Transactions of the ASME

Technical Editor
ARTHUR J. WENNERSTROM
Senior Associate Editor
G. K. Servoy
Associate Editors
Air Pollution Control
H. E. HESKETH
Diesel and Gas Engine Power
G. VAN DE MARK
Gas Turbine
G. OPDYKE
Power
R. W. PORTER
Advanced Energy Systems
T. M. BARLOW
Fuels
H. C. ORENDER
Nuclear Engineering
J. SUSNIR

BOARD ON COMMUNICATIONS
Chairman and Vice-President
MICHAEL J. RABINS

Members-at-Large
W. BEGELL
W. G. GOTTENBERG
D. KOENIG
M. KUTZ
F. LANDIS
J. W. LOCKE
J. E. ORTLOFF
C. PHILLIPS
H.C. REEDER
K. REID

President, FRANK M. SCOTT
Executive Director,
PAUL ALLMENDINGER
Treasurer, ROBERT A. BENNETT

PUBLISHING STAFF
Mng. Dir., Publ., J. J. FREY
Dep. Mng. Dir., Pub.,
JOS. SANSONE
Managing Editor,
CORNELIA MONAHAN
Production Editor,
JACK RUMMEL

The Journal of Engineering for Gas Turbines and Power (ISSN 0022-0825) is published quarterly for $90 per year by The American Society of Mechanical Engineers, 345 East 47th Street, New York, NY 10017. Second class postage paid at New York, NY and additional mailing offices. POSTMASTER: Send address change to The Journal of Engineering for Power, c/o The AMERICAN SOCIETY OF MECHANICAL ENGINEERS, P.O. Box 3199, Grand Central Station, New York, NY 10163.
CHANGES OF ADDRESS must be received at Society headquarters seven weeks before they are to be effective. Please send old label and new address.
PRICES: To members, $36.00, annually; to nonmembers, $90.00.
Add $6.00 for postage to countries outside the United States and Canada.
STATEMENT from By-Laws. The Society shall not be responsible for statements or opinions advanced in papers or ... printed in its publications (B 7.1, para. 3).
COPYRIGHT © 1984 by the American Society of Mechanical Engineers. Reprints from this publication may be made on condition that full credit be given the TRANSACTIONS OF THE ASME – JOURNAL OF ENGINEERING FOR POWER, and the author, and date of publication be stated.
INDEXED by the Engineering Index, Inc.

Journal of Engineering for Gas Turbines and Power

Published Quarterly by The American Society of Mechanical Engineers

VOLUME 106 • NUMBER 2 • APRIL 1984

TECHNICAL PAPERS

260 Interaction of Upstream Flow Distortions With High-Mach-Number Cascades (83-GT-137)
G. W. Englert

271 Development of Controlled Diffusion Airfoils for Multistage Compressor Application (83-GT-211)
D. E. Hobbs and H. D. Weingold

279 Redesign and Performance Analysis of a Transonic Axial Compressor Stator and Equivalent Plane Cascades With Subsonic Controlled Diffusion Blades (83-GT-208)
R. Dunker, H. Rechter, H. Starken, and H. Weyer

288 Experimental Cascade Analysis of a Transonic Compressor Rotor Blade Section (83-GT-209)
H. A. Schreiber and H. Starken

295 A Three-Dimensional Model for the Prediction of Shock Losses in Compressor Blade Rows (83-GT-216)
A. J. Wennerstrom and S. L. Puterbaugh

300 A Summary of Developments of the Mean-Streamline Method in China (83-GT-11)
R. Cai

306 A Streamline Curvature Method for Calculating S_1 Stream Surface Flow (83-GT-16)
S. K. Mao and D. T. Li

313 A Theory of Rotating Stall of Multistage Axial Compressors: Part I—Small Disturbances (83-GT-44)
F. K. Moore

321 A Theory of Rotating Stall of Multistage Axial Compressors: Part II—Finite Disturbances (83-GT-45)
F. K. Moore

327 A Theory of Rotating Stall of Multistage Axial Compressors: Part III—Limit Cycles (83-GT-46)
F. K. Moore

337 Wall Boundary Layer Development Near the Tip Region of an IGV of an Axial Flow Compressor (83-GT-171)
B. Lakshminarayana and N. Sitaram

346 Theory of Blade Design for Large Deflections: Part I—Two-Dimensional Cascade (83-GT-124)
W. R Hawthorne, C. Wang, C. S. Tan, and J. E. McCune

354 Theory of Blade Design for Large Deflections: Part II—Annular Cascades (83-GT-125)
C. S. Tan, W. R. Hawthorne, J. E. McCune, and C. Wang

366 Measurements of the Flow From a High-Speed Compressor Rotor Using a Dual Probe Digital Sampling (DPDS) Technique (83-GT-215)
R. P. Shreeve and F. Neuhoff

376 A Rapid Blade-to-Blade Solution for Use in Turbomachinery Design (83-GT-67)
E. R. McFarland

383 Prediction of Cascade Flow Fields Using the Averaged Navier-Stokes Equations
S. J. Shamroth, H. McDonald, and W. R. Briley

391 Boundary Layer and Loss Measurements on the Rotor of an Axial-Flow Turbine (83-GT-4)
H. P. Hodson

400 Flow in a Turbine Cascade: Part I—Losses and Leading-Edge Effects (83-GT-68)
J. Moore and A. Ransmayr

409 Flow in a Turbine Cascade: Part II—Measurement of Flow Trajectories by Ethylene Detection (83-GT-69)
J. Moore and B. L. Smith

414 An Experimental and Computational Study of Transonic Three-Dimensional Flow in a Turbine Cascade (83-GT-12)
J.-J. Camus, J. D. Denton, J. V. Soulis, and C. T. J. Scrivener

421 A Navier-Stokes Analysis of Three-Dimensional Turbulent Flows Inside Turbine Blade Rows at Design and Off-Design Conditions (83-GT-40)
C. Hah

430 Calculation of Three-Dimensional, Inviscid, Rotational Flow in Axial Turbine Blade Rows (83-GT-119)
W. Van Hove

Downloaded 03 Jun 2010 to 171.66.16.159. Redistribution subject to ASME license or copyright; see http://www.asme.org/terms/Terms_Use.cfm

(Contents Continued)

437 Experimental Study of the Three-Dimensional Flow Field in an Annular Turbine Nozzle Guidevane (83-GT-120)
C. H. Sieverding, W. Van Hove, and E. Boletis

449 Matrix Solution of Compressible Flow on S_1 Surface Through a Turbomachine Blade Row With Splitter Vanes or Tandem Blades (83-GT-10)
Wu Chung-Hua and Wang Baoguo

455 Experimental Study of Centrifugal Impeller Discharge Flow in Vaneless and Vaned Diffusers
M. Inoue and N. A. Cumpsty

468 Distinction Between Different Types of Impeller and Diffuser Rotating Stall in a Centrifugal Compressor With Vaneless Diffuser (83-GT-61)
P. Frigne and R. Van Den Braembussche

475 Performance Evaluation of Centrifugal Compressor Impellers Using Three-Dimensional Viscous Flow Calculations (83-GT-62)
J. Moore, J. G. Moore, and P. H. Timmis

482 A CAD Method for Centrifugal Compressor Impellers (83-GT-65)
H. Krain

489 On the Evaluation of Reynolds Number and Relative Surface Roughness Effects on Centrifugal Compressor Performance Based on Systematic Experimental Investigations (83-GT-118)
H. Simon and A. Bulskamper

502 An Investigation of the Flow Characteristics and of Losses in Radial Nozzle Cascades (83-GT-126)
S. G. R. Hashemi, R. J. Lemak, and J. A. Owczarek

511 Optimization of the Three-Dimensional Flow Path in the Scroll-Nozzle System of a Radial Inflow Turbine (83-GT-127)
E. A. Baskharone

516 Three-Dimensional Flow Measurements in a Turbine Scroll (83-GT-128)
W. Tabakoff, B. V. R. Vittal, and B. Wood

523 Three-Dimensional Inviscid Computation of an Impeller Flow (83-GT-210)
T. C. Prince and A. C. Bryans

529 Book Reviews
H. Saunders

TECHNICAL BRIEFS

445 Modifications of the Ives-Liutermoza Conformal-Mapping Procedure for Turbomachinery Cascades (83-GT-116)
W. J. Rae

ANNOUNCEMENTS

270 Change of address form for subscribers
287 Mandatory excess-page charge notice
530 Information for authors

Downloaded 03 Jun 2010 to 171.66.16.159. Redistribution subject to ASME license or copyright; see http://www.asme.org/terms/Terms_Use.cfm

Interaction of Upstream Flow Distortions With High-Mach-Number Cascades

G. W. Englert
Aerospace Research Engineer,
Lewis Research Center,
Cleveland, Ohio 44135

This analytical study models features of the interaction of flow distortions, such as gusts and wakes, with blade rows of advance-type fans and compressors having high-tip Mach numbers. A typical distortion is assumed to have harmonic time dependence and is described, at a far upstream location, in three orthogonal spatial coordinates by a double Fourier series. It is convected at supersonic velocity relative to a linear cascade described as an unrolled annulus. Conditions are selected so that the component of this velocity parallel to the axis of the turbomachine is subsonic, permitting interaction between blades through the upstream as well as downstream flow media. A strong, nearly normal shock is considered in the blade passages which is allowed curvature and displacement. The flows before and after the shock are linearized relative to uniform mean velocities in their respective regions. Solution of the descriptive equations is by adaptation of the Wiener-Hopf technique. This enables a determination of distortion patterns through and downstream of the cascade, and of pressure distributions on the blade surfaces. Details of interaction of the distortion with the in-passage shock are discussed. Influences of amplitude, wavelength, and phase of the distortion on lifts and moments of cascade configurations are presented. Numerical results are clarified by reference to an especially orderly pattern of upstream vortical motion in relation to the cascade parameters.

Introduction

Associated with high performance axial fans and compressors of aircraft engines are slender blades with high-tip Mach numbers [1]. Such blade rows may be vulnerable to distortions of the oncoming airstream such as atmospheric gusts, wakes from upstream struts and guide vanes, and maldistributions in air inlets and ducts, all of which tend to force the blades into vibratory motions. Such distortions can have a pronounced three-dimensional nature, as evidenced, for example, in the measurements of Wagner and Okiishi [2], Lakshminarayana and Davino [3], Shaw and Williams [4], and Zonars [5].

Of concern is the influence of strong shocks occurring in blade passages. When such shocks couple to the distortion pattern they can have an oscillatory influence on the blade pressure distributions, forces, and moments. The influence of the blade row on the distortion is also of importance since it passes on to influence other components of the propulsion system.

The recent linearized theory of Goldstein, Braun, and Adamczyk [6], which analyzes unsteady flow in supersonic cascades with strong in-passage shocks, is adapted to the distortion problem in the investigation reported herein. The flutter boundary conditions of [6] are, however, replaced with those of the three-dimensional distortion of Goldstein [7]. This distortion profile (Fig. 1) has components parallel to,

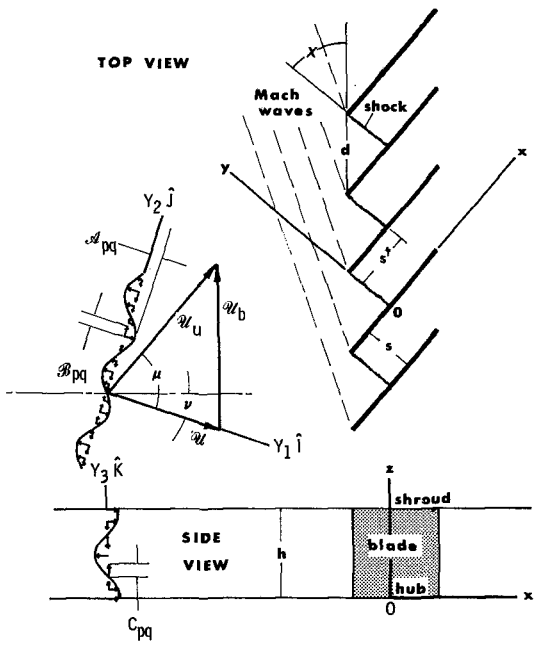


Fig. 1 Orientation of upstream distortion with respect to cascade

Contributed by the Gas Turbine Division of THE AMERICAN SOCIETY OF MECHANICAL ENGINEERS and presented at the 27th International Gas Turbine Conference and Exhibit, London, England, April 18–22, 1982. Manuscript received at ASME Headquarters January 10, 1983. Paper No. 82-GT-137.

Copyright © 1984 by ASME
Downloaded 01 Jun 2010 to 171.66.16.70. Redistribution subject to ASME license or copyright; see http://www.asme.org/terms/Terms_Use.cfm

and in two directions transverse to, a mean flow velocity, $\mathfrak{U}$. Relative to the cascade, the mean velocity, $\mathfrak{U}_u$, is supersonic in this study. The component of $\mathfrak{U}_u$ parallel to the axis of the turbomachine is, however, subsonic. The Mach waves from the leading edges of the blades then extend forward of the edge of each successive blade, permitting interaction between blades through the supersonic, as well as the subsonic, flow media. This is usually the case of interest in advance type fans and compressors.

The cascade (Fig. 1) is envisioned as an "unrolled annulus" which translates with a blade velocity $\mathfrak{U}_b$. Integral multiples of distortion wavelength must, however, equal a mean circumferential distance along the face of the blade row. Spanwise flow distributions are considered at limited blade aspect ratios, although centrifugal and Coriolis forces are neglected. Within the confines of linearized theory, blade thickness, camber, and angle of attack make no contribution to the unsteady forces (ch. 3 of [7]). Such time-independent effects can therefore be superposed on the results of this study in which the blades take the form of flat parallel plates.

The splitting theorem (ch. 5 of [7]) provides clarification in the formulation and aids in the solution of problems of interest herein. This theorem states that any linearized description of an inviscid compressible fluid can be decomposed into two noninteracting *motions*, one of which is vortical and the other acoustic in nature.

The vortical motion is solenoidal. Its substantial derivative is equal to zero; thus, it is transported as if frozen into the flow. Shear layers, for example, are vortical in nature, and are an effective means of forming flow distortions. In the flutter analysis of [6] the vortical motion first occurs at the shock.

The acoustic motion, on the other hand, is irrotational and has a velocity potential which satisfies the convective wave equation. The acoustic motion must satisfy blade-jump conditions [8], be continuous across streamlines extending upstream and downstream from the blades, have outgoing waves at ∞, and satisfy the Kutta condition at the trailing edges. Both motions herein will satisfy blade-to-blade periodicity relations [9].

Separation of the flow into two distinct (sub and supersonic) regions permits solution of the potential part of the flow field in each one by adaptation of the Wiener-Hopf technique [6]. In the first region, a supersonic flow extends from upstream infinity to a cascade which extends to downstream infinity. In the second region, a subsonic flow is guided by parallel blade passages from upstream infinity, past the trailing edges, and on to downstream infinity. The supersonic solution is independent of downstream influence, and the subsonic solution is kept sufficiently arbitrary to satisfy shock boundary conditions. Matching of solutions at the shock interface involves inversion of a large nearly diagonal matrix. This is easily done numerically.

In the present effort as well as in [6], the shock is assumed to be located at an arbitrarily small distance inside the leading edge of the blade so that it doesn't disturb the supersonic flow on the upper surface in this region.

Formulation

The upstream flow distortion of interest is vortical and thus it is transported as if frozen into the flow. The sum of the vortical and acoustic motion must satisfy the wall tangency condition. Selection of the far upstream velocity distribution of the distortion thus determines the vortical motion in the entire supersonic region as well as the inviscid boundary condition to be met by the acoustic motion on the cascade surfaces upstream of the shock.

Vortical Motion Upstream of Shock. A mathematical expression, which is sufficiently general to describe the essential characteristics of the vortical velocity upstream of the shock for many applications of interest, is given by the double Fourier series (ch. 5 of [7]).

$$\mathbf{v} = \sum_{p,q} [(\hat{I}\mathfrak{A}_{pq} + \hat{J}\mathfrak{B}_{pq})\cos(\pi q Y_3/h) + KC_{pq}\sin(\pi q Y_3/h)]e^{i2\pi p Y_2/L\cos\nu} \quad (1)$$

For each set of Fourier indices the distortion amplitudes are $\mathfrak{A}_{pq}$, $\mathfrak{B}_{pq}$, and C_{pq} for motion in the three orthogonal directions $\hat{I}$, $\hat{J}$, and $\hat{K}$. As in [7], there is an integral number, p, of distortion wavelengths parallel to the face of the blade row where L is a mean circumferential distance. The spanwise wavelength is the hub-to-shroud distance, h, divided by Fourier index, q. Distance and velocity are non-

Nomenclature[1]

A,a = distortion amplitudes in x- and y-directions of Fig. 1
$\mathfrak{A},\mathfrak{B},C$ = distortion amplitudes in I,J,K directions of Fig. 1
B_n = coefficients in description of subsonic acoustic motion in (47)
$b_{i,j}$ = coefficients in description of subsonic vortical flow in (16)
c = chord
d = mean circumferential distance between blades, Fig. 1
f = arbitrary function
h = blade height
i = $(-1)^{1/2}$
k_u,k_d = wave numbers = $M_u\omega_u/\beta_u^2$ and $M_d\omega_d/\beta_d^2$, respectively
k_q = spanwise wave number = $\pi q/h$
L = mean circumferential distance along blade row
$\mathfrak{L}$ = lift
M = Mach number
$\mathfrak{M}$ = moment
N = integral number of distortion transverse wavelengths in distance $s^\dagger$ along x
P_u,P_d = amplitudes of p_u, p_d
p_u,p_d = pressure perturbation nondimensionalized by $\rho_u\mathfrak{U}_u^2$
p,q = Fourier indices in (1)
S = solidity = chord/blade gap = 1/dimensionless d
s = interblade distance along y in Fig. 1
$s^\dagger$ = $(\sin\chi)/S$ as in Fig. 1
t = time nondimensionalized by multiplying by $\mathfrak{U}_u/c$
$\mathfrak{U}$ = mean velocity
$\mathbf{U},\mathbf{V},\mathbf{W}$ = amplitudes of $\mathbf{u},\mathbf{v},\mathbf{w}$
$\mathbf{u},\mathbf{v},\mathbf{w}$ = total, vortical, and acoustic velocity perturbations nondimensionalized by $\mathfrak{U}_u$
x,y,z = blade coordinates (Fig. 1) nondimensionalized by blade chord
$\tilde{x}_u,\tilde{x}_d$ = $x+s^\dagger$ and $x+s^\dagger-1$, respectively
Y_1,Y_2,Y_3 = orthogonal coordinates in a fixed frame upstream of cascade
β_u,β_d = $(M_u^2-1)^{1/2}$ and $(1-M_d^2)^{1/2}$, respectively

[1] The velocity and pressure perturbations downstream of the shock are the differences between actual and mean downstream values; however, they are nondimensionalized by the undisturbed upstream quantities $\mathfrak{U}_u$ and $\rho_u\mathfrak{U}_u^2$.

Downloaded 01 Jun 2010 to 171.66.16.70. Redistribution subject to ASME license or copyright; see http://www.asme.org/terms/Terms_Use.cfm

dimensionalized by blade chord and mean upstream velocity, $\mathfrak{U}_u$ of Fig. 1, respectively.

Transformation of equation (1) to blade coordinates (x, y, z) moving with velocity $\mathfrak{U}_b$ relative to $\mathfrak{U}$ gives the vortical motion a harmonic time dependence. In this system

$$\mathbf{v}_u = ae^{-i\omega_u t}\cos(k_q z)\mathbf{V}_u \tag{2a}$$

where time has been nondimensionalized by $\mathfrak{U}_u/c$, where

$$\mathbf{V}_u = \begin{bmatrix} V_1^{(u)} \\ V_2^{(u)} \\ V_3^{(u)} \end{bmatrix} = e^{i\omega_u (x+s^\dagger + y\cot\mu)} \begin{bmatrix} A/a \\ 1 \\ (C/a)\tan(k_q z) \end{bmatrix} \tag{2b}$$

and spanwise wave number, k_q, is equal to $\pi q/h$. The exponent in equation (2b) sets the interblade phase angle, σ, as

$$\sigma = \omega_u (s^\dagger + s\cot\mu) \tag{3}$$

The x- and t-dependence in equations (2a) and (2b) together satisfy the condition that the substantial derivative, $D\mathbf{v}_u/Dt$, is equal to zero. The components of the distortion amplitudes in the x-, y-, z-directions are now

$$a = -\mathfrak{A}_{pq}\sin\mu + \mathfrak{B}_{pq}\cos\mu \tag{4a}$$

$$A = \mathfrak{A}_{pq}\cos\mu + \mathfrak{B}_{pq}\sin\mu \tag{4b}$$

and, by the solenoidal condition on $\mathbf{v}_u$,

$$C = -2iph\mathfrak{B}/qL\cos\nu = -\frac{2i\pi p}{k_q L\cos\nu}(a\cos\mu + A\sin\mu) \tag{4c}$$

Since final results can be superposed, only one set of Fourier components will be carried through the analysis; thus the p and q indices will normally be omitted from the flow variables.

Acoustic Motion Upstream of Shock. The total motion, $\mathbf{u}_u = \mathbf{v}_u + \mathbf{w}_u$, will satisfy the inviscid tangency condition at the blade surface if the normal component of the acoustic (potential) motion satisfies

$$w_2^{(u)} = \frac{\partial \varphi_u}{\partial y} = -a\cos(k_q z)e^{i\omega_u (x+s^\dagger + n s\cot\mu - t)} \tag{5}$$

for $-s^\dagger < x - ns^\dagger < 0$, $0 < z < h$, and $n = 0, \pm 1, \pm 2, \cdots$. By inspection, the solution to the linearized convective wave equation

$$(\nabla^2 - M_u^2 D^2/Dt^2)\varphi_u = 0 \tag{6}$$

which satisfies equation (5) is of the form

$$\varphi_u = -a\cos(k_q z)e^{-i\omega_u t}\Phi_u(x,y) \tag{7}$$

Thus

$$\mathbf{w}_u = ae^{-i\omega_u t}\cos(k_q z)\mathbf{W}_u \tag{8a}$$

where

$$\mathbf{W}_u = \begin{bmatrix} -\partial\Phi_u/\partial x \\ -\partial\Phi_u/\partial y \\ k_q\tan(k_q z)\Phi_u \end{bmatrix} \tag{8b}$$

Note that the z-components of both equations (2) and (8) individually satisfy the flow tangency condition at both the hub and shroud.

Pressure, p_u, is associated with the acoustic motion, satisfies the wave equation, and can also be expressed in the form

$$p_u = -ae^{-i\omega_u t}\cos(k_q z)P_u(x,y) \tag{9a}$$

where

$$P_u = \left(i\omega_u - \frac{\partial}{\partial x}\right)\Phi_u \tag{9b}$$

Thus, use of equation (1) for the description of the upstream distortion permits reducing the solution of the acoustic motion to a form in which the z-dependence is factored from the remaining two dimensions. The only influence of the spanwise velocity on amplitude, Φ, enters through the wave number, k_q, which is a constant.

The solution for $\Phi_u(x,y)$ by use of the Wiener-Hopf technique is given in Appendix A.

Vortical Motion Downstream of Shock. The third dimension in this study prevents use of the stream function of [6] for the vortical subsonic motion. A sufficiently general solution for the velocity $\mathbf{v}_d$ can, however, be constructed as follows: Let $\mathbf{v}_d$ take the form

$$\mathbf{v}_d = a\cos(k_q z)e^{i(\omega_d x - \omega_u t)}[\Omega_1(y), \Omega_2(y), \tan(k_q z)\Omega_3(y)] \tag{10}$$

which satisfies the spanwise wall tangency condition and has a substantial derivative equal to zero. To satisfy periodicity let

Nomenclature (cont.)

γ = ratio of specific heats of an ideal gas
γ_u, γ_d = $(\alpha^2 - k_u^2 - k_q^2/\beta_u^2)^{1/2}$ and $(\alpha^2 - k_d^2 + k_q^2/\beta_d^2)^{1/2}$, respectively
δ = imaginary part of integration contour for Φ_u
δ_j^i = Kronecker delta; = 0 if $i \neq j$; = 1 if $i = j$
ϵ_u, ϵ_d = small damping terms in γ_u and γ_d, respectively
θ = arbitrary variable illustrating periodicity relation
μ = angle between upstream and blade coordinate systems in Fig. 1
ν = direction of transport of upstream distortion with respect to axis of turbomachine
ρ = density
σ = interblade phase angle defined by (3)
Φ = amplitude of φ
φ = velocity potential
χ = stagger angle = $\nu - \mu$
Ψ_u, Ψ_d = $(\omega_u^2 + k_q^2)^{1/2}$ and $(\omega_d^2 + k_q^2)^{1/2}$, respectively
ψ_u, ψ_d = $(k_u^2 + k_q^2/\beta_u^2)^{1/2}$ and $(k_d^2 - k_q^2/\beta_d{}^2)^{1/2}$, respectively
ω = frequency = $2\pi p\mathfrak{U}_b/L$ in dimensional form
ω_u, ω_d = reduced frequencies $\omega c/\mathfrak{U}_u$ and $\omega c/\mathfrak{U}_d$, respectively

Subscripts

b = blade
d,u = downstream and upstream of shock, respectively
m,n = integers
p,q = Fourier indices describing upstream distortion
s = shock
1,2,3 = correspond to I,J,K and to x,y,z = directions in upstream distortion and in blade coordinate systems of Fig. 1, respectively

Superscripts

d,u = downstream and upstream of shock, respectively
$+,-$ = upper and lower half planes of Fourier transformed, α, space
$\tilde{}$ = implies both vortical and acoustic properties when on v or φ
$\hat{}$ = unit vector

Downloaded 01 Jun 2010 to 171.66.16.70. Redistribution subject to ASME license or copyright; see http://www.asme.org/terms/Terms_Use.cfm

$$e^{i\omega_d(x+ns^\dagger)}\Omega(y+ns)=e^{in\sigma}e^{i\omega_d x}\Omega(y) \tag{11}$$

for blade number $n=0, \pm1, \pm2, \cdots$. The solenoidal condition will be invoked later, completing the splitting theorem requirements for $\mathbf{v}_d$ to be vortical.

It is anticipated that a part, $\tilde{\mathbf{v}}_d$ of $\mathbf{v}_d$ can be found which is both vortical and acoustic. Combining $\tilde{\mathbf{v}}_d$ with the potential flow, $\mathbf{w}_d$, may then simplify determination of the remaining part of $\mathbf{v}_d$. Such a procedure is used to advantage in [6]. Associated with $\tilde{\mathbf{v}}_d$ is a potential $\tilde{\varphi}_d$ such that $\nabla\tilde{\varphi}_d=\tilde{\mathbf{v}}_d$, and since $\nabla\cdot\tilde{\mathbf{v}}_d=0$, it follows that $\nabla^2\tilde{\varphi}_d=0$. Since $\tilde{\mathbf{v}}_d$ is vortical, $\tilde{\varphi}_d$ makes no contribution to the pressure distribution. Let $\tilde{\varphi}_d$ take the form.

$$\tilde{\varphi}_d=a\cos(k_q z)e^{i(\omega_d x-\omega_u t)}f(y) \tag{12}$$

For $\tilde{\varphi}_d$ to satisfy Laplace's equation, f must satisfy

$$-(\omega_d^2+k_q^2)f+f''=0 \tag{13}$$

A solution of equation (13) which enables $\tilde{\varphi}_d$ to satisfy periodicity as well as to cancel the normal component of $\mathbf{v}_d$ at the blade surfaces is

$$f=\frac{\Omega_2(ns)}{\Psi_d\sinh(\Psi_d s)}\{\cosh(\Psi_d s)\cosh[\Psi_d(y-ns)] - \cosh[\Psi_d(y-ns-s)]\} \tag{14}$$

where $\Psi_d=\sqrt{\omega_d^2+k_q^2}$. The subscripts 1, 2, 3, on Ω identify the components of Ω in the x, y, and z directions, respectively.

Substitution of equations (10), (12), and (14) into the identity

$$\mathbf{v}_d\equiv(\mathbf{v}_d-\nabla\tilde{\varphi}_d)+\nabla\tilde{\varphi}_d \tag{15}$$

shows that the first term $(\mathbf{v}_d-\nabla\tilde{\varphi}_d)$ makes no contribution to the blade boundary conditions (since its y-component vanishes at $y=n\ s$), although it does contribute to the matching of flows at the shock boundary. With sufficient generality the strictly vortical part of equation (15) can thus be sufficiently described by Fourier sine and cosine series as

$$\mathbf{v}_d(x,y,z)=a\cos(k_q z)e^{i(\omega_d x-\omega_u t)} \times \begin{bmatrix} \sum_{m=1}^{\infty} b_{1,m}\cos(m\pi y/s) \\ i\sum_{m=1}^{\infty} b_{2,m}\sin(m\pi y/s) \\ -k_q\tan(k_q z)\sum_{m=1}^{\infty} b_{3,m}\cos(m\pi y/s) \end{bmatrix} \tag{16}$$

and the $\nabla\tilde{\varphi}_d$ part of equation (15) will be included in $\mathbf{w}_d=\nabla\varphi_d$.

The solenoidal condition has already been invoked in $\tilde{\mathbf{v}}_d$. Using it in equation (16) for $\mathbf{v}_d$ gives

$$\omega_d b_{1,m}+\frac{m\pi}{s}b_{2,m}+ik_q^2 b_{3,m}=0 \tag{17}$$

Acoustic Motion Downstream of Shock. The acoustic field downstream of the shock is composed of two parts. An infinite "duct" solution, to the convective wave equation, having downstream running waves accounts for shock boundary conditions. A "cascade" solution, on the other hand, gives the upstream (or reflected) waves. Each solution, as well as the vortical motion of the preceding section, individually satisfies the wall tangency condition. The sum of the two acoustic solutions must satisfy the Kutta condition. In both solutions the velocity potential, φ_d, again takes the form

$$\varphi_d(x,y,z)=a\cos(k_q z)e^{-i\omega_u t}\Phi_d(x,y) \tag{18}$$

The procedure to obtain the combined potential $\Phi_d=\Phi_d^{\text{duct}}+\Phi_d^{\text{cascade}}$ is given in Appendix B.

Relations Across Shock. The mean flow satisfies the Rankine-Hugoniot relations. Shock curvature and displacement are treated as perturbations as in [10]. The downstream vorticity, longitudinal velocity, and pressure are related to the corresponding upstream quantities by the following three equations

$$u_1^{(d)}=-\frac{M_u^2+1}{2M_u^2}p_d+u_1^{(u)}+\frac{1}{2}\left[M_u^2+1-\frac{\gamma-1}{\gamma+1}\frac{\beta_u^4}{M_u^2}\right]p_u \tag{19}$$

$$\frac{\partial}{\partial y}\left[p_d-\left(M_u^2+\frac{\gamma-1}{\gamma+1}\beta_u^2\right)p_u\right]= (\gamma+1)\frac{M_u^2M_d^2}{\beta_u^2\beta_u^2}\left[\left(\frac{\partial v_2^{(d)}}{\partial x}-\frac{\partial v_1^{(d)}}{\partial y}\right)-\frac{\mathfrak{U}_u}{\mathfrak{U}_d}\left(\frac{\partial v_2^{(u)}}{\partial x}-\frac{\partial v_1^{(u)}}{\partial y}\right)\right] \tag{20}$$

and

$$\frac{\partial}{\partial z}\left[p_d-\left(M_u^2+\frac{\gamma-1}{\gamma+1}\beta_u^2\right)p_u\right]= (\gamma+1)\frac{M_u^2M_d^2}{\beta_u^2\beta_d^2}\left[\left(\frac{\partial v_3^{(d)}}{\partial x}-\frac{\partial v_1^{(d)}}{\partial z}\right)-\frac{\mathfrak{U}_u}{\mathfrak{U}_d}\left(\frac{\partial v_3^{(u)}}{\partial x}-\frac{\partial v_1^{(u)}}{\partial z}\right)\right] \tag{21}$$

These equations differ from those of [6] by addition of an upstream vorticity and a spanwise distribution of pressure and velocity.

Matching of Solutions at Shock Boundary. The final step in the overall procedure is the matching of sub- and supersonic solutions at the shock interface. The three shock equations supply just sufficient additional information to evaluate the arbitrary coefficients B_n and $b_{j,m}$, $j=1,2,3$ in the description of the subsonic acoustic and vortical motions of Appendix B and equation (16) respectively. Details of the solution procedure are given in Appendix C.

Complex variables are used throughout the solution. The real and imaginary parts of the answer then yield two solutions, one of which (the imaginary part) is for a distortion which lags the other (real part) by a phase angle of $\pi/2$.

Results

Variables which may be arbitrarily (independently) selected for input into the formulation for the general case are ratio of specific heats, γ, Mach number, M_u, two of the three angles, μ, ν, and χ, cascade parameters, S, h, and either phase angle, σ, or frequency, ω_u, along with distortion parameters, L/p, q, and either amplitudes, a and A or $\mathfrak{C}$ and $\mathfrak{B}$.

Reference Conditions. Certain combinations of variables give a very orderly upstream distortion (vortical) motion which in turn, through the blade-surface boundary condition, results in an especially clean acoustic motion upstream of the shock. Numerical results based on such flows are relatively easy to interpret and should aid in the analysis of more general cases which are within the capability of the theory.

As in Fig. 2, let $\nu=0$ and $-\mu=\chi=$ wave angle given by $\sin^{-1}(1/M_u)$. Then $-\cot\mu=\beta_u=s/s^\dagger$. Let one transverse wavelength fit the distance $\beta_u s$ along x, and let $s^\dagger=N\beta_u s$ for integer N. Then $\beta_u^2=1/N$, and $M_u=(1+1/N)^{1/2}$. This wave pattern has a negative phase along $\Delta y=s$, which offsets the phase of the cycle along $\Delta x=\beta_u s$, leaving $\sigma=2\pi(N-1)$. Using equation (3) along with $d=1/S=s^\dagger(1+\cot^2\mu)$, it follows that $\omega_u=2\pi(N-1)S(1+\cot^2\mu)\ /\ (1-\cot^2\mu)$. The lowest N which clearly permits a subsonic mean axial velocity

Downloaded 01 Jun 2010 to 171.66.16.70. Redistribution subject to ASME license or copyright; see http://www.asme.org/terms/Terms_Use.cfm

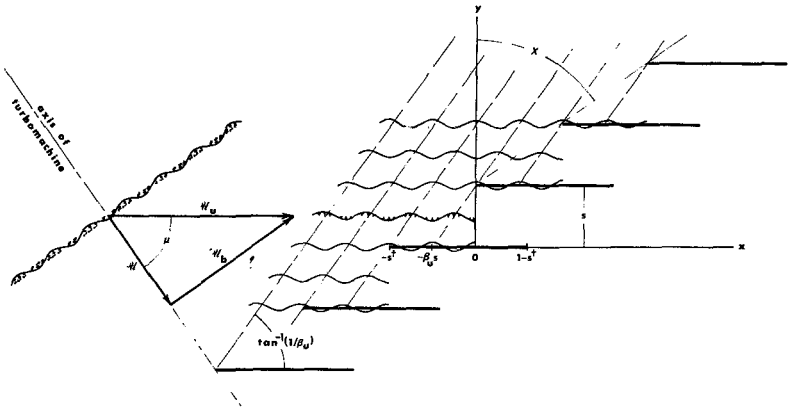


Fig. 2 Select distortion (vortical) pattern of v_2 entering blade channels for use as a reference condition: $N=2$, $\sigma=2\pi$, $M_u=(3/2)^{1/2}$, $\chi=-\mu=\tan^{-1}(2)^{1/2}$, and $A=0$

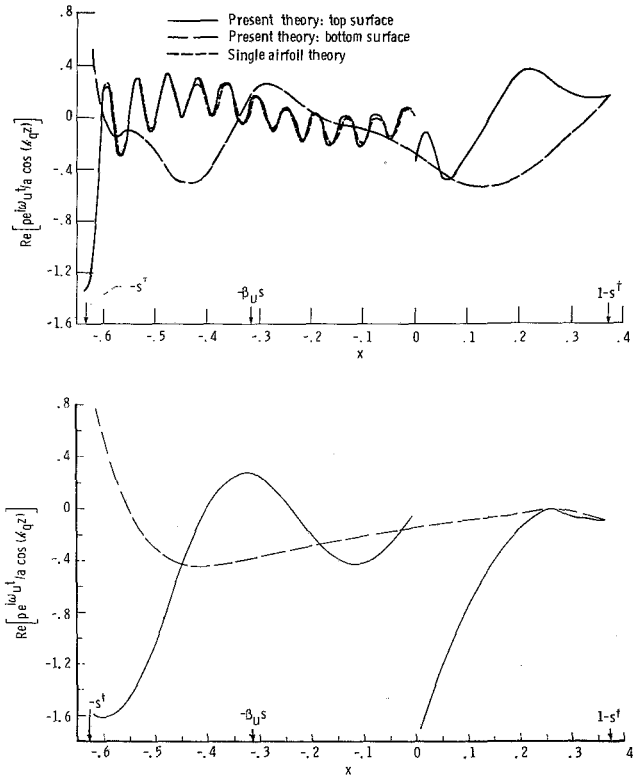


Fig. 3 Pressure distribution on zeroth blade: (a) distortion and cascade at basic reference conditions of Fig. 2 along with $S=1.3$, $\omega_u=20.0$, and $k_q=\pi/3$; (b) distortion and cascade conditions same as Fig. 3(a), except that σ and ω_u are reduced to $2\pi/8$ and 20.0/8, respectively

has a value of 2. For $N=2$, $\sigma=2\pi$, $M_u=(3/2)^{1/2}$, and $\chi=-\mu=\tan^{-1}\sqrt{2}$. Selecting a solidity of 1.3 then gives $\omega_u=20.0$ (which is the passing frequency) and circumferential wavelength $L/p=d=0.769$. Amplitude ratio A/a is set equal to 0. Amplitude ratio C/a is then equal to $-4.7\ i/k_q$ by equation (4c). These results, along with $\gamma=7/5$ and $k_q=\pi/3$ will be used as the basic reference condition for the numerical results herein.

Influence of Distortion on Blade Pressure Distribution. Pressure distribution along the upper and lower surfaces of the blades is given in Fig. 3(*a*) at the basic ordered condition. The short dashed line in the supersonic region represents a single airfoil solution [11]. Consistent with the reference cascade conditions in Fig. 2, the input to the airfoil theory is a transverse distortion having a wavelength equal to $s^\dagger/2$. The resulting pressure distribution is normalized to match that of the cascade solution at the leading edge. The short wavelength (high frequency) of the Bessel function solution of the airfoil is characteristic of the cascade solution also.[2] In the cascade, this short wavelength characteristic is carried a short distance downstream of the shock. The periodicity relation, $\Phi(x,y)=e^{-i\sigma}\Phi(x+s^\dagger, y+s)$, is used in equation (59) of Appendix B to relate pressure on the lower surface of blade 1 to the lower surface of blade 0.

A second cascade solution (not shown) for a distortion with a phase angle of $\pi/2$ with respect to that of Fig. 3(*a*) is obtained from $Im[pe^{i\omega_u t}/a\ \cos(k_q z)]$. This has the same wavelength characteristics and, in the supersonic region, agrees with single airfoil theory. Consistent with shock curvature and displacement, the pressure perturbation amplitude increased for the imaginary part but decreased for the real part of the solution across this boundary for the reference conditions of Fig. 3(*a*).

The solution for Fig. 3(*b*) is based on the same set of parameters (for the ordered vortical motion) as Fig. 3(*a*), except σ, and therefore ω_u by equation (3), are reduced from the basic reference conditions by a factor of 1/8. Single airfoil theory is no longer close to these results and has been omitted. Trends are quite smooth and, of course, much more gradual than those of Fig. 3(*a*).

At very low interblade phase angles, $<(0.01)$, the pressure profile (not shown) across the channel is quite uniform and the pressure amplitude in back of the shock on the upper surface approaches that on the lower surface near the leading edge.

Influence of Cascade on Distortion Profile. Figure 4 uses the same basic reference conditions as Fig. 3(*a*). Envision Fig. 4 as a view of two blade channels in the $x-y$-plane. Located at various x stations are y distributions of the real part of the solution for the three *transverse* components of velocity in $u_2=v_2+w_2$. Far upstream of the cascade, the amplitude of the acoustic motion (given by the short dashed line) goes to zero; however, the vortical motion (long dashed line) is transported undiminished as if frozen in the flow. In the

[2]Use of a reduced frequency of 20 thus permits comparison of two mathematical solutions to the linearized convected wave equation (6). It is possible that equation (6) may not offer a suitably accurate description of the motion, however, at such a high frequency. See, for example, ch. 1 of [12].

Downloaded 01 Jun 2010 to 171.66.16.70. Redistribution subject to ASME license or copyright; see http://www.asme.org/terms/Terms_Use.cfm

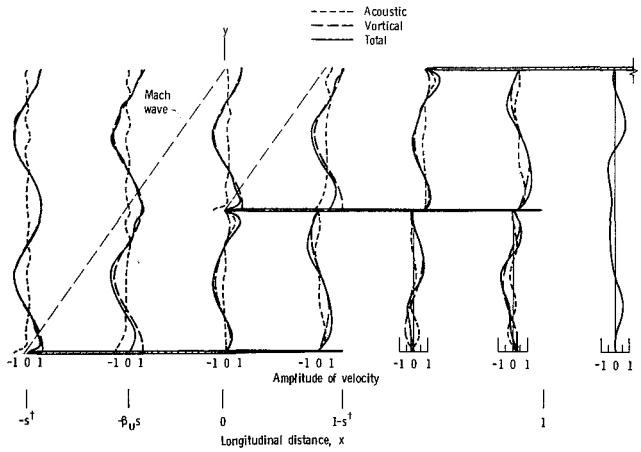


Fig. 4 Channelwise distribution of *y*-components of velocity at various longitudinal locations along blades (distortion and cascade conditions same as in Fig. 3(*a*))

vicinity of the cascade, the acoustic motion with its characteristic short wavelength, due to diffraction about the leading edges, becomes apparent. Once inside a leading edge Mach wave, the transverse component of the acoustic velocity, $w_2^{(u)}$, is noticeably large only in the vicinity of the blade surface. The amplitude of the total motion, $u_2^{(u)}$, away from the wall is then mainly comprised of the relatively long wavelength vortical motion, $v_2^{(u)}$. At x locations between the trailing edges of adjacent blades the amplitude of the acoustic motion becomes quite prominent, where diffraction is again encountered to satisfy the Kutta condition. Eventually $w_2^{(d)}$ decreases at large x to the asymptotic value of $x=\infty$. The amplitude of the vortical motion continues undiminished far downstream of the cascade.

The y-distributions of the longitudinal component of the acoustic motion, $w_1^{(u)}$, have much the same nature as the transverse component $w_2^{(u)}$. Although A, and therefore $v_1^{(u)}$, are zero, a longitudinal component of vortical velocity, $v_1^{(d)}$, arises at the shock. Beyond this station both longitudinal acoustic and vortical motions have trends with x much like those of $w_2^{(d)}$ and $v_2^{(d)}$. Recall that part of the vortical motion, $\tilde{\mathbf{v}}_d$ has been included in Φ_d, thus simplifying the wall boundary condition.

The y-distribution of the spanwise component of the acoustic motion, $w_3^{(u)}$, also follows a pattern somewhat similar to $w_2^{(u)}$. The influence of the shock on $v_3^{(d)}$ is small, but quite pronounced on $w_3^{(d)}$ for the particular set of conditions of Fig. 4.

The z-distributions of vortical and acoustic motions are not plotted since, by equations (2), (8), (16), and (18), they simply vary as $\cos(k_q z)$ for the transverse components in both subsonic and supersonic regions.

Influence of Distortion and Cascade Parameters on Lift and Moment. Lift, $\mathfrak{L}$, and moment, $\mathfrak{M}$, were obtained by integration of the pressure distributions over the blade surfaces. Moments were taken about the midchord of the blade located at $x=1/2-s^\dagger$. Plotting the real versus imaginary part of such descriptive variables (ch. 9 of [13]) enables determination of their magnitude as a function of phase angle of the gust. Such plots are useful in aeroelasticity studies wherein the distortion acts as a forcing function in the nonhomogeneous part of the differential stability equation. The phase of the forces and moments due to the distortion is then made available for study with respect to the motion of the structural system.

The contribution of shock movement to lift is shown in Fig. 5(*a*). As in [6], the shocks are assumed to be attached to the lower surfaces of the blades (Fig. 1) arbitrarily near their leading edges. The allowed displacements, x_s, of the shock

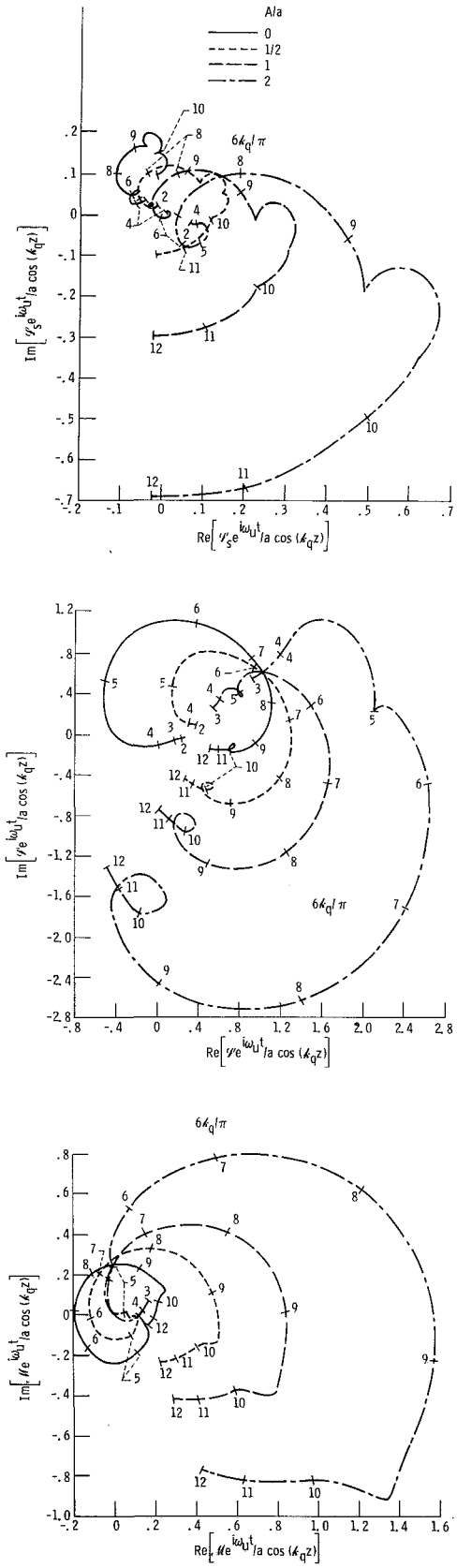


Fig. 5 Influence of azimuthal wave number, k_q and distortion amplitude ratio, A/a, on lift and moment: (*a*) shock induced lift, $\mathfrak{L}_s$; (*b*) total lift, $\mathfrak{L}$; (*c*) moment, $\mathfrak{M}$

Downloaded 01 Jun 2010 to 171.66.16.70. Redistribution subject to ASME license or copyright; see http://www.asme.org/terms/Terms_Use.cfm

footprints on the upper blade surface, however, cause a lift $\mathfrak{L}_s$, with amplitude equal to $(\bar{p}_d - \bar{p}_u)x_s$ within the confines of linearized theory. Here $\bar{p}_u$ and $\bar{p}_d$ are the steady pressures before and after the shock. This effect is included in the total lift and moment of Figs. 5(*b*) and (*c*). These figures are arbitrarily plotted at an interblade angle of 1/8 that of the reference set of conditions as in Fig. 3(*b*).

The variables h and q enter the equations for velocity potential (therefore for lift and moment) only as q/h, and thus their influence can be expressed by spanwise wave number $k_q = \pi q/h$. This wave number should be most influential on amplitudes Φ_u and Φ_d, when it is greater than circumferential wave numbers k_u and k_d, respectively. This trend is illustrated in Fig. 5 by the large distance between tick marks on these curves at high k_q. Increase of upstream distortion longitudinal to transverse amplitude ratio, A/a, tends to increase the magnitude of $\mathfrak{L}$ and $\mathfrak{M}$ at large k_q while preserving the spirallike k_q-dependence. Cusps and/or loops characterize both the $\mathfrak{L}_s$ and $\mathfrak{L}$ curves. The magnitude of $\mathfrak{L}_s$ is a significant part of $\mathfrak{L}$.

Concluding Remarks

Selection of a combination of cascade and distortion parameters for a very orderly initial vortical motion gives in turn, through use of the blade surface boundary condition, an especially orderly acoustic motion as well. Numerical results based on such flows are relatively easy to interpret and aid in the analysis of more general cases which are within the capability of the theory. At these special conditions the supersonic pressure distribution reduces to shapes predicted by single airfoil theory.

At high solidity the periodic pattern of the downstream running waves in the subsonic region of the cascade is quite evident in the blade pressure distribution. Influence of the reflected, or forward-running, waves is mostly confined to within a relatively small distance of the trailing edges on the upper surfaces but is apparent over the distance $1 - 2s^\dagger < x \le 1 - s^\dagger$ on the lower surfaces.

References

1 Fleeter, S., "Aeroelasticity Research for Turbomachine Applications," *Journal of Aircraft*, Vol. 16, No. 5, May 1979, pp. 320–326.

2 Wagner, J. H., and Okiishi, T. H., "Analysis of Multistage Axial-Flow Turbomachine Wake Production, Transport, and Interaction," TCRL-10, ISU-ERI-AMES-78173, Iowa State University of Science and Technology, Ames, Iowa, Dec. 1977.

3 Lakshminarayana, B., and Davino, R., "Mean Velocity and Decay Characteristics of the Guidevane and Stator Blade Wake of an Axial Flow Compressor," ASME JOURNAL OF ENGINEERING FOR POWER, Vol. 102, No. 1, Jan. 1980, pp. 50–60.

4 Shaw, R. J., Williams, R. C., and Koncsek, J. L., "Tilt Nacelle Aerodynamics and its Application to Fan Blade Stresses," *Journal of Aircraft*, Vol. 16, No. 9, Sept. 1979, pp. 591–598.

5 Zonars, D., "Problems on Inlets and Nozzles," The Seventh Congress of the International Council of the Aeronautical Sciences, ICAS Paper 70-47, Rome, Italy, Sept. 14–18, 1970.

6 Goldstein, M. E., Braun, W., and Adamczyk, J. J., "Unsteady Flow in a Supersonic Cascade with Strong In-Passage Shocks," *Journal of Fluid Mechanics*, Vol. 83, part 3, Dec. 1977, pp. 569–604.

7 Goldstein, M. E., *Aeroacoustics*, McGraw-Hill, New York, 1976.

8 Lane, F., and Friedman, M., "Theoretical Investigation of Subsonic Oscillatory Blade-Row Aerodynamics," NACA TN-4136, 1958.

9 Lane, F., "System Mode Shapes in the Flutter of Compressor Blade Rows," *Journal of Aeronautical Science*, Vol. 23, No. 1, Jan. 1956, pp. 54–66.

10 Moore, F. K., "Unsteady Oblique Interaction of a Shock Wave with a Plane Disturbance," NACA TR-1165, 1954.

11 Kaji, S., "Noncompact Source Effect on the Prediction of Tone Noise from a Fan Rotor," *Aeroacoustics: Fan Noise and Control; Duct Acoustics; Rotor Noise*, edited by I. R. Schwartz, H. T. Nagamatsu, and W. C. Strahle, *Progress in Astronautics and Aeronautics*, Vol. 44, American Institute of Aeronautics and Astronautics, New York, 1976, pp. 55–81.

12 Miles, J. W., *The Potential Theory of Unsteady Supersonic Flow*, Cambridge, University Press, 1959.

13 Bisplinghoff, R. L., Ashley, H., and Halfman, R. L., *Aeroelasticity*, Addison-Wesley, Cambridge, Mass., 1955.

14 Noble, B., *Methods Based on the Wiener-Hopf Technique for the Solution of Partial Differential Equations*, Pergamon Press, New York, 1958.

15 Roos, B. W., *Analytic Functions and Distributions in Physics and Engineering*, John Wiley, New York, 1969.

16 Peirce, B. O., *A Short Table of Integrals*, 3d rev. ed., Ginn and Co., Boston, 1929.

APPENDIX A

Solution for Acoustic Motion Upstream of Shock

Substitution of equation (7) into equation (6) gives

$$\left[-\beta_u^2\frac{\partial^2}{\partial x^2} + \frac{\partial^2}{\partial y^2} + 2iM_u k_u \beta_u^2 \frac{\partial}{\partial x} + \left(\beta_u^4 k_u^2 - k_q^2\right)\right]\Phi_u = 0 \tag{22}$$

A solution by separation of variables is $\exp\{-i[(\alpha - M_u k_u)x + \beta_u \gamma_u y]\}$ where α is an arbitrary constant and $\gamma_u \equiv (\alpha^2 - k_u^2 - k_q^2/\beta_u^2)^{1/2}$. Multiplying this result by $f(\alpha)\exp[-i(\alpha - M_u k_u)s^\dagger]$ and integrating over admissible values of α is also a solution of the linear homogeneous equation (22), where $f(\alpha)$ is yet to be determined.

Next, following the procedure of Lane and Friedman [8], apply this result to each of n-blades using the local coordinate system $x_n = x - ns^\dagger$, $y_n = y - ns$ and specify that $f_n(\alpha)$ must satisfy the periodicity condition [9]

$$f_n(\alpha) = e^{in\sigma} f_o(\alpha) \tag{23}$$

for $n = 0, \pm 1, \pm 2, \cdots$. A solution with jump conditions across the nth blade in proper form is then

$$\Phi_{u,n}(x_n, y_n) = \frac{\operatorname{sgn} y_n}{2\pi}\int_{-\infty+i\delta}^{\infty+i\delta} f_n(\alpha)\, e^{-i(\alpha - M_u k_u)s^\dagger} e^{-i[(\alpha - M_u k_u)x_n + \beta_u \gamma_u |y_n|]}\, d\alpha \tag{24}$$

where $\operatorname{sgn} y = \pm 1$ for $y \gtrless 0$. The branch points for γ_u are set at $\pm(\psi_u + i\epsilon_u)$ where $\psi_u^2 = k_u^2 + k_q^2\beta_u^2$ and ϵ_u is a small damping term. Now, as in [6], let $\delta = M_u \epsilon_u$ and $Im\, k_u = \epsilon_u$, then along the integration contour of equation (24) $Im(\alpha - M_u k_u) = 0$, $Im\, \gamma_u > 0$, and $|\exp\{i[(\alpha - M_u k_u)ns^\dagger + \beta_u \gamma_u |y_n|]\}| < 1$. Summing the contribution of each blade to the potential yields a geometric series which can be expressed in closed form as

$$\Phi_u(x,y) = \sum_{n=-\infty}^{\infty} \Phi_{u,n}(x_n, y_n) = \frac{1}{2\pi}\int_{-\infty+i\epsilon_u M_u}^{\infty+i\epsilon_u M_u} f_o(\alpha)\Lambda_u(\alpha, y) e^{-i(\alpha - M_u k_u)(x+s)^\dagger}\, d\alpha \tag{25}$$

where

$$\Lambda_u(\alpha, y) \equiv \frac{1}{2i}\left[\frac{e^{i(\Delta_u^- + \beta_u \gamma_u y)}}{\sin \Delta_u^-} + \frac{e^{i(\Delta_u^+ - \beta_u \gamma_u y)}}{\sin \Delta_u^+}\right] \quad \text{for } 0 \le y \le s \tag{26}$$

and

$$\Delta_u^\pm \equiv \frac{1}{2}(\sigma - M_u k_u s^\dagger + \alpha s^\dagger \pm \beta_u \gamma_u s) \tag{27}$$

Applying the flow tangency relation (5) to the surface of the $n = 0$ blade yields

$$-W_2^{(u)} = \frac{\partial \Phi_u}{\partial y} = \frac{1}{2\pi}\int_{-\infty+i\epsilon_u M_u}^{\infty+i\epsilon_u M_u} f_o(\alpha)\kappa_u(\alpha, 0) e^{-i(\alpha - M_u k_u)\tilde{x}_u}\, d\alpha = e^{i\omega_u \tilde{x}_u} \tag{28}$$

for $\tilde{x}_u \equiv x + s^\dagger > 0$ and where

$$\kappa_u(\alpha, 0) \equiv \partial \Lambda_u / \partial y \Big|_{y=0} \tag{29}$$

Downloaded 01 Jun 2010 to 171.66.16.70. Redistribution subject to ASME license or copyright; see http://www.asme.org/terms/Terms_Use.cfm

The potential of the irrotational field produced upstream of the cascade must be continuous across lines $y=ns$ extending forward of the leading edges of the blades. Applying this boundary condition to equation (24) at the zeroth blade yields

$$\frac{1}{2\pi}\int_{-\infty+i\epsilon_u M_u}^{\infty+i\epsilon_u M_u} f_o(\alpha)e^{-i(\alpha-M_u k_u)\tilde{x}_u}\,d\alpha=0 \text{ for } \tilde{x}_u<0 \tag{30}$$

Equations (28) and (30) are in the form of the upwash and continuity expressions of [8]. They differ from those of [6] only by the presence of k_q/β_u^2 in γ_u and by the distortion pattern, $e^{i\omega_u\tilde{x}_u}$, replacing the flutter motion on the right side of equation (28). The integrals in both of these equations are in the form of inverse Fourier transforms forming a two-part boundary value problem which can be solved for $f_o(\alpha)$ by the Wiener-Hopf technique [14]. Utilizing unilateral Fourier transforms [15] over $\tilde{x}_u$, the two equations are combined and then factored and decomposed into parts which are analytic in respective half planes as in Appendix B of [6], have a common region of analaticity between them, and vanish at ∞. The solution is completed by use of Liouville's theorem giving

$$f_o(\alpha)=\frac{i\kappa_u^-\left(\frac{k_u}{M_u}-i\epsilon_o\right)}{\left(\alpha-\frac{k_u}{M_u}+i\epsilon_o\right)k_u^+(\alpha)} \tag{31}$$

Here ϵ_o is a damping term on the distortion to ensure convergence as $\tilde{x}_u\to\infty$ and can be set equal to zero upstream of the shock.

The solution for $f_o(\alpha)$ required that $k_u(\alpha)$ could be factored as $\kappa_u(\alpha,0)=\kappa_u^+(\alpha)/\kappa_u^-(\alpha)$ where $\kappa_u^+(\alpha)$ and $\kappa_u^-(\alpha)$ are analytic and nonzero in the upper ($Im\ \alpha>M_u\epsilon_u$) and lower ($Im\alpha<M_u\epsilon_u$) half-planes, respectively. The factoring procedure of Appendix C of [6] yields the results

$$\kappa_u^-(\alpha)=e^{-i\alpha(s^\dagger-\beta_u s)/2}\prod_{n=-\infty}^{\infty}(1-\alpha/\nu_n^+) \tag{32}$$

and

$$\kappa_u^+(\alpha)=e^{-i\alpha(s^\dagger-\beta_u s)/2}\,\frac{\beta_u\gamma_u}{2}\sin(\beta_u\gamma_u s)\times\left[\left(\frac{d_u^\dagger}{2}\right)^2\nu_o^+\nu_o^-\prod_{\substack{n=-\infty\\ \neq 0}}^{\infty}\left(\frac{d_u^\dagger}{2n\pi}\right)^2\nu_n^+\nu_n^-\right]^{-1}\times\left[\prod_{n=-\infty}^{\infty}\left(1-\frac{\alpha}{\nu_n^-}\right)\right]^{-1} \tag{33}$$

where

$$d_u^\dagger=(s^{\dagger 2}-\beta_u^2 s^2)^{1/2} \tag{34}$$

$$\nu_n^\pm=\Gamma_n^{(u)}\frac{s^\dagger}{d_u^\dagger}\pm\frac{\beta_u s}{d_u^\dagger}\left[(\Gamma_n^{(u)})^2-k_u^2-\frac{k_q^2}{\beta_u^2}\right]^{1/2} \tag{35}$$

and

$$\Gamma_n^{(u)}=(2n\pi+M_u k_u s^\dagger-\sigma)/d_u^\dagger \tag{36}$$

Equations (32) to (36) differ from those of [6] only by the presence of k_q in the definitions of γ_u and $\nu_n^\pm$.

Substitution of equation (31) into equation (25) enables determination of $\Phi_u(x,y)$ by the method of residues. The path of integration is closed in the upper half-plane for $x<-\beta_u(s-y)$ and in the lower half-plane for $x>-\beta_u(s-y)$. The results are

$$\Phi_u(x,y)=-is\,\kappa_u^-\left(\frac{k_u}{M_u}\right)\times\sum_{n=-\infty}^{\infty}\frac{e^{-i[(\nu_n^+-M_u k_u)\tilde{x}_u+\frac{y}{s}(d_u^\dagger\Gamma_n^{(u)}-\nu_n^+ s^\dagger)]}}{\left(\nu_n^+-\frac{k_u}{M_u}\right)[\kappa_u^-(\nu_n^+)]'(d_u^\dagger\Gamma_n^{(u)}-\nu_n^+ s^\dagger)}$$

$$\text{for } x\le-\beta_u(s-y) \tag{37a}$$

where

$$[\kappa_u^-\nu_n^+]'\equiv d\kappa_u^-(\nu_n^+)/d\nu_n^+$$

and

$$\Phi_u(x,y)=-e^{i\omega_u\tilde{x}_u}\left\{\frac{\cosh[\Psi_u(y-s)]-e^{i(\sigma-\omega_u s^\dagger)}\cosh(\Psi_u y)}{\Psi_u\sinh(\Psi_u s)}\right\}+\sum_{n=0}^{\infty}\cos\left(\frac{n\pi y}{s}\right)\left[\frac{e^{i(M_u k_u-\lambda_n^{(u)})x}Q_n^+}{\frac{k_u}{M_u}-\lambda_n^{(u)}}+\frac{e^{i(M_u k_u+\lambda_n^{(u)})x}Q_n^-}{\frac{k_u}{M_u}+\lambda_n^{(u)}}\right]$$

$$\text{for } x>-\beta_u(s-y) \tag{37b}$$

where

$$Q_n^\pm=\frac{e^{i(\sigma-n\pi)}-e^{i(M_u k_u\mp\lambda_n^{(u)})s^\dagger}}{\pm\lambda_n^{(u)}\beta_u^2 s(1+\delta_n^o)}\,\frac{\kappa^-(k_u/M_u)}{\kappa^-(\pm\lambda_n^{(u)})} \tag{38}$$

$$\lambda_n^{(u)}=\left[\left(\frac{n\pi}{B_u s}\right)^2+k_u^2+\left(\frac{k_q}{\beta_u}\right)^2\right]^{1/2},\quad\text{and } \Psi_u=(\omega_u^2+k_q^2)^{1/2} \tag{39}$$

Substitution of equation (37) into equations (8) and (9) determines the velocity of the acoustic motion and the pressure in the supersonic region ahead of the shock.

APPENDIX B

Solution for Acoustic Motion Downstream of Shock

An infinite "duct" solution to the convected wave equation for downstream running waves can be obtained by use of the method of separation of variables. This gives the result

$$\Phi_d^{\text{duct}}(x,y)=\frac{1}{i}\sum_{n=0}^{\infty}B_n\frac{e^{i\eta_n^+ x_d}\cos(n\pi y/s)}{\frac{k_d}{M_d}-\lambda_n^{(d)}} \tag{40}$$

where

$$\eta_n^\pm=-M_d k_d\pm\lambda_n^{(d)} \tag{41}$$

and

$$\lambda_n^{(d)}=i[(n\pi/\beta_d s)^2-k_d^2+k_q^2]\beta_d^{2\,1/2} \tag{42}$$

By ch. 5 of [7], the cascade potential for upstream running waves can be expressed as

$$\Phi_d^{\text{cascade}}(x,y)=\frac{1}{2i}\int_{-\infty}^{\infty}\frac{f_o(\alpha)\Lambda_d(\alpha,y)}{\alpha+k_d/M_d}e^{-i(\alpha+M_d k_d)\tilde{x}_d}\,d\alpha \tag{43}$$

where, in slightly different nomenclature than [7]

$$\Lambda_d\equiv\frac{1}{2i}\left[\frac{e^{i\Delta_d^+-\beta_d\gamma_d y}}{\sin\Delta_d^+}+\frac{e^{i\Delta_d^-+\beta_d\gamma_d y}}{\sin\Delta_d^-}\right] \tag{44}$$

Downloaded 01 Jun 2010 to 171.66.16.70. Redistribution subject to ASME license or copyright; see http://www.asme.org/terms/Terms_Use.cfm

$$\Delta_d^{\mp} \equiv \frac{1}{2}(\sigma + M_d k_d s^{\dagger} + \alpha s^{\dagger}) \pm \beta_d \gamma_d s/2i \tag{45}$$

and

$$\gamma_d \equiv (\alpha^2 - k_d^2 + k_q^2/\beta_d^2)^{1/2} \tag{46}$$

For this linear problem, where superposition applies, let

$$f_o = \frac{1}{\pi} \sum_{n=0}^{\infty} B_n f_{o,n}(\alpha) \tag{47}$$

By equations (43) and (47) the zero upwash condition will be satisfied if

$$\int_{-\infty}^{\infty} f_{o,n}(\alpha)\, \kappa_d(\alpha,0) e^{-i(\alpha - M_d k_d)\tilde{x}_d}\, d\alpha = 0 \text{ for } \tilde{x}_d < 0 \tag{48}$$

where

$$\kappa_d(\alpha,0) \equiv -\partial \Lambda_d/\partial y\Big|_{y=0} (\alpha + k_d/M_d)^{-1} \tag{49}$$

A relation specifying zero pressure jump across lines extending in the downstream direction from the trailing edges of the blades is obtained by substituting equations (40) and (43) to (47) into $P_d = (i\omega_d - \partial/\partial x)(\Phi_d^{\text{duct}} + \Phi_d^{\text{cascade}})$ and utilizing the periodicity relation. The resulting expression can be reduced to

$$\int_{-\infty}^{\infty} f_{o,n}(\alpha) e^{-i\alpha \tilde{x}_d} d\alpha = \pi e^{i(\eta_n^+ + M_d k_d)\tilde{x}_d} [e^{i(\eta_n^+ s^{\dagger} - \sigma + n\pi)} - 1] \text{ for } \tilde{x}_d > 0 \tag{50}$$

Solution of equations (48) and (50) again constitutes a Wiener-Hopf problem which can be solved in much the same manner as in the supersonic case yielding

$$f_{o,n}(\alpha) = \frac{\kappa_d^-(-\lambda_n^{(d)})}{2i(\alpha + \lambda_n^{(d)})\kappa_d^-(\alpha)} [1 - e^{i(\eta_n^+ s^{\dagger} - \sigma + n\pi)}] \tag{51}$$

Here it is assumed that κ_d can be factored into the form $\kappa_d^-(\alpha)/\kappa_d^+(\alpha)$ where $\kappa_d^+(\alpha)$ and $\kappa_d^-(\alpha)$ are analytic and nonzero in upper and lower half planes, respectively. To perform this factorization substitute equation (44) into equation (49) and obtain

$$(\alpha + k_d/M_d)\kappa_d(\alpha,0) = \beta_d \gamma_d \sinh(\beta_d \gamma_d s)/(2 \sin\Delta_d^+ \sin\Delta_d^-) \tag{52}$$

The numerator of equation (52) can be factored by the Weierstrass factorization formula [15]. Page 40 of [14] is helpful for application of this theorem to the denominator. Choose the half planes as in Fig. 8 of [6] but with branch points of γ_d at $\pm(\psi_d + i\epsilon_d)$ where $\psi_d^2 = k_d^2 - k_q^2/\beta_d^2$. Then

$$\kappa_d^-(\alpha) = \frac{(\alpha - \psi_d)\sin(\beta_d \psi_d s) e^{i\alpha b/\pi}}{\psi_d[\cos(\beta_d \psi_d s) - \cos(\sigma + M_d k_d s^{\dagger})](1 - \alpha/\alpha^+{}_o)} \times \prod_{n=1}^{\infty} \frac{1 - \alpha/\lambda_n^{(d)}}{(1 - \alpha/\alpha_n^+)(1 - \alpha/\alpha^+{}_n)} \tag{53}$$

and

$$\kappa_d^+(\alpha) = \frac{(\alpha + k_d/M_d)(1 - \alpha/\alpha_o^-) e^{i\alpha b/\pi}}{\beta_d(\alpha + \psi_d)} \prod_{n=1}^{\infty} \frac{(1 - \alpha/\alpha_n^-)(1 - \alpha/\alpha^-{}_n)}{1 + \alpha/\lambda_n^{(d)}} \tag{54}$$

where

$$b \equiv s^{\dagger}\left[\frac{1}{2}\pi - \tan^{-1}(s\beta_d/s^{\dagger})\right] + s\beta_d \ell n(2s\beta_d/d_d^{\dagger}) \tag{55}$$

$$\Gamma_n^{(d)} \equiv (2n\pi - \sigma - M_d k_d s^{\dagger})/d_d^{\dagger} \tag{56}$$

$$d_d^{\dagger} \equiv (s^{\dagger 2} + \beta_d^2 s^2)^{1/2} \tag{57}$$

$$\alpha_n^{\pm} \equiv \Gamma_n^{(d)} \frac{s^{\dagger}}{d_d^{\dagger}} \pm i \frac{\beta_d s}{d_d^{\dagger}} \left[(\Gamma_n^{(d)})^2 - k_d^2 + \frac{k_q^2}{\beta_d^2}\right]^{1/2} \tag{58}$$

and ψ_d is equal to $|k_d^2 - k_q^2/\beta_d^2|^{1/2}$ and $i\,|k_q^2/\beta_d^2 - k_d^2|^{1/2}$ for k_d^2 greater than and less than k_q^2/β_d^2, respectively. Equations (53) to (58) reduce to those of Appendix E of [6] as $k_q \to 0$. Substitution of equation (51) and (44) to (47) into equation (43) gives an integral expression for Φ_d^{cascade} which can be evaluated by use of the residue theorem. The integrand of equation (43) can be expressed as $I = I_1 - I_2$ where the α dependence enters I_1 as

$$\cosh[\beta_d \alpha(y-s)] / [\beta_d \alpha^2 \kappa_d^+(\alpha)\sinh(\beta_d \alpha s)\exp(i\alpha \tilde{x}_d)] \quad \text{as } \alpha \to \infty$$

and I_2 as

$$\cosh(\beta_d \alpha y) / \{\beta_d \alpha^2 \kappa_d^+(\alpha)\sinh(\beta_d \alpha s)\exp[i\alpha(\tilde{x}_d - s^{\dagger})]\} \quad \text{as } \alpha \to \infty$$

For I_1, the path of integration must be closed in the upper half-plane (UHP) for $\tilde{x}_d < 0$ and LHP for $\tilde{x}_d > 0$. The path for I_2 must be closed in UHP for $\tilde{x}_d < s^{\dagger}$ and LHP for $\tilde{x}_d > s^{\dagger}$. Finally, the total amplitude, Φ_d, for $0 \le y \le s$ is obtained by combining Φ_d^{duct} with Φ_d^{cascade}.

The results for $0 \le y \le s$ are

$$\Phi_d(x,y) = \frac{1}{i} \sum_{n=0}^{\infty} \left[\frac{B_n e^{i\eta_n^+ x}}{\frac{k_d}{M_d} - \lambda_n^{(d)}} + \sum_{m=0}^{\infty} B_m K_{mn} \frac{e^{i\eta_n^- \tilde{x}_d}}{\frac{k_d}{M_d} + \lambda_n^{(d)}} \right] \cos\left(\frac{n\pi y}{s}\right)$$

$$\text{for } 0 \le x < 1 - s^{\dagger} \tag{59a}$$

$$\Phi_d(x,y) = \frac{1}{i} \sum_{n=0}^{\infty} B_n \left[\frac{\cos\left(\frac{n\pi y}{s}\right) e^{i[\eta_n^+ (x - s^{\dagger}) + \sigma - n\pi]}}{\left(\frac{k_d}{M_d} - \lambda_n^{(d)}\right)\left[e^{-i(\eta_n^+ s^{\dagger} - \sigma + n\pi)} - 1\right]} + \frac{e}{2}^{i\eta_n^+} \left[e^{i(n\pi - \sigma)} - e^{-i\eta_n^+ s^{\dagger}}\right] \times \left\{ \frac{\kappa_d^-(-\lambda_n^{(d)})\cosh[\Psi_d(y-s)] e^{i\omega_d \tilde{x}_d}}{\left(\lambda_n^{(d)} - \frac{k_d}{M_d}\right)\kappa_d^-\left(-\frac{k_d}{M_d}\right)\left[\cosh(\Psi_d s) - \cos(\sigma - \omega_d s^{\dagger})\right]} + \sum_{m=-\infty}^{\infty} \frac{\cos\left[\left(1 - \frac{y}{s}\right)(d_d^{\dagger}\Gamma_m^{(d)} - s^{\dagger}\alpha_m^-)\right] \mathcal{K}_m^-(\lambda_n^{(d)})}{\left(\alpha_m^- + \frac{k_d}{M_d}\right) e^{i(\alpha_m^- + M_d k_d)\tilde{x}_d}} \right\} \right]$$

$$+ \frac{1}{i} \sum_{n=0}^{\infty} \sum_{m=0}^{\infty} B_m K_{m,n} \frac{\cos\left(\frac{n\pi y}{s}\right) e^{i[\eta_n^- (\tilde{x}_d - s^{\dagger}) + \sigma + n\pi]}}{\left(\frac{k_d}{M_d} + \lambda_n^{(d)}\right)\left[e^{-i(\eta_n^- s^{\dagger} - \sigma - n\pi)} - 1\right]}$$

Downloaded 01 Jun 2010 to 171.66.16.70. Redistribution subject to ASME license or copyright; see http://www.asme.org/terms/Terms_Use.cfm

$$\text{for } 1-s^{\dagger}<x<1 \qquad (59b)$$

and

$$\Phi_d(x,y)=\frac{1}{i}\sum_{n=0}^{\infty}B_n\frac{e^{i\eta_n^+}}{2}[e^{i(n\pi-\sigma)}-e^{-i\eta_n^+ s^{\dagger}}]$$

$$\left\{\frac{\kappa_d^-(-\lambda_n^{(d)})\{\cosh[\Psi_d(y-s)]-\cosh(\Psi_d y)e^{i(\sigma-\omega_d s^{\dagger})}\}}{\left(\lambda_n^{(d)}-\frac{k_d}{M_d}\right)\kappa_d^-\left(-\frac{k_d}{M_d}\right)\left[\cosh(\Psi_d s)-\cos(\sigma-\omega_d s^{\dagger})\right]}e^{i\omega_d\bar{x}}\right.$$

$$+\sum_{m=0}^{\infty}\frac{\cos\left[\left(1-\frac{y}{s}\right)(d_d^{\dagger}\Gamma_m^{(d)}-s^{\dagger}\alpha_m^-)\right]-\cos\left[\frac{y}{s}(d_d^{\dagger}\Gamma_m^{(d)}-s^{\dagger}\alpha_m^-)\right]e^{i[\alpha^+(\sigma_m^-+M_d k_d)s^{\dagger}]}}{\left(\alpha_m^-+\frac{k_d}{M_d}\right)e^{i(\alpha_m^- M_d k_d)\bar{x}_d}}$$

$$\left.\mathcal{K}_m^-(\lambda_n^{(d)})\right\}\quad\text{for } 1\le x \qquad (59c)$$

where

$$K_{m,n}\equiv\frac{e^{i\eta_m^+}}{2(1+\delta_n^0)}\left[e^{(i(m\pi-\sigma)}-e^{-i\eta_m^+ s^{\dagger}}\right]\left[e^{i(\sigma-\eta_m^+ s^{\dagger}+n\pi)}-1\right]$$

$$\frac{k_d^-(-\lambda_m^{(d)})(\lambda_n^{(d)}+k_d/M_d)}{k_d^+(\lambda_n^{(d)})(\lambda_n^{(d)}+\lambda_m^{(d)})\beta_d^2 s\lambda_m^{(d)}}, \qquad (60)$$

$$\mathcal{K}_m^-(\lambda_n^{(d)})\equiv\frac{\kappa_d^-(-\lambda_n^{(d)})(d_d^{\dagger}\Gamma_m^{(d)}-\alpha_m^- s^{\dagger})}{k_d^-(\alpha_m^-)d_d^{\dagger}(s^{\dagger}\Gamma_m^{(d)}-\alpha_m^- d_d^{\dagger})(\alpha_m^-+\lambda_n^{(d)})\sin(\alpha_m^- s^{\dagger}-d^{\dagger}\Gamma_m^{(d)})} \qquad (61)$$

$\Psi_d\equiv\sqrt{\omega_d^2+k_q^2}$, and δ_n^o is the Kronecker delta.

APPENDIX C

Solution for Coefficients in Description of Subsonic Acoustic and Vortical Motions

Determination of the coefficients B_m of equation (59) and $b_{j,n}$ $(j=1,2,3)$ of equations (16) and (17) is made possible with the additional information supplied by the shock relations, equations (19) to (21). Equation (20) can easily be combined with equations (21), (2) and (16) to yield

$$\frac{\partial}{\partial y}(v_3^{(u)}-v_3^{(d)})=k_q\tan(k_q z)(v_2^{(d)}-v_2^{(u)}) \qquad (62)$$

since the z-dependence enters only through $\cos(k_q z)$. Combining equation (62) with equations (2), (16), and solenoidal condition (17), and utilizing orthogonality relations between sine terms, permits determination of $b_{1,n}$ and $b_{3,n}$ in terms of $b_{2,n}$ and known quantities. The downstream vortical velocity of equation (16) can now be expressed as

$$\mathbf{v}_d(x,y,z)=a\cos(k_q z)e^{i(\omega_u t+\omega_d x)}$$

$$\times\begin{bmatrix}-\sum_{m=1}^{\infty}\left[\frac{1+(k_q s/m\pi)^2}{\omega_d s/m\pi}b_{2,m}+\frac{2isR_m(k_q/\pi\omega_d)^2}{m\exp(i\omega_d x)}\right]\cos\left(\frac{m\pi y}{s}\right)\\ i\sum_{m=1}^{\infty}b_{2,m}\sin(m\pi y/s)\\ -k_q\tan(k_q z)\sum_{m=1}^{\infty}\left[\frac{sb_{2,m}}{im\pi}+\frac{2sR_m}{m\pi^2\omega_d\exp(i\omega_d x)}\right]\cos\left(\frac{m\pi y}{s}\right)\end{bmatrix} \qquad (63)$$

where

$$R_m=\omega_d e^{i\omega_u s^{\dagger}}\left[1+i\frac{C\omega_u\cot\mu}{ak_q}\right]$$

$$\frac{m[1-(-1)^m\exp(i\omega_u s\ ctn\ \mu)]}{m^2-[\omega_u s(ctn\mu)/\pi]^2}\quad\text{for } m\ge 1=0$$

$$=0\text{ for } m=0 \qquad (64)$$

Use of equations (2), (7), (9), (37b), (18), (59a), and (63) for velocities and pressures in shock relations (19) and (20) and utilizing equations (377), (378), (488), (489) and (592) of [16] gives the following equation for B_n in implicit form

$$\left[a_n^+-\delta_o^n\frac{k_q^2(2M_u^2M_d^2-M_u^2-M_d^2)}{\beta_d^4M_u^2}\right]B_n$$

$$+\left[a_n^--\delta_o^n\frac{k_q^2(2M_u^2M_d^2-M_u^2-M_d^2)}{\beta_d^4M_u^2}\right]e^{-i\eta_n^-(1-s^{\dagger})}\sum_{m=0}^{\infty}B_m K_{m,n}$$

$$=-i\left\{\frac{2M_d^2}{\beta_d^4}\left\{\left[\left(\frac{n\pi}{s}\right)^2+\omega_d^2+k_q^2\right]\left[\frac{k_u M_u-\lambda_n^{(u)}}{k_u/M_u-\lambda_n^{(u)}}Q_n^+\right.\right.\right.$$

$$+\frac{k_u M_u-\lambda_n^{(u)}}{k_u/M_u+\lambda_n^{(u)}}Q_n^--\frac{1}{2}\left(M_u^2+1-\frac{\gamma-1}{\gamma+1}\frac{\beta_u^4}{M_u^2}\right)Q_n^++\left.\left.\frac{t_{2,n}-t_{1,n}}{1+\delta_n^o}\right]\right.$$

$$+(1-\delta_n^o)\left(\cot\mu-\frac{\mathfrak{U}_u}{\mathfrak{U}_u}\frac{a}{A}\right)\left[\left(\frac{n\pi}{s}\right)^2+k_q^2\right]t_{1,n}/\cot\mu\Big\}$$

$$+\frac{2(1-\delta_n^o)}{\gamma+1}\left(\frac{\beta_u}{\beta_d M_u}\right)^2\left[\left(\frac{n\pi}{s}\right)^2+k_q^2\right]\left(M_u^2+\frac{\gamma-1}{\gamma+1}\beta_u^2\right)$$

$$\left.(Q_n^++Q_n^-)-i(1-\delta_n^0)\left(\frac{2k_q M_d}{\pi}\right)^2\frac{sR_n}{n\beta_d^4}\right\} \qquad (65)$$

where

$$a_n^{\pm}\equiv(\lambda_n^{(d)})^2\pm 2M_d k_d\lambda_n^{(d)}+(k_d/M_u)^2 \qquad (66)$$

$$t_{1,n}\equiv\frac{2\omega_u A}{sa}\cot(\mu)e^{i\omega_u s^{\dagger}}\frac{e^{i(n\pi+\omega_u s\cot\mu)}-1}{\left(\frac{n\pi}{s}\right)^2-(\omega_u\cot\mu)^2} \qquad (67)$$

Downloaded 01 Jun 2010 to 171.66.16.70. Redistribution subject to ASME license or copyright; see http://www.asme.org/terms/Terms_Use.cfm

$$t_{2,n} \equiv \frac{2\omega_u}{s} e^{i\omega_u s^\dagger} \frac{e^{i(\sigma-\omega_u s^\dagger + n\pi)} - 1}{\left(\frac{n\pi}{s}\right)^2 + \omega_u^2 + k_q^2} \tag{68}$$

The left side of equation (65) reduces to (3.33) of [6] as $k_q \to 0$. The right side of equation (65), however, replaces the flutter terms of [6] for this distortion problem. Solution of equation (65) for B_n is by inversion of an infinite matrix. The off-diagonal elements of this matrix came from the second term of equation (65), which represents acoustic waves reflected from the back end of the cascade. These are rapidly decaying waves for $(n\pi/\beta_d s)^2 + (k_q/\beta_d)^2 > k_d^2 = M_d^2\omega_d^2/\beta_d^4$ so that, in practice, equation (65) can be approximated by a nearly diagonal matrix. This can be further truncated to a reasonably small number of terms. Numerical results suggest that as few as 10 terms along the diagonal may, at times, give satisfactory results at values of reduced frequency less than one. Once the B_n are known the coefficient $b_{2,n}$ in the Fourier series of equation (63) can be obtained from shock relation equation (20) as

$$b_{2,n} = \frac{n\pi}{s}\omega_d \Bigg\{ B_n + e^{-i\eta_n^-(1-s^\dagger)} \sum_{m=0}^{\infty} B_m K_{m,n} - i\Bigg[\Bigg(M_u^2 + \frac{\gamma-1}{\gamma+1}\beta_u^2\Bigg)(Q_n^+ + Q_n^-) + \frac{2(\gamma+1)s}{n}\left(\frac{k_q}{\pi\omega_d}\right)^2\left(\frac{M_u M_d}{\beta_u\beta_d}\right)^2 R_n$$

$$+ \frac{(\gamma+1)t_{1,n}}{\cot\mu}\left(\frac{M_u M_d}{\beta_u\beta_d}\right)^2\left(\cot\mu - \frac{a}{A}\frac{\mathfrak{U}_u}{\mathfrak{U}_d}\right)\Bigg]\Bigg\} \tag{69}$$

$$\div (\gamma+1)\left(\frac{M_u M_d}{\beta_u\beta_d}\right)^2\left[\omega_d^2 + \left(\frac{n\pi}{s}\right)^2 + k_q^2\right]$$

Use of equation (69) in equation (63) determines the subsonic vortical velocity for $0 \le y \le s$ and $x > 0$, whereas use of partial derivatives of equation (59) in equation (18) determines the corresponding acoustic velocity components. Use of equation (37) in equation (8), along with equation (2) and (4), gives the acoustic and vortical velocities for $0 \le y \le s$ and $x < 0$. Pressure can be obtained by use of equation (9) and its subsonic counterpart $p_d = ae^{-i\omega_u t}\cos(k_q z)\ (i\omega_d - \partial/\partial x)\Phi_d$. Extension of equations to other blades and channels is simply by use of the periodicity condition $\theta_n(x + ns^\dagger, ns + y) = e^{in\sigma}\theta_o(x,y)$, where θ can be any of the physical variables Φ_u, V_u, P_u, Φ_d, V_d, and P_d as in [6].

Downloaded 01 Jun 2010 to 171.66.16.70. Redistribution subject to ASME license or copyright; see http://www.asme.org/terms/Terms_Use.cfm

Development of Controlled Diffusion Airfoils for Multistage Compressor Application

D. E. Hobbs
Research Engineer.

H. D. Weingold
Senior Research Scientist.

Pratt & Whitney Aircraft,
Engineering Division,
United Technologies Corporation,
East Hartford, Conn. 06108

A series of Controlled Diffusion Airfoils has been developed for multistage compressor application. These airfoils are designed analytically to be shock-free at transonic Mach numbers and to avoid suction surface boundary layer separation for a range of inlet conditions necessary for stable compressor operation. They have demonstrated, in cascade testing, higher critical Mach numbers, higher incidence range, and higher loading capability than standard series airfoils designed for equivalent aerodynamic requirements. These airfoils have been shown, in single and multistage rig testing, to provide high efficiency, high loading capability, and ease of stage matching, leading to reduced development costs and improved surge margin. The Controlled Diffusion Airfoil profile shapes tend to have thicker leading and trailing edges than their standard series counterparts, which lead to improved compressor durability.

Introduction

This paper reports the development of a new compressor airfoil type that is being used to replace most standard series airfoils in Pratt & Whitney Aircraft advanced compression systems such as the PW2037 high- and low-pressure compressors. Standard series airfoils, such as the NACA 400[1], the NACA 65/Circular Arc, or the Double Circular Arc airfoils, which have been used in most current production compressors, were adaptations, for compressor application, of shapes that were developed and optimized for isolated airfoil application, or were empirically derived shapes. Their development preceded the availability of analytical procedures capable of predicting transonic cascade aerodynamics.

Controlled Diffusion Airfoils are designed and optimized specifically for subsonic and transonic cascade application. Through control of the diffusion on the airfoil suction surface, significant boundary layer separation can be avoided over the entire range of airfoil operation. For transonic applications, diffusion from supersonic to subsonic local surface velocity can be accomplished without developing shock waves. A family of airfoils, capable of achieving these conditions, has been developed which can be described by a small number of geometric parameters.

Experimental testing of a number of Controlled Diffusion Airfoil cascades, between 1978 and 1981, has demonstrated the capability of achieving low loss at elevated Mach number, increased incidence range at elevated Mach number, high loading levels, and thicker leading and trailing edges without performance penalty. These qualities can be utilized to achieve high compressor efficiency, fewer compressor blades and vanes, improved stability, improved durability and reduced development cost.

The development of this airfoil family required prior technology improvements in analytical techniques and in cascade test procedures. Computer programs have been developed which are capable of efficiently computing transonic cascade aerodynamics with varying streamtube area and radius change. This capability has been combined with viscous boundary layer analyses to predict laminar, transitional, and turbulent boundary layer development and potential separation. These programs have been supplemented by empirical corrections to analytical turning, supplied by an extensive cascade test program. All of these capabilities have been combined in an extremely rapid computer interactive direct design system, capable of designing a Controlled Diffusion Airfoil for a specific requirement and predicting its off-design performance.

Discussion

Background. The abrupt increase in loss and decrease in turning of a cascade of compressor airfoils, as incident Mach number increases, is analagous to the transonic drag rise experienced by isolated airfoil sections. As Mach number increases, local patches of supersonic flow appear on airfoil surfaces, usually terminated by shock waves. The total pressure loss of the shock plus the losses caused by shock-induced boundary layer separation combine to limit the low loss Mach number range of a cascade of airfoils. To improve compressor efficiency, airfoil sections usually have been selected having thinner leading edges at higher Mach numbers, in order to increase the transonic drag rise Mach

[1] NACA 400 – NACA four digit airfoil with location of maximum camber fixed at 40 percent chord – NACA X4XX.

Contributed by the Gas Turbine Division of THE AMERICAN SOCIETY OF MECHANICAL ENGINEERS and presented at the 28th International Gas Turbine Conference and Exhibit, Phoenix, Arizona, March 27–31, 1983. Manuscript received at ASME Headquarters January 4, 1983. Paper No. 83-GT-211.

Copyright © 1984 by ASME
Downloaded 01 Jun 2010 to 171.66.16.70. Redistribution subject to ASME license or copyright; see http://www.asme.org/terms/Terms_Use.cfm

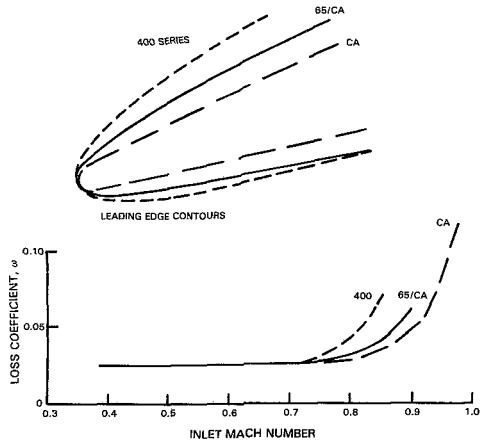


Fig. 1 To achieve low loss as Mach number increases, standard series airfoils are chosen having thinner leading edges

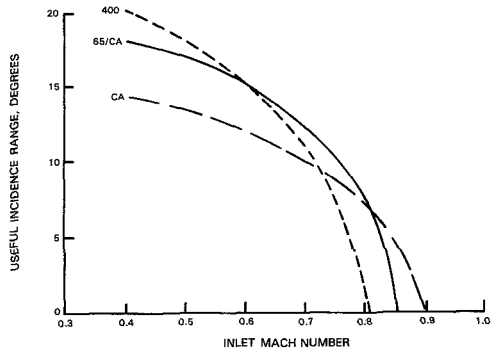


Fig. 2 Higher Mach number standard series airfoils have reduced incidence range

number, Fig. 1. However, this selection usually results in decreased useful incidence angle range (loss coefficient less than 0.04) and decreased durability, Fig. 2.

Whitcomb et al. [1], in 1965, demonstrated experimentally the existence of shockless supercritical flows for isolated airfoil sections. By developing shapes which could diffuse from locally supersonic velocities to subsonic velocities without shock waves, Whitcomb substantially increased the drag rise Mach number of his supercritical wing sections over existing airfoil sections of similar thickness. This capability also suggested that these shapes could be further optimized to reduce boundary layer drag, since the absence of shock waves would permit potential flow analytical solutions to be employed in conjunction with standard boundary layer procedures. Bauer, Garabedian, and Korn [2, 3, 4] provided analytical design procedures for supercritical wing sections which, through solution of the potential equation in the complex hodograph plane, permitted an airfoil shape to be derived from a specified shockless surface Mach number distribution.

Feasibility Demonstration. The current study was motivated by a desire to determine if shockless transonic airfoils could be designed for compressor application, thereby permitting more robust airfoils to be designed for higher Mach numbers or improving the compressor efficiency potential through increases in the critical Mach number. In 1974, Korn [5, 6] extended the previous isolated airfoil design procedure to cascade airfoils. In a cooperative program with Pratt & Whitney Aircraft, a supercritical cascade section was designed by Korn in 1974. It was tested in the transonic cascade facility of the DFVLR (Deutsche Forschungs und Versuchsanstalt fur Luft und Raumfahrt) in 1976 as reported by Stephens [7]. The test verified the shockless nature of the flow field and the attached viscous boundary layer. The airfoil exhibited excellent aerodynamic performance at off-design conditions as well as at its design point, indicating that shocks developing at off-design conditions were relatively weak and did not significantly degrade the airfoil's performance. This was important for compressor airfoil application since compressor airfoils must operate stably and efficiently over a range of incident Mach number and flow angles.

Although these test results demonstrated the feasibility of supercritical compressor airfoil design, the Korn hodograph procedure did not represent a practical compressor airfoil design capability for several reasons; the airfoils designed tended to have undesirable structural properties, the program could not compute at high solidity, and it did not permit streamtube thickness or streamtube radius to vary through the cascade, as occurs for most compressor airfoils. In addition, since it was strictly a design procedure, it could not be used to estimate the off-design capabilities of the airfoils designed. Recently, Sanz [8] has reduced the limitations on solidity of the Korn program.

First Practical Demonstration. Ives and Liutermoza [9, 10] developed a procedure in 1975 which was capable of calculating transonic flows at practical solidities with varying streamtube thickness, and, because it could calculate weak shock waves, could be used to calculate off-design performance. When combined with a boundary layer calculation [11] and a coordinate smoothing routine in a computer interactive design procedure, it provided a means of designing durable, structurally sound cascade airfoils capable of meeting shockless transonic design point conditions for turning at minimum total pressure loss, as well as insuring a reasonable range of efficient, stable off-design performance. Criteria were then developed to describe airfoil surface Mach number distributions to best achieve the aerodynamic design objectives (Fig. 3). These are:

Nomenclature

AVDR = axial velocity density ratio – streamtube inlet height/exit height, H_1/H_2
B = airfoil chord
BX = airfoil axial chord
DF = diffusion factor $(1 - V_2/V_1) + (\tau/B)\left(\frac{V_1\cos\beta_1 - V_2\cos\beta_2}{2V_1}\right)$
H = streamtube height normal to blade-to-blade plane
M = Mach number
P = static pressure
P_T = total pressure
Re = Reynolds number based on inlet velocity and chord, VB/ν
t = airfoil maximum thickness
V = velocity
β = air angle measured from tangential
ν = kinematic viscosity
σ = solidity, B/τ
τ = cascade gap, pitch
ω = loss coefficient = $(P_{T1} - P_{T2})/(P_{T1} - P_1)$

Subscripts

1 = cascade upstream inlet plane
LE = cascade airfoil leading edge plane
TE = cascade airfoil trailing edge plane
2 = cascade downstream exit plane
x = axial direction

Downloaded 01 Jun 2010 to 171.66.16.70. Redistribution subject to ASME license or copyright; see http://www.asme.org/terms/Terms_Use.cfm

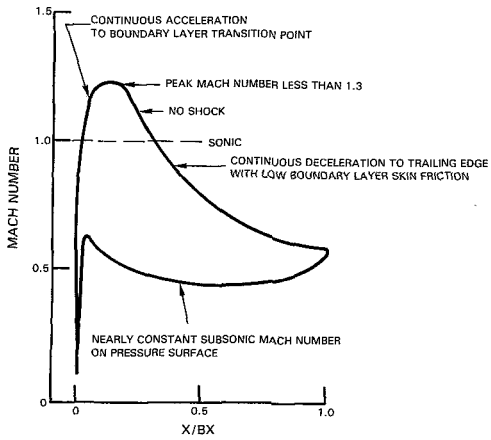


Fig. 3 Controlled diffusion airfoil aerodynamic design criteria

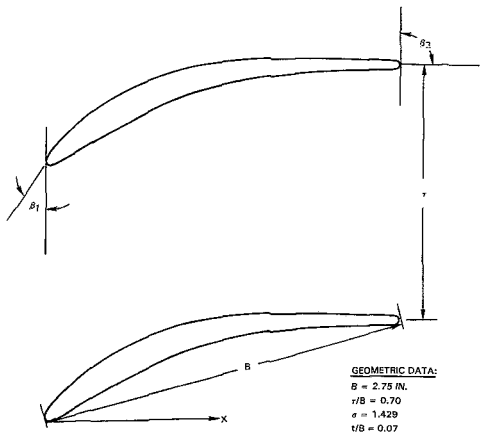


Fig. 4 Supercritical fan exit guide vane cascade geometry

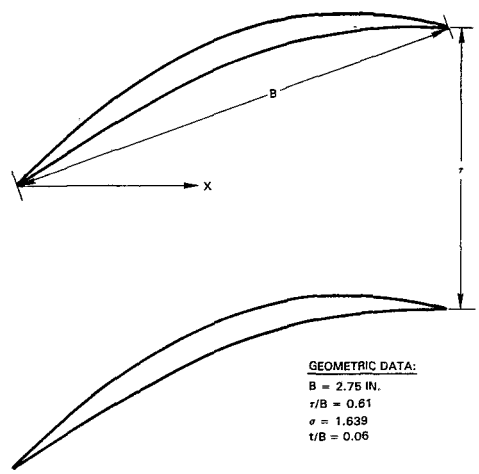


Fig. 5 Comparison multiple circular arc fan exit guide vane geometry

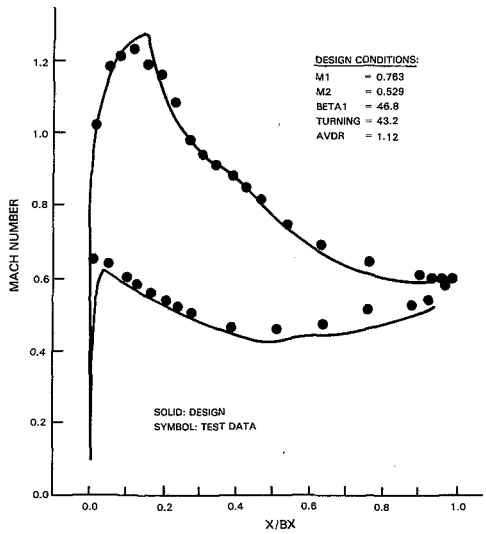


Fig. 6 Supercritical exit guide vane design experimental Mach number distribution closely achieved design distribution

1 A continuous acceleration from the leading edge to the peak Mach number on the airfoil suction surface, to avoid premature laminar boundary layer separation or transition

2 A peak Mach number less than 1.3 to avoid boundary layer separation, which could be induced by a severe shock wave boundary layer interaction should a shock develop at off-design conditions

3 A continuous, shock-free deceleration from the peak suction surface Mach number to the trailing edge, maintaining a turbulent boundary layer with a low level of skin friction and avoiding separation ahead of the trailing edge

4 A nearly constant subsonic Mach number distribution on the pressure surface

The Ives and Liutermoza procedure was used to design a fan exit guide vane section, under Naval Air Systems Command Contract N00019-77-C-0546 [12], to provide a demonstration of a supercritical cascade airfoil satisfying practical compressor aerodynamic and structural requirements. The design requirements were those of the mean section of the exit guide vane of a 1600 ft/s tip speed fan, tested previously under NASA Contract NAS3-10482 [13]. The design objectives were inlet Mach number of 0.76, inlet flow angle of 46.8 deg, turning of 43.2 deg to an axial discharge angle, and a streamtube contraction ratio (AVDR) of 1.124. The design iteration yielded a cascade having a solidity of 1.43 and a diffusion factor of 0.54, (Fig. 4). The airfoil was tested in the DFVLR transonic cascade facility in 1978. For comparison, a multiple circular arc airfoil (MCA) (Fig. 5) was designed to meet the same aerodynamic requirements, resulting in a solidity of 1.64 and a design diffusion factor of 0.51. It was also tested at the DFVLR cascade facility.

The design point surface Mach number distribution is depicted in Fig. 6, incorporating the features described above. Superimposed is the experimental Mach number distribution derived from static pressure taps on the airfoil surfaces corresponding to one gap, i.e., the suction surface taps and pressure surface taps were on consecutive airfoils. It can be seen that the airfoil closely matched its design Mach number distribution. In this figure, and in all subsequent figures, inlet Mach number is adjusted from the upstream measurement station to the plane of the cascade leading edge by accounting for streamtube contraction due to side wall boundary layer growth. The analysis of the static pressure data at several test points, used to arrive at this adjustment, is described at length in [12]. The loss of the cascade as a function of inlet angle and Mach number is illustrated in Fig. 7. The airfoil maintained low loss and excellent incidence angle range until its design Mach number was exceeded. The minimum loss as a function of Mach number is depicted in Fig. 8, compared to that achieved for the Multiple Circular Arc cascade. The supercritical exit guide vane section had significantly lower loss up to its critical Mach number. As illustrated in Fig. 9, the supercritical exit guide vane achieved and maintained its design exit angle, with little deviation, over a wide range of incidence angle and Mach number. The comparison MCA

Downloaded 01 Jun 2010 to 171.66.16.70. Redistribution subject to ASME license or copyright; see http://www.asme.org/terms/Terms_Use.cfm

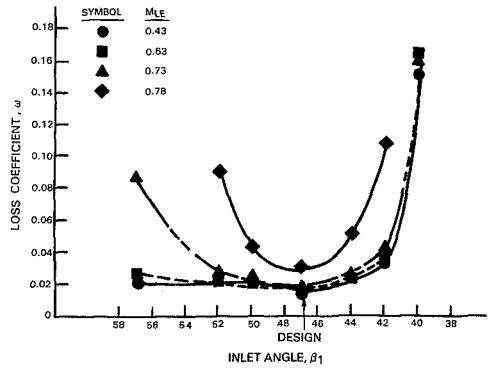


Fig. 7 Supercritical exit guide vane achieved low loss and wide incidence range at all Mach numbers below critical

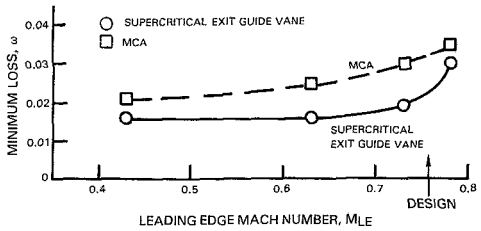


Fig. 8 Minimum loss of the supercritical exit guide vane was significantly below that of the comparison multiple circular arc design

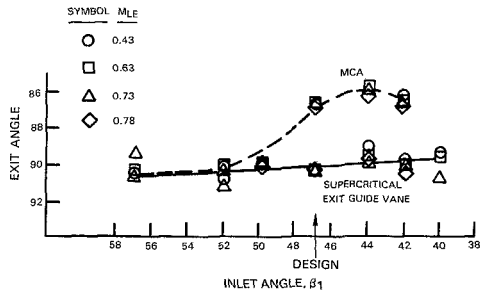


Fig. 9 Supercritical exit guide vane maintained its design exit angle over a wide range of incidence angle and Mach number. The comparison MCA design had significant deviation at design incidence and positive incidence angles.

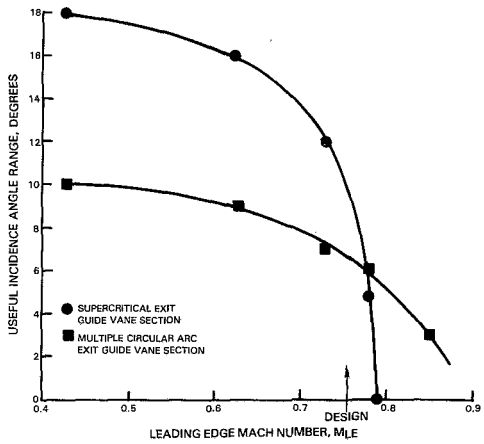


Fig. 10 The supercritical exit guide vane had superior incidence range to the MCA airfoil

airfoil experienced significant underturning at design incidence angle and all positive incidence angles. Similarly, the incidence range of the supercritical exit guide vane section was significantly higher than the MCA section, until design Mach number was exceeded, Fig. 10. For this comparison, incidence range was defined by the airfoils reaching an absolute loss level of 0.04 at each side of the loss bucket.

The supercritical fan exit guide vane test, besides demonstrating that a supercritical cascade section could be designed to meet practical compressor airfoil requirements, also demonstrated additional desirable aerodynamic and structural benefits. The cascade had excellent low-Mach-number performance due to the attached boundary layer design. It had excellent incidence range at all Mach numbers up to critical Mach number, demonstrating that the design rules adopted avoided strong shock wave boundary layer interactions at off-design conditions. The airfoil had little deviation in turning angle over its useful incidence and Mach ranges, also due to its attached boundary layer design. The airfoil's thick leading and trailing edges, relative to comparable high-Mach-number airfoils, promised improved durability. This successful test prompted the further development of airfoils obeying these design criteria for application to most compressor airfoil requirements from low to transonic Mach numbers.

Development of a Series of Controlled Diffusion Airfoils – Design. A series of eight airfoils of this type, designated Controlled Diffusion Airfoils "A" through "H" were designed and tested from 1978 to 1981, covering the range of airfoil requirements for an advanced multistage compressor. In addition, several standard series airfoils (NACA 400, NACA 65/CA, DCA), designed for identical aerodynamic requirements, were tested for direct comparison of their performance to the Controlled Diffusion Airfoils.

In order to design this large number of Controlled Diffusion Airfoil sections, and to provide a practical engineering design procedure for the hundreds of sections required for a typical high-pressure compressor, improvements were made to the analytical procedures. The improved design calculation utilized the Caspar, Hobbs, and Davis finite area solution of the compressible potential equation [14, 15, 16]. This procedure performs its computations in the physical cascade plane and avoids the complexity of conformal mapping, used in the Ives program, and its attendant difficulties at high solidity. The boundary layer calculation incorporated an improved laminar/turbulent transition calculation [17], a laminar separation and reattachment calculation [18], and a lateral streamtube contraction effect using the Mangler transformation. The inviscid analysis, the boundary layer calculation and empirically modified deviation corrections, were combined in an extremely fast computer interactive design system which requires only 13 CPU seconds on the IBM 3081 computer per cascade analysis.

Since the design method is a direct iterative procedure, speed of convergence is dependent upon the quality of the initially guessed airfoil contour. An analysis of several converged designs permitted development of a geometric construction procedure which, for most cases, satisfies all the above aerodynamic and structural criteria with the initial airfoil contour. This construction synthesizes the meanline and thickness distribution of a Controlled Diffusion Airfoil from a distribution of circular arcs and ellipses. The parameters for these curves are functionally related to the aerodynamic requirements. The current design procedure selects an airfoil, using this construction, and then utilizes the analytical program to verify the required range of off-design performance. Modifications are made to the initial parameter selection if added incidence or Mach range is required.

Development of a Series of Controlled Diffusion Airfoils – Cascade Test Procedure. The eight Controlled Diffusion Airfoils designed using this procedure and their comparison standard series airfoils were tested in the United Technologies Research Center High-Speed Cascade Tunnel from 1978 to

Downloaded 01 Jun 2010 to 171.66.16.70. Redistribution subject to ASME license or copyright; see http://www.asme.org/terms/Terms_Use.cfm

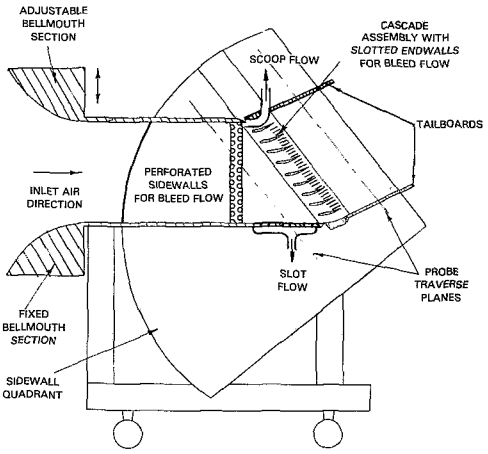


Fig. 11 Schematic of the United Technologies Research Center High-Speed Cascade Tunnel

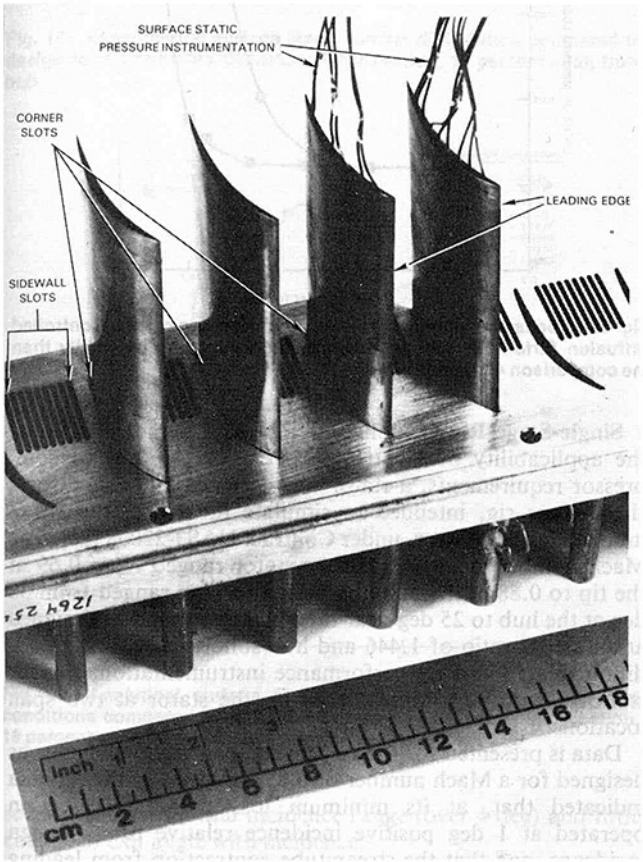


Fig. 12 A dual system of slots is used to control AVDR and corner boundary layers

1981 [19]. This facility (Fig. 11) has been utilized extensively for compressor airfoil testing since 1967 and is the latest in a series of cascade tunnels which have been used by Pratt & Whitney Aircraft to provide compressor airfoil design correlations since 1944. This facility, which has test capabilities similar to the DFVLR cascade tunnel, is an open circuit tunnel which uses pressurized air exhausting through the test section to atmospheric pressure. It is capable of testing airfoils of 4-in. span and 2-in. chord over a range of inlet Mach number from 0.4 to choke and over a Reynolds number range from Re = 400,000 to Re = 800,000, satisfactory for most compressor airfoil requirements.

Tunnel side wall boundary layers are removed by perforated plates upstream of the test section, and top and bottom wall boundary layers are removed by a scoop on the top wall and slots on the bottom wall. Tailboards are used to control periodicity within the cascade pack. Axial velocity density ratio, AVDR, is varied using a system of side wall suction slots located within the cascade pack, aft of the minimum pressure region of the airfoil flow field, to avoid recirculation, Fig. 12. A completely independent suction system is used to remove corner boundary layers through slots at the intersection of the airfoil suction surface with the side walls, to prevent spanwise flow of boundary layer fluid.

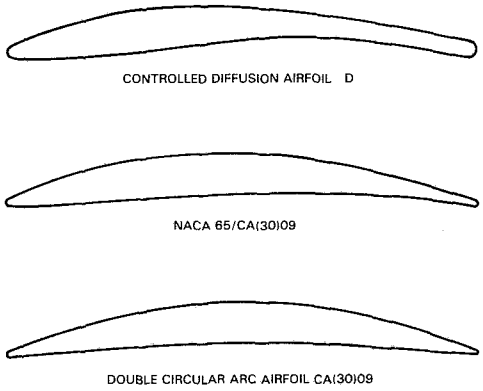


Fig. 13 Controlled Diffusion Airfoil "D" has more robust leading and trailing edges than standard series comparison airfoils

Airfoils are set in at constant stagger; the number of airfoils depending on stagger, gap chord ratio and inlet angle. The entire cascade is supported between drums which are rotated relative to the inlet section to achieve a desired inlet angle. Test procedure is to vary Mach number and AVDR at each inlet angle, and to vary the inlet angle from choke to stall to completely define the incidence and Mach number ranges of the cascade airfoil, and its response to streamtube contraction.

Data acquisition includes an upstream traverse for total pressure and flow angle, a downstream traverse over six gaps for exit angle and total pressure, static pressures on the side walls at the upstream and downstream traverse locations and at intermediate axial stations, and static pressures on the airfoil surfaces, defining one gap. Data is reduced for each airfoil individually to eliminate the effects of any residual nonperiodicity in the upstream conditions.

Development of a Series of Controlled Diffusion Airfoils – Cascade Test Results. Comparison cascade tests were run for a series of design conditions intended to demonstrate the range of application for which Controlled Diffusion Airfoils could offer improved aerodynamic and structural performance.

Controlled Diffusion Airfoil "D" is compared to a Double Circular Arc airfoil and to a NACA 65/CA profile cascade, both typically used for high transonic Mach number requirements. As can be seen in Fig. 13, the profile of the Controlled Diffusion Airfoil is considerably more robust at leading and trailing edges than the Double Circular Arc airfoil and, at the trailing edge, the 65/CA airfoil. All three cascades were designed for an inlet Mach number of 0.7, inlet angle of 30 deg, flow turning of 13.6 deg, AVDR of 1.07, solidity of 0.933, and maximum thickness of 9 percent of chord. Their relative performance is compared in Figs. 14 and 15. At their minimum loss incidence, Fig. 14, the Controlled Diffusion Airfoil had higher critical Mach number than either of the two comparison airfoils, despite its more robust profile. In addition, it had superior incidence angle range to the two comparison cascades at all Mach numbers tested, Fig. 15.

A comparison to a low-Mach-number airfoil type is illustrated in Figs. 16, 17, and 18. A NACA 400 series airfoil

Downloaded 01 Jun 2010 to 171.66.16.70. Redistribution subject to ASME license or copyright; see http://www.asme.org/terms/Terms_Use.cfm

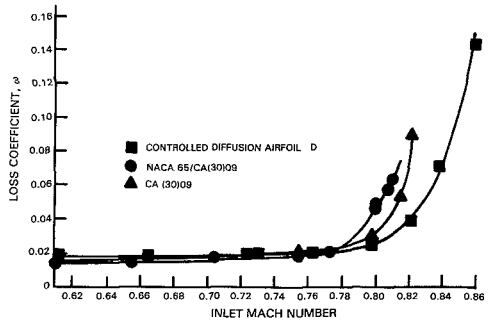


Fig. 14 Controlled Diffusion Airfoil "D" had higher critical Mach number than the comparison standard series airfoils when compared at their minimum loss incidence angles

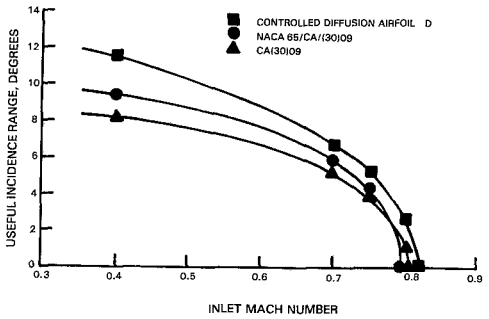


Fig. 15 Controlled Diffusion Airfoil "D" had superior incidence angle range at all Mach numbers

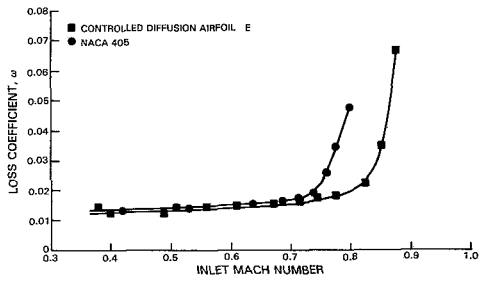


Fig. 16 Controlled Diffusion Airfoil "E" had higher critical Mach number and equivalent loss at low Mach number to the NACA 400 series comparison airfoil

is compared to Controlled Diffusion Airfoil "E." Both airfoils were designed for inlet flow angle of 30 deg, flow turning of 15 deg, AVDR of 1.07, solidity of 0.870, and maximum thickness 5 percent of chord. The Controlled Diffusion Airfoil, although designed for a high-Mach-number requirement, 0.80, exhibited equivalent minimum loss and incidence range, even at the low-Mach-numbers (less than 0.5) for which the NACA 400 series airfoil would be applied (Figs. 16, 17). The relative loading capability of the two airfoils is illustrated in Fig. 18. For Mach numbers below 0.65, to avoid critical Mach number problems for the NACA 400 series airfoil, the loading for each airfoil was varied by changing incidence angle and by applying suction to the cascade endwalls, thus lowering AVDR, until the airfoil stalled. The data points obtained during this procedure were plotted as loss verus D factor. For clarity, for each airfoil the minimum loss data points, at each D factor level, were joined by a line and then the points above the line were eliminated. The remaining locus of minimum loss points, illustrated in Fig. 18, represents the low loss loading limits for each airfoil. This is somewhat analogous to an isolated airfoil lift to drag curve. It can be seen that the Controlled Diffusion Airfoil was capable of sustaining a much higher loading than was the NACA 400 series airfoil.

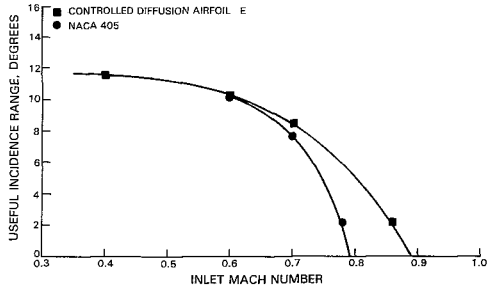


Fig. 17 Controlled Diffusion Airfoil "E" had higher incidence range than the comparison NACA 400 series airfoil at high-Mach-number and equivalent range at low-Mach-number

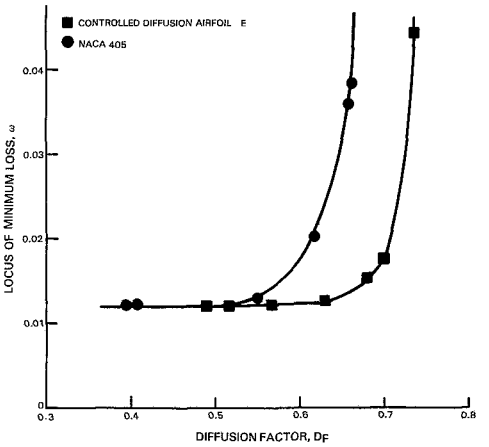


Fig. 18 Locus of minimum loss – maximum loading points. Controlled Diffusion Airfoil "E" had significantly higher loading capability than the comparison 400 series airfoil.

Single-Stage Rig Demonstration. As a demonstration of the applicability of Controlled Diffusion Airfoils to compressor requirements, a stator was designed and tested for a single-stage rig, intended to simulate the front stage of a multistage compressor, under Contract NAS3-22008 [20]. The Mach number incident upon the stator ranged from 0.69 at the tip to 0.88 at the hub and design turning ranged from 33 deg at the hub to 25 deg near the tip. The stator was designed at an aspect ratio of 1.446 and hub solidity of 1.429. In addition to standard rig performance instrumentation, surface static pressure taps were placed on the stator at two span locations.

Data is presented for the 16 percent span section which was designed for a Mach number of 0.85. Analysis of the rig data indicated that, at its minimum loss point, this section operated at 1 deg positive incidence relative to its design incidence, and that the streamtube contraction from leading to trailing edge was 13 percent higher than anticipated. This can be seen by comparing the measured Mach number distribution to the design Mach number distribution, Fig. 19. When the rig incidence angle and streamtube contraction are used in the analytical cascade calculation of [16], using streamtube area change to simulate the effect of radius change, the analtyical Mach number distribution closely matches the experimental distribution, Fig. 20.

No indication of shock wave formation is evident in the analysis, which would indicate a sharp discontinuity if a shock were present. The boundary layer calculation [11] indicated no separation. We conclude that there is also no experimental evidence for shock wave formation or boundary layer separation, based on the agreement of the analytical and experimental Mach number distributions. The 16 percent span section loss and exit angle are presented in Fig. 21. It can be seen that, even at its high incident Mach number of 0.85, the

Downloaded 01 Jun 2010 to 171.66.16.70. Redistribution subject to ASME license or copyright; see http://www.asme.org/terms/Terms_Use.cfm

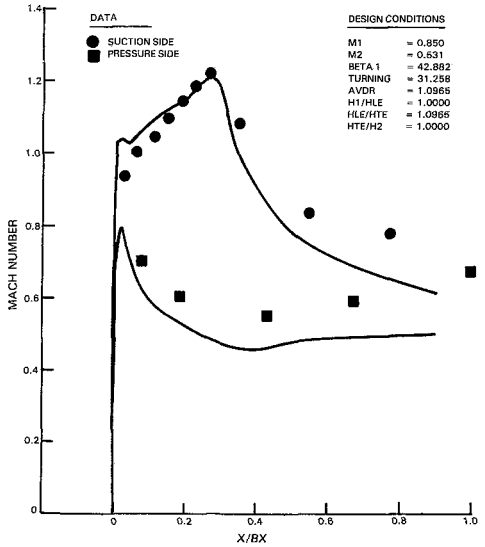


Fig. 19 Experimental surface Mach number distribution compared to design for a Controlled Diffusion stator section, 16 percent span from hub

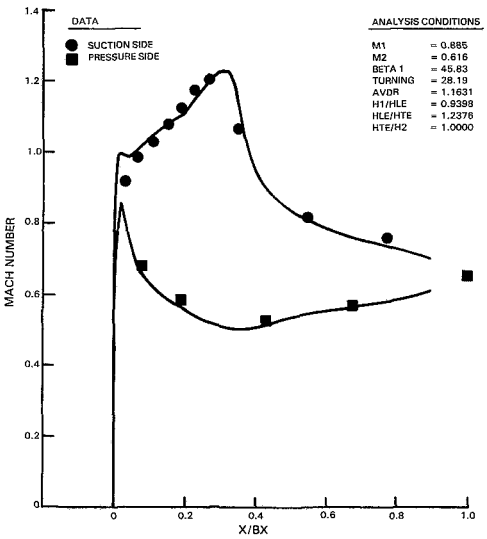


Fig. 20 Analytical surface Mach number distribution at rig inlet conditions compared to data for a Controlled Diffusion stator section, 16 percent span from hub, at leading edge plane Mach 0.85

section has substantial incidence range (over 4 deg) and little change of exit angle with incidence.

A comparison is made between the performance of the Controlled Diffusion Airfoil stator and a Multiple Circular Arc stator tested in the same rig under NASA Contract NAS3-20809, "Study of Blade Aspect Ratio on a Compressor Front Stage," [21]. Although the two tests do not strictly constitute a back-to-back comparison, since the axial location of the two stators, and hence the inlet Mach number, were not identical, by comparing the stators at equivalent inlet Mach number, a reasonable comparison can be made. In Fig. 22, the minimum full span losses of the two stators are compared as a function of mass average inlet Mach number, indicating that the Controlled Diffusion Airfoil stator had lower full span loss at every equivalent condition through its design speed. Figure 23 presents the spanwise distribution of loss for the two stators at their minimum loss points. For this comparison, the Multiple Circular Arc stator is illustrated at 95 percent rotor speed, to equalize its inlet Mach number to that of the Controlled Diffusion Airfoil stator at 100 percent rotor speed. The

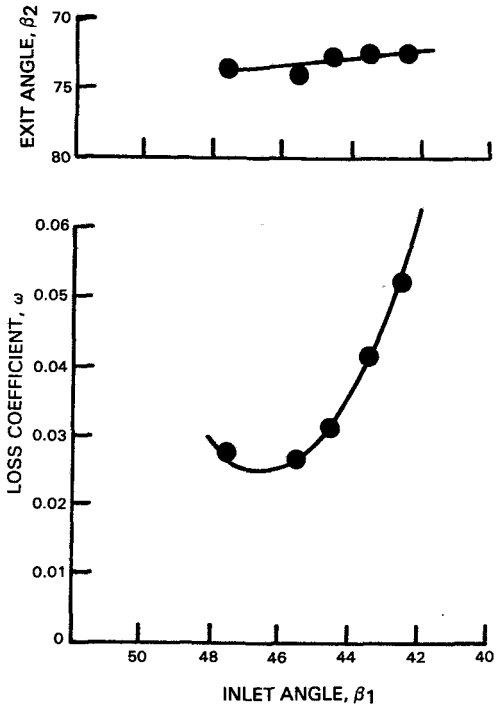


Fig. 21 Performance of Controlled Diffusion stator section, 16 percent span from hub, at Mach number 0.85

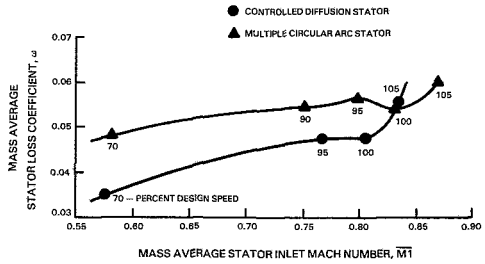


Fig. 22 Minimum full span average loss of the Controlled Diffusion stator is less than that of a multiple circular arc stator tested in the same single-stage rig, at equivalent inlet Mach numbers, through design speed

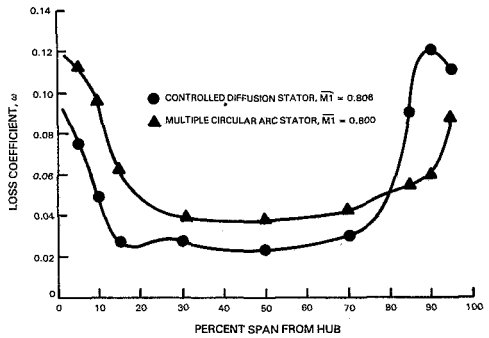


Fig. 23 A Comparison of the spanwise loss distributions of the Controlled Diffusion stator at its 100 percent speed minimum loss point and the multiple circular arc stator at its 95 percent speed minimum loss point indicates that, at equivalent Mach number, the Controlled Diffusion stator had lower loss over the core flow region

superiority of the Controlled Diffusion Airfoil stator is evident for the core flow region.

Multistage Application. As a result of the performance benefits demonstrated in cascade and rig testing, the Con-

Downloaded 01 Jun 2010 to 171.66.16.70. Redistribution subject to ASME license or copyright; see http://www.asme.org/terms/Terms_Use.cfm

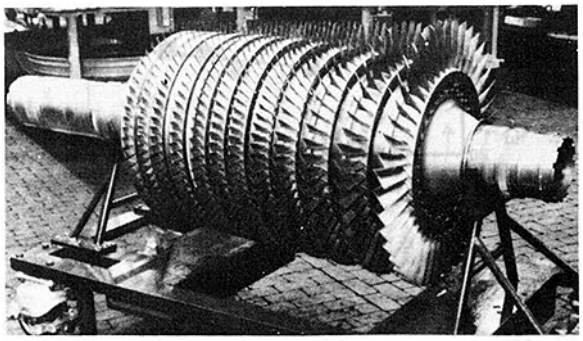


Fig. 24 PW2037 high-pressure compressor rig rotor employing controlled diffusion airfoils

trolled Diffusion Airfoils, developed in this project, have been incorporated in the Pratt & Whitney Aircraft Energy Efficient Engine High Pressure Compressor, developed under Contract NAS3-20646, and in the compressor of the PW2037 Advanced Transport Engine, Fig. 24. Both compressors were tested during 1981. The data available do not permit definitive evaluation of the Controlled Diffusion Airfoil performance in the multistage environment. However, both compressors achieved stable, efficient operation in their initial builds.

Conclusions

A new series of airfoils has been developed for multistage compressor application employing advanced transonic cascade computational capability to control the diffusion rate on the airfoil suction surface. A geometric construction has been developed which, for most applications, provides an initial airfoil shape capable of achieving design criteria intended to prevent the development of shock waves or boundary layer separation on the airfoil suction surface and provide a range of efficient, stable operation.

Cascade testing has demonstrated the feasibility of achieving shock-free transonic cascade operation, the ability of Controlled Diffusion Airfoils to provide increased incidence range, increased critical Mach number and more durable airfoil shapes for high transonic Mach number requirements, and ability to provide higher loading capability and equivalent incidence range for low-Mach-number applications. Prevention of boundary layer separation provides reduced exit angle deviation and reduced sensitivity of deviation to incidence angle.

Single-stage compressor testing has demonstrated that Controlled Diffusion Airfoils can provide efficient, shock-free performance, with wide incidence range and insensitive exit angle deviation in a high-Mach-number compressor environment. Improved incidence range can provide increased compressor surge margin and ease of stage matching in a multistage environment, leading to reduced development cost.

Controlled Diffusion Airfoils have been incorporated in Pratt & Whitney Aircraft advanced multistage compressors.

Acknowledgment

The authors wish to acknowledge John F. Dannenhoffer, III and David Spear for their contributions to the analytical procedures; Joseph Lubenstein, Alan Ross, and Brian Robideau for development of the airfoil geometric design procedure; William Taylor and John Horan for their experimental cascade test support; and Roy Behlke and James Brooky for the analysis of the single-stage test results. Part of this effort was supported by NASC Contract N00019-77-C-0546, technical monitor Dr. Max Platzer, and NASA Contract NAS3-22008, technical monitor Thomas Gelder.

References

1 Whitcomb, R. T., and Clark, L. R., "An Airfoil Shape for Efficient Flight at Supercritical Mach Numbers," NASA TMX-1109, May 1965.

2 Bauer, F., Garabedian, P., and Korn, D., "Supercritical Wing Sections," *Lecture Notes in Economics and Mathematical Systems*, Vol. 66, Springer-Verlag, New York, 1972.

3 Bauer, F., Garabedian, P., Korn, D., and Jameson, A., "Supercritical Wing Sections II," *Lecture Notes in Economics and Mathematical Systems*, Vol. 108, Springer-Verlag, New York, 1975.

4 Bauer, F., Garabedian, P., and Korn, D., "Supercritical Wing Sections III," *Lecture Notes in Economics and Mathematical Systems*, Vol. 150, Springer-Verlag, New York, 1977.

5 Korn, D. G., "Numerical Design of Transonic Cascades," Courant Institute of Mathematical Science, ERDA Mathematics and Computing Lab. Report C00-3077-72, Jan. 1975.

6 Garabedian, P., and Korn, D., "A Systematic Method for Computer Design of Supercritical Airfoils in Cascade," *Communications on Pure and Applied Mathematics*, Vol. XXIX, 1976.

7 Stephens, H. E., "Application of Supercritical Airfoil Technology to Two-Dimensional Compressor Cascades: Comparison of Theoretical and Experimental Results," *AIAA Journal*, Vol. 17, No. 6, June 1979.

8 Sanz, J. M., "Design of Supercritical Cascades with High Solidity," AIAA 82-0954, St. Louis, June 1982.

9 Ives, D. C., and Liutermoza, J. F., "Analysis of Transonic Cascade Flow Using Conformal Mapping and Relaxation Techniques," *AIAA Journal*, Vol. 5, No. 5, May 1977.

10 Ives, D. C., and Liutermoza, J. F., "Second Order Accurate Calculation of Transonic Flow Over Turbomachinery Cascades," *AIAA Journal*, Vol. 17, No. 8, Aug. 1979.

11 McNally, W. D., "Fortran Program for Calculating Compressible Laminar and Turbulent Boundary Layers in Arbitrary Pressure Gradients," NASA TND-5681, May 1970.

12 Stephens, H. E., and Hobbs, D. E., "Design and Performance Evaluation of Supercritical Airfoils for Axial Flow Compressors," Final Report for NASC Contract N00019-77-C-0546, PWA Report FR 11455, June 1979.

13 Sulam, D. H., Keenan, M. S., and Flynn, J. T., "Single-Stage Evaluation of Highly-Loaded Multiple-Circular-Arc Rotor High-Mach-Number Compressor Stages," NASA CR-7264, PWA-3772.

14 Caspar, J. R., Hobbs, D. E., and Davis, R. L., "The Calculation of Two-Dimensional Compressible Potential Flow in Cascades Using Finite Area Techniques," *AIAA Journal*, Vol. 18, No. 1, Jan. 1980.

15 Caspar, J. R., "A Model Problem Study of Transonic Potential Flow Procedures," AIAA 80-0337, Jan. 1980.

16 Caspar, J. R., "Unconditionally Stable Calculation of Transonic Potential Flow Through Cascades Using and Adaptive Mesh for Shock Capture," ASME Paper 82-GT-238, London, Apr. 1982.

17 Dunham, J., "Prediction of Boundary Layer Transition on Turbomachinery Blades," AGARD-AG-164, Dec. 1972.

18 Roberts, W. B., "Calculation of Laminar Separation Bubbles and their Effect on Airfoil Performance," AIAA 79-0285, Jan. 1979.

19 Taylor, W. E., "UTRC Variable Geometry High-Speed Cascade Tunnel Facility," UTRC Report R80-231889-5, Apr. 1980.

20 Canal, E., Chisholm, B. C., Lee, D., and Spear, D. A., "Study of Controlled Diffusion Stator Blading, I. Aerodynamic and Mechanical Design Report," NASA CR-165500, Jan. 1981.

21 Behlke, R. F., Brooky, J. D., Canal, E., "Study of Blade Aspect Ratio on a Compressor Front Stage—Final Report," NASA CR-159556, Nov. 1980.

Downloaded 01 Jun 2010 to 171.66.16.70. Redistribution subject to ASME license or copyright; see http://www.asme.org/terms/Terms_Use.cfm

Redesign and Performance Analysis of a Transonic Axial Compressor Stator and Equivalent Plane Cascades With Subsonic Controlled Diffusion Blades

R. Dunker

H. Rechter

H. Starken

H. Weyer

Propulsion Institute, DFVLR,
5000 Köln 90,
West Germany

In order to verify a new controlled diffusion blade design concept, the stator of an existing transonic axial compressor stage was redesigned. Stator and equivalent cascade tests revealed the potential of such blades for a considerably higher aerodynamic loading than it has been applied up to now. The design procedure is described, and the results of plane cascade and stage testing are submitted, including performance analysis of both cascade and stator blade sections, at design and off-design operating conditions. The blade profile shapes and cascade geometries were calculated by means of an inverse, two-dimensional method taking also into account the axial velocity density ratio (AVDR). This design concept is essentially based on prescribed blade pressure distributions, which are optimized with respect to the blade boundary layer development. The flow phenomena are illustrated by means of loss and flow turning investigations, blade pressure distributions, and laser velocimetry data. The test results reveal that the two-dimensional approach applied is quite promising for the three-dimensional blade design. Finally, overall and blade element performance comparisons between the original NACA 65 profiled stator and the redesigned one demonstrate the favorable flow behavior of the new stator, as well as the great potential of the controlled diffusion blade concept.

Introduction

Future aircraft propulsion systems will require compressors with higher pressure ratios and efficiencies than currently in use in order to reduce fuel consumption as well as engine size and weight. This implies compressor stages with transonic or even supersonic relative inflow velocities to the rotors and supercritical flow conditions for the stators. Conventional blade design techniques may be called in question to meet the corresponding blade loadings. Therefore, research and development activities are concentrated on establishing new blade design methods and investigating their capabilities by means of cascade and stage experiments.

Within these research and development activities, it is intended at the DFVLR Propulsion Institute to design an advanced highly loaded compressor stage that could be representative for the inlet stage of a multistage core compressor. This program relies on experience with a single-stage axial transonic compressor, which has been investigated extensively in the past, and on cascade results obtained with a new inverse blade calculation method. In order to reduce risk and costs, it was considered necessary as a first step to apply the controlled diffusion concept to subsonic cascades and to prove its capability under the three-dimensional flow conditions of a turbomachine. For this purpose the stator blades of the aforementioned transonic stage have been redesigned using the inverse calculation method.

Contributed by the Gas Turbine Division of THE AMERICAN SOCIETY OF MECHANICAL ENGINEERS and presented at the 28th International Gas Turbine Conference and Exhibit, Phoenix, Arizona, March 27–31, 1983. Manuscript received at ASME Headquarters January 4, 1983. Paper No. 83-GT-208.

Stage Design Consideration

The aerodynamic design considerations and the various experimental investigations of the original stage are discussed in detail in [1–3]. Therefore, only a brief description of the main parameters will be presented in the following:

The original machine was a single-stage axial transonic compressor without inlet guide vanes designed for a total pressure ratio of 1.51 and a mass flow rate of 17.3 kg/s at a blade tip speed of 425 m/s.

The rotor inlet diameter was 400 mm with a hub-to-tip ratio of 0.5. The maximum inlet Mach number obtained a value of 1.37, and the maximum diffusion factor was evaluated to be 0.52. The rotor consisted of 28 MCA-profiled blades with a tip chord length of 60 mm, which resulted in quite usual blade solidities between 1.34 and 2.

Copyright © 1984 by ASME
Downloaded 01 Jun 2010 to 171.66.16.70. Redistribution subject to ASME license or copyright; see http://www.asme.org/terms/Terms_Use.cfm

Table 1 Design performance parameters for stator UKS compared to some data of original stator NACA 65

Stator UKS/31

Number of blades: 31

Sec. no.	R^* %	R mm	Z_{LE} mm	Z_{ST} mm	Z_{TE} mm	Sec. no.	Ma_{LE}	β_{LE}	β_{TE}	Ω
Hub	0	117.50	123.60	139.0	160.87	Hub				
1	10	124.55	123.60		160.87	1	0.6775	133.4	90.0	1.0400
2	30	138.65	123.55		161.50	2	0.6352	129.2		1.0573
3	50	152.75	123.31		161.10	3	0.6012	128.6		1.053
4	70	166.85	123.46		161.33	4	0.5776	127.4		1.0622
5	90	180.95	123.46		161.00	5	0.5700	127.4	90.0	1.0893
Tip	100	188.00	123.46	139.0	161.00	Tip				

Stator NACA 65/60

Number of blades: 60

Sec. no.	c mm	σ	t_m/c	D_{ol}	Sec. no.	c mm	σ	t_m/c	D_{ol}
Hub	40.00	1.6795	0.06		Hub	30.00	2.4419	0.08	
1		1.5845		0.5259	1		2.2852		0.3996
2		1.4233		0.4578	2		2.0317		0.3417
3		1.2920		0.4664	3		1.8367		0.3171
4		1.1829		0.4524	4		1.6828		0.3075
5		1.0906		0.4340	5		1.5615		0.3251
Tip	40.00	1.0498	0.06		Tip	30.00	1.5143	0.08	

The stator had 60 blades which were composed of NACA 65 profiles with circular arc camberlines. The maximum inlet Mach number was 0.7, the diffusion factor was estimated to be about 0.42.

For the stator redesign, the original flowpath of the stage was retained. The positions of the blade leading edges were also unchanged for the new stator. Thus, the distance between rotor trailing and stator leading edge was the same for both the old and the new stator. In order to retain the conditions of continuity and especially of radial equilibrium, it is normally required for a stage redesign with altered stator blading to adjust the flow path downstream of the rotor. In this case, however, the aforementioned procedure has to be employed for reasons of manufacturing, costs, and time.

The design flow parameters were taken from blade leading and trailing edge values, which has been experimentally obtained with the original stator when operating at design speed with maximum efficiency for a mass flow of 17.15 kg/s. These data are summarized in Table 1, and the corresponding cascade notations are illustrated in Fig. 1.

Having in mind the last two paragraphs and considering usual procedures of turbomachinery design, it is conceivable

Nomenclature

c = chord length

D_{01} = diffusion factor, equal to $1-(w'_{TE}/w'_{LE})+|((rw'_\Theta)_{TE}-(rw'_\Theta)_{LE})/((r_{TE}+r_{LE})\sigma(w'_{LE}))|$

i = incidence angle

M,Ma = Mach number

$\dot{m}_{red}$ = reduced mass flow (equivalent mass flow) $\dot{m}_{red}=\dot{m}\cdot\sqrt{\Theta'}/\delta$

n = rotative speed

n_A = design speed (20.260 rpm)

p = static pressure

p_t,p_{tot} = total pressure

R,r = radius

R^* = relative blade height from hub (percent), equal to $(R-R_{hub})/(R_{tip}-R_{hub})\cdot 100$

t = blade pitch

t_m = maximum profile thickness

T_t = total temperature

w = velocity

X,x = Cartesian coordinate

x/c = relative blade chord

Y,y = Cartesian coordinate

Z = coordinate along machine axis

Z,z = Cartesian coordinate

β = flow angle against circumferential direction

β_s = stagger angle

γ = ratio of specific heats

Δ = difference

δ = ratio of rotor-inlet total pressure to standard pressure of 10.13 N/cm^2

η_{is} = stage isentropic efficiency, equal to $(\Pi_{tot})^{(\gamma-1)/\gamma}-1)/(\Delta T_t/T_{t1})$

Θ = ratio of rotor-inlet total temperature to standard temperature of 288.15 K

Π_{tot} = stage total pressure ratio

ρ = density

σ = solidity, ratio of chord to spacing, $\sigma=c/t$

Ω = axial velocity density ratio (AVDR), equal to $(\rho_2 w_2 \sin\beta_2)/(\rho_1 w_1 \sin\beta_1)$

ω = total pressure loss coefficient, equal to $(p_{t1}-p_{t2})/(p_{t1}-p_1)$; and $((p'_{tid})_{TE}-(p'_t)_{TE})/((p'_t)_{LE}-(p)_{LE})$

Subscripts

is = isentropic

LE = blade leading edge

m = maximum value

ST = stacking line

TE = blade trailing edge

Θ = tangential direction

1 = inlet plane

2 = outlet plane

$*$ = related value

$'$ = relative to blade

Downloaded 01 Jun 2010 to 171.66.16.70. Redistribution subject to ASME license or copyright; see http://www.asme.org/terms/Terms_Use.cfm

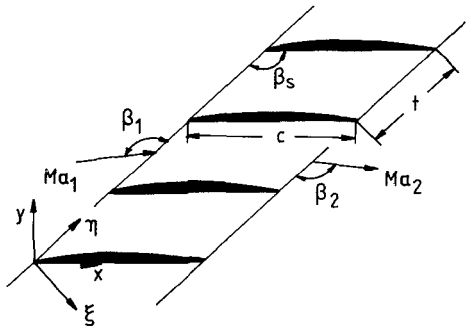


Fig. 1 Cascade notation

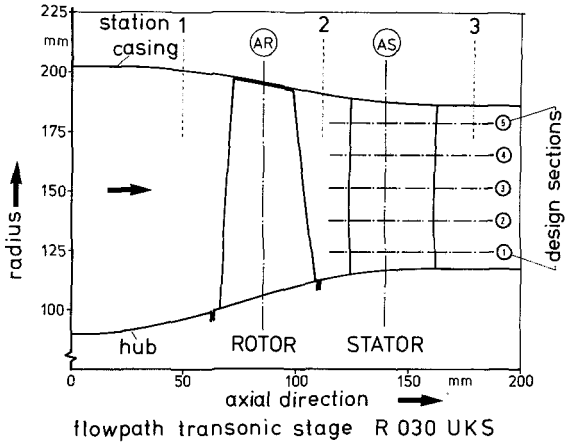


Fig. 2 Flow path geometry of stage R 030-UKS and design stator blade sections

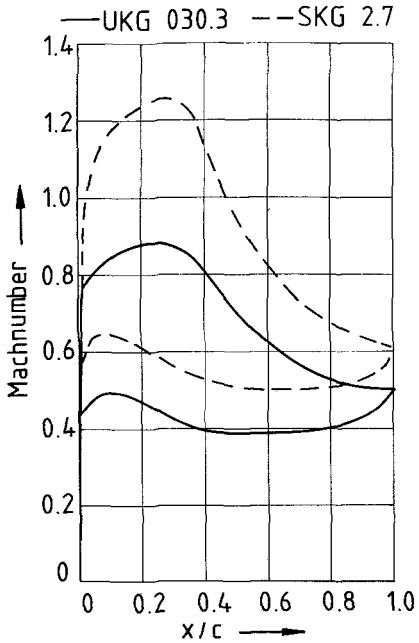


Fig. 3 Prescribed Mach number distribution for blade design of stator midsection (UKG 030.3) and reference distribution (SKG 2.7)

that differences may be expected to some extent between the performance characteristics of the new stage and the reference one.

The main features of the new stator blading may be described briefly as follows:

- The number of blades has been reduced from 60 to 31.
- The blade chord length has been enlarged from 30 to 40 mm in order to have enough profile thickness available for installation of surface pressure taps; this means an effective reduction of blade number by about 1.7.
- The maximum diffusion factor could be increased to a value of 0.55 due to the experience gained with former cascade investigations.

The flow path of the redesigned stage is shown in Fig. 2; geometric data and blade element parameters are presented in Table 1. The stator blading has been designed by means of five sections parallel to the axis. These blade sections are indicated in Fig. 2 by circled numbers.

The following sections of this paper deal with two main aspects of the stator redesign:

At first, the blade design concept itself and the main design details of the aforementioned sections are described. Three sections (near hub, at midspan height, and near tip) were tested in the transonic cascade tunnel. The main results are submitted and discussed.

In the second part of our paper, studies are presented that concern the analysis of the new stage and the original one. The overall performance of the new stage is discussed; the blade element performance of both stages is compared taking also into account the results of the cascade tests. Additional flow phenomena presented include blade surface pressure distributions measured for the previously mentioned sections of the redesigned stator blades, as well as laser velocimetry data that were elaborated within this stator.

Cascade Investigations

Stator Blade Design.

Background. In common design practice, profile series, together with empirically derived correlations for flow losses and flow turning, are used to develop compressor bladings. With higher stage loadings, however, classical profile shapes often exhibit undesired losses. Especially when they are tested under supercritical flow conditions, one can always observe strong shock waves terminating the supersonic regions. A boundary layer thickening or even separating due to shock-boundary layer interaction takes place. The result is an excessive total pressure loss, which reduces blade efficiency and operating range.

These shock-induced flow losses stimulated the development of new blade design concepts based on advanced numerical methods rather than profile series. Apart from the supercritical flow case, it is worthwhile in general to start blade designs with consideration to boundary layer characteristics, thus establishing a procedure that covers the whole velocity range from incompressible to supercritical flow conditions. This method has to begin with a blade pressure distribution that is shock-free and which provides an unseparated boundary layer. The next problem is to find the related airfoil contour which generates this prescribed pressure distribution when operating under design conditions.

Several attempts have been made since 1974 to establish such a new design system for compressor cascades and to demonstrate its potential (see [4–9]). Meanwhile the name "controlled diffusion concept" has come into use to characterize these ideas.

In order to verify the controlled diffusion concept in a three-dimensional flow field Pratt & Whitney Aircraft is now conducting a test program in cooperation with NASA. A single stage controlled diffusion demonstrator was designed for this purpose. Reference [10] presents the aerodynamic design details. The blade design was done using a direct flow calculation method based on the blade-to-blade method of Caspar, Hobbs and Davis [11].

Similar investigations have been performed at the DFVLR

Downloaded 01 Jun 2010 to 171.66.16.70. Redistribution subject to ASME license or copyright; see http://www.asme.org/terms/Terms_Use.cfm

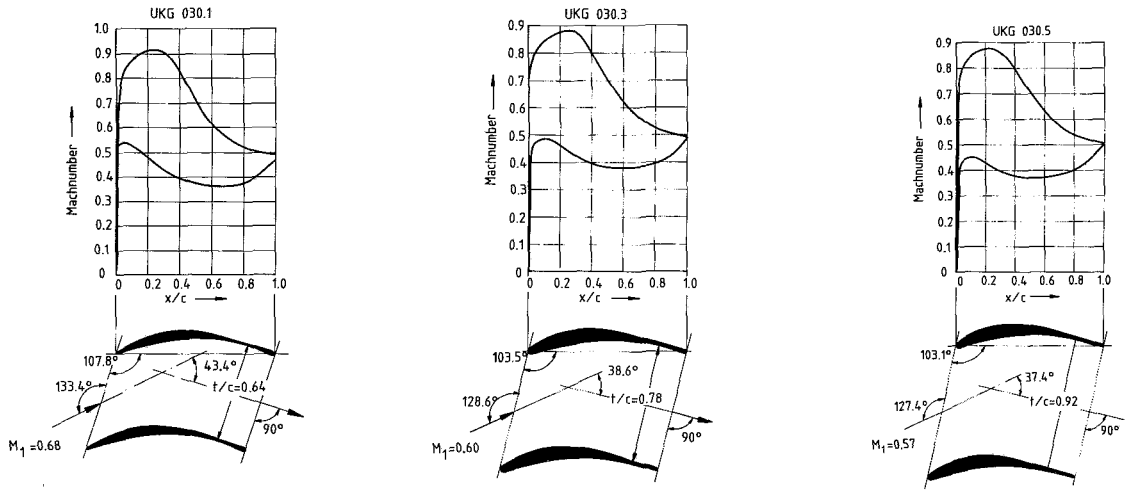


Fig. 4 Surface Mach number distributions and results of cascade design calculations

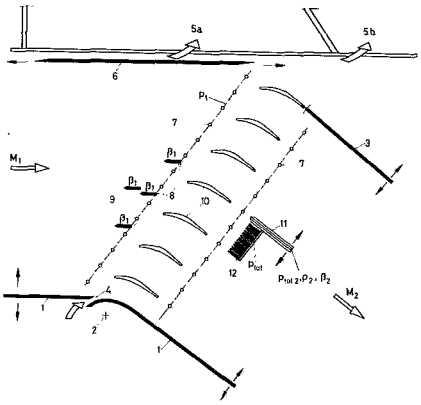


Fig. 5 Test section of the DFVLR transonic cascade tunnel

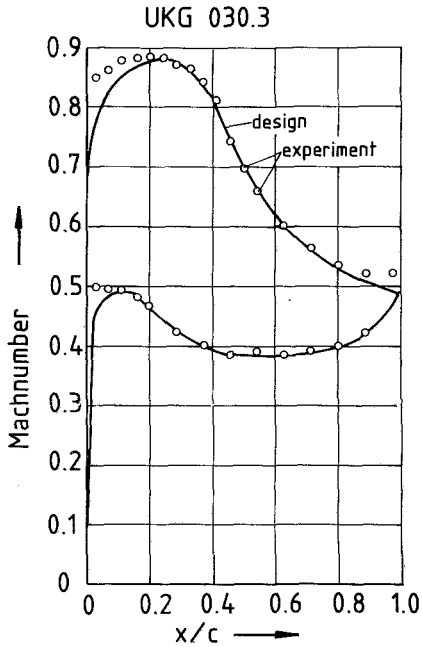


Fig. 6 Results of cascade tests: surface Mach number distribution (comparison design-experiment) at design point conditions

Propulsion Institute since 1978. The stator of an existing transonic axial compressor stage, originally consisting of NACA 65-blades, was redesigned for a considerably higher aerodynamic loading using Schmidt's inverse calculation method for the blade design [6, 7].

Design Procedure. Schmidt's method utilizes the plane cascade model which takes into account the axial velocity density ratio (AVDR). In order to design a complete stator by means of this method, a sufficient number of blade sections covering the blade height has to be specified. From these sections the final blade is derived by an appropriate interpolation procedure. It has to be mentioned that Schmidt's method cannot allow for a radius change up to now; thus, the design sections had to be parallel to the machine axis rather than on stream surfaces.

Five sections were selected as shown in Fig. 2. The aerodynamic and geometrical parameters of these sections are summarized in Table 1. Schmidt's method requires the velocity triangle and the blade pressure distribution as input data for each blade section.

The blade pressure distributions were prescribed on the basis of the experience gained with the two former supercritical cascade designs SKG 1.3 and SKG 2.7 [7, 8]. The SKG 2.7 cascade obtained the best agreement between measured and prescribed data. Therefore, its blade pressure distribution type was chosen as a reference for the new stator airfoils. Figure 3 presents the blade surface Mach numbers of the stator midsection, termed UKG 030.3, in comparison to the Mach number distribution of the SKG 2.7 cascade. The main characteristics of these distributions are:

- The suction surface leading edge region maintains a continuous acceleration up to the peak Mach number at approximately 30 percent chord length in order to provide a favourable pressure gradient for keeping the boundary layer laminar.
- Diffusion from peak Mach number is controlled on the rear portion of the airfoil in order to keep the boundary layer shape factor within the range of an unseparated turbulent boundary layer.
- The design pressure distributions of blade sections all were of the same type. Boundary layer calculations were performed using the integral method of Walz [12] to accomplish controlled diffusion without separation.

The results of the inverse flow field calculations are shown in Fig. 4. It displays the calculated airfoil shapes of three sections (hub, midspan, tip), termed UKG 030.1,3, and 5 in

Downloaded 01 Jun 2010 to 171.66.16.70. Redistribution subject to ASME license or copyright; see http://www.asme.org/terms/Terms_Use.cfm

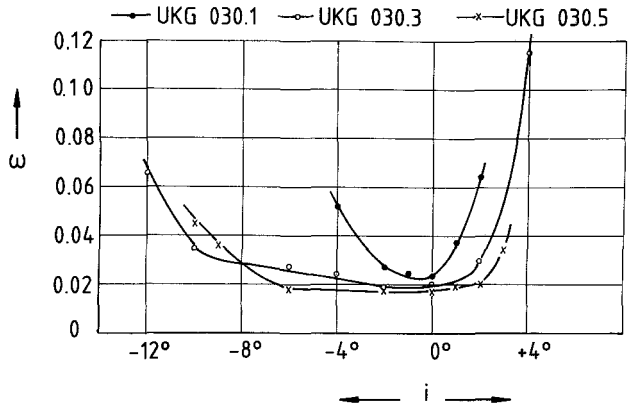


Fig. 7 Results of cascade tests: total pressure loss coefficient versus incidence angle at design inlet Mach number

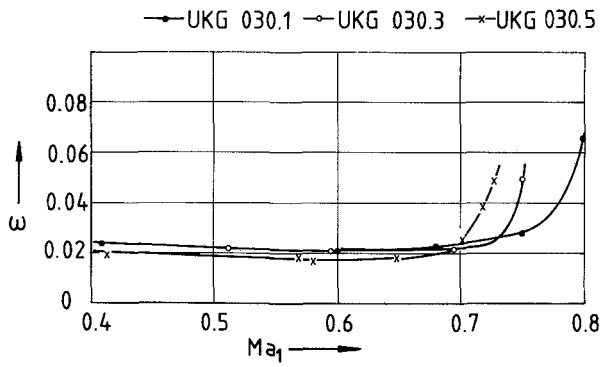


Fig. 8 Results of cascade tests: total pressure loss coefficient versus inlet Mach number at zero incidence

cascade formation together with the prescribed Mach number distributions.

Cascade Tests.

Test Facility. The DFVLR transonic cascade tunnel is already described in detail in [13]. Extensive information can also be found in [5] and [9]. A schematic sketch of the test section is presented in Fig. 5.

The cascade models usually consist of six blades with a chord length of 70 mm. In order to control the periodicity of inlet and outlet flow, the following instrumentation is provided: Static wall tapping upstream and downstream of the cascade parallel to the inlet and outlet plane (Fig. 5, position no. 7); three wedge type directional probes upstream of the cascade (position no. 8); and one probe further ahead of the center passage (position no. 9) in order to check the inlet flow direction.

The inlet Mach number is calculated from a mean value of the static pressure taps upstream of the cascade and from the total pressure measured in the settling chamber upstream of the test section inlet nozzle (position not to be seen in Fig. 5). Outlet total pressure, static pressure, and flow angle are measured with a combination probe traversing at midspan position (position no. 11). Fixed to this probe is a total pressure rake covering one blade pitch (position no. 12). Due to limited blade thickness, in most cases two blades have to be instrumented with static pressure taps. One blade is pressure tapped on the suction surface and the other on the pressure surface. Both are arranged in the center of the cascade formation (position no. 10). Thus, the blade surface pressures are recorded in the same blade passage.

In the cascade tunnel, several devices are available for the simulation of the infinite straight cascade model. These include a movable lower endwall (position no. 1), a part of which can be turned round position no. 2, a slot injection (position no. 4), a tailboard linked to the upper blade (position no. 3) and an upper endwall suction system whereby the air is removed through slots into two suction chambers (position no. 5*a*, *b*) which can be closed by a movable plate (position no. 6).

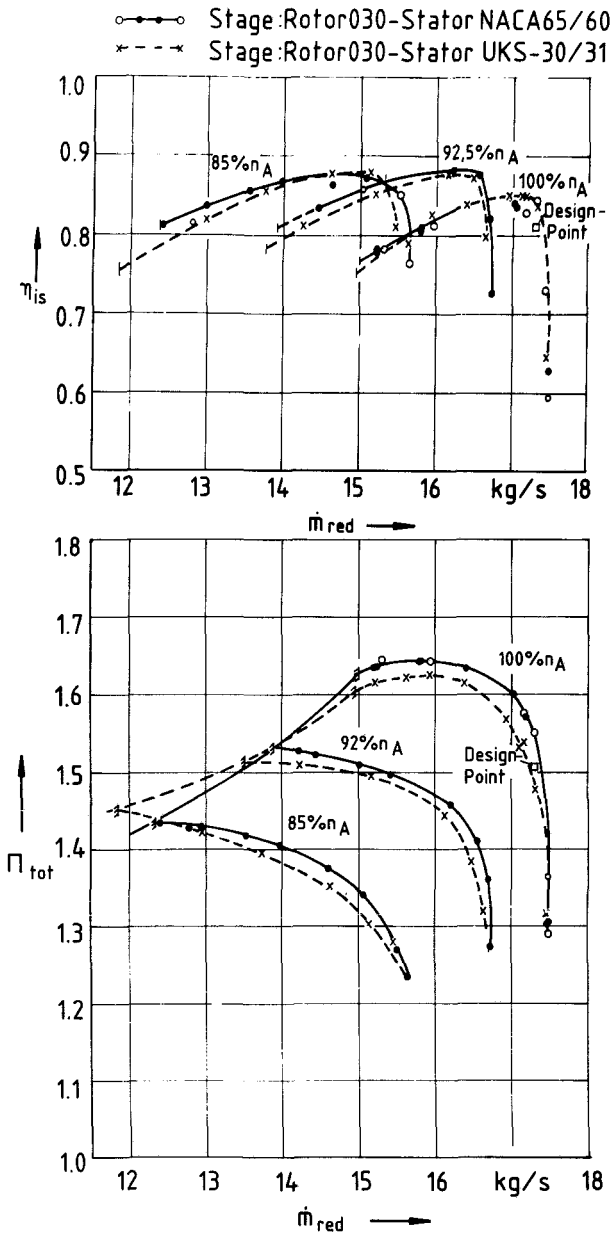


Fig. 9 Effects of stator redesign with controlled diffusion blades on overall performance

Test Results.

Three airfoils were tested:

UKG 030.1 (hub section)

UKG 030.3 (midsection)

UKG 030.5 (tip section)

Full details of the test results are given in [14]. In the following chapter only a short selection is presented.

The cascade performance for all three airfoils was first measured under design conditions, and the best match to the design Mach number distribution was thereby found. Figure 6 presents the result of the UKG 030.3 cascade (stator midsection), comparing the design distribution to experimentally determined values. The agreement is satisfactory. This was

Downloaded 01 Jun 2010 to 171.66.16.70. Redistribution subject to ASME license or copyright; see http://www.asme.org/terms/Terms_Use.cfm

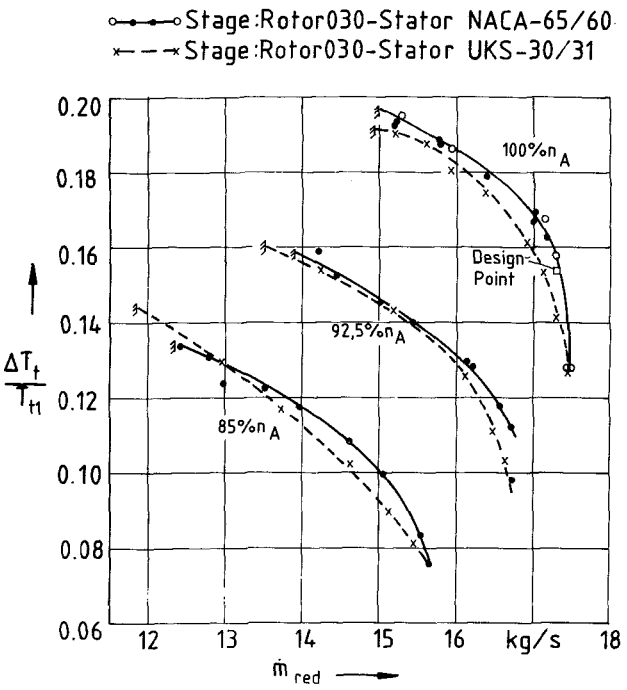


Fig. 10 Effects of stator redesign on overall total temperature rise

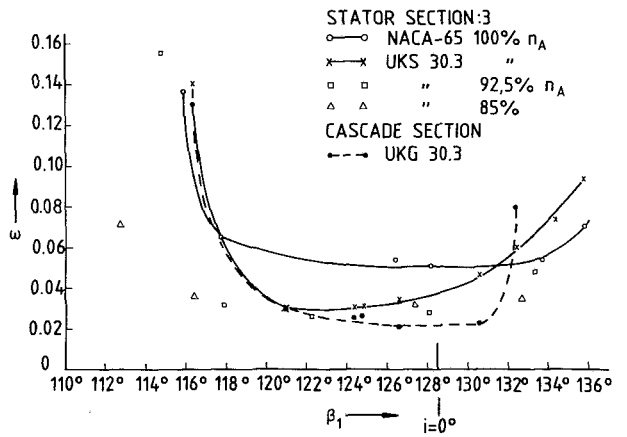


Fig. 11 Total pressure loss versus inlet flow angle for stator blade section 3 at 50 percent span from hub

also found for the two other cascades, in spite of some deviations in the leading edge regions due to inaccuracies of the inverse calculation method which have been discussed in detail in [7] and [8].

The flow conditions were also systematically varied over a wide range of inlet flow angles and inlet Mach numbers in order to determine the off-design performance of the cascades.

Total pressure loss characteristics of all three cascades varying the inlet flow angles at design Mach numbers are shown in Fig. 7. The chosen inlet angles corresponded to an incidence angle range from −12 to +4 deg. The midsection and the tip section cascade had a considerable broad useful operating range of more than 10 deg. The hub section cascade, however, turned out to have a significantly smaller range which must be attributed to the higher loading of this section. The losses at zero incidence (design conditions) were found to be around a value of 2 percent. The exit flow angles were 90 deg or even less over a wide incidence range and thus met the design objective.

Varying the inlet Mach numbers from 0.4 up to 0.8 at zero

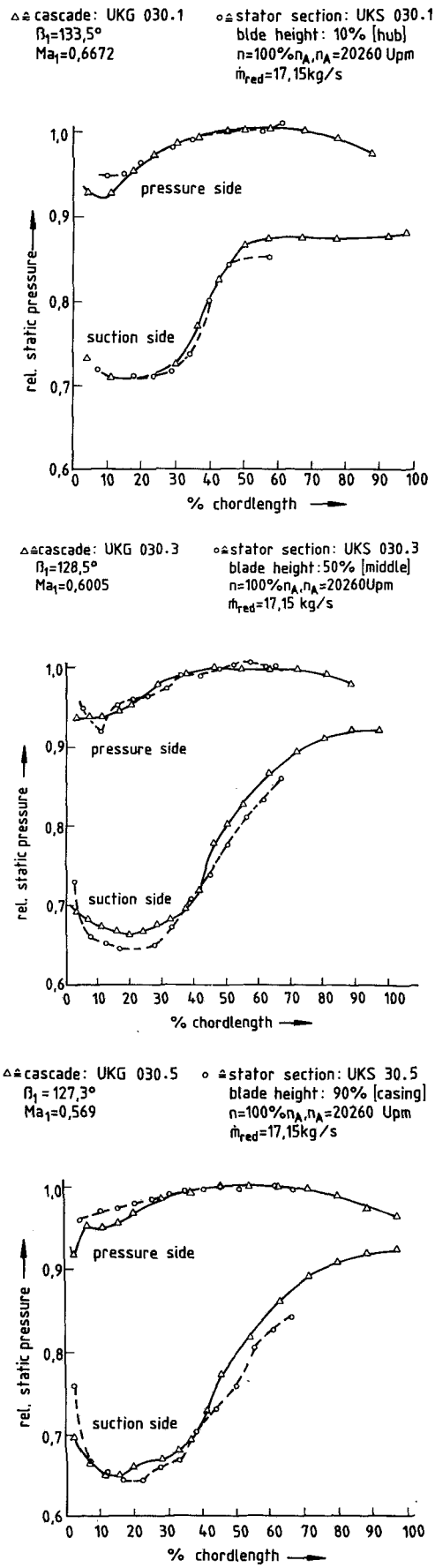


Fig. 12 Blade surface pressure distribution versus chord length for blade sections 1, 3 and 5 with reference static pressure at 45 percent chord for cascade and stage tests each

Downloaded 01 Jun 2010 to 171.66.16.70. Redistribution subject to ASME license or copyright; see http://www.asme.org/terms/Terms_Use.cfm

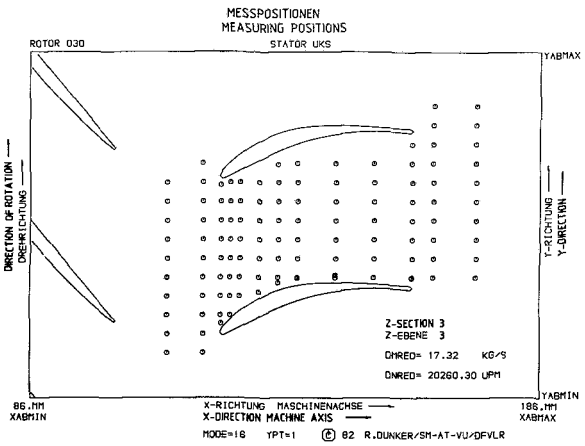


Fig. 13 L2F measuring positions in one blade channel of stator UKS for Cartesian section at 50 percent span

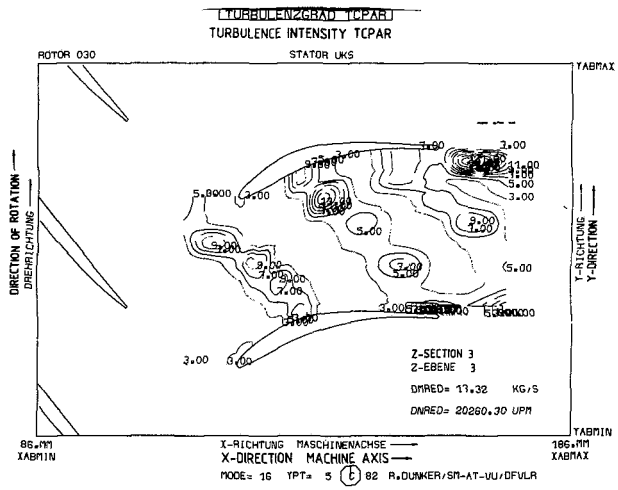


Fig. 14 Distribution of turbulence intensity parallel to local main flow direction (TCPAR) throughout one stator blade channel as in Fig. 13 at a distinct rotor blade setting

incidence, the obtained loss characteristics of all three cascades exhibited similar features (Fig. 8). The losses remained constant around a value of 2 percent over a large inlet velocity range up to values which exceeded the design objective. Beyond an inlet Mach number of 0.7, however, the losses of all three cascades increased considerably.

Comparing Stage Investigations

Overall Stage Performance Comparisons. In order to prove the validity of the stator redesign, the performance of the new stage R 030-UKS (UKS: stator blade row for subcritical inlet conditions) was measured and compared to the performance of the original stage R 030-NACA 65. The stage comparison was expected to reveal to what extent the performance, the operating range and the flow field would change considering the substantially reduced number of stator blades.

Test Procedure. The stage performance was investigated within the rotor speed range from 85 to 100 percent of design speed. For each flow, the data were taken in 15 radial positions, which were located upstream of the rotor (station 1, see Fig. 2) in the gap between rotor and stator (station 2) and downstream of the stage (station 3). At station 3, the instrumentation was also circumferentially traversed to 11 positions across the stator gaps. The axial location of the test planes is shown in Fig. 2. The survey measurement data consisted of total pressure, total temperature, and flow angle. Static pressures were measured at hub and casing of the instrumentation stations. The flow itself was measured with a Venturi nozzle. A more complete description of the instrumentation and test procedure is given in [2].

Calculation Procedure. The performance analysis is based only on the flow data downstream of the stator (station 3, Fig. 2). The pressures and temperatures at station 2 were determined as follows:

Within the iterative calculation procedure, at each radial survey position, total pressure and total temperature were transferred from station 3 to 2 in agreement with the actual streamlines. The circumferentially area-averaged total temperature of station 3 was assumed to be equal to the total temperature in station 2. The area-averaged mean value of the total pressure outside of the stator blade wake region, which had to be determined individually, was used as the total pressure in station 2. The radial distributions of static pressure and flow angle were calculated considering continuity of mass flow and radial equilibrium. Measured airflow and rotative speed were inputs.

All data were corrected to standard day conditions based on rotor inlet conditions. Overall total pressure and total temperature ratios rely on an energy average of the pressures and temperatures obtained from the calibrated survey instrumentation. Blade element data for the stator blade row were referred at the blade leading and trailing edges of the design sections. More details of the calculation procedure are given in [2].

Results and Discussions. An assessment of the effects of both stator blade rows is made by comparing the performance characteristics. Figures 9 and 10 present the overall performance of both stages. The data of the stage R 030-UKS are marked by cross symbols, the data of the reference stage R 030-NACA 65 are represented by full dots.

Figures 9 and 10 reveal that the new stage has lower total pressure ratios and total temperature rises, respectively, at design and off-design speeds (85 and 92.5 percent). At design speed the corresponding isentropic efficiencies (top diagram of Fig. 9) of both stages are quite well within normal data scattering. At off-design, the new stage obtained a lower efficiency except the peak value.

At first the discrepancies of total pressure and total temperature rise for both stages were attributed to some extent to the application of different measuring techniques. The results of the original stage relied on measurements with pressure and temperature rakes downstream of the stator. For the investigation of the new stage, however, single-probes for temperature and pressure were used exclusively. In order to exclude uncertainties of the different instrumentation the original stage R 030-NACA 65 was again tested with the single-probe instrumentation at design speed. The results are presented by the open circular symbols in Fig. 9. They confirm the original values obtained with the rake instrumentation.

One reason for the stage performance alteration might be unsteady flow phenomena affecting the total pressure readings downstream of the stator [16]. However, the stator flow analysis by means of laser anemometry revealed a very smooth outlet flow. Therefore, turbulence level has to be considered to have some influence on pressure probing.

Another reason might be the altered flow field caused by the annulus geometry kept constant for both stages. One interesting aspect to be noted here is that static pressure rise and its radial distribution of the new stage have changed at constant mass flow compared to the original stage. Discussing these phenomena in detail would go beyond the scope of this paper; therefore, this topic will be dealt with in another publication.

Downloaded 01 Jun 2010 to 171.66.16.70. Redistribution subject to ASME license or copyright; see http://www.asme.org/terms/Terms_Use.cfm

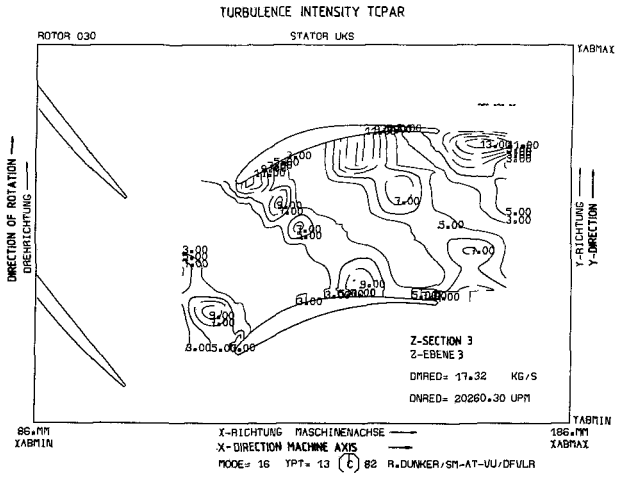


Fig. 15 Distribution of turbulence intensity (TCPAR) as in Fig. 14, but at altered rotor blade setting by one half rotor blade pitch

Blade Element Performance. As an example, Fig. 11 presents the stator blade element performance for section 3 at 50 percent span. The total pressure loss coefficient is plotted versus inlet flow angle for the redesigned airfoil at 85,92.5 and 100 percent speed designated by triangles, rectangles and cross symbols, respectively. These data are compared to the results of the original NACA 65 blade section at 100 percent speed represented by the open circular symbols and the corresponding cascade results marked by the dashed line with full dots. The cascade loss coefficient was interpolated to meet the inlet Mach numbers and AVDR values of the stage at design speed.

The comparison of the results of the original and new blade profiles demonstrates a substantial reduction of the controlled diffusion blade pressure loss between choke and design incidence; the choke line is slightly shifted to higher incidence. Beyond the design incidence the flow losses increase considerably exceeding even the NACA 65 blade losses and announcing a reduced stall margin.

The cascade results reveal a steep increase of the flow losses near stall incidence compared to the stator results with the stall margin itself considerably decreased. The reasons are believed to be unsteady stator inlet flow and three-dimensional flow interference of adjacent stator blade sections.

At 85 and 92.5 percent speed, the pressure loss level keeps almost unchanged compared to design speed; choke and stall incidence are shifted to lower and higher inlet flow angles, respectively.

Blade Surface Pressure Distribution. Detailed measurements of the blade surface pressure distributions were performed for the five design blade sections at design and off-design operating conditions. In order to install as many surface pressure taps as possible, the blade thickness and the blade chord length had to be enlarged. Thus, the blades could be provided with 14 taps on the suction and pressure side from leading edge up to 60 percent chord length. This instrumentation was chosen to investigate whether the favorable behavior of the new controlled diffusion blades can be obtained even under the real flow conditions within a turbomachine, i.e., unsteady inlet flow to the stator, high positive and negative incidence angles, and three-dimensional flow effects. Therefore, it was of special interest to compare the stator blade pressure distributions to those of the plane cascades. It has to be considered, however, that the measured static pressures of the stator are mean values, which could be affected by the unsteady through flow.

In Fig. 12, the blade surface pressures are plotted versus chord length for the three blade sections at 10, 50, and 90 percent span at the design mass flow of the new stator. The stage results (open circular symbols) are compared to the cascade tests results (triangular symbols). The absolute values of the static pressures depend on the inlet total conditions, which are essentially different for both the cascade and stage tests. Therefore, the absolute static pressure, which had been measured at 45 percent chord length on the blade pressure side of both the cascade and the corresponding stator blade section, was selected as the reference value.

Figure 12 reveals a quite satisfactory agreement of the cascade and stator blade pressure distributions, except for the minor acceleration of the stator flow near the leading edge on the suction surface. The stage tests were carried out with the compressor mass flow adjusted to the value of the stator redesign. Due to alteration of static pressure rise, already mentioned, the stator inlet parameters might have been changed, particularly the inlet flow angles. The separate tests on overall and blade element performance using conventional probes revealed stator inlet flow angle variation of about 1 deg negative incidence at the hub to 4 deg negative incidence at the tip.

Laser Measurements. Detailed optical measurements throughout the new stator blade row have been performed by means of a L2F-anemometer [15] to investigate the unsteady three-dimensional stator flow. The fluctuating flow vectors within the stator have been studied at different operating conditions.

The flow field within one stator blade channel, which is time-dependent observed from the rotor's position, was split up into 16 time intervals over one rotor blade pitch in each measuring point by means of a trigger unit. Ahead of the stator blade row the survey data were measured in several radial positions, whereas throughout the blade channel the measurements were only performed along sections 1,3, and 5. Because of their complexity these investigations are not yet finished.

Some preliminary results are shown in Figs. 14 and 15. The data presented were taken at the original stage design point from the midsection of one blade channel for two rotor blade settings which differ by one half of the rotor blade pitch. Figure 13 gives the information about the location of the measuring points in axial and pitchwise direction.

The distribution of the turbulence intensity parallel to the local main flow direction is illustrated in Figs. 14 and 15. The turbulence degree was believed most appropriate to analyze the rotor blade wake traveling throughout the stator blade channel. The rotor blade wakes become visible as areas of increased turbulence degree. When moving downstream the wakes are getting wider due to mixing and change their slope due to the mean velocity difference between stator blade suction and pressure side.

In the example shown here, no shift of the rotor blade wakes towards the stator blade pressure side is observed, which means that the slip velocity inside the rotor wake is close to zero within the stator blade channel. Indeed, the L2F-data confirm that the slip velocity decays very rapidly from rotor outlet to stator inlet.

The dots of high turbulence within the rotor wakes could be identified as vortices shed from the rotor blades; the Strouhal number of vortex shedding equals nearly that one of a flat plate with the maximum blade thickness.

This experimental and analytic work on the three-dimensional unsteady stator flow will be continued.

Conclusions

The stator of an existing transonic axial compressor stage was redesigned applying a new design concept for controlled

Downloaded 01 Jun 2010 to 171.66.16.70. Redistribution subject to ASME license or copyright; see http://www.asme.org/terms/Terms_Use.cfm

diffusion blades at subsonic flow. The design conditions of the new stator corresponded to the best point of the original stage at design speed. In order to verify the design concept, stage and cascade tests were performed.

The results of cascade testing indicate that the controlled diffusion airfoils have met their design requirements and have operated efficiently over a wide range of aerodynamic conditions. The test data taken at design point conditions exhibit a good match between measured and design Mach number distributions. Thus an attached suction side boundary layer could be obtained resulting in low losses and exit flow angles within the design specifications. The nearly constant exit angles over a wide range of test conditions were accomplished by means of the controlled diffusion technique.

The results of stage testing demonstrate that the new airfoils operate efficiently under three-dimensional turbomachinery conditions. The objectives of the redesign could be achieved taking into account the foregoing special conditions. In spite of reducing the number of blades by over 30 percent, combining a lower stage weight with a higher blade loading, a sufficient off-design performance was obtained with the new stage.

Furthermore the results of cascade and stage tests confirm that the controlled diffusion blade design concept is a reliable method. A substantial advantage of this concept is its close foundation in flow physics, which provides a potential for further improvements in turbomachinery blade design.

References

1 Strinning, P., and Dunker, R., "Aerodynamische Auslegung und Schaufelauslegung einer transsonischen Axialverdichterstufe," FVV-Forschungsbericht, Heft 178, 1975.

2 McDonald, P. W., Bold, C. R., Dunker, R. J., and Weyer, H. B., "A Comparison Between Measured and Computed Flow Fields in a Transonic Compressor Rotor," ASME JOURNAL OF ENGINEERING FOR POWER, Vol. 102, Oct. 1980.

3 Dunker, R. J., and Hungenberg, H., "Transonic Axial Compressor Using Laser Anemometry and Unsteady Pressure Measurements," *AIAA Journal*, Vol. 18, No. 8, Aug. 1980.

4 Korn, D., "Numerical Design of Transonic Cascades," ERDA Research and Development Report 000-3077-72, Courant Inst. Math. Sci., New York University, Jan. 1975.

5 Stephens, H. E., "Application of Supercritical Airfoil Technology to Compressor Cascades: Comparison of Theoretical and Experimental Results," AIAA Paper No. 78-1138, Seattle, Wash., July 1978.

6 Schmidt, E., "Numerische Berechnung und experimentelle Untersuchung des transsonischen Strömungsfeldes in stark umlenkenden Schaufelgittern," Diss. Univ. Stuttgart, 1976.

7 Schmidt, E., "Computation of Supercritical Compressor and Turbine Cascades With a Design Method for Transonic Flows," ASME JOURNAL OF ENGINEERING FOR POWER, Vol. 102, Jan. 1980.

8 Rechter, H., Schimming, P., and Starken, H., "Design and Testing of Two Supercritical Compressor Cascades," ASME Paper No. 79-GT-11, San Diego, Calif., 1979.

9 Stephens, H. E., and Hobbs, D. E., "Design and Performance Evaluation of Supercritical Airfoils for Axial Flow Compressors," Pratt & Whitney Aircraft, Report FR 11 455, June 1979.

10 Canal. E., et al., "Study of Controlled Diffusion Stator Blading, 1. Aerodynamic and Mechanical Design Report," NASA-CR-165500, Jan. 1981.

11 Caspar, J. R., Hobbs, D. E., and Davis, R. L., "Calculation of Two Dimensional Potential Cascade Flow Using Finite Area Methods," *AIAA Journal*, Vol. 18, No. 1, 1980, pp. 103–109.

12 Walz, A., "Strömungs- und Temperaturgrenzschichten," G. Braun, Karlsruhe 1968.

13 Starken, H., Breugelmans, F. A. E., and Schimming, P., "Investigation of the Axial Velocity Density Ratio in a High Turning Cascade," ASME Paper No. 75-GT-25, Houston, Texas, 1975.

14 Rechter, H., and Steinert, W., "Die Auslegung von Verdichtergittern nach vorgegebener Profildruckverteilung und ihre experimentelle Untersuchung," DFVLR-FB, (report to be published).

15 Schodl, R., "Laser Dual Beam Method for Flow Measurements in Turbomachines," ASME Paper No. 74-GT-157, 1974.

16 Ball, C. L., "private communication,"

Downloaded 01 Jun 2010 to 171.66.16.70. Redistribution subject to ASME license or copyright; see http://www.asme.org/terms/Terms_Use.cfm

Experimental Cascade Analysis of a Transonic Compressor Rotor Blade Section

H. A. Schreiber

H. Starken

Institut für Antriebstechnik, DFVLR,
5000 Cologne 90,
West Germany

A transonic compressor rotor blade cascade was tested in order to elucidate the flow behavior in the transonic regime and to determine the performance characteristic in the whole operating range of a rotor blade section. The experiments have been conducted in a transonic cascade wind tunnel, which enables tests even at sonic inlet velocities. The influence of the upstream Mach number between 0.8 and 1.1 and the inlet flow angle between choking and stalling of the blade row was investigated. The effect of the axial velocity density ratio (AVDR) could be studied by applying an endwall suction device. Furthermore, the level of the shock losses was determined from a wake analysis. A final comparison of cascade losses and those of the corresponding rotor blade element shows good agreement which underlines the applicability of the cascade model in the design of axial flow turbomachines.

Introduction

An improvement of the aerodynamic technology of axial flow compressors requires a comprehensive understanding of the flow phenomena that occur within the blade passages. In particular, the flow field within a transonic compressor rotor is extremely complex. In its relative frame range exist mixed subsonic and supersonic flow regions, as well as oblique and normal shock waves induced by the blades.

In recent years, considerable progress, achieved by both advanced computational and experimental techniques, has been made in the analysis of the transonic blade-to-blade flow.

New computational methods handle the inviscid transonic turbomachine flow, including the prediction of shock waves [1–4]. The results are encouraging; however, very often due to numerical problems and also due to viscous effects (in particular, the effect of shock boundary layer interactions), the theoretical models have difficulties in satisfactorily matching experimental results. Differences occur primarily in the prediction of the velocity level in the blade passage and the shock location, and in the flow angles and Mach numbers in the downstream portion.

On the other hand, advanced measurement techniques, especially the nonintrusive laser velocimetry, provide deep insight into the transonic flow fields [1, 5, 6]. Most methods are able to determine velocity contours and even shock locations, and in the mean time, some are even able to analyze real three-dimensional velocity vectors. The determination of density and total pressure losses, however, is still rather difficult.

A second experimental approach in analyzing the blade element flow is in the investigation of cascades in wind tunnels. Here the determination of the flow values is rather convenient and much more reliable. The essential advantage of cascade tests, however, is the ability to vary independently aerodynamic parameters such as inlet Mach number, inlet flow angle, static pressure increase, and even the blade channel stream tube convergence expressed by the axial velocity density ratio. The possible operating range in cascade investigations, therefore, is much more extended than in measurements at the corresponding blade element of a real compressor. The blade element within the compressor only allows the combination of the aerodynamic parameters corresponding to the operating conditions of the engine. For this reason, the cascade investigations easily enable a better understanding of the flow phenomena and help to find some reliable data of the blade element performance [7] and optimization criteria for new blade profile designs. In addition, a verification of theoretical blade design methods is possible, which will be important in the near future.

This paper describes the test results of a transonic compressor rotor blade section conducted in a cascade wind tunnel of the DFVLR in Cologne. The main objective of the tests was to analyze the complete operating range of the cascade in the transonic regime from Mach numbers 0.8 to 1.1. Inlet Mach numbers beyond 0.9 are of particular interest because here only very few experimental cascade results are available. Furthermore, the wide range of the cascade operating conditions allows a comparison to corresponding rotor blade element results.

Rotor Blade Element and Operating Range

The cascade was derived from a rotor blade element of a DFVLR transonic research compressor stage (Fig. 1), whose internal flow field was investigated in detail by the application

Contributed by the Gas Turbine Division of THE AMERICAN SOCIETY OF MECHANICAL ENGINEERS and presented at the 28th International Gas Turbine Conference and Exhibit, Phoenix, Arizona, March 27–31, 1983. Manuscript received at ASME Headquarters January 4, 1983. Paper No. 83-GT-209.

Copyright © 1984 by ASME
Downloaded 01 Jun 2010 to 171.66.16.70. Redistribution subject to ASME license or copyright; see http://www.asme.org/terms/Terms_Use.cfm

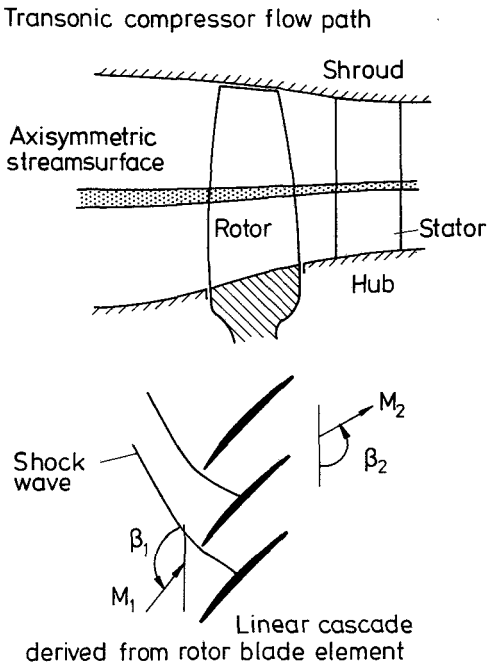


Fig. 1 Transonic compressor geometry and cascade section

of advanced testing techniques [5]. Therefore, several measurement data of the rotor blade element performance exist. This stage was designed for a total pressure ratio of 1.51 and a relative tip Mach number of 1.38. The investigated cascade is derived from the rotor blade midsection at 45 percent blade height. Its design relative inlet Mach number is $M_1 = 1.09$ and the flow turning is $\theta = 12.5$ deg. The main deceleration is achieved by a quasi normal shock wave located ahead of the blade passage (Fig. 1). The blade sections of the rotor are designed on axisymmetric stream surfaces with multiple circular arc profiles [8]. The midspan blades have an overall camber of 14.9 deg, but the blade suction side camber of the supersonic entrance region is kept low to reduce the supersonic expansion ahead of the shock wave.

The cascade was derived from the rotor blade geometry defined on the conical stream surface by projecting the profile coordinates to a cylindrical surface (cascade projection). Thus, the cascade has a constant gap from inlet to outlet corresponding to the gap at the stacking point of the rotor blade element. As the stream surface inclination within the rotor is on the order of 3 deg, the cascade profile shape differs only very little from that of the original rotor blade element.

The test conditions for the cascade investigations have been selected in such a way, that the inlet Mach number and inlet flow angle range is in accordance with the relative upstream values of the rotor blade element. To illustrate the upstream values, in Fig. 2 the inlet flow angles are plotted against the relative inlet Mach numbers. The solid symbols represent rotor results at the blade leading edge at 70, 85, 92.5, and 100 percent wheel speed and different mass flows between wide open discharge and near compressor stall. Contrary to the rotor tests at constant wheel speeds, where upstream flow angles and Mach numbers vary simultaneously, the cascade

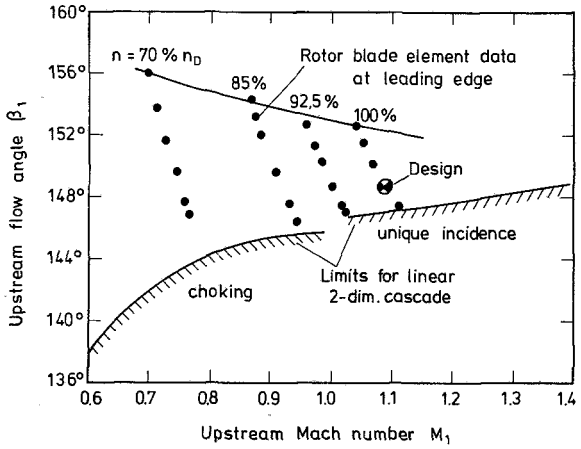


Fig. 2 Range of inlet flow conditions of the investigated rotor blade element

upstream flow angle variation has been carried out at constant upstream Mach numbers ($M_1 = 0.82, 0.92, 1.02$, and 1.1).

The essential boundaries of the operating range of the rotor blade section, as well as for the corresponding cascade, are blade choking at negative incidences and blade stall at high positive incidences with unacceptable loss increase. In Fig. 2, the calculated minimum incidence limits are plotted for the two-dimensional cascade. Thereby, the influence of any axial stream sheet thickness variation (AVDR) is neglected.

At subsonic flow the limit is determined by assuming a sonic line within the throat cross section of the blade channel. Reaching an upstream Mach number near to 1.0, this limit passes over to the supersonic choking limit known as "unique incidence." The latter was calculated by a simple wave analysis, taking the influence of the blunt leading edge and the detached bow shock wave into account [9]. The determination of the choking limit in the range around $M_1 = 1.0$ is much more complex, because additional shock losses which arise upstream of the throat and induced viscous losses due to shock boundary layer interactions shift this limit to somewhat higher positive incidences. In the present cascade tests, the minimum inlet flow angles have been selected according to the calculated limits in Fig. 2.

The test program provided a variation of the upstream Mach number, M_1, the upstream flow angle, β_1, and the axial velocity density ratio (AVDR) simulated by an endwall suction device.

Cascade Wind Tunnel and Its Operation

Before discussing the cascade results, a brief description is given of the transonic cascade tunnel and the operating procedures used to obtain reliable data.

The transonic tunnel of the DFVLR in Cologne is a closed-loop, continuously running facility which provides an inlet Mach number range from 0.2 to 1.4. It is equipped with a flexible half-symmetrical nozzle and a variable height adjustment for the flat lower half. Due to this flexibility, the test section can be adjusted to all compressor cascade configurations. Figure 3 shows a schematic drawing of the test

Nomenclature

M = Mach number
n = rotative speed (rpm)
p = static pressure
p_o = total pressure
w = velocity
x/l = relative blade chord
β = flow angle with respect to cascade front
ρ = density
ω = loss coefficient, $(p_{01} - p_{02})/(p_{01} - p_1)$
Ω = axial velocity density ratio, $(\rho_2 w_2 \sin\beta_2)/(\rho_1 w_1 \sin\beta_1)$

Subscripts

1 = uniform inlet conditions
2 = uniform outlet conditions

Downloaded 01 Jun 2010 to 171.66.16.70. Redistribution subject to ASME license or copyright; see http://www.asme.org/terms/Terms_Use.cfm

section with the investigated cascade installed. For operation in the transonic and supersonic range, the upper wall of the test section is slotted and equipped with a suction device. The suction enables a continuous transition from subsonic to supersonic flow and even stable test conditions at inlet Mach numbers of 1.0. Additional suction capability is available for side wall boundary layer removal ahead of the test section and through chordwise slotted cascade endwalls within the blade passages.

Compressor cascade tests in the transonic and supersonic inlet Mach number regime require a special throttle device in the downstream area of the blade row. This is necessary because at subsonic choked, supersonic unstarted-choked, and supersonic started cascade flow conditions the back pressure can be varied independently of the upstream flow conditions. But also at higher inlet flow angles and unchoked conditions, the back pressure must be controlled to achieve the desired incidence. The necessary throttle system is combined with two tailboards hinged to the trailing edges of the outermost blades. The bottom tailboard consists of a closed box with a slotted surface in which the back pressure is transferred upstream.

As long as the cascade is choked and the inlet flow field is independent of the back pressure, the adjustment of the desired flow conditions is relatively easy. Tests at relatively high positive incidences, however, are rather problematic, because the back pressure must be increased sufficiently by the throttle system. Consequently, a strong dependency arises between the inlet flow field, the periodicity, and the prescribed back pressure. This may have been the main reason why in former cascade tests the high positive incidence angle range (above the "unique incidence" limit) was avoided.

Still unsolved is the exact determination of the inlet flow angle at transonic and supersonic speeds. Due to the extreme sensitivity of the transonic flow, it is not possible to use flow direction probes. For the present test, therefore, the flow angle was assumed to be parallel to the tunnel axis. Simultaneously, the periodicity was checked by the wall static pressure distributions and the shock locations in the Schlieren pictures. The tests have been run with six blades of 167-mm span and a chord length of 90 mm.

Wake flow measurements at midspan position were obtained by traversing a combination probe for static pressure, total pressure, and flow direction. Two neighboring blades have been instrumented to measure the surface pressure distribution; the upper one for the pressure surface and the lower one for the suction surface.

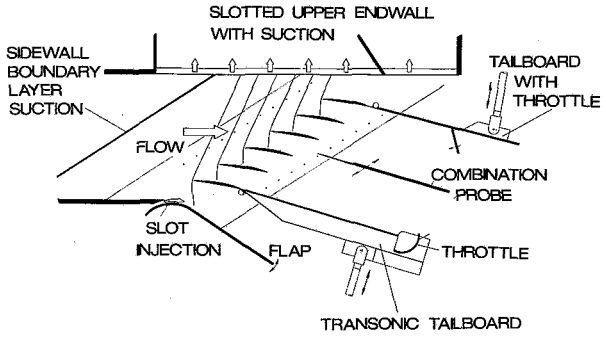


Fig. 3 Test section of the DFVLR transonic cascade facility

Cascade Test Results

To analyze the complete cascade operating range, an upstream Mach number variation was performed from 0.82 to 1.1 together with an inlet flow angle variation as large as possible. During the first test series, the cascade was investigated with solid endwalls without boundary layer removal within the blade passages. Thus, the axial streamtube convergence due to thickening of the endwall boundary layer could not be controlled; however, a better observation of the shock wave location was possible. In a second test series an endwall suction device was employed, which allowed a sufficient variation of the midspan axial velocity density ratio (AVDR).

Influence of Inlet Mach Number. Some of the obtained results will be discussed here. Of particular interest is the influence of the inlet Mach number on the cascade flow field passing from subsonic to supersonic velocity. For some typical test points at the minimum incidence limit, the Mach

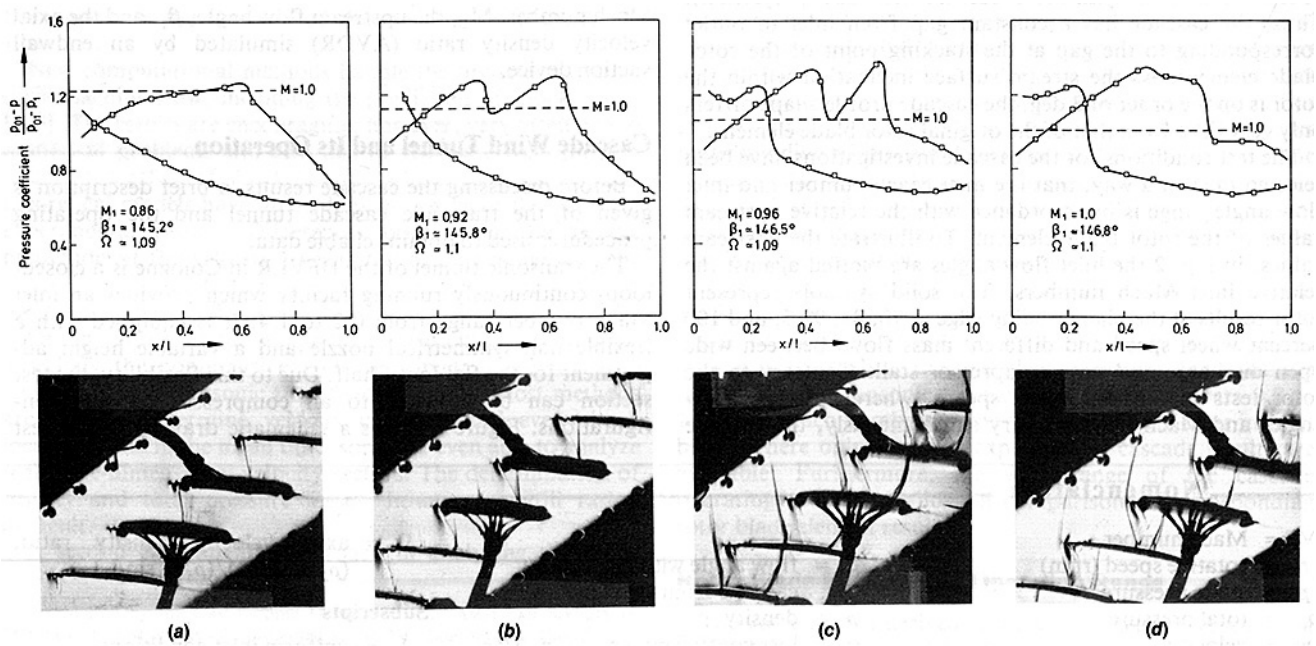


Fig. 4(a–d) Influence of inlet Mach number on blade pressure distribution and shock location at choked flow conditions

Downloaded 01 Jun 2010 to 171.66.16.70. Redistribution subject to ASME license or copyright; see http://www.asme.org/terms/Terms_Use.cfm

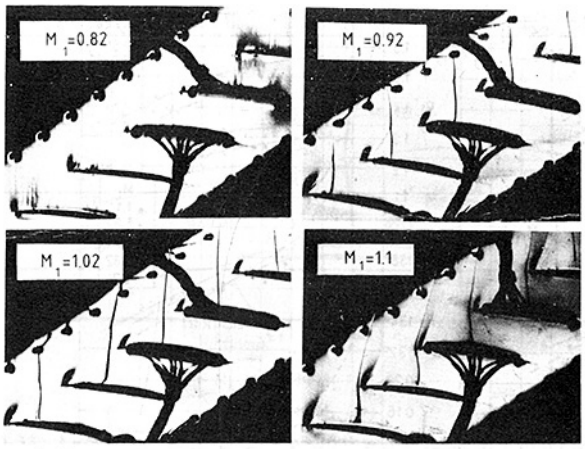


Fig. 5 Influence of inlet Mach number on shock wave position at β_1 = 148.5 deg (AVDR $\Omega \cong 1.1 - 1.17$; corresponding pressure distributions see Fig. 6)

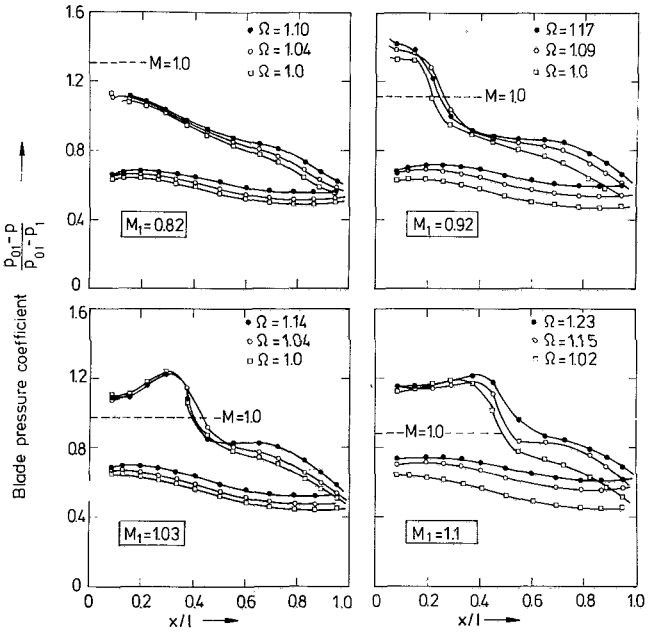


Fig. 6 Influence of axial velocity density ratio Ω on surface pressure distribution at various inlet Mach numbers (β_1 − 148.5 deg)

number influence on the flow field is illustrated by surface pressure distributions and Schlieren photographs in Fig. 4. For all the test points the inlet Mach number has reached its maximum, because the cascade chokes due to sonic velocity within the blade passage throats.

An increase of the inlet Mach number from 0.86 to 1.0 is only possible if the inlet flow angle is increased simultaneously from β_1 = 145.2 to 146.8 deg.

At an inlet Mach number of 0.86, the suction side pressure distribution of Fig. 4(*a*) shows a continuous expansion from subsonic to just sonic velocities near the passage entrance. The back pressure is high enough to avoid a supersonic acceleration downstream of the throat. Thus, only a weak shock wave can be observed.

If the inlet Mach number is increased to 0.92 (Fig. 4(*b*)) a supersonic pocket appears upstream of the throat terminated by a normal shock wave. Behind this shock, the flow is reaccelerated to sonic velocity in the throat followed by a weak supersonic expansion and a relatively strong passage shock. The blade pressure distribution of Fig. 4(*b*) with its two suction side peaks is rather typical for the MCA-blades at

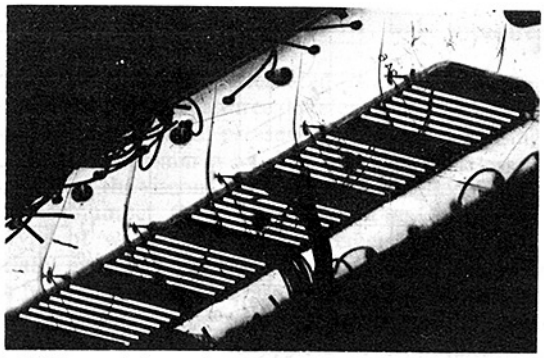


Fig. 7 Schlieren photograph of the test section with chordwise slotted endwalls ($M_1 \cong 1.0$)

choked flow conditions. A similar flow field can be observed at M_1 = 0.96 (Fig. 4(*c*)). The supersonic area, however, is increased and the peak Mach number ahead of the first shock is already as high as 1.2.

Reaching M_1 = 1.0, the supersonic flow area extends to the whole entrance region of the suction surface, and the first shock wave attaches to the leading edge of the adjacent blade (Fig. 4(*d*)). The suction surface Mach number in front of the shock is 1.28. A final normal shock wave within the blade passage induces a boundary layer separation with relatively high total pressure losses.

The Mach number influence at the design inlet flow angle (β_1 = 148.5 deg) is shown in the Schlieren pictures of Fig. 5 and in the blade pressure distributions of Fig. 6. At this incidence, the supersonic area arises directly behind the leading edge. With increasing inlet Mach number, the terminating normal shock wave is shifted further downstream.

Influence of AVDR. In addition to inlet Mach number and flow angle the axial velocity density ratio (AVDR) Ω is a very important parameter in cascade tests. It describes the midspan axial stream sheet thickness variation from cascade inlet to outlet. In the past the AVDR influence on blade element performance at subsonic flow has been pointed out by several authors. It has a considerable influence on the blade surface pressure distribution, the static pressure increase, and the flow turning.

For experimental investigations in transonic and supersonic flow, however, the test facility must be equipped with an effective suction system to enable sufficient endwall boundary layer removal. In the cascade facility used, the suction system enabled an AVDR variation between Ω = 1.0 (two-dimensional flow) and $\Omega = 1.1 - 1.25$ (closed suction) even at supersonic speeds up to M_1 = 1.25. In spite of the chordwise suction slots, an observation of the shock location by a Schlieren system was still possible (Fig. 7). The influence of the suction system on the stream tube near the cascade endwall is not investigated in detail, but this is of secondary interest because only the midspan stream sheet thickness distribution is considered to determine the AVDR. Experience has so far confirmed the assumption of a linear AVDR variation from cascade inlet to exit plane.

The variation of the blade surface pressure distributions at design incidence (β_1 = 148.5 deg) and inlet Mach numbers between 0.82 and 1.1 are presented in Fig. 6 for three different AVDR values. At this incidence angle the variation of the blade passage flow is similar at subsonic as well as supersonic inlet Mach numbers.

The AVDR influence on the blade element performance is illustrated in Fig. 8. Different inlet Mach numbers at three inlet flow angles (β_1 = 147 deg which corresponds to "unique incidence," β_1 = 150 deg, and 151.5 deg) are shown. With increasing AVDR, a considerable reduction of the static

Downloaded 01 Jun 2010 to 171.66.16.70. Redistribution subject to ASME license or copyright; see http://www.asme.org/terms/Terms_Use.cfm

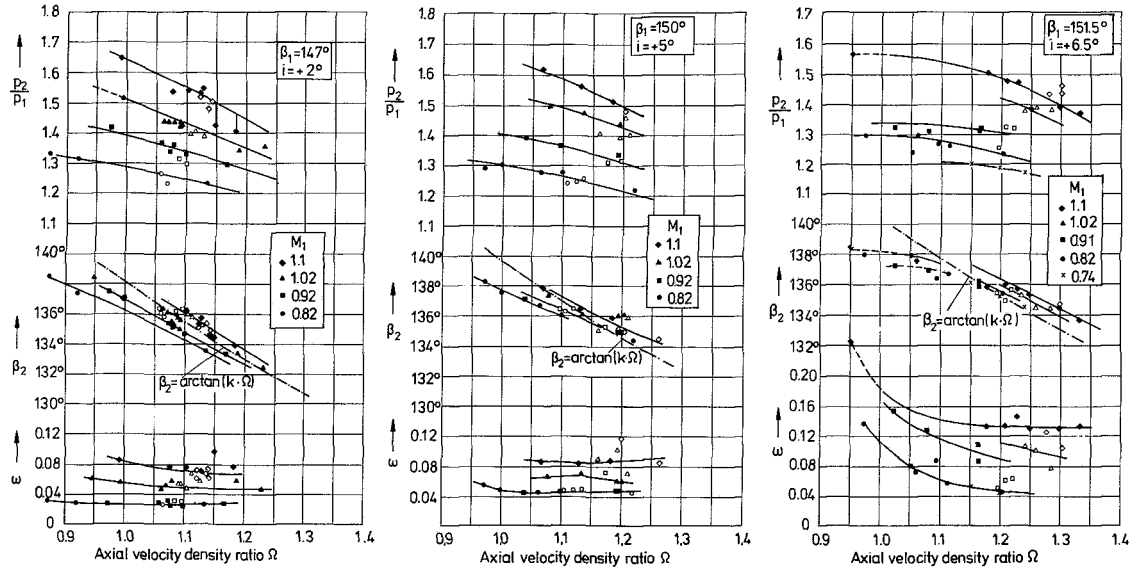


Fig. 8(*a–c*) Variation of cascade static pressure ratio, downstream flow angle, and loss coefficient with axial velocity density ratio, Ω (solid symbols: slotted endwalls with suction; open symbols: solid endwalls)

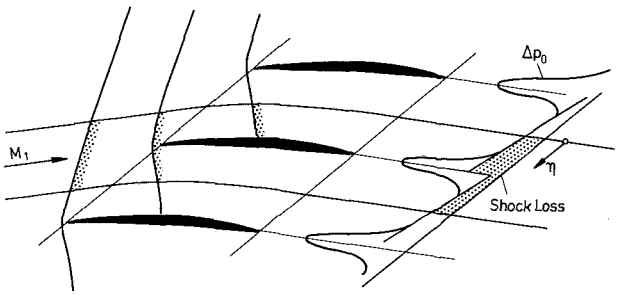


Fig. 9 Total pressure losses and assumed distribution of shock losses behind a transonic compressor cascade

pressure ratio, p_2/p_1, can be observed. Parallel to this, the downstream flow angle decreases nearly linearly, which corresponds to an increase of the flow turning.

The dependency of the downstream flow angle on the AVDR can be approximated easily by the assumption of a constant circumferential component of the velocity density value

$$\rho_2 w_2 \sin\left(\beta_2 - \frac{\pi}{2}\right) = \text{const} \tag{1}$$

Then the following linear dependency between $\tan\beta_2$ and Ω can be derived

$$\tan\beta_2 = K \cdot \Omega \tag{2}$$

The slope factor, $K = d(\tan\beta_2)/d\Omega$, can be calculated from any known (measured) β_2-Ω-combination. This theoretical relation is included in Fig. 8(*a–c*) by dashed-dotted lines. It is supposed that this relation is universal and not restricted to any special test section geometry or suction system. The slope factor, K, is primarily a function of the absolute value of the downstream flow angle β_2.

The behavior of the total pressure losses with changing AVDR is very surprising (lower part of Fig. 8). Although the blade surface velocity distribution is considerably influenced by the AVDR, the total pressure losses change only very little.

A reduction of the AVDR would allow a considerable increase of the blade loading without changing the loss level (Fig. 8(*a*) and 8(*b*)). At relatively high positive incidences,

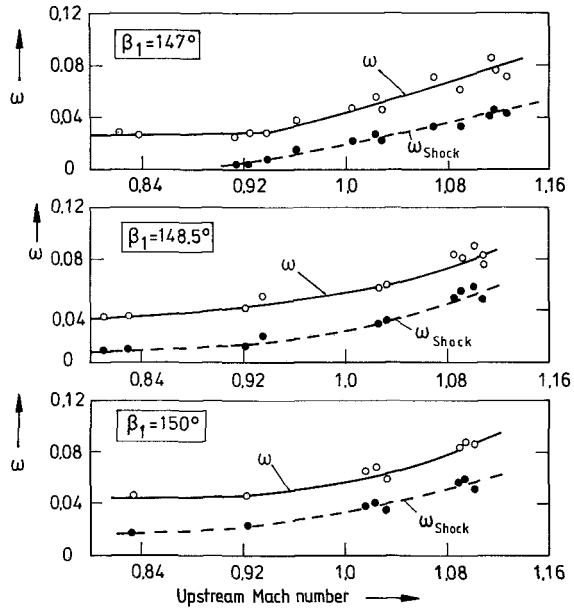


Fig. 10 Measured total pressure losses and corresponding shock losses reduced from wake analysis

however, when boundary layer separations occur, low losses can only be obtained at higher Ω values (Fig. 8(*c*)).

Shock Losses. An essential part of the total pressure losses of transonic and supersonic cascades is due to shock waves arising in the entrance region and the passage of the blades. Depending on inlet Mach number and inlet flow angle, the level of the shock losses of the present cascade reaches up to 40–60 percent of the overall losses. An exact analysis of these losses is of particular interest for the verification of new or existing theoretical loss models.

The measured total pressure losses in the blade wakes consist of viscous losses, including the effect of the shock boundary layer interaction and the total pressure losses due to the passage shock, the detached bow shock ahead of the blade leading edge, and one oblique shock emanating from the bow wave of the blade below into the upstream flow area.

Downloaded 01 Jun 2010 to 171.66.16.70. Redistribution subject to ASME license or copyright; see http://www.asme.org/terms/Terms_Use.cfm

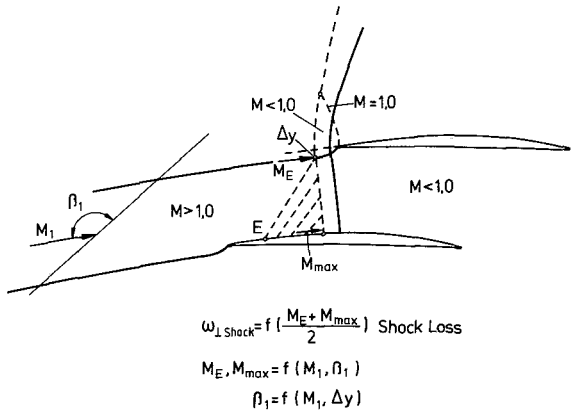


Fig. 11 Flow model for calculating shock wave losses as a function of inlet flow angle (dashed lines correspond to increased inlet flow angle)

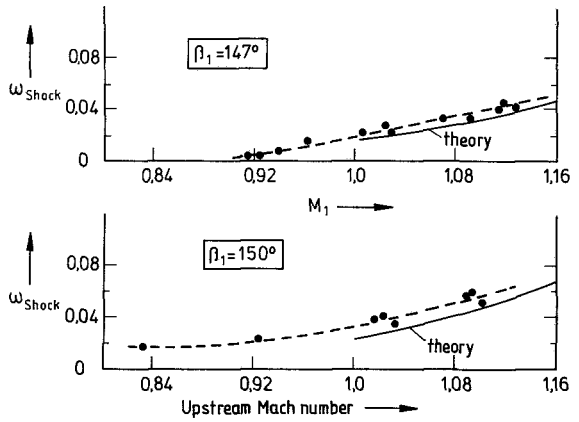


Fig. 12 Comparison of measured and calculated shock losses

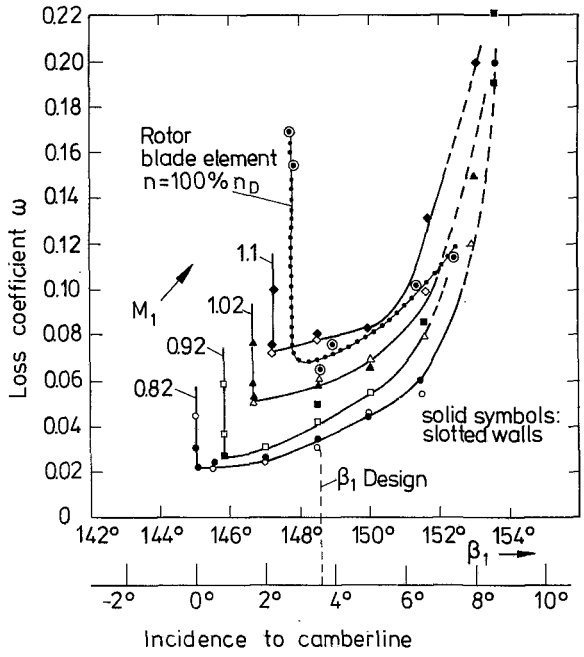


Fig. 13 Comparison of total pressure loss coefficient of rotor blade element and cascade (AVDR of the cascade tests: Ω ≈ 1.1 – 1.17)

Assuming a wake model as shown in Fig. 9, shock losses and viscous losses can be separated. In the measurement plane behind the cascade, the shock losses are recognized outside of the viscous wake. For some characteristic test points in the Mach number range from 0.82 to 1.1, wake measurements have been analyzed.

Figure 10 shows the measured overall losses and the separated shock losses at three different inlet flow angles. The gradual rise of the total pressure losses with increasing inlet Mach number is primarily a function of the shock losses. This indicates that the viscous losses do not strongly depend on the inlet Mach number. On the other side, it may be possible that this type of wake analysis overpredicts the shock losses, especially at higher positive incidences where losses due to shock boundary layer interactions could be included.

A comparison of the reduced experimental shock losses with calculated shock losses, however, indicates good agreement between experiment and theory (Fig. 12). The loss model used here [9] is similar to the one of Miller and Hartmann [10] but considers the influence of the blunt leading edge and simulates the influence of the inlet flow angle by a variation of the stagnation streamline shift, Δy, (see Fig. 11).

Comparison With Rotor Blade Element Data

The cascade tests with AVDR variation indicate that the total pressure losses are nearly independent of the AVDR. Therefore, one diagram with $\Omega \cong 1.1$–1.17 is sufficient to present the losses in the whole incidence range. Figure 13 shows the total pressure loss coefficient as a function of the inlet flow angle for different inlet Mach numbers. With increasing Mach number, the losses increase continuously and there is a considerable reduction of the incidence range. Primarily, the shifting of the choking limit (indicated by the left vertical branches of the loss curves) reduces the incidence range.

At all inlet Mach numbers investigated, the loss minimum was obtained near or at choking conditions. However, the back pressure behind the cascade must be high enough to avoid a supersonic expansion within the blade passage. At supersonic inlet speed the minimum loss point corresponds to a flow configuration with a normal shock located just at the blade passage entrance.

For comparison, the experimental total pressure losses of the corresponding rotor blade section (45 percent blade height at 100 percent wheel speed [4, 5]) are plotted in the same diagram. Due to different operating conditions of the compressor (wide open discharge, peak efficiency, near surge), the relative inlet Mach number to the rotor blade element is not constant. Therefore, the comparable cascade data are located between the loss curves of $M_1 = 1.1$ and 1.02. The AVDR values of the rotor blade element (defined between leading and trailing edge plane) vary between $\Omega = 1.15$–1.18.

The overall loss behavior of the rotor blade element and the cascade is very similar, with even the level of the losses being nearly identical. The two rotor test points with open discharge and low back pressure, however, show incidences which are about 0.6 deg higher than those of the comparable cascade test points. This can be explained by a higher AVDR value ($\Omega = 1.22$) of the rotor blade element compared to the cascade ($\Omega = 1.12$), which causes a shift of the choking limit to higher incidences.

A comparison of downstream flow angles of rotor and cascade at the same AVDR also shows satisfactory agreement. The comparison of the cascade surface velocity distributions with Laser-2-Focus results from the rotor blade element [4, 5] are not yet completed, but first results indicate good agreement in the velocity level and the shock wave position.

Conclusion

Cascade tests are a convenient tool to clarify the behavior of the complex transonic axial compressor blade element flow

Downloaded 01 Jun 2010 to 171.66.16.70. Redistribution subject to ASME license or copyright; see http://www.asme.org/terms/Terms_Use.cfm

within the whole operating range. The experiments provide detailed information about shock location, shock losses, blade surface pressure distributions, and overall performance. The total pressure losses of the presented cascade agree very well with the data obtained behind the corresponding blade element of the transonic compressor rotor. These results confirm the value of the cascade experiment as an analytical as well as a design tool for transonic turbomachines.

References

1 Chima, R. V., and Strazisar, A. J., "Comparison of Two- and Three-Dimensional Flow Computations With Laser Anemometer Measurements in a Transonic Compressor Rotor," ASME Paper No. 82-GT-302, Apr. 1982.

2 Sarathy, K. P., "Computation of Three-Dimensional Flow Fields Through Rotating Blade Rows and Comparison With Experiment," ASME JOURNAL OF ENGINEERING FOR POWER, Vol. 104, Apr. 1982, pp. 394–402.

3 Singh, U. K., "A Computation and Comparison With Measurements of Transonic Flow in an Axial Compressor Stage With Shock and Boundary Layer Interaction," ASME JOURNAL OF ENGINEERING FOR POWER, Vol. 104, Apr. 1982, pp. 510–515.

4 McDonald, P. W., Bolt, C. R., Dunker, R. J., Weyer, H. B.,"A Comparison between Measured and Computed Flow Fields in a Transonic Compressor Rotor," ASME JOURNAL OF ENGINEERING FOR POWER, Vol. 102, Oct. 1980, pp. 883–891.

5 Dunker, R. J., and Hungenberg, H. G., "Transonic Axial Compressor Using Laser Anemometry and Unsteady Pressure Measurements," *AIAA Journal*, Vol. 18, No. 8, Aug. 1980.

6 Wisler, D. C., "Shock Wave and Flow Velocity Measurements in a High Speed Fan Rotor Using the Laser Velocimeter," ASME Paper 76-GT-49.

7 Schreiber, H. A., and Starken, H., "Evaluation of Blade Element Performance of Compressor Rotor Blade Cascades in Transonic and Low Supersonic Flow Range," Fifth International Symposium on Air Breathing Engines, Bangalore, India, Feb. 16–22, 1981, pp. 67–1, 9.

8 Frost, G. R., Hearsey, R. M., and Wennerstrom, A. J., "A Computerprogram for the Specification of Axial Compressor Airfoils," ARL 72-0171, Dec. 1972.

9 Starken, H., "Untersuchung der Strömung in ebenen Überschallverzögerungsgittern," *DLR-Forschungsbericht, 71-99, 1971.*

10 Miller, G. R., and Hartmann, M. J., "Experimental Shock Configuration and Shock Losses in a Transonic Compressor Rotor at Design Speed," NACA RM E58A14b, June 5, 1958.

APPENDIX

Cascade Geometry

Gap-chord ratio	$t/1 = 0.621$
Stagger angle	$\beta_s = 138.51$ deg
Relative blade thickness	$d/1 = 0.05$
Blade camber	$\phi = 14.9$ deg

Profile Coordinates

Suction surface		Pressure surface	
XS/L	*YS/L*	*XD/L*	*YD/L*
0.003405	0.004271	0.004256	−0.003335
0.018243	0.006895	0.019226	−0.002395
0.047702	0.011922	0.048956	−0.000672
0.076930	0.016698	0.078410	0.000853
0.105934	0.021222	0.107595	0.002195
0.134720	0.025490	0.136517	0.003367
0.163294	0.029501	0.165183	0.004381
0.191659	0.033254	0.193599	0.005249
0.219822	0.036745	0.221771	0.005984
0.247786	0.039975	0.249707	0.006596
0.275556	0.042940	0.277411	0.007095
0.303135	0.045641	0.304891	0.007491
0.330526	0.048074	0.332151	0.007795
0.357733	0.050240	0.359198	0.008014
0.384757	0.052136	0.386038	0.008158
0.411602	0.053762	0.412676	0.008236
0.438270	0.055117	0.439117	0.008254
0.464763	0.056199	0.465368	0.008222
0.491082	0.057008	0.491434	0.008146
0.517230	0.057544	0.517320	0.008032
0.543208	0.057804	0.543031	0.007889
0.569017	0.057789	0.568573	0.007722
0.594658	0.057498	0.593950	0.007537
0.619550	0.056941	0.618526	0.007336
0.643650	0.056039	0.642264	0.007077
0.667529	0.054931	0.665802	0.006751
0.691190	0.053473	0.689146	0.006361
0.714635	0.051719	0.712305	0.005913
0.737866	0.049672	0.735285	0.005409
0.760884	0.047338	0.758094	0.004854
0.783692	0.044719	0.780738	0.004252
0.806292	0.041821	0.803224	0.003605
0.828685	0.038648	0.825558	0.002916
0.850873	0.035202	0.847746	0.002189
0.872858	0.031489	0.869795	0.001426
0.894639	0.027511	0.891710	0.000631
0.916220	0.023272	0.913496	−0.000196
0.937600	0.018775	0.935159	−0.001050
0.958781	0.014024	0.956705	−0.001930
0.979763	0.009021	0.978138	−0.002835
1.000550	0.003769	0.999454	−0.003769

Downloaded 01 Jun 2010 to 171.66.16.70. Redistribution subject to ASME license or copyright; see http://www.asme.org/terms/Terms_Use.cfm

A Three-Dimensional Model for the Prediction of Shock Losses in Compressor Blade Rows

A. J. Wennerstrom

S. L. Puterbaugh

Aero Propulsion Laboratory
(AFWAL/POTX)
Wright Patterson AFB, Ohio 45433

A design trend evident in newly evolving aircraft turbine engines is a reduction in the aspect ratio of blading employed in fans, compressors, and turbines. As aspect ratio is reduced, various three-dimensional flow effects become significant which at higher aspect ratios could safely be neglected. This paper presents a new model for predicting the shock loss through a transonic or supersonic compressor blade row operating at peak efficiency. It differs from the classical Miller-Lewis-Hartmann normal shock model by taking into account the spanwise obliquity of the shock surface due to leading-edge sweep, blade twist, and solidity variation. The model is evaluated in combination with three test cases. Each was a low-aspect-ratio transonic stage which had exceeded its efficiency goals. Use of the revised shock loss model contributed 2.11 points to the efficiency of the first test case, 1.08 points to the efficiency of the second, and 1.38 points to the efficiency of the third.

Introduction

A design trend evident in newly evolving aircraft turbine engines is a reduction in the aspect ratio of blading employed in fans, compressors, and turbines. As aspect ratio is reduced, various three-dimensional flow effects become significant which, at higher aspect ratios, could safely be neglected. This paper presents a new model for predicting the shock loss in a compressor blade row that takes into account the three-dimensionality of the shock surface. The work described in this paper was inspired by the observations of Prince [1], who noted that spanwise obliquity of shock surfaces might explain some of the apparent discrepancies seen in data concerning the shock structure of some fans and compressors. Prince observed that all data studied to-date suggested a qualitative view of the three-dimensional shock structure in which the shock, viewed on stream surfaces of revolution, varied from an orientation normal to the relative flow at high back pressures to an axial orientation at lower back pressures. For the shock loss model described in this paper, we have chosen to assume that the shock is normal to the inlet relative flow direction on each stream surface of revolution. A three-dimensional view of the shock structure is shown in Fig. 1. The fact that the shock vanishes near the hub has been ignored for the purpose of this purely geometric illustration. The normal shock assumption renders this model applicable to an operating point near peak efficiency which, for most fans and compressors, will occur at a slightly higher pressure ratio than a typical engine operating line design point. The model thus constructed is essentially a three-dimensional version of the Miller-Lewis-Hartmann [2] model, which has enjoyed widespread use since its publication.

Contributed by the Gas Turbine Division of THE AMERICAN SOCIETY OF MECHANICAL ENGINEERS and presented at the 28th International Gas Turbine Conference and Exhibit, Phoenix, Arizona, March 27–31, 1983. Manuscript received at ASME Headquarters January 4, 1983. Paper No. 83-GT-216.

Calculation Approach

The calculation begins in a manner similar to the Miller-Lewis-Hartmann approach in that a shock line is constructed on each stream surface, extending from the leading edge of one blade to the suction surface of the adjacent blade and normal to the relative inflow direction. The upstream shock Mach numbers are also obtained in a manner similar to the Miller-Lewis-Hartmann model. At the leading edge, the Mach number is considered equal to the relative inlet Mach number. At the suction surface impingement point, the Mach number is assumed to be that resulting from a Prandtl-Meyer expansion (or compression) from the relative inlet value through

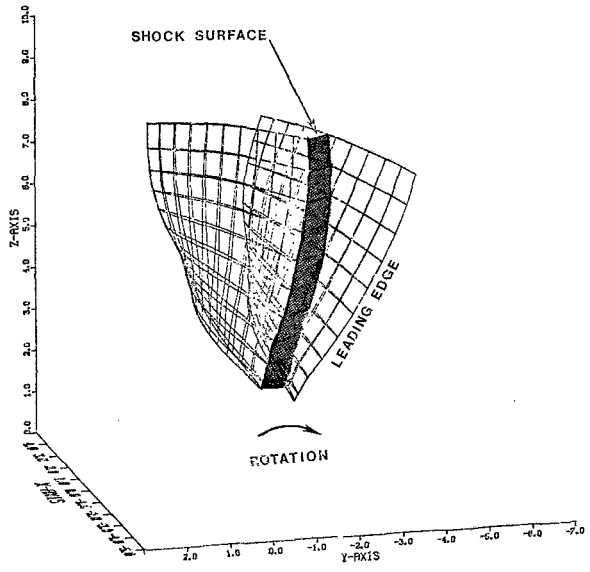


Fig. 1 Geometry of shock surface

Copyright © 1984 by ASME
Downloaded 01 Jun 2010 to 171.66.16.70. Redistribution subject to ASME license or copyright; see http://www.asme.org/terms/Terms_Use.cfm

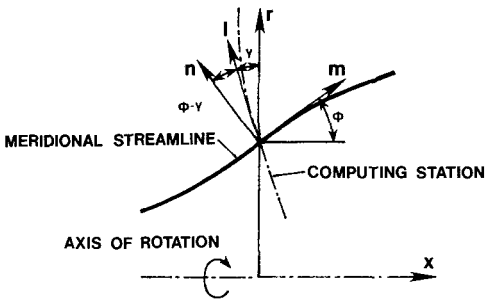


Fig. 2 Meridional plane

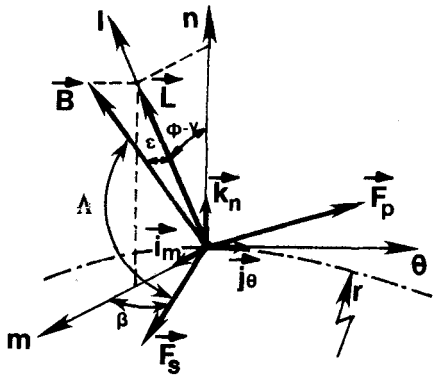


Fig. 3 Intrinsic coordinates

an angle equal to the difference between the relative inlet flow angle and the suction surface angle at the impingement point.

From this point on, the calculation departs from the Miller-Lewis-Hartmann approach. The suction surface impingement points so defined comprise the locus of points of a line which is typically swept back relative to the flow as one proceeds from hub to tip. The angle of the shock surface relative to the upstream flow is calculated at the leading edge and at the shock impingement point on each stream surface using equation (1).

$$\Lambda = \cos^{-1}[\cos\ \beta\ \cos\ \epsilon\ \sin(\phi-\gamma) - \sin\ \beta\ \sin\ \epsilon] \qquad (1)$$

The variables used in this equation are defined in Figs. 2 and 3. This angle, which is 90 deg plus the sweep angle, is a function of stream surface slope, ϕ, the blade lean angle, ϵ, the relative flow angle, β, and either the computing station lean angle, γ, at the leading edge or the impingement line lean angle at the impingement point. The blade lean angle used is that relative to the computing station at the leading edge or the impingement line at that location. Properties across the shock are then calculated in the standard fashion for oblique shocks using the normal shock relations and an upstream Mach number equal to

$$M_x = M|\sin\Lambda| \qquad (2)$$

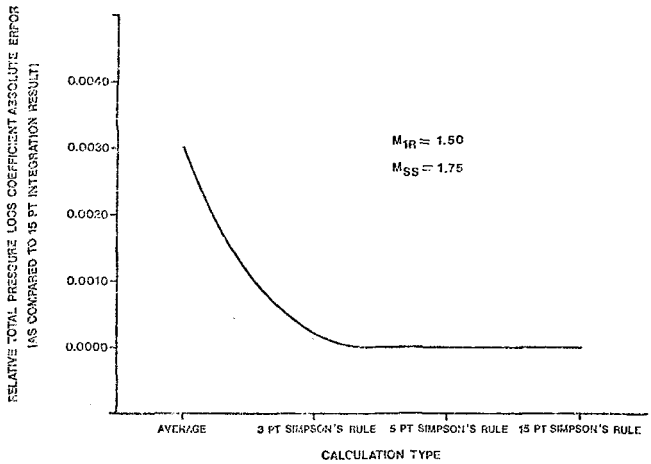


Fig. 4 Loss error from averaging

where M is the approach Mach number at the point in question.

In addition to introducing shock obliquity, one more departure is made from the Miller-Lewis-Hartmann shock model. In the original model, the two Mach numbers obtained on each stream surface were simply averaged to obtain an upstream shock Mach number used to calculate the shock pressure ratio. In this new model, we have chosen to integrate along the shock to obtain the pressure ratio since the total pressure ratio is not a linear function of Mach number or obliquity. Both Mach number and shock surface obliquity have been assumed to vary linearly from leading edge to the impingement point on each stream surface. Simpson's Rule integrations using three, five, and fifteen points were compared with each other and with the simple average used by Miller-Lewis-Hartmann. The results are illustrated in Fig. 4.

The integration approach was selected in preference to the simple average because it produced a more conservative result; i.e., a higher loss. However, a three-point integration was selected as being entirely adequate in relation to the probable accuracy of such a loss prediction.

Miller, Lewis, and Hartmann did not address the question of shock loss in the region of high subsonic Mach numbers, when the relative inlet Mach number is subsonic but is still high enough to produce a finite shock loss due to a transonic bubble on the suction surface. A shock loss model is required for this region in order to avoid the discontinuous onset of shock loss upon reaching the sonic radius. The model chosen by the authors is patterned after one described in [3], modified appropriately for shock obliquity. It is applied to the region within which the relative inlet Mach number is less than 1.0, but the mean shock Mach number calculated according to equation (3) is greater than 1.0

Nomenclature

- $\mathbf{B}$ = vector tangent to blade surface and computing station surface
- $\mathbf{F}_p$ = vector normal to the blade surface
- $\mathbf{F}_s$ = vector tangent to a blade in a stream surface
- $\mathbf{i}_m$ = unit vector; see Fig. 3
- $\mathbf{j}_\theta$ = unit vector; see Fig. 3
- $\mathbf{k}_n$ = unit vector; see Fig. 3
- l = coordinate along a computing station
- $\mathbf{L}$ = vector coincident with l coordinate direction
- m = meridional intrinsic coordinate
- M_{1R} = inlet relative Mach number
- M_{ss} = suction surface Mach number at shock impingement
- M_x = shock approach Mach number
- n = normal intrinsic coordinate
- r = radius from axis of symmetry
- β = relative flow angle
- γ = computing station lean angle
- ϵ = blade lean angle
- θ = angular coordinate about axis of symmetry
- Λ = angle between $\mathbf{B}$ and $\mathbf{F}_s$
- σ = solidity
- Φ = stream surface pitch angle
- $\bar{\omega}$ = relative total pressure loss coefficient

Downloaded 01 Jun 2010 to 171.66.16.70. Redistribution subject to ASME license or copyright; see http://www.asme.org/terms/Terms_Use.cfm

Table 1 (for specific heat ratio = 1.3996)

Streamline number	Mach rel. in.	Expansion angle	M-L-H shock loss	L. E. sweep	Imping. line sweep	Oblique shock loss
1	0.661	3.557	0.0	38.854	40.852	0.0
3	0.681	4.522	0.0	37.135	40.880	0.0
5	0.746	7.020	0.0	32.969	32.006	0.0
7	0.847	7.855	0.0	26.821	24.679	0.0
9	0.964	7.726	0.00553	21.185	20.962	0.00051
11	1.091	7.080	0.02031	18.749	23.127	0.00907
13	1.223	5.799	0.04296	18.137	21.190	0.02407
15	1.352	4.487	0.07430	17.201	19.574	0.04976
17	1.465	2.771	0.10382	15.839	21.433	0.07339
19	1.565	1.035	0.13094	14.314	24.031	0.09449
21	1.667	−0.783	0.15958	12.043	24.504	0.12276

$$\bar{M}_x = \frac{M_{1R}}{2} |\sin\ \bar{\Lambda}| (M_{1R} + M_i) \qquad (3)$$

M_i is the Mach number resulting from a Prandtl-Meyer expansion from Mach 1.0 through an angle equal to the relative turning angle up to the suction surface impingement line, M_{1R} is the relative inlet Mach number, and $\bar{\Lambda}$ is the average value of shock surface angle relative to the flow. Within this transition region, the blade-to-blade integration is not performed, and the shock pressure ratio is obtained directly using the Mach number defined by equation (3).

Test Results

The shock model just described was incorporated as an option into the axisymmetric, streamline-curvature-type computer program [4] currently used for compressor design by the Aero Propulsion Laboratory. It was evaluated with three axial compressor designs which shared the common characteristics of low aspect ratio, tip relative Mach numbers in the range of 1.5 to 1.7, and higher than expected efficiency demonstrated at design speed. The loss model of [4] assumed the total loss to be the sum of shock loss plus a diffusion loss predicted on the basis of a Loss Parameter versus Diffusion Factor correlation. Since the test cases were designed using different Loss Parameter correlations, the first step in the evaluation was to choose a single correlation for Loss Parameter versus Diffusion Factor against which all test cases could be evaluated on a common basis. The first test case chosen was the compressor described in [5], which was also one of the test cases used by Prince in [1]. The data used for this paper were taken from [6]. Detailed rotor as well as stage performance data were available for this case, so it was used as the basis for correction of the correlation. In particular, it had been observed that the stator loss had been overestimated, so the largest correction was made in this area. The correlation selected for evaluation of all test cases is shown in Fig. 5.

The physical characteristics for the rotor of the first test case are:

Rotor inlet hub/tip radius ratio	0.312
Average rotor span/chord ratio	1.320
Rotor tip relative Mach number	1.667
Rotor tip speed	457 m/s

A meridional plane view of the rotor is shown in Fig. 6. Table 1 presents a detailed breakdown of parameters entering into the shock loss computation across the span of the rotor. The levels of sweep at the leading edge and at the impingement line are shown, as well as the relative total pressure loss coefficient attributable to shock loss computed both with the Miller-Lewis-Hartmann method and the new method. Table 2

Table 2

	M-L-H model	New model	Exp. results
Total pressure ratio	2.026	2.061	2.058
Isentropic efficiency, %	86.96	89.07	88.90

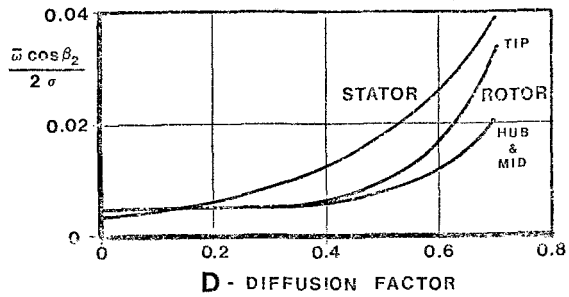


Fig. 5 Loss parameter correlation used

presents a comparison of the stage performance of this machine, predicted using the Miller-Lewis-Hartmann shock loss model, using the new oblique shock loss model, and as experimentally measured at peak efficiency at design speed. The predictions were both made using the spanwise work distribution experimentally determined at the stage exit, which corresponded to a higher pressure ratio than the initial design. This work distribution cancelled the effect of inaccuracy in the original prediction of rotor deviation angle and was felt to pose a more valid test of the loss models. As shown in Table 2, the new oblique shock model predicted as isentropic efficiency 2.11 points higher than the Miller-Lewis-Hartmann model.

The second test case was a fan designed by Teledyne CAE using the same design computer program [4]. The basic physical characteristics of the rotor from this stage are:

Rotor inlet hub/tip radius ratio	0.333
Average rotor span/chord ratio	1.788
Rotor tip relative Mach number	1.550
Rotor tip speed	480 m/s

Although its tip speed is higher than that of the first test case, the rotor tip relative Mach number is lower because it was designed for a lower specific flow rate. A meridional plane view of this rotor is illustrated in Fig. 7. Table 3 presents the same data shown for the first test case in Table 1, and similarly, Table 4 compares the stage performance as predicted with both shock loss models and as experimentally measured. In this case, the increase in efficiency due to use of the oblique shock model was reduced to 1.08 points due to

Downloaded 01 Jun 2010 to 171.66.16.70. Redistribution subject to ASME license or copyright; see http://www.asme.org/terms/Terms_Use.cfm

Table 3 (for specific heat ratio = 1.3996)

Streamline number	Mach rel. in.	Expansion angle	M-L-H shock loss	L. E. sweep	Imping. line sweep	Oblique shock loss
1	0.731	6.267	0.0	29.164	24.778	0.0
2	0.746	7.138	0.0	28.105	24.822	0.0
3	0.793	8.811	0.0	26.684	24.110	0.0
4	0.869	9.753	0.00048	22.600	17.712	0.0
5	0.961	9.406	0.00882	17.872	12.410	0.00393
6	1.060	9.308	0.02460	15.776	11.082	0.02533
7	1.163	8.426	0.04211	13.875	11.240	0.03797
8	1.265	6.915	0.06188	11.576	12.878	0.05305
9	1.361	5.284	0.08333	7.634	16.437	0.07035
10	1.452	4.353	0.11114	0.642	21.608	0.09428
11	1.549	2.932	0.13957	−6.599	22.229	0.12434

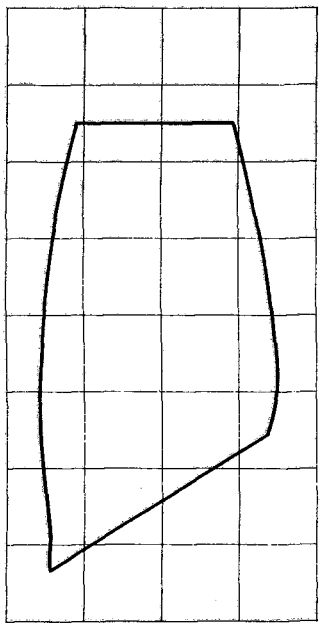


Fig. 6 Meridional view of rotor 1

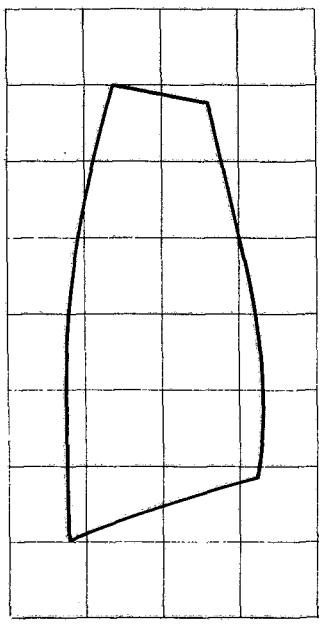


Fig. 7 Meridional view of rotor 2

Table 4

	M-L-H model	New model	Exp. results
Total pressure ratio	1.691	1.691	1.683
Isentropic efficiency, %	85.86	86.94	87.48

reductions in both sweep and Mach number. Also, the overall prediction is still 0.54 point below the experimental result.

The third test case chosen was a stage designed and tested in-house having characteristics substantially different from the first two. This stage, designed for a core compressor, had inlet guide vanes producing counterswirl to raise the inlet relative Mach number to the rotor. The basic physical characteristics of the rotor from this stage are:

Rotor inlet hub/tip radius ratio	0.643
Average rotor span/chord ratio	0.556
Rotor tip relative Mach number	1.493
Rotor tip speed	381 m/s

Inlet guide vane losses and outlet flow angles predicted by a three-dimensional viscous flow analysis, circumferentially averaged, were used to provide input to the present computations. The new loss model was used to predict rotor and stage performance. A meridional plane view of this rotor is illustrated in Fig. 8, in which the large difference relative to the first two examples is readily apparent. Table 5 presents, for this test case, computational results comparable to Tables 1 and 3. Table 6 compares the stage performance as predicted with both shock loss models and as experimentally measured. In this case, the increase in efficiency predicted as a result of the new shock loss model was 1.38 points; again, less than the calibration case because of reduced sweep and Mach number. More significant is the accuracy of the absolute level of this prediction because of the substantially different characteristics of this stage relative to the first two examples.

Conclusions

The foregoing examples do not conclusively prove the validity of the new shock model. However, they do illustrate the magnitude of the reduction in loss, or increase in efficiency, which might be expected as a result of including shock surface obliquity in shock loss calculations. Some of the imprecision in predicting the performance of the sample test cases is likely to be contained in the oversimplification associated with lumping all other losses into a Loss Parameter/Diffusion Factor Correlation. Many variations of the original Lieblein correlation are known to exist. Data points for lower values of aspect ratio and higher values of

Downloaded 01 Jun 2010 to 171.66.16.70. Redistribution subject to ASME license or copyright; see http://www.asme.org/terms/Terms_Use.cfm

Table 5 (for specific heat ratio = 1.3996)

Streamline number	Inlet rel Mach no.	Expansion angle	M-L-H shock loss	L. E. sweep	Imping. line sweep	Subject shock loss
1	0.908	11.644	0.005	28.89	25.84	0.0
3	1.031	9.404	0.021	23.59	19.83	0.013
5	1.158	7.667	0.037	18.74	16.03	0.025
7	1.285	5.544	0.059	15.90	17.68	0.041
9	1.402	4.363	0.091	13.69	27.21	0.054
11	1.493	7.250	0.152	6.98	21.52	0.126

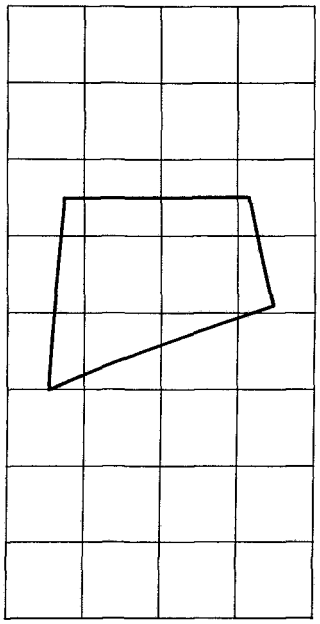


Fig. 8 Meridional view of rotor 3

sweep are currently lacking. More of this type of data will be needed to provide a definitive proof of concept.

A second conclusion reached is that significant potential may exist to employ sweep as a compressor design variable. Within the limits permitted by rotor blade stress, the deliberate incorporation of sweep may permit compressor efficiency to be maintained at higher tip speeds or, alternatively, higher efficiency to be achieved at conventional tip speeds.

One unresolved question concerns the behavior of the flow in close proximity to the outer casing. The Mach numbers immediately downstream of the shock front at the casing in all test cases were subsonic. A velocity vector passing through a shock surface inclined with respect to the casing would be turned toward or away from the casing, depending upon the direction of inclination. Since this is clearly impossible, it is

Table 6

	M-L-H model	New model	Exp. results
Total pressure ratio	2.281	2.309	2.300
Isentropic efficiency, %	84.84	86.22	85.76

presumed that, in a limited region close to the casing, the shock probably merges into something resembling a lambda shock as it approaches the casing boundary layer and a rapid readjustment in radial velocity occurs in the subsonic region. This would be consistent with the shock smearing and lower overall pressure rise typically observed with overrotor dynamic pressure measurements. At sufficiently high values of Mach number and obliquity to produce supersonic flow downstream of the principal shock surface, a reflected shock extending a short distance in from the casing seems the most likely solution.

Acknowledgment

The authors wish to extend their appreciation to Teledyne CAE for permission to use the data pertaining to the second test case.

References

1 Prince, D. C., Jr., "Three-Dimensional Shock Structures for Transonic/Supersonic Compressor Rotors," *Journal of Aircraft*, Vol. 17, No. 1, Jan. 1980, pp. 28–37.

2 Miller, G. R., Lewis, G. W., and Hartmann, M. J., "Shock Losses in Transonic Compressor Blade Rows," ASME *Transactions*, Vol. 83, Series 4, No. 3, July 1961, pp. 235–242.

3 Creveling, H. F., and Carmody, R. H., "Axial Flow Compressor Design Computer Programs Incorporating Full Radial Equilibrium, Part II," NASA CR-54531, June 1968.

4 Hearsey, R. M., "A Revised Computer Program for Axial Compressor Design," ARL TR 75-0001, Vols. I and II, A009273 and A009157 Jan. 1975.

5 Wennerstrom, A. J., and Frost, G. R., "Design of a 1500 ft/sec, Transonic, High-Through-Flow, Single-Stage Axial-Flow Compressor With Low Hub/Tip Ratio," AFAPL-TR-76-59, ADB016386, Oct. 1976.

6 Law, C. H., DeRose, R. D., Gurecki, D. J., and Strain, E. C., "Investigation of a High-Through-Flow, Single-Stage Axial-Flow Compressor with Tip Clearance Increased 0.010 Inch (Configuration 2)," AFWAL-TR-80-2079, ADB059621, Apr. 1981.

Downloaded 01 Jun 2010 to 171.66.16.70. Redistribution subject to ASME license or copyright; see http://www.asme.org/terms/Terms_Use.cfm

A Summary of Developments of the Mean-Streamline Method in China

R. Cai
Institute of Engineering Thermophysics,
Academia Sinica,
Beijing, People's Republic of China

The mean-streamline method (MSLM) proposed by Wu more than 30 years ago has been further developed in many ways in China since the fifties. Major progress in this method is summarized here. This progress includes: a completely analytical solution of the inverse problem which is extremely quick and more accurate than the original solution, the extension of MSLM to the axisymmetrical flow channels, the extension of the calculation range to transonic flow and nonisentropic flow, the estimation of applicable limits of MSLM, the improvement of MSLM with higher order derivatives, and the development of practical computer programs. The comparison of the calculation results with the experimental data is good, and the method has been widely applied in China with good success.

Introduction

The mean-streamline method (MSLM) proposed by C. H. Wu [1] more than 30 years ago has been adopted worldwide. In fact, its Russian translation [2] was published only a few months later than the original paper, and the paper has been selected by many authors of various countries as a reference. Since Wu returned to China in the fifties, he and his assistants have been successfully developing this method. The major achievements (which were previously published in Chinese) are summarized here.

Before introducing these developments, it is appropriate to briefly review the main concept of MSLM in its original form [1].

If the shape of a certain stream line and the variation of a certain physical quantity along the stream line of a plane cascade channel are known (Fig. 1), it is possible to derive expressions for the first and higher partial derivatives of Wz, Wy, and ρ with respect to the y-direction from basic equations of the steady inviscid isentropic two-dimensional flow and the following derivative relation

$$\frac{\partial}{\partial z} = \frac{d}{dz} - \tan\beta \frac{\partial}{\partial y} \tag{1}$$

In early practice, the mean streamline (MSL) $y_m(z)$, which divides the channel flow into two equal parts, and the axial specific mass flow, q_{zm}, along MSL were selected as the primary input (Fig. 1).

The velocity component field and the density field in the channel can then be expressed in a Taylor series expansion and the coordinates of channel boundary can also be obtained by numerical integration of the specific mass flow along the y-direction at each z station. Many examples show that the first three terms in the Taylor series are sufficiently accurate for most engineering calculations of typical subsonic turbine cascades.

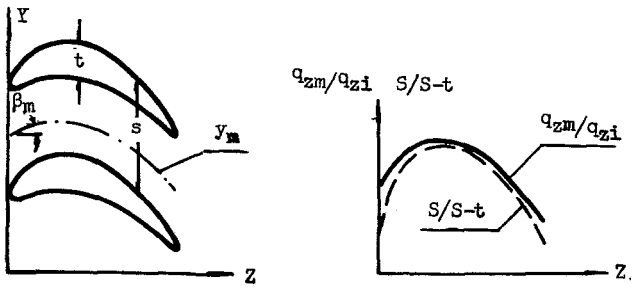


Fig. 1 Symbols used in MSLM

When solving direct problems, it is recommended that one makes an initial guess of the shape of MSL y_m (e.g., the geometrical mean line of the channel) and the distribution of the axial reduced specific mass flow, q_{zm}/q_{zi}, along this line (e.g., a function roughly proportional to $s/s-t$). Then, one can compute the channel boundary coordinates and velocity distribution. If the boundary coordinates do not fit the given data, y_m and q_{zm}/q_{zi} are modified according to one-dimensional flow relation and successive approximations are made.

The inverse problem was solved in the early days as a direct problem with a given cascade shape by experience. If the velocity distribution is not satisfied, it must be improved by progressively changing the given shape.

It is evident that MSLM can also be extended to cascades lying on an arbitrary surface of revolution [3–5]. The calculation procedure and equations are quite similar to that of the planar case.

Early Work in China

From the middle of the fifties to the early sixties, Chinese

Contributed by the Gas Turbine Division of THE AMERICAN SOCIETY OF MECHANICAL ENGINEERS and presented at the 28th International Gas Turbine Conference and Exhibit, Phoenix, Arizona, March 27–31, 1983. Manuscript received at ASME Headquarters November 30, 1982. Paper No. 83-GT-11.

Copyright © 1984 by ASME
Downloaded 01 Jun 2010 to 171.66.16.70. Redistribution subject to ASME license or copyright; see http://www.asme.org/terms/Terms_Use.cfm

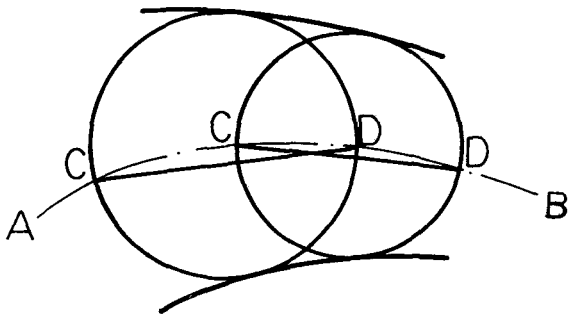


Fig. 2 Estimation of MSL

scientists applied MSLM to design and calculate many practical turbine cascades. The results and experiences gained in this period were summarized briefly in [6]. The main contents include:

1 For solving direct problems, the MSL in an incompressible plane turbine cascade can be obtained fairly accurately by graphic method as the envelope of chords CD shown in Fig. 2, and the MSL in a subsonic plane turbine cascade would shift toward the curve AB in Fig. 2, connecting the centers of inscribed circles of the channel about one-fourth of the distance between this envelope and the AB curve.

2 It is better to use the 60 percent streamline for the starting streamline instead of the MSL when calculating a reactive turbine cascade. The flow rate between the 60 percent streamline and the suction surface is 60 percent of the total flow rate of the cascade channel.

3 It is advantageous to smooth the value obtained by numerical differentiation.

Analytical Solution

A completely analytical solution form has been obtained, and has been found to be extremely simple and more accurate than the original MSLM [7–10]. The numerical differentiation and integration in the original MSLM is a somewhat cumbersome procedure and is a source of calculation error. The numerical method is perhaps a useful tool for direct problems, but it is not a necessary one for inverse problems.

Instead of $y_m(z)$ and $q_{zm}(z)$ in early works, the variation of Laval number along MSL $\lambda_m(z)$ and $y_m(z)$ are given for a plane cascade to simplify calculation and to make transonic calculation possible, then the following equations can be derived to determine the partial derivatives of q_z and λ with respect to y [7]

$$\frac{1}{q_z}\frac{\partial q_z}{\partial y}=\left[\beta' \ \frac{\lambda'}{\lambda}\right]\cdot\begin{bmatrix} B_1-B_{14} \\ B_2-B_2 \end{bmatrix}\cdot\begin{bmatrix} 1 \\ M^2 \end{bmatrix}/\cos\beta \tag{2}$$

$$\frac{1}{\lambda}\frac{\partial \lambda}{\partial y}=\left[\beta' \ \frac{\lambda'}{\lambda}\right]\cdot\begin{bmatrix} B_7 \\ B_8 \end{bmatrix} \tag{3}$$

$$\frac{1}{q_z}\frac{\partial^2 q_z}{\partial y^2}=\left[\beta'^2 \ \beta'' \ \beta\frac{\lambda'}{\lambda} \ \frac{\lambda''}{\lambda} \ \left(\frac{\lambda'}{\lambda}\right)^2\right]$$

$$\cdot\begin{bmatrix} B_3 & B_{15} & (2-\gamma)B_{20} & 0 \\ B_4 & -3B_{16} & 0 & 0 \\ B_5 & B_{17} & (7-3\gamma)B_{16} & 0 \\ B_6 & B_{18} & -B_{20} & 0 \\ 0 & B_{19} & B_{21}-\gamma B_6 & -\gamma B_{20} \end{bmatrix}\cdot\begin{bmatrix} 1 \\ M^2 \\ M^4 \\ M^6 \end{bmatrix}\Big/\cos\beta \tag{4}$$

$$\frac{1/8}{\Lambda}\frac{\partial^2 \lambda}{\partial y^2}=\left[\beta'^2 \ \beta'' \ \beta\frac{\lambda'}{\lambda} \ \frac{\lambda''}{\lambda} \ \left(\frac{\lambda'}{\lambda}\right)^2\right]$$

$$\cdot\begin{bmatrix} B_9 & 0 & 0 \\ 2B_{10} & 0 & 0 \\ B_{11} & -B_{10} & 0 \\ B_{12} & B_{13} & 0 \\ B_{13} & 0 & \gamma B_{13} \end{bmatrix}\cdot\begin{bmatrix} 1 \\ M^2 \\ M^4 \end{bmatrix} \tag{5}$$

In the preceding formulas, where B_i are various simple trigonometric functions of β, their definition can be found in the Appendix.

The cascade channel boundary coordinates and the resultant velocity distribution can then be obtained directly with von Mises transformation (noticing that $dy=d\psi/q_z$) and Taylor series expansion [8, 9]

$$y=y_m+\frac{\Delta\psi}{q_{zm}}-\frac{1}{2}\left(\frac{1}{q_z}\frac{\partial q_z}{\partial y}\right)_m\cdot\left(\frac{\Delta\psi}{q_{zm}}\right)^2+$$

$$+\frac{1}{6}\left[3\left(\frac{1}{q_z}\frac{\partial q_z}{\partial y}\right)^2-\frac{1}{q_z}\frac{\partial^2 q_z}{\partial y^2}\right]_m\left(\frac{\Delta\psi}{q_{zm}}\right)^3+\cdots \tag{6}$$

Nomenclature

B_i = trigonometric function of β (see Appendix)
F = force
l = stream line coordinate
M = Mach number
n = coordinate normal to stream line
Q = heat
q = reduced specific mass flow, $\rho w/\rho_* w_*$
r = radius
s = spacing or entropy
T = temperature
t = blade thickness
W = velocity
x = meridional stream line coordinate (see Fig. 4)
y = coordinate (see Fig. 1)
z = coordinate (axial direction)
β = $\tan^{-1}(dy/dz)$
γ = specific heat ratio
λ = Laval number, W/W_*
ρ = density
σ = $\tan^{-1}(dr/dz)$
τ = normal thickness of stream filament of revolution
φ = angular coordinate
$\Delta\psi$ = difference of stream functions
Ω = curvature of stream line
ω = angular speed of rotor

Subscripts

e = exit
i = inlet, various numbers
l = stream direction component
m = on the mean (selected) stream line
x = meridional streamline direction component
y = tangential component
z = axial component
$*$ = critical

Superscript

$'$ = d/dz
= divided by Ω_m

Downloaded 01 Jun 2010 to 171.66.16.70. Redistribution subject to ASME license or copyright; see http://www.asme.org/terms/Terms_Use.cfm

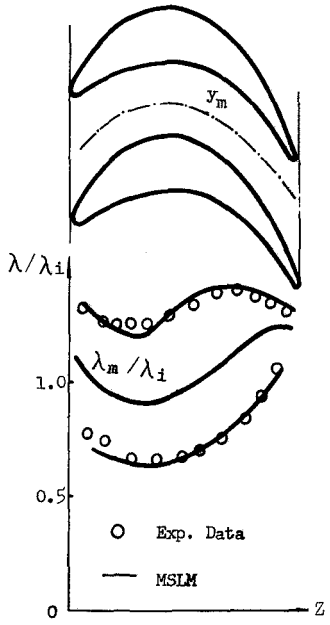


Fig. 3 Comparison of calculated and experimental data

$$\lambda=\lambda_m\left[1+\left(\frac{1}{\lambda}\frac{\partial\lambda}{\partial y}\right)_m\cdot(y-y_m)+\right.$$
$$\left.+\frac{1}{2}\left(\frac{1}{\lambda}\frac{\partial^2\lambda}{\partial y^2}\right)_m\cdot(y-y_m)^2+\cdots\cdots\right] \quad (7)$$

It is thus obvious that the whole computation is extremely simple. When the analytical functions of $y_m(z)$ and $\lambda_m(z)$ are given, the differentiation of these two functions can be made analytically and functions β', β'' and λ', λ'' can be obtained easily and exactly. The whole computation is a straightforward one using only equations (2–7). Years ago, one could calculate a good cascade design within eight hours using a slide rule, because there was no numerical differentiation. However, with the modern computer, the whole computation is carried out in less than 1 s [11]. Due to the simplification, a small portable calculator, such as Texas Instruments TI 59, is sufficient for programming [12].

In the case of programming, the computer can not differentiate analytically as a human being does. This difficulty can be surmounted, however, by the following ways [11]: First, some analytical functions of $y_m(z)$ and $\lambda_m(z)$ in common use are chosen, so that their derivatives are obtained beforehand and put into the code. Second, if an arbitrary analytical function is chosen, an accurate enough numerical differentiation can also be obtained by selecting a very small appropriate difference increment, because the analytical functions of $y_m(z)$ and $\lambda_m(z)$ have been given.

Selection of independent design functions $y_m(z)$ and $\lambda_m(z)$ is an important point for the inverse problem. Many analytical functions were tried and their effect was analyzed qualitatively according to aerodynamic concept also. It is recommended that a circular arc, or $\beta''=0$ curve, be selected to be y_m in the upstream region of an axial flow turbine cascade channel ($\beta_m \geq 0$ in Fig. 1) and a catenary curve, or $\beta''=0$ curve, should be selected in the downstream region ($\beta_m \leq 0$ in Fig. 1). An elliptical arc or parabolical curve, or $d^2\beta/dy^2=0$ curve, is selected to be y_m of an axial flow compressor cascade channel. Of course, when different curves are used together to be MSL in a cascade channel, y_m, β_m, β_m', and β_m'' must all be continuous at the connecting point. The value of β_m at leading edge station is recommended to be β_i.

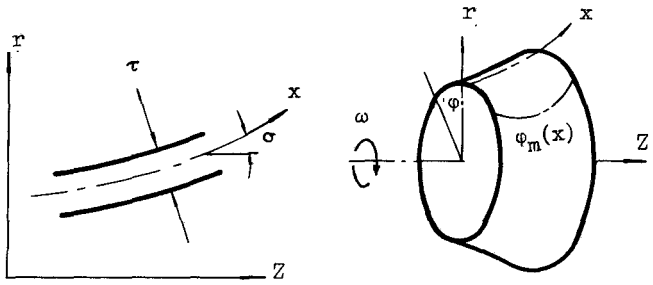


Fig. 4 Revolutionary stream surface and coordinates

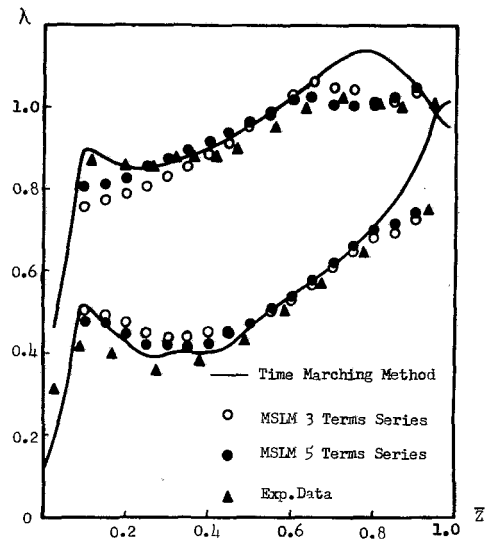


Fig. 5 Calculation example of transonic turbine cascade

For reactive turbine cascade, β_m is suggested to be several degrees larger than β_i. The value of β_m at the trailing edge station should be β_e. In the case of $\lambda_m \to 1$, it is suggested that $|\beta_m|$ is somewhat less than $|\beta_e|$. $\lambda_m(z)$ is recommended to be a monotonic function, and it is suggested that λ_m' near the downstream front approximates to zero. λ_m at leading or trailing edge station is recommended to be (1.10–1.35) λ_i or (1.02–1.08) λ_e, but not larger than 1 for subsonic cascades. The larger coefficient corresponds to a thicker blade thickness near front or higher Laval number. The values of β_i, β_e, λ_i, λ_e, and of the cascade solidity are given for an inverse problem.

Evidently, there are difficulties in calculating the direct problem with the analytical solution, this is because successive approximation with analytical functions is not an easy job. But if one is skillful at this method and knows how to adjust the shape of various analytical curves, it is still possible to do the analytical solution. For example, a NACA turbine cascade is solved by this method and its calculated result is compared with experimental data as shown in Fig. 3 [7]. It can be seen that $\lambda_m(z)$ of this cascade is not monotonic and this cascade is perhaps not a good design.

Of course, the aforementioned analytical solution and its merit can also be extended to cascades lying on an arbitrary stream surface of revolution [10]. In this case, the equations are similar to the plane case. There are merely some additional terms in the partial derivatives of $q_{xm}(x)$ and $\lambda_m(x)$ such as terms including $1/\tau$. $d\tau/dx$, $\sin\sigma/r$ and $\omega\sin\sigma/W$ (see Fig. 4).

With the concept and equations of MSLM and the analysis of the order of magnitude, the influence of the thickness of stream filament of revolution, of the inclined angle of the

Downloaded 01 Jun 2010 to 171.66.16.70. Redistribution subject to ASME license or copyright; see http://www.asme.org/terms/Terms_Use.cfm

stream surface of revolution, and of the rotating speed of the rotor were studied [10]. It was found that the variation of thickness (equivalent to AVDR) has a most important influence in a general axial turbomachinery cascade, and the plane cascade assumption is probably unjustified not only for a long blade stage but also for a short blade stage with low aspect ratio and significant divergent or convergent angle in the meridional plane.

Extension to Other Flows

1 Originally, MSLM was only used to calculate the flow in turbine cascade channels or centrifugal compressor impeller channels [1, 5]. However, the flow in axial flow compressor cascade channels is somewhat similar to a part of the turbine cascade channels, so that there is no reason why it is not possible to calculate the former with MSLM [7]. Indeed, there have been many successful compressor cascade designs since the middle of the sixties, using MSLM.

2 Expansion along the y- or φ-direction is particularly suitable for cascade channels. But it is not suitable to flow channels with very large turning angle and with inlet and exit section approximately normal to streamlines. In that case, it is more appropriate to expand along the normal direction of the mean streamline. The formulas suitable for normal expansion can be obtained simply by replacing $\partial/\partial y$, β and d/dz in equations (2-7) with $\partial/\partial n$, 0 and d/dl [13].

It is evident that normal expansion equations are simpler than (2-7). However, the total calculation may not be simpler because there is an additional coordinate transformation from (l, n) to (z, y).

3 It is well known that the solution of two-dimensional transonic flow problem is not easy because there are two different kinds of flow regions described by two different types of differential equations. However, with one-dimensional flow, there has been a very simple analytical solution suitable for both subsonic and supersonic flow, so it is reasonable to suggest that the difficulty in calculating two-dimensional transonic flow can be solved by splitting the calculation into two one-dimensional flow calculations just as MSLM does [14]. Indeed, when MSLM is improved by analyzation and choosing $\lambda_m(z)$ instead of $q_{zm}(z)$ as independent variable, it is more convenient to prove this feasibility and more possible to obtain the necessary operational accuracy needed for transonic flow.

Evidently, the calculation of one-dimensional flow along MSL is not difficult; it is only necessary to check whether the Taylor series expansion across the mean streamline is feasible in a transonic flow region. Of course, it is impossible to expand by Taylor series with finite terms when there is discontinuity, so MSLM can not be applied to transonic flow with strong shock. However, for other transonic flow without shock or with a weak shock, expansion is feasible for both subsonic and supersonic flow regions because the partial derivative derived from the basic equation for subsonic and supersonic flow are the same and there is no singularity in derived expressions in MSLM at $M=1$. Moreover, the difference between one-dimensional supersonic and subsonic flow is merely that $q(M)$ is a monotonic decreasing function or increasing function, and there is a maximum at $M=1$. Then, if MSLM can be applied for transonic flow, the following relations must be satisfied: $\partial q_1/\partial n=0$, $\partial^2 q_1/\partial n^2<0$ at $M=1$, $\partial\lambda/\partial n$ and $\partial q_1/\partial n$ have the same sign at $M<1$ and the opposite sign at $M>1$. According to those normal expansion equations it can be seen that all these relations do hold true in expressions in MSLM.

Recently, many transonic cascades have been designed and calculated by MSLM. For examples, the calculated and experimental results of a transonic turbine cascade are shown in Fig. 5 [19]. It can be seen that the agreement is good.

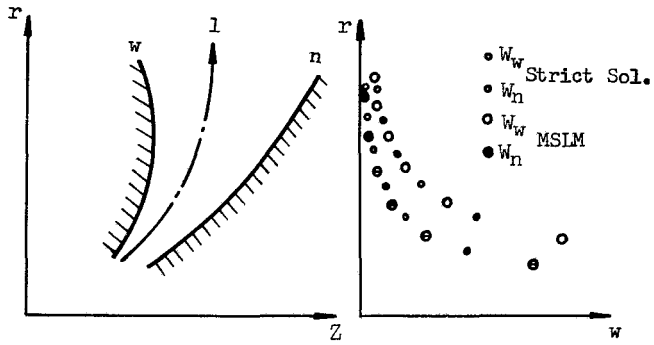


Fig. 6 Calculation example of axisymmetric channel

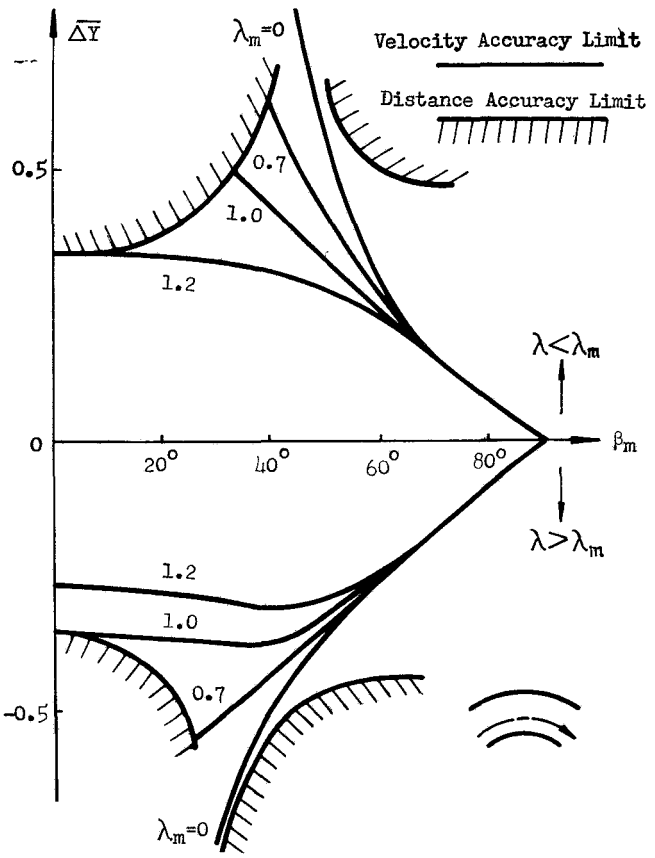


Fig. 7 The permitted expansion distance of MSLM in vortex flow

4 It is a general practice now to give an entropy increase calculated from experimental data as an input to approximately account for the viscous effect. Many authors have chosen the simplified steady nonviscous momentum equation and steady adiabatic energy equation as basic equations, but there is a question of inconsistency when this is done. For adding a simple consideration of loss in MSLM in a consistent manner, a simple flow model was proposed and the resulting equations of MSLM are given in [15]. This model includes fictitious heat transfer, $dQ=Tds$, and fictitious volumetric force, F, in flow directions between every nonviscous flow element and a fictitious surrounding. It is also assumed that the fictitious work $Fdl/\rho=dQ=Tds$ and $\partial s/\partial\varphi=0$ can be applied to obtain simple results and to simulate approximate flow conditions in cascades. Of course, some terms including ds/dx are added into the derived expressions. This approach has been programmed.

5 Axisymmetrical annular flow is also a two-dimensional flow, so it is possible to calculate the axisymmetrical flow

Downloaded 01 Jun 2010 to 171.66.16.70. Redistribution subject to ASME license or copyright; see http://www.asme.org/terms/Terms_Use.cfm

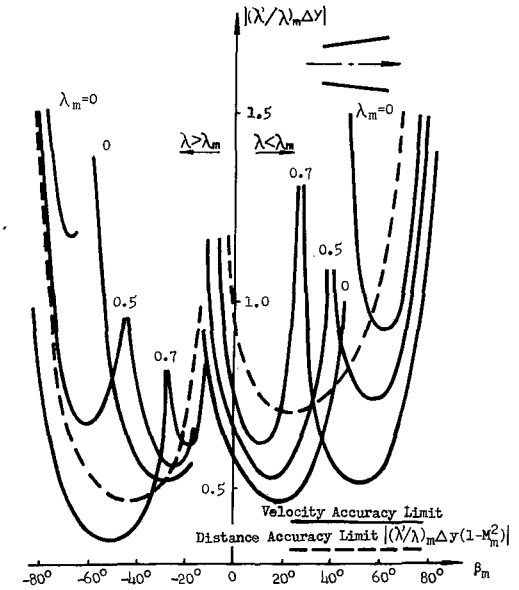


Fig. 8 The permitted expansion distance of MSLM in source flow

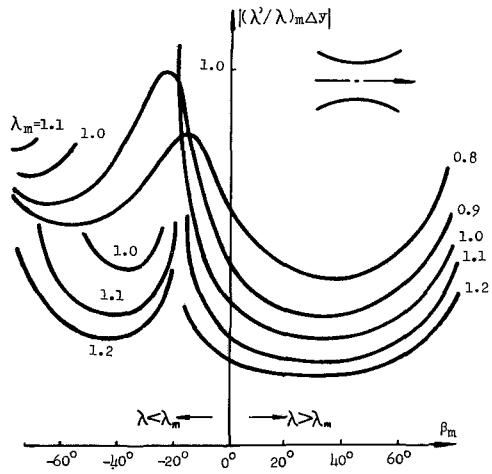


Fig. 9 The permitted expansion distance of MSLM in λ'_m = constant flow

channel, such as the annular passage of turbomachine, with MSLM. Three sets of equations suitable for different type of this flow are given in [16]. The expressions of partial derivatives are similar to that of plane flow, except that some terms, such as $1/r$, are added to them. One of the calculated examples is shown in Fig. 6, where an axisymmetrical channel having analytical solution is computed by MSLM. The comparison of results obtained in analytical solution and by MSLM is fairly good.

Accuracy of MSLM

Many examples obtained so far in typical turbine and compressor cascades indicate that the first three terms in the Taylor series of MSLM are sufficient for engineering accuracy and can be extended to transonic field as well. Indeed, all these examples are checked only as specific cases and so the conclusion can not be considered to be universal. It is better to derive the general error equations rigorously as far as possible in order to ascertain limits of applicability of this method.

The essence of MSLM is to correct the one-dimensional flow on MSL to two-dimensional over the entire channel by Taylor series expansion across the MSL. Therefore, it is more accurate when the flow field does not deviate much from the one-dimensional flow or when the partial derivatives across the MSL and the distance of expansion are small. When the turning of flow is more gentle (that is, the radius of curvature of mean stream line, Ω_m, is larger or the β'_m is smaller), and when the acceleration $(\lambda'/\lambda)_m$ of flow is smaller, the deviation of flow field from the one-dimensional flow is smaller. The basic correcting terms in MSLM equations are $\Delta y/\Omega_m$ or $\beta'_m\Delta y$, $(\lambda'/\lambda)_m\Delta y$, etc. It is possible to separate the calculation errors of MSLM basically into two parts: one is due to pure turning and the other is due to pure acceleration. Their values can be obtained by comparison between the solutions of MSLM and the rigorous solutions of the pure turning flow and the pure accelerating flow, respectively. Moreover, since the analytical solution of MSLM has already been obtained, it is possible to derive the error equations expressed in analytical forms.

Of course, the exact value of calculation error of arbitrary flow is by no means the sum of these two terms mentioned above. Nevertheless, the influence of turning or acceleration is considered originally as a small term in MSLM, so that the effect of higher order terms in the error can be neglected.

The details of the derivation of error equations is given in [17]. It is only necessary to point out here that there is no throat in source flow, so the fluid does not pass a sonic section and the transonic flow does not exist. Therefore, it is only possible to compare the solution of MSLM using second-order derivatives in transonic region of pure acceleration flow with the improved MSLM using fourth-order normal expansion terms [18]. Because our purpose is to determine the small calculation error of the second-order MSLM, it can be assured that the error of the fourth-order MSLM can be reduced to a very small amount in this case, and the solution of the fourth-order MSLM will approximate the rigorous solution.

If 4 percent is chosen as the permissible maximum error of λ and Δy, the permissible maximum expansion distance, Δy, for pure turning flow is plotted in Fig. 7. According to this figure, the MSLM can be applied effectively to calculate the subsonic and transonic turning flow in general cascades, and the applicable limits can be found.

The permissible maximum absolute value of $(\lambda'/\lambda)_m\Delta y$ for pure subsonic and transonic accelerating flow is shown in Figs. 8 and 9, respectively. This parameter is basically determined by the velocity accuracy limit. The permissible value of $(\lambda'/\lambda)_m\Delta y$ can be larger than or equal to 0.2–0.4, depending on Mach number and direction of expansion; and it is possible to calculate subsonic and most transonic accelerating flow accurately with MSLM.

This analysis is conditioned upon a strong discontinuity not existing in the flow (including discontinuity in derivative). A discontinuity may exist, however, when the flow is supersonic. For modern low transonic cascades with inlet $M<1$, designers always attempt to avoid the appearance of such a discontinuity, so that this analysis is still valid for low transonic cascades.

MSLM With Higher-Order Derivatives—Computer Code for Direct Problem

Evidently, the calculation error of MSLM can be lowered by using more expansion terms. The equations including partial derivatives up to fourth-order suitable for cascades lying on arbitrary surface of revolution were derived in [19]. This derivation is similar to that done by Wu in [1] and [3] for first- and second-order derivatives, and is rigorous. Similarily, the cascades channel boundary coordinates can also be obtained directly with von Mises transformation.

With these equations, computer codes with higher-order

Downloaded 01 Jun 2010 to 171.66.16.70. Redistribution subject to ASME license or copyright; see http://www.asme.org/terms/Terms_Use.cfm

derivatives have been successfully programed for direct and inverse problems of plane cascades or cascades lying on arbitrary stream surface of revolution [19]. In the direct problem there are some necessary measures adopted to improve the program:

1 Correcting the $y_m(z)$ and $q_{zm}(z)$ of MSL by one-dimensional considerations and introducing a relaxation factor (0.1–0.5, lower value for higher Mach number and earlier corrections) to improve the convergence

2 Smoothing the values obtained by numerical differentiation to reduce the accumulated error

3 Approximating the new $y_m(z)$ and $q_{zm}(z)$ by least squares in the successive approximation to avoid unreasonable results

4 Increasing the Mach number step by step and/or using 60 percent streamline instead of 50 percent streamline to enable one to calculate high subsonic and transonic cascades

An example of plane cascades computed by this direct problem code is shown in Fig. 5. It can be seen that the agreement of computed result of MSLM and experimental data is good, and the data obtained with fourth-order partial derivatives is better than that obtained with second-order partial derivatives, particularly near the leading edge. The computing time needed for a complete calculation is still very short, less than 1 min by computer.

Summary

It can be concluded from the materials presented herein that the MSLM developed by scientists in China, led by Prof. Wu, is capable of designing and calculating a great variety of flow channels. This includes subsonic and transonic cascades, axisymmetrical channels and others. Speed is extremely fast and accuracy is sufficient for most engineering calculations. This method has been applied widely and successfully in China (for example, see [20] and [21]). However, it is unsuitable for flow with extremely large curvature and acceleration or for flow regions having strong shocks. Furthermore, MSLM is essentially a channel calculation method, so it is not capable of calculating the flow field outside the channel.

Acknowledgment

The author acknowledges the guidance of Prof. C. H. Wu and the help of many colleagues in the past 26 years and during the preparation of this paper.

References

1 Wu, Chung-hua, and Brown, C. A., "A Theory of the Direct and Inverse Problems of Compressible Flow Past Cascade of Arbitrary Airfoils," *J.A.S.*, Vol. 19, No. 3, Mar. 1952, pp. 183–196.

2 *Ibid.* (in Russian), "Sbornik Perevodov," *Voprosy Raketnoy Tehkniki*, IIL, 1953, No. 1.

3 Wu, Chung-hua, Brown, C. A., and Prian, V. D., "An Approximate Method of Determining the Subsonic Flow in an Arbitrary Stream Filament of Revolution Cut by Arbitrary Turbomachine Blades," NACA TN 2802, 1952.

4 Wu, Chung-hua, "A Method to Determine the Compressible Fluid Flow in Cascade Lying along Arbitrary Stream Filament of Revolution and the Design of Such Cascade," *Journal of Mechanical Engineering*, (Chinese), Vol. 4, No. 1, 1956, pp. 21–46.

5 Wu, Chung-hua, "A Theory of the Direct and Inverse Problems of Compressible Flow Past Cascade of Arbitrary Blade Sections Lying in Arbitrary Stream Filament of Revolution in Turbomachine," *Scientia Sinica*, Vol. 8, No. 12, Dec. 1959, pp. 1529–1557.

6 Liu, K., Hsueh, M., and Wu, C. H., "Aerothermodynamic Analysis and Design of Turbomachines," *Journal of Mechanical Engineering*, (Chinese), Vol. 11, No. 1, 1963, pp. 1–28.

7 Cai, R., "The Analytical Solution of MSLM for 2-D Cascades," *Journal of Mechanical Engineering*, (Chinese), Vol. 14, No. 1, 1966, pp. 17–49.

8 Liu, K., Private Communication, 1964.

9 Ruan, Z., and Liu, Y., Bachelor theses, China University of Science and Technology, 1964.

10 Cai, R., "A Method of Designing Axial Flow Turbomachine Cascades along an Arbitrary Stream Filament of Revolution," *Journal of Mechanical Engineering*, (Chinese), Vol. 15, No. 1, 1979, pp. 24–36.

11 Cai, R., and Shen, J., "The MSLM Program for Designing Plane Cascades and Some Calculated Results," *Journal of Engineering Thermophysics*, (Chinese), Vol. 2, 1981, pp. 114–120.

12 Cai, R., "Design Program of MSLM for Subsonic and Transonic Flow with Texas TI59 Portable Calculator," Research Report 81-25, Inst. Engg. Thermophysics, Academia Sinica, 1981.

13 Li, F., Bachelor thesis, China University of Science and Technology, 1964.

14 Cai, R., "The Calculation of Transonic Flow in 2-D Cascades," *Journal of Engineering Thermophysics*, (Chinese), Vol. 1, No. 3, 1980, pp. 223–229.

15 Cai, R., "A Simple Self-Consistent Model of Simulating Flow Loss with Entropy only and Its Application in MSLM," Research Report 81-48, Inst. Engg. Thermophysics, Academia Sinica, 1981.

16 Cai, R., "MSLM for Solving Potential Flow in Axisymmetric Annular Passage," *Journal of Mechanical Engineering*, (Chinese), Vol. 15, No. 2, 1979, pp. 53–64.

17 Cai, R., "The Accuracy of MSLM in Subsonic and Transonic Regions," *Proceedings of 5th ISABE*, Paper No. 71, Feb. 1981.

18 Cai, R., "The Semianalytical Equations of Fourth-order MSLM for Designing Transonic Nozzles," Research Report 80-Aero-016, Inst. Engg. Thermophysics, Academia Sinica, 1980.

19 Wang, Z., and Cai, R., "MSLM with Higher-Order Derivatives and the Computer Code," paper presented at 3rd Annular Symposium of Chinese Society of Engineering Thermophysics, 1982.

20 Wu, W., Zhu, R., and Liu, C., "Computational Design of Turbomachine Blades," *Journal of Aircraft*, Vol. 17, No. 5, May 1980, pp. 319–325.

21 Academia Sinica and Shenyang Aeroengine Co., "Theory, Method and Application of Three-dimensional Flow Design of Transonic Axial-Flow Compressor," *Journal of Engineering Thermophysics*, (Chinese), Vol. 1, No. 1, 1980, pp. 44–54.

APPENDIX

B_i Functions

$$B_1 = \cos\beta(2\cos^2\beta - 1) \qquad B_2 = 2\cos^2\beta\sin\beta$$
$$B_3 = \cos\beta(12\cos^4\beta - 11\cos^2\beta + 1) \qquad B_4 = \cos^2\beta\sin\beta(4\cos^2\beta - 1)$$
$$B_5 = 2\cos^2\beta\sin\beta(8\cos^2\beta - 3) \qquad B_6 = \cos^3\beta(3 - 4\cos^2\beta)$$
$$B_7 = \cos^2\beta \qquad B_8 = \cos\beta\sin\beta$$
$$B_9 = \cos^2\beta(5\cos^2\beta - 3) \qquad B_{10} = \cos^3\beta\sin\beta$$
$$B_{11} = \cos\beta\sin\beta(6\cos^2\beta - 1) \qquad B_{12} = \cos^2\beta(1 - 2\cos^2\beta)$$
$$B_{13} = \cos^4\beta \qquad B_{14} = \cos^3\beta$$
$$B_{15} = \cos^3\beta(6 - 11\cos^2\beta) \qquad B_{16} = \cos^4\beta\sin\beta$$
$$B_{17} = \cos^2\beta\sin\beta(6 - 26\cos^2\beta) \qquad B_{18} = \cos^3\beta(5\cos^2\beta - 3)$$
$$B_{19} = \cos^3\beta(10\cos^2\beta - 9) \qquad B_{20} = \cos^5\beta$$
$$B_{21} = \cos^3\beta(6 - 7\cos^2\beta)$$

Downloaded 01 Jun 2010 to 171.66.16.70. Redistribution subject to ASME license or copyright; see http://www.asme.org/terms/Terms_Use.cfm

A Streamline Curvature Method for Calculating S_1 Stream Surface Flow

S. K. Mao
Engineer.

D. T. Li
Associate Engineer.

Harbin Steam Turbine Plant,
Harbin, Heilongjiang Province,
People's Republic of China

A streamline curvature method for calculating S_1 surface flow in turbines is presented. The authors propose a simple method in which a domain of calculation can be changed into an orderly rectangle without making coordinate transformations. Calculation results obtained on subsonic and transonic turbine cascades have been compared with those of experiment and another theory. Good agreement has been found. When calculating blade-to-blade flow velocity at subsonic speed, a function approximation technique can be used in lieu of iteration method in order to reduce calculation time. If the calculated flow section is of a mixed (subsonic-supersonic) flow type, a Boolean expression obtained from the truth table of flow states is proposed to judge the integrated character of the mixed flow section. Similarly, another Boolean expression is used to determine whether there exists a "choking" of the relevant section. Periodical conditions are satisfied by iterating the first-order derivative of stagnation streamline, which is formed simultaneously. It can be proved that the stagnation streamline formed in this way is unique.

Introduction

According to C. H. Wu's theory, the fluid flow in turbomachinery can be represented by the flow on the S_1 and S_2 stream surface [1].

The S_1 stream surface is warped in space [3]. To simplify the problem, one can assume the S_1 stream surface to be an arbitrary surface of revolution, for cascades of which Wu and others had long ago given computation and design methods [4, 5, 6]. The stream curvature method proposed in this paper can be used to calculate S_1 stream surface without making any simplifications.

Though the equation itself is to some extent characterized by universality (i.e., three-dimensional with the nonuniformity of peripheral parameters and the changes of entropy being taken account of), we still used the plane cascade data to test the validity of the method referred to earlier. With this aim in mind, all equations used in computations are two dimensional. A subsonic cascade with known test results has been calculated by using the said method. Comparison of calculated and test results shows fairly good agreement.

With the development of high output steam and gas turbines the calculation of transonic flow past cascades has become one of the most urgent problems demanding early solution. Theory and computational practices have shown that the streamline curvature method can be applied to calculate both subsonic and isentropic transonic flow [7, 8, 9]. This has been borne out by our own computational practices

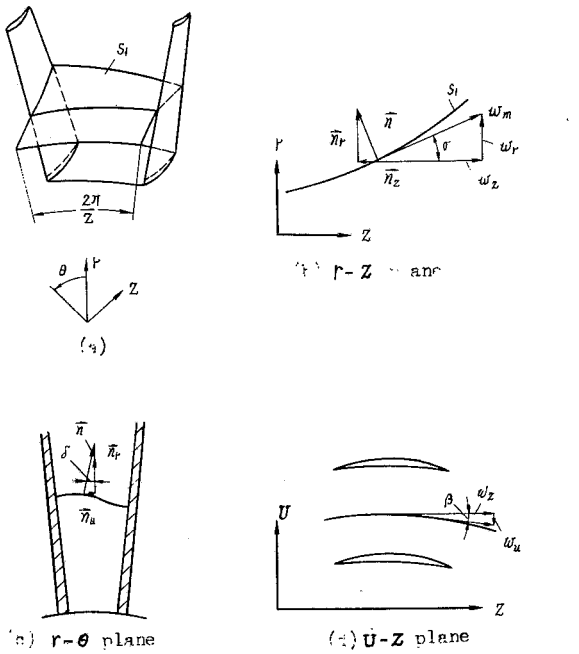


Fig. 1 Definition of flow angles

[10, 11]. We have calculated the transonic cascade flow given in [12]. The computation results have been compared with those of the hodograph method. Fairly good agreement has been found.

For ease of flow rate integration and adjustment of flow and streamline locations during the computation process,

Contributed by the Gas Turbine Division of THE AMERICAN SOCIETY OF MECHANICAL ENGINEERS and presented at the 28th International Gas Turbine Conference and Exhibit, Phoenix, Arizona, March 27-31, 1983. Manuscript received at ASME Headquarters December 3, 1982. Paper No. 83-GT-16.

Copyright © 1984 by ASME
Downloaded 01 Jun 2010 to 171.66.16.70. Redistribution subject to ASME license or copyright; see http://www.asme.org/terms/Terms_Use.cfm

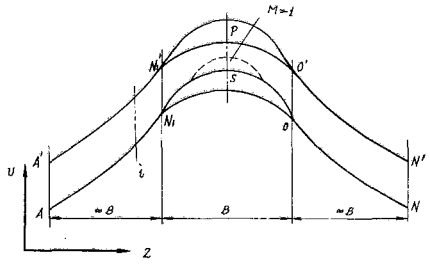


Fig. 2 Mixed flow type cascade

there usually exists the need to transform the flow domain into a rectangular domain in some transformation plane, which will make the calculation process somewhat complicated. By way of simple remoulding of the streamline first- and second-order derivative at various node points in the flow domain, we have transformed the flow domain into an orderly rectangle. As a consequence, the aim of coordinate transformation has been attained without incurring any attendant complexities.

A rather difficult problem during the flow field calculation is the determination of stagnation streamlines downstream and upstream of cascade with periodical conditions being satisfied at the same time. The method proposed by D. H. Wilkinson consists in iteration of stagnation streamline locations and the formation of stagnation streamlines while simultaneoulsy satisfying periodical conditions [13]. We resolved the problem by the iteration of the first-order derivative of stagnation streamline. This method has two advantages: (*a*) the accuracy is higher than that attainable by the iteration of locations; (*b*) the stagnation streamline achieved by the iteration of the streamline first-order derivative is unique. We will give a proof of this.

During the calculation process, the suction surface velocity, W_s, can be determined by iteration to make the calculated flow rate, G_{cal}, satisfy relevant requirements. The higher the degree of approximation of G_{cal} to inlet flow rate, the smaller the W_s increment, consequently, the longer the computation time. Under subsonic flow conditions an improvement of this situation by use of function approximation is possible. A three-point parabola can be used to approximate the $G_{cal} - W_s$ curve.

In the central portion of the blade suction surface given by Hobson, there exists a supersonic zone (see Fig. 2). When solving by iteration for such a subsonic-supersonic mixed flow, one may encounter the problem of ascertaining whether the calculated section pertains to subsonic or supersonic flow. Only on the basis of the general character of the said section is it possible to determine the direction of velocity iteration (increasing or decreasing). From the truth table of flow, a Boolean expression for judging the character of the said section may be obtained. On the basis of the Boolean expression value, one can determine the direction of velocity iteration. The ascertainment of choking is an important problem during transonic cascade calculations by the streamline curvature method. In [14] it has been proved by mathematical analytical method that there is no solution for flow equation if there exists choking. We have also established whether there is choking or not by using another Boolean expression obtained from a truth table of flow states.

The Equation of Motion of S_1 Stream Surface and Its Difference Schemes

For the adiabatic steady flow of compressible ideal gas on S_1 stream surface, the equation of motion can be derived as follows

$$\frac{\partial W^2}{r\partial\theta} + \xi_1(\theta)\, W^2 + \xi_2(\theta) = 0 \tag{1}$$

where

$$\xi_1(\theta) = -\frac{2}{B'}\left\{\frac{dtg\beta}{dZ} - tg\delta\frac{dtg\sigma}{dZ} + \frac{1}{r}\left[tg\beta tg\sigma + (1+\epsilon)^2 tg^2\beta tg\delta\right] + \frac{2\epsilon}{r}tg\beta tg\sigma\right\} \tag{2a}$$

$$\xi_2(\theta) = -(tg\beta - tg\delta tg\sigma)\frac{dW_z^2}{dZ} - 2\left(\frac{\partial I}{r\partial\theta} - rW^2 tg\delta - T\frac{\partial S}{r\partial\theta}\right) \tag{3a}$$

In $\xi_1(\theta)$

$$B' = (\sec^2\sigma + tg^2\beta) \tag{4a}$$

$$\epsilon = \frac{u}{W_u} \tag{5}$$

For the derivation of equation (1) see the Appendix.

If the flow is isentropic and inlet parameters are uniform, then in equation (2*a*)

$$\frac{\partial I}{r\partial\theta} = \frac{\partial S}{r\partial\theta} = 0$$

In the case, if S_1 is an arbitrary surface of revolution, we have

Nomenclature

F, F' = output values of Boolean expressions
G_{cal} = calculated flow rate
G_{pre} = flow rate calculated on the basis of given inlet conditions
H = channel height
$\bar{H}$ = channel relative height
I = generalized enthalpy
i = calculation station notation in the Z-direction
i = gas enthalpy
j = calculation station notation in the U-direction
M = Mach number
m = notation of the last calculation station in the U-direction
$\mathbf{n}$ = normal unit vector on stream surface
P = pressure
p = pressure surface
S = gas entropy
s = suction surface
T = absolute temperature
U = plane ordinate
u = blade tangential velocity
W = relative velocity
ω = blade angular velocity
r,θ,z = coordinates of cylindrical coordinate system
μ = flow rate accuracy
μ_1 = relaxation factor
β,δ,σ = gas flow angle defined in Fig. 1

Superscript

p = iteration times

Subscripts

r,θ,z = components of three coordinates
s = values at the suction surface
i,j = notations of calculation stations in the Z and U direction, respectively
1, 2 = cascade inlet and outlet value, respectively
u = disk tangential component

Downloaded 01 Jun 2010 to 171.66.16.70. Redistribution subject to ASME license or copyright; see http://www.asme.org/terms/Terms_Use.cfm

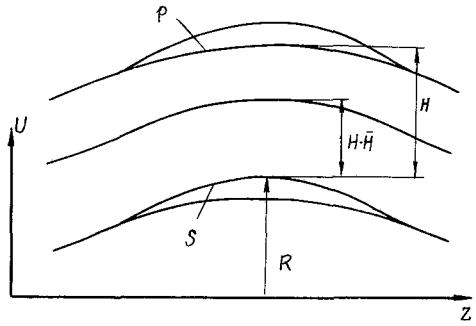


Fig. 3 Definition of H, $\bar{H}$, R

$$\xi_1'(\theta) = -\frac{2}{B'}\left[\frac{dtg\beta}{dZ} + \frac{1}{r}tg\beta tg\sigma(1+2\epsilon)\right] \tag{2b}$$

$$\xi_2'(\theta) = -tg\beta\frac{dW_z^2}{dZ} \tag{3b}$$

If S_1 is a plane, then

$$\xi_1''(\theta) = -\frac{2}{B''}\frac{dtg\beta}{dZ} \tag{2c}$$

$$\xi_2''(\theta) = -tg\beta\frac{dW_z^2}{dZ} \tag{3c}$$

In equation (2c)

$$B'' = (1+tg^2\beta) \tag{4b}$$

In case of S_1 being a plane, the equation of motion is

$$\frac{\partial W^2}{\partial U} - \frac{2}{(1+tg^2\beta)}\frac{dtg\beta}{dZ}W^2 - tg\beta\frac{dW_z^2}{dZ} = 0 \tag{6}$$

This is the basic equation for calculating plane cascades. The central difference scheme of this equation has been chosen as the equation for computation purposes, for in [15] it has been explained that the central difference in the U-direction is applicable without exception to subsonic, sonic, and supersonic flow regimes.

At the same time, for a certain station, i, in the Z-direction, from equation (6) we can obtain

$$W_{(j+1)}^2 = (U_{(j+1)} - U_{(j-1)})\left[\frac{2W_{(j)}^2}{(1+tg^2\beta_{(j)})}\left(\frac{dtg\beta}{dZ}\right)_{(j)} + tg\beta_{(j)}\left(\frac{dW_z^2}{dZ}\right)_{(j)}\right] + W_{(j-1)}^2 \tag{7}$$

In equation (7), when solving for velocity $W_{(j+1)}$ at node points $(j+1)$, the velocities at node points j and $j-1$ have to be used. However, at the initial stage of computation there is only an assumed velocity, W_s, on the blade suction surface. Because of this, when solving for $W_{(j=1)}$, one has to employ a one-sided difference, i.e.,

$$W_{(j=1)}^2 = W_{(j=0)}^2\left[1 + \frac{2}{(1+tg^2\beta_{(j=0)})}\left(\frac{dtg\beta}{dZ}\right)_{(j=0)} + tg\beta_{(j=0)}\left(\frac{dW_z^2}{dZ}\right)_{(j=0)}\right] \tag{8}$$

For various node points of $j=2\sim M$, equation (7) should be used.

Calculation Domain and Boundary Conditions

Calculation domain: $AN_1SONN'O'PN_1'A'A$, domain width $\approx 3B$ (Fig. 2).

Boundary conditions: At inlet $\overline{AA'}$, the initial value M_1, β_1, P_1, i_1 are known. At outlet $\overline{NN'}$, the initial value β_2 is given. Later on, in making calculations, the accurate value β_2 can be obtained by consecutive corrections on the basis of flow rate G_{pre} determined by inlet conditions.

The periodical conditions are satisfied on AN_1, $A'N_1'$ and ON, O'N'.

At location B before and after the cascade the flow field is uniform.

The Treatment of the First- and Second-Order Derivatives of Streamlines

With this method all calculations are done in the flow domain, namely, in coordinates U and Z, resulting in a simple and easy computation process. However, to facilitate the integration of flow rate and the adjustment of streamline locations, it is necessary to remould the expression format of the first- and second-order derivative of streamlines as follows

$$tg\beta = \frac{dU}{dZ} = \frac{d}{dZ}(H\cdot\bar{H}+R) \tag{9}$$

where, for the meaning of R, $\bar{H}$, and H, see Fig. 3.

The development of the aforesaid equation will yield

$$tg\beta = H\frac{d\bar{H}}{dZ} + \bar{H}\left[\frac{d}{dZ}(H+R) - \frac{dR}{dZ}\right] + \frac{dR}{dZ} \tag{10}$$

In the same way, $dtg\beta/dZ$ may be written as

$$\frac{dtg\beta}{dZ} = \frac{d^2R}{dZ^2} + 2\frac{d\bar{H}}{dZ}\left[\frac{d(H+R)}{dZ} - \frac{dR}{dZ}\right] + \bar{H}\left[\frac{d^2(H+R)}{dZ^2} - \frac{d^2R}{dZ^2}\right] + H\frac{d^2\bar{H}}{dZ^2} \tag{11}$$

In equations (10) (11),

$$\frac{dR}{dZ}, \frac{d(H+R)}{dZ}, \frac{d^2R}{dZ^2}, \frac{d^2(H+R)}{dZ^2}$$

constitute the first-order and second-order derivative of suction and pressure surface streamlines. Thus, the first- and second-order derivatives of streamlines in flow fields are all expressed as functions of the first- and second-order derivatives of suction and pressure surface and first- and second-order derivative of the relative height, $\bar{H}$. Moreover, the variation range of the relative height, $\bar{H}$, is the same for all stations in the Z-direction, namely, $0\sim 1$. As a result, in making calculations, the computation domain becomes the rectangular domain of $0\sim 1$. This will greatly facilitate the calculation process.

The Determination of Velocity of Various Node Points in the U-Direction

In calculating the velocity in the U-direction of various node points of a station i on the Z-axis by use of difference equation (7) or (8), suction surface velocity $W_{(j=0)}$ during the first iteration is an assumed value. On this basis, further iterations can be made until the flow rate accuracy, μ, of the said calculated section satisfies relevant requirements. The equation of flow rate accuracy can be written as follows

$$\mu = \frac{G_{pre} - G_{cal}}{G_{pre}} \leq \text{given value} \tag{12}$$

If $\mu >$ given value, then the formula $W_{(j=0)}$ should be iterated in accordance with the following equation

$$W_{(j=0)}^{(p+1)} = W_{(j=0)}^{(p)}\left[1 + \left(\frac{G_{pre} - G_{cal}}{G_{pre}}\right)\mu_1\right] = W_{(j=0)}^{(p)} + \Delta W_{(j=0)} \tag{13}$$

where μ_1, relaxation factor ($\mu_1 < 1$), P, the number of times of iteration.

Downloaded 01 Jun 2010 to 171.66.16.70. Redistribution subject to ASME license or copyright; see http://www.asme.org/terms/Terms_Use.cfm

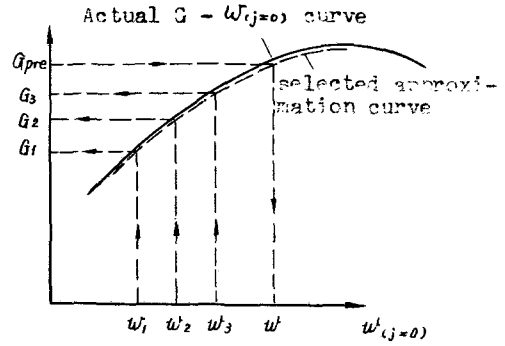


Fig. 4 Approximation curve of $G_{cal} - W_{(j=0)}$

Table 1 The truth table of flow states for judging the section character

DG	0	0	0	0	1	1	1	1
DW	0	0	1	1	0	0	1	1
DP	0	1	0	1	0	1	0	1
F	0	1	1	0	1	0	0	1

The more G_{cal} approximates G_{pre}, the smaller $\Delta W_{(j=0)}$ becomes. Therefore, there will be a relatively large number of times of iteration. The use of function approximation method will make it possible to decrease the number of times of iteration. A parabola can be selected to approximate $W_{(j=0)} - G_{cal}$ curve. The parabola equation is written as

$$G = aW^2_{(j=0)} + bW_{(j=0)} + c \tag{14}$$

At first, set the three values of $W_{(j=0)}$ as W_1, W_2, and W_3. Determine accordingly the three values of calculated flow rates, G_{cal}, namely, G_1, G_2, and G_3. In this manner, based on equation (14), three coefficients, a, b, and c, may be determined. Then, from G_{pre} with the help of the determined values, a, b, and c, the required suction surface velocity $W_{(j=0)}$ can be readily calculated, which will markedly decrease the number of times of iteration.

The aforementioned method is applicable to calculations of subsonic flows.

During calculations of the blade profile given in [12] there exists in the blade profile central portion a supersonic region (Fig. 2). When determining the velocity of various node points on the quasi-orthogonal line passing through the supersonic zone, it is first of all necessary to know the character of this section. When the suction surface velocity $W_{(j=0)}$ of the said section is increasing (or decreasing), the calculated flow rate, G_{cal}, may be also increasing (or decreasing). In such a case, we designate this subsonic-supersonic mixed type section as a section having the subsonic character. On the other hand, if with the increase of $W_{(j=0)}$ (or decrease) there is a decrease of G_{cal} (or increase), then we classify such a section as having the supersonic character. During the iteration of suction surface velocity of subsonic-supersonic mixed type section, it is essential to make revisions in the following iteration equation to accommodate the two different kinds of flow character

$$W^{(p+1)}_{(j=0)} = W^{(p)}_{(j=0)}\left[1 + \left(\frac{G_{pre} - G_{cal}}{G_{pre}}\right)\mu_1 \cdot \mu_4\right] \tag{15}$$

where μ_4 can be given the value of $+1$ or -1, depending on the section character (subsonic or supersonic). The character of μ_4 can be determined by the value of a Boolean expression obtained from the truth table of flow states as follows

$$d\omega = W^{(p)}_{(j=0)} - W^{(p-1)}_{(j=0)},\ dp = G^{(p)}_{cal} - G^{(p-1)}_{cal},\ dg = G_{pre} - G^{(p)}_{cal}$$

and let us suppose when dw, dp, dg are greater than 0, the Boolean values DW, DP, and DG will be 1; when dw, dp, dg are less than zero, let the Boolean values be zero. Thus, on the basis of the relationship between subsonic and supersonic flows, the following truth table of flow states may be obtained.

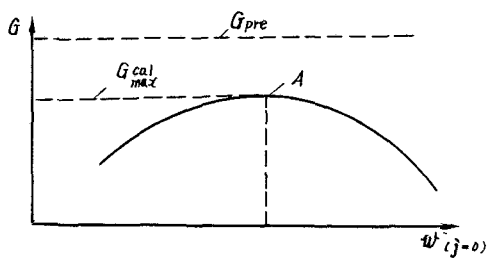


Fig. 5 The relationship of calculated flow rate and inlet flow rate in case of choking

In the table, F denotes output. When $F = 0$, $\mu_4 = -1$; when $F = 1$, $\mu_4 = 1$. From Table 1, we can obtain the Boolean expression when $F = 1$ as follows:

$$F = \overline{DG}\cdot\overline{DW}\cdot DP + \overline{DG}\cdot DW\cdot\overline{DP} + DG\cdot\overline{DW}\cdot DP + DG\cdot DW\cdot DP$$

or

$$F = \overline{DG}\cdot BA + DG\cdot\overline{BA} \tag{16}$$

where $BA = DW\cdot\overline{DP} + \overline{DW}\cdot DP$

Equation (16) may be used to determine whether μ_4 should assume a value of 1 or -1.

In the same way, we can use the truth table of flow states with or without choking occurring to ascertain whether the section is choked or not. The choking condition present on a certain $i - i$ section in the Z-direction of the channel may be seen from Fig. 5.

In this section

$$G_{\substack{cal \\ max}} < G_{pre} \tag{17}$$

Let us assume

$$d\omega 1 = W^{(p-1)}_{(j=0)} - W^{(p-2)}_{(j=0)}\ ,\quad d\omega 2 = W^{(p)}_{(j=0)} - W^{(p-1)}_{(j=0)},$$

$$dp1 = G^{(p-1)}_{cal} - G^{(p-2)}_{cal}\ ,\quad dp2 = G^{(p)}_{cal} - G^{(p-1)}_{cal},$$

$$dg1 = G_{pre} - G^{(p-1)}_{cal}\ ,\quad dg2 = G_{pre} - G^{(p)}_{cal} \tag{18}$$

Assume that when $dw1$, $dw2$, $dp1$, and $dp2$ are greater than zero, their Boolean values DW1, DW2, DP1, and DP2 will be 1, and when $dw1$, $dw2$, $dp1$, and $dp2$ are less than zero, the corresponding Boolean values are zero. Then, we can obtain the following truth table of flow states of striding over point A or not by means of two consecutive iterations (P times and $P+1$ times or $P-1$ and P times).

After adding two "AND gate," DG1 and DG2 (they are the Boolean values of $dg1$ and $dg2$) we have the following Boolean expression signifying choking

$$F' = DP1\cdot\overline{DP2}\cdot DG1\cdot DG2(DW1\cdot DW2 + \overline{DW1}\cdot\overline{DW2})$$

$F' = 1$ means there is choking, while $F' = 0$ denotes the absence of choking.

The Fullfilment of Periodical Conditions, the Formation of Stagnation Streamlines and Their Uniqueness

Periodical conditions are physically self-evident; i.e., in the disk peripheral direction all flow parameters are periodical, which should be satisfied during the calculations process. D. H. Wilkinson, by way of iterating the locations of stagnation streamlines, has achieved this aim [13]. In this connection,

Downloaded 01 Jun 2010 to 171.66.16.70. Redistribution subject to ASME license or copyright; see http://www.asme.org/terms/Terms_Use.cfm

Table 2 The truth table of flow states of striding over point A or not

DW1	1	1	1	1	1	1	1	1	0	0	0	0	0	0	0	0
DW2	1	1	1	1	0	0	0	0	1	1	1	1	0	0	0	0
DP1	1	1	0	0	1	1	0	0	1	1	0	0	1	1	0	0
DP1	1	0	1	0	1	0	1	0	1	0	1	0	1	0	1	0
F'	0	1	0	0	0	0	0	0	0	0	0	0	0	1	0	0

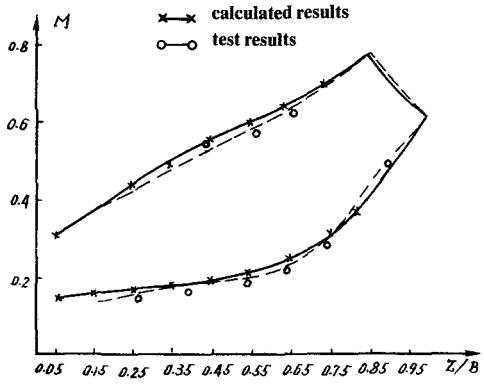


Fig. 6 Velocity distribution of the subsonic cascade

there is a problem of uniqueness of the stagnation streamline. This is because outside the cascade, on two arbitrary streamlines separated by a pitch distance in the U-direction, there exists periodicity. Moreover, the flow rate between these two streamlines equals inlet flow.

The use of iteration of the first-order derivative of stagnation streamline not only results in a higher accuracy than achievable in the case of iterating streamline locations, but it enables us to obtain streamlines which are unique. We can proceed with the proof of this uniqueness as follows.

For ease of description, two boundary streamlines are designated by subscripts, s and p; $tg\beta$, $dtg\beta/dz$ denoted by T and DT. The periodical conditions can be given as

$$\left.\begin{aligned} W_s &= W_p \qquad (19\text{-}1)\\ T_s &= T_p \qquad (19\text{-}2)\\ \mathrm{DT}_s &= \mathrm{DT}_p \qquad (19\text{-}3)\end{aligned}\right\} \tag{19}$$

The derivation process that follows is performed for the station i on the Z-axis. To minimize the use of written symbols, we have done away with subscripts of all parameters. Only in the case when there are in the same equation both i station parameters and $i+1$ or $i-1$ station parameters is the relevant subscript i marked for identification purposes.

Our aim is under the original conditions of $W_s \neq W_p$ to satisfy equation (19) by giving T_s an increment ΔT_s. To accomplish this, the increment of velocity gradient $\partial W/\partial U$ caused by ΔT_s must first be determined. Then, for the various terms on the right and left side of the equation, solve for partial derivative with respect to T_s. After making rearrangements and reductions we have

$$\frac{\partial}{\partial T_s}\left(\frac{\partial W}{\partial U}\right) = BW \tag{20}$$

where

$$B = \left[-DT\frac{2T}{(1+T^2)^2} + \frac{1}{(1+T^2)^2}\frac{1}{\Delta Z}\right] + \frac{1}{2W^2}\left(\frac{dW_z^2}{dZ}\right) \tag{21}$$

where $\Delta Z = Z_{(i)} - Z_{(i-1)}$

Equation (21) can be approximated as

$$\Delta\left(\frac{\partial W}{\partial U}\right) = BW \cdot \Delta T_s \tag{22}$$

Equation (22) may be written as a difference scheme as follows

$$(W'_{(j+1)} - W'_{(j)}) - (W_{(j+1)} - W_{(j)}) = B_{(j)} W_{(j)} (U_{(j+1)} - U_{(j)}) \cdot \Delta T_s \qquad (j=0, 1, \ldots, M-1) \tag{23}$$

where the parameter with superscript "′" stands for the parameter value in the presence of increment ΔT_s. Write and express equation (23) as several equations numbering M. Adding the various terms on the right and left sides of the equations and, depending on periodical conditions, let $W'_{(j=0)} = W'_{(j=M)}$, and we have

$$\Delta T_s = \frac{-W_p + W_s}{\sum_{j=0}^{M-1} B_{(j)} W_{(j)} (U_{(j+1)} - U_{(j)})} \tag{24}$$

where all parameters in $B_{(j)}$ are known values determined in the preceding cycle. As a result, ΔT_s can be calculated.

The stagnation streamline obtained by iterating the first-order derivative of stagnation streamline is unique, which can be proved in the following way.

First, when the first-order derivative $tg\beta$ of streamline is the continuous function of Z, let the equation $tg\beta = dU/dZ = f(Z)$ be defined in a closed domain $[Z_0, Z_n]$ and be continuous, then there must exist a unique stagnation streamline passing through stagnation point 0 (z_0, U_0) and satisfying the aforesaid requirements.

Proof: Take the Lipschitz constant $N=0$. Since $\partial f/\partial U = 0 = N$, from the theorem of the presence and uniqueness of ordinary differential equation solution for the first-order separable variable, we can state that there exists the curve satisfying the aforesaid requirements and, moreover, the curve is unique. In fact

$$\frac{dU}{dZ} = f(Z)$$

therefore

$$U = \int_{z_0}^{z} f(Z)\,dZ + U_0 \tag{25}$$

Here ends the proof.

In our practical computatons, the known quantities are the first-order derivatives $tg\beta_{(i)}$, $(i=0, 1, \ldots, n)$ of streamlines on various stations in the Z-direction and the coordinates (Z_0, U_0) of stagnation point 0. We must choose an interpolation function to approximate the streamline passing through the point 0. This is an interpolation problem. The quadratic spline interpolation function has been chosen as the interpolation function $S(z)$. In what follows, let us prove that there exists an unique solution for such an interpolation problem.

Proof: Let us set a division for the interval $[a, b]$

$$\pi: a = Z_0 < Z_1 < \ldots < Z_n = b$$

The quadratic spline function with the inner points Z of the said division as the node points can be written as

$$S(Z) = \alpha_0 + \alpha_1 Z + \alpha_2 Z^2 + \sum_{j=1}^{n-1} C_j (Z - Z_j)_+^2 /2!$$

where there are $n+2$ constants to be determined. The number of given conditions is precisely also $n+2$. Since $S'(Z)$ is the division linear function, it satisfies for the interval (Z_i, Z_{i+1}) the following interpolation conditions $S'(Z_i) = U'_i$, $S'(Z_{i+1}) = U'_{i+1}$. Consequently, we have

Downloaded 01 Jun 2010 to 171.66.16.70. Redistribution subject to ASME license or copyright; see http://www.asme.org/terms/Terms_Use.cfm

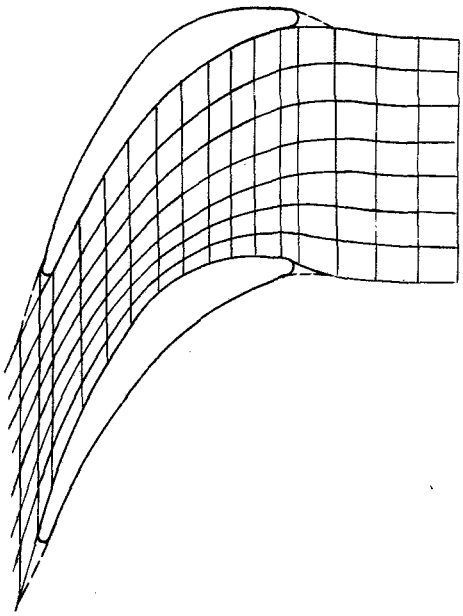


Fig. 7 Flow pattern of the subsonic cascade

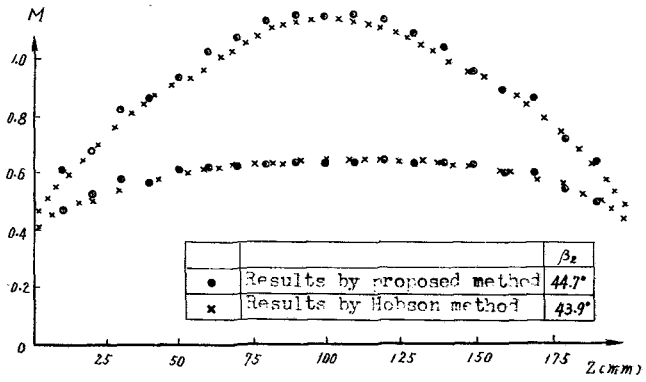


Fig. 8 Comparison of calculated results obtained by use of the proposed method with those of the Hobson method

$$S'(Z)=\frac{Z_{i+1}-Z}{Z_{i+1}-Z_i}U_i'+\frac{Z-Z_i}{Z_{i+1}-Z_i}U_{i+1}'=\frac{Z_{i+1}-Z}{h_i}U_i'+\frac{Z-Z_i}{h_i}U_{i+1}'$$

$$Z\epsilon[Z_i, Z_{i+1}]$$

After first integration, it yields

$$S(Z)=\frac{(Z-Z_i)^2}{2hi}U_{i+1}'-\frac{(Z_{i+1}-Z)^2}{2h_i}U_i'+d_i \qquad (26)$$

$$Z\epsilon[Z_i, Z_{i+1}]$$

Since $S(Z)$ is a continuous function, hence $S(Z_{i-0})=S(Z_{i+0})$

Thence

$$\frac{h_{i-1}}{2}U_i'+d_{i-1}=-\frac{h_i}{2}U_i'+d_i$$

where $h_{i-1}=Z_i-Z_{i-1}$

$$\therefore d_i=d_{i-1}+U'(h_{i-1}-h_i)/2\,,\ (i=1,2,\ldots n-1) \qquad (27)$$

$$\therefore d_{n-1}=U_n-\frac{h_{n-1}}{2}U_n' \qquad (28)$$

From equations (27) and (28) $d_i(i-1,\ 2,\ \ldots,\ n-1)$ is determined as unique. Substituting it into equation (26) yields a unique solution. Our proof ends here.

It should be pointed out that if a cubic spline is chosen as the approximation function, we can also prove its uniqueness. However, in this case, owing to the fact that the number of factors to be determined will be greater by one than in the case of the quadratic spline, it is necessary to supplement a known condition to make things rational.

The condition to be added is that the second-order derivative of streamlines on the outlet station should be zero. This is reasonable to expect, for after the outlet there exists a straight line. Due to space limitations we will not go into details here. It should be noted that because of the rationality of problem presentation there exists more than one uniqueness proof method.

Calculation Results

For subsonic flows the known test results of a plane cascade were used. The velocity distributions are shown in Fig. 6. The tested value of the outlet angle is 19 deg 58 min, calculated value of same is 20 deg 24 min. The streamlines of a full flow field are shown in Fig. 7. In Fig. 8 the calculated results of Hobson's transonic blade profile are shown.

References

1 Wu, C. H., "A General Theory of Three-Dimensional Flow in Subsonic and Supersonic Turbomachines of Axial, Radial, and Mixed-flow Types," NACA TN 2604, 1952.

2 Wang, C. J., "Lectures on Three-Dimensional Flows," (in Chinese), Harbin Polytechnical Institute, Harbin, 1976.

3 Sheng, T. K., Jiang, J. K., and Chu, S. T., "Quasi-orthogonal Method for Calculating Three-Dimensional Flows in Turbomachinery: Part II," (in Chinese), Futan University, Shanghai, 1978, pp. 9-19.

4 Wu, C. H., "A Solution for Compressible Gas Flow Past Cascade of Arbitrary Surface of Revolution and the Design Method of such a Cascade," (in Chinese), *Journal of Mechanical Engineering*, June 1956.

5 Liu, K. L., and Dao, C., "A General Solution for the Aerodynamic Direct and Inverse Problems of Cascades of Arbitrary Surface of Revolution," (in Chinese), Status Report of the Institute of Mechanics of the Chinese Academy of Sciences, July 1967.

6 Chen, W. W., "Aerodynamic Calculation and Design of Cascades of Arbitrary Surface of Revolution," (in Chinese), Research Report, Design Department of Harbin Steam Turbine Plant, Jan. 1976.

7 Binden, T. P., and Carmichael, A. D., "Streamline Curvature Analysis of Compressible and High Mach Number Cascade Flows," *Journal of Mechanical Engineering Science*, Vol. 13, No. 5, 1971, pp. 344-357.

8 Research Division No. 3 of the Chinese Academy of Sciences, "The Solution of Aerodynamic Problems by the Method of Iterating Streamlines," (in Chinese), Technical Report, Chinese Academy of Sciences, Jan. 1977.

9 Perkins, H. J., and Horlock, H. J., "Flow Calculations in Turbomachinery, a Collection of Translated Papers," (in Chinese), Dong Fang Steam Turbine Plant, Chengdu, 1978, pp. 3-5.

10 Mao, S. K., and Shi, W. K., "A Treatise on the Stream Curvature Method for Calculating S_1 Stream Surface Flow," (in Chinese), *Journal of Marine Boilers and Turbines*, Dec. 1978, pp. 1-12.

11 Mao, S. K., and Li, D. T., "A Treatise on the Stream Curvature Method for Calculating S_1 Stream Surface Flow Part II," (in Chinese), *Third Symposium on Marine Turbomachinery*, Chinese Society of Shipbuilding, Sept. 1981, pp. 1-14.

12 Hobson, D. E., "Transonic Turbine Blade Design by the Hodograph Method," CUED-A-Turbo/TR 40, Nov. 1972.

13 Wilkinson, D. H., "Calculation of Blade-to-Blade Flow in a Turbomachine by the Stream Curvature Method," ARC R&M 3704, 1970.

14 Wan, P. C., "The Direct Problem of Aerodynamic Calculation in Turbomachines and the Adjustment of Flow Rate," (in Chinese), presented at the Third Conference of the Chinese Society of Thermophysics, 1980.

15 Lu, S. J., and others, *Mixed Difference Method for Calculating Transonic Steady Potential Flow*, (in Chinese), National Defense Industry Press, 1979, pp. 35-44.

APPENDIX

The Derivation of Equation of Motion for S_1 Stream Surface

Let the relative cylindrical coordinate system be r, θ, Z. Blades rotate at a constant velocity (Fig. 1). In this coordinate system, the momentum equation of the adiabatic flow for a compressible ideal gas can be written as

Downloaded 01 Jun 2010 to 171.66.16.70. Redistribution subject to ASME license or copyright; see http://www.asme.org/terms/Terms_Use.cfm

$$\frac{DW_r}{dt}-\frac{(W_u+U)^2}{r}=-\frac{1}{\rho}\frac{\partial P}{\partial r} \tag{29}$$

$$\frac{DW_u}{dt}+\frac{W_r\cdot W_u}{r}+2\omega W_r=-\frac{1}{\rho}\frac{\partial P}{r\partial\theta} \tag{30}$$

$$\frac{DW_z}{dt}=-\frac{1}{\rho}\frac{\partial P}{\partial Z} \tag{31}$$

The S_1 stream surface equation is $s_1(r, \theta, Z) = 0$

Since the flow is irrotational, there exists the following equation for the stream surface

$$\mathbf{n}\cdot\mathbf{W}=0$$

where $\mathbf{n}$ denotes the normal unit quantity of S_1 stream surface. Equation (32) can be written as

$$n_r dr+rn_u d\theta+n_z dZ=0 \tag{32}$$

The variation rate of a quantity, q, on the S_1 surface with respect to θ, Z can be given by the following

$$\left.\begin{aligned}\frac{1}{r}\frac{\bar{\delta}q}{\partial\theta}&=\frac{1}{r}\frac{\partial q}{\partial\theta}-\frac{n_u}{n_r}\frac{\partial q}{\partial r}\\ \frac{\bar{\delta}q}{\partial z}&=\frac{\partial q}{\partial z}-\frac{n_z}{n_r}\frac{\partial q}{\partial r}\end{aligned}\right\} \tag{33}$$

where "–" notation means that the relevant term pertains to the stream surface. This is true for all other equations that follow.

Using equations (32) and (33), one may rewrite equations (29) and (30) as

$$\frac{\bar{D}W_r}{dt}-\frac{(W_u+U)^2}{r}=-\frac{1}{\rho}\frac{\partial P}{\partial r} \tag{34}$$

$$\frac{\bar{D}W_u}{dt}+\frac{W_u W_r}{r}+2W_r\omega=-\frac{1}{\rho}\frac{\bar{\delta}P}{r\partial\theta}-\frac{n_u}{n_r}\frac{1}{\rho}\frac{\partial P}{\partial r} \tag{35}$$

let us assume

$$\left.\begin{aligned}tg\delta&=\frac{n_u}{n_r}\\ tg\sigma&=\frac{W_r}{W_z}\\ tg\beta&=\frac{W_u}{W_z}\end{aligned}\right\} \tag{36a}$$

Taking note of equation (32), we may write equation (36*a*) as

$$\left.\begin{aligned}tg\delta&=-\frac{W_r}{W_u}=\frac{n_u}{n_r}\\ tg\sigma&=\frac{W_r}{W_z}=\frac{-n_z}{n_r}\\ tg\beta&=\frac{W_u}{W_z}=\frac{-n_z}{n_u}\end{aligned}\right\} \tag{36b}$$

Substituting equation (34) into equation (35), eliminating term $-1/\rho\ \partial P/\partial r$ and using the relationship of equation (36*b*) we have

$$-\frac{1}{\rho}\frac{\bar{\delta}P}{r\partial\theta}=\frac{W^2}{B'}\left\{\frac{\bar{D}tg\beta}{dZ}-tg\delta\frac{\bar{D}tg\sigma}{dZ}+\frac{1}{r}[tg\beta tg\sigma+(1+\epsilon)^2 tg^2\beta tg\delta]-\frac{2\epsilon}{r}tg\beta tg\sigma\right\}+\frac{1}{2}\frac{\bar{D}W_z^2}{dZ}(tg\beta-tg\delta\cdot tg\sigma) \tag{37}$$

where $B' = (\sec^2\sigma + tg^2\beta)$, $\epsilon=\dfrac{u}{W_u}$.

From the definition of generalized enthalpy $I = i + W^2/2 - u^2/2$ and the first law of thermodynamics

$$\frac{1}{\rho}\nabla P=\nabla I-\frac{1}{2}\nabla W^2+\frac{1}{2}\nabla U^2-T\nabla S \tag{38}$$

Substituting equation (37) into equation (38) yields the equation of motion on the S_1 surface as follows

$$\frac{\bar{\delta}W^2}{r\partial\theta}-\frac{2W^2}{B'}\left\{\frac{\bar{D}tg\beta}{dZ}-tg\delta\frac{\bar{D}tg\sigma}{dZ}+\frac{1}{r}[tg\beta tg\sigma+(1+\epsilon)^2 tg\beta tg\delta]+\frac{2\epsilon}{r}tg\beta tg\sigma\right\}-\frac{\bar{D}W_z^2}{dZ}(tg\beta-tg\delta tg\sigma)-2\left(\frac{\bar{\delta}I}{r\partial\theta}-rW^2tg\delta-T\frac{\bar{\delta}S}{r\partial\theta}\right)=0 \tag{39}$$

or

$$\frac{\bar{\delta}W^2}{r\partial\theta}+\xi_1(\theta)W^2+\xi_2(\theta)=0 \tag{40a}$$

where

$$\xi_1(\theta)=-\frac{2}{B'}\left\{\frac{\bar{D}tg\beta}{dZ}-tg\delta\frac{\bar{D}tg\sigma}{dZ}+\frac{1}{r}[tg\beta tg\sigma+(1+\epsilon)^2 tg^2\beta tg\delta]+\frac{2\epsilon}{r}tg\beta tg\sigma\right\}$$

$$\xi_2(\theta)=-\frac{\bar{D}W_z^2}{dZ}(tg\beta-tg\delta tg\sigma)-2\left(\frac{\bar{\delta}I}{t\partial\theta}-rW^2tg\delta-T\frac{\bar{\delta}S}{r\partial\theta}\right)$$

Keeping in mind that all derivatives in equations (39) and (40*a*) pertain to the S_1 surface, we can discard "–", and obtain

$$\frac{\partial W^2}{r\partial\theta}+\xi_1(\theta)W^2+\xi_2(\theta)=0 \tag{40b}$$

Downloaded 01 Jun 2010 to 171.66.16.70. Redistribution subject to ASME license or copyright; see http://www.asme.org/terms/Terms_Use.cfm

A Theory of Rotating Stall of Multistage Axial Compressors: Part I—Small Disturbances[1]

F. K. Moore
Sibley School of Mechanical and Aerospace Engineering, Cornell University, Ithaca, N.Y. 14853

An analysis is made of rotating stall in compressors of many stages, finding conditions under which a flow distortion can occur which is steady in a traveling reference frame, even though upstream total and downstream static pressure are constant. In the compressor, a pressure-rise hysteresis is assumed. Flow in entrance and exit ducts yield additional lags. These lags balance to give a formula for stall propagation speed. For small disturbances, it is required that the compressor characteristics be flat in the neighborhood of average flow coefficient. Results are compared with the experiments of Day and Cumpsty. If a compressor lag of about twice that due only to fluid inertia is used, predicted propagation speeds agree almost exactly with experimental values, taking into account changes of number of stages, stagger angle, row spacing, and number of stall zones. The agreement obtained gives encouragement for the extension of the theory to account for large amplitudes.

Introduction

In recent years, experimental studies and reviews by Greitzer, Day, and Cumpsty [1, 2, 3] have clarified and redefined the problem of rotating stall of axial flow compressors, giving a new emphasis to the compressor of many stages. At low flows, virtually all compressors exhibit zones of stalled flow which propagate tangentially, with blade passages cyclically stalling and recovering in the manner first described by Emmons [4].

However, when the compressor has many stages (about three seems to suffice), the stall patterns seem to be simpler and presumably more predictable than when the compressor consists of a single row or stage. Early reviews [5] convey this impression, but it remained for Day, Greitzer, and Cumpsty [3] to describe what one might call the kinematics of rotating stall. They demonstrated, for example, that the stall pattern in "deep stall" tends to run straight through the machine, with an especially abrupt transition at the trailing edge of the stall zone.

Theoretical studies in the past [6–9] have attempted to understand rotating stall for a single stage under the natural impression that if one could properly relate the Emmons type of stalling-unstalling episodes to the individual cascade characteristics, then one could proceed to synthesize a theory for multistage machines. This approach, though logical, has not been fruitful. In effect, rotating stall is too universal a phenomenon and depends on too many variables; single-stage analysis does not yield critical conditions meaningful for whole-compressor performance, especially in deep stall.

In the present three-part study, we explore the idea that rotating stall theory should begin with the compressor of many stages, operating in stall. Doing this, we will not emphasize the problem of "stall inception," but, rather, try to incorporate in the theory the kinematic features of deep stall described by Day, Cumpsty, and Greitzer [3]. Greitzer and Cumpsty [10] have presented a semiempirical analysis of deep-stall propagation speed which is in this same spirit.

In this paper (Part I), a single dynamic hysteresis is assumed for the blade-passage force function and conditions are derived for the occurrence of a weak stall pattern which is steady in some rotating frame of reference. From this analysis we find a formula for stall propagation speed which agrees well with experimental data, if the single lag parameter is properly chosen.

In Part II, the analysis is extended to describe the stall patterns of arbitrary velocity amplitude which can occur when the quasi-steady compressor characteristic is either flat (deep stall) or else curved as it would be at stall inception. Wave forms for velocities and pressure are found, as well as propagation speeds and the distortion of the compressor characteristic due to rotating stall.

In Part III, a compressor characteristic is adopted which has the realistic feature of an unstalled region with peak pressure rise, a deep-stall valley, and a steep resistance to reversed flow. Rotating stall then is found to have the nature of a limit cycle, familiar in the classical van der Pol problem of nonlinear mechanics [11]. Results include a prediction of stall recovery as flow coefficient is increased.

The present paper, though limited in results to weak disturbances, will include certain developments in forms suitable for more general application in subsequent parts.

Support for this work by NASA-Lewis during the author's sabbatic leave from Cornell is gratefully acknowledged, as

[1] Research performed at NASA-Lewis Research Center, Cleveland, Ohio

Contributed by the Gas Turbine Division of THE AMERICAN SOCIETY OF MECHANICAL ENGINEERS and presented at the 28th International Gas Turbine Conference and Exhibit, Phoenix, Arizona, March 27–31, 1983. Manuscript received at ASME Headquarters, December 20, 1982. Paper No. 83-GT-44.

Copyright © 1984 by ASME
Downloaded 01 Jun 2010 to 171.66.16.70. Redistribution subject to ASME license or copyright; see http://www.asme.org/terms/Terms_Use.cfm

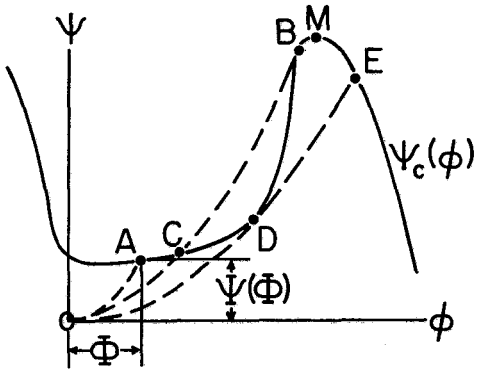


Fig. 1 Constant-speed compressor characteristic, $\psi_c(\phi)$, and operating points, $\Psi(\Phi)$; upstream total to downstream static pressure rise versus axial flow coefficent

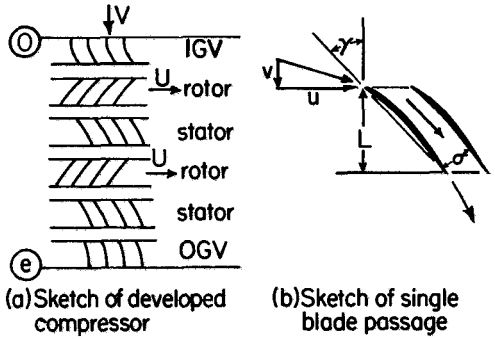


Fig. 2 Sketch of compressor configuration. Number of stages is arbitrary; two are shown. Radial effects are neglected. Entrance and exit planes are denoted by ⓞ and ⓔ. Blading is symmetrical.

well as helpful discussions with C. L. Ball, Lonnie Reid, and M. E. Goldstein in the course of the study.

The Compressor

The compressor is assumed to have a constant-speed characteristic as sketched in the solid line of Fig. 1. We will denote the upstream total (p_T) to downstream static (p_s) pressure-rise coefficient by ψ_c, in the absence of rotating stall

$$\frac{p_s - p_T}{\rho U^2} \equiv \psi_c(\phi) \tag{1}$$

The axial flow coefficient, ϕ, has the average value, Φ

$$\frac{v}{U} \equiv \phi; \quad \frac{V}{U} \equiv \Phi. \tag{2}$$

The characteristic ψ_c will be considered to be single-valued, as shown. Throttle settings, indicated by dashed parabolic lines, will intersect the characteristic and establish operating points (A–E on the sketch) about which rotating stall might occur. Points B and D in the sketch would indicate limits of a quasi-steady hysteresis loop (B – C – D – E) due (we assume) purely to the way the throttle parabolas intersect the characteristic. In Parts II and III, we shall permit the net pressure rise (Ψ) to depend on the existence of rotating stall. For example, the operating point in rotating stall for the Φ indicated at point A might actually lie above or below the characteristic curve.

The compressor has N stages, with IGV and OGV rows providing zero incidence at design. Blading and design vector diagrams are symmetrical (50 percent reaction) as sketched in Fig. 2. Radial effects will be neglected, and flow will be considered incompressible.

Flow Disturbance in the Compressor

First, a disturbance will be postulated to exist in the compressor, steady in a circumferentially moving frame. This disturbance implies disturbances in the flow fields entering and leaving the compressor. The plan of this study is to find the requirement that such a set of disturbances exists, even though pressures far upstream and downstream remain constant; in effect, to find eigensolutions and eigenvalues for the whole system. We begin by describing the disturbance of a single blade passage.

Disturbance in a Blade Passage. When rotating stall occurs flow velocities will change locally and in time. We will assume that when axial flow is slowly reduced, keeping U constant, flow fields of rotor and stators remain symmetrical, though pressure rise and deviation should change. In other words, the quasi-steady velocity triangles remain symmetrical, and corresponding pressure changes are equal. Pressure rise in each row is assumed to depart slightly from the quasi-steady, however.

The static pressure rise through each row will be assumed to have the form

$$\frac{\Delta p}{\frac{1}{2}\rho U^2} = F(\phi) - \tau(\phi)\dot{\phi} \tag{3}$$

whether rotor or stator.

The quasi-steady pressure-rise coefficient, F, might have

Nomenclature

a_n, b_n = Fourier coefficient of $g(\theta)$, equation (18a)
D = mean wheel diameter
F = steady pressure rise coefficient in blade passage, equation (3)
f = stall propagation-speed coefficient, equation (11) and Fig. 4
g = axial flow coefficient perturbation in compressor, equation (4)
h = transverse velocity coefficient perturbation at entrance, equation (15)
K_I = pressure-rise parameter at IGV entrance, equation (8)
k = parameter relating actual compressor-row lag to interia lag of blade passage only
L = depth of row in axial direction, Fig. 2(b)
m = parameter defining lag tendency outside compressor, equation (34)
N = number of stages in compressor core
n = wave number, corresponding to number of stall cells
P = pressure coefficient, equation (24)
p = static pressure
U = wheel speed at mean wheel diameter
u = transverse velocity in laboratory frame
V = average axial velocity
v = axial velocity
x = circumferential distance, in stall-zone frame, equation (5)
y = distance normal to compressor face, in flow direction, Figs. 4, 5
γ = stagger angle of blades, Fig. 2

Downloaded 01 Jun 2010 to 171.66.16.70. Redistribution subject to ASME license or copyright; see http://www.asme.org/terms/Terms_Use.cfm

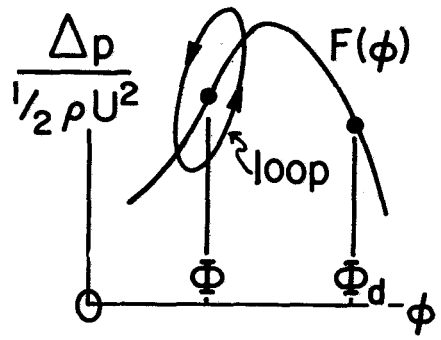


Fig. 3 Assumed form of blade-passage pressure-rise function

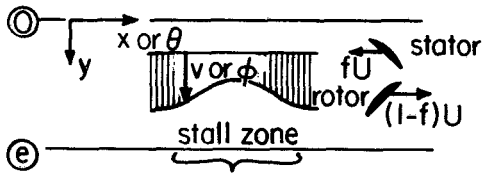


Fig. 4 Sketch showing axial stall zone in compressor, in coordinates fixed in the stall zone which, in laboratory coordinates, is moving to the right at speed, fU

the form sketched in Fig. 3. Assigning the same F to each row, and properly taking account of dynamic pressure, $F(\phi)$ will yield the ψ_c of Fig. 1. The occurrence of a maximum of F, and the drop of F as ϕ is reduced, will signify stall of a blade passage.

The second term describes hysteresis due either to flow acceleration, flow separation, or viscous processes in the blade passage. It is written in the sense that if ϕ is decreasing, then there is an extra force which is positive. At any flow coefficient, therefore, we assume a counterclockwise dynamic hysteresis loop, as sketched in Fig. 4. The parameter, τ, will generally be a function of ϕ, of course. However, throughout this study, we will take τ to be constant, and the same for rotors and stators.

Because equation (3) will be considered to apply equally to the rotor and stator rows, in effect we disregard centrifugal and secondary-flow phenomena. In fact, for symmetric blading, τ would be the same for rotors and stators. For guide vanes, we will adopt the same equation, using subscripts to distinguish them from the stage elements.

Stall Pattern of the Compressor. If, by symmetry, rotor and stator blade passages show no deviation under disturbance, and no flow development takes place between rows (as if there is zero inter-row spacing), then continuity will require that all instantaneously connected blade passages have the same axial velocity. Therefore, any disturbance of axial velocity would be purely circumferential, however many stages there are, and whatever the speed of propagation of the disturbance pattern. Further study might show that dynamic effects will require modification of this symmetry argument.

Under present assumptions, a stall pattern, shown shaded on Fig. 4, must proceed straight through the machine. This is consistent with observations of deep stall. Obviously, if reaction is not 50 percent or blades are of unequal axial length, if compressibility or centrifugal effects were significant, or if circumferential flow between rows is allowed, then the straight-through pattern would not be correct.

Next we assume that a disturbance pattern is steady in some rotating frame of reference. If the compressor is "unwrapped" as in Fig. 4, the disturbance is moving to the right with speed fU relative to stators. The "stall propagation speed" f is unknown; it is to be found as an eigenvalue of the disturbance, so to speak. Relative to the disturbance, stators are moving to the left with speed fU and rotors are therefore moving to the right with speed $(1-f)U$. The axial flow coefficient in this frame takes the form

$$\phi = \Phi + g(\theta) \tag{4}$$

where g represents a steady disturbance. Again referring to Fig. 4, distance x is measured to the right, so that

$$\theta = 2x/D \tag{5}$$

where D is the mean diameter of the compressor. If the disturbance of ϕ is purely circumferential, then equation (3) applies equally to each blade row, and pressure-rise may be accumulated through the compressor purely as a function of θ, or equivalently, x.

The time derivative, $\dot{\phi}$, must be expressed in terms of the steady disturbance described in equation (4) and Fig. 4; it signifies the rate of increase of ϕ experienced by a blade passage as it traverses the postulated stall disturbance. Thus from equations (4) and (5)

$$\dot{\phi} = g'(\theta)\,\dot{\theta} = g'(\theta)\,\frac{2\dot{x}}{D} \tag{6}$$

Figure 4 sketches the situation: The solid line represents the steady but disturbed flow, $\phi(\theta)$. Stator blades moving to the left at speed fU experience an increase of ϕ depending on the local gradient of ϕ (that is, $\phi'(\theta)$) and the relative speed $\dot{x} = -fU$. Similarly, a rotor moves in the same gradient with speed $\dot{x} = (1-f)U$. For stators and rotors separately

Nomenclature (cont.)

ϵ = amplitude parameter of disturbance, equation (19)
θ = angular location, in stall-zone frame, equation (5)
λ = collection of terms analogous to oscillator mass, equation (39)
ρ = density
σ = normal blade passage width, Fig. 2(*b*)
τ^* = reduced time lag, equation (45)
τ = coefficient of pressure-rise hysteresis, equation (3)
Φ = average flow coefficient, V/U
ϕ = flow coefficient, v/U
$\dot{\phi}$ = velocity potential, equation (13)
Ψ = upstream total to downstream static pressure-rise coefficient existing during operation
ψ_c = compressor characteristic in absence of rotating stall, Fig. 1
$\bar{\psi}$ = stream function, equation (23)

Superscripts

• = time derivative
= = ordinary differentiation

Subscripts

d = design conditions
e = at compressor exit
IV = inlet guide vane
OV = outlet guide vane
s = far downstream static conditions
T = far upstream total conditions
0 = just ahead of compressor entrance
∞ = far upstream static conditions

Downloaded 01 Jun 2010 to 171.66.16.70. Redistribution subject to ASME license or copyright; see http://www.asme.org/terms/Terms_Use.cfm

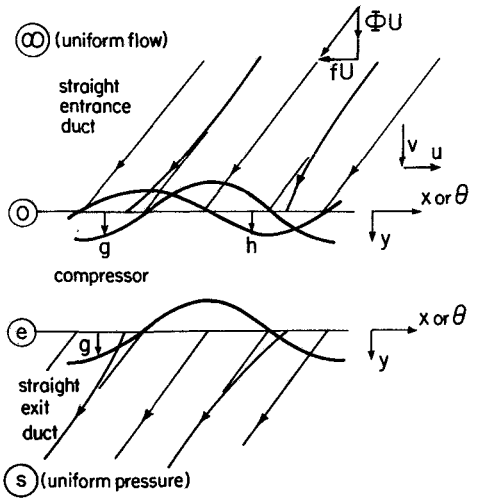


Fig. 5 Sketches of flows in straight entrance and exit ducts, coordinates fixed in disturbance. At the compressor exit, $u = -fU$.

$$\dot{\phi}_{\text{stator}} = -g'(\theta)\frac{2U}{D}f \tag{7a}$$

$$\dot{\phi}_{\text{rotor}} = g'(\theta)\frac{2U}{D}(1-f) \tag{7b}$$

Since it is intended to accumulate forces through the compressor, we will find use for the combined pressure-rise expression for a single stage

$$\left(\frac{\Delta p}{\frac{1}{2}\rho U^2}\right)_{\text{stage}} = 2F(\phi) - \tau g'(\theta)\frac{4U}{D}\left(\frac{1}{2}-f\right) \tag{8}$$

Guide Vanes. The OGV is assumed to have no deviation, and will therefore deliver flow in a purely axial direction to the diffuser. A hysteresis term (equation (3)) applies with a value of τ_{OV} presumably different from the τ applicable to stators and rotors of the stages.

It will be assumed that IGV's are purely axial at entrance. When rotating stall occurs, there will be (as we shall find) a transverse velocity disturbance at the compressor (IGV) entrance. In this paper, we will consider this velocity disturbance small compared to V. Regarding the IGV as a nozzle, its entering velocity will therefore depart from the local value of v only to second order in small quantities. Accordingly, although there must be a rather abrupt pressure rise crossing the entrance plane of the IGV's, it too will be of second order in flow deflection. By our previous stage symmetry argument, we should expect the IGV discharge angle to be the same as the OGV entrance angle. Thus, recalling equation (3), there should be negative value of F for the IGV nozzle, just equal to the positive value for the OGV passage acting as a diffuser, even though ϕ varies. Again a hysteresis term should apply, and, for OGV and IGV together, one has, corresponding to equation (8),

$$\left(\frac{\Delta p}{\frac{1}{2}\rho U^2}\right)_{\substack{\text{guide}\\ \text{vanes}}} (\tau_{IV}+\tau_{OV})g'(\theta)\frac{2U}{D}f + K_I h^2 \tag{9}$$

where $K_I h^2$ represents the coefficient of abrupt pressure rise at the IGV entrance.

Upstream Disturbance

Far upstream, we imagine a reservoir of total pressure, p_T, constant whether or not rotating stall is in progress. Between that reservoir and the compressor face is a flow passage of some possibly complex shape ("Gooseneck"). In that region, a flow disturbance will develop, if rotating stall exists. In this study, we shall assume the entrance region to be a straight, uniform channel. In that case, if the flow upstream has uniform velocity and pressure

$$p_\infty = p_T - \frac{1}{2}\rho V^2 \tag{10}$$

and V will be the average velocity of any disturbance that arises downstream.

Velocity Field. In the channel, disturbances will be considered irrotational as well as incompressible. Thus, Laplace's equation applies. For convenience, we adopt the coordinate system of Fig. 4, so that the velocity components far upstream ($y = -\infty$) are

$$\frac{u_\infty}{U} = -f; \quad \frac{v_\infty}{U} = \frac{V}{U} \equiv \Phi \tag{11}$$

At the compressor face, equation (4) applies

$$\frac{v}{U} = \phi = \Phi + g(x) \tag{12}$$

The resulting steady streamline pattern in the entrance duct region will be as sketched in Fig. 5. It will be necessary to know the pressure disturbance at the compressor face, and, for this, the value of u there is needed. We may write a disturbance velocity potential

$$\frac{u}{U} = -f + \tilde{\phi}_x; \quad \frac{v}{U} = \Phi + \tilde{\phi}_y \tag{13}$$

with $\tilde{\phi}$ vanishing when $y = -\infty$, and at $y = 0$

$$(\tilde{\phi}_y)_0 = g(\theta) \tag{14}$$

where g is arbitrary but periodic, with wavelength $\pi D/n$. The wave number, n, is introduced to account for the possibility of multiple-cell stall. The required u-velocity at the compressor face will henceforth be designated as $h(x)$

$$(\tilde{\phi}_x)_0 = h(\theta) \tag{15}$$

In general, h is the Hilbert transform of g

$$h(\theta) = -\frac{1}{\pi}\int_{-\infty}^{\infty}\frac{g(\xi)d\xi}{\theta-\xi} \tag{16}$$

Takata and Nagano [9] integrated this relation numerically for certain unsteady disturbances. If g is periodic, it may be shown that equation (16) yields

$$h = -\frac{1}{\pi}\int_0^{2\pi} g'(\xi)\ln\left|\sin\frac{\theta-\xi}{2}\right| d\xi \tag{17}$$

If $g(\theta)$ has a Fourier series

$$g(\theta) = \sum_1^\infty (a_n \sin n\theta + b_n \cos n\theta) \tag{18a}$$

then

$$\tilde{\phi}(y,\theta) = \sum_1^\infty \frac{D}{2n} e^{n\frac{2y}{D}}(a_n \sin n\theta + b_n \cos n\theta) \tag{18b}$$

which satisfies equation (14) and vanishes at $y = -\infty$. The corresponding u and v velocities both vanish as they should at $y = -\infty$, and

$$h(\theta) = \sum_1^\infty (a_n \cos n\theta - b_n \sin n\theta) \tag{18c}$$

For example, if g is a harmonic wave

$$g = \epsilon\Phi \sin n\theta; \quad h = \epsilon\Phi \cos n\theta \tag{19}$$

ϵ being an amplitude parameter.

Downloaded 01 Jun 2010 to 171.66.16.70. Redistribution subject to ASME license or copyright; see http://www.asme.org/terms/Terms_Use.cfm

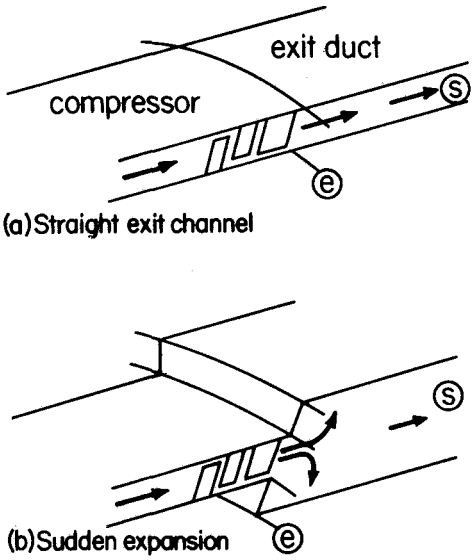


Fig. 6 Sketches of extreme exit-duct configuration

Pressure Field. In the disturbance coordinates, the steady Bernoulli equation applies

$$p_\infty + \frac{1}{2}\rho U^2(f^2+\Phi^2) = p_0 + \frac{1}{2}\rho U^2[(-f+h)^2+(\Phi+g)^2] \quad (20)$$

where p_0 is the pressure at the compressor face, just ahead of the IGV. Recalling equation (10), one finds

$$\frac{p_0-p_T}{\rho U^2} = -\left(\frac{1}{2}\Phi^2+\Phi g+\frac{1}{2}g^2-fh+\frac{1}{2}h^2\right) \quad (21)$$

If g is a weak harmonic wave, equation (19), with ϵ assumed small compared to 1, would provide

$$\frac{p_0-p_I}{\rho U^2} = -\frac{1}{2}\Phi^2 - \epsilon(\Phi^2 \sin n\theta - f\Phi\cos n\theta) \quad (22)$$

to first order in ϵ.

If the channel is not straight, or if the flow in the channel is not irrotational, equations (21) and (22) would require modification.

Downstream Disturbance

Far downstream, we imagine a flow of uniform static pressure (p_s), but no necessarily constant velocity; a shear flow might be the final result. The flow is expected to emerge from the OGV in an axial direction (viewed in stator coordinates) but with varying pressure (p_e) and perhaps vorticity. The actual exit-flow device, or diffuser, is very important in this regard, and we will limit this discussion to two types, a straight channel, and a sudden expansion. These two extreme types perhaps bracket the possibilities.

Straight Channel. If there is a straight, constant-area channel downstream of the compressor exit (Fig. 6(*a*)) then the Euler equations must be solved in the region sketched in Fig. 5. Defining a stream function for that region

$$\frac{u}{U} = \tilde{\psi}_y; \quad \frac{v}{U} = \phi = -\tilde{\psi}_x \quad (23)$$

and expressing pressure in the dimensionless form

$$\frac{p_s-p}{\rho U^2} \equiv P \quad (24)$$

where p_s is the (constant) downstream static pressure, one may write the Euler equations as

$$-P_x = -\tilde{\psi}_y\tilde{\psi}_{xy} + \tilde{\psi}_x\tilde{\psi}_{yy}; \quad -P_y = \tilde{\psi}_y\tilde{\psi}_{xx} - \tilde{\psi}_x\tilde{\psi}_{xy} \quad (25)$$

Boundary conditions at the rear face of the compressor (subscript e) at $y=0$ are

$$(\tilde{\psi}_y)_e = -f; -(\tilde{\psi}_x)_e = \Phi + g(x) \quad (26)$$

and far downstream (subscript s) at $y=\infty$, the pressure must become uniform, but vortical velocity disturbances may survive

$$P_s = 0 \quad (27)$$

In formulating a solution of the system of equations (25–27), we should recall that only P is needed, in its relation to the disturbance function $g(x)$. Equation (25) can be converted to

$$\frac{1}{2}\nabla^2 P = -\tilde{\psi}_{xx}\tilde{\psi}_{yy} + (\tilde{\psi}_{xy})^2 \quad (28)$$

and equations (25) and (26) yield

$$(P_y)_e = -fg'(x) \quad (29)$$

Of course, one or the other of equation (25) must be included with equation (28). However, if the disturbance is weak, then the right side of equation (28) is of second order, and equation (28) is simply Laplace's equation

$$\nabla^2 P = 0 \quad (30)$$

The desired solution for P can be found directly, using equations (27) and (29) as boundary conditions.

In fact, the function $-P/f$ would correspond to the x-derivative of a velocity potential, vanishing at $y=\infty$, of which $g(x)$ is the y-derivative at $y=0$. But that is precisely the relationship between g and h defined in equations (14) and (15). Taking account of the difference of direction of y between the two cases, one may immediately conclude that

$$P_e = fh; \quad P_e \equiv \frac{p_s-p_e}{\rho U^2} \quad (31)$$

This is not a general result, because the right side of equation (28) was set equal to zero. It is, however, correct to first order in small quantities if, for example, equation (19) applies, and may be a useful relation even if disturbances are not weak.

If disturbances are indeed weak, equations (25) and (31) may be used to find the velocity field in the straight channel. The result for $\tilde{\psi}$ is

$$\tilde{\psi} = \frac{D}{2n}\left\{-\Phi n\left(\theta+2\frac{f}{\Phi}\frac{y}{D}\right) + \epsilon\frac{\Phi^2}{\Phi^2+f^2}\left[f\sin n\left(\theta+2\frac{f}{\Phi}\frac{y}{D}\right) + \Phi\cos n\left(\theta+2\frac{f}{\Phi}\frac{y}{D}\right) + \frac{f}{\Phi}e^{-2n\frac{y}{D}}(-\Phi\sin n\theta + f\cos n\theta)\right]\right\} \quad (32)$$

If disturbances are of finite strength, and if $g(\theta)$ can be expressed as a Taylor series in ϵ, then the full equation (28) could be made the basis of a method of successive approximations.

Sudden Expansion. If there is a sudden large transverse (radial) expansion just at the OGV exit, as sketched in Fig. 6(*b*), then the exit flow would be like a jet emerging from a long slot. While the jet velocity would vary circumferentially on a scale comparable to wheel diameter, the pressure matching of the jet to the receiver would occur on the scale of blade height. Since the receiver pressure could be considered constant, the jet exit pressure could also be considered constant. In the extreme of an orifice-like diffuser

$$p_e = p_s \quad (33)$$

Downloaded 01 Jun 2010 to 171.66.16.70. Redistribution subject to ASME license or copyright; see http://www.asme.org/terms/Terms_Use.cfm

This is the simplest possible assumption about pressure change at the compressor exit [9]. Of course, it envisages an extremely short diffuser, which would generally not be acceptable because of its low efficiency.

Apparently, the general problem of finding the pressure change at the compressor exit is quite difficult, both to define and to solve. The specifics of diffuser configuration would greatly affect the result. Here, we have found expressions for two extreme cases which may possibly bracket typical practical situations. We may, for convenience, write them in the form

$$P_e = \frac{p_s - p_e}{\rho U^2} = (m-1)fh \tag{34}$$

where $m=1$ would signify a sudden area change, and $m=2$ would signify a straight channel. We will regard m, therefore, as a somewhat arbitrary parameter of our problem.

Requirements for Rotating Stall

The various pressure relations may now be combined to express a statement that pressures remain constant in upstream and downstream reservoirs, even though an unsteady disturbance occurs in the compressor which connects them. We have already specified that the disturbance is steady when viewed in a frame rotating with velocity, fU.

Pressure Match. We require that $p_s - p_T$ be constant, or

$$\underbrace{\frac{p_0 - p_T}{\rho U^2}}_{\text{entrance duct}} + \underbrace{\frac{p_e - p_0}{\rho U^2}}_{\text{compressor}} + \underbrace{\frac{p_s - p_e}{\rho U^2}}_{\text{exit duct}} = \underbrace{\frac{p_s - p_T}{\rho U^2}}_{\text{reservoirs}} \equiv \Psi \tag{35}$$

The first term is given by equation (21), the third by equation (34), and the second by application of equation (9) for guide vanes and equation (8) for each of N stages. The result may be written

$$\left[\frac{2UN\tau}{D}\left(\frac{1}{2}-f\right) - \frac{U(\tau_{IV}+\tau_{OV})}{D}f\right]g'(\theta) - mfh + \frac{1}{2}h^2 - \frac{1}{2}K_I h^2 + \Psi - \left[NF(\phi) - \frac{1}{2}\phi^2\right] = 0 \tag{36}$$

It is obvious that the last quantity in brackets is the compressor characteristic function that would apply in the absence of rotating stall; that is, the curve $\psi_c(\phi)$ shown on Fig. 1.

$$\psi_c(\phi) \equiv NF(\phi) - \frac{1}{2}\phi^2 \tag{37}$$

It should be emphasized that while $\psi_c(\phi)$ is a given feature of the compressor, it is not the same as Ψ; the latter is the pressure rise actually produced, with rotating stall (if it occurs) in progress. While ψ_c is, in principle, given, it is not the characteristic usually measured in tests of compressors subject to rotating stall. One might rather say that Ψ is the usually measured quantity; here, it is part of the answer.

The problem now is to find what values of parameters such as f, m, Ψ, or features of the function $\psi_c(\phi)$, permit nonzero solutions of the pair of equations (36) and (17).

Weak Disturbances. In this paper, we will restrict disturbances to be weak. Thus, we neglect the terms $(1/2)h^2$ and $(1/2)K_I h^2$ appearing in equation (36). Also, since ϕ will remain close to Φ during a weak disturbance, we keep only the first two terms of the Taylor series

$$\psi_c(\phi) = \psi_c(\Phi) + \psi_c'(\Phi)g + \frac{1}{2}\psi_c''(\Phi)g^2 + \ldots \tag{38}$$

For convenience, we define

$$\lambda \equiv \frac{2UN\tau}{D}\left(\frac{1}{2}-f\right) - \frac{U(\tau_{IV}+\tau_{OV})}{D}f \tag{39}$$

so that equation (36) becomes

$$\lambda g'(\theta) - mfh - \psi_c' g + \Psi - \psi_c(\Phi) = 0 \tag{40}$$

By definition, the average value of g over a cycle must vanish. Also, if the flow far upstream is purely axial, no average swirl can arise between there and the compressor entrance if the flow is irrotational. Therefore, the average value of h must also vanish. These conditions would apply even for strong waves, but in the present case, integrating equation (40) over a cycle shows that

$$\Psi - \psi_c(C) = 0 \tag{41}$$

In other words, for weak waves, there is no vertical displacement of the operating point from the rotating-stall-free characteristics; it is as indicated for point A of Fig. 1.

Presumably, g and h have Fourier series with coefficients related by equations (18(a) and 18(c)). Because equation (40) is linear, each coefficient is independently fixed. Using only the a_n terms, we find by substitution

$$(\lambda n - mf)a_n \cos n\theta - \psi'(\Phi)a_n \sin n\theta = 0 \tag{42}$$

The conditions for a weak periodic wave of arbitrary amplitude are therefore that $\lambda n = mf$, that $\psi_c'(\Phi) = 0$, and that $\Psi = \psi_c(\Phi)$. The first of these may be solved for propagation-speed coefficient, f

$$f = \frac{1/2}{1 + m\dfrac{D}{2UnN\tau} + \dfrac{\frac{1}{2}(\tau_{IV}+\tau_{OV})}{N\tau}} \tag{43}$$

This is the chief result of our analysis, and will be discussed fully in the next section. The second requirement

$$\psi_c'(\Phi) = 0 \tag{44}$$

means that the local curve of ψ_c must be flat. This could be true in the deep-stall region (points like A or C in Fig. 1), and is true at the maximum of the characteristic (point M). In the latter case, equation (44) would be a conditon for stall inception, agreeing with the classical stability requirement. On the descending branch of the speed line, equation (44) would not be satisfied; we interpret that to mean not that rotating stall cannot occur, but rather that it cannot be weak. In fact, ψ_c' can be interpreted as a negative damping factor; since equations (18) indicate that $g = -h'$, equation (40) is that of a harmonic oscillator,

$$\lambda h'' - \psi_c' h' + mfh = 0$$

with homogeneous boundary conditions, a wave must decay if ψ_c' is negative, or be amplified if ψ_c' is positive. In neither case could a permanent oscillation exist.

Equations (41), (43), and (44) therefore give the conditions for a steady rotating stall of weak amplitude to exist, when reservoir pressures are both constant.

Stall Propagation Speed

We next discuss the implications of equation (41) and compare its predictions with experiment [2]. Equation (43) is essentially a balance of disturbance phase lags inside and outside the compressor.

The External Lag Parameter. The parameter, m, appears in equation (43). It was defined in equation (34) as a measure of the strength of the lagging pressure term fh arising in the exit duct. The same lag term arises from the entrance duct (the term fh in equation (21)) assuming ideal flow in a straight

Downloaded 01 Jun 2010 to 171.66.16.70. Redistribution subject to ASME license or copyright; see http://www.asme.org/terms/Terms_Use.cfm

channel. We should admit the possibility that in the entrance flow, too, configuration or loss effects might affect lag. Thus, where the two lags are added to give mfh in equation (36), we should imagine m to be a net lag parameter depending on the combined contributions of both entrance and exit flows.

The Compressor Lag Parameters. The lag, τ, defined in equation (3), depends on the aerodynamics of a blade passage, sketched in Fig. 2(b). Whatever its physical nature, it should scale with axial passage length, L, and axial velocity, V. We are then led to define a dimensionless lag

$$\tau^* \equiv \frac{\Phi U \tau}{L} \tag{45}$$

in terms of which equation (43) becomes

$$f = \frac{1/2}{1 + \frac{m\Phi}{n}\frac{D}{2NL}\frac{1}{\tau^*} + \frac{1}{N}\frac{\tau_v^*}{\tau^*}} \tag{46}$$

The lags for guide vanes are assumed equal.

It is perhaps of interest to note the value of τ^* that would represent "apparent mass" or inertia only. Referring to Fig. 2(b), we see that a mass $\rho L\sigma/\cos\gamma$ of fluid is accelerating in a blade passage at a rate $U\dot{\phi}/\cos\gamma$ requiring the force provided by an additional pressure rise $(\Delta p)_A$

$$\frac{(\Delta p)_A}{\frac{1}{2}\rho U^2} = -\frac{2}{\cos^2\gamma}\frac{L}{U}\dot{\phi} \tag{47}$$

Comparing equation (3) we see that, due to inertia in blade passages only, $\tau^* = 2\Phi/\cos^2\gamma$. The stagger angle, γ, is roughly $\tan^{-1}(1/2\ \Phi_d)$ where Φ_d is design flow coefficient. We write

$$\tau^* = \frac{2\Phi}{\cos^2\gamma}k \tag{48}$$

where a factor k has been included because, often, the interrow gap is quite large. If the gap were a multiple $k-1$ of L, then τ^* would be proportional to k.

Other effects having to do with separation or secondary flows will also influence τ^*. If these could be represented by suitable choice of k, it would be appropriate to write equation (46) in the following form

$$f = \frac{1/2}{1 + \frac{m}{k}(\cos^2\gamma)\frac{1}{2n}\frac{D}{2NL} + \frac{\tau_v^*}{\tau^*}\frac{1}{N}} \tag{49}$$

We will use k as a general "uncertainty factor" comparing actual τ to blade-passage inertia lag. It is interesting that the external and internal lag parameters enter equation (49) only in their ratio, m/k.

Qualitative Results for Propagation Speed. Equation (46) shows certain general trends:

1 Propagation speed is less than 50 percent of U, unless τ is negative. Actually, negative lag has been argued to occur at stall of isolated airfoils [12], and $f > 1/2$ is generally associated with single-stage experiments [2, 5]. Perhaps these results are consistent.

2 Increasing number of stages (N) increases f toward 1/2. This result has been found by Cumpsty and Greitzer [10]. It is important that N multiplies τ^* in equation (1.46). If τ is very small, being proportional to blade chord, it might at first be thought to make a negligible contribution to pressure rise (equation (3)), and therefore not be proper to include in a disturbance analysis. This argument might be valid for single-row problems. However, a small lag per row will accumulate over many rows in a multistage compressor to make a large overall lag; it is the latter which governs rotating stall. The same idea is expressed by noting the group $D/2NL$ in equation (49); it describes the shape factor of the whole compressor when viewed from the side. Typically it would be of order 1, while for a single row, D/L would be much larger—typically about 15.

3 Multicell stalls have higher propagation speeds. The mode number, n, represents number of stall cells.

4 Increased lag (larger k) tends to increase propagation speed.

5 Especially if design flow coefficient, Φ_d, is small, smaller Φ_d (or larger stagger angle) will increase f.

6 If the net external phase-shift parameter, m, is made smaller, f is increased. For a typical engine, m is probably near 2. If the diffuser is a sudden area change at the rear face of the compressor, $m=1$. If circumferential velocity were suppressed in the inlet flow, m might also decrease by 1. A value of $m=0$ may be theoretically possible, if circumferential velocity is suppressed in both entrance and exit flows.

7 Guide vanes have litte effect on f in multistage compressors.

Table 1 Propagation speed coefficient

Φ_d	γ (deg)	N	n	Ref. [2]	f (percent) Equation (49) $k/m=1$	f (percent) Equation (49) $k/m=2$
0.35	50	1	1	19	11	16
			6	31	23	26
			12	66	26	27
0.35	50	3	1	32	23	29
			4	40	34	37
			12	60	38	39
0.35 (reducing spacing)	50	3	1	27	23	29
			5	54	35	38
0.55	35	1	1	15	9	14
		2	1	22	15	21
		3	1	26	20	26
		4	1	31	23	30
1.00	20	1	1	11	8	12
		2	1	20	14	20
		3	1	24	18	25
		4	1	28	22	28

Chord = 17.8 mm
Mean diameter: 320 mm

Comparison with Day and Cumpsty's Data. The foregoing results may be compared with the propagation speed data of Day and Cumpsty [2]. Table 1, in the first 5 columns, collects some of their results for various designs, number of stages, and number of stall cells. Of single-cell cases ($n=1$), only the full-span results are included, because the present paper assumes full-span stall, in effect. Multiple-cell cases are included, but it should be noted that all of them are part-span. Guide vanes have a smaller average incidence than core blades, by about a factor of 2. Therefore relative velocities are lower. As a rough estimate, we will assume τ_v to be the average of equation (48) and $2\Phi k$. In that case

$$\frac{\tau_v^*}{\tau^*} = \frac{1}{2}(1+\cos^2\gamma) \tag{50}$$

For the experiments [2] the blade chord is 17.8 mm, and the mean diameter is about 320 mm. The spacing between rows is about one chord width. In that case, if inertia were the only source of lag, we would expect $k=2$. There appears to be a fairly long straight section before the diffuser, and so one

Downloaded 01 Jun 2010 to 171.66.16.70. Redistribution subject to ASME license or copyright; see http://www.asme.org/terms/Terms_Use.cfm

would expect $m=2$. Equation (49) shows that k and m enter in the ratio, k/m. The last two columns of numbers are the theoretical predictions of equation (49) for two values of k/m, the first being for the expected $k/m=1$ ($k=2$, $m=2$), and the second for $k/m=2$. The latter would apply if k were 4 instead of 2 owing to separation hysteresis, or perhaps if the exit acted like an orifice so that $m=1$ instead of 2. The former would be a more likely combination ($m=2$, $k=4$).

Comparing the theoretical and experimental columns, it is clear that equation (49) gives all the proper trends of f with γ, N, and n. We should keep in mind that the theory does not contemplate the part-span stall patterns found experimentally for multiple zones, so agreement for n different from 1 is perhaps fortuitous. The theory probably does not apply well to single-stage situations. Therefore, the most appropriate comparisons are for $n=1$, $N=2$, 3, 4. These cases are enclosed in boxes in the Table, for emphasis.

Table 1 clearly indicates that $k/m=2$ is the best choice for agreement, and the agreement could hardly be closer, for intermediate and high-Φ_d builds. For low Φ_d, full agreement would require a somewhat higher value of k/m, about 3 instead of 2. Perhaps the higher stagger angle causes more hysteresis due to separation.

In the low-Φ_d experiments, a reduced spacing gave a substantially lower speed. In that case, we would expect to reduce the factor k to account for the smaller mass of fluid undergoing oscillation. Because spacing was originally one-chord length, it seems reasonable to reduce k by a factor of 2. Indeed, Table 1 shows that $k/m=1$ gives a prediction having the same relation to experiment for reduced spacing as $k/m=2$ had for the wider spacing. Also, it was mentioned that $k/m=3$ gives exact agreement with experiment for the wider spacing; $k/m=1.5$ gives exact agreement for reduced spacing. Thus, we may add spacing to the list of compressor parameters whose influence on propagation speed is well predicted by equation (49).

Finally, we should note that Cumpsty and Day [10] have derived an equation for propagation speed based on a consideration of pressure jumps across the boundaries of deep-stall zones, together with certain observations of compressor test results. Their equation also predicts the correct trend with number of stages.

Concluding Remarks

The present analyis shows that rotating stall can be considered an eigenfunction of a compressor-inlet-diffuser system if a single lag process occurs in the generation of force by a blade passage, and, at least for weak amplitude, if there is a flat total-to-static pressure rise characteristic in the neighborhood of the average flow coefficient set by the throttle.

The predicted propagation speed depends on various features of the compressor, and follows very closely the trends of experimental observations as those features are changed. The lag processes originating in the compressor (k), and those originating outside the compressor in the entrance duct and the diffuser (m) require more study from a fundamental point of view.

The present analysis, being based on small perturbations, has limited value. First, actual perturbations in deep stall are not small, nor are amplitudes arbitrary. Therefore, there is little guidance from the present analysis as to how compressor parameter changes might help to control or eliminate the phenomenon. However, the results of the present analysis perhaps do give encouragement for the study of finite amplitude oscillations using similar physical assumptions.

Parts II and III of this study report such extensions. In Part II, we keep the restriction to a flat characteristic, but allow the amplitude to be finite. Results will include a measure of how the mean performance is affected by the existence of rotating stall, as well as certain interesting velocity and pressure profiles. In Part III, we attempt to relate rotating stall to the complete characteristic curve. Results include an indication of when the "blockage" model [3] applies, and also predict that rotating stall becomes impossible beyond some value of flow coefficient, probably indicating the onset of stall recovery.

References

1 Greitzer, E. M., "Review—Axial Compressor Stall Phenomena," ASME *Journal of Fluids Engineering*, Vol. 102, June 1980, pp. 134–151.

2 Day, I. J., and Cumpsty, N. A., "The Measurement and Interpretation of Flow Within Rotating Stall Cells in Axial Compressors," *Journal of Mechanical Engineering Sciences*, Vol. 20, 1978, pp. 101–114.

3 Day, I. J., Grietzer, E. M., and Cumpsty, N. A., "Prediction of Compressor Performance in Rotating Stall," ASME JOURNAL OF ENGINEERING FOR POWER, Vol. 100, Jan. 1978, pp. 1–14.

4 Emmons, H. W., Pearson, C. E., and Grant, H. P., "Compressor Surge and Stall Propagation," ASME *Transactions*, Vol. 27, Apr. 1955, pp. 455–469.

5 Graham, R. M., and Guentert, E. C., "Compressor Stall and Blade Vibration," Chapter XI in *Aerodynamic Design of Axial-Flow Compressors*, NASA SP-36, 1965.

6 Sears, W. R., "Rotating Stall in Axial-Flow Compressors," *Zeitschrift fur Angewandte Mathematik und Physik*, Vol. 6, No. 6, 1955, p. 429–455.

7 Marble, F. E., "Propagation of Stall in a Compressor Blade Row," *Journal of the Aeronautical Sciences*, Vol. 22, 1955, pp. 541–554.

8 Stenning, A. H., Kriebel, A. R., and Montgomery, S. R., "Stall Propagation in Axial-Flow Compressors," NACA TN 3580, 1956.

9 Takata, H., and Nagano, S., "Nonlinear Analysis of Rotating Stall," ASME JOURNAL OF ENGINERING FOR POWER, Oct. 1972, pp. 279–293.

10 Cumpsty, N. A., and Grietzer, E. M., "A Simple Model for Compressor Stall-Cell Propagation," ASME JOURNAL OF ENGINEERING FOR POWER, Vol. 104, Jan. 1982, pp. 170–176.

11 Stoker, J. J., *Nonlinear Vibrations*, ch. 5, Interscience, New York, 1950.

12 Moore, F. K., "Lift Hysteresis at Stall as an Unsteady Boundary-Layer Phenomenon," NACA TN 3571, 1951.

Downloaded 01 Jun 2010 to 171.66.16.70. Redistribution subject to ASME license or copyright; see http://www.asme.org/terms/Terms_Use.cfm

A Theory of Rotating Stall of Multistage Axial Compressors: Part II—Finite Disturbances[1]

F. K. Moore
Sibley School of Mechanical and Aerospace Engineering, Cornell University, Ithaca, N.Y. 14853

A small-disturbance theory of rotating stall in axial compressors is extended to finite amplitude, assuming the compressor characteristic is a parabola over the range of the disturbance. An exact solution is found which requires the operating point to be at the minimum or maximum of the parabola. If the characteristic is flat in a deep-stall regime, the previous harmonic solution applies with neither reverse flow or "unstalling." If the characteristic is concave upward in deep stall, the disturbance has a skewed shape, steeper at the stall-zone trailing edge as experiment shows. Propagation speed is only slightly affected by this nonlinearity. Near stall inception, negative curvature in combination with multiple stall zones can limit the nonlinear oscillation, in the manner of "progressive" stall. If, as seems likely, lag at stall inception is negative (opposite to inertia), propagation speed exceeds 1/2 wheel speed, as experiments suggest.

Introduction

In Part I ("Small Disturbances") [1], it was shown how a combination of three lags, pertaining to entrance-flow passage, compressor blade passage, and exit-flow passage permit the occurrence of a flow distortion which is steady in a moving frame of reference. In principle, the entrance and exit lags are easily calculated, while the blade-passage lag is difficult to define and infer from tests. Comparison with measurements of rotating-stall propagation speed made by Day and Cumpsty [2] support the idea that the blade-passage effect is largely inertial, in deep stall.

The lag per row was represented as a factor, k, of the purely inertial value for a blade passage. If the inter-row gap is equal to the blade depth, then k would be about 2, still considering only inertia but including the mass of fluid occupying the inter-row space. The combined lag effects of entrance and exit flows was represented by the factor, m; if long straight passages describe both entrance and exit configurations, then $m=2$.

For small perturbations, k and m enter as a ratio in the formula for propagation speed. If the ratio is taken as 2 (about twice what we would expect on purely inertial grounds), agreement with experiment is very complete, suggesting that a single compressor lag parameter, if suitably chosen, could lead to a quite complete description of rotating stall.

Small perturbations restrict wave forms to be harmonic, which is quite unlike the wave forms actually observed [2]. Furthermore, the amplitude is unspecified in a linear analysis. Thus, although a good prediction of propagation speed is encouraging, the important questions about rotating stall have to do with disturbances of finite amplitude. Specifically:

1 What is the effect on average pressure-rise performance caused by rotating stall?

2 Are there circumstances which limit the amplitude of oscillation? If so, "progressive stall" may be indicated.

3 Are there ranges of flow coefficient for which rotating stall is forbidden? If so, "stall recovery" may be indicated.

In considering these questions, we should, if possible, allow the assumed compressor characteristic to depart from a constant value during the oscillation of flow coefficient.

In this paper, we investigate the finite-strength disturbances permitted when the characteristic is either flat or has constant curvature. Notation will be as defined in Part I, except for quantities appearing for the first time; these appear in the Nomenclature.

Solutions of the Pressure Equation

The Disturbance Equations. We recall the basic pressure-match equation, equation (36) of Part I, and incorporate equations (37) and (39)

$$\lambda g'(\theta) - mfh + \frac{1}{2}(1-K_I)h^2 + \Psi - \psi_c(c) = 0 \qquad (1)$$

where g and h are the axial and circumferential velocity disturbances, related by the Fourier series (equation (18)) of Part I, or the equivalent statement

$$h + ig = \text{analytic function of } (e^{i\theta}) \qquad (2)$$

[1] Research performed at NASA-Lewis Research Center

Contributed by the Gas Turbine Division of THE AMERICAN SOCIETY OF MECHANICAL ENGINEERS and presented at the 28th International Gas Turbine Conference and Exhibit, Phoenix, Arizona, March 27-31, 1983. Manuscript received at ASME Headquarters December 20, 1982. Paper No. 83-GT-45.

Copyright © 1984 by ASME
Downloaded 01 Jun 2010 to 171.66.16.70. Redistribution subject to ASME license or copyright; see http://www.asme.org/terms/Terms_Use.cfm

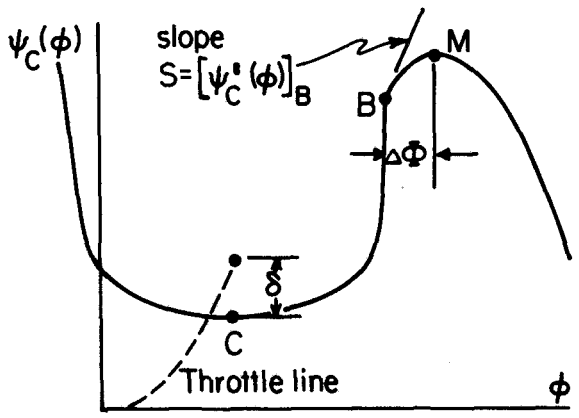


Fig. 1 Constant-speed compressor characteristic in the absence of rotating stall

We will assume that the rotating stall-free characteristic function remains well represented, over the range of the oscillation, by the first three terms of a Taylor series (equation (38) of Part I) about the mean flow Φ

$$\psi_c(\phi)=\psi_c(\Phi)+\psi_c'(\Phi)g+\frac{1}{2}\psi_c''(\Phi)g^2+\ldots \tag{3}$$

We will find that no solutions are possible unless $\psi_c'(\Phi)=0$, even for finite disturbances. Such a term would represent a damping effect, even for finite disturbances, and must be discarded if only the three terms of equation (3) are considered. The reasons why this is true will be made clear later, especially in Part III.

Equation (1) now becomes

$$\lambda g'(\theta)-mfh+\frac{1}{2}(1-K_I)h^2-\frac{1}{2}\psi_c''(\Phi)g^2+\delta=0 \tag{4}$$

where δ is the performance increase (perhaps negative) due to rotating stall

$$\delta\equiv\Psi-\psi_c(\Phi) \tag{5}$$

A typical function $\psi_c(\Phi)$ and positive δ are sketched in Fig. 1.

The second term of equation (4) embodies the factor m, introduced in Part I to account for lags external to the compressor. This factor was found to be 2 for small disturbances of a straight-channel exit. In the present paper, we are concerned with finite disturbances, and a more complete accounting for downstream pressure recovery is no doubt needed. The necessary analysis would be very arduous and not justified for a particular highly idealized exit channel. For a sudden exit expansion, we argued that $m=1$, and this result is independent of amplitude. Therefore, the term mfh will be retained because it is proper when $m=1$, and may be empirically justified for other values of m. Further research on this point is required.

The disturbances, g and h, governed by equation (4) are periodic (but not necessarily harmonic) and have vanishing averages over a cycle: in the case of g because it is defined as a departure from average axial velocity, and in the case of h, because net circulation in the entrance flow is assumed to remain zero. Therefore, integrating equation (4) over a cycle shows that, when nonlinear terms involving h^2 and g^2 are included, the constant δ cannot be zero, as it was in the linear analysis of Part I.

A General Solution. In Part I, equations (2) and (4) had a simple harmonic solution because the last three terms of equation (4) were absent. Here, those terms are kept, and appropriate nonlinear periodic solutions are sought. It happens that a general solution, believed to be unique, can be written down at once

$$h+ig=A\frac{e^{in\theta}}{1+\eta e^{in\theta}} \tag{6a}$$

or

$$h=\frac{A(\cos n\theta+\eta)}{1+\eta^2+2\eta\cos n\theta};\quad g=\frac{A\sin n\theta}{1+\eta^2+2\eta\cos n\theta} \tag{6b}$$

where A and η are constants to be determined by satisfying equation (4). In order that h and g have Fourier series in θ of the form of equations (18) of Part I, it is necessary that $|\eta|<1$. Equation (6*a*) is clearly a special case of equation (2), and the previous linear solution is recovered by setting $\eta=0$.

The forms of these velocity traces are shown for various values of η between 0 and 1, on Fig. 2. The axial-flow disturbance, g, is antisymmetric and is traveling to the right. Its negative portion represents a "stall zone"; if A is positive, its "trailing edge" is steeper.

In presenting the results for A and η obtained by substitution into equation (4), we note that f is not known and recall that

$$\lambda=\frac{2UN\tau}{D}\left(\frac{1}{2}-f\right)-\frac{2U\tau_v}{D}f \tag{7}$$

if the lags for IGV and OGV are equal. Thus, a free constant will remain after η, A, and δ are given in terms of f. Results are

$$\frac{\lambda n}{mf}=\frac{(1-\eta^2)\psi_c''+(1-5\eta^2)(1-K_I)}{(1+\eta^2)\psi_c''+(1-3\eta^2)(1-K_I)} \tag{8}$$

$$A=\frac{4mf\eta}{\psi_c''}\frac{(1-\eta^2)\psi_c''+(1-3\eta^2)(1-K_I)}{(1+\eta^2)\psi_c''+(1-3\eta^2)(1-K_I)} \tag{9}$$

$$\delta=\frac{Amf}{8\eta^2}[4\eta-Amf(\psi_c''+1-K_I)] \tag{10}$$

The next step will describe rotating-stall features implied by

Nomenclature

A = amplitude coefficient of disturbance, equation (6*a*)
A_1, A_2 = stream-tube areas at entrance to IGV, Fig. 3
a = dimensionless reciprocal time lag, $D/(2UNt)$
B = denotes "break" of characteristic, Fig. 1
C = denotes minimum of deep-stall characteristic, Fig. 1
C_p = disturbance of static-pressure rise coefficient across the compressor, equation (18)
M = denotes maximum of characteristic at stall inception, Fig. 1
S = slope of characteristic at "break point," B, Fig. 1
Δp = pressure recovery at entrance to IGV, equation (11)
$\Delta\Phi$ = difference of flow coefficient at points, M and B, of Fig. 1
η = nonlinearity parameter of disturbance, equation (6*a*)
δ = performance increase due to rotating stall, equation (5)

Subscripts

m = amplitude of axial velocity disturbance
mm = conditions when axial velocity disturbance amplitude has its largest permitted value

Downloaded 01 Jun 2010 to 171.66.16.70. Redistribution subject to ASME license or copyright; see http://www.asme.org/terms/Terms_Use.cfm

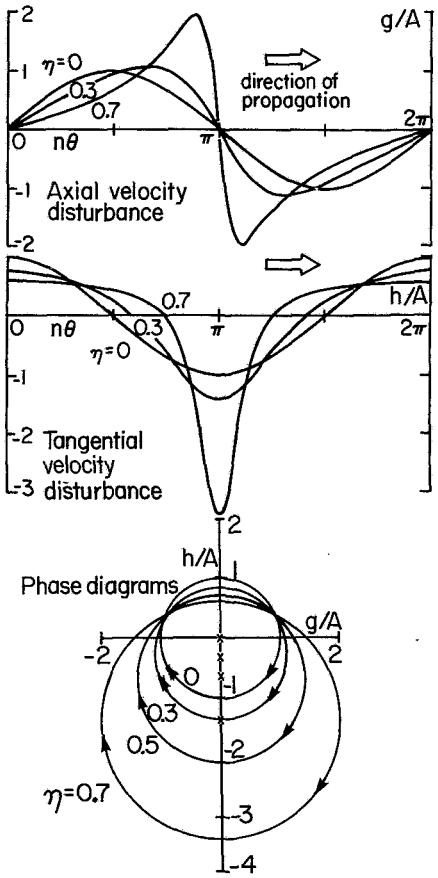


Fig. 2 Nonlinear velocity disturbances, for various values of amplitude parameter η, from equations 6(*a*) and 6(*b*)

equations (8–10). First, we should specify the parameters $\psi_c''(\Phi)$ and K_I.

In these equations, K_I is the coefficient of pressure recovery in the entrance of the IGV passage, owing to the fact that a transverse velocity disturbance makes an incoming stream tube somewhat narrower than the IGV entrance. Figure 3 sketches the process. The conservative estimate of this effect is gotten by assuming the area increase is sudden. The usual pressure-rise formula in such a case is

$$\frac{\Delta p}{\rho(V^2+u^2)} = \frac{A_1}{A_2}\left(1-\frac{A_1}{A_2}\right)$$

but the geometry of Fig. 3 shows that $A_1/A_2 = V/\sqrt{V^2+u^2}$. Since $V = U\phi$ and $u = Uh$ in stator coordinates, we may conclude that

$$\frac{\Delta p}{\rho U^2} = \phi^2[\sqrt{1+(h/\phi)^2}-1] = \frac{1}{2}h^2K_I \tag{11}$$

the last member of the equation being the definition of K_I. The quantity $1-K_I$ which appears in equations (8–10) is the head loss coefficient due to oblique entrance to the IGV. Clearly, it is a function of h itself, and therefore cannot properly be used in equation (4) as a constant. Fortunately, the magnitude of $1\text{-}K_I$ is very small, not exceeding 10 percent unless h/ϕ exceeds 0.7. Therefore, one is probably justified in neglecting the head-loss effect represented by $1-K_I$, and equations (8–10) become

$$\frac{\lambda n}{mf} = \frac{1-\eta^2}{1+\eta^2} \tag{12}$$

$$A = \frac{4mf}{\psi_c''}\frac{\eta(1-\eta^2)}{1+\eta^2} \tag{13}$$

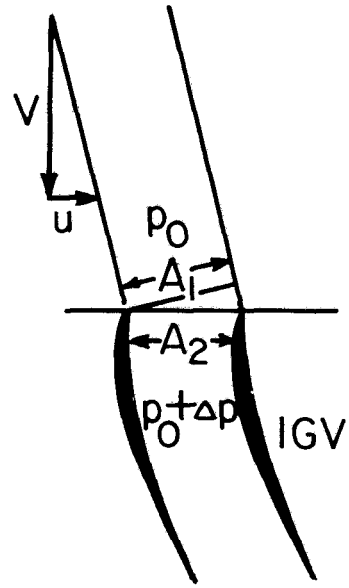


Fig. 3 Sketch of the increase of stream-tube area from A_1 to A_2 upon entry into an IGV passage, owing to transverse disturbance velocity, u

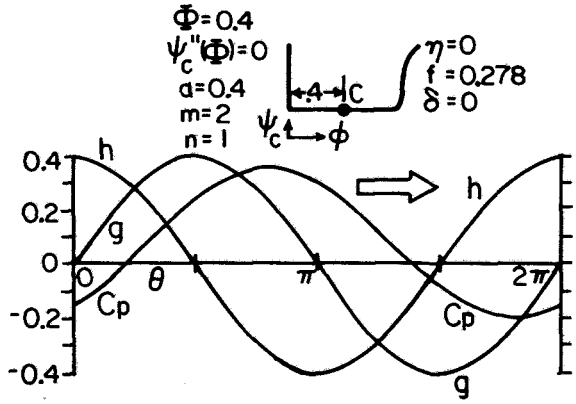


Fig. 4 Velocity and pressure disturbances for a flat characteristic ($\psi_c''(\Phi)=0$) in deep stall. Stall zone is $180 < \theta < 360$ deg, where $g < 0$.

$$\delta = \frac{4(mf)^2}{\psi_c''}\frac{\eta^2(1-\eta^2)}{(1+\eta^2)^2} \tag{14}$$

We bear in mind that λ is a given function of f (equation (7)), and therefore equation (12) is an equation connecting f and η. In fact, equation (12) may be replaced by

$$f = \frac{1/2}{1+\dfrac{\tau_v/\tau}{N}+\dfrac{am}{n}\dfrac{1-\eta^2}{1+\eta^2}} \tag{15}$$

where the symbol a is introduced to define the group

$$a \equiv \frac{D}{2UN\tau} = \frac{D}{NL}\frac{\Phi}{2\tau^*} \tag{16}$$

and the last expression results from equation (45) of Part I. In discussing compressors of many stages, one might well neglect the second term of the denominator of equation (15), finding

$$f = \frac{1/2}{1+\dfrac{am}{n}\dfrac{1-\eta^2}{1+\eta^2}} \tag{17}$$

Downloaded 01 Jun 2010 to 171.66.16.70. Redistribution subject to ASME license or copyright; see http://www.asme.org/terms/Terms_Use.cfm

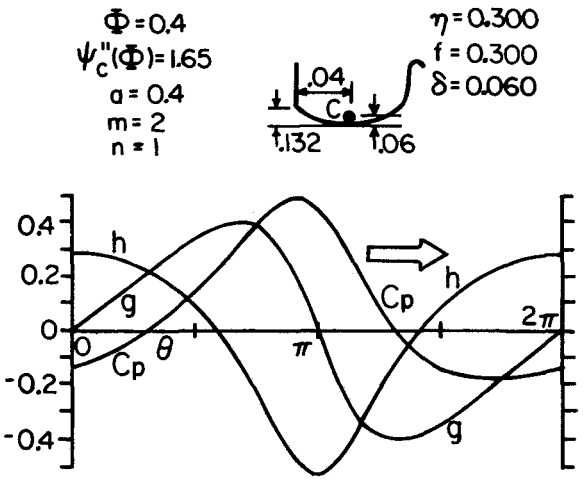


Fig. 5 Velocity and pressure disturbances for a concave characteristic ($\psi_c''(\Phi) > 0$) in deep stall. Stall zone is $180 < \theta < 360$ deg, where $g < 0$.

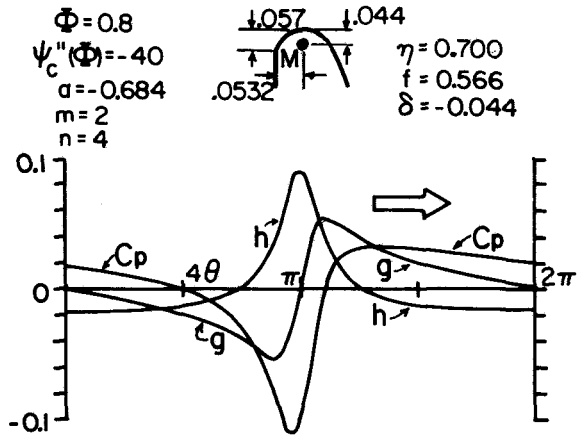


Fig. 6 Velocity and pressure disturbances for a convex characteristic ($\psi_c''(\Phi) < 0$) at incipient stall (note expanded scales). Stall zone is $0 < 4\theta < 180$ deg, where $g < 0$.

Pressure Disturbance. We should record for subsequent use an expression for pressure-rise fluctuation, because that is a quantity more easily measured than the velocity components represented by g and h. Equations (8) and (9) of Part I and the present equations (4) and (5), with $K_I = 1$, yield the static pressure rise across the compressor

$$C_p \equiv \frac{p_e - p_0}{\rho U^2} - \left[\frac{1}{2}\Phi^2 + \Psi(\Phi)\right] = -mfh + \Phi g + \frac{1}{2}g^2 + \frac{1}{2}h^2 \tag{18}$$

Included in brackets on the left of this equation are certain quantities which will be constant during any rotating-stall process. Quantities which will fluctuate are on the right side, and they are the ones of most interest.

Amplitude of Solution. We have noted that equation (6*b*) describes an oscillation of axial flow (g) that is symmetrical: its amplitude can be found using equations (13) and (17) to be

$$g_m = \frac{2m}{\psi_c''} \frac{\eta}{\left(1 + \frac{am}{n}\right) + \eta^2\left(1 - \frac{am}{n}\right)} \tag{19}$$

with η being an amplitude parameter as yet undetermined.

As a function of η, the disturbance amplitude, g_m, might be limited in some circumstances. According to equation (19), the maximum value that g_m can assume is

$$g_{mm} = \frac{m}{\psi_c''} \frac{1}{\sqrt{1 - (am/n)^2}} \tag{20}$$

when

$$\eta_{mm} = \sqrt{\frac{1 - (am/n)}{1 + (am/n)}} \tag{21}$$

In such a case, equations (17) and (14) give

$$f_{mm} = \frac{1/2}{1 - (am/n)^2}; \quad \delta_{mm} = -\frac{m^2}{\psi_c''} \frac{am/n}{[1 - (am/n)^2]} \tag{22}$$

Because η is restricted to be less than 1, equation (21) shows that this particular limiting solution is possible only if a is negative, and that requires τ to be negative; in effect, the hysteresis loop of Fig. 3 of Part I would be clockwise in such a case.

If, on the other hand, a is positive, equation (19) shows that maximum would occur when $\eta = 1$, taking the value $g_{mm} = m/\psi_c''$.

Next, we should apply these results for interesting choices of ψ_c'', indicated on Fig. 1. There are two types of points where the characteristic (in absence of rotating stall) is horizontal ($\psi_c''(\Phi) = 0$) but yet has nonzero curvature. They are indicated on Fig. 1 as points C and M. At point C, the curvature $\psi_c''(\Phi)$ is positive, while at M it is negative.

Deep Stall

Flat Characteristic. At a point such as C of Fig. 1, we first consider the possibility that $\psi_c'' = 0$ everywhere in the range of oscillation. In that case, equation (19) shows that η must be zero if g_m is to be finite, and equations (17) and (14) give

$$f = \frac{1/2}{1 + (am/n)}; \quad \delta = 0 \tag{23}$$

This is simply the harmonic solution discussed in Part I, with, according to equation (6*b*),

$$h = g_m \cos n\theta; \quad g = g_m \sin n\theta$$

We conclude that in a region where the characteristic is flat, the solution is the linear one with arbitrary amplitude, even though a nonlinear solution is allowed. This result perhaps explains the surprising outcome of Part I, that a small-perturbation theory yields a good representation of stall propagation speed, even though the actual stall amplitude is large. For realistic comparison with experiment, the lag τ, and hence a, is positive, corresponding to values of $f < 1/2$.

The amplitude cannot actually be unlimited, of course. We suppose that this linear solution will be appropriate for rather small mean flow coefficients, so that the oscillation does not intrude into the rising part of the characteristic, with "unstalling" becoming a feature of the oscillation. In the same way, we would forbid the flow to reverse, imagining an abrupt rise of the characteristic below $\phi = 0$. If this is true, the oscillation should have an amplitude limited by Φ itself. That is

$$h = \Phi \cos n\theta; \quad g = \Phi \sin n\theta \tag{24}$$

Although the velocity components are harmonic, the pressure fluctuation is not, according to equation (18): If $n = 1$

$$C_p = \frac{1}{4}\Phi^2 - mf\Phi\cos\theta + \Phi^2\sin\theta \tag{25}$$

If, for example, $\Phi = 0.4$, $a = 0.4$, and $m = 2$, the velocity and pressure-rise fluctuations would be shown in Fig. 4. The pressure trace is also harmonic. The propagation is toward the right of the figure, at a speed (f) of 0.278. In this case, of course, $\delta = 0$, because $\eta = 0$. The operating point lies at point C, on the characteristic, as indicated in the sketch.

Downloaded 01 Jun 2010 to 171.66.16.70. Redistribution subject to ASME license or copyright; see http://www.asme.org/terms/Terms_Use.cfm

Concave Characteristic. Next we consider the possibility that $\psi_c'(\Phi)$ is slightly positive, or concave, as at point C of Fig. 1. Again, we expect that a is positive (on the ground that deep stall seems always to have $f < 1/2$). In that case, the greatest possible value of η would be 1, but then only if ψ_c'' is larger than m/g_m according to equation (19). For realistic diagram shapes, ψ_c'' must be much less than m/Φ, and we therefore conclude that η is quite small in these cases.

From equation (19), setting $g_m = \Phi$ and making η small gives

$$\eta = \frac{\psi_c''}{2m}\left(1 + \frac{am}{n}\right) \tag{26}$$

Substitution of equation (26) into previous equations will give corrections of order ψ_c'' to the flat-characteristic solutions. While the predicted traces of g and h as well as δ, will change to first order in ψ_c'', the value of f will be affected only to second order.

If $\psi_c'' > 0$, then A is positive and the velocity traces are as in Fig. 2, with an axial flow disturbance (g) which is steepest at the stall-zone "trailing edge," as experiments have shown [2]. By way of example, we modify the example displayed in Fig. 4, by making $\psi_c''(\Phi) = 1.65$; the changed characteristic is sketched in Fig. 5. Equation (18) gives the corresponding pressure trace, C_p. Pressure rise as well as axial velocity demonstrate the steep "trailing edge" found experimentally.

Incipient Stall

Convex Characteristic. At a point such as M, the value of ψ_c'' is negative. At a given speed, as flow coefficient, Φ, is reduced, rotating stall can first appear at point M. The characteristic of Fig. 1 is drawn to show some degree of overturn to the left of M, terminated in an abrupt drop at point B. At that point, we imagine a certain positive slope, S, to occur. The final slope, S, depends on the compressor; lightly-loaded compressors tend to permit a large S before a steep break occurs. If a parabola is used to represent the curve in the stall-inception zone, centered on point M, one could relate S to ψ_c'' and the distance, $\Delta\Phi$, between points B and M on the diagram

$$\Delta\Phi = S/\psi_c'' \tag{27}$$

As we have seen, a stall oscillation about point M would have a maximum permissible amplitude g_{mm} depending on the sign of τ (or a)

$$\left.\begin{aligned} g_{mm} &= \frac{m/\psi_c''}{\sqrt{1-(am/n)^2}}, \quad a<0 \\ &= m/\psi_c'', \quad a>0 \end{aligned}\right\} \tag{28}$$

If this maximum amplitude exceeds the $\Delta\Phi$ between points B and M, then the oscillation could easily extend into the deep stall zone, and a different type of larger amplitude oscillation would result, of the sort to be discussed in Part III of this series. On the other hand, if $g_{mm} < \Delta\Phi$, the oscillation could be limited to the vicinity of point M, governed purely by the local convex parabolic segment. This latter situation would presumably relate to "progressive" stall.

Because $\psi_c''(\Phi) < 0$, equation (13) shows that $A < 0$. Thus, the trace of g in Fig. 2 is reversed in sign, and now it is the cell "leading edge" that is the steeper. The proper value of η can be found from equation (19), if g_m is fixed.

Progressive Stall. Pursuing this idea further, we can relate g_{mm} and $\Delta\Phi$ from equations (27), (28) to arrive at the criteria for limited, or progressive-type stall

$$S > \frac{m}{\sqrt{1-(am/n)^2}}, \quad a<0 \tag{29}$$

$$S > m, \quad a>0 \tag{30}$$

These equations indicate that progressive stall is favored if:

1 S is large. Experience confirms that a delayed "break," and hence large S, favors progressive stall.

2 m is small. That is, an abrupt expansion at exit as opposed to a long, straight discharge would favor progressive stall. It is not known whether experience confirms this prediction.

3 n is large, if $a < 0$ (clockwise hysteresis). Large n denotes many stall cells, and experience is quite definite that progressive stall is associated with multiple stall cells [2]. We find that n is relevant only if $a < 0$ and, therefore, $f > 1/2$ (equation (22)). It is also usually found that progressive stall has this feature as well (see [2] or Table 1 of Part I), and we conclude that clockwise hysteresis ($a < 0$, $\tau < 0$) is quite typical in these "soft-stall" cases. Theoretically, it has been argued [3] that lift hysteresis of a single airfoil is of this sense if its stall process is a progressive advance of trailing-edge separation as opposed to the more abrupt leading-edge stall. In the former case, lift curves are rounded, while in the latter case, an abrupt break occurs. Thus, there is some basis for expecting $\tau < 0$ for progressive compressor stall.

4 a is small, if $a < 0$. Actually, am and n should be considered together; equation (17) provides

$$\frac{am}{n} = \frac{Dm}{2UNn\tau} \tag{31}$$

This grouping suggests that large τ favors progressive stall, as does a large product Nn. Perhaps it may be inferred that large n is especially required for single-stage ($N=1$) progressive stall, whereas multistage machines can have progressive stall which does not split up into multiple cells, because Nn is large even if $n = 1$. Experimental results tend to support this idea.

Figure 6 shows velocity and pressure-rise fluctuations calculated for a limited oscillation of the sort just discussed with a negative and ψ_c'' quite large and negative, n was taken to be 4, and the stall point M was considered to occur at $\Phi = 0.8$. The amplitude is only 0.053, but η is quite large because ψ_c'' is large, and the traces are quite far from harmonic shape. Propagation speed is greater than 1/2, and axial velocity changes most rapidly at the cell leading edge, in contrast to the case when $\psi_c'' > 0$. This result is in contrast to the known tendency of deep-stall wave forms to be steeper at the cell trailing edge [4]. Probably, the differing curvatures of ψ_c are important in this regard. Perhaps it would be useful to investigate this aspect of progressive stall experimentally.

Limitations of the Analysis. Multicell progressive stall is usually also part-span stall [2]. The present analysis assumes two-dimensional flow; in effect, full-span disturbances are assumed. The importance of this inconsistency with observations is difficult to assess.

The foregoing analysis does not show that rotating-stall oscillations must extend to the allowed amplitude limits, or that the oscillation will choose, so to speak, to adopt a zone number appropriate to progressive stall. Neither is it shown that the oscillation will become of the large-amplitude type just because it is not limited to remain above point B. These questions are ones for future research, probably to be answered by studying limit cycles emerging from equation (4). The present analysis is intended to suggest features to look for, in those more complete and inevitably more complex and confusing solutions.

Finally, we should recall the criterion $\psi_c'(\Phi) = 0$, mentioned following equation (3). Of course, a throttle setting need not correspond to $\Phi'(\Phi) = 0$. However, a purely periodic wave cannot occur, governed by a purely parabolic characteristic

Downloaded 01 Jun 2010 to 171.66.16.70. Redistribution subject to ASME license or copyright; see http://www.asme.org/terms/Terms_Use.cfm

unless that is true, even if the motion is nonlinear. The reason for this result, which will be made clear in Part III, is essentially that mentioned in Part I; namely, that $\psi_c'(\Phi)$ would be an amplification coefficient in equation (3). If $\psi_c'(\Phi)=0$, then any oscillation would grow until it encountered new features of the function $\psi_c(\Phi)$, beyond the range of the assumed parabola, such as a resistance to reversed flow, and this encounter would lead finally to a limit cycle. If $\psi_c'(\Phi) < 0$, then the oscillation would presumably disappear by damping.

Thus, if Φ is intermediate between points B and M, rather than at M, an oscillation would presumably amplify to include some involvement with the steep drop at B. This case is beyond the scope of this paper.

Concluding Remarks

Finite-amplitude rotating stall has been analyzed for cases in which it may be assumed that the constant-speed characteristic is parabolic in flow coefficient with rotating stall absent. It was found that a periodic solution (neither damped nor amplified) requires a horizontal slope of that characteristic at the given average flow. Presumably, if the slope were negative, the oscillation would be damped, but if it were positive, the oscillation would grow until new features of the characteristic curve (reverse flow or stall recovery) become influential.

In "deep stall," if the characteristic is flat, the solution differs only slightly from the linear one, perhaps explaining why propagation speeds from Part I agree so well with experiment. In this case (Figs. 4 and 5), the oscillation would presumably be limited by reverse-flow resistance, provided flow coefficient is quite low (less than half the coefficient at stall). At larger flow coefficients, even if the characteristic is locally flat, interaction with the unstalled part of the characteristic will occur, and the resulting motion will become nonharmonic on that account. This is the subject of Part III of this series.

The characteristic function $\psi_c(\phi)$ we have used is artificial in the sense that it is defined in the absence of rotating stall, and therefore is not normally measured in compressor tests. However, it is perfectly well defined physically, and could be measured in experiments designed to suppress rotating stall. It is defined for the compressor alone, and therefore one is free to manipulate exit and entrance conditions in order to prevent rotating stall, and also to eliminate any irrelevant hysteresis effects of a control throttle.

In incipient stall conditions, the stall oscillation may be limited in amplitude by a strong reverse curvature of the characteristic, permitting a progressive type of stall. If the characteristic "turns over," so that the break of the speed line is delayed substantially below maximum pressure rise, then this limited solution is favored. If the force lag is negative (opposite in sense to the effect of inertia) then two notable results appear: the propagation speed exceeds $1/2\ U$, and the limited-amplitude solution is favored for multiple cells. Because experiments usually show these same features, the inference seems warranted that lag (τ) is indeed negative in the incipient or progressive stall region.

In the deep-stall region, nonlinearity associated with concave curvature of the characteristic provides a steepening of the stall-zone trailing edge, as experiments show, provided lag (τ) is positive. Probably, then, lag should be taken positive in deep stall, and negative in incipient stall. Experiments are needed to establish these blade-passage lags.

Theory and experiment are both needed to describe the entrance and exit flows, especially for the relation between axial and transverse velocity disturbances. The present theory shows that rotating stall is sensitive to these conditions (lumped, in the present theory, in the parameter, m), and practical control means could well evolve from such a study.

A new type of experiment is needed to find the compressor characteristic in the absence of rotating stall, and free of irrelevant throttle hysteresis. Experiments have suggested that exhaust to low pressure through a high-resistance screen may suppress rotating stall even at fully stalled flow rates, and also that unwanted throttle effects can be eliminated by lowering pressure behind the throttle (see [4], Fig. 19). Therefore, it seems feasible in principle to measure $\psi_c(\phi)$.

The present theory shows that the characteristics with and without rotating stall are different (δ represents that difference) and thus that rotating stall affects average compressor performance. Ultimately one can envisage a theory in which surge and rotating stall are integrated, rather than being considered separate and independent phenomena. One would then be able to deal with engine dynamics on a fundamental basis.

A nonlinear, unsteady model of rotating stall has been presented by Takata and Nagano [5] for single rows and pairs of rows; in it they permit the upstream potential flow and downstream vortical flow to be unsteady and make the required calculations numerically. One of their equations can be specialized for steady disturbances and purely inertial compressor lag to give the first two terms of equation (1) with $m = 1$ (constant exit pressure). Their treatment of blade-row losses and pressure rise is quite different from that used here, and seems quite unsuitable for multistage compressors. Their chief concern was to analyze the growth of initially weak disturbances into rotating stall of single rows and stages.

In the next and concluding paper of this series, oscillations will be allowed to interact with the entire characteristic diagram, so that resistance to reverse flow and "unstalling" affect the disturbance pattern.

References

1 Moore, F. K., "A Theory of Rotating Stall of Multistage Axial Compressors: Part I — Small Disturbances," ASME Paper No. 83-GT-44, 28th International Gas Turbine Conference, Mar. 1983, pp. 313–320.

2 Day, I. J., and Cumpsty, N. A., "The Measurement and Interpretation of Flow within Rotating Stall Cells in Axial Compressors." *Journal of Mechanical Engineering Sciences*, Vol. 20, 1978, pp. 101–114.

3 Moore, F. K., "Lift Hysteresis at Stall as an Unsteady Boundary-Layer Phenomenon," NACA TN 3571, 1955. Also, Hartunian, R. A., "Research on Rotating Stall in Axial-flow Compressors. Part I. On Lift Hysteresis at Maximum Lift Including Effect of Camber," WADC TR 59-75, Jan. 1959.

4 Day, I. J., Greitzer, E. M., and Cumpsty, N. A., Stall," ASME JOURNAL OF ENGINEERING FOR POWER, Vol. 100, Jan. 1978, pp. 1–14.

5 Takata, H., and Nagano, S., "Nonlinear Analysis of Rotating Stall," ASME JOURNAL OF ENGINEERING FOR POWER, Oct. 1972, pp. 279–293.

Downloaded 01 Jun 2010 to 171.66.16.70. Redistribution subject to ASME license or copyright; see http://www.asme.org/terms/Terms_Use.cfm

A Theory of Rotating Stall of Multistage Axial Compressors: Part III—Limit Cycles[1]

F. K. Moore
Sibley School of Mechanical and Aerospace Engineering, Cornell University, Ithaca, N.Y. 14853

A theory of rotating stall, based on single parameters for blade-passage lag and external-flow lag and a given compressor characteristic yields limit cycles in velocity space. These limit cycles are governed by Liénard's equation with the characteristic playing the role of nonlinear damping function. Cyclic integrals of the solution determine stall propagation speed and the effect of rotating stall on average performance. Solution with various line-segment characteristics and various throttle settings are found and discussed. There is generally a limiting flow coefficient beyond which no solution is possible; this probably represents stall recovery. This recovery point is independent of internal compressor lag, but does depend on external lags and on the height-to-width ratio of the diagram. Tall diagrams and small external lags (inlet and diffusor) favor recovery. Suggestions for future theoretical and experimental research are discussed.

Introduction

In Part I, it was shown [1] that a simple time lag of blade-passage force, accumlated in a multistage compressor and suitably matched with lags arising in entrance and exit flows, permits rotating stall as a kind of eigensolution of the equations for weak disturbances. A prediction of stall propagation and speed results, and it agrees well with the experiment discussed by Day, Greitzer and Cumpsty (D.G.C.) [3].

In Part II, finite amplitude disturbances were considered [2] in conjunction with compressor characteristics (upstream total to downstream static pressure rise, versus axial flow coefficient) which have parabolic shape over the range of fluctuation. It was found that, if the characteristic diagram is flat, the linear, harmonic solution of Part I applies, presumably limited by resistance to reverse flow. If the diagram is concave the disturbance wave is distorted, with the reduced-flow (stall) zone being steeper at its trailing edge, as observed by D.G.C. If the diagram is convex, as at stall inception, the disturbance is of limited amplitude, especially for multiple-zone stalls when the lag is negative. In this case, propagation speed would exceed 50 percent of wheel speed. These last results may relate to "progressive stall" often observed near the inception point.

None of the foregoing results indicate "recovery"; clearly, a more complete diagram must be used, incorporating unstalled and probably, reversed-flow segments. Use of a more complete diagram should also provide estimates of the effect of the presence of rotating stall on the average compressor performance. This, then, is the theme of this paper, to analyze the recovery phenomenon and other results which would come from using a complete performance diagram, and allowing oscillations to enter both unstalled and reverse-flow regions. We will find "limit cycles" which are more complex than the circles in phase space which arose in Parts I and II, and, under certain conditions, these limit cycles will appear to describe "relaxation oscillations," which we will argue represent recovery from rotating stall. Throughout, simple assumptions about internal and external lags will be maintained as in Parts I and II.

Notation is the same as that defined in Parts I and II; new quantities appear in the Nomenclature.

Support for this work by NASA-Lewis Research Center, during the author's sabbatic leave from Cornell is gratefully acknowledged, as well as helpful discussions with C. L. Ball and L. Reid of NASA, and E. M. Greitzer of MIT.

The Cycle Equation

We return to the basic equation (1) of Part II. It permits finite amplitude disturbances of axial velocity (g) and transverse velocity (h) at entrance, as functions of angle (θ) around the compressor. Assuming zero entrance loss at the IGV entrance

$$\lambda g'(\theta) - mfh + \Psi - \psi_c(\phi) = 0 \qquad (1)$$

Lags are embodied in the parameters, λ and mf, where f is propagation speed coefficient, and m reflects inlet and outlet flow lags; if the exit flow is a sudden expansion, and entrance flow is potential, then $m=1$. If the exit is a straight duct, then we know only that $m=2$ for small disturbances. We assume that m is constant for large disturbances as well, with $m=2$ being appropriate for compressors followed by long diffusers. Research is needed to give a more complete picture of exit lag effects. Here, we will show the importance of m, or the

[1] Research done at Lewis Research Center, Cleveland, Ohio.

Contributed by the Gas Turbine Division of THE AMERICAN SOCIETY OF MECHANICAL ENGINEERS and presented at the 28th International Gas Turbine Conference and Exhibit, Phoenix, Arizona, March 27-31, 1983. Manuscript received at ASME Headquarters December 20, 1983. Paper No. 83-GT-46.

Copyright © 1984 by ASME
Downloaded 01 Jun 2010 to 171.66.16.70. Redistribution subject to ASME license or copyright; see http://www.asme.org/terms/Terms_Use.cfm

phenomena it imperfectly represents, for rotating stall. The compressor lag is embodied in the parameter λ, also related to f according to equation (16) to follow.

The last two terms of equation (1) refer to the compressor diagram, sketched in Fig. 1. To define $\psi_c(\phi)$, we imagine a test in which ϕ is varied from design to reverse flow, but rotating stall is suppressed by forcing axial velocity to remain circumferentially uniform (a high-drag screen at exit would work, in principle). In that case, ψ_c would be the characteristic measured in the absence of rotating stall. An operating point of the compressor (with axial velocity no longer constrained to be constant) would lie on a throttle line, but at Ψ, either above or below the characteristic. Thus, δ represents the effect of rotating stall on performance at a given average flow coefficient $\phi=\Phi$. It will be convenient to define the characteristic function relative to the intersection of $\psi_c(\phi)$ and $\phi=\Phi$. Thus

$$\Psi-\psi_c(0)\equiv\delta;\psi_c(\phi)-\psi_c(0)\equiv G(g) \tag{2}$$

and equation (1) becomes

$$\lambda g'(\theta)-mfh-G+\delta=0 \tag{3}$$

This is the equation to be solved in this paper.

If one finds the disturbance functions $g(\theta)$ and $h(\theta)$, the disturbance of static-pressure rise through the compressor can be found from equation (18) of Part II. Aside from constants, relative to ρU^2 it is

$$C_p=-mfh+\Phi g+\frac{1}{2}(g^2+h^2) \tag{4}$$

This formula assumes full pressure recovery at the IGV entrance.

Relation of h to g. In order to solve equation (3) it is necessary to connect the functions h and g. If the upstream flow is potential flow in a straight duct, then $h(\theta)$ is the Hilbert transform of $g(\theta)$, given for periodic functions by equation (17) of Part I

$$h=-\frac{1}{\pi}\int_0^{2\pi} g'(\xi)\ln\left|\sin\frac{\theta-\xi}{2}\right|d\xi \tag{5}$$

Because g is defined as a difference from average axial velocity, the average $\oint g d\theta = 0$. It can be shown from equation (5) that it is also true that the average $\oint h d\theta = 0$. Physically, this means that no swirl can be created in the entering potential flow.

Although equation (5) could be numerically incorporated into equation (3), it would be desirable to use some simpler relation, such as the one which is valid for single-cell stall and small perturbations, according to equation (19) of Part I, with $n=1$

$$h'(\theta)=-g \tag{6}$$

This equation is true for the first terms of Fourier series derivable from equation (5); in other words, it is exact if g is purely harmonic. Because we are concerned with "deep stall" in this paper, for which experiments [3, 6] show single-cell stall, we will assume $n=1$. Actually, results for higher modes can be inferred by substituting the appropriate multiple of wheel diameter in the parameter, a, of equation (16) to follow.

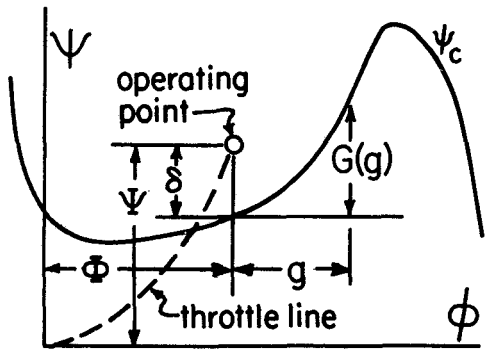


Fig. 1 Sketch of notation on compressor performance diagram, of total-to-static pressure rise (ψ_c) versus flow coefficient (ϕ) in absence of rotating stall. Operating point in rotating stall is δ above steady diagram.

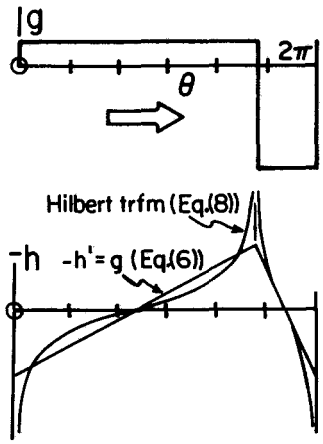


Fig. 2 Comparison of correct determination of h from g (equation (8)) with generally approximate equation (6) for a step wave (β = 0.8)

The nonlinear solution, equation (6b) of Part II, can be manipulated to yield

$$h'=-\left(1-2\frac{\eta}{A}h\right)g \tag{7}$$

and one could consider making more general use of such a nonlinear relation in equation (3), rather than equation (6).

We shall see that a "blockage" function has particular relevance to recovery. That is, $g(\theta)$ might be a step function as shown in Fig. 2. The example chosen has a "blockage" of $1-\beta$ = 20 percent. Such a "relaxation oscillation" will

Nomenclature

A = amplitude, equation (8)
$\mathfrak{B}$ = width of characteristic, Fig. 4(a)
$\mathfrak{C}$ = rise of deep-stall line, Fig. 4(a)
$\mathfrak{D}$ = slant of unstalled leg, Fig. 4(a)
$\mathfrak{E}$ = slant of reverse-flow leg, Fig. 4(a)
$\mathfrak{F}$ = height of drop into stall, Fig. 4(a)
$G(g)$ = characteristic function, rotating stall absent, Figs. 1 and 4(a)
g = axial velocity disturbance, equation (4), Part I
h = circumferential velocity disturbance, equation (15) of Part I
β = throttle setting, Fig. 4(a)
δ = increment of performance due to rotating stall (Fig. 1)

Superscripts

$\hat{}$ = (caret) transformation defined by equation (11)
$\hat{\hat{}}$ = (double caret) after change of scale so that width of characteristic is 1

Subscript

cr = critical or recovery value

Downloaded 01 Jun 2010 to 171.66.16.70. Redistribution subject to ASME license or copyright; see http://www.asme.org/terms/Terms_Use.cfm

provide a severe test of the reasonableness of equation (6). Substitution into equation (5) gives the corresponding $h(\theta)$

$$h = \frac{A}{\pi\beta(1-\beta)} \ln \left| \frac{\sin\left(\frac{\theta}{2} - \pi\beta\right)}{\sin\frac{\theta}{2}} \right| \tag{8}$$

with A being the amplitude of the g oscillation. Equation (8) is shown on Fig. 2; the result is singular at the two values of θ where g jumps. For comparison, we show equation (6). Apparently, equation (6) represents the correct Hilbert transform quite well on the average. Equation (7) would be inappropriate because it would not have the correct antisymmetry about the midpoints of the stalled and unstalled zones. We are therefore emboldened to adopt equation (6) for general use in equation (3); it is correct in the small perturbation (harmonic) limit, and has the correct antisymmetry as well as a reasonable amplitude in the "blockage" limit.

Liénard's Equation. Equation (6) permits the transformation of equation (3) into a generalization of the classical van der Pol equation [4], with the characteristic function, $G(g)$, playing the role of damping function. From equation (6),

$$g'(\theta) = -g\, dg/dh \tag{9}$$

In phase space, equation (3) becomes

$$\lambda g g'(h) + mfh + G - \delta = 0 \tag{10}$$

The following transformations and shift of origin (and sign) of h

$$\left.\begin{aligned} \hat{G} &= \frac{G(g)}{(mf)^2};\ \hat{\delta} \equiv \frac{\delta}{(mf)^2} \\ \hat{h} &\equiv -\frac{h}{mf} + \hat{\delta};\ \hat{g} \equiv \frac{1}{mf}\sqrt{\frac{\lambda}{mf}}\, g \end{aligned}\right\} \tag{11}$$

yield a new expression for angle θ

$$d\theta = -\frac{dh}{g} = \sqrt{\frac{\lambda}{mf}}\frac{d\hat{h}}{\hat{g}} \tag{12}$$

and yield the Liénard equation [4]

$$\hat{g}\hat{g}'(\hat{h}) + \hat{h} = \hat{G}(\hat{g}) \tag{13}$$

Equation (12) provides, for a complete cycle

$$\oint \frac{d\hat{h}}{\hat{g}} = 2\pi\sqrt{\frac{mf}{\lambda}} \tag{14}$$

and the requirement $\oint h\, d\theta = 0$, where equations (11) and (12) are used, becomes

$$\oint \frac{\hat{h}\, d\hat{h}}{g} = \left(2\pi\sqrt{\frac{mf}{\lambda}}\right)\hat{\delta} \tag{15}$$

If $\hat{G}$ were given, equation (13) could be solved, and mf/λ found from equation (14). However, λ and f are related (equation (7) of Part II, neglecting effect of guide vanes for present purposes) by the definition

$$\lambda \equiv \frac{1}{a}\left(\frac{1}{2} - f\right);\ a \equiv D/(2UN\tau) \tag{16}$$

where a is a reciprocal compressor time lag, in effect (equation (16), Part II). Therefore, f itself can be found. Then, the characteristic displacement $\hat{\delta}$ (or δ) comes from equation (15). Actually, of course, $G(g)$ would normally be given, rather than $\hat{G}(\hat{g})$, and therefore equations (13) and (14) would have to be solved simultaneously.

Under the foregoing transformations, equation (4) becomes

$$C_p = (mf)^2(\hat{h} - \hat{\delta}) + \Phi mf\sqrt{\frac{mf}{\lambda}}\,\hat{g} + \frac{(mf)^3}{2\lambda}\left[\hat{g}^2 + \frac{\lambda}{mf}(\hat{h} - \hat{\delta})^2\right] \tag{17}$$

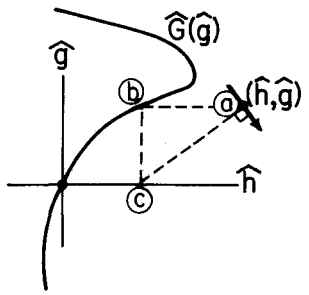


Fig. 3 Geometrical solution of the Liénard Equation (equation (13))

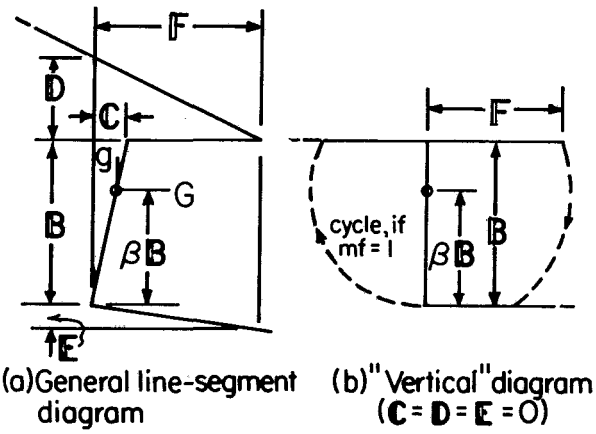


Fig. 4 Line-segment characteristic diagrams of function $G(g)$, oriented as in Fig. 3

Figure 3 sketches the usual geometrical construction for solving Liénard's equation [4]. The characteristic is reoriented (compare Fig. 1) to correspond to the classical damping function. Hereafter, in discussing solutions of equation (13), we will use this convention without further comment. At a point (a) during an oscillation, where the values $\hat{h}$ and $\hat{g}$ apply, one locates point (b), so that the line (a) – (b) has a length $\hat{h} - \hat{G}(\hat{g})$. The line (b) – (c) has the length $\hat{g}$. The negative reciprocal of the ratio of these lengths is, by equation (13) just $\hat{g}'(\hat{h})$ or the slope of the trajectory of the oscillation. Thus, that trajectory is locally perpendicular to the line (a) – (c), as sketched in Fig. 3. This geometrical method gives a quick sense of the progress of any oscillation in phase space.

Line-Segment Characteristic. In the rest of this paper, we will consider the function, G, to be various special cases of the line-segment diagram shown in Fig. 4(*a*). The quantities $\mathfrak{B}$ – $\mathfrak{F}$ are parameters of the diagram to be specified. The throttle setting is specified by β. We would usually consider the origin of ϕ to be at $\beta = 0$, so $\beta\,\mathfrak{B} = \Phi$.

A particularly simple but nontrivial case is sketched in Fig. 4(*b*). It is a "vertical" diagram in which the unstalled leg is vertical ($\mathfrak{D} = 0$) as is the reverse-flow leg ($\mathfrak{E} = 0$). The deep-stall leg is horizontal ($\mathfrak{C} = 0$). The circular arcs shown dashed in the sketch will be discussed later.

Some Limit-Cycle Examples

For purposes of illustration, we first pose a series of "indirect" problems, in which we specify $\hat{G}(\hat{g})$, find the resulting oscillation, determine f, and then infer the function $G(g)$. We note that equations (13–15) are invariant to a uniform change of scale. Thus, for example, we may imagine our diagram of $\hat{G}$ to be scaled so that its width is exactly 1; in

Downloaded 01 Jun 2010 to 171.66.16.70. Redistribution subject to ASME license or copyright; see http://www.asme.org/terms/Terms_Use.cfm

other words, so that $\hat{g} = g/\mathfrak{G}$. On this basis, we assume our diagrams of $\hat{G}$ to have width 1, with the scale of $\hat{h}$ suitably adjusted. Figure 5 shows a particular choice of diagram shape, double carets signifying the scale adjustment just discussed.

1 Suppose $\beta = 0.5$, and an oscillation begins at a point such as P. An analytic solution of equation (13) can easily be found for any part of an oscillation for which $\hat{G}(g)$ is a straight line, and these solutions can be pieced together to form a continuous trajectory in phase space. In this case, the trajectory is at first a growing spiral (the construction of Fig. 3 suggests this result directly) which grows until it encounters reverse-flow resistance, and then becomes momentarily "unstalled." After about three circuits, the oscillation becomes self-duplicating; that is, a "limit cycle" of the sort familiar in nonlinear mechanics, and in fact which is classically illustrated by van der Pol's equation with an S-shaped damping function. The usual compressor diagram, when properly oriented, is of that classical shape.

The initial amplification in this example is due to the deep-stall slope being positive. If it were negative, the oscillation would locally damp. In any case, the peak of $\hat{G}$ being to the right of the reverse-flow corner is amplifying, for an oscillation which is already strong enough. The slopes of unstalled and reverse-flow legs being negative are (locally) limiting. Thus, the oscillation, as it grows, ultimately settles into a limit cycle.

2 The limit cycle depends on the throttle setting (β) for a given diagram. Figure 6 shows the effect. Various symbols on the cycle traces serve to relate each trace to the value of β indicated in the legend and along the deep-stall line where each cycle is centered. It is noteworthy that if β is somewhat less than 0.5, the cycle is "caught" by reverse-flow resistance, but it never unstalls. As β is increased toward 1, the cycle is proportionately more unstalled, perhaps failing to be "caught" by the reverse-flow leg. As β approaches 1, the "release point" moves closer to the maximum-$\hat{G}$ corner, and, in fact, the unstalled part of the cycle tends to hug the unstalled leg of the diagram. If β is slightly greater than 1, the unstalled leg actually catches the trajectory before it reaches the corner, and a rapidly damped oscillation follows (because the unstalled leg has negative slope).

Table 1 shows the results when equations (14) and (15) are used to find f and hence $G(g)$ and δ. We assume $m = 2$, and $a = 1$, in order to make the example definite. The actual $\mathfrak{F}$ is only about 43 percent of $\mathfrak{G}$; rather a lightly loaded compressor. The value of f is about 0.26, tending to increase as β increases. As is obvious from Fig. 6, the δ needed to bring the average h to zero is greatest when $\beta = 0.5$; that cycle lies more to the right than the others.

Figure 7 shows the profiles of $g(\theta)$ which may be derived from Fig. 6 and equation (12). The wave is propagating to the right. Thus, the fraction of circumference with reduced flow becomes less as β increases, as one would expect. There is a tendency, not very strong, for the "trailing edge" of the reduced-flow (stall) zone to be steeper than the leading edge, for the lower flow rates, as observed by D.G.C. [1].

3 The limit cycle depends on the diagram "tallness." Figure 8 shows how the limit cycle changes when β is kept at 0.9, but the scale of $\hat{G}$ is changed by factors of 2 and 3 beyond the case shown in Fig. 6 (and repeated in Fig. 8 for comparison). Obviously, as scale of $\hat{G}$ increases, the cycle follows the unstalled leg very closely indeed, releasing just at the top point of the diagram in the limit. The reverse-flow leg is also

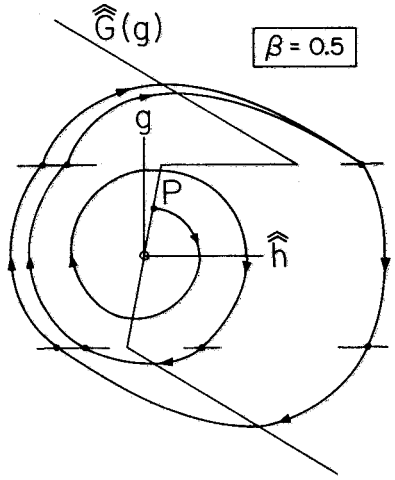


Fig. 5 Development of limit cycle for $\beta = 0.5$. Oscillation begins at point P. After three cycles, negligible changes. See Table 1 for diagram parameters corresponding to assumed $\hat{\hat{G}}(g)$.

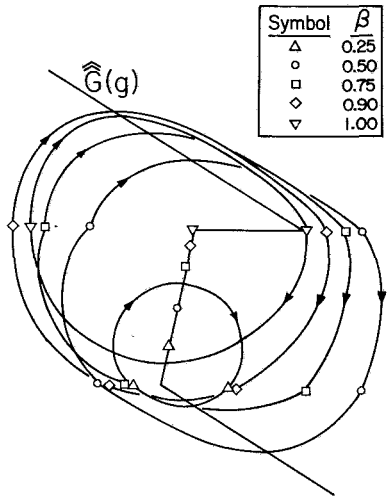


Fig. 6 Effect of throttle setting (β) on limit cycles; for the same given $\hat{\hat{G}}(g)$. See Table 1 for the corresponding diagram parameters.

Table 1 Results for limit-cycle examples[a]

Symbol	β	$\sqrt{\frac{mf}{\lambda}}$	$\hat{\hat{\delta}}$	f	$\sqrt{\lambda mf}$	$\mathfrak{F}/\mathfrak{G}$	$\delta/\mathfrak{F}$
△	0.25	1.028	0.043	0.26	0.50	0.45	0.048
○	0.50	1.076	0.221	0.26	0.60	0.45	0.246
□	0.75	1.084	0.190	0.26	0.50	0.45	0.121
◇	0.90	1.151	−0.032	0.29	0.50	0.45	−0.036
▽	1.00	1.336	0.068	0.32	0.48	0.43	0.076
◇	0.90	1.151	−0.032	0.28	0.50	0.45	−0.036
◇	0.90	1.178	0.387	0.37	0.44	0.78	0.215
◇	0.90	2.400	0.766	0.426	0.36	0.96	0.284

[a]Shapes of $\hat{\hat{G}}(g)$, as in Figs. 5 and 8, defined by reference to Fig. 4: $\hat{\mathfrak{G}} = 1$; $\hat{\mathfrak{D}} = \hat{\mathfrak{E}} = 9/16$; $\hat{\mathfrak{F}} = 0.9$; $\hat{\mathfrak{C}} = 0.2$. In Fig. 8, $\hat{\mathfrak{F}}$ and $\hat{\mathfrak{C}}$ multiplied by 1, 2, 3. $m = 2$, $a = 1$.

Downloaded 01 Jun 2010 to 171.66.16.70. Redistribution subject to ASME license or copyright; see http://www.asme.org/terms/Terms_Use.cfm

followed closely, and, again, release occurs close to the lower corner of the diagram. These effects of diagram tallness will be of great significance in our subsequent discussion of recovery.

The last three rows of Table 1 show the completed calculations. Even in the most extreme case, $\mathcal{F}$ is only about equal to $\mathcal{B}$. In that case, f has increased to 0.43, and δ has increased dramatically, as Fig. 8 suggests it should.

Figure 9 shows $g(\theta)$ for the most extreme case, to be compared with the profile $\beta = 0.9$ in Fig. 7. The stalled angle is reduced, and the expected steepness of the stall trailing edge is very definite. The intercepts of a horizontal line ($\hat{G} = 0$) with the unstalled and reversed legs are shown ("unstall g" and "reverse g" to indicate how well this profile conforms to blockage ideas, namely that the flow is either stalled or unstalled. The concept seems not to be very useful in this case. Also shown is the pressure-rise disturbance, C_p, obtained from equation (17), with $\mathcal{B}$ taken to be 1.

We proceed now to analysis of the direct problem, in which a simple "vertical" shape of $G(g)$ is given, and we will pay particular attention to indications of stall recovery as the throttle is opened.

Ideal-Diagram Solutions

Vertical Diagram. The "vertical" diagram of Fig. 4(b) has only $\mathcal{F}$ and $\mathcal{B}$ as parameters, and, because the equations are invariant to overall scale change, only the single parameter $\mathcal{F}/\mathcal{B}$ is significant, along with throttle setting β.

The limit cycle in this case is simply described in the h, $\hat{g}$ plane. Reference may be made to Fig. 4(b), imagining it to be transformed to $\hat{h}$ and $\hat{g}$, or as if $mf = 1$. Equation (13) tells us that the cycle follows the unstalled leg ($\hat{g}' = 0$) until the peak of $\mathcal{F}$ is reached ($\hat{h} = \hat{G}_{\max}$). The cycle leaves that corner, and is governed by $\hat{G}(\hat{g}) = 0$. In that part of the cycle, equation (13) is satisfied by a circular arc centered at (0, 0). It is shown dashed on Fig. 4(b). The arc will intersect the reverse-flow leg as shown, provided the diagram is tall enough.

In the $\hat{h}$, $\hat{g}$ plane, "tallness" will depend on f as well as $\mathcal{F}/\mathcal{B}$, because of the transformations, equations (11) and (12). The height-to-width ratio will be

$$\frac{\mathcal{F}/\mathcal{B}}{\sqrt{\lambda mf}}$$

in the $\hat{h}$, $\hat{g}$ plane. Thus, if f is near 0.5, so that λ is small, then any diagram will be "tall" in the $\hat{h}$, $\hat{g}$ plane, and, incidentally, the cycle will always reach the reverse-flow line.

The cycle will then follow the reverse flow line until the corner is reached at $\hat{h} = 0$. Then another circular arc governs the return to the unstalled condition. This second arc will reach the unstalled line only if $\beta > 0.5$. If $\beta < 0.5$, the arc will simply complete a circle back to the starting point. This solution corresponds to the purely harmonic wave (limited by reverse-flow resistance) discussed in Part II.

It is a simple matter to evaluate the cyclic integrals, equations (14) and (15) in these cases. Along the arc segments, the differential $d\hat{h}/\hat{g}$ is simply the angle increment along the arc. Therefore, according to equation (12), the real angle change, $d\theta$, is simply $\sqrt{\lambda/mf}$ times the angle of arc in the $\hat{h}$, $\hat{g}$ plane. An immediate conclusion may be drawn: Fig. 4(b) shows that the arc from unstalled to reverse condition generally subtends a smaller angle than the return. Therefore, the drop into stall is more abrupt than the recovery. Since the stall zone is traveling in the positive θ direction (Fig. 4 of Part I), the drop into stall is the "trailing edge" of the stall zone, in D.G.C.'s terminology [3], and, in keeping with their observations, the trailing edge of the zone is predicted always to be steeper than the "leading edge."

The foregoing simple calculations were made for various $\mathcal{F}/\mathcal{B}$, λ, and mf, subject to the requirement of equation (14), and finding δ from equation (15). Typical results are shown

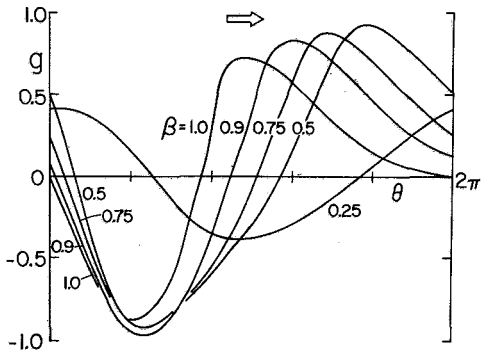


Fig. 7 Axial-velocity disturbance around the compressor for the various throttle settings given in Fig. 6. Here, $\mathcal{B} = 1$.

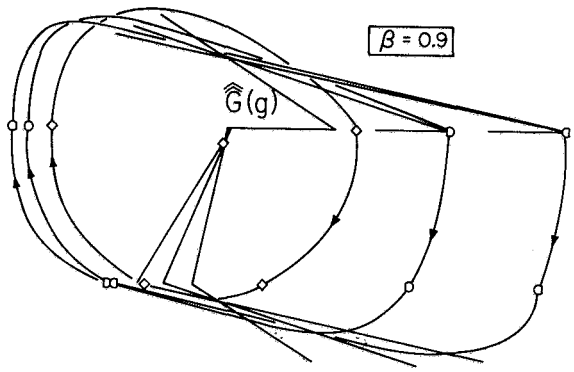


Fig. 8 Effect of changes of diagram height (scale of $\hat{G}$). See Table 1 for the numerical values.

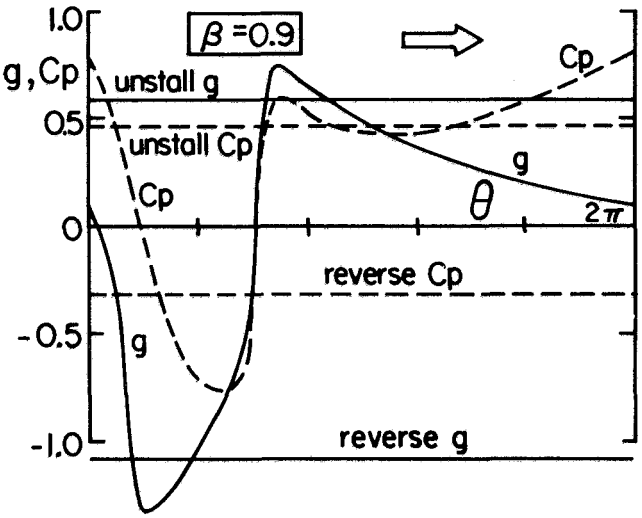


Fig. 9 Axial velocity (g), static pressure-rise (C_p) disturbances, for β = 0.9 and the most extreme case of Fig. 8 (Symbol ◇, see Table 1)

for $\mathcal{F}/\mathcal{B} = 1$ on Fig. 10. The solid-line results do not depend on compressor lag (a); only when the definition of λ (equation (16)) is introduced, overlaid on Fig. 10 as dot-dashed lines, does a become a factor. The intersections of dashed and solid lines provide the solution shown in Fig. 11 for the special cases of $m = 2$ and $a = 0.3$ and 0.6.

These solutions describe two regimes: The harmonic wave, for which $\delta = 0$, when $\beta < 0.5$, and a rather different wave when $\beta > 0.5$. The velocity, pressure-rise and phase diagrams for these two cases (with $a = 0.6$) are shown as the first and second rows of Fig. 12. The steeper "trailing edge" is evident in $g(\theta)$ for $\beta > 0.5$.

It is obvious from Fig. 10 that the external lag parameter

Downloaded 01 Jun 2010 to 171.66.16.70. Redistribution subject to ASME license or copyright; see http://www.asme.org/terms/Terms_Use.cfm

(m) is more significant than the internal one, especially for the larger values of β. The speed, f, is restricted to less than 0.5. Therefore, if m is small, say 1, rotating-stall solutions might be forbidden entirely. Even if $m=2$, no solution is possible when $\beta > 0.801$. In the next paragraphs, this point will be discussed more fully.

The Recovery Limit. When $m=2$, a limit is reached when $\beta=0.801$. At that limit, which is independent of a, the speed, f, goes to 0.5, and so does $\delta/\mathcal{F}$. The third row of Fig. 12 shows the corresponding traces. The axial velocity becomes a pure step wave and the circumferential velocity is a saw tooth. (This type of "relaxation oscillation" was discussed earlier in connection with Fig. 2.)

The phase diagram becomes a rectangle because λ has approached zero. From equation (10) one would expect dg/dh to become infinite when $\lambda\to 0$. Another way to see this result is to recall that the cycle includes arcs in the $\hat{h}$, $\hat{g}$ plane, in which the diagram is infinitely "tall" when $\lambda\to 0$. That is, while g changes by $\mathcal{G}$, equation (12) says that g changes only to order $\mathcal{G}\sqrt{\lambda}$ when λ is small. Thus, the arcs depart to a vanishing degree from $\hat{h}=\mathcal{F}/(1/2)m$ when stalling or $\hat{h}=0$ when unstalling. The result in the original frame of reference is a rectangular cycle.

Pursuing further the effort to interpret the limiting solution physically, we may focus attention on equation (14). Essentially, it is the requirement that the cycle complete itself in the angular distance 2π. Now if we specify a large β, then $\hat{g}$ is a small constant quantity on the unstalled leg of the cycle. The coordinate $\hat{h}$ must change by a certain amount essentially fixed by the height of the diagram ($\mathcal{F}$). Thus, the contribution of the unstalled leg to the integral $\oint d\hat{h}\,(\hat{g}$ will be of the order $\mathcal{F}/[(1-\beta)\mathcal{G}\sqrt{\lambda}]$, and equation (14) suggests that if β is too near 1, the unstalled leg will use up all the allowed range of θ. Clearly, β may be permitted to be largest when the other terms of the integral are minimized. This occurs when the stalling and unstalling arcs have the least angle in the $\hat{h}$, $\hat{g}$ plane, namely zero when $\lambda\to 0$, and the negative-$\hat{h}$ portion of the unstalled leg is minimized; again, when $\lambda\to 0$. In the $\lambda\to 0$ limit, the reverse flow leg is longest, but $\hat{g}$ is larger there, and so the contribution to β is less important.

In summary, as the throttle is opened, a limiting condition is reached such that the cycle spends too much time unstalled to permit the required pressure changes of stalling and unstalling to occur. This description would seem to fit the phenomenon of "stall recovery" [3]. It is significant that δ is quite large (about (1/2)$\mathcal{F}$) when the critical $\beta=\beta_{cr}$ is reached. If this is true, a discontinuity of Ψ is predicted to occur when $\beta=\beta_{cr}$. The geometry of Fig. 1 suggests that a slightly more open throttle line than that for β_{cr} would have no nearby performance line to intersect, and a jump across to the unstalled line (i.e., recovery from stall) would have to occur.

The value $\beta_{cr}=0.801$ applies only for a vertical characteristic with $\mathcal{F}/\mathcal{G}=1$ and $m=2$. The general results for a vertical characteristic are

$$\beta_{cr}(1-\beta_{cr})=\frac{\mathcal{F}/\mathcal{G}}{\pi m};\ \frac{\delta_{cr}}{\mathcal{F}}=\frac{1}{2} \tag{18}$$

which appear as the lowest curves on Fig. 14. If the diagram is

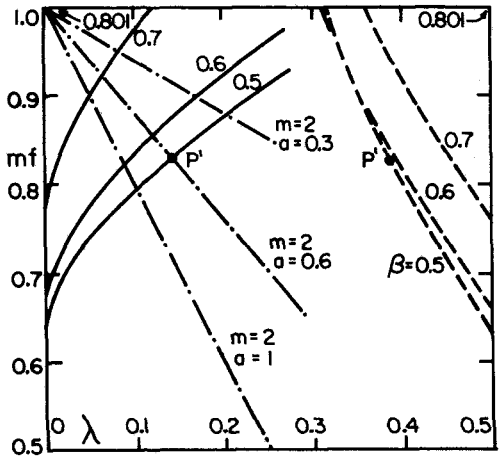


Fig. 10 λ and δ (shown dashed) versus mf for various β and $\mathcal{F}/\mathcal{G}=1$. The definition of $\lambda=(1/a)[(1/2)-f]$ overlaid (dot-dashed). Point P' gives the solution for $\beta=0.5$ when $a=0.6$, $m=2$.

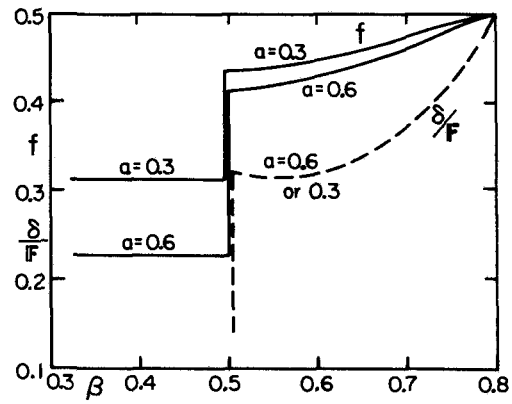


Fig. 11 Propagation speed (f) and performance rise due to rotating stall (δ) shown dashed versus throttle setting (β), for $m=2$ and $\mathcal{F}/\mathcal{G}=1$. No solution for $m=1$. Note that $\beta_{cr}=0.801$ is independent of lag (a), and that $\delta=0$ for $\beta<0.5$

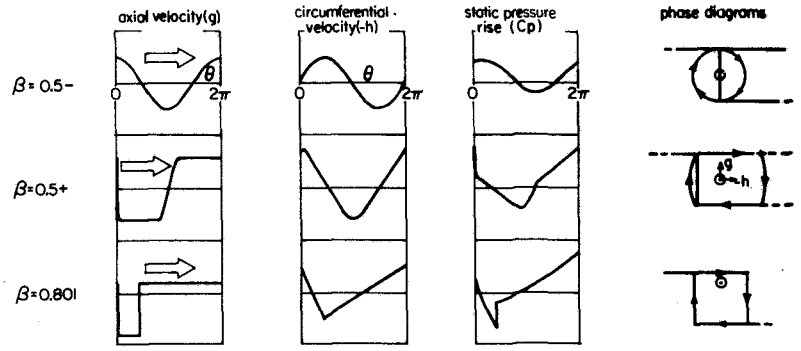


Fig. 12 Theoretical velocity and pressure "traces and phase diagrams for a particular vertical characteristic and three values of β ($\beta_{cr}=0.801$), $m=2$, $a=0.6$. Arrow denotes direction of propagation.

Downloaded 01 Jun 2010 to 171.66.16.70. Redistribution subject to ASME license or copyright; see http://www.asme.org/terms/Terms_Use.cfm

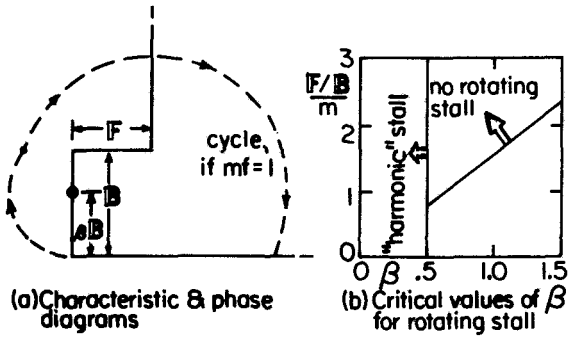


Fig. 13 Results for step-type characteristics, $m=2$

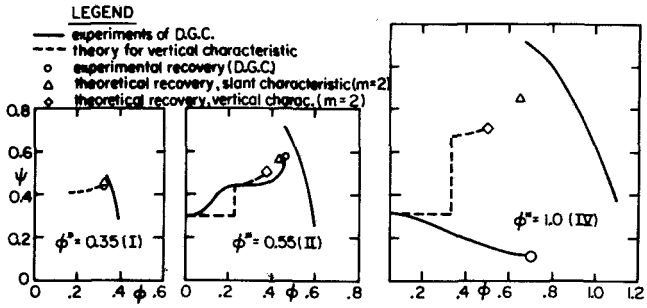


Fig. 15 Comparison of theoretical predictions with cases I, II, and IV (50 percent reaction) of Day, Greitzer and Cumpsty (D.G.C.), [3]

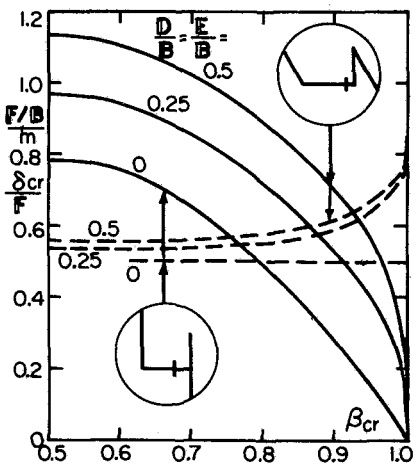


Fig. 14 Effect of slant characteristic on recovery throttle setting (β_{cr}) and performance rise at recovery (δ_{cr}), shown dashed, for $\mathcal{E}=\mathcal{D}$

less "tall," β_{cr} can approach 1. On the other hand, if $\mathcal{F}/\mathcal{B}$ exceeds $(1/4)\pi m$, no rotating stall other than the harmonic variety can occur.

In general, a tall diagram (large $\mathcal{F}/\mathcal{B}$) and a small value of m favor recovery. The role of m is particularly significant. We have inferred that m is about 2 for a compressor with a straight outlet. If m were reduced to 1 by using a sudden expansion, rotating stall could be largely suppressed, according to the present analysis, when $\mathcal{F}/\mathcal{B}$ is greater than about 0.8. Thus, changes in external lag mechanisms could be very effective for relatively "tall" diagrams, it would seem.

The Step Diagram. Another sort of ideal, simple diagram would continue to have $\mathcal{C}=\mathcal{E}=0$, but $\mathcal{D}=\infty$ rather than 0. Figure 13(*a*) shows such a "step" diagram, together with a phase diagram in the $\hat{h}$, $\hat{g}$ plane (as if $mf=1$). Such an extended unstalled plateau seems a possible model for Iura and Rannie's diagram [5], but is not typical of modern compressors.

The results show a lower, rather than an upper limit for rotating stall. It is

$$\beta_{cr}=2\frac{\mathcal{F}/\mathcal{B}}{\pi m} \tag{19}$$

shown in Fig. 13(*b*). If the diagram is tall enough, there is a forbidden gap between $\beta=0.5$ and β_{cr} where a rotating-stall solution is impossible. This is true only if $\mathcal{F}/\mathcal{B}$ exceeds $(1/4)\pi m$, which is quite tall. For smaller values of $\mathcal{F}/\mathcal{B}$, there is no critical case, and solutions for f are quite far from 0.5. For example, if $F/B=0.5$, $m=2$, and $a=0.6$, the speed, f, would remain in quite a narrow range: 0.35 at $\beta=0.5$ and 0.25 at $\beta=1.5$.

Recovery for Line-Segment Characteristic

We now return to the more general line-segment characteristic shown in Fig. 4(*a*), and look for the effect to nonzero $\mathcal{C}$, $\mathcal{D}$, and $\mathcal{E}$. The general solution is easy to find, but hard to discuss because there are so many parameters to consider; the previous section describing Figs. 6–9 will suffice for illustration. If we consider only recovery, simplifications are available; f approaches 0.5, λ approaches 0, and compressor lag (a) become irrelevant.

As $\lambda\to 0$, we have seen how the transformation equation (12) makes the diagram "taller" in the $\hat{h}$, $\hat{g}$ plane without limit, so that, as in the vertical diagram case, the unstalling and stalling legs are lines of constant $\hat{h}$. The deep-stall slope, $\mathcal{C}$, becomes irrelevant except in finding δ, provided $\mathcal{C}$ is positive. If $\mathcal{C}$ is negative, the cycle would presumably follow the deep-stall leg and release at the corner $g=(1-\beta)\mathcal{B}$. We do not consider this possibility any further in the present paper. With $\mathcal{C}>0$, the only change from the vertical-diagram analysis is that the integral of $d\hat{h}/\hat{g}$ must be carried out along the slanted lines defined by $\mathcal{D}$ and $\mathcal{E}$. When this is done, the following formulas for recovery result

$$\frac{\mathcal{F}/\mathcal{B}}{\pi m}=1/\ln\left[\left(1+\frac{\mathcal{D}/\mathcal{B}}{1-\beta_{cr}}\right)^{\mathcal{B}/\mathcal{D}}\left(1+\frac{\mathcal{E}/\mathcal{B}}{\beta_{cr}}\right)^{\mathcal{B}/\mathcal{E}}\right] \tag{20}$$

$$\frac{\delta_{cr}}{\mathcal{F}}=\frac{\mathcal{F}/\mathcal{B}}{\pi m}\left[\frac{1-\beta_{cr}+\mathcal{D}/\mathcal{B}}{(\mathcal{D}/\mathcal{B})^2}\ln\left(1+\frac{\mathcal{D}/\mathcal{B}}{1-\beta_{cr}}\right)-\frac{\mathcal{B}}{\mathcal{D}}+\frac{\beta_{cr}+\mathcal{E}/\mathcal{B}}{(\mathcal{E}/\mathcal{B})^2}\ln\left(1+\frac{\mathcal{E}/\mathcal{B}}{\beta_{cr}}\right)-\frac{\mathcal{B}}{\mathcal{E}}\right] \tag{21}$$

These formulas reduce to equation (18) when $\mathcal{E}$ and $\mathcal{D}$ are set equal to zero. The formula for δ is valid even if $\mathcal{C}$ is not zero, so long as δ is measured from the reverse flow corner at $g=-\beta\mathcal{B}$.

Figure 14 shows the effect of "slant," choosing $\mathcal{D}=\mathcal{E}$ for convenience. Clearly, slant increases the value of β_{cr}; in other words, it delays recovery. It remains true, however, that a tall diagram with small m will favor recovery. Figure 14 shows how the maximum value of $\mathcal{F}/m\mathcal{B}$, which occurs at $\beta_{cr}=0.5$, depends on the slant parameter $\mathcal{D}/\mathcal{B}$. The more slanted the characteristic, the taller may be the diagram before the rotating-stall limit descends to $\beta_{cr}=0.5$. Figure 14 also suggests that for realistic slants of about 0.5, recovery occurs in a fairly narrow range of β (between 0.9 and 1.0 for $\mathcal{F}/\mathcal{B}<0.7$m). In D.G.C. [3], it is suggested that experiments indicate reccovery when a certain critical blockage (about 0.7) occurs. The present analysis is not quite consistent with this idea because β_{cr} is not the same as blockage. If β_{cr} is near 1, and $\mathcal{D}/\mathcal{B}=0.4$, then the two ideas do happen to agree.

The dashed lines of Fig. 14 show that δ_{cr} is not greatly affected by slant unless β_{cr} is quite near 1. Of course, that is the region where recovery is generally predicted.

Downloaded 01 Jun 2010 to 171.66.16.70. Redistribution subject to ASME license or copyright; see http://www.asme.org/terms/Terms_Use.cfm

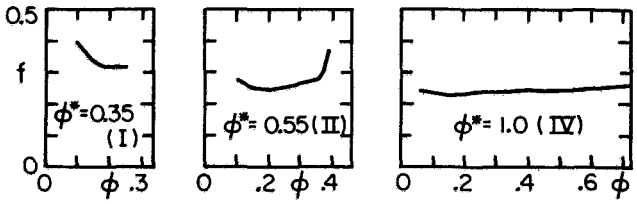


Fig. 16 Propagation speed versus flow coefficient for cases I, II, and IV shown on Fig. 15 (from Fig. 18 of Day's thesis [6]). Right margin of each diagram is at recovery value of ϕ.

Comparison With Experiment

Comparison of the present theory with experiment is handicapped by ignorance of the rotating-stall-free characteristic $\psi_c(\phi)$. In prinicple, it could be measured, but heretofore there has not been sufficient reason to do so. Nevertheless, in Part I, it was shown that theoretical predictions of propagation speed (f) agreed well with experiment. Here, we are concerned chiefly with recovery, and we may appeal to D.G.C. [3] for evidence.

Recovery. Figure 15 shows characteristics measured and reported by D.G.C. These appear as solid lines, with the recovery point indicated by a circle. Three different loadings are included, all at 50 percent reaction. For theoretical predictions, we have assumed that the shutoff head describes a constant value of deep-stall, ψ_c and calculated values of δ are applied relative to that level of ψ_c.

Therefore, if vertical diagrams were used, the theory would follow the dashed lines shown in each of the three cases. The average slant of the unstalled leg gives a basis for estimating the recovery point by use of equations (20) and (21). These points are triangles, and are presumably better estimates than the diamonds which terminate the vertical-characteristic results.

The "low-ϕ^*" (Case I) results are not very informative. The "intermediate-ϕ^*" (Case II) results show excellent agreement, even including a suggestion of transition from harmonic to limit-cycle waves. The "high-ϕ^*" (Case IV) is reasonable as regards β_{cr}, but quite poor as regards vertical shift of Ψ. Probably, the slope, $\mathcal{C}$, of the deep-stall ψ_c, should be taken as negative. If so, the integral, $\oint d\hat{h}/\hat{g}$, should be recalculated. It seems doubtful, however, that such a revision would give such a low value of Ψ at recovery. Perhaps the throttle plays a special role in recovery when the characteristic descends to such a low limit.

In all cases, it is worth noting that recovery, both in theory and experiment, is close to the break-point of the characteristic. That is, $\beta \approx 0.95$ at recovery. Perhaps this may prove a more basic concept than blockage.

Propagation Speed. Figure 16 shows the propagation speeds which correspond to the Cases I, II, and IV of Fig. 15. These speeds, given in Day's thesis [6], relate to theory just as recovery does in Fig. 15, if we recall that f should approach 0.5 ($\lambda \to 0$) at recovery, according to Fig. 11.

The low-ϕ^* Case I does not show the predicted rise of f toward 0.5, but the measurements do not extend to recovery; perhaps the rise would indeed occur if recovery were more closely approached.

The intermediate-ϕ^* Case II does show the predicted rise; perhaps the good agreement in this case is related to the good agreement of recovery prediction and experiment shown for Case II in Fig. 15. The high-ϕ^* Case IV shows the least agreement; the experiments show no rise, all the way up to recovery. Possibly this is an effect of throttle characteristic.

Iura and Rannie [5] also report a propagation speed which remains nearly constant right up to recovery. In their experiments, the compressor has an extended plateau of pressure beyond the stall point, somewhat like the steep characteristic of Fig. 13. In that case, we would in fact predict a nearly flat value of f.

Further comparisons of theory with experiment will require, on the one hand, a more thorough theoretical exploration of the parameters of the problem, and on the other hand, new measurements of rotating-stall-free compressor characteristic maps.

Concluding Remarks

The problem of rotating stall has been difficult largely because it occurs in such a complex parameter space. Perhaps the best service theory can provide in such a situation is to suggest priorities among these parameters, rather than to predict the resulting phenomenon in detail. The present set of three reports is set forth in this spirit. The most important results seem to be the following:

1 The recovery from rotating stall seems basically predictable. It depends on the compressor's steady characteristic; primarily its "tallness" (the height of the drop into stall compared with the diagram width), and secondarily the slope of the unstalled characteristic. Tallness favors early recovery. The slope of the reverse-flow resistance is of minor significance, as is the slope of the deep stall line, provided that slope is positive. If it is negative, the throttle curve may be important; otherwise, the throttle characteristic is unimportant.

Recovery does not depend on compressor lag (dynamic hysteresis), but it depends very much on the lags originating in the entrance and exit flows. Small external lags favor recovery. It seems likely that the most directly effective design change would be to reduce the lag in the exit duct.

2 The characteristic with rotating stall suppressed must be found experimentally to form a proper basis for further theoretical refinements. Discharge to a very low pressure through a dense screen at exit would force circumferentially uniform axial flow, and suppress rotating stall. Also, it would be important to suppress any effects of finite throttle-line slope, such as steady hysteresis about stall. Again, discharge to a low pressure would tend to steepen the throttle lines in the necessary way.

3 Research is needed on entrance flow fields and, especially, diffusers with transversely nonuniform flow. Dynamic (lag) effects are very important, more so than compressor blade-row dynamics.

4 Theoretical limit-cycle analysis can easily be extended to include a wider class of hypothetical characteristic diagrams, and a certain "exact" entrance and exit-flow relation. It is felt that these should proceed in parallel with the studies discussed in 2 and 3 above.

References

1 Moore, F. K., "A Theory of Rotating Stall of Multistage Axial Compressors, Part I. Small Disturbances," ASME Paper No. 83-GT-44, 28th International Gas Turbine Conference, Mar. 1983, pp. 313-320.

2 Ibid. Part II. "Finite Disturbances," ASME Paper No. 83-GT-45.

3 Day, I. J., Greitzer, E. M., and Cumpsty, N. A., "Prediction of Compressor Performance in Rotating Stall," ASME JOURNAL OF ENGINEERING FOR POWER, Vol. 100, Jan. 1978, p. 1-14.

4 Stoker, J. J., *Nonlinear Vibrations in Mechanical and Electrical Systems*, Interscience, New York (1970), ch. 5.

5 Iura, T., and Rannie, W. D., "Experimental Investigations of Propagating Stall in Axial-Flow Compressors," ASME *Transactions*, Apr. 1954, pp. 463-471.

6 Day, I. J., "Axial Compressor Stall," Ph.D. dissertation, Cambridge University Engineering Department, 1976.

Downloaded 01 Jun 2010 to 171.66.16.70. Redistribution subject to ASME license or copyright; see http://www.asme.org/terms/Terms_Use.cfm

DISCUSSION

J. T. Lewis[1]

Dr. Moore is to be complimented on this contribution to the understanding of the performance characteristics of multistage compressors operating in rotating stall. The insight gained as to the interaction of the compressor's pumping characteristic with the inlet and discharge flow fields presents a convenient arena within which specific elements of the model can be scrutinized. This discussion is intended to support (and emphasize) Dr. Moore's concluding remark that research is needed on entrance flow fields.

Through the cooperation of Dr. E. M. Greitzer at the Massachusetts Institute of Technology, the FORTRAN coding for a numerical solution of Dr. Moore's model was made available to United Technologies Corporation, Pratt & Whitney Aircraft (P&WA). Automated iteration routines were added and the program was streamlined by P&WA to allow the "cause and effect" relationships of the model to be thoroughly investigated in a relatively short time. The test case to be considered here involved the $\phi^* = 1.0$, three-stage configuration from Day's disseration ([6], Part III). Figure 17 shows the axisymmetric pumping characteristic, ψ_c, that was selected for this study. (The positively sloped portion of the characteristic is an arbitrary straight-line connection between the unstalled (data) characteristic and a reverse flow characteristic based on an analytical prediction.) Also shown on this figure is the measured characteristic in rotating stall, Ψ, and the value of Ψ calculated by the model at $\Phi = 0.3$. (This Φ was chosen because Day's dissertation includes detailed time-averaged measurements at this flow.) As Dr. Moore has previously noted, the agreement in the Ψ level is poor.

The crux of the problem appears to be directly related to the basic nature of the flow field prediction; specifically, the prediction of the Cx/U profile, $\phi(\theta)$. A comparison of the predicted and measured $\phi(\theta)$ profiles is shown in Fig. 18. (The angular alignment is arbitrary.) Outwardly, the comparison looks good, but upon closer examination, one realizes that the major portion of the cycle is made up of nearly linear excursions of the negatively sloped portions of the unstalled and backflow ψ_c characteristics, with the transitions between these characteristics being quite abrupt. The data, on the other hand, suggest a more "cellular" or "parallel compressor" distribution. This predicted ϕ profile will necessarily result in a ψ_c profile versus θ such as shown in Fig. 19. The basic pressure rise equation (Moore's equation (3.1) gives

$$\Psi = \frac{1}{2\pi}\int_0^{2\pi} (\psi_c(\phi) + mfh(\theta) - \lambda g'(\theta))\, d\theta$$

$$= \frac{1}{2\pi}\int_0^{2\pi} \psi_c(\phi)\, d\theta$$

since the integrals of $h(\theta)$ and $g'(\theta)$ over a cycle must be zero. In applying this equation to the profile of Fig. 19, one notes first that ψ_c varies nearly linearly with θ over the unstalled and backflow characteristics and, second, that the transition regions contribute very little to the integral (thus suggesting that the exact shape of ψ_c between the stable unstalled and backflow legs probably is of secondary importance). This will result in a prediction of

$$\Psi \approx \tfrac{1}{2}(\psi_{c_{\max}} + \psi_{c_{\min}})$$

in all cases, and the data do not generally support this result.

In our evaluation of the model, input parameters were systematically varied in an attempt to alter the basic shape of the calculated ϕ profile. This was not successful, however, as none of the variables seemed to exert a first-order effect. An example is shown in Fig. 20, where the compressor lag parameter λ was both halved and doubled. The external lag parameter, m, was varied from 2.0 to 1.5 with the only effect being a steepening of the transition regions. Otherwise the shape of the ϕ profile was unchanged.

Toward understanding why the predicted ϕ profile exhibits

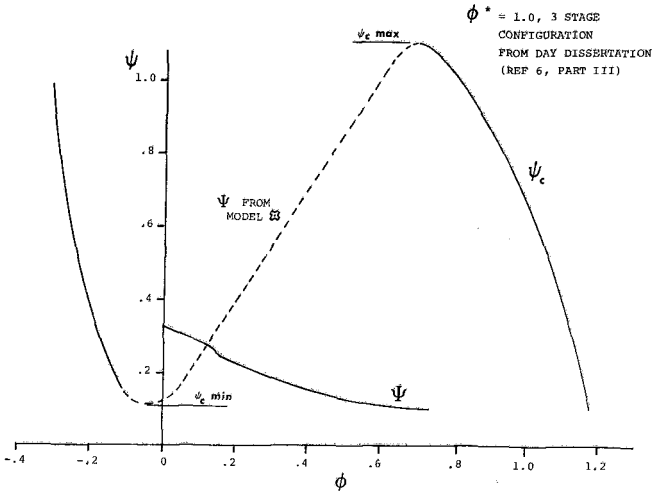


Fig. 17 Axisymmetric pumping characteristic

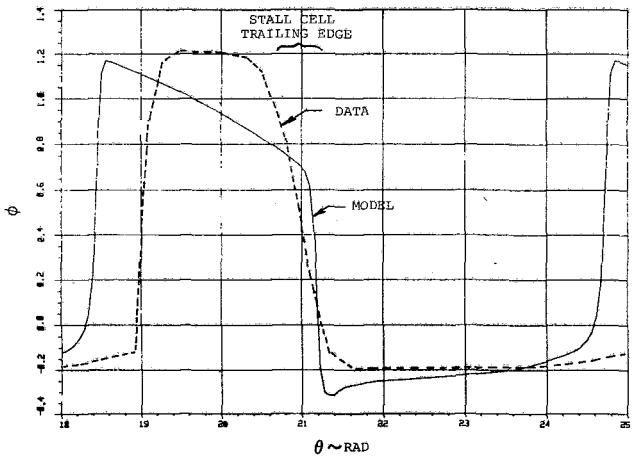


Fig. 18 Comparison of predicted inlet *Cx/U* profile with data

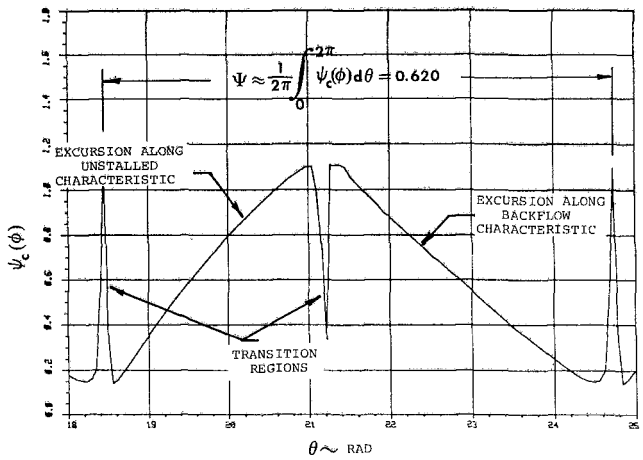


Fig. 19 Variation in pumping profile over a stall cycle

Toward understanding why the predicted ϕ profile exhibits

[1] Assistant Project Engineer, Government Products Division, Pratt & Whitney Aircraft, West Palm Beach, Fla. 33402

Copyright © 1984 by ASME
Downloaded 01 Jun 2010 to 171.66.16.70. Redistribution subject to ASME license or copyright; see http://www.asme.org/terms/Terms_Use.cfm

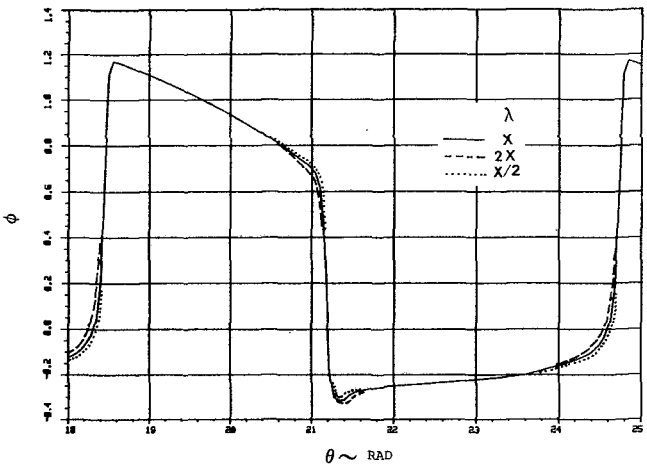


Fig. 20 Effect of compressor lag term

this unalterable shape, it is suggested that the problem may lie in the assumption of potential flow in the upstream channel. Recent post-stall data obtained at P&WA have shown that considerable backflow exists in the stalled cell, and this backflow can extend upstream as far as a compressor diameter or so. It is difficult to imagine that the interaction of this backflow with the incoming (net) flow would be potential, i.e., irrotational. Compounding the problem is the lack of experimental data—understandable in light of the difficulty involved in obtaining such measurements—from which one could deduce a more suitable representation.

At any rate, it appears as if the accuracy of the model, at least as far as the Ψ prediction is concerned, depends almost entirely on the shape of the ϕ profile. This is an important observation, since it allows one to properly focus future studies.

Author's Closure

I am grateful to Mr. Lewis for his interest and appreciate very much the useful contribution he has made in providing the foregoing very informative discussion.

Understanding, now lacking, of entrance and exit flows with reversal is badly needed for further progress in the study of rotating stall, and I believe Mr. Lewis is quite correct in emphasizing that Day's Case IV [3] must involve reverse-flow considerations that are not included in the theory. It may be helpful to remark that Case IV is quite peculiar in its very low value of Ψ in deep stall; Case II (Fig. 15 of the present paper) shows a rising characteristic in deep stall and agrees well with the theory. Which behavior is more typical? Perhaps, as Fig. 23 of [3] suggests, the rising type is at least very common among axial compressors.

In terms of the present theory, one might say that Case IV behaves as if the reverse-flow resistance were very low; if that were true, the predicted limit cycle would be of the type shown by the symbol Δ ($\beta = 0.25$) in Fig. 6, which is not "caught" by the reverse-flow leg of the diagram. One result would be that δ would be nearly zero, so that the deep-stall Ψ could indeed remain low, as in Case IV. Case IV has a very low stagger angle (20 deg), and it seems conceivable that a low resistance to reverse flow is implied.

Mr. Lewis and I differ somewhat in our views of the importance of the axial profile. I feel that the profile should be just one of the results of a theory, along with pressure rise (Ψ), propagation speed, and recovery point. In none of those features does the theory successfully predict Case IV! It would be interesting to see how the axial profile, calculated by Mr. Lewis's method, would compare with experiment for Case II, for which theory seems more successful in other respects.

Downloaded 01 Jun 2010 to 171.66.16.70. Redistribution subject to ASME license or copyright; see http://www.asme.org/terms/Terms_Use.cfm

Wall Boundary Layer Development Near the Tip Region of an IGV of an Axial Flow Compressor

B. Lakshminarayana

N. Sitaram

Department of Aerospace Engineering,
The Pennsylvania State University,
University Park, Pa. 16802

The annulus wall boundary layer inside the blade passage of the inlet guide vane (IGV) passage of a low-speed axial compressor stage was measured with a miniature five-hole probe. The three-dimensional velocity and pressure fields were measured at various axial and tangential locations. Limiting streamline angles and static pressures were also measured on the casing of the IGV passage. Strong secondary vorticity was developed. The data were analyzed and correlated with the existing velocity profile correlations. The end wall losses were also derived from these data.

Introduction

Inlet guide vanes (IGV) are often used for the improvement in the stage efficiency and the operating range of axial flow compressors. Also, a recent study [1], has shown that an appreciable increase in the useful operating range of an axial flow rotor is obtained with a freely rotating IGV compared to the rotor without IGV. Very little information is available on the flow field inside IGV passages. Most of the experimental data available consists of radial survey at the IGV exit, with no blade-to-blade measurements. An exception to this is the investigation by Kolesnikov [2], who made a blade-to-blade survey of the velocity and the pressure fields at an IGV exit.

The flow enters axially into the IGV and is accelerated through the passage. The flow in the end wall region is three-dimensional and cannot be estimated from the two-dimensional cascade data or theories. The losses in this region are also large, and the flow turning is much more than that of the two-dimensional flow. These complexities arise due to the development of secondary flows generated by the turning of the incoming wall boundary layer, as shown in Fig. 1. Moreover, the incoming flow to the succeeding row (i.e., rotor) would be significantly affected by these flows. Hence, the present investigation is undertaken to understand the end wall flow in an IGV in a real environment.

Recent attempts to develop computer codes to solve the Navier-Stokes equations in the end wall region have underscored the need for comprehensive and scientific quality data. Langston et al. [3] provided such detailed measurements of the flow in the end wall region of a turbine cascade, and Flot [4] presented similar data for a compressor cascade. A comprehensive review of the end wall flows is given in [5]. The present study is complementary to these studies, and provides a complete and comprehensive set of data on the end wall flow for verification of computer codes.

The data were acquired in a single-stage axial flow compressor facility using a miniature five-hole probe, and is analyzed for the streamwise and the crossflow velocity profiles. A loss correlation and various other boundary layer parameters are derived from the data.

Experimental Facility, Technique and Accuracy

The single-stage axial flow compressor facility at the Turbomachinery Laboratory of the Department of Aerospace Engineering at The Pennsylvania State University was used in the present experimental investigation. A detailed description of the facility is given by Lakshminarayana [6]. The compressor stage was designed by Smith [7] who investigated the secondary flows phenomena in blade passages. The hub-to-tip diameter ratio is 0.5, with the tip diameter equal to 0.932 m. The inlet guide vane row has 43 blades. All the measurements are taken at a midspan inlet velocity of 29.04 m/s, giving a flow coefficient (based on the rotor tip speed) of 0.556. Other details are given in [5]. The blade element data are tabulated in Table 1.

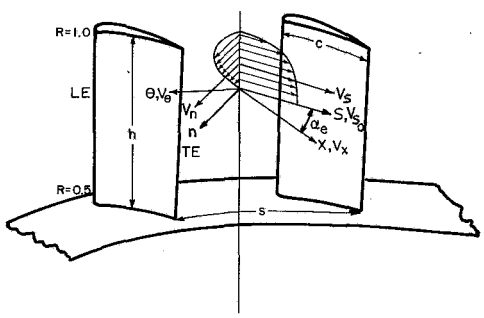


Fig. 1 Nature of end wall flow in the inlet guide vanes and the notation used

Contributed by the Gas Turbine Division of THE AMERICAN SOCIETY OF MECHANICAL ENGINEERS and presented at the 28th International Gas Turbine Conference and Exhibit, Phoenix, Arizona, March 27-31, 1982. Manuscript received at ASME Headquarters December 27, 1982. Paper No. 83-GT-171.

Copyright © 1984 by ASME
Downloaded 01 Jun 2010 to 171.66.16.70. Redistribution subject to ASME license or copyright; see http://www.asme.org/terms/Terms_Use.cfm

Table 1 Blade element data and design parameters near the IGV tip

	Quantity	$R=0.95$	$R=1.00$
Design	Profile thickness distribution	NACA 65-010 modified to have a 1% chord trailing edge radius	
	Camber line type	Circular arc	
	Camber angle ϕ (deg)	37.3	42.9
	Stagger angle γ (deg)	18.6	21.0
	Chord C (cm)	10.37	10.91
	Spacing S (cm)	6.48	6.82
	Solidity $\sigma=C/S$	1.6	1.6
	Thickness ratio t/c (%)	8.80	8.29
	Flow inlet angle α_1 (deg)	0	0
	Flow exit angle α_2 (deg)	29.85	34.1
	Lift coefficient C_l (based on cascade mean velocity)	0.690	0.802
Experimental	Flow inlet angle α_1 (deg)	0	0
	Flow exit angle $\bar{\alpha}_2$ (deg)	31.8	54.5 (at $R=0.995$)
	Axial velocity $\bar{V}_x/V_{x_{1_{ms}}}$	0.990	0.507 (at $R=0.995$)
	Tangential velocity $\bar{V}_\theta/V_{x_{1_{ms}}}$	0.614	0.712 (at $R=0.995$)
	Static pressure coefficient $\bar{C}_{p_s}$	−1.228	−1.266

A miniature five-hole probe of 1.65-mm (0.066-in.) dia, shown in Fig. 2, was used to measure the IGV end wall flow at various axial and tangential stations, shown in Fig. 4. The calibration and interpolation techniques of [8] were used. This probe was selected because of its small dimensions, which will enable accurate measurement of the thin wall boundary layers at the inlet and inside the IGV passages. The measurements were taken utilizing a ±0.2 psi range Validyne DP-15 pressure transducer. The speed of the compressor was measured by a photo cell arrangement and was controlled to an accuracy of ±1 rpm (approximately 0.1 percent). Day-to-day variation of atmospheric pressure and temperature were noted and used to correct the measured pressures of the five-hole probe.

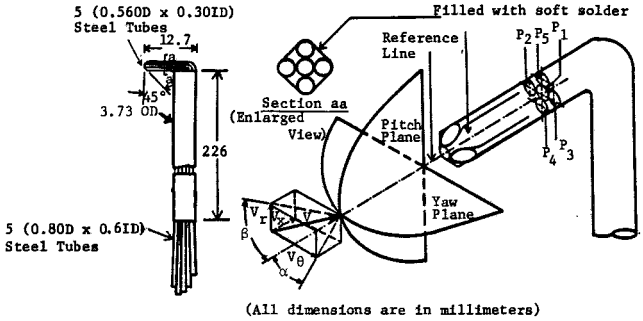


Fig. 2 Miniature five-hole probe

The axial and tangential movement of the probe was achieved by a simple tangential traverse mechanism. Axial traverse slots enable small axial movements of the traverse mechanism. The tangential movement was achieved by means of rollers moving in a slotted arc in the traverse mechanism. The traverse mechanism was capable of 0.05 deg movement in the tangental direction. The probe was mounted in a radial

Nomenclature

C = chord length
C_p = static pressure coefficient = $(p_l-p_1)/\frac{1}{2}\rho V^2_{x1_{ms}}$
C_{ploss} = stagnation pressure loss coefficient = $(P_{01}-P_{0l})/\frac{1}{2}\rho V^2_{x1_{ms}}$
F = blade force per unit span = $2\pi\rho r_2 V_{x_2}(V_{\theta_2}-V_{\theta_1})$
H = shape factor = δ^*/θ^*
n = exponent in the power law for the streamwise velocity profile
P_o = stagnation pressure
PS,SS = pressure and suction surface, respectively
p = static pressure
P_{o_1} = stagnation pressure at inlet (local radius)
R = nondimensional radius $= r/r_t$
r = radius
r,θ,x = cylindrical coordinate system (Fig. 1)
s,n,r = streamwise coordinate system (s is along the edge of the boundary layer, n is perpendicular to s and radial direction, see Fig. 1)
t = blade maximum thickness
U = blade speed
V = flow velocity
X = axil distance from the leading edge
YS = normalized distance (w.r.t. local blade spacing) along the tangential direction measured from the suction surface
Y^+ = $V_e(r_t-r)/\nu$
Z = nondimensional axial distance from the leading edge = X/C_{t_x}
α = absolute flow angle = $\tan^{-1}(V_\theta/V_x)$, deg
α_l = limiting streamline angle, deg
β = radial angle = $\tan^{-1}(V_r/V_x)$, deg
δ = boundary layer thickness
δ^* = displacement thickness
η = $(r_t-r)/\delta_t$
ψ_s = $2(p-p_a)/\rho V_1^2$
θ^* = momentum thickness
ϵ = error in measured velocity $(V/V_{\text{actual}}-1)$
ν = kinematic viscosity, tangential force defect $= \frac{1}{r F_{\theta e}}\int_{r_t-\delta_t}^{r_t}(F_{\theta_e}-F_\theta)\,r\,dr$
$\bar{\phi}$ = flow coefficient, V_x/U_t
$\Delta\beta,\Delta\alpha,\Delta\psi_s$ = error in β,α,ψ_s, respectively

Subscripts

a = atmosphere
e = boundary layer edge
l = local
ms = midspan
o = stagnation quantities
p,s = pressure surface, suction surface, respectively
r,θ,x = along r, θ, x directions, respectively (Fig. 1)
s,n,r = along s, n, r directions, respectively (Fig. 1)
t,w = tip and wall, respectively
1,2 = blade inlet and exit, respectively

Superscripts

$\overline{\quad}$ = passage-averaged quantities
$\underline{\quad}$ = averaged over the annulus wall boundary layer

Downloaded 01 Jun 2010 to 171.66.16.70. Redistribution subject to ASME license or copyright; see http://www.asme.org/terms/Terms_Use.cfm

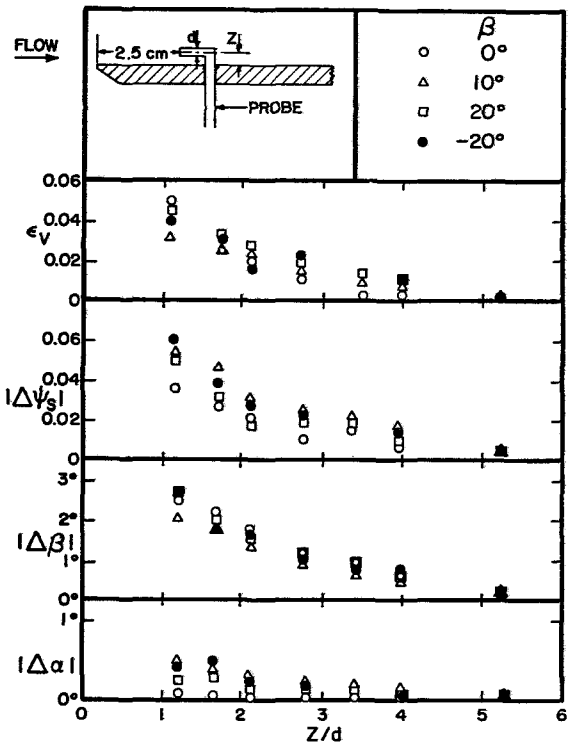


Fig. 3 Wall vicinity effect on five-hole probe

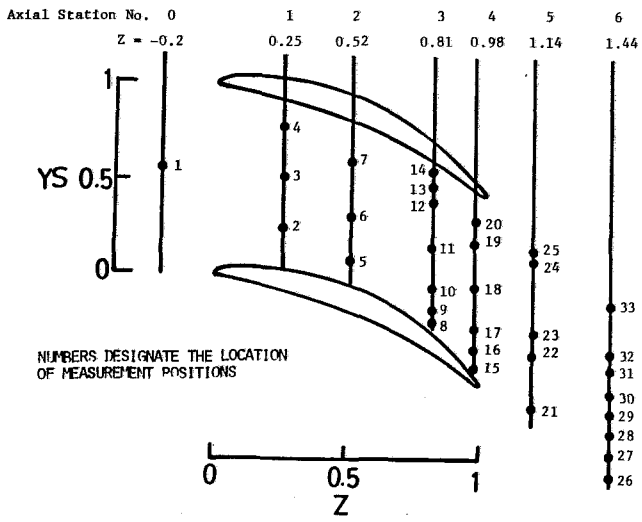


Fig. 4 IGV end wall flow measurement positions

traverse mechanism which is capable of moving the probe in 0.025 mm (0.001 in.) steps. The probe orientation with the axial direction was measured by means of a protractor mounted on the radial traverse mechanism and was accurate to within 0.5 deg.

The probe was passed through the holes drilled in the casing. The gap between the 6.35-mm-dia holes and 3.73-mm-dia probe stem was filled with a steel tube of proper dimension. The steel tube was almost flush with the casing inner surface. To measure the probe orientation, the probe was nulled in the free-stream region of the IGV inlet, and its orientation was marked on the protractor. At every measurement position, the probe was aligned in the free-stream region at that passage location, and its orientation was noted on the protractor. The difference between these two readings gives the free-stream yaw angle. The flow angles inside wall boundary layers were determined likewise. The pitch angle derived from the probe measurements was the radial angle, since the probe was in the radial direction. The gap between the probe and slot was filled up with a dense foam, which was contoured to the inner curvature of the window (casing). This arrangement was quite satisfactory, and there was no leakage or flow disturbance due to the foam. The small gap between the blade and the window was filled with epoxy.

The estimated experimental accuracies are as follows:

Axial and tangential position of the probe:	0.8 mm (1/32 in.)
Radial position of the probe:	0.025 mm (0.001 in.)
Radial and tangential angles:	±1 deg (execpt very close to the end wall and in the blade wake near the blade)
RPM of the compressor:	±1 rpm
Static and Stagnation pressures:	2% of dynamic head based on tip speed
Limiting streamline angle:	1 deg

The probe error due to the wall vicinity effect was determined, experimentally, using the arrangement shown as an insert in Fig. 3. The procedure was similar to that described in [9]. The distance Z between the center line of the probe and the wall was varied. The results are shown in Fig. 3. The error in the yaw angle α (angle in the cylindrical plane) is less than ± 0.5 deg, even for $Z/d = 1.2$. The maximum error in the angle β (which is a measure of the radial velocity) is ± 2.5 deg. The maximum error for ψ_s and velocity are 6 and 5 percent, respectively. The error is negligibly small beyond two probe diameters from the wall. The correction due to the wall vicinity effect is not incorporated in the data presented in this paper, as it is very small for the streamwise (V_s) and crossflow (V_n) velocities. The error is negligible for the angle β. The error is appreciable for the radial velocity (V_r). Hence data on radial velocity are not included in this paper. The uncorrected data for the radial velocity can be found in [5].

The locations of measuring stations are shown in Fig. 4 at $R = 1.0$. The boundary layer parameters at these locations are listed in Table 2.

Experimental Results and Interpretation

The flow data in the end wall region is presented and interpreted here. Tabulated data are available from the authors. The boundary layer parameters at all the stations are given in Table 2.

Limiting Streamline Angles and Wall Static Pressures. The traces of the limiting streamlines are obtained by injecting ammonia gas at a controlled rate on to an Ozalid paper fixed to the casing inside the blade passage and at the exit. A large number of 1.5-mm-dia holes were drilled on the casing, and these were used to pass ammonia gas. The measurements were taken at different locations than indicated in Fig. 4. The limiting streamline angle distribution derived from these traces is shown in Fig. 5. The angles apply to the tail ends of the arrows. The deviation from the blade surface is small near the leading edge. Beyond an axial position of 0.25 chord downstream of the leading edge, the flow deviations are strong, with the flow turning more towards the suction surface. This is to be expected as the crosswise pressure gradients are large downstream of the leading edge to the trailing edge (see Fig. 6).

The holes that were used for the limiting streamline angle measurements were utilized to measure the static pressures on the casing in the IGV blade passage and at the exit region. The static pressure coefficient (C_p) distribution thus obtained is shown in Fig. 6. The inlet C_p is nearly uniform and zero.

Downloaded 01 Jun 2010 to 171.66.16.70. Redistribution subject to ASME license or copyright; see http://www.asme.org/terms/Terms_Use.cfm

Table 2 IGV end wall flow parameters

Measurement position no.	Z	YS	V_e m/s	α_e (deg)	β_e (deg)	δ mm	δ_s^* mm	θ_s^* mm	δ_x^* mm	θ_x^* mm
1	−0.20	0.530	29.04	0.0	0.0	5.92	0.790	0.450	0.790	0.450
2	0.25	0.287	34.74	25.33	−1.46	5.87	0.733	0.276	0.677	0.239
3	0.25	0.543	31.69	15.90	−2.55	7.55	0.884	0.419	0.867	0.399
4	0.25	0.821	24.64	29.47	−0.20	6.99	1.213	0.674	1.253	0.622
5	0.52	0.231	36.87	22.93	−7.63	6.99	0.953	0.474	0.980	0.476
6	0.52	0.469	32.86	25.38	−4.64	6.99	0.967	0.491	1.066	0.537
7	0.52	0.747	30.60	19.63	−2.77	8.67	1.454	0.877	1.583	0.892
8	0.81	0.133	33.63	30.95	2.85	9.79	1.774	1.271	1.695	1.050
9	0.81	0.190	35.52	23.65	0.38	9.23	1.153	0.664	1.160	0.631
10	0.81	0.304	35.14	28.41	−1.47	12.54	2.499	1.330	2.628	1.209
11	0.81	0.532	34.37	26.28	−1.41	10.86	2.386	1.528	2.652	1.385
12	0.81	0.791	30.37	28.28	−5.29	9.23	0.856	0.404	1.028	0.539
13	0.81	0.848	29.84	30.43	−4.12	10.86	1.107	0.576	1.570	0.772
14	0.81	0.930	28.01	33.51	−1.37	9.23	1.003	0.508	0.969	0.445
15	0.98	0.062	34.16	35.10	−1.11	17.57	3.753	3.007	4.117	2.431
16	0.98	0.162	32.84	32.55	−0.88	8.67	2.326	1.484	2.693	1.220
17	0.98	0.276	33.73	29.73	−1.02	10.58	1.995	1.298	2.304	1.215
18	0.98	0.500	32.14	28.66	−0.43	8.67	2.016	1.290	2.225	1.171
19	0.98	0.727	32.86	29.34	−1.65	13.65	1.278	0.799	1.360	0.787
20	0.98	0.841	30.97	34.84	2.06	15.33	2.984	2.571	4.050	2.687
21	1.14	0.100	19.98	43.86	0.28	20.92	5.817	4.867	4.938	3.102
22	1.14	0.392	31.06	31.00	−1.18	14.21	1.412	0.899	1.930	1.105
23	1.14	0.500	32.44	30.24	−0.65	14.21	2.534	1.798	3.173	1.698
24	1.14	0.878	30.83	34.36	−0.08	17.57	2.842	1.419	3.663	1.850
25	1.14	0.936	31.87	33.60	−0.60	15.89	3.171	1.694	3.673	1.768
26	1.44	0.090	30.98	36.63	−5.74	15.89	4.106	2.295	4.500	1.797
27	1.44	0.208	31.69	33.69	−5.05	10.86	2.656	1.652	3.264	1.378
28	1.44	0.300	31.93	32.76	−3.82	10.81	2.924	1.670	3.342	1.362
29	1.44	0.427	31.10	32.03	−4.23	10.86	2.297	1.447	2.933	1.298
30	1.44	0.523	31.12	31.89	−4.89	10.86	1.522	1.048	2.020	1.170
31	1.44	0.654	31.39	32.63	−4.28	10.86	1.447	0.992	1.891	1.121
32	1.44	0.740	30.21	35.16	−8.07	10.86	0.795	0.319	0.883	0.389
33	1.44	0.950	18.82	35.90	1.93	14.21	−3.611	−6.841	−1.022	−1.842

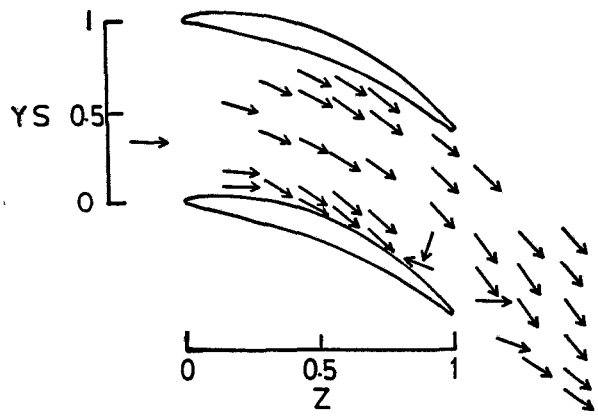


Fig. 5 Limiting streamline angle distribution on the IGV end wall

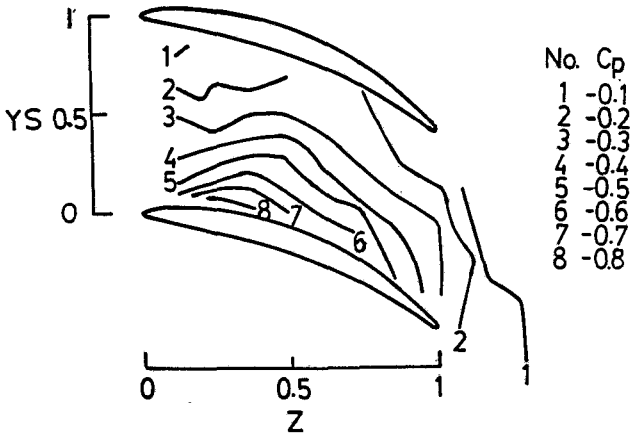


Fig. 6 Static pressure distribution on the IGV end wall

Large crosswise pressure gradients exist inside the IGV blade passage. The static pressure gradients in the tangential direction are smaller near the trailing edge. The crosswise pressure gradients are negligibly small beyond the trailing edge. The streamwise pressure gradient increases towards the trailing edge.

Boundary Layer Profiles. The annulus wall boundary layer profiles at all of the 33 measurement positions are given in Fig. 7. The velocity components are shown in the s, n coordinate system illustrated in Fig. 1. The s coordinate is along the streamwise direction at the edge of the annulus wall boundary layer, and n is normal to it (Fig. 1). Hence the velocity components are given by

$$\left.\begin{aligned} V_s &= V\cos(\alpha-\alpha_e) \\ V_n &= V\sin(\alpha-\alpha_e) \end{aligned}\right\} \quad (1)$$

where α_e is the flow angle at the edge of the boundary layer. The edge of the annulus wall boundary layer is determined from the location where the changes in stagnation pressure, total velocity, and flow angle are small. This method proved to be satisfactory, and the accuracy is 1.65 mm (i.e., the radial step size towards the boundary layer edge).

The boundary layer thickness is small (about 6mm) at the IGV inlet and increases continuously downstream of the IGV passage. The inlet boundary layer (Fig. 4, Station 1) is two-dimensional and the crossflow are negligible up to a quarter-chord. The boundary layer is turbulent throughout.

At $Z = 0.25$ and tangential locations 2 to 4 (Fig. 4), a small crossflow is observed on the pressure side, and its magnitude decreases continuously to negligible values as the suction side (station 2) is approached. Compared to the inlet profile the boundary layer profiles undergo large changes near the

Downloaded 01 Jun 2010 to 171.66.16.70. Redistribution subject to ASME license or copyright; see http://www.asme.org/terms/Terms_Use.cfm

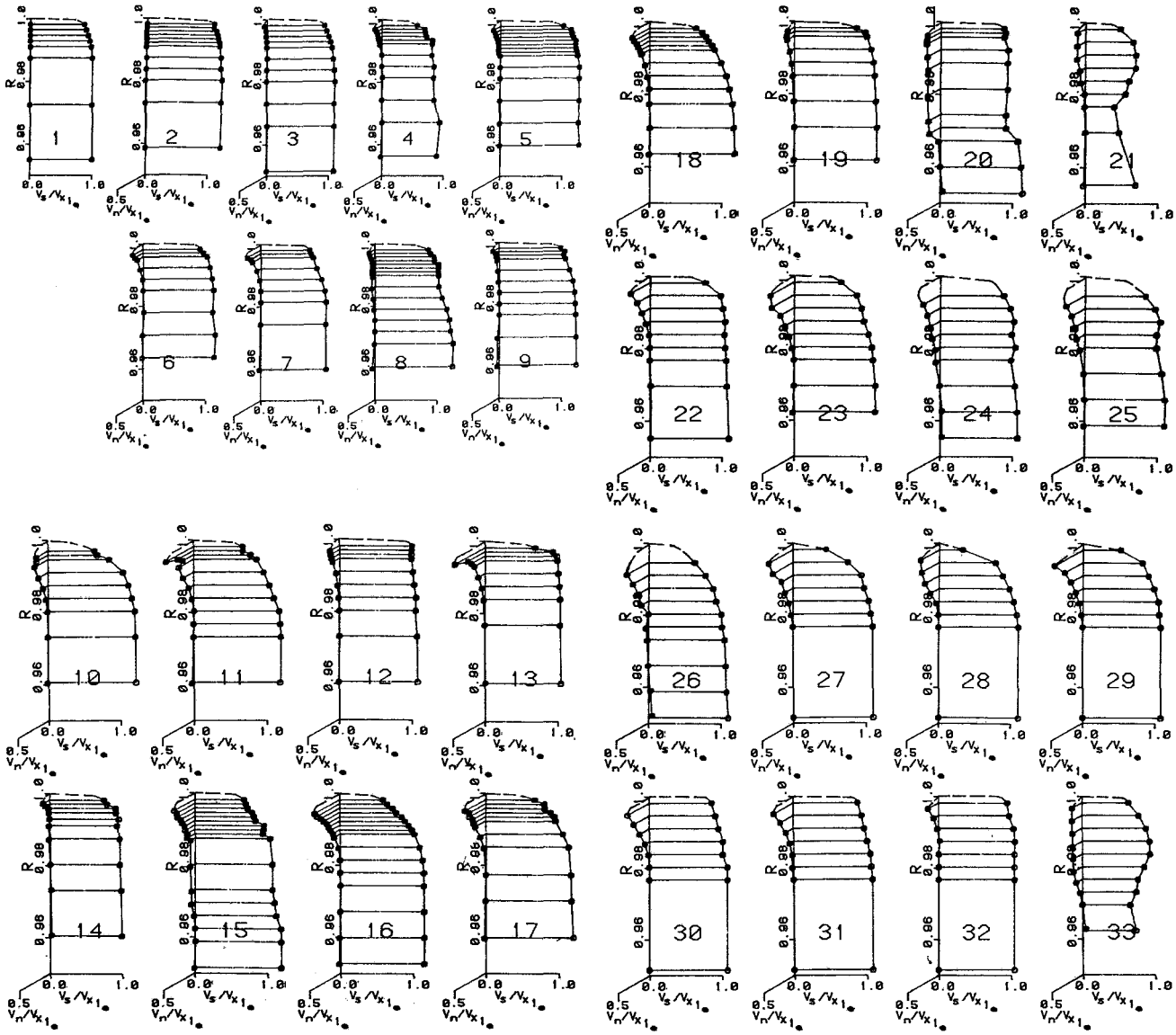


Fig. 7 Streamwise and crossflow velocity profiles

pressure side and negligible changes from midpassage to the suction side.

Near the midchord, $Z = 0.52$, the measured streamwise and crossflow velocity profiles are similar to those observed at $Z = 0.25$, but the crossflows exist at all the passage locations in this region, with maximum values occurring near the pressure side. These values are nearly 50 percent of the streamwise velocity. The annulus wall boundary layer growth is also substantial in this region.

At $Z = 0.81$ (Fig. 7, Stations 8–14), rapid growth in the annulus wall boundary layer is evident. Comprehensive measurements are available at this station, including data very close to the blade surfaces. The crossflow velocities are negligibly small near blade surfaces, but reach high values near the midpassage (Stations 10 and 11), with peak values (as high as 50 percent of the streamwise velocity) occurring near the pressure surface at Station 13. Most of the rapid growth in the boundary layer occurs between the midpassage and the suction side. A wake type of profile, observed near the suction surface (Station 8), may be due to the fact that, because the blade surface is warped, the radial survey includes different blade boundary layer locations. The limiting streamline angle plot (Fig. 5) indicates the presence of large flow-angle changes at this axial locations.

Data near the trailing edge at $Z = 0.98$ (Fig. 7, Stations 15–20) indicate that the boundary layers are thicker than those at $Z = 0.81$. The crossflows are considerably larger than those at other axial stations. The trend in the crossflows observed earlier ($Z = 0.25$ to 0.81), namely, smaller crossflows near the suction surface and larger crossflows near the pressure surface, is reversed at this station. The crossflows are generally higher near the suction surface, with maximum values reaching about 100 percent of the local streamwise velocity. The boundary layer thickness is maximum near the suction surface and decreases toward the pressure surface.

Large changes occur as the flow leaves the trailing edge. The boundary layer thickness near the suction surface shows a tendency to decrease (compare Stations 17 and 22), while the annulus wall boundary layer thickness near the pressure surface increases as it leaves the trailing edge (compare Stations 20 and 24).

As the flow proceeds downstream from $Z = 1.14$, the boundary layer thickness grows rapidly at approximately the middle third of the passage (Stations 26–29), while the

Downloaded 01 Jun 2010 to 171.66.16.70. Redistribution subject to ASME license or copyright; see http://www.asme.org/terms/Terms_Use.cfm

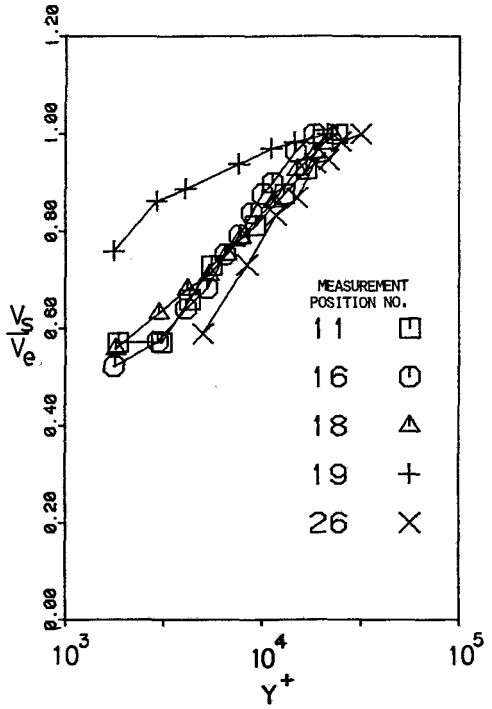


Fig. 8 Streamwise velocity profile in logarithmic form

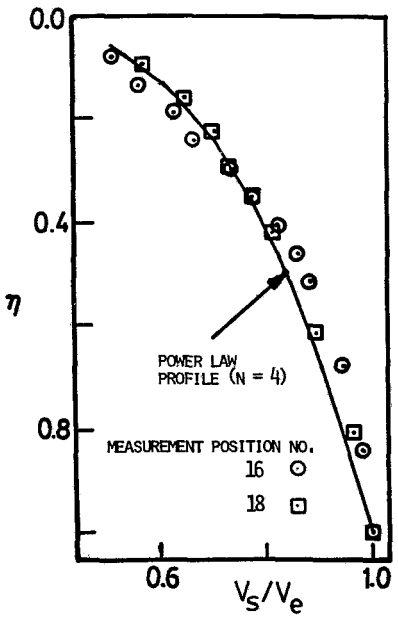


Fig. 9 Streamwise velocity profile in power law form

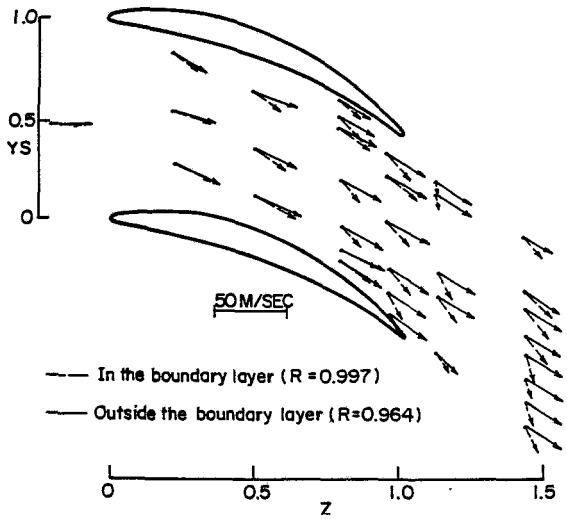


Fig. 10 Velocity vectors in the x-θ plane at R = 0.997, 0.964

pressure surface boundary layer (Stations 30–32) decreases near the suction side (Station 33) of the adjoining passage. Comparing the data at Stations 3, 6, 11, 18, 23, and 29 (which are approximately along the mean streamline), it is evident that most of the boundary layer growth occurs between midchord and the trailing edge, beyond which it remains nearly frozen.

The unusual shape of the boundary layers at positions 21 and 33 (Fig. 7) is probably due to the fact that this radial traverse is in the wake, which is not radial. Also, the axial distance between the probe and the IGV trailing edge varies with the radial positions of the probe. Hence, the probe also senses different axial development of the wake. The crossflows are still large, even at this location.

The radial velocity distribution across the passage at various axial and radial stations are presented and interpreted in [5]. Since the error in the radial velocity and the radial angle measurement is appreciable, in view of the spatial resolution and the wall vicinity effect, the radial velocity plots should be viewed with caution.

A logarithmic plot of the mean velocity profile at some locations (Stations 11, 16, 18, 19, and 26) is shown in Fig. 8. Except for the inaccuracy in the measurements close to the annulus wall, the data seem to indicate the existence of the logarithmic region. The wake region (the region following the "law of the wall" region) is either small or nonexistent in most of the IGV end wall boundary layer data. The presence of the logarithmic region could not be confirmed in thin boundary layers (such as Sations 1–7 and 11–14, etc.), where there are not enough data points.

The streamwise velocity profile was also plotted in power law form to check the validity of the power law profiles. The plots at two typical stations are shown in Fig. 9. The exponent at these locations is found to be 1/4, which is in conformity with the adverse pressure gradient measured at these locations. The exponent at most other locations ranged from 1/7 to 1/12. The existence of power law profiles is confirmed at most locations, although deviations are observed in regions where the boundary layer is thin or affected by the blade boundary layer or wake. However, attempts to compare crossflow velocities with the expressions given by Mager [10], Johnston [11], and Horlock [12] have not been successful. Most of these models are developed for curved flows with negligible streamwise pressure gradients. The presence of favorable streamwise pressure gradients may be responsible for the discrepancy between correlations and the data.

Streamwise and Secondary Flow Velocity Vector Plots. The velocity vectors in the $x-\theta$ plane at two radii (R = 0.964 and 0.997) are shown in Fig. 10. At Z = 0.25, the boundary layer velocity vector is smaller in magnitude than the velocity vector in the free stream, but the direction is the same, except near the pressure surface. The free-stream velocity deviates considerably from the blade surfaces. Beyond Z = 0.25, the velocity in the boundary layer deviates considerably, both in magnitude and direction, from the velocity vector in the free stream. The difference in the directions of velocity vectors in the boundary layer and free stream increases with the axial distance, thus indicating the increasing strength of the secondary flow. The overturning in the boundary layer is substantial beyond midchord and continues far downstream.

Downloaded 01 Jun 2010 to 171.66.16.70. Redistribution subject to ASME license or copyright; see http://www.asme.org/terms/Terms_Use.cfm

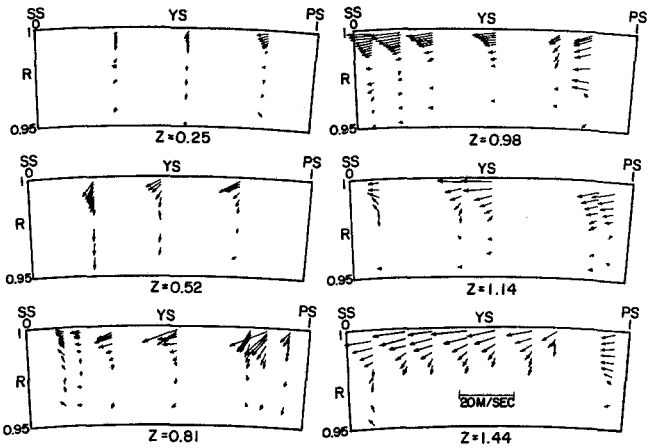


Fig. 11 Secondary velocity vectors in the r-θ plane (resultant of cross flow and radial velocities)

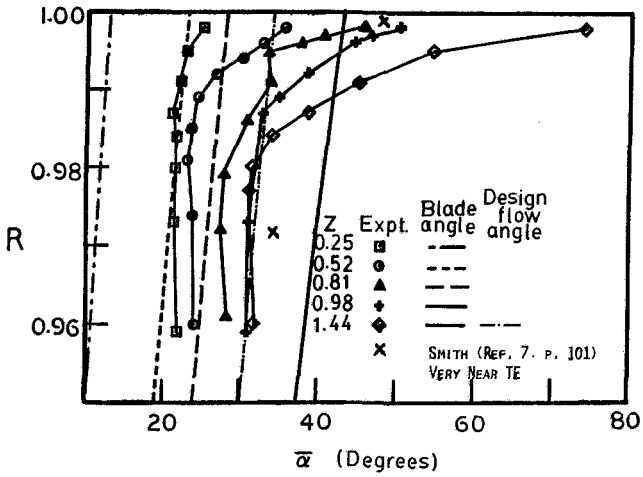


Fig. 13 Radial variation of passage-averaged flow angles

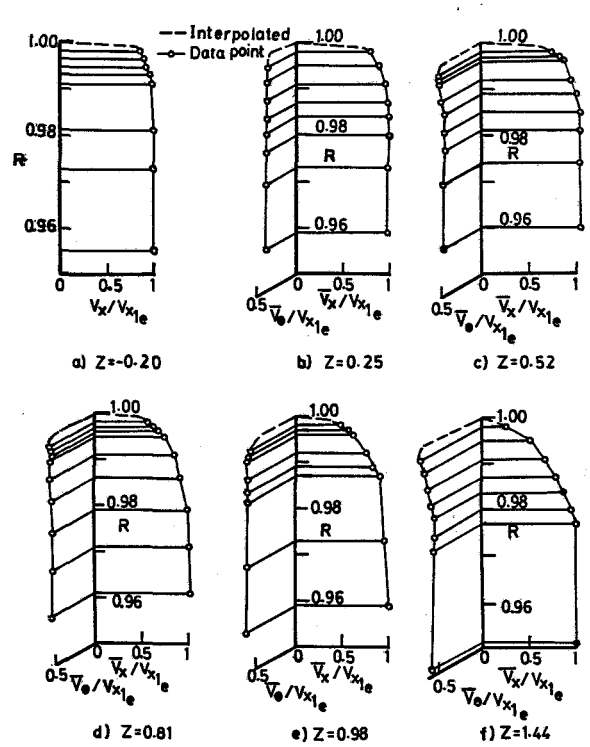


Fig. 12 Passage-averaged boundary layer profiles

The sudden increase in overturning as the flow leaves the pressure surface cannot be explained on the basis of classical secondary flow theories, which do not predict the changes in the streamwise boundary layer, which apparently causes it.

The secondary flow velocity vector plots at various axial stations (Z = 0.25 to Z = 1.44) are shown in Fig. 11. Even though the radial velocity data may be in error, especially near the wall, due to reasons mentioned earlier, a vectorial plot of the secondary flow velocities provides a qualitative understanding of the flow field. The primary streamline is assumed to follow the measured flow at the edge of the local annulus wall boundary layer. At Z = 0.25, the crossflow velocities and the radial velocities are small at most of the tangential locations. At Z = 0.52, appreciable radial velocities (pressure to suction surface) are observed. Except in the corner between the pressure surface and the wall, the usual secondary flow pattern is observed at this location. Near the pressure surface, the flow is inward at most axial locations, which is opposite to the trend predicted by secondary flow theories. It should be borne in mind that these IGV's were designed to have a strong radial variation of circulation (see [7]) in a direction to produce radially inward flow on the pressure side. In fact at R = 0.931, Smith [7] measured a jump in V_r in this direction of 0.12 $V_{x_{1e}}$. The velocity vectors at Z = 1.44 clearly indicate the conventional secondary flow in a developed state, with a large accumulation of low energy fluid near the suction side.

Passage-Averaged Properties of the Annulus Wall Boundary Layer. The radial variations of the axial and the tangential velocities, averaged over the blade passage, is shown in Fig. 12.

At IGV entry, the flow is axial and the boundary layer is very thin. As the flow proceeds downstream, the boundary layer thickness increases, and the axial velocity gradient also increase. The tangential velocities show different trends from the axial velocities. At most of the axial stations, the tangential velocity is almost constant along the radius. At Z = 0.52 and 1.44, slight increases in the tangential velocities near the casing are observed. The boundary layer profile at Z = 1.44 is not included because of insufficient data at this location. Three of the measurement positions are in the wake region here.

The passage-averaged flow angles ($\bar{\alpha}$) are shown in Fig. 13. The camber line angles and the design outlet angle are also compared. Flow overturning and its radial extent increase with the axial distance from the IGV leading edge. The flow overturning near the casing is large, beyond (Z = 0.25) as is confirmed by the limiting streamline angle measurements shown in Fig. 5. This is evidenced by the observed suction peak at this station. It is interesting to note that a large increase in overturning occurs beyond the trailing edge, caused mainly by a reduction in axial velocity (Fig. 7). This indicates that caution should be exercised in interpreting the secondary flow data acquired far downstream. At the exit, the flow is slightly underturned near the outer edge of the boundary layer relative to the design, but the design angles are thought to be lower than those of a two-dimensional flow.

The passage-averaged and overall stagnation pressure-loss coefficients are shown in Figs. 14 and 15, respectively. They are defined as follows

$$\bar{C}_{p_{\text{loss}}} = \int_{\theta_s}^{\theta_p} V_x C_{p_{\text{loss}}} d\theta \Big/ \int_{\theta_s}^{\theta_p} V_x d\theta$$

and

$$\bar{\bar{C}}_{p_{\text{loss}}} = \int_{r_t-\delta_t}^{r_t} \left[\int_{\theta_s}^{\theta_p} V_x C_{p_{\text{loss}}} d\theta\right] dr \Big/ \int_{r_t-\delta_t}^{r_t} \left[\int_{\theta_s}^{\theta_p} V_x d\theta\right] dr$$

Downloaded 01 Jun 2010 to 171.66.16.70. Redistribution subject to ASME license or copyright; see http://www.asme.org/terms/Terms_Use.cfm

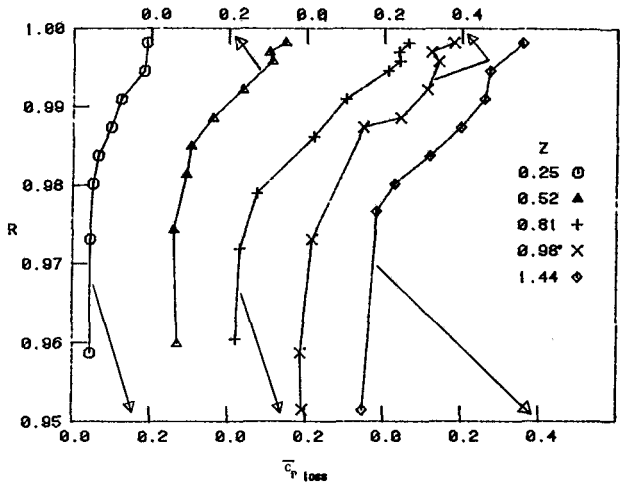


Fig. 14 Radial variation of passage-averaged stagnation pressure loss coefficient

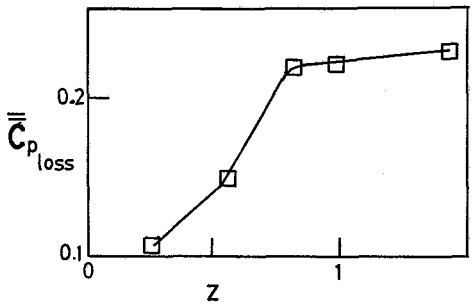


Fig. 15 Axial variation of overall stagnation pressure loss coefficient

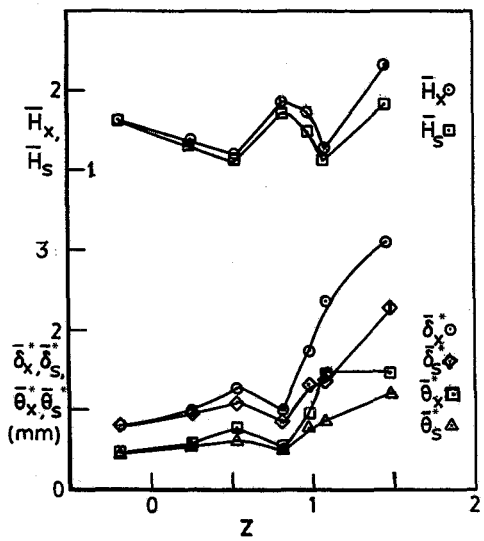


Fig. 16 Axial variation of passage averaged boundary layer integral parameters

The overall loss coefficient increases rapidly between Z = 0.52 and 0.81. Overall and passage-averaged stagnation pressure-loss coefficients at axial station Z = 1.14 are not shown, due to the insufficient number of measurement

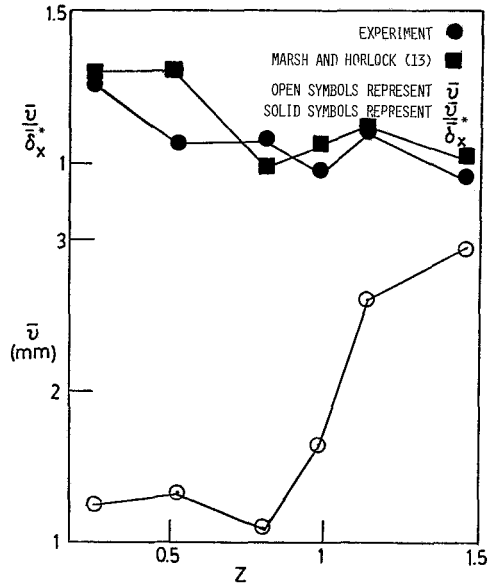


Fig. 17 Axial variation of passage-averaged force defect thicknesses

stations across the passage. The overall loss coefficient increases linearly along the passage from zero at Z = 0 to Z = 0.81. It should be emphasized here that the loss coefficient $\bar{\bar{C}}_{p_{loss}}$ is not for the entire blade row, but only for the end wall region inside the wall boundary layer. The integrated losses ($\bar{\bar{C}}_{p_{loss}}$) remain nearly constant beyond the trailing edge region.

The passage-averaged boundary layer integral quantities are presented in Fig. 16. The velocity profiles are first passage-averaged and then integrated along the radius. The momentum and displacement thicknesses, both in the axial and streamwise directions, show a rapid increase beyond Z = 0.82 and up to Z = 1.44. The axial shape factor is higher than the streamwise shape factor. The local value of displacement and momentum thicknesses are tabulated in Table 2.

Passage-averaged values of tangential force defect thicknesses v and v/δ_x^* are shown in Fig. 17. The force defect thickness, v, decreases slightly from Z = 0.25 to 0.52, beyond which the variation is small. The values of v/δ_x^* are compared with the theory of Marsh and Horlock [13]. Their analysis shows that

$$v/\delta_x^* = \left(1+\frac{1}{H_x}\right)\left[\frac{d\,\alpha_e/dx}{\frac{1}{\cos^2\alpha_e}\frac{d\alpha_e}{dx}+\frac{\tan\alpha_e}{V_{x_e}}\frac{dV_{x_e}}{dx}}\right]$$

Since V_{x_e} is fairly constant within the IGV passage

$$\frac{dV_{x_e}}{dx}=0$$

Hence,

$$v/\delta_x^* = \left(1+\frac{1}{H_x}\right)\cos^2\alpha_e$$

Their results show decreasing v/δ_x^* with Z, leveling off at Z = 0.98. Comparison with the experimental v/δ_x^* shows that the agreement between the analysis and experimental data is very good.

Conclusions

The annulus wall boundary layer and secondary flow

Downloaded 01 Jun 2010 to 171.66.16.70. Redistribution subject to ASME license or copyright; see http://www.asme.org/terms/Terms_Use.cfm

development inside the blade passage of an inlet guide vane row of a low-speed, axial flow compressor is reported. The experimental data consist of velocity and pressure field measurements. This set of data is believed to be the first of its kind, obtained in a real environment. The following important conclusions are drawn from this investigation.

1 Strong secondary vorticity is developed, giving rise to highly three-dimensional flow in the IGV end wall region, with considerable flow deviation from the inviscid flow.

2 The character of the flow changes considerably along the axial distance. The boundary layer near the suction surface is thinner than that near the pressure surface in the first half of IGV chord length. Beyond this point, the trend reverses. These results are qualitatively consistent with the free-stream velocity distribution.

3 The crossflow velocities are substantially close to the pressure surface and negligibly small near the suction surface at the quarter-chord point.

4 Large crossflows are observed at about 80 percent of chord. Both the flow data and the flow visualization on the annulus wall confirm this trend. Appreciable changes in the streamwise velocity and crossflow velocity profiles and the boundary layer thickness occur near the trailing edge and in the downstream regions. The boundary layer thickness decreases on the pressure side and increases near the suction side as the flow proceeds downstream of trailing edge.

5 The streamwise velocity profiles can be well represented by the logarithmic law of the wall and the power law profiles. However, crosswise profiles are not well represented by the correlations developed for the three-dimensional (bounded or unbounded) turbulent boundary layers.

6 Large flow overturning exists near the annulus wall. Substantial overturning is observed at and beyond the quarter-chord point. Substantial flow angle deviations are observed even beyond the trailing edge. A small region of underturning is observed near the edge of the annulus wall boundary layer.

7 The displacement and momentum thicknesses increase very slowly from the leading edge to $Z = 0.81$, beyond which the increase is much more rapid.

8 Good agreement is obtained between the theoretical and the experimental values of ν/δ^*.

Acknowledgment

This work was supported by the National Aeronautics and Space Administration through Grant No. NSG 3032, with Dr. P. M. Sockol as the Technical Monitor. The authors would like to express their appreciation for the comments and criticism received by the anonymous reviewers. These have been incorporated into the revised paper.

References

1 Venkatarayalu, N., Prithvi Raj, D., and Narayanamurthi, R. G., "Influence of Freely Rotating Inlet Guide Vanes on the Return Flows and Stable Operating Range of an Axial Flow Fan," ASME JOURNAL OF ENGINEEIRNG FOR POWER, Vol. 102, 1980.

2 Kolesnikov, Yu. N., "Investigation of Losses of Total Pressure in the Inlet Guide Vane of an Axial Flow Compressor," in *Blade Machines and Jet Devices*, U.S. Air Force, FTD-MT-24-69-68, 1968.

3 Langston, L. S., Nice, M. L., and Hooper, R. M., "Three-Dimensional Flow Within a Turbine Blade Passage," ASME JOURNAL OF ENGINEERING FOR POWER, Vol. 99, 1977, pp. 21–28.

4 Flot, R., "Contribution a L'Etude des ecoulements secondaires dan les compresseurs axiaus," Docteur-ingenieur thesis, Universite De Lyon, 1975.

5 Sitaram, N., and Lakshminarayana, B., "Blade End Wall Flow and Overall Performance of an Axial Compressor Stage," NASA CR 3671, 1983.

6 Lakshminarayana, B., "An Axial Flow Compressor Facility With Instrumentation for Relative Flow Measurement," ASME *Journal of Fluids Engineering*, Vol. 102, 1980.

7 Smith, L. H., Jr., "Three-Dimensional Flow in Axial-Flow Turbomachinery," Wright Air Development Center Technical Report 55-348, Vol. I, Aug. 1955.

8 Treaster, A. L., and Yocum, A. M., "The Calibration and Application of Five Hole Probes," *ISA Transactions*, Vol. 18, No. 3, 1979, pp. 23–34.

9 Sitaram, N., Lakshminarayana, B., and Ravindranath, A., "Conventional Probes for the Relative Flow Measurement in a Turbomachinery Rotor Blade Passage," ASME JOURNAL OF ENGINEERING FOR POWER, Vol. 103, No. 2, Apr. 1981, pp. 406–414.

10 Mager, A., "Generalization of Boundary Layer Momentum Integral Equations to Three-Dimensional Flow Including Those of Rotating Systems," NASA Report No. 1067, 1952.

11 Johnston, J. P., "On the Three-Dimensional Turbulent Boundary Layer Generated by Secondary Flow," ASME *Journal of Basic Engineering*, Vol. 81, No. 3, 1960, p. 233.

12 Horlock, J. H., "Crossflows in Bounded Three-Dimesional Turbulent Boundary Layers," *Journal of Mechanical Engineering Sciences*, Vol. 15, No. 4, 1973, pp. 274–284.

13 Marsh, H., and Horlock, J. H., "Wall Boundary Layers in Turbomachines," *Journal of Mechanical Engineering Sciences*, Vol. 14, No. 6, 1972, pp. 411–423.

Downloaded 01 Jun 2010 to 171.66.16.70. Redistribution subject to ASME license or copyright; see http://www.asme.org/terms/Terms_Use.cfm

W. R. Hawthorne
Cambridge University Engineering Laboratory,
Cambridge, England

C. Wang
Tsing Hua University,
People's Republic of China

C. S. Tan

J. E. McCune

Gas Turbine and Plasma Dynamics Laboratory,
Massachusetts Institute of Technology,
Cambridge, Mass. 02139

Theory of Blade Design for Large Deflections: Part I—Two-Dimensional Cascade

As a step in the development of an analytical method for designing highly loaded, three-dimensional blade profiles for axial compressors and turbines, a simple two-dimensional method was first investigated. The fluid is assumed to be incompressible and inviscid, the blades of negligible thickness, and the mean tangential velocity is prescribed. The blades are represented by a distributed bound vorticity whose strength is determined by the prescribed tangential velocity. The velocity induced by the bound vortices is obtained by a conventional Biot-Savart method assuming a first approximation to the blade profile. Using the blade surface boundary condition, the profile is then obtained by iteration. It is shown that this procedure is successful even for large pitch-chord ratios and large deflections. In order to develop a method for use in three dimensions, the velocity is divided into a pitchwise mean value and a value varying periodically in the pitchwise direction. By using generalized functions to represent the bound vorticity and a Clebsch formulation for the periodic velocity, series expressions are obtained which can be adapted to three-dimensional problems. Several numerical results were obtained using both approaches.

1 Introduction

This paper and its companion (Part II) [1] describe the first stage in the development of a method for designing three-dimensional blade profiles for axial compressors and turbines to produce large deflections and specified whirl or tangential velocities. Several authors, [2, 3, 4, 5] have described methods of designing three-dimensional blade profiles for small deflections in which the blades introduce only small velocity perturbations and a linearized theory may be used. The large deflection nonlinear theory has been developed here in the first instance for the two-dimensional flow through a linear cascade, primarily in order to explore and test methods which would be suitable for use in the design of annular cascades. The fluid is assumed to be incompressible and inviscid and the blades are assumed to have zero thickness and incidence so that there are no stagnation points at the leading edges. The overall deflection and the schedule of pitchwise averaged tangential velocity $\bar{V}_y$ is prescribed at all points within the blade row.

The paper presents first the development of a theory in which the effect of the blades is represented by a distribution of bound vorticity whose strength is determined from the prescribed tangential velocity schedule and which is distributed along assumed blade profiles. The velocity induced by bound vorticity is determined by familiar methods. The expression for the blade profile obtained from the boundary condition at the blade surface is then solved iteratively.

The foregoing procedure which we called the Biot-Savart method is geometrically complicated for use in the three-dimensional case, so we have adopted the Clebsch formulation of the equations of motion as in previous work by the authors and others on the nonaxisymmetric flows entering axial compressor blade rows, as well as in blade wake flows and secondary flows [6–10].

When the problem is formulated in terms of the Clebsch transformation, it enables the flow field, periodic in the pitchwise direction, to be expressed in the form of a series. As before, the equations and the nonlinear boundary condition on the blade surface can be solved for the blade shape in a simple iterative manner. The resulting solution not only gives the blade shape but also the pressure distribution—and the entire flow field if desired.

It should be emphasized that it is not the intention in this paper to present a two-dimensional design method in competition with those of Costello [11], Wilkinson [13], or of Novak and Haymann-Haber [14], the latter of which is similar in spirit to the method based on the Clebsch formulation.

2 Two-Dimensional Cascade Theory

2.1 The Biot-Savart Approach. A common conventional analysis of the potential flow of an incompressible fluid through a two-dimensional cascade assumes that thin blades may be represented by bound vortices of strength $\gamma(x)$

Contributed by the Gas Turbine Division of THE AMERICAN SOCIETY OF MECHANICAL ENGINEERS and presented at the 28th International Gas Turbine Conference and Exhibit, Phoenix, Arizona, March 27-31, 1983. Manuscript received at ASME Headquarters December 22, 1982. Paper No. 83-GT-124.

Copyright © 1984 by ASME
Downloaded 01 Jun 2010 to 171.66.16.70. Redistribution subject to ASME license or copyright; see http://www.asme.org/terms/Terms_Use.cfm

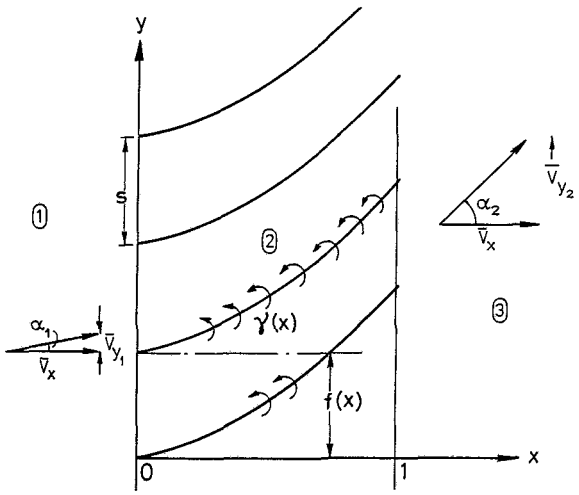


Fig. 1 Two-dimensional cascade: notation

distributed along the camber lines, Fig. 1. The complex potential for the flow induced by such an array of vortices may be written

$$w = -\frac{i}{2\pi}\int_0^1 \gamma(t)\, ln \sinh \frac{\pi}{s}(z-z_0)dt \tag{1}$$

Here

$$w=\phi+i\psi,$$
$$z=x+iy,$$
$$z_0=t+if(t)$$

where z_0 defines the location of the vorticity of strength $\gamma(t)$ on the blade with the leading edge at the origin. The blade spacing or pitch is s, the leading edge of each blade is at $x = 0$, and the trailing edge at $x = 1$, so that all dimensions are scaled by the axial width. We use a right-hand rule to define the sign of the vorticity which is here opposite to that used in conventional two-dimensional airfoil theory. This is done to avoid confusion in the three-dimensional analysis.

We define the blade surfaces by

$$\alpha = y - f(x) = 0, \pm ns \tag{2}$$

where n is an integer.

In conventional cascade theory the flow velocity, $\hat{\mathbf{v}}$, induced by the vortices given by (1), is superimposed on a mean flow which is the vector mean of the upstream and downstream flow so that

$$\mathbf{V} = \mathbf{e}_x \bar{V}_x + \mathbf{e}_y \frac{\bar{V}_{y1}+\bar{V}_{y2}}{2} + \hat{\mathbf{v}} \tag{3}$$

where $\mathbf{e}_x$ and $\mathbf{e}_y$ are unit vectors in the x- and y-direction, respectively, the subscripts x and y denote axial and tangential directions, respectively, 1 and 2 are far upstream and downstream values, and a bar superscript denotes a pitchwise mean value, i.e.,

$$\bar{\mathbf{V}} = \frac{1}{s}\int_0^s \mathbf{V}\, dy \tag{4}$$

The velocity $\hat{\mathbf{v}}$ in (3) induced by the bound vorticity is given by

$$\frac{dw}{dz} = \hat{v}_x - i\,\hat{v}_y = -\frac{i}{2s}\int_0^1 \gamma(t)\, \coth \frac{\pi}{s}(z-z_0)\,dt$$

$$= \frac{-i}{2s}\int_0^1 \gamma(t)\, \frac{\sinh \frac{2\pi}{s}(x-t) - i \sin \frac{2\pi}{s}[y-f(t)]}{\cosh \frac{2\pi}{s}(x-t) - \cos \frac{2\pi}{s}[y-f(t)]}\,dt \tag{5}$$

The boundary conditions upstream and downstream are satisfied by (3) and (5) provided that

$$\bar{V}_{y2} - \bar{V}_{y1} = \frac{1}{s}\int_0^1 \gamma(x)\,dx \tag{6}$$

and, defining a mean boundary vorticity

$$\bar{\gamma}(x) = \gamma(x)/s = \frac{d\bar{V}_y}{dx} \tag{7}$$

we may also write

$$\bar{V}_y = \bar{V}_{y1} + \int_0^x \bar{\gamma}(t)\,dt \tag{8}$$

The remaining boundary condition is on the thin blades. The condition for a zero velocity normal to the blade surface may be written

$$\mathbf{V}_{bl} \cdot \nabla \alpha = 0 \tag{9}$$

where

$$\mathbf{V}_{bl} = (\mathbf{V}^+ + \mathbf{V}^-)/2 \tag{10}$$

i.e., the mean of the velocities on the upper (pressure) surface, $\mathbf{V}^+$, and the lower (suction surface, $\mathbf{V}^-$, Fig. 1, respectively. We note that

$$|\,\mathbf{V}^- - \mathbf{V}^+\,| = \gamma(x) \tag{11}$$

Nomenclature

$\mathbf{e}$ = unit vector
i = imaginary number $\sqrt{-1}$
Im = imaginary part of
m = integer
n = integer
p = pressure
Re = real part of
s = blade spacing or pitch
S = periodic saw tooth function
$\mathbf{V}$ = velocity vector
$\hat{\mathbf{v}}$ = velocity induced by the bound vorticity
w = complex potential
(x,y) = Cartesian coordinate system as shown in Fig. 1
z = coordinate of a point in the complex $x-y$ plane
z_o = location of bound vorticity on blade with leading edge at the origin
α = without subscript refers to blade surface with subscript 1 or 2 refers to the blade angle
δ = Dirac delta function
γ = strength of bound vorticity along camber lines
λ = scalar
μ = scalar
ϕ = real part of complex potential or velocity potential
ψ = imaginary part of complex potential or stream function
Ω = vorticity

Subscripts

bl = at the blade
x = in the x-direction or differentiation wrt x
y = in the y-direction or differentiation wrt y
1 = far upstream or upstream of the blade leading edge
2 = within the blade or far downstream
3 = downstream of the blade trailing edge

Superscripts

$-$ = pitchwise mean value
$+$ = pressure surface
$-$ = suction surface
$'$ = differentiation wrt argument

Downloaded 01 Jun 2010 to 171.66.16.70. Redistribution subject to ASME license or copyright; see http://www.asme.org/terms/Terms_Use.cfm

We may write the blade boundary condition (9) in the form

$$\bar{V}_x \frac{df}{dx} = \frac{\bar{V}_{y1} + \bar{V}_{y2}}{2} + \hat{\mathbf{v}}_{bl} \cdot \nabla \alpha \tag{12}$$

Now

$$\begin{aligned} \hat{\mathbf{v}}_{bl} \cdot \nabla \alpha &= \hat{v}_{ybl} - \hat{v}_{xbl} f' \\ &= \mathrm{Re}(\hat{v}_{xbl} - i\, \hat{v}_{ybl})\,(i - f') \\ &= -Im(1 + i f') \frac{dw}{dz}\Big|_{bl} \end{aligned} \tag{13}$$

where $f' = df/dx$.

Writing $w = F(z)$,

$$\frac{dw}{dz}\Big|_{bl} = F'(x + if)$$

Hence (13) becomes

$$\hat{\mathbf{v}}_{bl} \cdot \nabla \alpha = -Im \frac{d}{dx} F(x + if)$$

so that (12) becomes

$$\frac{df}{dx} = \frac{\tan \alpha_1 + \tan \alpha_2}{2} - Im \frac{1}{\bar{V}_x} \frac{d}{dx} F(x + if)$$

or, using (5),

$$\frac{df}{dx} =$$

$$\frac{s}{4\pi} \int_0^1 \frac{\bar{\gamma}(t)}{\bar{V}_x} \frac{d}{dx} ln\left(\cosh \frac{2\pi}{s}(x - t) - \cos \frac{2\pi}{s}[f(x) - f(t)]\right) dt$$

$$+ \frac{\tan \alpha_1 + \tan \alpha_2}{2} \tag{14}$$

If $f = 0$ at $x = 0$, the leading edge, (14), may be integrated to give

$$f =$$

$$\frac{s}{4\pi} \int_0^1 \frac{\bar{\gamma}(t)}{\bar{V}_x} ln\left\{ \frac{\cosh \frac{2\pi}{s}(x - t) - \cos \frac{2\pi}{s}[f(x) - f(t)]}{\cosh \frac{2\pi t}{s} - \cos \frac{2\pi}{s} f(t)} \right\} dt$$

$$+ x \frac{\tan \alpha_1 + \tan \alpha_2}{2} \tag{15}$$

The procedure for solution is to assume that $\bar{\gamma}(x)$ or $\bar{V}_y$ is known and substitute initial values of f and df/dx in the r.h.s. of (14) and (15) and iterate.

It is convenient to use the mean streamlines to give the initial values of f. It is found that up to quite large values of the pitch, s, convergence can be obtained fairly rapidly particularly if a relaxation factor is introduced. Details of the numerical procedure are given in the Appendix.

3 The Clebsch Approach for Two- and Three-Dimensional Blade Rows

Section 2.1 shows the use of the Biot-Savart Law for the determination of the camber line for two-dimensional cascade. However, its use for three-dimensional annular blade rows is complicated and a simpler method is to be preferred. For this reason, the Clebsch transformation was adopted in the procedure for determining the blade shape required to produce a specified mean tangential or swirl velocity schedule in an annular blade row. The two-dimensional cascade was the starting point for the development of this procedure.

3.1 Clebsch Formulation of Steady Rotational Flow. In the Clebsch formulation of steady rotational flow, the velocity vector, $\mathbf{V}$ is decomposed into a "potential" part as well as a rotational part. Thus $\mathbf{V}$ is written in the form of a sum

$$\mathbf{V} = \nabla \phi + \lambda \nabla \mu \tag{16}$$

where ϕ, λ, μ are scalars, and the term $\lambda \nabla \mu$ is that part of the velocity vector which accounts for the rotationality of the flow (see Lamb [15], p. 248). By taking the curl of equation (16), we obtain the vorticity as

$$\underset{\sim}{\Omega} = \nabla \lambda \times \nabla \mu \tag{17}$$

The Clebsch formulation has been used extensively in studies of rotational flows, e.g., shear and skew flows, [10] wake flows, [6, 7, 8, 9], and in nonaxisymmetric flows, i.e., inlet distortion studies [7]. The scalars λ and μ are related to appropriate physical surfaces in the flow, e.g., Bernoulli surfaces (constant stagnation pressure, etc.), sheets of vorticity (wakes from blades) and drift surfaces. In this paper, we shall relate the scalars λ and μ to the blade circulation and a function of the blade shape. The Clebsch approach is developed here for the two-dimensional cascade and then, in a second paper [1], it is applied in the derivation of the flow in annular blade rows.

4 The Clebsch Approach for Two-Dimensional Cascades

The bound vorticity on the blades can be written in terms of a periodic delta function, viz:

$$\Omega = (\nabla \bar{V}_y \times \nabla \alpha) s \sum_{m=-\infty}^{\infty} \delta(\alpha - ms) \tag{18}$$

Hence, in the blade row the mean vorticity becomes

$$\begin{aligned} \bar{\Omega} &= (\nabla \bar{V}_y \times \nabla \alpha) \frac{1}{s} \int_0^s s \sum_{-\infty}^{+\infty} \delta(\alpha - ms)\, dy \\ &= \nabla \bar{V}_y \times \nabla \alpha \end{aligned} \tag{19}$$

where the integral is taken over the complete blade pitch including the blade. In equations (18) and (19), s is the blade spacing.

A Clebsch formulation for the mean velocity is then $0 < x < 1$

$$\bar{\mathbf{V}} = \nabla \phi(x) + \bar{V}_y \nabla \alpha = \mathbf{e}_x \bar{V}_x + \mathbf{e}_y \bar{V}_y \tag{20}$$

We note that the curl of (20) gives (19) as it should.

We obtain the complete velocity field by adding a velocity periodic in y

$$\mathbf{v}_2 = \nabla \phi_2 - S(\alpha) \nabla \bar{V}_y \tag{21}$$

Now

$$\begin{aligned} \underset{\sim}{\Omega} &= \nabla \times \bar{\mathbf{V}} + \nabla \times \underset{\sim}{\mathrm{v}}_2 \\ &= (\nabla \bar{V}_y \times \nabla \alpha)(1 + S'(\alpha)) \end{aligned}$$

On comparing this with (18), we find

$$S'(\alpha) = s \sum_{m=-\infty}^{\infty} \delta(\alpha - ms) - 1$$

Lighthill [16] shows that a periodic delta function may be expressed in a Fourier series, i.e.,

$$s \sum_{m=-\infty}^{\infty} \delta(\alpha - ms) = \sum_{m=-\infty}^{\infty} \exp\left(im \frac{2\pi\alpha}{s}\right)$$

so that $S(\alpha)$ is the periodic "saw-tooth" function given by

Downloaded 01 Jun 2010 to 171.66.16.70. Redistribution subject to ASME license or copyright; see http://www.asme.org/terms/Terms_Use.cfm

$$S(\alpha) = +2\mathrm{Re}\sum_{n=1}^{\infty} e^{in\frac{2\pi}{s}\alpha} \Big/ \left(\frac{in\,2\pi}{s}\right) \tag{22}$$

We separate the flow regime into three zones (Fig. 1).

(*i*) upstream of the cascade in which the flow is irrotational with velocity

$$\mathbf{V} = \bar{V}_x \mathbf{e}_x + \bar{V}_{y1}\mathbf{e}_y + \mathbf{v}_1$$

where

$$\mathbf{v}_1 = \nabla\phi_1 \tag{23}$$

represents a periodic velocity which vanishes far upstream of the cascade.

(*ii*) A flow within the blade row given by

$$\mathbf{V} = \bar{V}_x\hat{\mathbf{e}}_x + \bar{V}_y\hat{\mathbf{e}}_y + \mathbf{v}_2 \tag{24}$$

where $\mathbf{v}_2$ is given by (21).

(*iii*) Downstream of the cascade in which the flow is irrotational with velocity

$$\mathbf{V} = \bar{V}_x\hat{\mathbf{e}}_x + \bar{V}_{y2}\hat{\mathbf{e}}_y + \mathbf{v}_3$$

where

$$\mathbf{v}_3 = \nabla\phi_3 \tag{25}$$

represents the periodic velocity which vanishes far downstream of the cascade.

At the leading and trailing edges the boundary conditions are

at $x = 0$

$$\mathbf{v}_1 = \mathbf{v}_2$$

and at $x = 1$

$$\mathbf{v}_2 = \mathbf{v}_3 \tag{26}$$

The remaining boundary condition is at the blade surfaces which may be expressed as

$$\mathbf{V}_{bl}\cdot\nabla\alpha = 0$$

or

$$\bar{V}_x\frac{df}{dx} = \bar{V}_y + \mathbf{v}_{bl}\cdot\nabla\alpha \tag{27}$$

Applying the continuity condition to expressions (23), (24), (25), and (26) we obtain

$$\nabla^2\phi_1 = 0 \tag{28a}$$

$$\nabla^2\phi_2 = \nabla\cdot(S(\alpha)\nabla\bar{V}_y) \tag{28b}$$

and

$$\nabla^2\phi_3 = 0 \tag{28c}$$

Expressions satisfying these equations are of the form

$$\phi_1 = \sum_{n=1}^{\infty} A_n e^{i\lambda_n y}e^{\lambda_n x} \tag{29a}$$

$$\phi_2 = \sum_{n=1}^{\infty} e^{i\lambda_n y}\left(B_{n1}e^{\lambda_n x} + B_{n2}e^{-\lambda_n x} + X_n(x)\right) \tag{29b}$$

$$\phi_3 = \sum_{n=1}^{\infty} C_n e^{i\lambda_n y}e^{-\lambda_n x} \tag{29c}$$

where

$$\lambda_n = n\,2\pi/s \tag{30}$$

and A_n, B_{n1}, B_{n2}, C_n are constants, and real parts are to be taken.

The expressions (29*a*) and (29*c*) satisfy the boundary conditions at infinity that the flow be uniform. The inhomogeneous part of (29*b*) may be obtained by substituting (29*b*) in (28*b*) giving

$$\sum_{n=1}^{\infty} e^{i\lambda_n y}(X_n'' - \lambda_n^2 X_n) = \nabla\cdot(S(\alpha)\nabla\bar{V}_y) \tag{31}$$

On substituting $\bar{\gamma}(x) = d\bar{V}_y/dx$ and using (22) for the sawtooth function series we obtain

$$X_n'' - \lambda_n^2 X_n = \frac{d}{dx}\frac{2\bar{\gamma}(x)}{i\lambda_n}e^{-i\lambda_n f(x)} \tag{32}$$

The solution by the method of variation of parameters gives

$$X_n = \int^x \frac{e^{\lambda_n(x-t)} - e^{-\lambda_n(x-t)}}{2\lambda_n}\frac{d}{dt}\left(\frac{2\bar{\gamma}(t)}{i\lambda_n}e^{-i\lambda_n f(t)}\right)dt + c_1e^{\lambda_n x} + c_2e^{-\lambda_n x} \tag{33}$$

The constants c_1 and c_2 in the last two terms depend on the limits in the integral and may be absorbed in the homogeneous part of ϕ_2 (29*b*). A convenient choice of limits gives

$$X_n(x) = \int_1^x \frac{e^{\lambda_n(x-t)}}{i\lambda_n^2}\frac{d}{dt}(\bar{\gamma}(t)e^{-i\lambda_n f})\,dt - \int_0^x \frac{e^{-\lambda_n(x-t)}}{i\lambda_n^2}\frac{d}{dt}(\bar{\gamma}(t)e^{-i\lambda_n f})\,dt \tag{34}$$

On integrating by parts we obtain

$$X_n(x) = \left(\frac{\bar{\gamma}(t)e^{-i\lambda_n f(t)}}{i\lambda_n^2}\right)_1^x - \left(\frac{\bar{\gamma}(t)e^{-i\lambda_n f(t)}}{i\lambda_n^2}\right)_0^x + \int_1^x \frac{e^{\lambda_n(x-t)}}{i\lambda_n}\bar{\gamma}(t)e^{-i\lambda_n f(t)}\,dt + \int_0^x \frac{e^{-\lambda_n(x-t)}}{i\lambda_n}\bar{\gamma}(t)e^{-i\lambda_n f(t)}\,dt \tag{35}$$

At this point we observe that if the Kutta condition at the trailing edge is to be satisfied then

$$\bar{\gamma}(1) = 0 \tag{36}$$

(see section (2.3) in Part II [1]) and that $\bar{\gamma}(x)$ is not likely to become singular except at the leading edge, where at the most it may have a logarithmic singularity since the total circulation round the blade must remain finite. For the moment, we shall assume that in this design problem we shall specify zero incidence at the leading edge so that

$$\bar{\gamma}(0) = 0 \tag{37}$$

and leave nonzero and singular values of $\bar{\gamma}(0)$ for later consideration. Hence (35) becomes

$$X_n(x) = \frac{-i}{\lambda_n}\int_0^x e^{-\lambda_n(x-t)}e^{-i\lambda_n f(t)}\bar{\gamma}(t)\,dt + \frac{i}{\lambda_n}\int_x^c e^{\lambda_n(x-t)}e^{-i\lambda_n f(t)}\bar{\gamma}(t)\,dt \tag{38}$$

On differentiating

$$X_n'(x) = i\int_0^1 \bar{\gamma}(t)e^{-\lambda_n|x-t|}e^{-i\lambda_n f(t)}\,dt - \frac{i2\bar{\gamma}(x)e^{-i\lambda_n f(x)}}{\lambda_n} \tag{39}$$

Hence

$$X_n'(0) = \lambda_n X_n(0) \tag{40a}$$

and

$$X_n'(1) = -\lambda_n X_n(1) \tag{40b}$$

Matching conditions at the leading edge $x = 0$ (equation (26)) yields

Downloaded 01 Jun 2010 to 171.66.16.70. Redistribution subject to ASME license or copyright; see http://www.asme.org/terms/Terms_Use.cfm

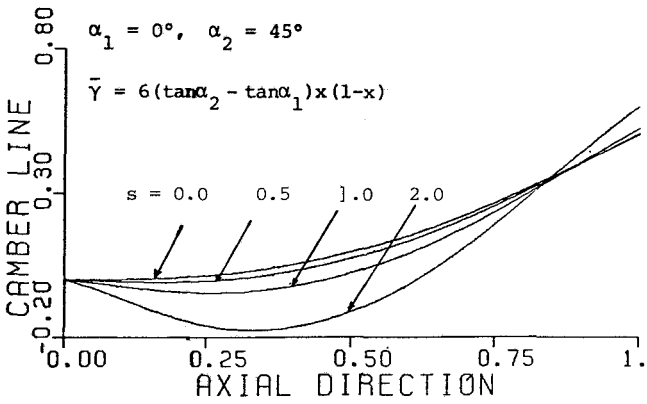


Fig. 2 Two-dimensional guide vane: profiles

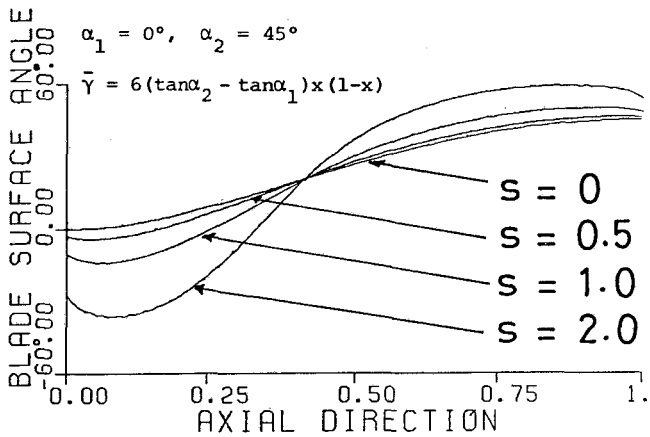


Fig. 3 Two-dimensional guide vane: blade surface angle

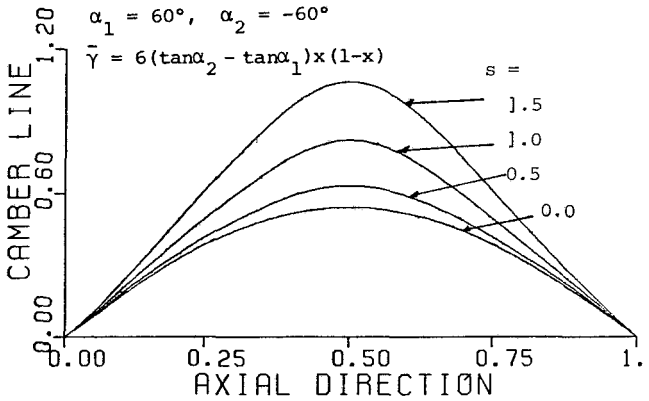


Fig. 4 Two-dimensional impulse turbine cascade

$$\phi_{1y} = \phi_{2y}$$

hence

$$A_n = B_{n_1} + B_{n_2} + X_n(0) \tag{41a}$$

and

$$v_{x_1} = v_{x_2} = \frac{\partial \phi_2}{\partial x} - \bar{\gamma}(0) S(\alpha)$$

or

$$\lambda_n A_n = \lambda_n B_{n_1} - \lambda_n B_{n_2} + X_n'(0) \tag{41b}$$

Equations (40*a*), (41*a*), (41b) yield

$$B_{n_2} = 0 \tag{42}$$

At the trailing edge, $x = 1$

$$\phi_{3y} = \phi_{2y}$$

hence

$$C_n e^{-\lambda_n} = B_{n_1} e^{\lambda_n} + X_n(1) \tag{43a}$$

and

$$v_{x_3} = v_{x_2} = \frac{\partial \phi_2}{\partial x} - \bar{\gamma}(1) S(\alpha),$$

$$-\lambda_n C_n e^{-\lambda_n} = \lambda_n B_{n_1} e^{\lambda_n} + X_n'(1) \tag{43b}$$

Equations (40*b*), (43*a*), and (43*b*) yield

$$B_{n_1} = 0 \tag{44}$$

Hence

$$v_{y_2} = \sum_{n=1}^{\infty} i\lambda_n X_n(x) e^{i\lambda_n y}$$

$$= \sum_{n=1}^{\infty} \int_0^1 \operatorname{sgn}(x-t)\, \bar{\gamma}(t) \exp(-\lambda_n |x-t| + i\lambda_n (y - f(t)))\, dt \tag{45}$$

where for $x > 0$, sgn $(x) = +1$ and for $x < 0$, sgn $(x) = -1$, and

$$v_{x_2} = \sum_{n=1}^{\infty} X_n'(x) e^{i\lambda_n y} - S(\alpha)\bar{\gamma}(x)$$

From (22) and (39)

$$v_{x_2} = \sum_{n=1}^{\infty} i \int_0^1 \bar{\gamma}(t) \exp\{-\lambda_n |x-t| + i\lambda_n (y - f(t))\}\, dt \tag{46}$$

These results may be used in (27) by writing $y = f(x)$ to obtain $\mathbf{v}_{bl}$.

As in section 2.1, equation (27) may be solved by iterative methods. Now

$$\sum_{n=1}^{\infty} x^n = \frac{x}{1-x} = \frac{1}{1-x} - 1$$

so that the series of exponential terms in (45) and (46) may be summed to give

$$\sum_{n=1}^{\infty} \exp\left\{-n \frac{2\pi}{s} (|x-t| - i(y - f(t)))\right\}$$

$$= \frac{\exp\left(\frac{2\pi}{s}|x-t|\right) - \cos\frac{2\pi}{s}(y-f) + i \sin\frac{2\pi}{s}(y-f)}{2\left(\cosh\frac{2\pi}{s}(x-t) - \cos\frac{2\pi}{s}(y-f)\right)} \tag{47}$$

Now noting that

$$\exp\left(\frac{2\pi}{s}|x-t|\right) = \cosh\frac{2\pi}{s}(x-t) + \operatorname{sgn}(x-t) \sinh\frac{2\pi}{s}(x-t)$$

the real parts of (45) and (46) become

$$v_{y_2} = \frac{1}{2} \int_0^1 \bar{\gamma}(t)\, dt \left(\frac{\sinh\frac{2\pi}{s}(x-t)}{\cosh\frac{2\pi}{s}(x-t) - \cos\frac{2\pi}{s}(y-f)} - \operatorname{sgn}(x-t) \right) \tag{48a}$$

Downloaded 01 Jun 2010 to 171.66.16.70. Redistribution subject to ASME license or copyright; see http://www.asme.org/terms/Terms_Use.cfm

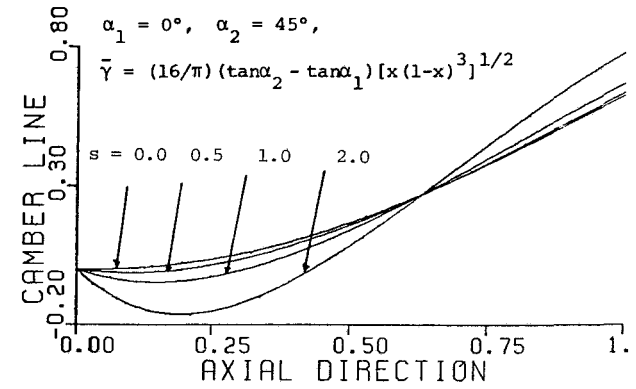


Fig. 5 Two-dimensional inlet guide vane: profiles

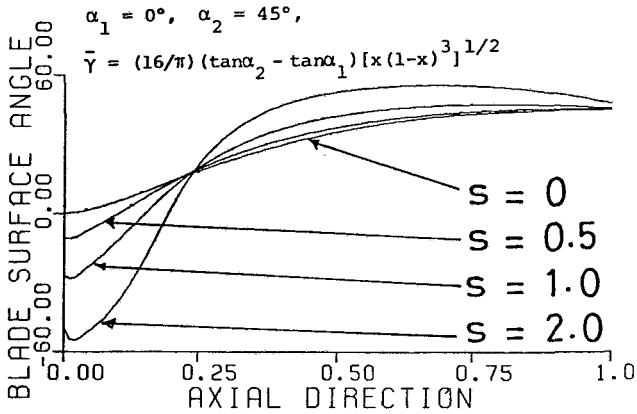


Fig. 6 Two-dimensional guide vane: blade surface angle

$$v_{x_2} = -\frac{1}{2}\int_0^1 \bar{\gamma}(t)\,dt\left(\frac{\sin\frac{2\pi}{s}(y-f)}{\cosh\frac{2\pi}{s}(x-t)-\cos\frac{2\pi}{s}(y-f)}\right). \tag{48b}$$

We note that

$$\mathbf{v}_{bl}\cdot\nabla\alpha = v_{y_{2bl}} - f'(x)\,v_{x_{2bl}} \tag{49}$$

and that

$$\frac{1}{2}\int_0^1 \operatorname{sgn}(x-t)\,\bar{\gamma}(t)\,dt = \frac{1}{2}\{(\bar{V}_y)_0^x - (\bar{V}_y)_x^1\} = \bar{V}_y - \frac{\bar{V}_{y_1}-\bar{V}_{y_2}}{2} \tag{50}$$

so that the result given in equation (14) may be recovered from (27), (48*a*), (48*b*), (49), and (50).

Most calculations were performed using the equations given in section 2, but some numerical results were obtained from the series solutions given above to explore results obtained from the three-dimensional analysis.

5 Results

Programs were written for the computation of the thin blade profiles in a two-dimensional cascade. As already noted, the fluid was assumed to be inviscid and incompressible. The variation along the chord of the strength of the bound vortices representing the blades was assumed initially to be parabolic, i.e., proportional to $x(1-x)$. The zero values of the vorticity at the trailing and leading edges given by this expression satisfy the Kutta condition at the trailing edge and give zero incidence at the leading edge.

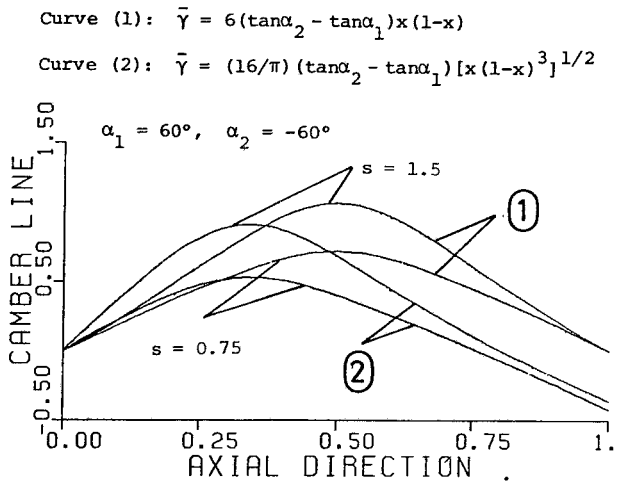


Fig. 7 Two-dimensional turbine cascade: effect of loading distribution

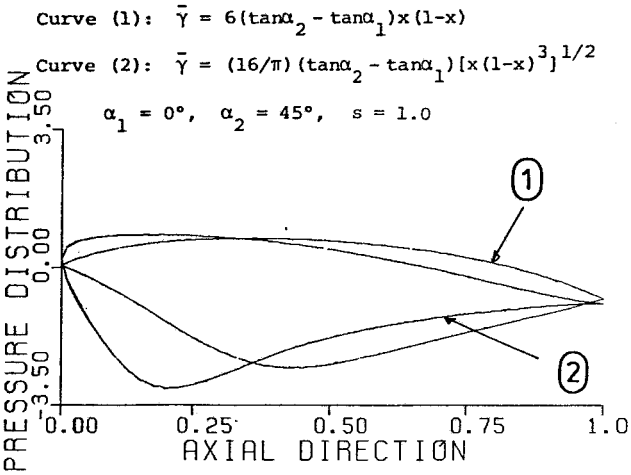


Fig. 8 Two-dimensional inlet guide vane: pressure distribution normalized by far upstream dynamic head

As already noted the objective was not to produce a two-dimensional design method but to prepare the way for a three-dimensional method by checking first whether the proposed iterative technique would be satisfactory, exploring the use of the Clebsch method and providing some basic results for comparison with three-dimensional solutions. For this reason, equations (A10) and (A11) were used in writing the programs in order to separate mean and periodic velocities. Only a few results are presented to show the limits reached in the numerous calculations.

Figures 2 and 3 show the profile and blade angles for a two-dimensional cascade with air inlet angle $\alpha_1 = 0$ deg and air outlet angle $\alpha_2 = 45$ deg, representing a row of inlet guide vanes. The computation involves an integration by a Newton-Cotes formula (Appendix) with the integral evaluated at 101 equally spaced points on the axial chord. However, the results given in Table I were obtained using 301 points and 18 iterations giving a maximum difference in the value of f (the y-coordinate of the blade profile) between the 17th and 18th iteration of 10^{-5} axial widths at any point.

It is of interest to note the reverse curvature of the blade near the trailing edge and the large negative blade angles required to obtain zero incidence at the leading edge.

A more stringent test of the iteration procedure is given by the design of an impulse blade with 120 deg deflection, Fig. 4. At pitch to the axial chord ratios above 1.5, convergence

Downloaded 01 Jun 2010 to 171.66.16.70. Redistribution subject to ASME license or copyright; see http://www.asme.org/terms/Terms_Use.cfm

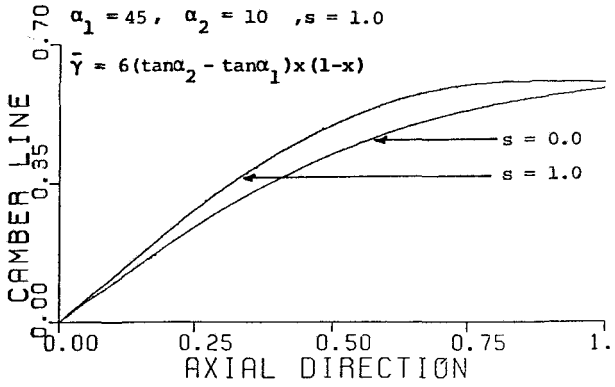


Fig. 9(a) Two-dimensional compressor cascade: profiles

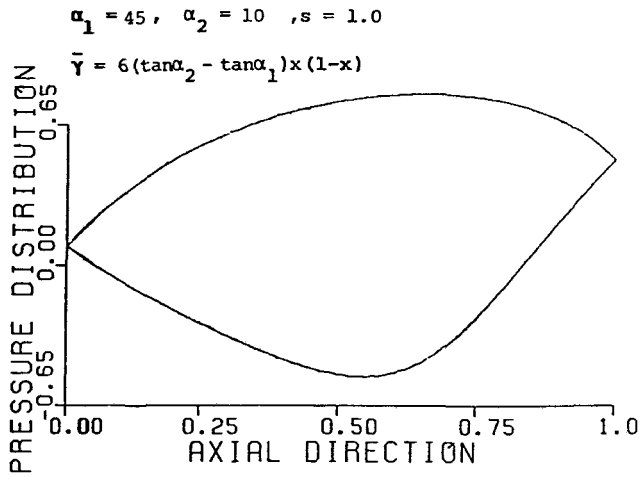


Fig. 9(b) Two-dimensional compressor cascade: pressure distribution normalized by far upstream dynamic head

becomes slow. Figures 5, 6, and 7 show the effect of a different loading, i.e.,

$$\bar{\gamma} \propto (\sin\beta - \frac{1}{2}\sin 2\beta) \tag{51a}$$

where

$$x = (1+\cos\beta)/2 \tag{51b}$$

Figures 5 and 6 show curves similar to these of Figs. 2 and 3 for inlet guide vanes, and Fig. 7 compares high deflection turbine cascades with different loadings.

The expression (51) brings the point of maximum loading, i.e., bound vortex strength, forward to one-quarter chord from the leading edge. Other loadings have been tried successfully, including one with a singularity at the leading edge as in the Glauert series for the bound vortex strength on an isolated aerofoil.

Some pressure distributions are shown in Figs. 8, 9, and 10 for two-dimensional cascades of inlet guide vanes, compressor cascades, and turbines with the different loadings.

Many other calculations were performed and the effect of number of terms used in the Clebsch method was explored. It was found that good accuracy was obtained with 15 or 20 terms.

6 Conclusions

The convergence of the iterative procedure for determining the blade profile using both the Clebsch and the Biot-Savart approach is satisfactory for the range of pitch-chord ratios and deflections of practical importance. Hence the procedure was adopted for use in the development of the theory of the

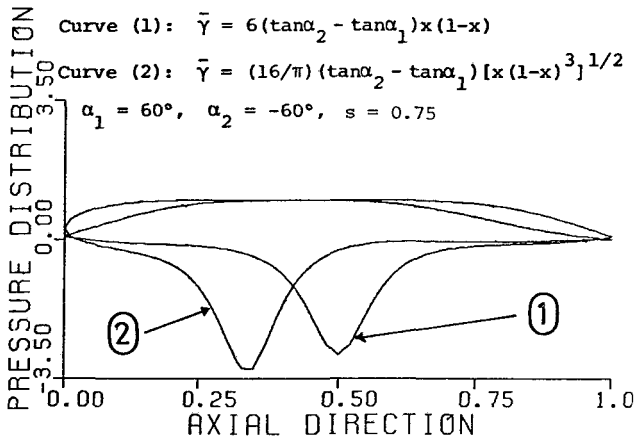


Fig. 10 Two-dimensional turbine cascade: pressure distribution normalized by far upstream dynamic head

Table 1 Two-dimensional inlet guide vane, $s = 1.0$

x	Mean streamline y-coordinate	Blade profile y-coordinate	Blade angle deg
0	0	0	−10.49768
0.05	0.00012	−0.01174	−14.23379
0.10	0.00095	−0.02438	−13.51160
0.15	0.00312	−0.03535	−10.76986
0.20	0.00720	−0.04312	−6.52426
0.25	0.01367	−0.04658	−1.10216
0.30	0.02295	−0.04491	5.14522
0.35	0.03537	−0.03749	11.79599
0.40	0.05120	−0.02399	18.40724
0.45	0.07062	−0.00424	24.58522
0.50	0.09375	0.02170	30.08641
0.55	0.12062	0.05360	34.80161
0.60	0.15120	0.09109	38.73239
0.65	0.18537	0.13369	41.95433
0.70	0.22295	0.18087	44.55325
0.75	0.26367	0.23204	46.61130
0.80	0.30720	0.28656	48.18797
0.85	0.35312	0.34374	49.30482
0.90	0.40095	0.40270	49.92021
0.95	0.45012	0.46230	49.84225
1.00	0.50000	0.52039	47.93311

design of three-dimensional annular cascades reported in Part II [1].

The work has been extended to radial cascades, e.g., diffuser vanes for centrifugal compressors, and needs to be extended to compressible flow and blades with thickness.

Acknowledgments

This research was partially supported by the Air Force Office of Scientific Research under Contract No. F49620-82-K-0002, Dr. J. D. Wilson, Program Manager. The authors are also grateful to the staff of the Gas Turbine and Plasma Dynamics Laboratory, M.I.T., and the Whittle Laboratory, University of Cambridge, and E. R. Beggs for their assistance.

References

1 Tan, C. S., Hawthorne, W. R., McCune, J. E., and Wang, C., "Theory of Blade Design for Large Deflections: Part II—Annular Cascades," ASME JOURNAL OF ENGINEERING FOR POWER, Vol. 106, April 1984, pp. 354–365.

2 McCune, J. E., "A Three-Dimensional Theory of Axial Compressor Blade Rows—Subsonic, Supersonic and Transonic," Ph.D. thesis, Cornell Univ., 1958 (see also USAFOSR TN-58-72, *J. Aerospace Sc.*, 544 and 616, 1958).

3 Okuroumu, O., and McCune, J. E., "Lifting Surface Theory of Axial Compressor Blade Rows: Part I—Subsonic Compressor; Part II—Transonic Compressor," *AIAA Journal*, Vol. 12, 1974, pp. 1363 and 1372.

4 Namba, M., "Lifting Surface Theory for a Rotating Subsonic or Transonic Blade Row," ARC R&M, #3740, 1974.

5 Homicz, G. F., and Lordi, J. A., "Three-Dimensional Lifting-Surface Theory for an Annular Blade Row," *AIAA Journal*, Vol. 19, No. 4, 1980, pp. 492–500.

Downloaded 01 Jun 2010 to 171.66.16.70. Redistribution subject to ASME license or copyright; see http://www.asme.org/terms/Terms_Use.cfm

6 Tan, C. S., "Three-Dimensional, Vorticity-Induced Flow Effects in Highly-Loaded Axial Compressors," Ph.D. thesis, Massachusetts Institute of Technology, June 1978 (also GT&PDL Report Nos. 131 and 151).

7 Hawthorne, W. R., McCune, J. E., Mitchell, N. A., and Tan, C. S., "Nonaxisymmetric Flow Through an Annular Actuator Disk; Inlet Distortion Problem," JOURNAL OF ENGINEERING FOR POWER, Vol. 100, 1978, p. 604.

8 Tan, C. S., "Vorticity Modelling of Blade Wakes Behind Isolated Annular Blade-Rows: Induced Disturbances in Swirling Flows," ASME JOURNAL OF ENGINEERING FOR POWER, Vol. 103, No. 2, Apr. 1981.

9 Tan, C. S., "Three-Dimensional Incompressible and Compressible Beltrami Flow Through a Highly-Loaded Isolated Rotor," MIT GT&PDL Report 147, 1980.

10 Hawthorne, W. R., "On The Theory of Shear Flow," MIT GTL Report 88.

11 Costello, G. R., Cummings, R. L., and Sinnette, J. T., "Detailed Computational Procedure for Design of Cascade Blades With Prescribed Velocity Distributions in Compressible Flows," NACA Report 1060, 1952.

12 Stanitz, J. D., "Design of Two-Dimensional Channels With Prescribed Velocity Distributions Along the Channel Walls," NACA Report 1115, 1953.

13 Wilkinson, D. H., "A Numerical Solution of the Analysis and Design Problems for the Flow Past One or More Aerofoils or Cascades," ARC R&M 3545, 1968.

14 Novak, R. A., Haymann-Haber, G., "A Mixed-Flow Cascade Passage Design Procedure Based on a Power Series Expansion," ASME Paper No. 82-GT-121.

15 Lamb, H., *Hydrodynamics*, 6th ed., Dover, 1945.

16 Lighthill, M. J., "An Introduction to Fourier Analysis and Generalized Functions," Cambridge University Press, 1969.

APPENDIX

The determination of the blade profile for the two-dimensional cascade by the Biot-Savart method requires the integration of the functions in equations (14) and (15), each of which has a singularity at $t = x$. As $t \to x$

$$f(x) - f(t) \to (x-t) f'(x) \tag{A1}$$

For $t \to x$, the terms in the integral in equation (14) may be expanded to give approximately

$$\frac{\bar{\gamma}(x)}{2} \frac{\frac{2\pi}{s}(x-t)\left(1+f'^2(x)\right)}{\frac{1}{2}\left(\frac{2\pi}{s}(x-t)\right)^2\left(1+f'^2(x)\right)} = \bar{\gamma}(x)/\left(\frac{2\pi}{s}(x-t)\right) \tag{A2}$$

Equation (14) then may be written

$$\frac{df}{dx} = (\tan\alpha_1 + \tan\alpha_3)/2 + \int_0^1 F_1(x,t)\,dt + \frac{s\bar{\gamma}(x)}{2\pi}\int_0^1 dt/(x-t) \tag{A3}$$

where

$$F_1(x,t) = \frac{\bar{\gamma}(t)}{2} \frac{\sinh\frac{2\pi}{s}(x-t) + f'(x)\sin\frac{2\pi}{s}(f(x)-f(t))}{\cosh\frac{2\pi}{s}(x-t) - \cos\frac{2\pi}{s}(f(x)-f(t))} - \frac{s\bar{\gamma}(x)}{2\pi}\frac{1}{(x-t)} \tag{A4}$$

and $\bar{V}_x$ is assumed to be unity. On taking the principal value of the second integral we obtain

$$\frac{df}{dx} - (\tan\alpha_1 + \tan\alpha_3)/2 + \int_0^1 F_1(x,t)\,dt + \frac{s\bar{\gamma}(x)}{2\pi}\ln\frac{x}{1-x} \tag{A5}$$

Because $\bar{\gamma}(0) = \bar{\gamma}(1) = 0$, the last term on the right-hand side of this equation vanishes at $x = 0$ and 1. The integrand $F_1(x,t)$ is now no longer singular as $F_1(x, t=x) = 0$ and the integral can be computed by any of the standard methods.

When $t \to x$ the integral in equation (15) has a term

$$\frac{s\gamma(t)}{4\pi}\ln\left\{\cosh\left(\frac{2\pi}{s}\overline{x-t}\right) - \cos\left(\frac{2\pi}{s}\overline{f(x)-f(t)}\right)\right\}$$

which approaches

$$\frac{s\bar{\gamma}(x)}{4\pi}\ln\left\{\left(\frac{2\pi}{s}\overline{x-t}\right)^2(1+f'^2(x))/2\right\} \tag{A6}$$

Equation (15) may then be written

$$f(x) = x(\tan\alpha_1 + \tan\alpha_3)/2 + \int_0^1 F_2(x,t)\,dt + \frac{s\bar{\gamma}(x)}{4\pi}\left\{\ln\left(\frac{2\pi}{s}2(1+f'^2(x))/2\right) + \int_0^1 \ln((x-t)^2)dt\right\} \tag{A7}$$

where $\bar{V}_x$ is assumed to be unity and

$$F_2(x,t) = \frac{s\bar{\gamma}(t)}{4\pi}\ln\left\{\frac{\cosh\frac{2\pi}{s}\overline{x-t} - \cos\frac{2\pi}{s}\overline{f(x)-f(t)}}{\cosh\frac{2\pi}{s}t - \cos\frac{2\pi}{s}f(t)}\right\}$$

$$- \frac{s\bar{\gamma}(x)}{4\pi}\ln\left\{\left(\frac{2\pi}{s}\overline{x-t}\right)^2(1+f'^2(x))/2\right\} \tag{A8}$$

The final expression for $f(x)$ is obtained by taking the principal value of the last integral in (A7),

$$f(x) = x(\tan\alpha_1 + \tan\alpha_3)/2 + \int_0^1 F_2(x,t)\,dt + \frac{s\bar{\gamma}(x)}{2\pi}\left\{\ln\frac{2\pi}{s} + \frac{1}{2}\ln\left(\frac{1+f'^2(x)}{2}\right) + x\ln x + (1-x)\ln(1-x) - 1\right\} \tag{A9}$$

It was convenient to rewrite equations (14) and (15) in the form

$$\bar{V}_x\frac{df}{dx} = \bar{V}_y + \frac{1}{2}\int_0^1 \bar{\gamma}(t)\left\{\frac{\sinh B + f'(x)\sin A}{\cosh B - \cos A} - \mathrm{sgn}(x-t)\right\}dt \tag{A10}$$

and

$$\bar{V}_x f(x) = \int_0^1 \bar{V}_y dx + \frac{1}{2}\int_0^1 \gamma(t)\left(\frac{s}{2\pi}\ln(\cosh B - \cos A) - |x-t|\right)_0^x dt \tag{A11}$$

Where $B = (2\pi/s)(x-t)$; $A = (2\pi/s)(f(x) - f(t))$. The singularities were removed from the integrals as before and the expression for $\bar{V}_y$ and its integral obtained analytically from the assumed value of the loading $\bar{\gamma}(x)$. When $\bar{\gamma}(0) \neq 0$, a singularity occurs in the integral when $t = 0$ which may be removed by similar techniques.

Downloaded 01 Jun 2010 to 171.66.16.70. Redistribution subject to ASME license or copyright; see http://www.asme.org/terms/Terms_Use.cfm

Theory of Blade Design for Large Deflections: Part II—Annular Cascades

C. S. Tan
Gas Turbine and Plasma Dynamics Laboratory, Massachusetts Institute of Technology, Cambridge, Mass. 02139

W. R. Hawthorne
Cambridge University Engineering Laboratory, Cambridge, England

J. E. McCune
Gas Turbine and Plasma Dynamics Laboratory, Massachusetts Institute of Technology, Cambridge, Mass. 02139

C. Wang
Tsing Hua University, People's Republic of China

A method of designing highly loaded blades to give a specified distribution of swirl is presented. The method is based on a newly developed, three-dimensional analysis. In the present application, the flow is assumed to be incompressible and inviscid (the annulus has constant hub and tip radii), and the blades are of negligible thickness. A simple free vortex swirl schedule is assumed. The flow velocity is divided into circumferentially averaged and periodic terms. The Clebsch formulation for the periodic velocities is used, and the singularities are represented by periodic generalized functions so that solutions may be obtained in terms of eigenfunctions. The blade profile is determined iteratively from the blade boundary condition. Results from the computer program show how blade number, aspect, and hub-tip ratios affect the blade shape. The blade profiles for a given swirl schedule depend not only on the aspect ratio but also on the stacking position (i.e., the chordwise location at which this thin blade profile is radial), and so too do the mean axial and radial velocities. These effects occur whether the number of blades is large or small, and we conclude that even in incompressible flow the blade element or strip theory is not generally satisfactory for the design of high-deflection blades. The analysis derives the geometrical conditions for the blade profiles on the walls of the annulus which are needed to satisfy the wall boundary conditions in the idealized flow, but which in any practical example will be modified by the presence of wall boundary layers and blade thickness. In the limit when the number of blades approaches infinity, a bladed actuator duct solution is obtained. The conditions for the blade profile at the walls are absent, but the stacking position and aspect ratio still affect the axial and radial velocity distributions for the same swirl schedule.

1 Introduction[1]

This is the second of two papers describing the first stage in the development of an analytical method for designing three-dimensional blade profiles for axial compressors and turbines to produce large deflections and specified whirl or tangential velocities. Several authors [2–5] have described methods of designing three-dimensional blade profiles for small deflections in which the blade introduce only small velocity perturbations and a linearized theory may be used. The large deflection nonlinear theory has been developed in the first instance for a single row of blades in annular ducts of constant hub and tip radius. The fluid is assumed to be incompressible and inviscid and the blades are assumed to have zero thickness and incidence so that there are no stagnation points at the leading edges. After geometrical parameters such as hub-tip ratio, number of blades, blade axial width, and rotational speed have been chosen, as well as the overall deflection, the schedule of pitchwise averaged tangential velocity, $\bar{V}_\theta$, is prescribed at all points within the blade row.

We have adopted the Clebsch formulations of the equations of motion as in previous work by the authors and others on the nonaxisymmetric flows entering axial compressor blade rows, as well as blade wake flows and secondary flows [6–10]. The equations and the nonlinear boundary condition on the blade surface are solved for the blade shape in a simple iterative manner. The resulting solution not only gives the blade shape but also the pressure distribution – and the entire flow field if desired.

The calculation procedure does not rely on any of the numerical schemes based, for instance, on the finite difference or finite volume methods which have been developed for the calculation of flow through blades of given shape [11,12]. The governing equations are solved by classical methods, i.e., all the variables determining the flow and blade profiles are expanded in series of smooth eigenfunctions [13], e.g., Fourier and Bessel functions and Chebyshev polynomials. These spectral methods [14] are capable of giving accurate results and establishing blade profiles which

[1] For the nomenclature, see Part I [1] or as explained in text or as shown in figures.

Contributed by the Gas Turbine Division of THE AMERICAN SOCIETY OF MECHANICAL ENGINEERS and presented at the 28th International Gas Turbine Conference and Exhibit, Phoenix, Arizona, March 27–31, 1983. Manuscript received at ASME Headquarters December 22, 1982. Paper No. 83-GT-125.

Copyright © 1984 by ASME
Downloaded 01 Jun 2010 to 171.66.16.70. Redistribution subject to ASME license or copyright; see http://www.asme.org/terms/Terms_Use.cfm

can then be used to test finite difference and other numerical methods.

In the first paper [1] the development of the method for the two-dimensional flow through a linear cascade has been reported; and it has been shown that the shape of the thin blade profile can be obtained by an iterative method using a Clebsch formulation of the equations for the velocity. In this paper the method is extended to the three-dimensional annular blade row. The boundary conditions at the annular walls, i.e., at the hub and tip, and the Kutta condition at the trailing edge require special consideration. It was found necessary to introduce an appropriate blade shape near the walls if computational difficulties were to be avoided. The determination of the blade shape from the boundary condition, i.e., no flow normal to the blade surface, requires the specification of some stacking condition, for example, that the leading edge be radial. When the number of blades approaches infinity, a limiting case described as the "bladed-actuator duct" is obtained. It is shown that even in this case the shape of the blade profile depends on the way in which each blade profile is stacked radially in relation to the adjacent blade profiles.

2 Formulation of Equations and Boundary Conditions

In the Clebsch formulation, the velocity vector **V** is written in terms of three scalars ϕ, λ, μ arranged in the form

$$\underset{\sim}{V} = \nabla\phi + \lambda\nabla\mu \tag{1}$$

where ϕ is the "potential" or irrotational part and term $\lambda\nabla\mu$ accounts for the rotationality of the flow (see Lamb [15], p. 248). By taking the curl of equation (1), we obtain the vorticity as

$$\underset{\sim}{\Omega} = \nabla\lambda \times \nabla\mu \tag{2}$$

The Clebsch formulation has been used extensively in studies of rotational flows, e.g., shear and skew flow [10] wake flows [6,8,9], and in nonaxisymmetric flows, i.e., inlet distortion studies [6,7]. The scalars λ and μ are related to appropriate physical surfaces in the flow, e.g., Bernoulli surfaces (constant stagnation pressure, etc.), sheets of vorticity (wakes from blades) and drift surfaces. In this paper, we shall relate the scalars λ and μ to the blade circulations and a function of the blade shape.

In Part I [1] the Clebsch approach was developed for the two dimensional cascade. The same approach will be further developed here for the blade-to-blade flow in the annular blade row.

2.1 Vorticity and Velocity in the Blade Row. We assume that the fluid is incompressible and inviscid and that a single row of blades of specified axial extent and negligible thickness is to be designed to produce a given mean tangential velocity in a long annular duct of constant hub (inner) and tip (outer) radii, i.e., $r = h$ and 1, respectively (see Figs. 1 and 2).

The blade shape is given by

$$\alpha = \theta - f(r,z) = m2\pi/B \tag{3}$$

where B is the number of blades and m is zero or an integer. The leading and trailing edges are at $z = 0$ and $z = c$, respectively.

We shall assume that the flow is irrotational throughout so that the only vorticity is the bound vorticity in the blade surfaces and there is no trailing vorticity due to spanwise variation of circulation about each blade. In the example to be presented, constant circulation (free vortex) blading will be assumed, and in fact we shall at first assume that

$$r\bar{V}_\theta = r\bar{V}_\theta(z) \tag{4}$$

within the blade row, where the superscript "$-$" defines a tangential mean, viz.,

$$\bar{\underset{\sim}{V}} = \frac{B}{2\pi}\int_0^{2\pi/B} \underset{\sim}{V}\, d\theta \tag{5}$$

where the integral is taken over the complete blade pitch including the blade.

As all the vorticity is contained in the blade surfaces, we may express it in terms of a periodic delta function, following closely the formulation in Part [1],

$$\underset{\sim}{\Omega} = \nabla \times \underset{\sim}{V} = (\nabla r\bar{V}_\theta \times \nabla\alpha)\delta_p(\alpha) \tag{6}$$

where

$$\delta_p(\alpha) = \frac{2\pi}{B}\sum_{m=-\infty}^{\infty}\delta(\alpha - m2\pi/B) = \sum_{m=-\infty}^{\infty}\exp(imB\alpha) \tag{7}$$

(see Lighthill [16])

The mean value is then obtained by noting that

$$\overline{\delta_p(\alpha)} = \frac{B}{2\pi}\int_0^{2\pi/B}\frac{2\pi}{B}\,\delta(\alpha - m2\pi/B)\,d\alpha = 1 \tag{8}$$

so that

$$\bar{\underset{\sim}{\Omega}} = \nabla \times \bar{\underset{\sim}{V}} = (\nabla r\bar{V}_\theta \times \nabla\alpha) \tag{9}$$

or

$$\bar{\underset{\sim}{\Omega}} = \left\{\frac{1}{r}\frac{\partial}{\partial z}r\bar{V}_\theta, \frac{\partial}{\partial z}\bar{V}_r - \frac{\partial}{\partial r}\bar{V}_z, \frac{1}{r}\frac{\partial}{\partial r}r\bar{V}_\theta\right\} \tag{10}$$

which offers a convenient check on the r- and z-components of (9).

Similarly, the velocities can be split into a mean velocity, $\bar{\mathbf{V}}$, and a periodioc velocity, $\mathbf{v}$; when $0 < z < c$.

$$\bar{\underset{\sim}{V}} = \nabla\bar{\phi}(r,z) + r\bar{V}_\theta\nabla\alpha = \mathbf{e}_r\bar{V}_r + \mathbf{e}_\theta\bar{V}_\theta + \mathbf{e}_z\bar{V}_z \tag{11}$$

where $\mathbf{e}_r$, $\mathbf{e}_\theta$, $\mathbf{e}_z$ are unit vectors in the r-, θ- and z- directions. directions.

In the region $0 < z < c$, again following the analysis given in Part I, we may write

$$\underset{\sim}{v}_2 = \nabla\phi_2 - S(\alpha)\nabla r\bar{V}_\theta \tag{12}$$

where

$$S'(\alpha) = 2\mathrm{Re}\sum_{n=1}^{\infty} e^{inB\alpha} \tag{13}$$

and

$$S(\alpha) = 2\mathrm{Re}\sum_{n=1}^{\infty}\frac{e^{inB\alpha}}{inB} \tag{14}$$

We can now derive the complete expressions for the mean and periodic velocities but, before doing this, we consider the boundary conditions at the hub and tip and on the blades, and the Kutta condition at the trailing edge.

2.2 A Kinematic Condition for the Blade Camber Line at the Boundary Walls

At the hub and tip both the mean and the periodic velocity normal to the walls must be zero. These boundary conditions can and will be satisfied by appropriate adjustments to the constants in the expressions for the velocities. It is, however, possible and necessary to deduce an important condition which materially assists in the computation of the blade shape at the hub and tip.

We first write the Kutta-Joukowski relation between lift and circulation in the form

$$\rho\underset{\sim}{V}_{bl} \times \underset{\sim}{\Omega} = (p^- - p^+)\nabla\alpha\,\delta_p(\alpha) \tag{15}$$

Downloaded 01 Jun 2010 to 171.66.16.70. Redistribution subject to ASME license or copyright; see http://www.asme.org/terms/Terms_Use.cfm

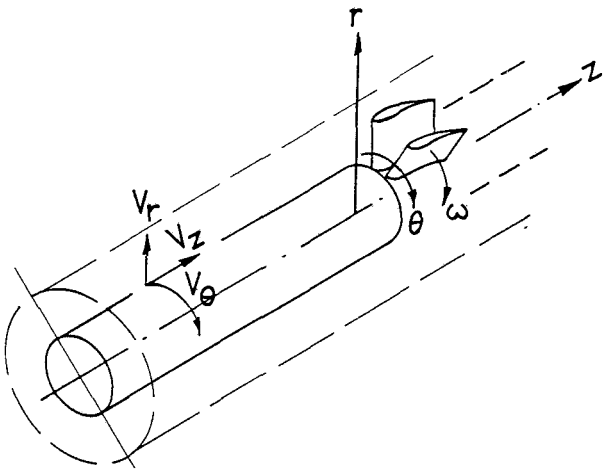


Fig. 1 Annular blade row of constant hub and tip diameter

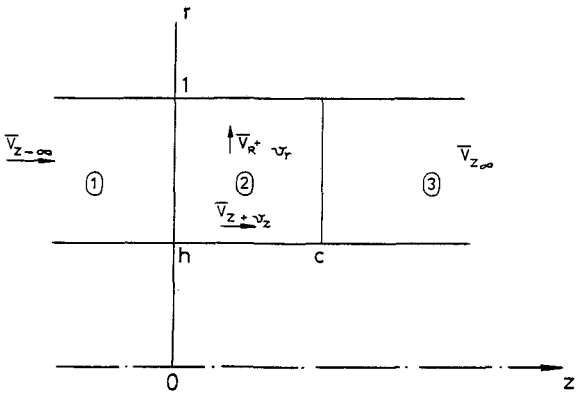


Fig. 2 Annular blade row: notation

where p^+ is the pressure on the upper surface and p^- is the pressure on the lower surface. In other words, the pressure goes from p^- to p^+ as θ increases across the blade. Because the (relative) stagnation pressure is constant

$$p^+ + \frac{1}{2}\rho \underset{\sim}{V}^+ \cdot \underset{\sim}{V}^+ = p^- + \frac{1}{2}\rho \mathbf{V}^- \cdot \mathbf{V}^- \tag{16}$$

{Note that $\mathbf{V}_{bl} = (\mathbf{V}^+ + \mathbf{V}^-)/2$} so that (15) becomes

$$\underset{\sim}{V}_{bl} \times \underset{\sim}{\Omega} = \underset{\sim}{V}_{bl} \cdot (\underset{\sim}{V}^+ - \underset{\sim}{V}^-) \nabla \alpha \delta_p(\alpha) \tag{17}$$

Further we note that

$$\underset{\sim}{V}_{bl} \times \underset{\sim}{\Omega} \cdot \nabla \alpha = \underset{\sim}{V}_{bl} \cdot (\underset{\sim}{V}^+ - \underset{\sim}{V}^-) \nabla \alpha \cdot \nabla \alpha \delta_p(\alpha)$$

or

$$\underset{\sim}{V}_{bl} \cdot \underset{\sim}{\Omega} \times \nabla \alpha = \underset{\sim}{V}_{bl} \cdot (\underset{\sim}{V}^+ - \underset{\sim}{V}^-) |\nabla \alpha|^2 \delta_p(\alpha) \tag{18}$$

from which we deduce that we may satisfy this equation by writing

$$(\underset{\sim}{V}^+ - \underset{\sim}{V}^-)\delta_p(\alpha) = \frac{\underset{\sim}{\Omega} \times \nabla \alpha}{|\nabla \alpha|^2} + K \nabla \alpha$$

where K is an arbitrary function. However, we know that $\mathbf{V}^+$ and $\mathbf{V}^-$ lie in the blade surface so that

$$(\underset{\sim}{V}^+ - \underset{\sim}{V}^-) \cdot \nabla \alpha \delta_p(\alpha) = 0$$

$$= \frac{\underset{\sim}{\Omega} \times \nabla \alpha \cdot \nabla \alpha}{|\nabla \alpha|^2} + K |\nabla \alpha|^2$$

The first term on the right-hand side is zero, being a triple vector product with two vectors the same so that $K = 0$. Hence

$$(\underset{\sim}{V}^+ - \underset{\sim}{V}^-)\delta_p(\alpha) = \frac{\underset{\sim}{\Omega} \times \nabla \alpha}{|\nabla \alpha|^2} \tag{19}$$

If the blades are rotating, we substitute the relative velocity, $\mathbf{W}$, for the absolute velocity $\mathbf{V}$, in equations (15) to (19) but note that $\mathbf{W}^+ - \mathbf{W}^- = \mathbf{V} - \mathbf{V}^-$, so that (19) applies to both rotating and stationary blade rows. In physical terms (19) represents the fact that the bound vorticity lies in the blade surface and is at right angles to the vector difference between the velocities on upper and lower surfaces.

We now introduce the wall boundary conditions at $r = h$ and 1 by letting $\mathbf{n}$ represent the unit vector normal to the wall $\mathbf{n} \cdot \mathbf{V}^+ = \mathbf{n} \cdot \mathbf{V}^- = 0$ or

$$\mathbf{n} \cdot (\underset{\sim}{V}^+ - \underset{\sim}{V}^-)\delta_p(\alpha) = \mathbf{n} \cdot \frac{\underset{\sim}{\Omega} \times \nabla \alpha}{|\nabla \alpha|^2} = 0 \tag{20}$$

Now $\tilde{\mathbf{\Omega}} = \nabla r \bar{V}_\theta \times \nabla \alpha$ may be substituted for $\mathbf{\Omega}$ in the above equation because the multiplying constant $2\pi/B$ does not affect the result.

Hence

$$\mathbf{n} \cdot ((\nabla r \bar{V}_\theta \times \nabla \alpha) \times \nabla \alpha) = 0 \tag{21}$$

or

$$\mathbf{n} \cdot ((\nabla \alpha \cdot \nabla r \bar{V}_\theta) \nabla \alpha - (\nabla \alpha \cdot \nabla \alpha) \nabla r \bar{V}_\theta) = 0$$

For the coordinate system of Fig. 1, $\underset{\sim}{n} = \underset{\sim}{\hat{e}}_r$ and (21) becomes

$$r^2 \frac{\partial f}{\partial r} \frac{\partial f}{\partial z} \frac{\partial r V_\theta}{\partial z} - \left(1 + r^2 \left(\frac{\partial f}{\partial z}\right)^2\right) \frac{\partial r \bar{V}_\theta}{\partial r} = 0 \tag{22}$$

which must be satisfied at the hub and tip, i.e., at $r = h$ and 1.0. As $r\bar{V}_\theta$ is specified, (22) leads to a relationship between $\partial f/\partial r$ and $\partial f/\partial z$ at the wall. If, as in the present example, $\partial r \bar{V}_\theta/\partial r$ is zero at the wall (and indeed everywhere), then $\partial f/\partial r$ must be zero there. At first sight, this condition may seem surprising, since it appears to be possible to violate it in practice without any ill effects. However, the flows studied here are irrotational and inviscid, and there is no attempt to model the wall boundary layers. In this idealized flow condition (22) is merely a consequence of applying the wall boundary condition $V_r = 0$ at $r = h, 1$. It is a consequence which would be eventually arrived at in a convergent computing process. We use it to shorten computing time and prevent divergence.

Condition (22) can be shown to be equivalent to the condition that the component of bound vorticity tangential to the wall must vanish at the wall. Such a condition is required to avoid the infinitely large induced velocities associated with discrete vortices near the walls. It has been noted by L.H. Smith [17], C.S. Tan [8,9], and A. Falcao [18], and is discussed further in section 4.

When $\partial r \bar{V}_\theta/\partial r$ is not zero at the wall it appears to be possible to obtain other values for $\partial f/\partial r$, but it should be noted that $\partial r \bar{V}_\theta/\partial z$ and $\partial f/\partial z$ may vanish at points on the blade surface at the wall leading to absurdly large values of $\partial f/\partial r$. For the sake of convenience and pending further investigations into methods of representing wall boundary layers for design methods, it seems desirable to make $\partial r \bar{V}_\theta/\partial r$ zero at the walls. This condition is not unfamiliar as it has had to be imposed in the study of flows in blade wakes [8,9,17] when no wall boundary layers are represented.

Although in practice there will be boundary layers and viscous effects on the walls, failure to use functions for f which satisfy the boundary condition (22) was found to lead to instabilities in the numerical calculations.

2.3 Kutta Condition at the Trailing Edge of Blades. Substituting for $\mathbf{\Omega}$ from equation (6) in equation (15), we have

Downloaded 01 Jun 2010 to 171.66.16.70. Redistribution subject to ASME license or copyright; see http://www.asme.org/terms/Terms_Use.cfm

$$\rho \underset{\sim}{V}_{bl} \times \frac{2\pi}{B} (\nabla r\bar{V}_\theta \times \nabla \alpha)\delta_p(\alpha) = (p^- - p^+)\nabla \alpha \delta_p(\alpha)$$

or

$$\underset{\sim}{V}_{bl} \times (\nabla r\bar{V}_\theta \times \nabla \alpha) = \frac{B}{2\pi} \frac{(p^- - p^+)}{\rho} \nabla \alpha \tag{23}$$

By making use of vector product formulae, equation (23) can further be rewritten as

$$(\underset{\sim}{V}_{bl} \cdot \nabla \alpha)\nabla r\bar{V}_\theta - (\underset{\sim}{V}_{bl} \cdot \nabla r\bar{V}_\theta)\nabla \alpha = \frac{B}{2\pi} \frac{(p^- - p^+)}{\rho} \nabla \alpha$$

However, the boundary condition at the blade requires

$$\underset{\sim}{V}_{bl} \cdot \nabla \alpha = 0$$

so that this equation becomes

$$\underset{\sim}{V}_{bl} \cdot \nabla r\bar{V}_\theta = -\frac{B}{2\pi} \frac{(p^- - p^+)}{\rho} \tag{24}$$

The Kutta condition demands that the pressure be continuous at the trailing edge; thus, we have, at the trailing edge that

$$\mathbf{V}_{bl} \cdot \nabla r\bar{V}_\theta = 0$$

i.e.

$$V_{z_{bl}} \frac{\partial r\bar{V}_\theta}{\partial z} + V_{r_{bl}} \frac{\partial r\bar{V}_\theta}{\partial r} = 0 \tag{25a}$$

or

$$\frac{\partial r\bar{V}_\theta}{\partial s} = 0 \tag{25b}$$

where s denotes distance along the blade in the direction of $\underset{\sim}{V}_{bl}$.

In the example chosen in the report $\partial r\bar{V}_\theta/\partial r = 0$, hence $\partial r\bar{V}_\theta/\partial z = 0$ at the trailing edge.

2.4 Blade Boundary Conditions and Stacking. The boundary condition on the blade may be written as for the two-dimensional cascade, but allowing for blade rotation.

$$\mathbf{W}_{bl} \cdot \nabla \alpha = 0$$

or

$$\bar{V}_z \frac{\partial f}{\partial z} = \frac{\bar{V}_\theta}{r} - \omega - \bar{V}_r \frac{\partial f}{\partial r} + \mathbf{v}_{bl} \cdot \nabla \alpha \tag{26a}$$

or

$$\bar{V}_{z\infty} \frac{\partial f}{\partial z} = \frac{\bar{V}_\theta}{r} - \omega + (\bar{V}_{z\infty} - \bar{V}_z) \frac{\partial f}{\partial z} - \bar{V}_r \frac{\partial f}{\partial r} + \mathbf{v}_{bl} \cdot \nabla \alpha \tag{26b}$$

The equations are to be solved for f by iteration, subject to the boundary conditions on the walls and at the leading and trailing edges.

The solutions for f are obtained by integration of (26) which cannot be completed without an integration constant in the form of some initial condition on f. One such condition would be, for instance, that the leading edges of the blades are radial. We need therefore to define a "stacking position," $z = z_{st}$ where $f(r,z_{st}) = f_{st}(r)$ would give the required initial condition for the generation of the blade profile.

At the stacking position the blade need not be radial but may take any prescribed shape, but for radial stacking position at $z = z_{st}$, we put $f(r,z_{st}) = 0$.

3 Equations for Velocities and Blade Shape

In this section we obtain expressions for the mean and periodic velocities which may then be used in the blade boundary condition (26) to obtain the blade shape by iteration.

3.1 The Mean Velocity and the Bladed Actuator Duct. The mean velocity may either be formulated using the Clebsch expression of (11) or in terms of the more familiar Stokes' stream function which has been used in through-flow and actuator disc calculations.

Both forms are useful and can be developed for the three regions, the upstream region, the blade region and the downstream region, corresponding to regions 1, 2, and 3 in Fig. 2. We shall use the Stokes' stream function here; the Clebsch expression is given in [20].

Let

$$\bar{V}_r = -\frac{1}{r} \frac{\partial \psi}{\partial z}, \quad \bar{V}_z = \frac{1}{r} \frac{\partial \psi}{\partial r} \tag{27}$$

where $\psi = \psi(r,z)$. These expressions satisfy the continuity equation and give from (10)

$$\frac{\partial^2 \psi}{\partial r^2} - \frac{1}{r} \frac{\partial \psi}{\partial r} + \frac{\partial^2 \psi}{\partial z^2} = -r\bar{\Omega}_\theta \tag{28}$$

Now $\bar{\Omega}_\theta = 0$ in regions (1) and (3) of Fig. 2 so that we can construct solutions

$$\psi_1 = \frac{r^2}{2} \bar{V}_{z\infty} + \sum_{p=1}^{\infty} A_p e^{\lambda_p z} r R_p(r) \tag{29}$$

$$\psi_3 = \frac{r^2}{2} \bar{V}_{z\infty} + \sum_{p=1}^{\infty} C_p e^{-\lambda_p z} r R_p(r) \tag{29}$$

In region (2)

$$\Omega_\theta = \hat{\mathbf{e}}_\theta \cdot \nabla r\bar{V}_\theta \times \nabla \alpha \tag{30}$$

so that the solution for ψ_2 will contain an inhomogeneous part

$$\psi_2 = \frac{r^2}{2} \bar{V}_{z\infty} + \sum_{p=1}^{\infty} r R_p(r) (B_{p1} e^{\lambda_p z} + B_{p2} e^{-\lambda_p z} + Z_p(z)) \tag{31}$$

The solution is then obtained conventionally by substituting the expressions for ψ in (28), separating the variables, applying the boundary conditions on the walls of the annulus, and matching the flow at the trailing and leading edges.

The results are for region (2)

$$\bar{V}_r = -\frac{1}{2} \sum_{p=1}^{\infty} R_p(r) \int_0^c \mathrm{sgn}(z-t) e^{-\lambda_p |z-t|} \frac{dr\bar{V}_\theta}{dt} \times \int_h^1 r R_p(r) \frac{\partial f}{\partial r} dr\, dt, \tag{32}$$

$$\bar{V}_z - \bar{V}_{z\infty} = -\frac{1}{2} \sum_{p=1}^{\infty} R_p{}^0(r) \int_0^c e^{-\lambda_p |z-t|} \frac{dr V_\theta}{dt} \times \int_h^1 r R_p(r) \frac{\partial f}{\partial r} dr\, dt \tag{33}$$

where

$$R_p(r) = \frac{1}{\sqrt{N_p}} \left(J_1(\lambda_p r) - \frac{J_1(\lambda_p)}{Y_1(\lambda_p)} Y_1(\lambda_p r) \right) \tag{34a}$$

with

$$N_p = \int_h^1 r \left(J_1(\lambda_p r) - \frac{J_1(\lambda_p)}{Y_1(\lambda_p)} Y_1(\lambda_p r) \right)^2 dr \tag{34b}$$

$$J_1(\lambda_p h) Y_1(\lambda_p) - J_1(\lambda_p) Y_1(\lambda_p h) = 0 \tag{34c}$$

and

Downloaded 01 Jun 2010 to 171.66.16.70. Redistribution subject to ASME license or copyright; see http://www.asme.org/terms/Terms_Use.cfm

$$R_p^0(r) = \frac{J_0(\lambda_p r) - \frac{J_1(\lambda_p)}{Y_1(\lambda_p)} Y_0(\lambda_p r)}{\sqrt{N_p}} \tag{35}$$

and sgn $(x) = +1$ for $x > 0$, $= -1$ for $x < 0$.

In the above analysis we have written

$$r\bar{V}_\theta = r\bar{V}_\theta(z)$$

and set $\bar{\gamma} = d_r\bar{V}_\theta/dz = 0$ at $z = 0$ and c, to satisfy the Kutta condition and to give zero incidence at the leading edge.

Before developing equations for the determination of the periodic velocity, v, it is useful to consider the limiting case when the number of blades, B, approaches infinity. As $B \to \infty$, $\mathbf{v} \to 0$ so that the last term in (26), $\underset{\sim}{v}_{bl} \cdot \nabla\alpha \to 0$, and

$$\bar{V}_z \frac{\partial f}{\partial z} = \frac{\bar{V}_\theta}{r} - \bar{V}_r \frac{\partial f}{\partial r} - \omega \tag{36a}$$

This equation has two unknowns, f, and say, ψ; it may be written

$$\frac{1}{r}\frac{\partial\psi}{\partial r}\frac{\partial f}{\partial z} - \frac{1}{r\partial z}\frac{\partial\psi}{\partial r}\frac{\partial f}{\partial r} = \frac{\bar{V}_\theta}{r} - \omega \tag{36b}$$

If a unique solution is to be obtained, another equation relating ψ and f is also required. It is clearly given by (28), viz:

$$\frac{\partial^2\psi}{\partial r^2} - \frac{1}{r}\frac{\partial\psi}{\partial r} + \frac{\partial^2\psi}{\partial z^2} = r\left(\frac{\partial r\bar{V}_\theta}{\partial z}\frac{\partial f}{\partial r} - \frac{\partial r\bar{V}_\theta}{\partial r}\frac{\partial f}{\partial z}\right) \tag{37}$$

To complete the limiting case a stacking condition must be prescribed and the Kutta condition (25) must be satisfied.

The wall boundary condition (22) does not apply to the actuator duct because $\underset{\sim}{V}^+$ and $\underset{\sim}{V}^-$ are not relevant. In fact, (22) is now replaced by an equation obtained by differentiating (36*b*) with respect to r, viz:

$$\frac{\partial}{\partial r}\left(\frac{1}{r}\frac{\partial\psi}{\partial r}\right)\frac{\partial f}{\partial z} + \frac{1}{r}\frac{\partial\psi}{\partial r}\frac{\partial^2 f}{\partial r\partial z} - \frac{\partial^2\psi}{\partial r\partial z}\frac{1}{r}\frac{\partial f}{\partial r} - \frac{\partial\psi}{\partial z}\frac{\partial}{\partial r}\frac{1}{r}\frac{\partial f}{\partial r} = \frac{1}{r^2}\frac{\partial r\bar{V}_\theta}{\partial r} - \frac{2}{r^3}r\bar{V}_\theta \tag{38}$$

Substituting for $\partial/\partial r\,[1/r\,\partial\psi/\partial r]$ in the first term from (37) and putting $\partial\psi/\partial z = 0$ at the wall, we obtain for $r = h$ and 1.0,

$$\frac{\partial f}{\partial r}\frac{\partial f}{\partial z}\frac{\partial}{\partial z}r\bar{V}_\theta - \left\{\frac{1}{r^2} + \left(\frac{\partial f}{\partial z}\right)^2\right\}\frac{\partial}{\partial r}r\bar{V}_\theta = -\frac{2}{r^3}r\bar{V}_\theta + \frac{\partial^2\psi}{\partial r\partial z}\frac{1}{r}\frac{\partial f}{\partial r} - \frac{1}{r}\frac{\partial\psi}{\partial r}\frac{\partial^2 f}{\partial r\partial z} \tag{39}$$

Equation (22) is obtained when the r.h.s of the above equation is zero, a condition which will not be normally obtained in the actuator duct solution. In fact, if $r\bar{V}_\theta = r\bar{V}_\theta(z)$ and we force $\partial f/\partial r$ to zero as for the finite number of blades, then the equation becomes

$$-\frac{2}{r^2}r\bar{V}_\theta = 0$$

which is unacceptable. We therefore conclude that in the actuator duct $\partial f/\partial r$ is not generally zero on the walls. When there is a finite number of blades the term $\partial/\partial r(\underset{\sim}{v}_{bl} \cdot \nabla\alpha)$ needs to be added to the r.h.s. of (38), and it may be shown by lengthy analysis that the presence of this term reduces the r.h.s. of (38) to zero.

We conclude therefore that in the limiting case of an infinite number of blades one may specify the mean tangential velocity, $\bar{V}_\theta$, but neither of the other velocities $\bar{V}_z$ nor $\bar{V}_r$ may be specified. This result has been recognized in the literature [19] although not always used. This analysis shows how the values depend for the present simple case on the blade stacking condition. One may refer to actuator ducts which are used to model blade rows as "bladed" actuator ducts, thereby implying that they satisfy the above relationships.

3.2 The Periodic Velocity. We represent the velocities in the three regions as

$$\mathbf{v}_1 = \nabla\phi_1, \qquad \mathbf{v}_3 = \nabla\phi_3 \tag{40}$$

and from (12)

$$\mathbf{v}_2 = \nabla\phi_2 - S(\alpha)\nabla r\bar{V}_\theta \tag{12}$$

$$\phi_1 = \sum_{n=1}^{\infty}\sum_{p=1}^{\infty} A_{np}e^{\lambda_{np}z}e^{inB\theta}R_{np}(r) \tag{41}$$

$$\phi_3 = \sum_{n=1}^{\infty}\sum_{p=1}^{\infty} C_{np}e^{-\lambda_{np}z}e^{inB\theta}R_{np}(r) \tag{42}$$

and

$$\phi_2 = \sum_{n=1}^{\infty}\sum_{p=1}^{\infty} e^{inB\theta}Z_{np}(z)R_{np}(r) \tag{43}$$

where

$$R''_{np} + \frac{1}{r}R'_{np} + \left(\lambda_{np}^2 - \frac{n^2B^2}{r^2}R_{np}\right) = 0 \tag{44}$$

$$R_{np} = \frac{1}{\sqrt{N_{np}}}\left\{J_{nB}(\lambda_{np}r) - \frac{J'_{nB}(\lambda_{np})}{Y'_{nB}(\lambda_{np})}Y_{nB}(\lambda_{np}r)\right\} \tag{45}$$

$$N_{np} = \int_h^1 r\left(J_{nB}(\lambda_{np}r) - \frac{J'_{nB}(\lambda_{np})}{Y'_{nB}(\lambda_{np})}Y_{nB}(\lambda_{np}r)\right)^2 dr \tag{46}$$

and the values of λ_{np} are determined from

$$J'_{nB}(\lambda_{np}h)\,Y'(\lambda_{np}) - J'_{nB}(\lambda_{np})\,Y'(\lambda_{np}h) = 0 \tag{47}$$

so that the boundary conditions of vanishing radial velocity at $r = h$ and 1 are satisfied. The homogeneous part of ϕ_2 has been omitted from (43), since it may be made to vanish by suitable choice of the limits of integration in the expressions for Z_{np} as shown in Part I.[1]

Now using (12) in the continuity relation

$$\nabla\cdot\underset{\sim}{v}_2 = 0,$$

$$\nabla^2\phi_2 = \nabla\cdot(S(\alpha)\nabla r\bar{V}_\theta) = \mathrm{Re}\,\nabla\cdot 2\sum_{n=1}^{\infty}\frac{e^{inB[\theta - f(r,z)]}}{inB}\nabla r\bar{V}_\theta \tag{48}$$

which reduces to

$$\sum_{p=1}^{\infty}(Z''_{np} - \lambda_{np}^2 Z_{np})R_{np} = \nabla\cdot\frac{2e^{-inBf}}{inB}\nabla r\bar{V}_\theta \tag{49}$$

On multiplying by $rR_{np}(r)$ and integrating from $r = h$ to 1 we obtain an equation for Z_{np} which may be solved by the method of variation of parameters to give

$$Z_{np} = \frac{2}{inB}\int_h^1\int_0^c \frac{e^{-\lambda_{np}|z-t|}}{2\lambda_{np}} \times rR_{np}(\nabla\cdot e^{-inBf}\nabla r\bar{V}_\theta)dr\,dt \tag{50}$$

For example if

$$r\bar{V}_\theta = r\bar{V}_\theta(z),$$

$$Z_{np} = \frac{1}{inB\lambda_{np}}\int_0^c e^{-\lambda_{np}|z-t|}\int_h^1 rR_{np} \times \frac{\partial}{\partial t}\bar{\gamma}(t)e^{-inBf(r,t)})dr\,dt \tag{51}$$

Downloaded 01 Jun 2010 to 171.66.16.70. Redistribution subject to ASME license or copyright; see http://www.asme.org/terms/Terms_Use.cfm

Table I Summary of three-dimensional computation for annular blade rows

$$\frac{d}{dz} r\bar{V}_\theta = C_0 z(c-z)$$

Run no.	h	c	ω	C_0	$r\bar{V}_{\theta 1}$	B	Z_{stack}
	Inlet guide vanes						
1	0.5	0.2	0	562.5	0	30	0
2	0.99	0.2	0	746.25	0	30	0
	Fan						
1000	0.4	0.2	$\sqrt{3}$	$120\sqrt{3}$	0	20	0
1001	0.4	0.2	$\sqrt{3}$	$120\sqrt{3}$	0	10	0
1002	0.4	0.2	$\sqrt{3}$	$120\sqrt{3}$	0	10	0.2
1003	0.4	0.2	$\sqrt{3}$	$120\sqrt{3}$	0	5	0.095
1005	0.4	0.2	$\sqrt{3}$	$120\sqrt{3}$	0	7	0
1006	0.4	0.2	$\sqrt{3}$	$120\sqrt{3}$	0	7	0.095
1007	0.4	0.2	$\sqrt{3}$	$120\sqrt{3}$	0	7	0.2
1010	0.4	0.1	$\sqrt{3}$	$960\sqrt{3}$	0	14	0
	Turbine						
903	0.6	0.13	5/3	−3037.5	1.2	20	0.063
909	0.6	0.13	5/3	−3037.5	1.2	∞	0.13
910	0.6	0.13	5/3	−3037.5	1.2	∞	0.003
911	0.6	0.13	5/3	−3037.5	1.2	∞	0.063
913	0.6	0.06	5/3	−24.300	1.2	40	0.0316

$$\frac{d}{dz} r\bar{V}_\theta = B_1\sqrt{z(c-z)\,(c-z)}$$

				B_1			
	Fan						
1100	0.4	0.2	3	$120\sqrt{3}/\pi$	0	7	0.095

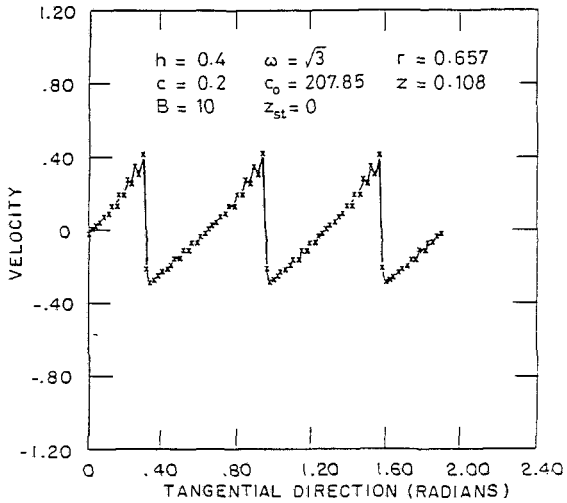


Fig. 3 Fan: circumferential variation of axial velocity, $\bar{\gamma} \propto z(c-z)$ (Run 1001)

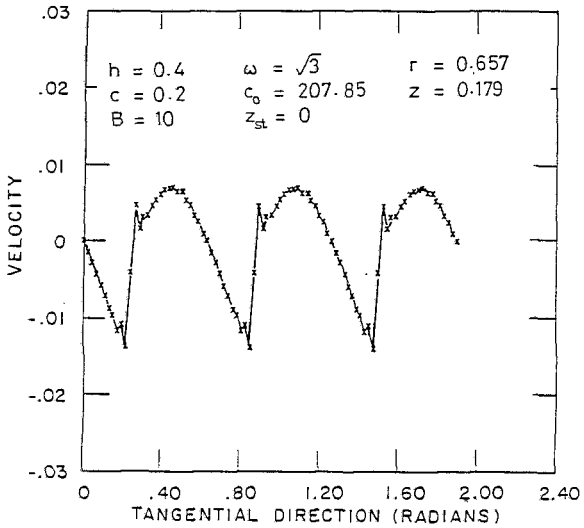


Fig. 4 Fan: circumferential variation of radial velocity, $\bar{\gamma} \propto z(c-z)$ (Run 1001)

If we integrate by parts with the assumption (25), namely $\bar{\gamma}(0) = 0$, we obtain

$$Z_{np} = -\frac{i}{nB}\int_0^z e^{-\lambda_{np}(z-t)}\bar{\gamma}(t)\left(\int_h^1 \rho R_{np}(\rho)e^{-inBf(\rho,t)}d\rho\right)dt + \frac{i}{nB}\int_z^c e^{\lambda_{np}(z-t)}\bar{\gamma}(t)\left(\int_h^1 \rho R_{np}(\rho)e^{-inBf(\rho,t)}d\rho\right)dt \tag{52}$$

and

$$Z'_{np} = \frac{i\lambda_{np}}{nB}\int_0^z \bar{\gamma}(t)e^{-\lambda_{np}(z-t)}\left(\int_h^1 \rho R_{np}(\rho)e^{-inBf(\rho,t)}d\rho\right)dt + \frac{i\lambda_{np}}{nB}\int_z^c \bar{\gamma}(t)e^{\lambda_{np}(z-t)}\left(\int_h^1 \rho R_{np}(\rho)e^{-inBf(\rho,t)}d\rho\right)dt + \frac{2i}{nB}\bar{\gamma}(z)\int_h^1 \rho R_{np}(\rho)e^{-inBf(\rho,z)}d\rho \tag{53}$$

The above results satisfy the boundary conditions at the hub and tip if $\partial f/\partial r = 0$ and also the matching condition at the leading and trailing edges, if

$$C_{np} = Z_{np}(c)e^{\lambda_{np}c},$$
$$A_{np} = Z_{np}(0)$$

The value of $\underset{\sim}{v}_{bl}$ required in (26) is obtained by setting $\theta = f$ in the expressions for the three components of $\underset{\sim}{v}_2$ derived from (12) and noting that $S(0) = 0$. The iterative procedure is further described in [20].

Downloaded 01 Jun 2010 to 171.66.16.70. Redistribution subject to ASME license or copyright; see http://www.asme.org/terms/Terms_Use.cfm

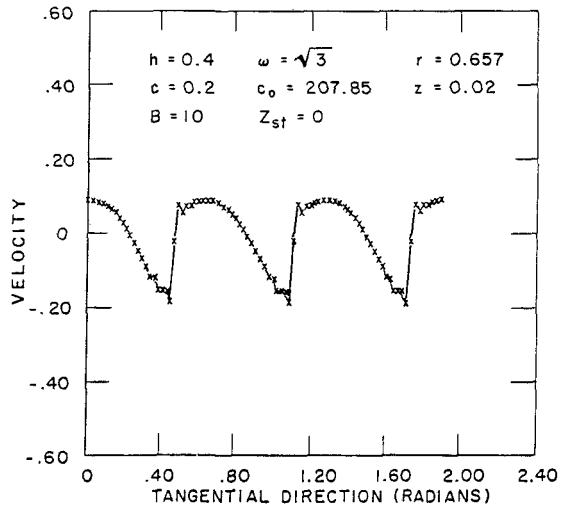


Fig. 5 Fan: circumferential variation of tangential velocity, $\bar{\gamma} \propto z(c-z)$ (Run 1001)

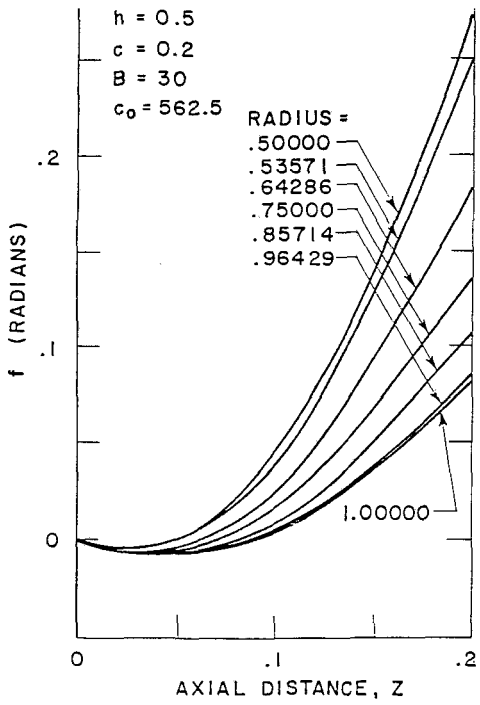


Fig. 6 Three-dimensional inlet guide vane profiles $\bar{\gamma} \propto z(c-z)$ (Run 1)

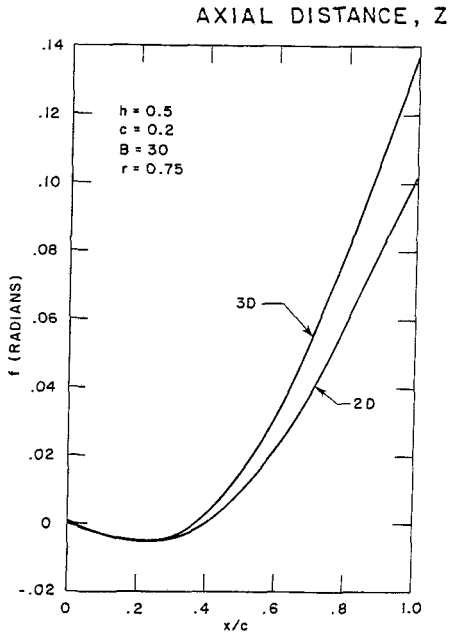


Fig. 7 Inlet guide vane: blade profile comparison between three-dimensional (mean diameter) and two-dimensional for same nominal flow angles and pitch-axial width ratios. $h=0.5$, $c=0.2$, $B=30$, $C_0=562.5$, $r=0.75$, $\alpha_1=0$, $\alpha_2=45$, $\bar{\gamma} \propto z(c-z)$ (Run 1)

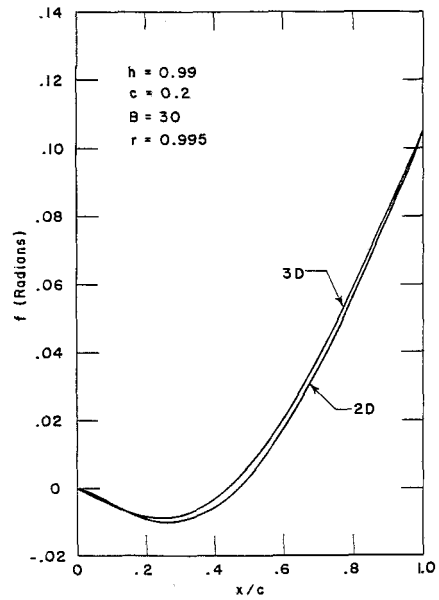


Fig. 8 Inlet guide vane: blade profile comparison between three-dimensional (mean diameter) and two-dimensional for same nominal flow angles and pitch-axial width ratios. $h=0.99$, $c=0.2$, $B=30$, $C_0=746.25$, $r=0.995$, $\alpha_1=0$, $\alpha_2=45$, $\gamma \propto z(c-z)$

4 Results

Programs were written for the computation of the thin blade profiles in a fixed or rotating cascade in an annulus of constant inner and outer radius. As already noted, the fluid was assumed to be inviscid and incompressible. The variation along the chord of the strength of the bound vortices representing the blades was assumed initially to be parabolic, i.e., proportional to $z(c-z)$. The zero values of the vorticity at the trailing and leading edges given by this expression satisfy the Kutta condition at the trailing edge and give zero incidence at the leading edge. The dependence of the vorticity on the axial distance only and not on the radius prescribes a constant circulation or "free vortex" type of blading with no trailing vorticity. Some results have been obtained with another loading distribution, i.e.,

$$\bar{\gamma} \propto (\sin\beta - \frac{1}{2}\sin 2\beta) \qquad (54a)$$

where

$$z = c(1+\cos\beta)/2 \qquad (55b)$$

This expression brings the point of maximum loading, i.e., bound vortex strength, forward to one-quarter chord from the leading edge.

The computations which have been performed using the three-dimensional program are summarized in Table 1 and Fig. 23.

The three-dimensional program was tested first to shown that it gave the required periodic discontinuity in velocity across the blade. Figures 3, 4, and 5 show the circumferential (θ-direction) variation of axial, radial and tangential velocities for a fan (Run 1001, Table 1) at a radial position $r = 0.65714$ and differing axial positions, chosen to show significant

Downloaded 01 Jun 2010 to 171.66.16.70. Redistribution subject to ASME license or copyright; see http://www.asme.org/terms/Terms_Use.cfm

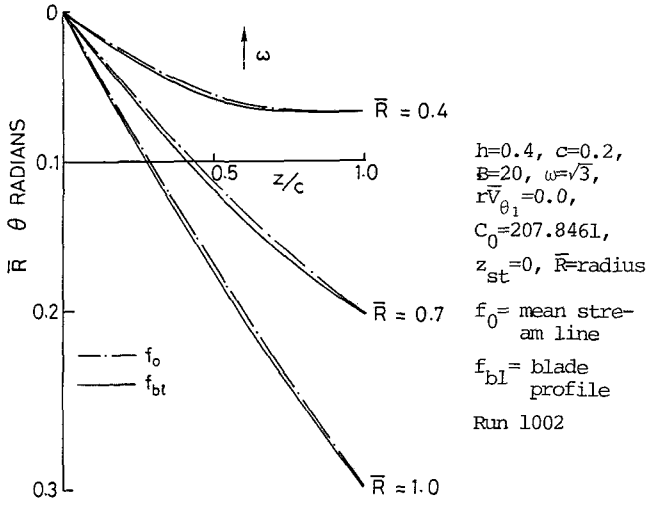


Fig. 9 Fan: 20 blades $h=0.4$, $c=0.2$, $B=20$, $\omega=\sqrt{3}$, $r\bar{V}_{\theta 1}=0.0$, $C_0=207.8461$, $z_{st}=0$, $\bar{R}$ = radius f_0 = mean stream line f_{bl} = blade profile Run 1002

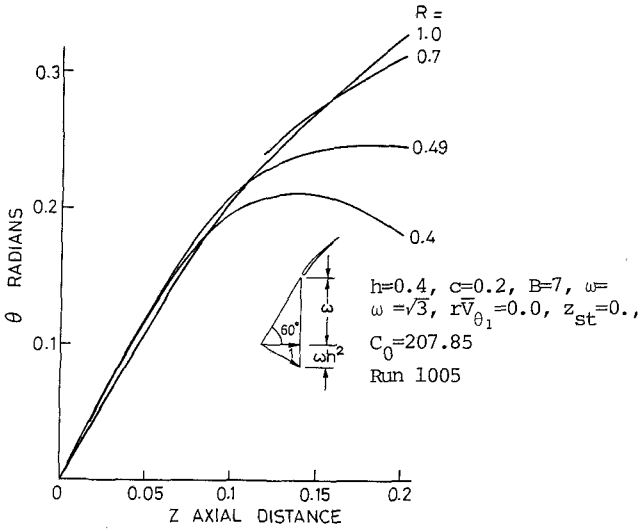


Fig. 11 Fan: 7 blades, radial leading edge $h=0.4$, $c=0.2$, $B=7$, $\omega=\omega=\sqrt{3}$, $r\bar{V}_{\theta 1}=0.0$, $z_{st}=0.$, $C_0=207.85$ Run 1005

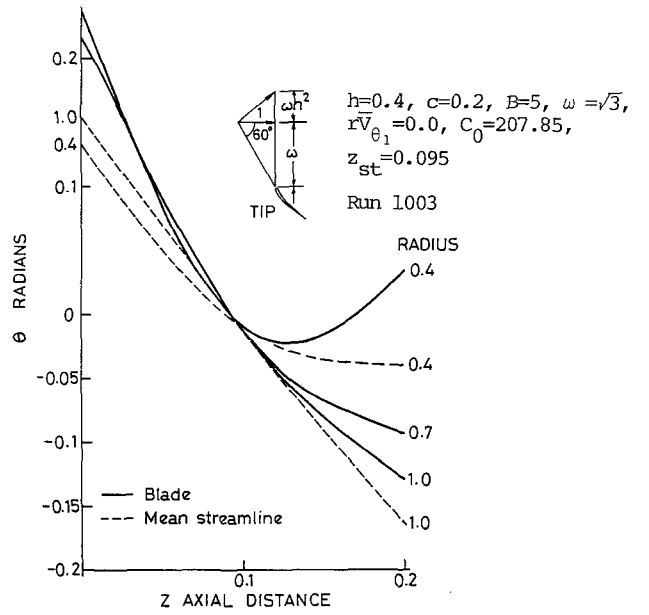


Fig. 10 Fan: 5 blades $h=0.4$, $c=0.2$, $B=5$, $\omega=\sqrt{3}$, $r\bar{V}_{\theta 1}=0.0$, $C_0=207.85$, $z_{st}=0.095$ Run 1003

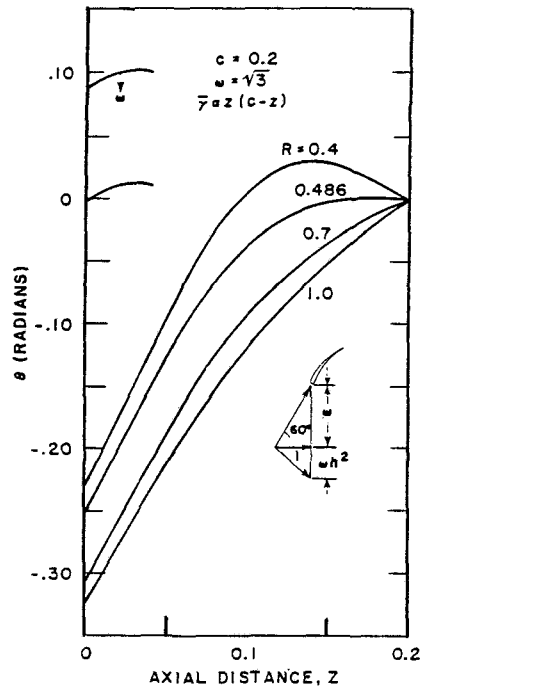


Fig. 12 Fan: 7 blades, radial trailng edge same data as Fig. 10, but $B=7$, $z_{st}=0.2$, Run 1007

periodic jumps in velocities across the blades. Their values may be computed from equation (19), i.e.,

$$\underset{\sim}{V}^{+} - \underset{\sim}{V}^{-} = \frac{2\pi}{B} \frac{(\nabla r V_\theta \times \nabla \alpha) \times \nabla \alpha}{|\nabla \alpha|^2} \tag{56}$$

from which the jumps in velocity may be obtained using the values of $\partial f/\partial r$ and $\partial f/\partial z$ obtained from the computer program. For instance, there is a jump in axial velocity of -0.72 units measured from the curve in Fig. 3. The corresponding value calculated from equation (4.2) is -0.71. The plotted and calculated values of the radial velocity jump from Fig. 4 are 0.019 and 0.023, respectively, and for the tangential velocity jump, from Fig. 5, are 0.27 and 0.24, respectively. The test is a severe one because the Gibbs phenomenon will occur in the determination of the velocities on a surface of the blades from a Fourier series in θ. Fortunately, the calculations for the blade surface do not suffer from this phenomenon because only the mean of the two velocities (i.e., $\mathbf{V}_{bl}$) is required.

The results for an inlet guide vane (Run 1, Table 1) are shown in Fig. 6. These vanes were designed for hub tip ratio of 0.5, a purely axial inlet velocity, i.e., an inlet flow angle of zero, and to give a nominal outlet angle of 45 deg at the mean diameter. The computed blade profile at the mean diameter is compared in Fig. 7 with a two-dimensional cascade profile for the same flow angles and pitch-chord ratio. As the hub-tip ratio is increased keeping the same flow angles at the mean diameter as before, the profile obtained should approach the two-dimensinal profile for the same flow angles and pitch-chord ratio. As a further test of the program, the inlet guide vane profile at the mean diameter for a hub-tip ratio of 0.99 was computed (Run 2) and is compared in Fig. 8 with the corresponding profile for a two dimensional cascade with the same pitch-chord ratio. On comparing Figs. 7 and 8, the convergence to the two-dimensional profile as the hub-tip ratio is increased is very apparent and in fact the difference

Downloaded 01 Jun 2010 to 171.66.16.70. Redistribution subject to ASME license or copyright; see http://www.asme.org/terms/Terms_Use.cfm

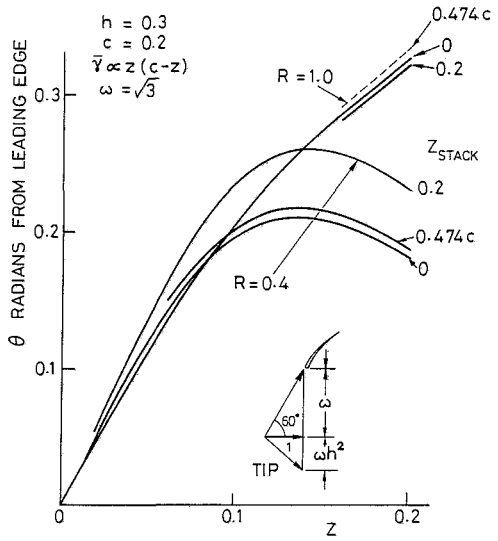


Fig. 13 Fan, 7 blades: effect of stacking on profile shape (Run 1005, 1006, 1007)

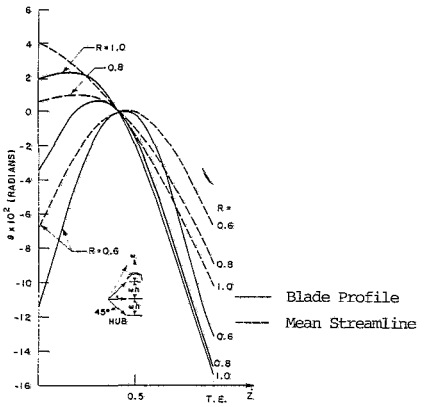


Fig. 14 Turbine rotor, 20 blades, stacked near midchord. $h = 0.6$, $c = 0.13$, $B = 20$, $\omega = 5/3$, $r\bar{V}_{\theta 1} = 1.2$, $C_0 = -3037.5$, $z_{st} = 0.063$, $\bar{\gamma} \propto z(c-z)$

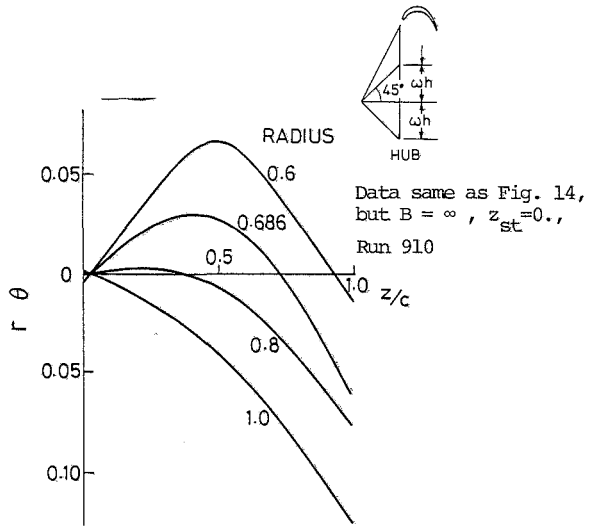


Fig. 15 Turbine, actuator duct, infinite number of blades: radial leading edge

between the three-dimensional and two-dimensional curves in Fig. 8 may be within the accuracy of the program. The two dimensional profiles were calculated by the method described in Part I [1].

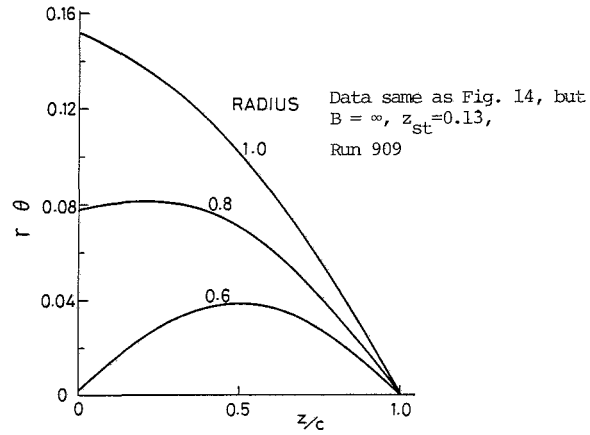


Fig. 16 Turbine, actuator duct: infinite number of blades, radial trailing edge

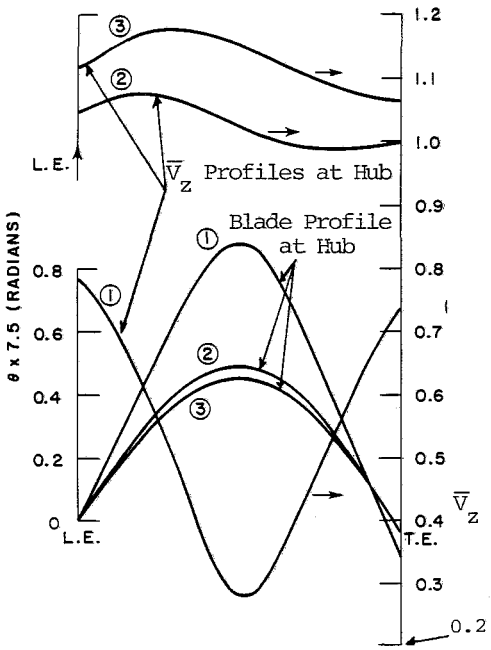


Fig. 17 Turbine, actuator duct: effect of stacking position on blade profiles and mean axial velocity at the hub. ①, stacking at .003 Run 910; ②, stacking at .063 Run 903; ③, stacking at .13 Run 909

During these computations the importance of satisfying the condition $\partial f/\partial r = 0$ at the walls, derived from equation (22), was clearly demonstrated by a failure of the iterative procedure to converge without this condition.

Several calculations were done for a fan with hub-tip ratio of 0.4, a relative air inlet angle at the tip of 60 deg, and a relative outlet angle of 0 deg at the hub. The results for 20 blades, Fig. 9, show a relatively small difference between the blade profiles and the mean streamlines, a difference which rapidly grows larger as the number of blades is reduced. With five blades, Fig. 10, convergence was only satisfactory when the blades were stacked radially near the midchord. However, results for a fan with seven blades were obtained for three different stacking positions. Figure 11 shows the profiles obtained when the leading edge is radial, and Fig. 12, when the stacking point is at the trailing edge.

The profiles obtained with the different stacking points are compared in Fig. 13 in which all three profiles have been made to start at the origin by translating them in the θ-direction.

Results were obtained for a turbine with no exit swirl, i.e.

Downloaded 01 Jun 2010 to 171.66.16.70. Redistribution subject to ASME license or copyright; see http://www.asme.org/terms/Terms_Use.cfm

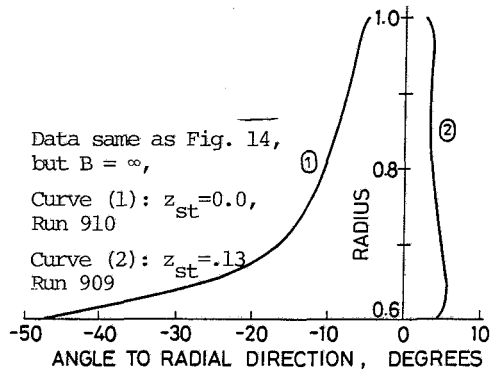


Fig. 18 Turbine, actuator duct: effect of stacking position on blade inclination near midchord

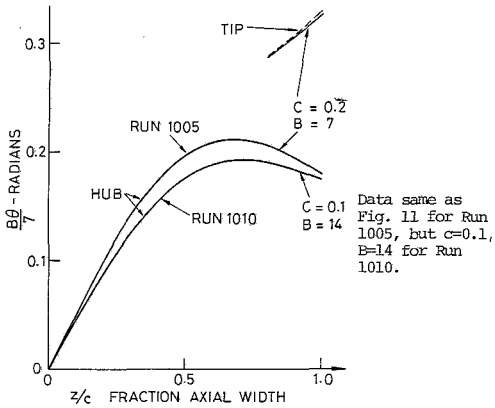


Fig. 19 Fan: effect of aspect ratio at fixed pitch-chord ratio on blade profiles

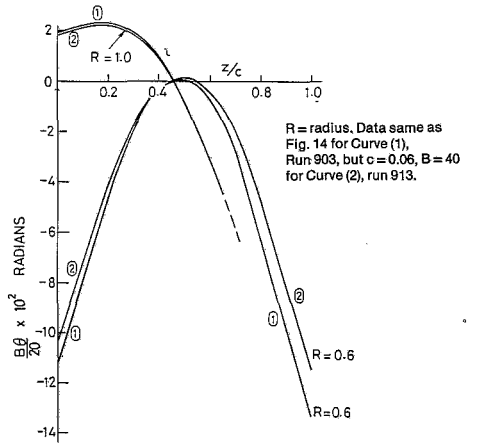


Fig. 20 Turbine: effect of aspect ratio at fixed pitch-chord ratio on the blade profiles

$\bar{V}_{\theta 2} = 0$, and a nominal 90 deg deflection impulse blade at the hub. The hub-tip ratio was 0.6, and the axial width was 0.13 to give an aspect ratio of 3 as on the fan. Figure 14 shows the profiles obtained with 20 blades stacked radially near the midchord position. Although convergence was obtained for this stacking position, it was not obtained with 20 or 30 blades stacked at the leading edge. To explore the reasons for the failure to converge, the number of blades was increased to infinity, i.e., the bladed actuator duct solutions were obtained with stacking at or near the leading and trailing edges and at the midchord position. Figures 15 and 16 show the blade profiles for stacking at leading and trailing edges, respectively. The large effect of stacking position on the blade

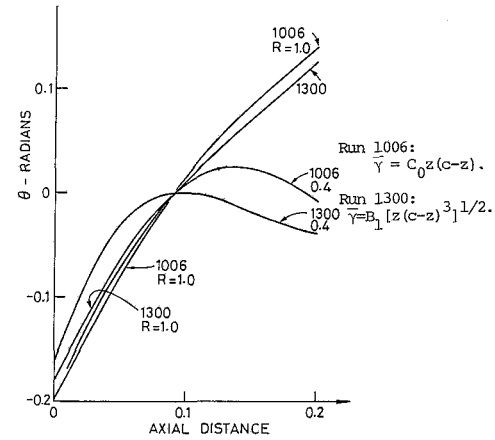


Fig. 21 Fan, 7 blades; effect of loading on the blade profiles. R = radius, z_{st} = .095

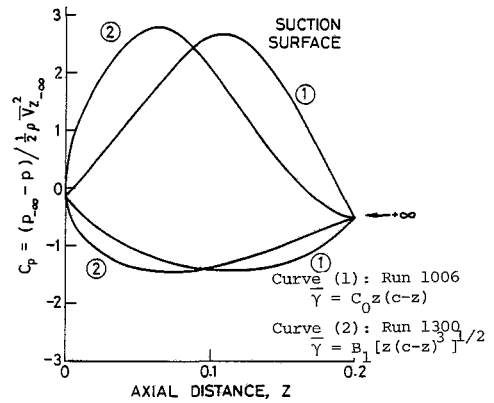


Fig. 22 Fan, 7 blades; effect of loading on pressure distribution at hub, z_{st} = 0.095

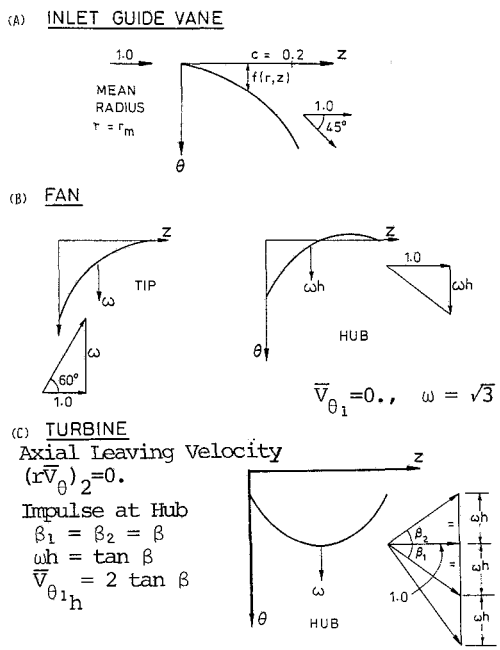


Fig. 23 Computational examples: (*a*) inlet guide vane, (*b*) fan rotor, (*c*) turbine rotor

profile at the hub is shown in Fig. 17. More striking is the effect on the mean axial velocity $\bar{V}_z$ at the hub also shown in Fig. 17. The curve labeled (1) shows that it falls to less than 30 percent of its upstream value when the blades are stacked

Downloaded 01 Jun 2010 to 171.66.16.70. Redistribution subject to ASME license or copyright; see http://www.asme.org/terms/Terms_Use.cfm

radially 0.025c from the leading edge. Convergence was not obtained for a stacking position at the leading edge, but at z_{st} = 0.05c it was obtained with a reduction of axial velocity at the hub to about half the upstream value. This steep decrease in axial velcoity as the stacking position approaches the leading edge suggests that the failure to converge is due to the reduction of the hub axial velocity to very small or even negative values. The physical explanation for this low axial velocity at the hub is that close to the hub $\partial f/\partial r$ reaches large values. In Fig. 18 we have taken a section of the blade at the plane z = 0.5c and plotted the angle of inclination of the blade to the radial direction for the two cases of the bladed actuator duct turbine (Runs 909 and 910) stacked at or near the leading and trailing edges, respectively. This angle is given by arctan-($r\partial f/\partial r$). At the hub for z_{st} = 0.025c the blade makes an angle of −47 deg with the radial direction. This large angle, coinciding with a high value of the bound vorticity which is at its maximum at z = 0.5c, leads to a high value of the tangential component of vorticity $\bar{\Omega}_\theta$ near the hub which is negative, as may be seen by studying Fig. 15 and either applying the right-hand screw rule or using the relationship

$$\bar{\Omega}_\theta = -\frac{d}{dz}(r\bar{V}_\theta)\frac{\partial f}{\partial r}$$

and remembering that drV_θ/d is negative. The high negative value of $\bar{\Omega}_\theta$ close to the hub induces a strong negative axial velocity at the hub and gives the result shown in Fig. 17.

As we have already seen from (22), when there is a finite number of blades it is necessary to make $\partial f/\partial r$ and therefore the angle of inclination of the blade zero at the walls to avoid infinite velocities. Nevertheless the inclination of the blade can still be large a short distance from the hub, see, for instance, Fig. 14 where there is a large average inclination (about 15 deg) between the midspan and the hub at the leading edge.

Because the flow near a wall may be represented by a vortex line and its image in the wall, a vortex line entering a wall at an angle from the radial direction other than zero is represented by a vortex line with a sharp kink, giving infinite velocities in the kink. If straight vortices are used to model swept wings, a similar problem arises at the junction between them.

As shown in (39), the actuator duct does not have the same wall boundary condition. A similar fundamental difference is found when first actuator discs and then spoke, i.e., radial vortices or lifting lines are used to represent a blade row. The rate of change of circulation around a spoke vortex in the direction normal to the wall must vanish at the wall if infinite velocities are to be avoided [8,9,17]. However, this condition need not be applied to the actuator disk because in the actuator disk and the actuator duct the vorticity is continuous and invariant in the tangential, θ, direction, and infinite velocities due to kinked vortex lines or discrete trailing vortices at the walls are not developed.

The effect of changes in aspect ratio was explored in Run 1010 for the fan with 7 blades by halving the chord and doubling the number of blades to keep the pitch chord ratio the same. Figure 19 shows that there is an appreciable increase in the camber at the hub as the aspect ratio is reduced. The results for the turbine Run 913 with 40 blades and a chord of 0.06 are shown in Fig. 20.

The effect of loading was explored in Run 1100 using equation (56) for the fan with blades stacked near the mid chord. Some of the results for the blade profiles and surface pressure distributions are shown in Figs. 21 and 22.

5 Summary and Conclusions

It has been shown that an iterative solution for the blade profiles of a large deflection three-dimensional cascade of normal solidity can be obtained by expanding the flow variables and the blade profile in series of smooth eigenfunctions (Fourier series, Chebyshev polynomials, and Bessel functions). This result has been shown for blades of zero thickness, invisicid ad incompressible flow, and the simple geometry of cylindrical annular walls. The Clebsch transformation has been used because it allows one to cast the equations of motion into a useful and convenient form in which the blades are represented by singularities; periodic generalized functions have been used to describe these singularities analytically.

Typical calculations for determining the blade profile are carried out for a free vortex annular cascade of constant hub and tip radii. In the course of the work, it was found necessary to introduce a geometrical condition for the blade shape at the annular walls (e.g., $\partial f/\partial r = 0$ at $r = h,1$), except when the number of blades is assumed to be infinite. In the determination of the blade shape for the annular cascade, a stacking requirement is needed, e.g., the choice of the axial distance at which the blade profile is radial, for instance. It has been shown that the stacking position can have a significant effect on the blade profile, the pressure distribution, and the radial and axial velocities. Changes in stacking position can lead to very small or possibly negative axial velocities.

The representation of blades by an actuator disk is well understood. By taking the number of blades to the limit of infinity, we obtain an *actuator duct* which, with the exception of the blade shape very close to the walls of the annulus, can be used to represent a row of blades, and it is shown that the radial and tangential velocities are dependent on the stacking position as well as on the swirl velocity schedule.

In the earlier work using the linearized theories and cascades of small deflection, it was shown that the three-dimensional effects were practically negligible in incompressible flow and that the "strip" theory was a fair approximation. However, in cascades of large deflection, this is not generally true. Several examples when strip theory does not apply have been demonstrated in the paper, for instance, by showing that changes of aspect ratio and stacking position affect the blade profiles.

The work needs to be extended to compressible flow, ducts of arbitrary geometry, and blades of finite thickness, including the effects of a stagnation point at the leading edge.

Acknowledgments

This research was partially supported by the Air Force Office of Scientific Research under contract no. F49620-82-K-0002, Dr. J. D. Wilson, Program Manager. The authors are also grateful to the staff of the Gas Turbine and Plasma Dynamics Laboratory, M.I.T., and the Whittle Laboratory, University of Cambridge, and E.R. Beggs for their assistance.

References

1 Hawthorne, W. R., Wang, C., Tan, C. S., and McCune, J. E., "Theory of Blade Design for Large Deflections, Part I: Two-Dimensional Cascade," ASME JOURNAL OF ENGINEERING FOR GAS TURBINES AND POWER, Vol. 106, April 1984, pp. 346–353.

2 McCune, J. E., "A Three-Dimensional Theory of Axial Compressor Blade Rows—Subsonic, Supersonic and Transonic,' Ph.D. thesis, Cornell Univ, 1958, (see also USAFOSR TN-58-72, *J. Aerospace Sc.*, 544 and 616, 1958.

3 Okuroumu, O., and McCune, J. E., "Lifting Surface Theory of Axial Compressor Blade Rows: Part I Subsonic Compressor: Part II—Transonic Compressor," *AIAA Journal*, Vol. 12, 1974, pp. 1363 and 1372.

4 Namba, M., "Lifting Surface Theory for a Rotating Subsonic or Transonic Blade Row," ARC R&M, #3740, 1974.

5 Homicz, G. F., and Lordi, J. A., "Three-Dimensional Lifting-Surface

Downloaded 01 Jun 2010 to 171.66.16.70. Redistribution subject to ASME license or copyright; see http://www.asme.org/terms/Terms_Use.cfm

Theory for an Annular Blade Row," *AIAA Journal*, Vol. 19, No. 4, 1980, pp. 492–500.

6 Tan, C. S., "Three-Dimensional, Vorticity-Induced Flow Effects in Highly-Loaded Axial Compressors," Ph.D. thesis, Massachusetts Institute of Technology, June 1978, (also GT&PDL Report Nos. 131 and 151).

7 Hawthorne, W. R., McCune, J. E., Mitchell, N. A., and Tan, C. S., "Non-axisymmetric Flow Through an Annular Actuator Disk; Inlet Distortion Problem," ASME JOURNAL OF ENGINEERING FOR POWER, Vol. 100, 1978, p. 604.

8 Tan, C. S., "Vorticity Modelling of Blade Wakes Behind Isolated Annular Blade-Rows: Induced Disturbances in Swirling Flows," ASME JOURNAL OF ENGINEERING FOR POWER, Vol. 103, No. 2, Apr. 1981.

9 Tan, C. S., "Three-Dimensional Incompressible and Compressible Beltrami Flow Through a Highly-Loaded Isolated Rotor," MIT GT&PDL Report 147, 1980.

10 Hawthorne, W. R., "On The Theory of Shear Flow," MIT GTL Report 88.

11 Thompkins, W., "An Experimental and Computational Study of the Flow in a Transonic Compressor Rotor," PhD thesis, Massachusetts Institute of Technology, 1976 (also Massachusetts Institute of Technology GTL Report No. 129, 1976.

12 Denton, J., "A Time-marching Method for Two-and Three-Dimensional Blade-To-Blade Flows," ARC R&M 3775, 1975.

13 Hildebrand, F. B., "Advanced Calculas for Applications," Prentice-Hall, 1976.

14 Gottlieb, D., and Orszag, S. A., "Numerical Analysis of Spectral Methods: Theory and Applications," CBMS-NSF Regional Conference Series in Applied Mathematics, SIAM, Philadelphia, 1977.

15 Lamb, H., *Hydrodynamics*, 6th ed., Dover, 1945.

16 Lighthill, M. J., "An Introduction to Fourier Analysis and Generalized Functions," Cambridge University Press, 1969.

17 Smith, L. H., "Secondary Flow in Axial-Flow Turbomachinery," ASME *Transactions*, 1955, p. 1065.

18 Falcao, A., "Three-Dimensional Flow Analysis in Axial Turbomachines," Ph.D. thesis, Cambridge University, 1970.

19 Marsh, H., "A Digital Computer Program for the Through-flow Fluid Mechanics in An Arbitrary Turbomachine Using a Matrix Method," ARC R&M #3509, 1968.

20 Tan, C. S., Wang, C., McCune, J. E., and Hawthorne, W. R., "Three-Dimensional Blade Design for Large Deflections Using An Analytical Theory," GT & PDL report No. 168, M.I.T., 1982 (also CUED/ATurbo/TR 115, Cambridge University Engineering Laboratory, 1982).

Downloaded 01 Jun 2010 to 171.66.16.70. Redistribution subject to ASME license or copyright; see http://www.asme.org/terms/Terms_Use.cfm

Measurements of the Flow From a High-Speed Compressor Rotor Using a Dual Probe Digital Sampling (DPDS) Technique

R. P. Shreeve
Director,
Turbopropulsion Laboratory,
Department of Aeronautics,
Naval Postgraduate School,
Monterey, Calif.

F. Neuhoff
Project Engineer,
Exotech Inc.

The flow from a high-speed rotor in a rotor-first arrangement has been measured using a "dual-probe, digital sampling (DPDS)" technique. The flow field was found to be steady in rotor coordinates (periodic in machine coordinates) outside the rotor wake, and three components of velocity and the pressure field were determined in this area. The wake regions were unsteady. In these regions the measurements based on ensemble averages of multiple samples did not follow the behavior established during calibration in steady uniform free-jet flow, except near the wake center. The broadening of the wake and three-dimensional effects in the flow field were measured at reduced throttle and increased speeds. The results serve to illustrate the potential of the measurement technique, on which the emphasis of the presentation is placed.

Introduction

The present work reports the first results in a program aimed at the determination of the flow field produced by a high-speed compressor rotor in a rotor-first arrangement. Details of the work are given in [1]. The purpose of the program is to obtain careful and detailed information with which to test the validity of computational descriptions of compressor flow fields. A small, 450 HP transonic single-stage axial compressor and test rig capable of continuous operation has been used. The rig was designed specifically to facilitate measurements of internal flow behavior. The present compressor stage is one of in-house design. Instrumentation was developed earlier and applied to measure time-averaged flow behavior through the compressor [2]. Concentration has been placed more recently on the determination of the detailed internal aerodynamics.

In order to measure the unsteady flow field one must either use high-response probes or an optical technique of some kind. While nonintrusive laser velocimetry techniques have many advantages, in a turbomachine they are normally able to measure only two components of the velocity. Furthermore, they do not provide measurements of the pressure field, and in highly unsteady flows, since LDV systems measure particle velocity, the accuracy must be questioned. There is good reason therefore to approach the problem of measuring the unsteady flow field in other ways, and ideally to obtain independent, redundant measurements of the same phenomena. The work reported here was such an attempt.

Controlled (phase-locked) digital sampling from Kulite transducers was adopted as a technique for defining both case wall pressure signatures and the periodic exit flow field from the rotor. Early results were reported, and a method was proposed in [3] for obtaining the full periodic velocity field at the rotor exit from measurements with two very simple Kulite probes. The present paper reports the first distributions measured of the velocity vector (magnitude, yaw angle, and pitch angle), across two rotor blade passages in both hub-to-shroud and blade-to-blade directions, made using the proposed technique. The attempt is made to introduce the measurement concept as simply and clearly as possible and to exhibit and discuss the type of results which have been achieved so far. This has required the omission of details of the calibration and verification tests and of factors found to be important in the development of the technique. These will be reported separately. References to existing reports are given.

Results are given of measurements made with two different sets of probes (referred to as first and second generation designs). The results of the first set of probes are discussed largely on the basis of qualitative behavior. The second generation probes were smaller in diameter and could be expected to better resolve the flow within the rotor blade wakes. Since measurement redundancy was inherent in the approach, it was shown definitively that the measurements obtained with the smaller probes outside the wakes, in regions of the flow which were periodic in the machine frame (steady with respect to the rotor), were valid. However,

Contributed by the Gas Turbine Division of THE AMERICAN SOCIETY OF MECHANICAL ENGINEERS and presented at the 28th International Gas Turbine Conference and Exhibit, Phoenix, Arizona, March 27-31, 1983. Manuscript received at ASME Headquarters January 4, 1983. Paper No. 83-GT-215.

Copyright © 1984 by ASME
Downloaded 01 Jun 2010 to 171.66.16.70. Redistribution subject to ASME license or copyright; see http://www.asme.org/terms/Terms_Use.cfm

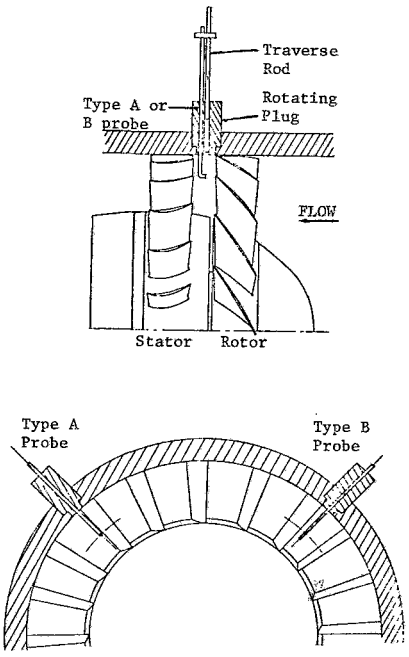


Fig. 1 Arrangement of probes in the compressor

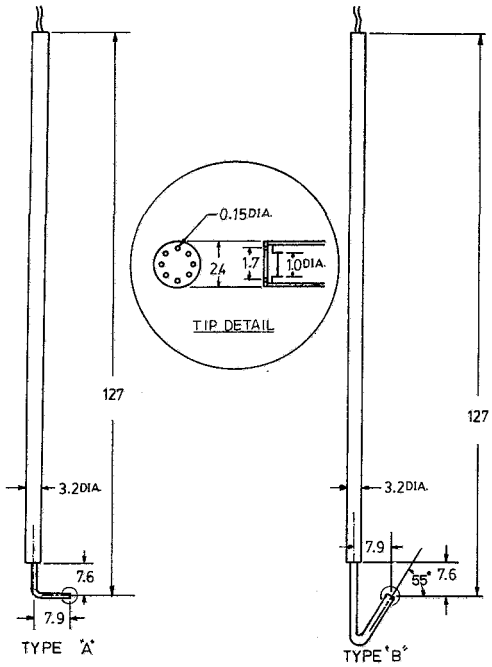


Fig. 2 Probe geometries (first-generation design)

measurements obtained in wake regions which were observed to be highly unsteady in the rotor frame could not generally be interpreted accurately on the basis of probe calibrations obtained in a steady flow. The implications of these observations are discussed.

DPDS Measurement Technique

The measurement approach derives from the need to measure a flow field which is, ideally, periodic at blade-passing frequency. Departures from periodicity might occur however as a result of either steady differences in the flow through different blade passages, or what would be viewed by an observer on the rotor as unsteady flow effects, which could be either periodic or random in nature.

The approach to be described here takes complete account of the steady differences in the flow between rotor blades by identifying and measuring behind specific blade passages. It then attempts to extract from the flow, which is unsteady to an observer on the rotor, its average behavior by ensemble-averaging readings taken on successive rotations. The concept of the measurement is therefore based on the contention that the flow to be measured is, on average, periodic and the task of the measurement is to establish that average behavior. The approach therefore is to attempt to measure that which a steady-flow analysis code for rotor flows attempts to predict.

The DPDS method uses two different high response, impact pressure probes, precisely controlled digital sampling so that the two probes measure at the same location in the rotor flow field, and a reduction procedure of the data from the two probes which is analogous to that used for multisensor (four- or five-hole) flow probes. These elements will be discussed here in turn, giving only details necessary to understand the measurement concept. Compressor hardware and test procedures will be given in the section which follows.

Probes. The two probes are inserted through the compressor case wall as shown in Fig. 1. The probes are separated peripherally, but the sensors at the tips are at the same radial position. The probes are, conceptually, simple impact probes with similar geometries at the very tip consisting of a semiconductor transducer protected by a vented plate, or screen (Fig. 2). The probes are mounted eccentrically in round plugs so that they can be rotated about a radial line through the sensor tip. The effect of rotation is to "yaw" the probe with respect to the machine axis. The two probes differ only in the angle of inclination of the tip section with respect to the machine axis. The "Type A" probe is at 0 deg to the axis. The "Type B" probe is hook-shaped, with the tip at either 55 deg to the machine axis (first generation design) or 35 deg to the machine axis (second generation design). Figure 2 gives the dimensions of the first generation of probes incorporating Kulite XB-093-25 transducers. Figure 3 shows a view of the tip of one of the second generation probes, which were smaller

Nomenclature

C_P = pressure coefficient
c_p = specific heat at constant pressure
c_{ij} = coefficients in calibration surface for X
d_{ij} = coefficients in calibration surface for ϕ
L,N = order of polynomial approximation
M = Mach number
p = pressure
T = temperature
V_t = limiting, or stagnation velocity, $(V_t = \sqrt{2c_pT_t})$
X = dimensionless velocity obtained by dividing velocity by V_t
α = yaw angle
β = pressure coefficient defined in equation (3)
γ = pressure coefficient defined in equation (4)
ϕ = pitch angle
$\epsilon_{\alpha,\phi,X}$ = error in α, ϕ, X, respectively

Subscripts

A = Type A probe
B = Type B probe
i,j = indices
max = maximum value
s = static (near static when used as A_s)
t = total (or stagnation) value
1,2,3,4 = combination probe sensors

Downloaded 01 Jun 2010 to 171.66.16.70. Redistribution subject to ASME license or copyright; see http://www.asme.org/terms/Terms_Use.cfm

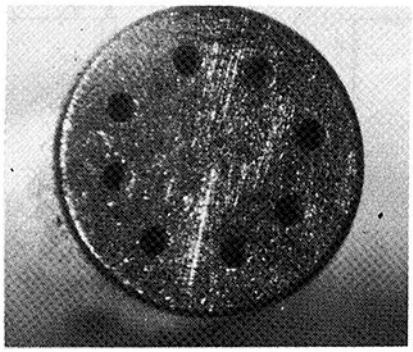


Fig. 3 View of probe tip (second generation, Type A or Type B). Diameter = 1.57 mm.

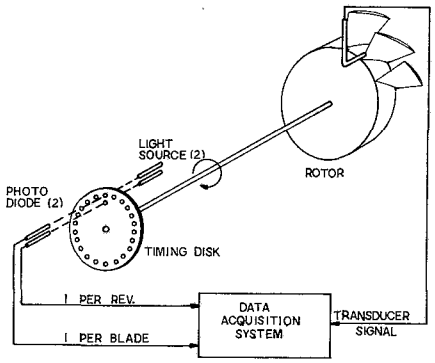


Fig. 4 Controlled (paced) sampling technique

everywhere in diameter (1.57 mm) and incorporated Kulite XB-063-25 transducers.

The frequency response of the probes is higher than can be measured in available calibration facilities. Oscilloscope traces of probe output in the rotor wake reported earlier [3] showed response well in excess of 100 KHZ. Since blade passing frequencies in the present machine can not exceed 9 KHZ (and in the present measurements did not exceed 6 KHZ), it is accepted that the probe output responds accurately to the pressure, velocity, and angle changes present in the flow field generated by the passing rotor.

Controlled Sampling. The DPDS technique requires that data be digitized from each of the two probes when they are at precisely the same location with respect to the rotor blading. In effect, the Type A and Type B probe readings are recorded at the same point in the rotor flow field, but at different times.

Precise control of the data acquisition is effected using a "Pacer" [4, 5]. As shown in Fig. 4, inputs to the Pacer are one-per-blade and one-per-rev. optical signals obtained from a timing disk on the compressor shaft. The Pacer "locks-on" to the blade-passing frequency and outputs from a PLL (phase-locked-loop) circuit a pulse-train at 128 times the blade passing frequency. The Pacer interrupts the "command" and "flag" lines between a Hewlett-Packard HP21MX computer and HP 5610 A/D converter. Conversion is allowed to occur when a programmed number of counts matches the number of pulses counted following a one-per-rev. reset pulse. Because of the "lock-on" feature of the PLL circuit, there are always 128 counts per passing blade passage, no matter what variations occur in the rotor speed. With the Type B probe peripherally displaced by 90 deg (4½ blade passages of the 18 bladed rotor) delaying the Type B conversion by 4½ × 128 = 576 counts ensures that the Type B probe reading is taken at precisely the same location in the rotor frame as the reading of the Type A probe.

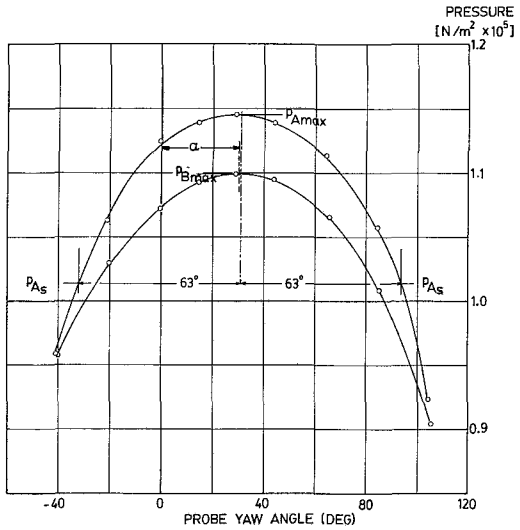


Fig. 5 Example of Type A and Type B probe data at one position in the rotor flow field

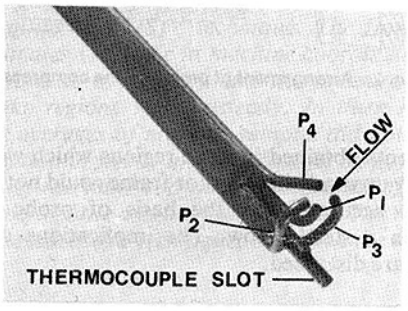
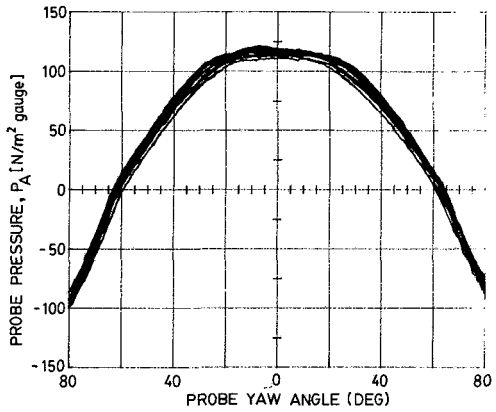


Fig. 6 Combination temperature-pneumatic flow probe

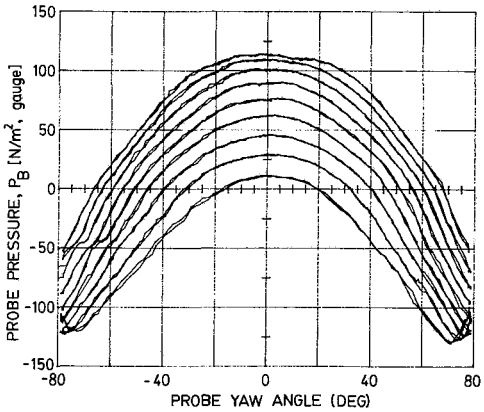
Thus a particular point in the rotor frame can be selected and with the Type A and Type B probes set to a particular yaw angle, each probe can be sampled. In order to average unsteadiness in the rotor flow, the readings can be taken any desired number of times and the ensemble averaged value computed.

Data Reduction. In order to obtain sufficient information from each point in the rotor flow field to determine completely the local average velocity vector (magnitude (X), yaw angle (α) and pitch angle (ϕ)), the Type A and Type B probes are set to a number of specific yaw angles (from five to nine typically) and ensemble averages of successive samples of the output voltages are recorded at each probe setting. From an on-line calibration procedure (described in the following section), the data are reduced to probe pressures. An example of a set of data taken at one position in the rotor flow field and reduced to pressures is shown in Fig. 5. Also shown in Fig. 5 is the result of fitting a fourth-order polynomial to the data from each probe. This procedure is used to define p_{Bmax}, the maximum value from the Type B probe, p_{Amax}, the maximum value from the Type A probe and p_{As}, the value of pressure from the Type A probe where the right and left branches of the output curve are separated by a difference in yaw angle of 126 deg. The data in Fig. 5 are viewed as if they were obtained in a uniform steady flow at an unknown Mach number, yaw angle, and pitch angle (which is equivalent to assuming that the probes respond without error or delay to the passing flow gradients). The unknown flow yaw angle is determined immediately as the Type B probe yaw angle corresponding to p_{Bmax}. (In practice, as seen in Fig. 5, the value corresponding to p_{Amax} may differ slightly as a result of curve fitting to the flatter characteristic of the Type A probe.)

Downloaded 01 Jun 2010 to 171.66.16.70. Redistribution subject to ASME license or copyright; see http://www.asme.org/terms/Terms_Use.cfm



(a) Type A Probe



(b) Type B Probe

Fig. 7 Probe calibration data at M = 0.4 and nine pitch angles from −15 deg to +25 deg

The situation is then very similar to that encountered in using a multisensor steady flow (or averaging) probe such as is shown in Fig. 6. The probe in Fig. 6 (which is in fact a combination temperature-pneumatic probe, shown in this figure without its fine-wire thermocouple sensor) is used by first rotating the probe about its shaft to balance the pressures at sensors p_2 and p_3 and reading the yaw angle from a scale. When balanced, the pressures at the sensors p_1, p_2 ($= p_3$) and p_4 are used through a calibration procedure to calculate the unknown Mach number and pitch angle. (The temperature is needed to calculate velocity.) The procedure used in reducing the data from Type A and Type B probes is to treat p_{Amax} as being equivalent to p_1, p_{As} as being equivalent to p_2, and p_{Bmax} as being equivalent to p_4, and to use the calibration procedure established for the multisensor probe.

The procedure is described in [6] for the combination probe and in [7] and the Appendix for the Type A and Type B probe system. In summary, the procedure establishes, from calibration data obtained with the probes mounted in a uniform steady free jet flow at controlled Mach numbers and pitch angles, surface approximations to the probe characteristics in the form

$$X = X(\beta,\gamma) = \sum_{i=1}^{L}\left[\sum_{j=1}^{N} c_{ij}\beta^{(j-1)}\right]\gamma^{(i-1)} \tag{1}$$

and

$$\phi = \phi(\beta,\gamma) = \sum_{i=1}^{L}\left[\sum_{j=1}^{N} d_{ij}\beta^{(j-1)}\right]\gamma^{(i-1)} \tag{2}$$

where β and γ are dimensionless pressure coefficients defined as

$$\beta = \frac{P_{\text{Amax}} - p_{\text{As}}}{P_{\text{Amax}}} \tag{3}$$

and

$$\gamma = \frac{p_{\text{Amax}} - p_{\text{Bmax}}}{p_{\text{Amax}} - p_{\text{As}}} \tag{4}$$

Once the coefficients c_{ij} and d_{ij} have been established from the calibration data (using procedures given in [8]), any set of data such as that shown in Fig. 5 can be reduced to obtain the local value of the dimensionless velocity and the pitch angle using first equation (3) and equation (4), followed by equation (1) and equation (2).

The following additional comments are made concerning the technique; the first concerns the necessity for using two probes. In principle, readings from a single probe at the maximum and from two other yaw angles are sufficient to determine calibration surfaces which depend on Mach number and pitch angle. In practice, however, the results are not useful because of the lack of sensitivity. To illustrate, calibration data from the Type A and Type B probes are shown in Fig. 7(*a*) and Fig. 7(*b*), respectively, (and discussed in the Appendix). The Type A probe output is quite insensitive to pitch angle variations in the range in which the pitch angle is to be measured. While it cannot be seen very clearly in Fig. 7(*a*), the Type A probe output is almost totally insensitive to either pitch or yaw angle variations in the range −10 deg to +10 deg and the value of p_{Amax} is then very close to the stagnation pressure. The value of p_{As} is close to (but not exactly equal to) local static pressure since the yaw angle at which static pressure is registered has been shown to be quite insensitive of Mach number and pitch angle [9]. Thus the Type A probe is by itself a Mach number indicator, which is insensitive to pitch angle. On the other hand, Fig. 7(*b*) shows that the Type B probe is particularly sensitive to pitch angle and this is in fact its purpose. Unfortunately, at large yaw angles the probe characteristics are not well behaved, and over what might be considered to be the useful range the shape of the characteristic is insensitive to pitch angle (and to Mach number). Therefore, only one probe yaw angle in addition to the maximum value can be considered to give independent information. Once again, a second probe is required.

Finally, two alternate techniques for representing and using the calibration data from the two-probe system to reduce data from the compressor have been reported [9, 10]. All the results reported in the following section however have been obtained using the surface approximation technique described above.

Compressor Measurements

Compressor. The compressor in which measurements were made is a single-stage machine with axial inlet flow to the rotor. Figure 1 shows the flow path to scale. The outside case wall diameter is 27.94 cm (11 in.) and the blade height is approximately 6.99 cm (2.75 in.), 4.83 cm (1.9 in.) and 4.56 cm (1.8 in.) at stations upstream of the rotor, downstream of the rotor, and downstream of the stator, respectively. The compressor is driven by a cold-air turbine supplied from a continuous laboratory air supply [11]. Instrumentation is provided to measure stage performance. Radial survey probes are used ahead of and between blade rows, and the case wall can be rotated to position instrumentation peripherally. A combination temperature-pneumatic probe of the type shown in Fig. 6 is positioned downstream of the rotor, peripherally displaced but at the same axial station as the two Kulite probes, and is used to obtain the time average velocity vector and temperature using the calibration procedure given in [6]. Data acquisition, recording, and reduction uses an HP21MX

Downloaded 01 Jun 2010 to 171.66.16.70. Redistribution subject to ASME license or copyright; see http://www.asme.org/terms/Terms_Use.cfm

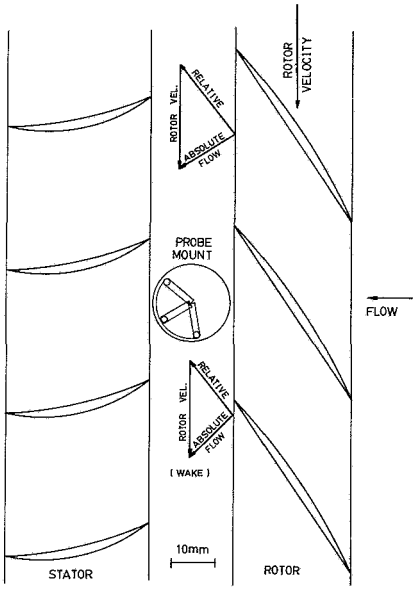


Fig. 8 Probe orientation and blading geometry at the case wall (shown to scale)

computer-controlled data system. The software is described in [7] and [12].

Pneumatic pressures are recorded using a Scanivalve, strain gauge transducer, signal conditioning, and DVM to an uncertainty of ± 25 N/m^2 (0.1 in. of water). Kulite differential transducer signal conditioning circuits output through a scanner to the DVM and through DATEL amplifiers to separate channels of a ± 1.0 V range HP 5610 a-d converter. On-line calibration ensures an uncertainty in Kulite pressure data to ± 0.002 of the pressure equivalent of the 1 V range, typically ± 50 N/m^2 (0.2 in. of water).

The geometry of the rotor and stator blading at the tip is shown to scale in Fig. 8. Also shown to scale is a radial view of the probe (either Type A or Type B) and the range of yaw angles within which it is rotated in the data acquisition process. Velocity diagrams typical of the flow within and outside the rotor wake are shown. It is noted that the rotor blade profile is flat on the pressure side and is a circular arc on the suction side. The stator blades are double circular arc.

Test Procedure. A procedure was used which acquired data sufficient to define the velocity distribution at one radial position across two adjacent blade passages. The procedure involved taking time-integrated data (using the DVM) required to calibrate the temperature-sensitive Kulite transducers on-line, and "Paced" data (using the A/D converter) at each of 256 positions (counts) with the probes set at up to nine different yaw angles. A sequence was selected such that the requirement for mechanically adjusting the probe yaw angles was minimized. It was the mechanical changes which largely determined the time required to acquire the data. The sequence was as follows:

(*i*) The compressor speed and throttle were adjusted to produce the desired operating condition. Complete steady-state performance data were recorded.

(*ii*) The combination probe was adjusted (balanced) to the time-average flow angle. The Type A and Type B probes were set to the same angle and data required to calibrate the Kulite transducers were recorded using the DVM. First the probe outputs were recorded when atmospheric, and four different levels of air pressure were applied to the reference side of the transducers. The slopes (voltage output versus differential pressure) of each transducer were automatically computed in the acquisition program using a least squares linear fit to the five data points. (This procedure was repeated after all the data were acquired. The data were only accepted if the two slopes were within ± 1.5 percent, whereupon mean values were used in the data reduction.)

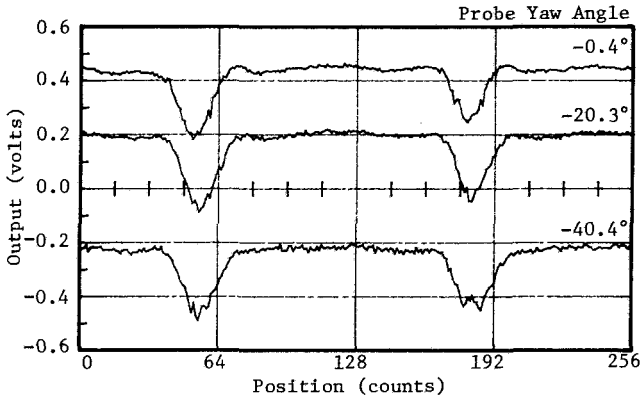


Fig. 9 Examples of paced data from the Type A probe

(*iii*) "Paced," digitized data were recorded at 256 positions (counts) across two selected blade spaces using a programmed number of samples (10 to 40) at each position. The ensemble average values at each position were stored. (A DO loop in the acquisition program was programmed from 1-256.)

(*iv*) Reference data for the compressor (speed, flow rate, etc.), data from the combination probe and time-averaged outputs of the Type A and Type B probes were recorded using the DVM.

(*v*) The Type A and Type B probes were yawed, in unison, to four angles in each direction from the time-average angle setting. At each setting the procedures in steps (*iii*) and (*iv*) above were repeated. Angles were chosen to range from -70 deg to $+80$ deg with respect to the time-average angle to best accommodate the expected flow yaw angle behavior within the rotor wakes.

Examples of the data obtained in step (*iii*) at three yaw angle settings of the Type A probe are shown in Fig. 9. The 256 data points at each probe yaw angle are shown plotted with the plotter pen down. The rotor blade wakes are evident, but it can be seen that the process of ensemble averaging (shown for 40 samples) produces relatively noise-free distributions of voltage output. The total quantity involved in one set of data and its general behavior is illustrated in Fig. 10. Results from both probes are shown for every fourth count of the first half of the 256 counts recorded. One eighth of the complete data set is therefore shown. The data reduction procedure to be outlined next uses the data which make up corresponding curves (at the same number of counts) in the two sections of Fig. 10. This is what is shown in Fig. 5.

Data Reduction. The reduction of probe voltage output to values of pressure requires a knowledge of the slope and the intercept of the transducer calibration curves. Since both are known to depend somewhat on temperature, and the exact temperature of the transducer immersed in the flow field is unknown, an on-line calibration procedure has been followed. First, the slopes were evaluated as described in the test procedure. The intercepts were obtained by assuming that the time-averaged output of the Type A and B probe system was consistent with the time-averaged behavior measured by the combination probe. The combination probe was used to obtain the time-averaged values of α, X, ϕ, p_t, and p_s. Corresponding values of $c_{p\mathrm{Amax}}$ and $c_{p\mathrm{Bmax}}$ were obtained from the definitions in equation A(1) and A(2). These pressures were then assumed to correspond to maximum values of the time-averaged outputs of the two probes, which fully determined the intercepts. Voltages from both probes were then reduced to pressures, β and γ were calculated using equation (3) and equation (4) for each set of data at each

Downloaded 01 Jun 2010 to 171.66.16.70. Redistribution subject to ASME license or copyright; see http://www.asme.org/terms/Terms_Use.cfm

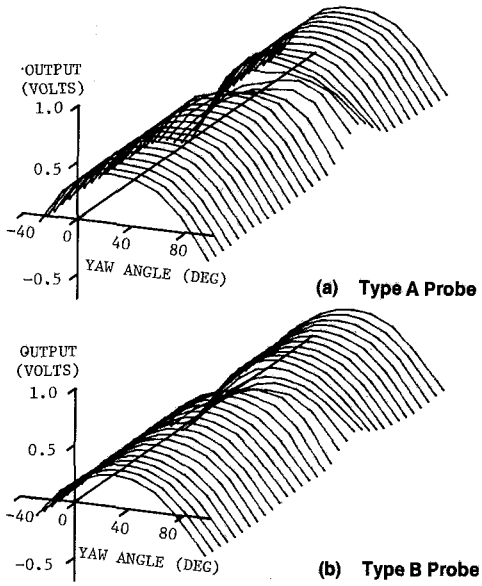


Fig. 10 Ensemble averaged DPDS data at one radial position (one blade passage, every 4th count = 1/8 total data set)

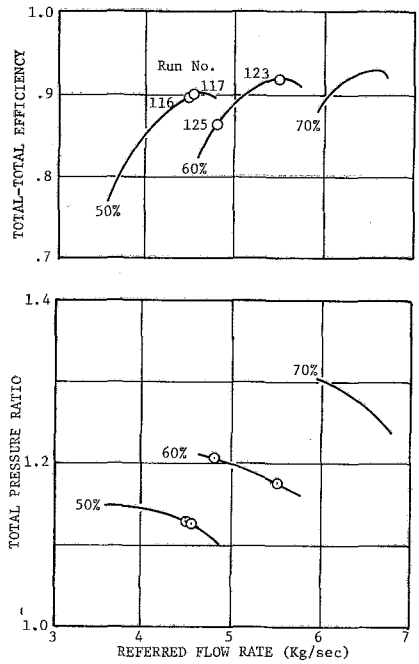


Fig. 11 Compressor stage performance at 50 percent, 60 percent, and 70 percent of design speed (30,460 rpm)

position (counts), and the values of X and ϕ were calculated using equation (1) and equation (2).

Results and Discussion

First-Generation Probe System. Results were obtained using the first-generation probe system with the compressor operating at 15,230 rpm (50 percent of design speed) and throttled to near peak efficiency. A partial map for the stage is shown in Fig. 11, and the machine condition for the first probe data is identified there as run 117. Data were obtained at eight radial positions from hub to tip across two blade passages. The resulting distributions of dimensionless velocity (X), yaw angle (α) and pitch angle (ϕ) are shown in Fig. 12. (It is noted that the limiting velocity, V_t, at room temperature is approximately 760 m/s (2500 ft/s).) Also shown in each distribution is the time-averaged value obtained from the combination probe.

In discussing the results, it is first noted that the data are shown plotted by the computer (pen down) without smoothing. From oscilloscope observations of probe outputs, the area of the rotor blade wake (which corresponds closely to where the yaw angle is increased) was clearly not periodic. In acquiring the data, 40 separate samples were taken at each point through the wakes and 15 were taken outside the wakes. The resulting ensemble averages are seen to result in a smooth and coherent distribution of flow characteristics throughout. It is noted that each data point shown was reduced from two sets (2 probes) of 9 ensemble averages (at each probe angle) digitized at quite different times in the acquisition process. The coherence of the behavior from point to point at a single radial position is therefore better than might have been expected. The clearly coherent changes in behavior observed with radial displacement is striking.

The agreement of the measurements with the time-average values is to be expected since the on-line calibration procedure forces the time averaged behavior of the Kulite system to duplicate that of the combination probe. However, it is noted that this simply fixes the intercepts for the transducers, and the paced data from which the data in Fig. 12 were reduced were otherwise obtained independently.

Qualitatively, the yaw angle distribution is as would be expected, with increased magnitudes resulting from lower relative velocity in blade wake regions. The absolute velocity magnitude appears to vary outside the wake nearer to the hub, with larger magnitudes from the suction side of the blades. The outermost distribution was taken 4.83 mm (0.19 in.) from the case wall and was probably influenced by case wall boundary layer and tip flow effects. This is most evident in the derived pitch angle which is seen to vary as much outside as inside the blade wakes.

The qualitative behavior of the results was examined using data obtained on the annulus centerline at the machine condition indicated as Run 116 in Fig. 11. The dimensionless velocity and yaw angle results at this condition are shown in Fig. 13, and three discrete conditions to be examined at counts 47, 88 and 95, respectively, are indicated. Count 47 is outside the wake, count 88 corresponds to the minimum velocity, and count 95 corresponds to the maximum yaw angle (which occurs at a velocity magnitude greater than the minimum). The velocity diagrams which correspond to the data at these three positions are shown in Fig. 14. It can be seen that the relative flow velocity vectors for the three positions and for the time-averaged condition are at 51 deg or 52 deg (50.8 deg was used in design). Hence a relative velocity which is almost constant in angle but wakelike in magnitude is implied by the reduced data. It can also be seen in Fig. 14 why the minimum in absolute velocity does not occur at the maximum yaw angle. If the relative flow angle were truly constant, then the absolute velocity vector would move along the broken line drawn parallel to this direction. The minimum velocity magnitude occurs where the absolute velocity is normal to the broken line (approximately true here at count 88), whereas the maximum yaw angle occurs where the magnitude of the relative flow velocity is a minimum. Hence the behavior of the derived velocity magnitude and angle is consistent with a nearly constant relative flow angle. The calculated distribution of the relative flow vector showing a nearly classic wake is shown in Fig. 15 for the data from Run 116.

Second-Generation Probe System. Data were obtained using the second-generation probe system on the centerline of the compressor annulus, at 18300 rpm (60 percent of design speed) at different compressor flow rates. The machine run conditions are indicated in Fig. 11. Run 123 was taken near peak efficiency while Run 125 was at more throttled con-

Downloaded 01 Jun 2010 to 171.66.16.70. Redistribution subject to ASME license or copyright; see http://www.asme.org/terms/Terms_Use.cfm

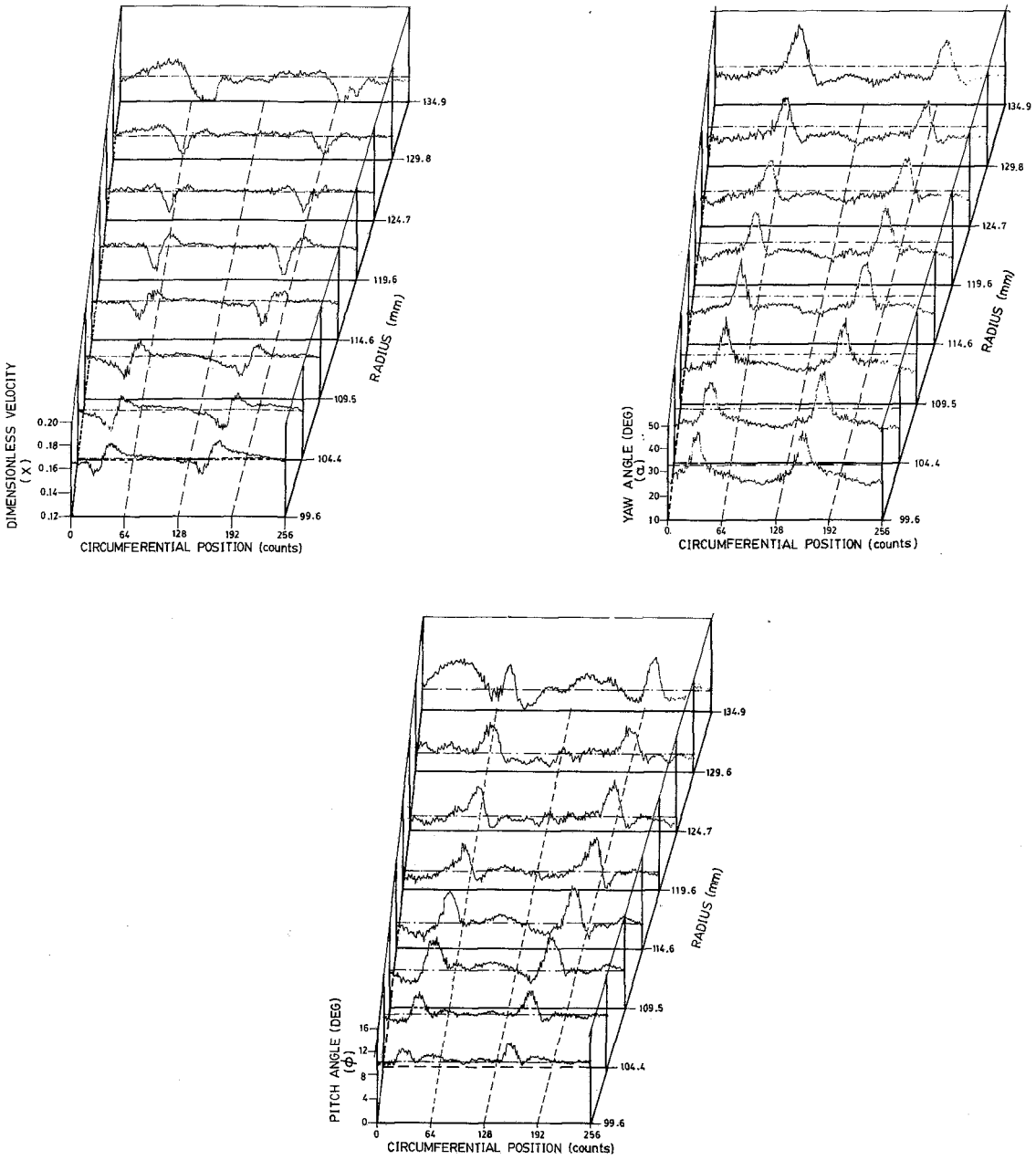


Fig. 12 Flow field from compressor rotor at 50 percent speed near peak efficiency using first-generation probes

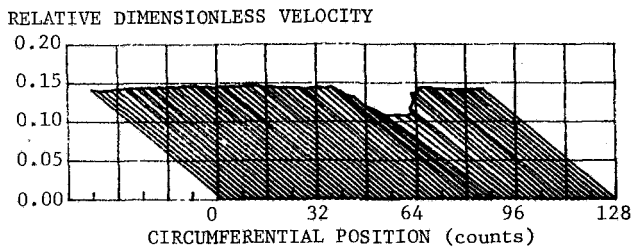


Fig. 13 Measurements at midspan at 50 percent speed (run 116, near peak efficiency)

ditions. Ensemble averages were taken over 40 samples at all blade-to-blade positions. The results are shown in Fig. 16.

It can be seen that as the compressor was throttled the average yaw angle increased, the change in yaw angle through the wake increased, and the wake width increased. There was also a significant change in pitch angle in the wake, with up to 12 deg positive increase indicated at the throttled condition. The pitch angle distribution outside the wake appeared to be little changed with throttling but showed greater variations than was observed at 50 percent speed. The velocity magnitude showed considerable change in the wake region; however, examination also showed that the variations in yaw angle and velocity magnitude remained consistent with almost constant relative flow angle for each set of data.

Verification of the Measurements. The qualitative behavior of the data has been discussed and has left few obvious questions. The question of quantitative accuracy remains. Fortunately, inherent in the measurement technique is measurement redundancy, which allows the accuracy to be verified. The verification at a given blade-to-blade position involves an examination of whether the data obtained there at the 9 yaw angles follow the same characteristic as that obtained during calibration in steady flow at the corresponding

Downloaded 01 Jun 2010 to 171.66.16.70. Redistribution subject to ASME license or copyright; see http://www.asme.org/terms/Terms_Use.cfm

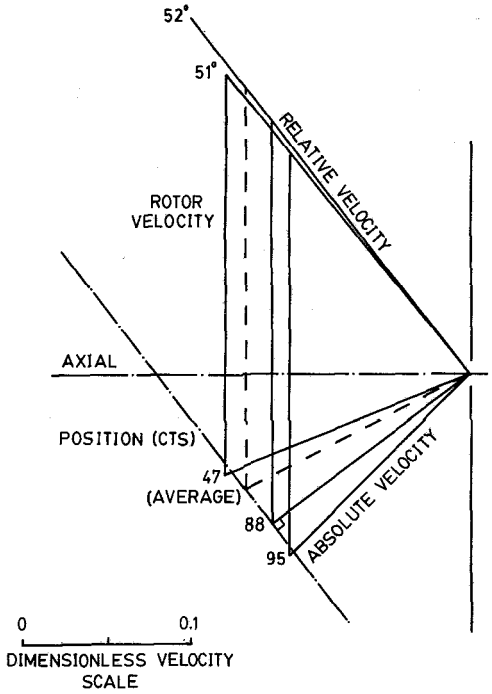


Fig. 14 Velocity diagrams for data in Fig. 13 (run 116)

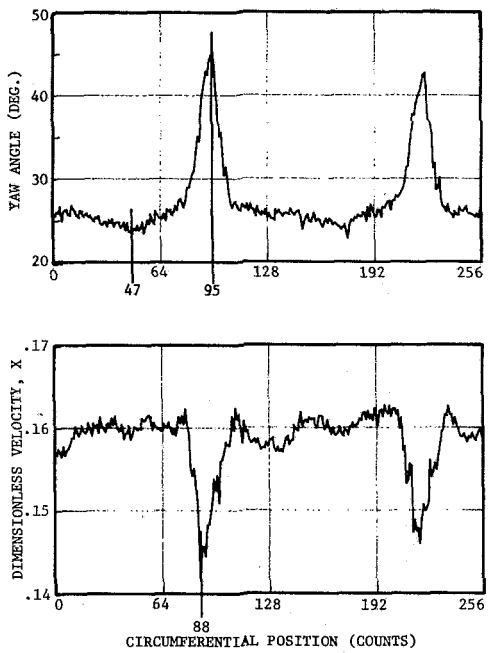


Fig. 15 Relative flow velocity vectors at midspan deduced from absolute measurements (run 116)

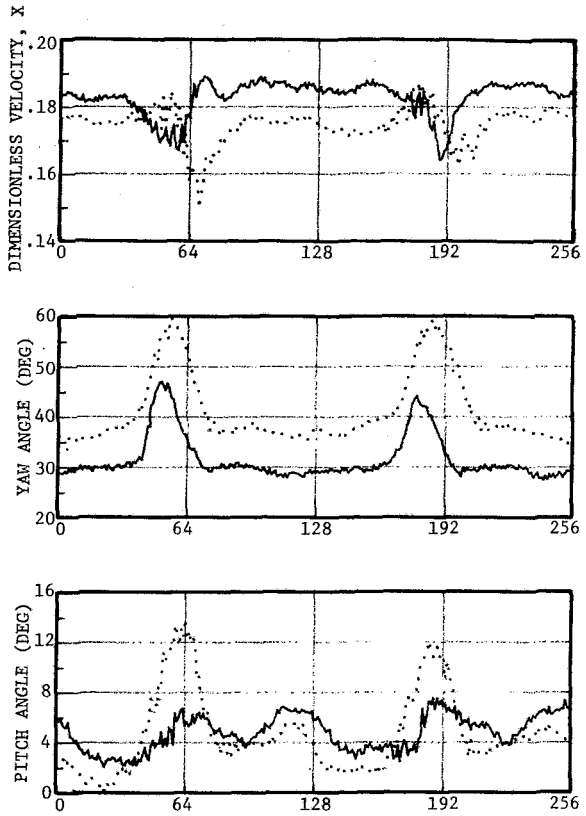


Fig. 16 Second-generation probe measurements at midspan at 60 percent speed (—— Run 123, peak efficiency; · · · · Run 125, throttled)

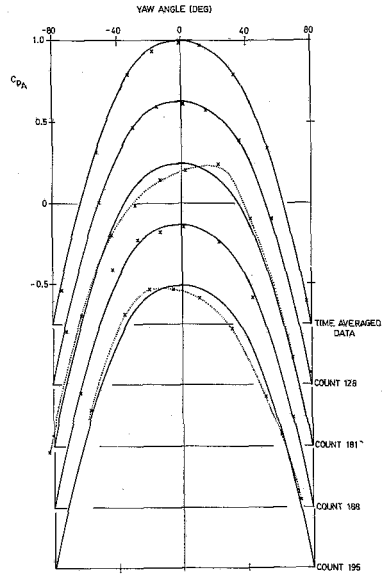


Fig. 17 Pressure coefficient versus yaw angle for Type A probe at specific positions in rotor flow field (Run 123: solid line is from calibration at $M = 0.4$, $\phi = 0$ deg)

Mach number and pitch angle. This has been done for one set of data taken with the Type A probe.

If the output of the Type A probe is represented as a pressure coefficient, C_{pA}, defined as

$$C_{pA} = \frac{p_A - p_s}{p_t - p_s} \tag{5}$$

it is found that C_{pA} depends very little on Mach number generally, and very little on pitch angle in the range -5 deg $< \phi < 20$ deg [9]. Thus when the local values of X (or Mach number) and ϕ have been derived, the local values of p_t and p_s are obtained by solving equation A(1) and equation A(2) using the measured values of p_{Amax} and p_{Bmax}. Values for C_{pA} can then be calculated using equation (5) for each probe yaw angle. These values can be imposed on the curve of C_{pA} versus α obtained at a similar Mach number and similar pitch angle during calibration.

This has been done for data obtained in Run 123 and the results are shown in Fig. 17. First, it can be seen that the time-averaged data obtained as a function of yaw angle closely approximated the behavior in steady flow. Also, data acquired outside the wake region (at count 128) was consistent

Downloaded 01 Jun 2010 to 171.66.16.70. Redistribution subject to ASME license or copyright; see http://www.asme.org/terms/Terms_Use.cfm

with steady-flow behavior. Inside the wake, however, it is clear that the behavior of the ensemble-averaged data do not follow the characteristic established in steady flow except at the very center (at count 188). Going into the wake (at count 181), the characteristic is skewed and the peak probe output is to the right. Coming out of the wake (at count 195), the characteristic is skewed, with the peak output to the left.

It must therefore be concluded that reduced data obtained outside the unsteady wake regions can be accepted to within the uncertainty derived from the measurement uncertainty. The reduced data for the area of the wake contains an unknown uncertainty for which an explanation is required. The values at the center of the wake, however, appear also to be verified.

Assumptions and Sources of Error. The assumption was made in the on-line calibration that the time-averaged behavior of the Kulite probe system could be equated to that given by the combination probe. This was supported in the verification check above; however, the result was that the absolute levels of the parameters derived from the Kulite probe system depended on the accuracy of the combination probe. Since averaging errors can occur in pneumatic probes (although as shown in [6] they are negligible for the conditions found behind the rotor at present speeds), errors in the pressure measurements of the combination probe sensors were assumed and the effect on the Kulite measurements was evaluated. It was found that assumed errors of as much as 10 percent in the pneumatic pressures gave rise to negligible differences in the velocity and yaw angle results and differences ranging from $-\frac{1}{2}$ deg to $+1$ deg in pitch angle results.

The source of the discrepancy in the behavior of the probes in the wake regions is not resolved. It is encouraging that the measurements near the wake center may be acceptable, since the knowledge of the wake width, the minimum velocity, and the conditions at the wake edge are sufficient for many engineering purposes. An attempt will be made, however, to resolve the remaining uncertainty in the method. Of the possible explanations, the suggestion that there is a varying temperature effect through the wake has been rejected since the thermal lag of the transducer sensor could not allow such a rapid response. The remaining potential explanations include:

(*i*) the steady flow error of probe measurement in a shear layer

(*ii*) differences in unsteady response at different yaw settings

(*iii*) incorrect averaging procedure in a flow in which Mach number and flow angle are unsteady and probe system response is nonlinearly dependent on both

A limited attempt has been made to investigate errors which might stem from the averaging procedure. However it is difficult to see why a lack of symmetry in the probe output could be caused this way. It is noted that the error which would normally result from the probe measurement in a steady shear layer is qualitatively consistent with the behavior observed, and this will be investigated further. The possibility of differences in unsteady response at different yaw angles is to be investigated in the near future by changing probe tip geometry.

Conclusions

The Dual Probe Digital Sampling (DPDS) technique was applied to measure the blade-to-blade and hub-to-tip flow field from two blade passages of a compressor rotor. All three components of the velocity were derived with relative success. The results showed a coherent and realistic behavior near peak efficiency at 50 percent speed. Broadening of the wake with increased yaw and pitch angles was measured at midspan when the compressor was throttled at 60 percent speed. Outside the wake regions, the flow was found to be steady in the rotor frame, and the data were shown through inherent measurement redundancy to be valid. Inside the wake regions, the flow was found to be unsteady in the rotor frame, and the reduced data contained an unknown uncertainty, except near the wake center where they are thought to be valid. Attempts are to be made to resolve the remaining uncertainty and to compare the measurements with those from an LDA system.

Acknowledgment

The work was supported by the Office of Naval Research, Power Program and Project Squid (Dr. A. D. Wood) and Naval Air Systems Command, Air Breathing Propulsion Program (Dr. G. Heiche). Essential contributions and dedicated support of Mr. J. E. Hammer are acknowledged.

References

1 Shreeve, R. P., and Neuhoff, F., "Measurements of the Flow From a High-Speed Compressor Rotor Using a Dual Probe Digital Sampling (DPDS) Technique," Naval Postgraduate School Technical Report NPS67-82-010, Sept. 1982.

2 Shreeve, R. P., Dodge, F. J., Hawkins, W. R., and Larson, V. J., "Probe Measurements of Velocity and Losses from a Small Axial Transonic Rotor," AIAA Paper No. 78-1198, AIAA 11th Fluid & Plasma Dynamics Conference, Seattle, Wash., July 10–12, 1978.

3 Shreeve, R. P., Simmons, J. M., Winters, K. A., and West, J. C., Jr., "Determination of Transonic Compressor Flow Field by Synchronized Sampling of Stationary Fast Response Transducers," Symposium on Non-steady Dynamics, ASME 1978 Winter Annual Meeting, San Francisco, Calif., Dec. 1978.

4 West, J. C., Jr., and Shreeve, R. P., "Digital Programmable Timing Device," U.S. Patent No. 4,181,962, Jan. 1, 1980.

5 McCarville, P. A., "Hardware and Software Improvements to a Paced Data Acquisition System for Turbomachines," Master's thesis, Naval Postgraduate School, June 1981.

6 Neuhoff, F., "Calibration and Application of a Combination Temperature-Pneumatic Probe for Velocity and Rotor Loss Distribution Measurements in a Compressor," Naval Postgraduate School Contractor Report NPS67-81-03CR, Dec. 1981.

7 Neuhoff, F., "Further Development of a Dual-Probe Digital Sampling (DPDS) Technique for Measuring Flow Fields in Rotating Machines," Naval Post-graduate School Contractor Report NPS67-82-01CR, Sept. 1982.

8 Zebner, H., "Procedure and Computer Program for the Approximation of Data (with Application to Multiple Sensor Probes), Naval Postgraduate School Contractor Report NPS67-80-01CR, Aug. 1980.

9 Shreeve, R. P., McGuire, A. G., and Hammer, J. A., "Calibration of a Two-Probe Synchronized Sampling Technique for Measuring Flows Behind Rotors," IEEE International Congress on Instrumentation in Aerospace Simulation Facilities, Monterey, Calif., Sept. 24–26, 1979 (published in ICIASF '79 Record, IEEE Cat. No. 79CH1500-8AES).

10 Adler, D., and Taylor, P. M., "A Procedure for Obtaining Velocity Vector From Two High Response Impact Pressure Probes," Naval Postgraduate School Technical Report NPS67-80-007, Aug. 1980.

11 Vavra, M. H., "Design Report of Hybrid Compressor and Associated Test Rig," Naval Postgraduate School Technical Report NPS-57Va73071A, July 1973.

12 Zebner, H., "Transonic Compressor: Program System TXCO for Data Acquisition and On-Line Reduction," Naval Postgraduate School Contractor Report NPS67-80-02CR, Oct. 1980.

APPENDIX A

Probe Calibration and Verification

The probes were calibrated separately in a 10.16-cm (4-in.)-dia free air jet exhausting to atmosphere [6, 7]. The probe mount allowed pitch angle to be set and the probes to be rotated in yaw. At each of six Mach numbers of the jet (0.2 to 0.7 in increments of 0.1) and at nine values of the pitch angle (-15 deg to 25 deg in increments of 5 deg); data from the probe were recorded digitally with reference data as the probe was yawed continuously from -80 deg to $+80$ deg and back.

Downloaded 01 Jun 2010 to 171.66.16.70. Redistribution subject to ASME license or copyright; see http://www.asme.org/terms/Terms_Use.cfm

300 values were recorded to describe the probe pressure versus yaw angle characteristic at each of the 54 combinations of the known jet Mach number (or dimensionless velocity) and pitch angle. Figure 7 shows examples of the data obtained. The average of the two sweeps, to and from, was used when this procedure was shown to give the correct result.

As described in [1], the 54 values of each of p_{Amax}, p_{As} and p_{Bmax} were obtained using numerical procedures, and the values of β and γ defined by equation (3) and equation (4) were calculated. Using the methods given in [8], the coefficients c_{ij}, d_{ij} in the surface approximation to the calibration data represented by equation (1) and equation (2) were calculated.

Surface approximations were similarly derived for the maximum output values of the two probes defined as pressure coefficients by the expressions

$$C_{p\text{Amax}} = \frac{p_{\text{Amax}} - p_s}{p_t - p_s} = C_{p\text{Amax}}(\phi) \tag{A1}$$

(which depended negligibly on Mach number) and

$$C_{p\text{Bmax}} = \frac{p_{\text{Bmax}} - p_s}{p_t - p_s} = C_{p\text{Bmax}}(X, \phi) \tag{A2}$$

which would be required in the on-line calibration procedure when the probes were applied.

To evaluate probable uncertainty in the measurements, the two probes were mounted in the free jet under known conditions and data acquired and reduced following procedures identical to those used in the compressor. The results are shown in the following table. It can be seen that in a steady uniform flow the maximum uncertainty in the velocity was 1.5 percent, in yaw angle, 0.8 deg and in pitch angle, 1.0 deg.

Table 1 Errors obtained in verification tests in steady flow

Test condition			Total measurement error		
X	ϕ (deg)	α (deg)	ϵ_X (%)	ϵ_ϕ (deg)	ϵ_α (deg)
.1420	0	0	−0.04	−0.04	−0.31
.1459	5	0	+1.49	−0.26	+0.11
.1459	5	0	+1.52	+0.21	−0.1
.1450	10	0	+1.28	−0.18	−0.24
.1448	15	0	−0.02	+0.18	+0.30
.170	10	0	+1.22	+0.22	−0.78
.170	10	5	−1.17	+1.03	−0.45
.170	10	10	−0.31	−0.2	−0.22
.2049	7	0	+0.53	−0.66	+0.18
.211	10	0	−0.31	−0.16	−0.2
.2052	13	0	+0.26	−0.21	−0.24

Downloaded 01 Jun 2010 to 171.66.16.70. Redistribution subject to ASME license or copyright; see http://www.asme.org/terms/Terms_Use.cfm

A Rapid Blade-to-Blade Solution for Use in Turbomachinery Design

E. R. McFarland
National Aeronautics and Space Administration, Lewis Research Center, Cleveland, Ohio 44135

A rapid technique for solving the blade-to-blade turbomachinery flow problem has been developed. Approximate governing flow equations, which include the effects of compressibility, radius change, rotation, and variable stream sheet thickness are solved using an improved panel method. The development and solution of these equations are described. Sample calculations are presented to illustrate the method's capabilities and accuracy.

Introduction

The design and study of turbomachinery rely heavily on the use of inviscid irrotational compressible blade-to-blade flow solutions. As a result, many methods and computer codes have been developed to solve this problem. The intent in presenting yet another of these blade-to-blade solutions is to provide the turbomachinery designer with a tool which has a better combination of solution speed, robustness, and versatility than previous methods.

The procedure solves the inviscid irrotational compressible blade-to-blade flow equations on a surface of revolution. One three-dimensional effect is modeled by including a variable stream sheet thickness. The governing equations are linearized by approximating the compressibility effects. These approximate equations are solved using an integral equation technique (panel method).

The method does have limitations and is intended primarily for use in preliminary design studies where a variety of blade shapes and flow conditions are to be analyzed. By using this technique the designer can produce blade shapes for analysis by more accurate, but presumably longer running, flow codes.

Specific features of the method are as follows: (*i*) computational time for a typical case run on the IBM 3033 computer at NASA Lewis Research Center is less than 4 CPU s. After an initial solution, additional solutions for variations in the inlet flow velocity, inlet flow angle, outlet flow angle, rotational speed, or a combination of these effects can be made at an additional expense of less than 0.5 CPU s per case. (*ii*) The method can be applied to all types of turbomachinery and flow conditions. However, the quality of the solution does vary with the particular problem being solved. The method loses accuracy as the flow becomes transonic, will not predict shocked flows, and does not accurately determine when a blade row is choked. In addition, the method also gives poorer solutions in the uncovered portions of the blade passage for lower solidity blade rows. (*iii*) Since a direct linear equation solver is used, a solution is always produced even if the blade shape is poorly described or extreme flow conditions are given. (*iv*) The method uses an integral equation solution so that the flow is only calculated on the blade surface. The flow can be calculated at points in the blade passage, but this is inefficient. (*v*) The solution does not require the use of a computational mesh or grid, so that almost any blade shape or body can be analyzed.

Contributed by the Gas Turbine Division of THE AMERICAN SOCIETY OF MECHANICAL ENGINEERS and presented at the 28th International Gas Turbine Conference and Exhibit, Phoenix, Arizona, March 27-31, 1983. Manuscript received at ASME Headquarters December 21, 1982. Paper No. 83-GT-67.

Analysis

The general blade-to-blade surface geometry is shown in Fig. 1, and an $r-z$ cut through the blade-to-blade surface is shown in Fig. 2. The surface in Fig. 1 corresponds to the S_1 surface described by Wu in [1]. The governing equations developed by Wu for inviscid, irrotational, compressible flow in the S_1 surface can be written as

Continuity

$$\frac{\partial}{\partial \varphi}(\rho b V_\varphi) + \frac{\partial}{\partial m}(r \rho b V_m) = 0 \tag{1}$$

Irrotationality

$$\frac{\partial}{\partial \varphi}(V_m) - \frac{\partial}{\partial m}(r V_\varphi) = 0 \tag{2}$$

where V_φ and V_m are absolute velocity components, ρ is the fluid density, b is the stream sheet thickness, and r is the local radius of the axisymmetric blade-to-blade surface.

In terms of flow relative to the blades the equations become

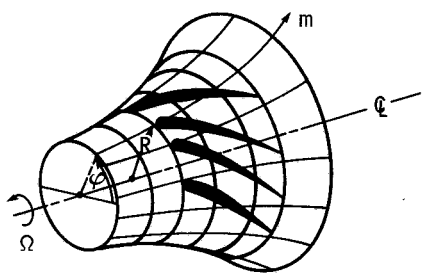


Fig. 1 Blade-to-blade surface of revolution

Copyright © 1984 by ASME
Downloaded 01 Jun 2010 to 171.66.16.70. Redistribution subject to ASME license or copyright; see http://www.asme.org/terms/Terms_Use.cfm

Continuity

$$\frac{\partial}{\partial \varphi}(\rho b W_\varphi) + \frac{\partial}{\partial m}(r \rho b W_m) = 0 \tag{3}$$

Irrotationality

$$\frac{\partial}{\partial \varphi}(W_m) - \frac{\partial}{\partial m}(r W_\varphi) = 2\Omega r \frac{dr}{dm} \tag{4}$$

where the relative components, W_φ and W_m, are given by

$$\begin{aligned} V_m &= W_m \\ V_\varphi &= W_\varphi + \Omega r \end{aligned} \tag{5}$$

and Ω is the angular velocity of the blades.

The radius, r, can be transformed out of the governing equations by using the same transformation as Kurmanov, Podvidz, and Stepanov [2].

$$y = \varphi; x = \int_{m_u}^{m} \frac{dm}{r}$$

or

$$\frac{\partial}{\partial y} = \frac{\partial}{\partial \varphi}; \frac{1}{r}\frac{\partial}{\partial x} = \frac{\partial}{\partial m} \tag{6}$$

and

$$W_x = r W_m; W_y = r W_\varphi$$

where r is a function of m only. In the present work, the velocity part of this transformation is modified to the following

$$W_x = r \rho b W_m; W_y = r \rho b W_\varphi \tag{7}$$

Note that the transformation preserves the relative flow angle from the $m-\varphi$ surface to the $x-y$ surface.

$$\tan(\alpha) = \frac{W_\varphi}{W_m} = \frac{W_y}{W_x}$$

Using this transformation, the governing equations become

Continuity

$$\frac{\partial}{\partial y}(W_y) + \frac{\partial}{\partial x}(W_x) = 0 \tag{8}$$

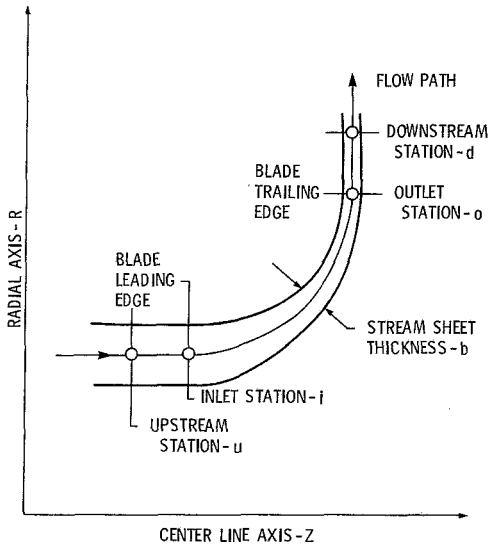


Fig. 2 R-Z cut through blade-to-blade surface

Irrotationality

$$\frac{\partial}{\partial y}\left(\frac{W_x}{\rho b}\right) - \frac{\partial}{\partial x}\left(\frac{W_y}{\rho b}\right) = 2\Omega r \frac{dr}{dx} \tag{9}$$

Expanding the irrotationality equation (9) gives

$$\frac{\partial}{\partial y}(W_x) - \frac{\partial}{\partial x}(W_y) + \frac{W_y}{\rho b}\frac{\partial}{\partial x}(\rho b) - \frac{W_x}{\rho b}\frac{\partial}{\partial y}(\rho b) = 2\Omega \rho b r \frac{dr}{dx} \tag{10}$$

The effect of the transformation on the governing equations has been to move the nonlinear terms from the continuity equation (8) to the irrotationality equation (10) and to have the radius explicitly appear in a single term.

Equation (10) is linearized by replacing (ρb) and W_y in the last three terms by estimated values, which are taken to be

Nomenclature

$As, Bs, \ldots, Ad$ = integral equation solution singularity influence coefficients
b = stream sheet thickness
m = meridional blade-to-blade surface coordinate
n = blade shape surface normal
r = radius from turbomachine centerline to blade-to-blade surface
S = blade row pitch or blade spacing in radians
s = blade surface distance
S_1, S_2 = blade-to-blade and midchannel surfaces
absolute velocity of flow
V = absolute velocity of flow
W = relative velocity of flow
w = disturbance relative velocity
x = transformed meridional coordinate
y = transformed tangential coordinate
α = flow angle on the blade-to-blade surface
Γ = blade row circulation
φ = tangential blade-to-blade surface coordinate
ρ = fluid density
σ, γ, δ = singularity strengths
θ = orientation of blade surface elements used in the integral equation solution angular velocity

Subscripts

c = known or constant value
est = estimated value
i,j,k = summation indices for singularity strengths
u,i,o,d = upstream, inlet, outlet, and downstream station of the blade row
n,t = surface normal and tangential components
onset = undisturbed flow
rb = integral terms contribution to solution velocity
p = arbitrary point on blade-to-blade surface
m,φ = on blade-to-blade surface of revolution
x,y = on transformed blade-to-blade surface
$*$ = transformed quantity

Overbars

$(\bar{\ })$ = mean quantity

Downloaded 01 Jun 2010 to 171.66.16.70. Redistribution subject to ASME license or copyright; see http://www.asme.org/terms/Terms_Use.cfm

functions of x only. With these approximations the governing equations become

Continuity

$$\frac{\partial}{\partial y}(W_y)+\frac{\partial}{\partial x}(W_x)=0 \tag{11}$$

Irrotationality

$$\frac{\partial}{\partial y}(W_x)-\frac{\partial}{\partial y}(W_y)= -\frac{W_{y_{\text{est}}}}{(\rho b)_{\text{est}}}\frac{d}{dx}(\rho b)_{\text{est}}+2\Omega(\rho b)_{\text{est}}r\frac{dr}{dx} \tag{12}$$

Equation Solution. Since equations (11) and (12) are linear, superposition of solutions may be used

$$\begin{aligned} W_x &= W_{x_c}+w_x \\ W_y &= W_{y_c}+w_y \end{aligned} \tag{13}$$

where W_{x_c} and W_{y_c} can be considered as components of a flow which is independent of y, and w_x and w_y are the disturbance to this known flow due to the blade presence. Substituting equations (13) into the governing equations gives

$$W_{x_c}=\text{constant} \tag{14a}$$

$$W_{y_c}=\text{constant}+\int_{(\rho b)_u}^{(\rho b)}\left(\frac{W_y}{\rho b}\right)_{\text{est}}d(\rho b) -2\Omega\int^{r}(\rho b)_{\text{est}}r\,dr \tag{14b}$$

$$\frac{\partial}{\partial x}(w_x)+\frac{\partial}{\partial y}(w_y)=0 \tag{14c}$$

$$\frac{\partial}{\partial x}(w_y)-\frac{\partial}{\partial y}(w_x)=0 \tag{14d}$$

In this study a solution to these equations was developed by using the integral equation approach of [3]. In the notation of this paper, the onset velocity [3] becomes

$$V_{x_{\text{onset}}}\Big|_{\text{ref[3]}}=W_{\text{onset}}\cos(\alpha)$$

$$V_{y_{\text{onset}}}\Big|_{\text{ref[3]}}=W_{\text{onset}}\sin(\alpha) +\int_{(\rho b)_u}^{(\rho b)}\left(\frac{W_y}{\rho b}\right)_{\text{est}}d(\rho b)-2\Omega\int_{r_u}^{r}(\rho b)_{\text{est}}r\,dr$$

and the distributed singularity expressions of reference [3] are used to satisfy equations (14c) and (14d). The resulting equations for the velocity components tangential and normal to the blade surface can be written as

$$W_{t_p}=W_{\text{onset}}\cos(\theta_p-\alpha)+W_{rb_p}\sin(\theta_p)+\sum_{i=1}^{n}As_{pi}\sigma_i +\sum_{j=1}^{n-1}Av_{pj}\gamma_j+\sum_{k=1}^{m}Ad_{pk}\delta_k \tag{15a}$$

$$W_{n_p}=-W_{\text{onset}}\sin(\theta_p-\alpha)-W_{rb_p}\cos(\theta_p)+\sum_{i=1}^{n}Bs_{pi}\sigma_i +\sum_{j=1}^{n-1}Bv_{pj}\gamma_j+\sum_{k=1}^{m}Bd_{pk}\delta_k \tag{15b}$$

where

$$W_{rb_p}=\int_{(\rho b)_u}^{(\rho b)}\left(\frac{W_y}{\rho b}\right)_{\text{est}}d(\rho b)-2\Omega\int^{r_p}(\rho b)_{\text{est}}r\,dr$$

The preceding equations, (15*a*) and (15*b*), correspond to equations (16*c*) and (16*d*) in [3]. The solution technique of [3] may now be applied directly using slightly modified boundary conditions.

Boundary Conditions. The boundary conditions for the relative transformed flow problem are

1 On the body surface

$$\mathbf{W}\cdot\mathbf{n}=W_n(s)=0 \tag{16a}$$

2 At the upstream boundary

$$\begin{aligned} W_x\Big|_u &= W_u\cos(\alpha_u)=W_{\text{onset}}\cos(\alpha)+w_{x_u} \\ W_y\Big|_u &= W_u\sin(\alpha_u)=W_{\text{onset}}\sin(\alpha)+w_{y_u} \end{aligned} \tag{16b}$$

3 At the downstream boundary

$$\begin{aligned} W_x\Big|_d &= W_d\cos(\alpha_d)=W_{\text{onset}}\cos(\alpha)+w_{x_d} \\ W_y\Big|_d &= W_d\sin(\alpha_d)=W_{\text{onset}}\sin(\alpha)+w_{y_d} \end{aligned} \tag{16c}$$

4 Circulation condition

$$\Gamma=S[(rV)_u-(rV)_d]=\oint r\mathbf{V}\cdot d\mathbf{s}$$

or in transformed variables

$$\frac{\Gamma}{S}=\left(\frac{W_y}{\rho b}\right)_u-\left(\frac{W_y}{\rho b}\right)_d+\Omega(r_u^2-r_d^2) \tag{16d}$$

and

$$\Gamma=\oint\frac{1}{\rho b}(\overline{W+\rho b\ \Omega r^2})\cdot(\overline{dx^2+dy^2})^{1/2} \tag{16e}$$

5 Far stream limits on w

$$\begin{aligned} w_{x_u}&=w_{x_d}\text{ --> }0\text{ as }x_u,x_d\text{ --> }\pm\infty \\ w_{y_u}&=-w_{y_d}\text{ as }x_u,x_d\text{ --> }\pm\infty \end{aligned} \tag{16f}$$

The foregoing conditions, along with the conservation of angular momentum (rV_φ = constant) in areas outside the blade row and equations (15) are used to develop a system of equations similar to equations (17–19) in [3]. This system of equations is solved by upper and lower triangular matrix decomposition.

Mean Flow and Stream Sheet Thickness Estimation. The solution of the governing equations requires that the integral terms in equation (14*b*) be known a priori. These terms can be approximated by using numerical integration and a one-dimensional estimate for the flow through the blade passage.

Three techniques have been used to estimate the one-dimensional flow in this study. The first is to use the blade shape and passage geometry to calculate approximate flow turning angles, flow areas, and stream sheet thicknesses. These quantities are then used with a one-dimensional continuity equation and the isentropic relations to calculate the mean flow velocity and density. The second technique is to specify or assume a mean flow velocity distribution through the blade row and to estimate the stream sheet thickness from the passage geometry (see Fig. 2). Isentropic relations are used to calculate the density. The simplest mean flow estimate is a linear distribution from blade inlet to exit based on the design velocity diagram. More complex distributions can be made depending on the type of turbomachinery being analyzed and one's knowledge of the flow. The third method is to use a midchannel stream surface flow solution, which corresponds to a S_2 surface in Wu's notation [1]. Such a solution can provide both the stream sheet thickness and mean velocity distributions.

All three techniques were used successfully in this study.

Downloaded 01 Jun 2010 to 171.66.16.70. Redistribution subject to ASME license or copyright; see http://www.asme.org/terms/Terms_Use.cfm

The quality of the overall solution produced by using any one of the mean flow estimates was dependent on the particular blade geometry being analyzed. For highly guided passages like those found in centrifugal machinery, the first technique produced very good results. In lower solidity blading where the flow angle can deviate significantly from the mean blade angle, the second method proved to give the best results. The use of a midchannel solution also provided good results for a number of cases, but its success depends on how well the midchannel solution models the flow turning through the blade row. In this work, the MERIDL computer code [4] was used to calculate the midchannel solutions and did provide good solutions for most cases. For flows where the mean flow is supercritical and the flow turning is controlled by the compressibility of the flow, only the second and third techniques gave resonable solutions.

Method Accuracy. In considering the overall accuracy of this solution, two sources of error are discussed. First is the approximations made in the governing equations. Second is the solution technique used in solving the equations.

By looking at the terms in equation (10) which are neglected or approximated in the final solution, the applicability and accuracy of the solution can be assessed. The only flow for which the solution is exact, in the sense that no approximation has been made to the governing equations, is incompressible flow with constant stream sheet thickness. With the introduction of a variable stream sheet thickness, an approximation of the W_y term is required. This term makes significant contributions to the solution when problems with large or rapid changes in stream sheet thickness are analyzed. The accuracy of the term is controlled by the estimate of W_y. At far stream stations the flow is modeled as being uniform, and the estimate of W_y as being independent of y is consistent. However, near or inside the blade row where blade surface curvatures strongly influence the flow, errors in the solution will occur. Compressible flow calculations require the inclusion of the change in density terms in equation (10). The more compressible the flow the more significant these terms become. In the solution equations used in this study, it is assumed that the density only varies in the meridional direction. Wood in [5] also makes the same assumption, and it is currently used in the TSONIC code [6] to calculate transonic flows. An estimate of tangential variations in density could have been included in the analysis, but this would require an approximate solution for the blade loading. Calculations indicate that the term is not significant for subcritical flows. However, inaccuracy in the solution will appear when high-speed flows with large blade loadings are being analyzed. Such flow occur in supercritical blade designs. The remaining term for change in density in the meridional direction is approximated by using a mean flow estimate to arrive at values of the tangential velocity component and the density. This term tends to dominate the solution as the compressibility effects increase. If the mean flow estimate does not approximate the local flow well, errors in the solution will occur.

Major sources of error in the solution technique are the integral equation solution and the numerical approximation of the integral terms in equations (15*a*) and (15*b*). The integral equation solution is second-order accurate in terms of the elements used to approximate the blade shape. Its accuracy was discussed in [3]. Numerical integration of the terms in equations (15*a*) and (15*b*) was accomplished using a simple trapezoidal method. Twenty-two integration points were used between the upstream and downstream boundaries of the flow field with 20 of the points placed between the blade row leading and trailing edges. The accuracy of this integration is consistent with the accuracy of the integral equation solution for a typical design calculation.

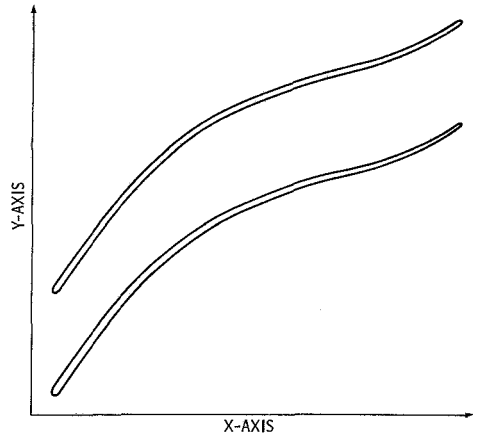


Fig. 3 Transform blade-to-blade surface—centrifugal impeller

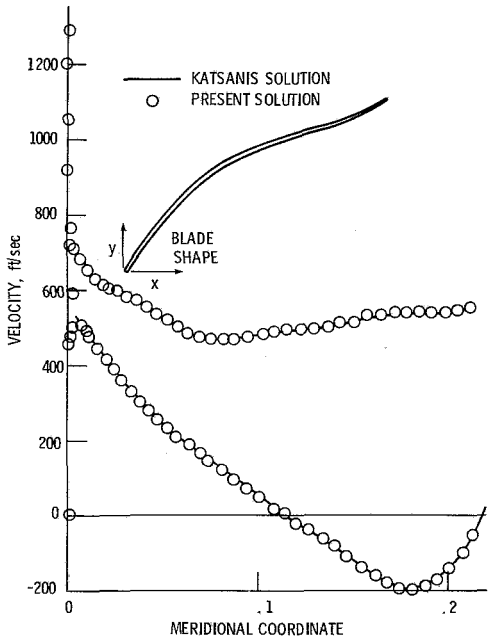


Fig. 4 Incompressible flow—constant stream sheet thickness

Solution Modifications. The solution can be modified to produce better results for certain problems. One possible modification is to specify a fictitious mean flow distribution or stream sheet thickness in order to account for viscous flow blockage effects. Another solution modification is to alter the transformation back to physical variables. The velocity transformation can be written as

$$W = \frac{W_*}{\rho br} = \frac{1}{rb}\left(\frac{1}{\rho}\right) W_*$$

where W is the physical velocity magnitude and W_* is the transformed velocity magnitude. This can be modified to a form similar to the Stockman-Lieblein compressibility correction [7].

$$W = \frac{1}{rb}\left(\frac{1}{\rho}\right)^{W_*/\tilde{W}_*} W_* \tag{17}$$

where $\tilde{W}_*$ is the transformed mean velocity magnitude at the same meridional location as W. This altered transformation models density variations in the tangential direction which

Downloaded 01 Jun 2010 to 171.66.16.70. Redistribution subject to ASME license or copyright; see http://www.asme.org/terms/Terms_Use.cfm

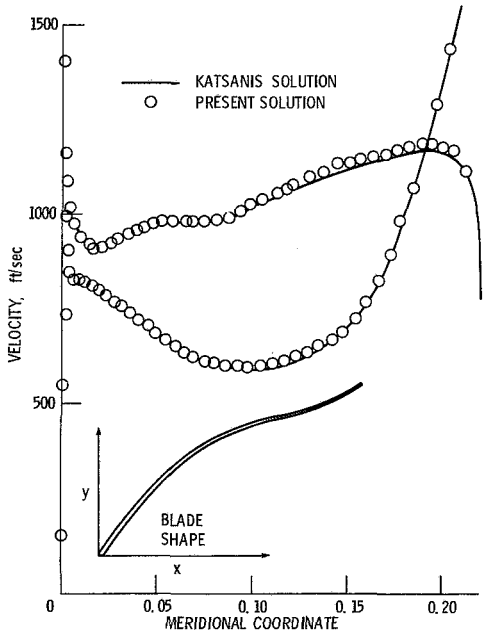


Fig. 5 Incompressible flow—variable stream sheet thickness

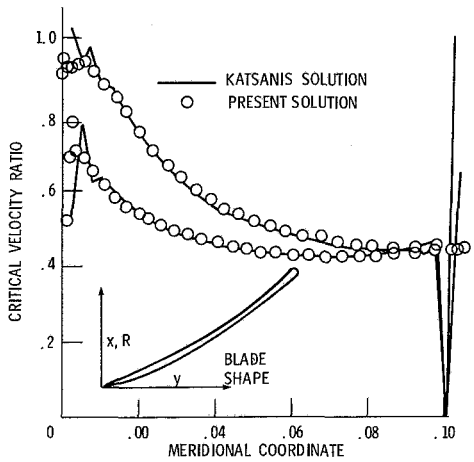


Fig. 6 Radial vane diffuser

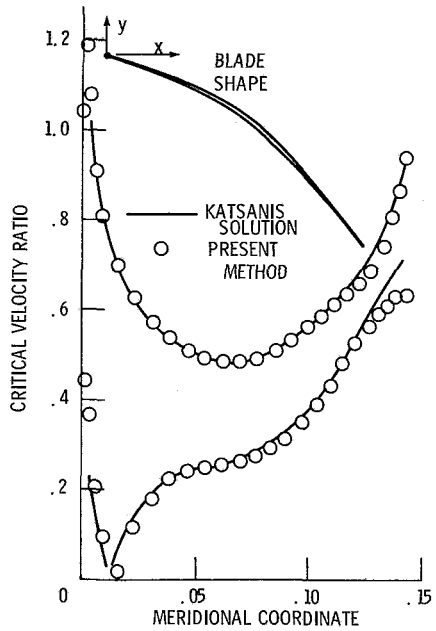


Fig. 7 Radial in—flow turbine

were suppressed by the approximations to the governing equations.

Additional solution modifications are possible. The problem with using solution modifications is that they usually produce better solutions only for a particular type of turbomachinery flow.

Sample Calculations and Discussion

The sample calculation problems were chosen to demonstrate the capabilities and accuracy of the method. The calculated flows range from incompressible to supercritical. Both centrifugal and axial turbomachinery blade rows are analyzed. All flows are calculated without taking into account viscous effects.

Incompressible Flow. Two incompressible flow cases are presented. In both cases a centrifugal compressor blade-to-blade geometry is considered. The transformed surface is shown in Fig. 3. The blade row is rotating at 68,000 rpm. In the first case a constant stream sheet thickness is assumed. Therefore no approximations are present in the governing equations. The calculated results are shown in Fig. 4, along with results from the finite difference solution of Katsanis [6]. The calculated surface velocities from the two solutions are in good agreement, including the region of reverse relative flow on the blade pressure surface. The second case differs slightly from the first. A variable stream sheet thickness is assumed, so that the method is solving approximate governing equations. The mean flow is estimated using the blade passage geometry. The assumed stream sheet variation has a ratio of 4.75 to 1 from the blade leading to trailing edge. The comparison of surface velocities with Katsanis [6] is shown in Fig. 5. Agreement between the two solutions is very good.

Compressible Flow, Subcritical. Three subcritical flow cases are presented. The density approximation will influence the solutions for these flows. The mean flows used in the solutions were determined from the blade passage geometry in the first and second cases and was specified in the third case.

The first calculation is for a radial diffuser. The critical velocity ratio at the blade inlet is 0.87 and at the outlet is 0.41. As shown in Fig. 6, the comparison with Katsanis is excellent except at the trailing edge. The trailing edge velocity spikes calculated by the Katsanis solution are due to the rapid turning of the inviscid flow around the rounded trailing edge of the blade. The real flow would separate, forming a viscous wake before such large velocity gradients could appear. In the present solution an extrapolation technique similar to Gostelow's [8] is used to eliminate these spikes.

The second case is a radial inflow turbine design by Klassen using the MERIDL and TSONIC computer codes [4, 6]. The critical velocity ratios across the blade row are 0.48 at the inlet and 0.88 at the exit. The flow incidence with the blade is 60 deg. Total turning of the flow is 100 deg. The rotational speed of the rotor is 100,000 rpm. A comparison of the present method with the TSONIC code solution is shown in Fig. 7. Some differences in the solutions do occur in the uncovered portions of the blade row at the inlet and outlet areas, but overall agreement is good.

The third subcritical case is a high-turning, low-solidity turbine vane. The vane has an axial solidity of 0.63, and a design turning of 75 deg. The ideal exit critical velocity is 0.896. Since the flow turning deviates significantly from the

Downloaded 01 Jun 2010 to 171.66.16.70. Redistribution subject to ASME license or copyright; see http://www.asme.org/terms/Terms_Use.cfm

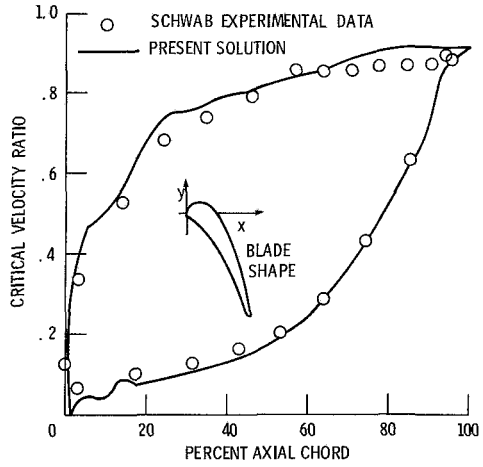


Fig. 8 High turning turbine vane

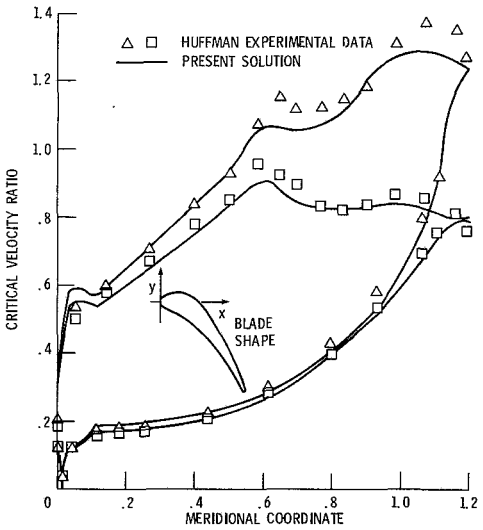


Fig. 9 Supercritical exit turbine vane

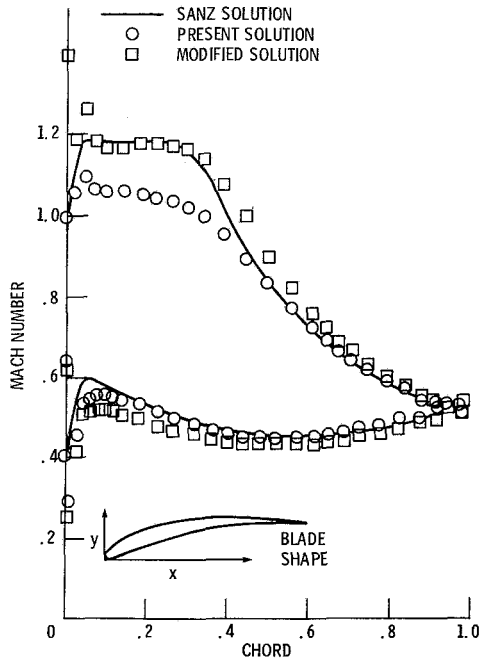


Fig. 10 Supercritical compressor blade

mean blade angle for this problem, it was necessary to specify the mean flow rather than calculating it using the blade passage geometry. A linear mean flow distribution was assumed based on the vane velocity diagrams. The experimental data of Schwab [9] is used for comparison in Fig. 8. The agreement is good.

Compressible Flow, Supercritical. Two supercritical cases are presented. The density approximation will have more of an effect in these cases than it had on the previous solutions. Solution modification techniques were used in calculating these flows.

The first case is a turbine vane which was designed by Detroit Diesel Allison and tested there by Huffman et al. [10]. The mean flow for this calculation was determined by using the blade geometry from the inlet to the throat and a linear distribution from the throat to the blade row outlet flow conditions. The comparision with experimental data is shown in Fig. 9 for both a supercritical and subcritical exit flow. The agreement for both cases is good. The calculated velocity is a little low on the suction surface near the throat and blade trailing edge.

The final case is a supercritical compressor blade designed by Sanz using the hodograph method of Bauer, Garabedian, and Korn [11]. The critical velocity ratio is 0.74 at the blade inlet and 0.58 at the outlet. The flow is turned through 29 deg by the cascade. The mean flow for the solution was calculated using the blade passage geometry. This case is a severe test of density approximation, since large blade loadings and high-speed flows are present. Solution comparisons are shown in Fig. 10. The circle symbols show the calculated results when the basic method is applied. The calculation does poorly in the region where the flow is transonic. The calculation in this region can be improved by using equation (17) to modify the solution as shown by the square symbols in the figure. However, the subsonic portion of the solution becomes poorer as a result.

As this case demonstrates, solution modification techniques can be used to match almost any known blade row flow. The difficulty with using solution modifications lies in their general application to the prediction of flows. Hopefully, specific modification techniques could be developed and applied to the prediction of flows in particular classes or types of turbomachinery.

Conclusion

The present method rapidly calculates surface velocities for a wide range of turbomachinery blade-to-blade flows. The method produces good results for subcritical flows. Supercritical flows can be calculated, but the solution accuracy is poor. Solution modifications can be made to improve the supercritical flow calculations, however, application of these modifications requires insight into the flow being analyzed and the modifications cannot be applied universally to all flows.

References

1 Wu, C., "A General Theory of Three-Dimensional Flow in Subsonic and Supersonic Turbomachines of Axial-, Radial-, and Mixed-Flow Types," NACA TN 2604, 1952.

2 Kurmanov, B., Podvidz, G., and Stepanov, G., "Analysis of Two-Dimensional Gas Flow in Turbomachinery Cascades by Means of Integral Equations," (*Akademiia Nauk SSSR, Izvestiia, Mekhanika Zhidkosti i. Gaza,*

Downloaded 01 Jun 2010 to 171.66.16.70. Redistribution subject to ASME license or copyright; see http://www.asme.org/terms/Terms_Use.cfm

July-Aug. 1977, pp. 90–97); *Fluid Dynamics*, Vol. 12, No. 4, Mar. 1978, p. 560–566.

3 McFarland, E. R., "Solution of Plane Cascade Flow Using Improved Surface Singularity Methods," ASME JOURNAL OF ENGINEERING FOR POWER, Vol. 104, No. 3, July 1982, pp. 668–674.

4 Katsanis, T., and McNally, W. D., "Revised FORTRAN Program for Calculating Velocities on the Hub-Shroud Midchannel Stream Surface of an Axial-, Radial-, or Mixed-Flow Turbomachine or Annular Duct, I - User's Manual," NASA TN D-8430, Mar. 1977.

5 Wood, J. R., "Improved Method for Calculating Transonic Velocities on Blade-to-Blade Stream Surfaces of a Turbomachine," NASA TP-1772, Apr. 1981.

6 Katsanis, T., "FORTRAN Program for Calculating Transonic Velocities on a Blade-to-Blade Stream Surface of a Turbomachine," NASA TN D-5427, Sept. 1969.

7 Lieblein, S., and Stockman, N. O., "Compressibility Correction for Internal Flow Solutions," *Journal of Aircraft*, Vol. 9, No. 4, Apr. 1972, pp. 312–313.

8 Gostelow, J. P., "Trailing Edge Flows Over Turbomachine Blades and Kutta-Joukowsky Condition," ASME Paper No. 75-GT-94, Mar. 1975.

9 Schwab, J. R., "Aerodynamic Performance of High Turning Core Turbine Vans in a Two-Dimensional Cascade," NASA TM-82894, 1982.

10 Huffman, G., McClure, R., Holtman, R., and Sinnett, G., "Results of a Two-Dimensional Turbine Cascade Test," Research Note 71-47, Detroit Diesel Allison, Indianapolis, Ind., 1971.

11 Bauer, F., Garabedian, P., and Korn, D., "Supercritical Wing Sections III," *Lecture Notes in Economics and Mathematical Systems*, Vol. 150, Springer-Verlag, New York, 1977.

Downloaded 01 Jun 2010 to 171.66.16.70. Redistribution subject to ASME license or copyright; see http://www.asme.org/terms/Terms_Use.cfm

Prediction of Cascade Flow Fields Using the Averaged Navier-Stokes Equations

S. J. Shamroth
Vice President

H. McDonald
President

W. R. Briley
Vice-President
Scientific Research Associates, Inc.,
Glastonbury, Conn. 06033

A numerical solution procedure for the ensemble-averaged, compressible, time-dependent Navier-Stokes equations is applied to predict the flow about a cascade of airfoils operating in the transonic flow regime. The equations are solved by the consistently split, linearized block implicit (LBI) method of Briley and McDonald. Boundary conditions are set so as to specify upstream total pressure and downstream static pressure. Turbulence is modeled by a mixing length model. Predictions are made for flow through a compressor cascade configuration. The method yields converged solutions within a relatively small number of time steps ($\approx$ 150), which give good comparisons with experimental data.

Introduction

One of the most important problems confronting the gas turbine design engineer focuses on the aerodynamic and heat transfer processes of the turbine rotor and stator stages. Poor estimates of flow conditions in these regions may lead to unnecessary high aerodynamic losses and/or potential catastrophic failure due to thermal loads. Although a complete solution of the turbine passage problem requires a full three-dimensional viscous analysis, including endwall effects, much relevant information can be gained by considering the flow through a two-dimensional cascade.

At the present time, possible approaches to the cascade flow analysis problem include (*i*) inviscid analyses (e.g., [1]), (*ii*) inviscid analyses with shear layer corrections (e.g., [2]), and (*iii*) full flow field analyses. Although inviscid analyses can give accurate predictions of the blade passage flow in some cases, they obviously are limited by (*i*) the necessity of assuming airfoil circulation to obtain a unique flow field prediction, (*ii*) neglect of shear layer displacement effects, and (*iii*) the inability to predict losses and heat transfer. Considering the first of these aspects, specification of the airfoil circulation may be both reasonable and straightforward for isolated sharp trailing edge airfoils at high Reynolds number operating below stall. However, proper specification of the circulation is not obvious for rounded trailing edge airfoils and also remains a problem in time-dependent flows or in flows about blades having trailing edge separation.

Inviscid flow analyses also are limited by their restricted treatment of shear layer displacement effects upon the pressure distribution development. In cases where the blade boundary layer remains thin, flow field predictions neglecting boundary layer displacement effects may be quite accurate. However, if the boundary layer does not remain thin, the actual pressure distribution generated in the flow may be affected significantly by the boundary layer development. The displacement effect is magnified in transonic flow where shock placement is very sensitive to the effective airfoil geometry and even small shear layer displacement effects can significantly affect the blade pressure distribution. Finally, inviscid analyses by themselves cannot predict aerodynamic losses or heat transfer rates.

The need for including shear-induced phenomena in a cascade analysis has led to several approaches. One approach modifies the inviscid solutions for boundary layer and wake effects via empirical data correlations or solves the boundary layer equations under the calculated inviscid pressure distribution. In regard to the first of these, although methods based upon data correlations can play a useful role in the design process, they are limited to flow conditions within the range of correlating data. The second approach is considerably more general and a review of boundary layer techniques for turbomachinery applications has been presented by McDonald [3]. When the boundary layer remains thin throughout the flow, as it does in many practical applications, the combined inviscid flow boundary layer analysis may give an adequate description of the flow, even if shear layer displacement effects on the pressure distribution are neglected. However, as previously discussed, in many practical applications severe pressure gradients, shock waves, or transonic effects can cause significant displacement effects, which in turn result in the actual pressure distribution being considerably different from that obtained via a purely inviscid analysis. In these situations, an analysis which solves an inviscid set of equations to obtain a blade pressure distribution and then solves a set of blade boundary layer equations under the influence of this pressure distribution to account for displacement effects is inadequate, and a solution recognizing the mutual dependence of the pressure distribution and blade shear layer development is required.

Contributed by the Gas Turbine Division for publication in the JOURNAL OF ENGINEERING FOR GAS TURBINE AND POWER. Manuscript received by the Gas Turbine Division February 8, 1983.

Copyright © 1984 by ASME
Downloaded 01 Jun 2010 to 171.66.16.70. Redistribution subject to ASME license or copyright; see http://www.asme.org/terms/Terms_Use.cfm

Two major approaches have been developed for such problems; these are the inviscid flow, boundary layer strong interaction analysis, and the full flow field analysis, where no distinction between the shear layers and the core flow is required.

A strong interaction analysis may take the form of either a forward-marching procedure or a global iteration. For regions where the inviscid flow is supersonic and thus described by hyperbolic equations, a solution can be forward-marched in space with the inviscid and viscous regions coupled on a station-by-station basis. The chief difficulty in this process is that mathematically stiff equations must be solved. Problems with stiff equations result from numerical solutions which can branch off the desired solution, thus producing a physically unrealistic result. In regions where the inviscid flow is subsonic, and thus described by elliptic equations, a forward-marching procedure without iteration is not physically realistic as a result of the upstream pressure propagation, and consequently, a sequence of inviscid and boundary layer solutions must be performed in a manner where each stage corrects the former one through a global iteration. In some instances, it becomes necessary to include the wake development in order to predict the loading satisfactorily. Additional problems occur in transonic cascades where mixed regions of flow are present and where small displacement effects may have considerable influence on shock location and overall pressure distribution. Further problems with the interaction approach concern representation of separated regions within the boundary layer and the necessarily arbitrary division of the flow field into viscous and inviscid portions.

The second approach used in obtaining solutions for flows in which shear induced phenomena significantly affect pressure distribution is the full flow field analysis. The full flow field analysis solves the entire flow field via a single set of equations, thus avoiding any need to divide the flow into viscous regions and inviscid rotational or irrotational regions. Two related approaches of this type for cascades have been used; one by Shamroth, Gibeling and McDonald [4], which is based upon the full ensemble-averaged Navier-Stokes equations, and a second approach based upon the so-called thin shear layer equations has been used by Steger, Pulliam and Chima [5]. The thin shear layer equations are an approximate form of the Navier-Stokes equations which contain all pressure and convective terms but retain only those viscous terms significant in thin shear layer flows in which streamlines are aligned with one coordinate; the remaining viscous terms are omitted from the analysis. The full flow field cascade analyses overcome many of the problems associated with boundary layer and wake strong interaction analyses as they avoid the need to divide the flow into different regions and eliminate the iterative marching between regions. When the averaged Navier-Stokes equations are used, the analysis contains all convective, pressure, and diffusion terms necessary to model large separated flow regions, and therefore, flows with significant separation or shear layers not aligned with one of the coordinates present no special problem when this set of equations is used. Furthermore, when full flow field cascade analyses are based upon time-dependent forms of the governing equations, these approaches can be used to study steady-state flows, should they exist, as the asymptote of time integration, and in addition, these procedures can be used to study transient effects. Retaining the transient computational capability must be weighed against the possible cost vis-á-vis some non-timelike integration scheme for solving the steady equations. It appears from the present calculations, and others, that retaining an implicit transient integration does not result in any penalty relative to alternate existing steady-state solution schemes. The present paper demonstrates the application of an averaged Navier-Stokes calculation procedure to subsonic and transonic cascade problems and gives an assessment of the procedure through specific comparisons with experimental data.

Analysis

The Governing Equations. The problems of interest in the present study are general cascade flow fields which may be transonic and may contain separated flow regions. Therefore, a Navier-Stokes analysis is required. However, even after deciding to use the ensemble-averaged Navier-Stokes equations, a further decision regarding dependent variables and precise equation form must be made. The problem is further complicated by the presence of a complex geometry which has required a reevaluation of the choice of equation form and dependent variables. The reevaluation by Shamroth, Gibeling, and McDonald [4] suggests the following formulation. The governing equations are transformed from the Cartesian coordinates x,y to a new set of coordinates ξ,η where

$$\xi=\xi(x,y,t)$$
$$\eta=\eta(x,y,t)$$
$$\tau=t \tag{1}$$

The specific choice of coordinates is discussed briefly in a later subsection. For two-dimensional flow with constant total temperature, the governing equations are then written in the form

$$\frac{\partial W}{\partial \tau}+\xi_t\frac{\partial W}{\partial \xi}+\xi_x\frac{\partial F}{\partial \xi}+\xi_y\frac{\partial G}{\partial \xi}+\eta_t\frac{\partial w}{\partial \eta}+\eta_x\frac{\partial F}{\partial \eta}+\eta_y\frac{\partial G}{\partial \eta}$$
$$=\frac{1}{\mathrm{Re}}\left[\xi_x\frac{\partial F_1}{\partial \xi}+\eta_x\frac{\partial F_1}{\partial \eta}+\xi_y\frac{\partial G_1}{\partial \xi}+\eta_y\frac{\partial G_1}{\partial \eta}\right] \tag{2}$$

where

$$D=\xi_x\eta_y-\xi_y\eta_x$$

$$W=\begin{bmatrix}\rho\\ \rho u\\ \rho v\end{bmatrix},\quad F=\begin{bmatrix}\rho u\\ \rho u^2+p\\ \rho uv\end{bmatrix},\quad G=\begin{bmatrix}\rho v\\ \rho uv\\ \rho v^2+p\end{bmatrix}\quad F_1=\begin{bmatrix}0\\ \tau_{xx}\\ \tau_{xy}\end{bmatrix}$$
$$G_1=\begin{bmatrix}0\\ \tau_{xy}\\ \tau_{yy}\end{bmatrix} \tag{3}$$

In equations (1–3) x and y are Cartesian coordinates, t is time, u and v are velocity components, ρ is density, p is pressure, and τ_{ij} is the stress tensor and Re is the Reynolds number. This formulation is termed the quasi-linear form and has been used successfully for a number of cascade and airfoil

Nomenclature

C_p = static pressure coefficient $(p-p_\infty)/1/2\rho_\infty u_\infty{}^2$
D = Jacobian of coordinate transformation
p = pressure
Re = Reynolds number
t = time
u,v = Cartesian velocity components
x,y = Cartesian coordinates
ξ,η = computational coordinates
ρ = density
τ = shear stress
σ = dissipation parameter

Subscript

∞ = upstream conditions

Downloaded 01 Jun 2010 to 171.66.16.70. Redistribution subject to ASME license or copyright; see http://www.asme.org/terms/Terms_Use.cfm

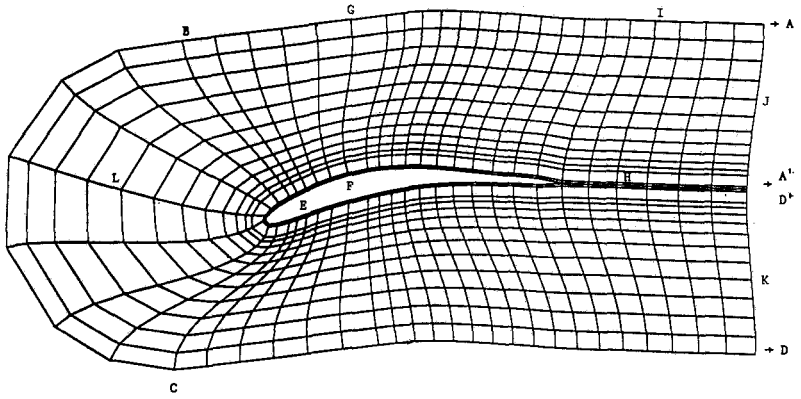


Fig. 1 Cascade coordinate grid—all grid points not included

calculations [4, 6–8] for both laminar and turbulent flow in the subsonic regime.

Numerical Procedure. The numerical procedure used to solve the governing equations is a consistently split, linearized block implicit (LBI) scheme developed originally by Briley and McDonald [9]. A conceptually similar scheme has been developed for two-dimensional MHD problems by Lindemuth and Killeen [10]. Since the procedure has been described in considerable detail elsewhere, it shall only be briefly outlined here. The reader interested in greater detail should refer to [9, 11]. The method can be briefly outlined as follows: the governing equations are replaced by an implicit, time-difference approximation, optionally a backward difference or Crank-Nicolson scheme. Terms involving nonlinearities at the implicit time level are linearized by Taylor expansion in time about the solution at the known time level, and spatial difference approximations are introduced. The result is a system of multidimenisonal coupled (but linear) difference equations for the dependent variables at the unknown or implicit time level. To solve these difference equations, the Douglas-Gunn [12] procedure for generating alternating-direction implicit (ADI) schemes as perturbations of fundamental implicit difference schemes is introduced. This technique leads to systems of coupled linear difference equations having narrow block-banded matrix structures which can be solved efficiently by standard block-elimination methods.

The method centers around the use of a formal linearization technique adapted for the integration of initial-value problems. The linearization technique, which requires an implicit solution procedure, permits the solution of coupled nonlinear equations in one space dimension (to the requisite degree of accuracy) by a one-step noniterative scheme. Since no iteration is required to compute the solution for a single time step, and since only moderate effort is required for solution of the implicit difference equations, the method is computationally efficient; this efficiency is retained for multidimensional problems by using ADI techniques. The method is also economical in terms of computer storage, in its present form requiring only two time-levels of storage for each dependent variable. Furthermore, the ADI technique reduces multidimensional problems to sequences of calculations which are one-dimensional in the sense that easily-solved, narrow, block-banded matrices associated with one-dimensional rows of grid points are produced.

Coordinate System. Although the governing equations have been written in a set of general spatial coordinates, the problem of choosing an appropriate specific coordinate system remains. To date, several possible coordinate generation procedures are available. These include conformal techniques, techniques based upon solution of a Poisson equation (e.g., [13]) and techniques based upon a constructive system. The present effort utilizes this latter approach (e.g. [14, 15]). In brief, two families of curves are found, the ξ = constant curves such as lines FG or HI in Fig. 1, and the η = constant curves such as ABCD or A′ED′ in Fig. 1. The coordinate system is constructed by first forming the inner loop A′ED′, which includes the blade and a coordinate branch cut emanating from the trailing edge. The blade shape may be specified either through an equation or through discrete coordinate points. If the latter technique is used, the blade surface is constructed through a curve fitting routine which fits both the shape and curvature of the blade surface. Construction of the inner loop is followed by construction of an outer loop AGBCD which consists of periodic line AB and CD and a frontal curve BC. Both the inner and outer loops are then represented by parametric curves

$$x=x(s), y=y(s) \tag{4}$$

where the parameter varies from zero to unity. The present coordinate generation process utilizes a two-part transformation to express x and y as functions of s. First x and y are expressed as a function of s', the physical distance along the curve. Then s' is related to s via a hyperbolic tangent parameterization centered about the leading edge for the inner loop and a cubic polynomial representation for the outer loop. The parametric representation is chosen so as to have rapid variation in the airfoil leading edge region. If N pseudo-raidal lines are to be used, the grid points on each loop are chosen as values

$$s_i\,(i-1)/(N-1) \qquad i=0, N-1$$

and points having the same value of s_i on the inner and outer loops define the end points for a given pseudo radial line (e.g., HI). Since the loops are parameterized so that s varies rapidly in the region of the leading edge, this process effectively packs points into the leading edge region. These points are then connected via a cubic curve which allows specification of the slope at each end point. For pseudoradial lines which intersect the inner loop downstream of a user specified location (usually $x/c \approx .05$), the slopes are specified so as to make the lines vertical at the outer loop and either vertical or normal at the inner loop end points. For pseudoradial lines whose intersection with the inner loop is upstream of this location a smooth variation of the angle with distance around the leading edge is specified. With this process, the pseudoradial lines are vertical as they pass through the periodic lines (BA and CD), and therefore, the metric data will be continuous across these lines. This process allows construction of all pseudoradial lines.

The second set of coordinate lines, the pseudoazimuthal

Downloaded 01 Jun 2010 to 171.66.16.70. Redistribution subject to ASME license or copyright; see http://www.asme.org/terms/Terms_Use.cfm

lines (e.g., JLK) are obtained by normalizing the length along each pseudoradial line with a hyperbolic tangent transformation that packs points near the airfoil surface (or branch cut). Then if M pseudoazimuthal lines are to be used, the grid point for the jth pseudoazimuthal point occurs at $r_j = (j-1)/(M-1)$ for each pseudoradial line. The actual system used in the present effort consisted of 113 points along each loop and 30 points along each pseudoradial line. The plot shown in Fig. 1 is a computer generated plot in which all grid points are not included. For clarity, radial lines in the vicinity of the leading edge were omitted, and loops in the vicinity of the blade surface were omitted, leading to the nonsmooth appearance of the grid. The actual grid spacing normal to the surface was 4.0×10^{-5} chords at the blade surface, and the spacing along the blade surface was 4.6×10^{-3} chords at the blade leading edge. In addition, the grid extended two chords downstream of the airfoil trailing edge.

It should be noted that this constructive procedure does not guarantee that the generated coordinate system be nearly orthogonal. In fact, the angle between coordinate lines of different families may become very small in certain regions, and it is even possible that coordinate lines of the same family may cross. These problems can be rectified by changing the parameterization coefficients for the inner and outer loops or adding additional prameterizations. Further details of the constructive coordinate generation process are given in the SRA report [4].

Boundary Conditions. Prior experience in solving a variety of equations has consistently indicated the important role boundary conditions play in determining accurate solutions and in obtaining rapid convergence. In [16], Moretti and Pandolfi point out that specification of boundary conditions first requires assumption of a physical model and then selection of boundary and initial conditions consistent with that model. Adopting a duct or wind tunnel as a model, prior experience has indicated a consideration of inviscid flow equations characteristics can be a very helpful tool in setting both inflow and outflow boundary conditions for the Navier-Stokes equations. Based upon these considerations, Briley and McDonald [17] and Moretti and Pandolfi [16] set stagnation pressure, P_o, and stagnation temperature, T_o, at a subsonic inflow boundary and static pressure, P, at a subsonic outflow boundary. This approach is taken in the present effort.

It has also been pointed out on a number of occasions that standard difference representations can introduce more variables from outside the computational domain into the problem than can be removed through specification of physical boundary conditions. These additional variables can be removed in a variety of ways; for example, by use of one-sided differencing, by use of equations applied in a one-sided manner at the boundaries or through so-called "extraneous boundary conditions." If extraneous conditions are utilized, they should be chosen to be as reasonable as possible from a physical point of view. The hypothesis is adopted that if a solution can be obtained with the extraneous boundary conditions applied, then any defective influence of these extraneous conditions will result only from the approximations inherent in them, and the solutions should be assessed in this manner.

With these considerations in mind, the following approach was taken in setting boundary conditions for the cascade flow field problem. Two physical boundary conditions are assumed for the upstream boundary and one for the downstream boundary. These represent items which would be set in a wind tunnel experiment and are the upstream stagnation pressure, the upstream flow angle, and the downstream static pressure. The "extraneous boundary conditions" chosen were first derivative of density at the upstream boundary and second derivatives of both velocity components. It should be noted that specifying stagnation pressure and incidence has several advantageous features. Since computation economics argues for placing grid points in the vicinity of the cascade and minimizing the number of grid points far from the cascade, the upstream and downstream computational boundaries should be set as close to the cascade as is practical. In addition, with the particular body-fitted coordinates used, as the upstream boundary moves further upstream, the angle between pseudoradial and pseudoazimuthal coordinate lines becomes smaller. Decreasing the coordinate angle causes the coordinate system to become less well conditioned and increases the role of cross-derivative terms in the equations. Both of these characteristics could be detrimental to the present numerical procedure, and therefore, they also argue for placing the upstream boundary as close to the cascade as possible. However, when the upstream boundary is placed close to the cascade, most flow function conditions on the boundary such as velocity will be influenced by the cascade and will not be known. However, as long as the upstream boundary is not in the region where viscous phenomena occur, the stagnation pressure is known, and therefore, this approach allows the upstream boundary to be placed relatively close to the cascade and still allows a physically reasonable boundary condition specification. In regard to the inlet flow angle, at present a given value is specified. However, a distribution of inlet flow angle along this boundary could be computed from a simpler potential flow analysis which encompassed a larger flow domain, and this could be imposed as a boundary condition for the present procedure. Such an approach could be updated in time by an interaction model to include a limited effect of shear layer development upon the upstream incidence. To date, this "interactive" approach has not been considered further. In the present application, the static pressure was set as the pressure at downstream infinity, and hence, it is assumed that the downstream boundary is located in a region where pressure is uniform. Both the upstream and downstream boundaries have boundary conditions associated with them which are nonlinear functions of the dependent variables. These are the specifications of total pressure on the upstream boundary and static pressure on the downstream boundary. These nonlinear boundary conditions are linearized in the same manner as the governing equations (via a Taylor expansion of the dependent variable in time) and then solved implicitly along with the interior point equations.

The final boundary conditions concern conditions along the solid surface and periodic lines. No-slip and no throughflow conditions were applied, leading to a specification of zero velocity on the surface. An inviscid transverse momentum equation was applied on the surface, leading to the boundary condition approximation of zero transverse pressure gradient being applied. Periodic boundary conditions were applied on the periodic lines.

Artificial Dissipation. The final item to be considered concerns the use of artificial dissipation. Since the calculations were at high Reynolds numbers typical of normal turbomachinery applications, it was necessary to add "artificial dissipation" terms to suppress central difference spatial oscillations. Such "artificial dissipation" could be added via the spatial differencing formulation (e.g., one-sided difference approximations for first derivatives) or by explicitly adding an additional dissipative type term. The present authors favor the latter approach since when an additional term is explicitly added, the physical approximation being made is usually clearer than when dissipative mechanisms are contained within numerical truncation errors, and further, explicit addition of an artificial dissipation term allows greater control over the amount of nonphysical dissipation being added. Obviously,

Downloaded 01 Jun 2010 to 171.66.16.70. Redistribution subject to ASME license or copyright; see http://www.asme.org/terms/Terms_Use.cfm

the most desirable technique would add only enough dissipative mechanism to suppress oscillations without deteriorating solution accuracy. Various methods of adding artifical dissipation were investigated in [18] and these were evaluated in the context of a model one-dimensional problem containing a shock with a known analytic solution (one-dimensional flow with heat tranfer). The methods considered included second-order dissipation, fourth-order dissipation, and pressure dissipation techniques.

As a result of this investigation, it was concluded that a second-order anisotropic artificial dissipation formulation suppressed spatial oscillations without impacting adversely on accuracy and could be used to capture shocks successfully. In this formulation the terms

$$\rho^{n-1} d_x \frac{\partial^2 \phi}{\partial x^2}, \quad \rho^{n-1} d_y \frac{\partial^2 \phi}{\partial y^2}$$

are added to the governing equations where $\phi = u$, v, and ρ for the x-momentum, y-momentum, and continuity equations, respectively. The exponent, n, is zero for the continuity equation and unity for the momenta equations. The dissipation coefficient, d_x, is determined as follows. The general equation has an x-direction convective term of the form $a\partial\phi/\partial x$ and an x-direction diffusion term of the form $\partial(b\partial\phi/\partial x)/\partial x$. The diffusive term is expanded

$$\partial(b\partial\phi/\partial x)/\partial x = b\,\partial^2\phi/\partial x^2 + \partial b/\partial x\,\partial\phi/\partial x \tag{5}$$

and then a local cell Reynolds number $\mathrm{Re}_{\Delta x}$ is defined for the x-direction by

$$\mathrm{Re}_{\Delta x} = |a - \partial b/\partial x|\,\Delta x/b \tag{6}$$

where b is the total or effective viscosity, including both laminar and turbulent contributions, and Δx is the grid spacing. The dissipation coefficient d_x is nonnegative and is chosen as the larger of zero and the local quantity $\mu_e(\sigma_x \mathrm{Re}_{\Delta x} - 1)$. The dissipation parameter σ_x is a specified constant and represents the inverse of the cell Reynolds number below which no artificial dissipation is added. The dissipation coefficient, d_y, is evaluated in an analogous manner and is based on the local cell Reynolds number $\mathrm{Re}_{\Delta y}$, grid spacing Δy for the y-direction, and the specified parameter σ_y. It should be noted that recently calculations have been run with artificial dissipation added in the conservative form $\partial(\rho^{n-1} d_x\ \partial\phi/\partial x)/\partial x$, and no significant difference between the forms was noted.

The question arises as to the values of σ_x and σ_y which should be chosen. This was assessed both through the model problem [18] and through calculations for a Jose Sanz compressor cascade. The model problem calculations are discussed in detail in [18]. The Sanz cascade was investigated through a series of calculations in [19], and has the blade shape shown in Fig. 1. The cascade has a solidity, $\sigma = c/H$, equal to approximately 0.94, and a stagger angle of -9.3 deg. For the purpose of the calculation, the trailing edge was brought to a cusp to allow use of a "C"-type coordinate grid. The solidity ratio is defined as the ratio of chord, c , to distance between periodic lines, H. The flow conditions chosen were Reynolds number based upon chord and downstream conditions of 1.2×10^6, which gives largely turbulent flow over the cascade, and a nominal approach Mach number of 0.75. The inlet flow angle was specified as 35.8 deg. Since the boundary conditions set total pressure at the upstream boundary and static pressure at the downstream boundary, the Mach number on the upstream boundary is not set a priori but evolves from the solution and is controlled by the ratio of these quantities.

The calculations were carried out on a highly stretched grid having 113 pseudoazimuthal points and 30 pseudoradial points; i.e., referring to Fig. 1, 113 pseudo-radial lines such as A A′ and 30 pseudo-azimuthal loops A′ E D′ were used. Grid points were packed to obtain high resolution both in the vicinity of the blade surface and in the vicinity of the blade leading edge. The first point off the surface was placed at 0.00004 chords from the surface; in contrast, the distance between grid points in the center region of the passage reached a value of 0.06 chords. Similarly, the distance between grid points on the blade surface in the vicinity of the blade stagnation point was also kept small having a value of .0046 chords at the blade leading edge. In contrast, the grid spacing at the downstream boundary was 0.16 chords, the downstream boundary being taken two chords downstream of the blade trailing edge.

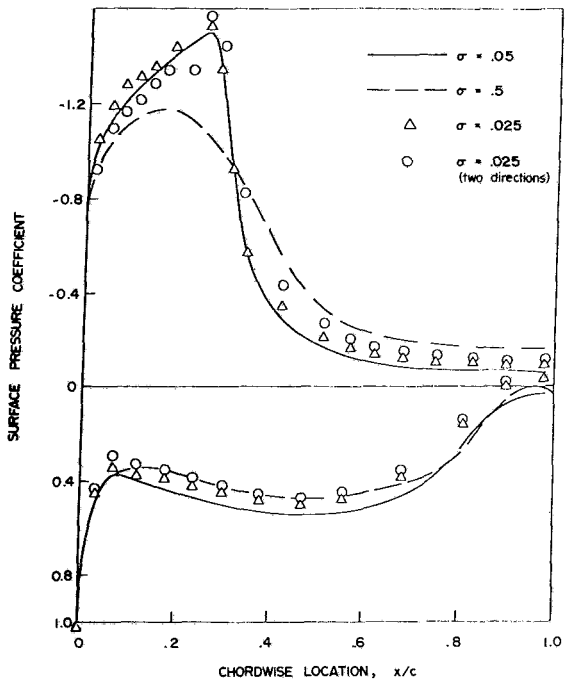


Fig. 2 Surface static pressure coefficient

The results in Fig. 2 were obtained by calculations which varied only in the values of σ_x and σ_y. In the first three calculations, $\sigma_x = .5$, .05, and .025 and $\sigma_y = .5$; in the final calculation, both σ_x and σ_y were set to 0.025. As can be seen, setting σ_x to 0.5 smears the solution considerably and leads to physically unrealistic results. This is consistent with the model problem solution in [18]. However, the results for $\sigma_x = .05$ and $\sigma_x = .025$ were nearly identical, thus indicating that the results obtained when $\sigma_x = .05$ do not change when σ_x is reduced to .025 and that the solution is insensitive to the choice of σ in this range. Furthermore, reducing σ_y from 0.5 to 0.025 when σ_x is held 0.025 causes little change in the solution, the only change being a small oscillation prior to the shock pressure rise. In reducing σ_y, it was noted that in this particular case the grid resolution normal to the surface was only marginal, and on the basis of prior experience, it was felt that with the addition of a few more grid points the oscillation in the region of the shock could have been eliminated. These results indicate that the values chosen for σ_x should be .05, whereas the results seen relatively insenstive to σ_y. The calculations presented subsequently are for $\sigma_x = .05$ and $\sigma_y = 0.5$. Further, widespread use of the controlled addition of second-order artificial dissipation by the present authors in other problems has led to the conclusion that σ less than or equal to .05 gives generally very acceptable results.

Results

Calculations were run for the compressor cascade con-

Downloaded 01 Jun 2010 to 171.66.16.70. Redistribution subject to ASME license or copyright; see http://www.asme.org/terms/Terms_Use.cfm

figurations of [20, 21], and compared with experimental data. The calculations were initiated by assuming constant velocity magnitude flow with a boundary layer correction on the airfoil surface. The calculation was run first as a variable viscosity laminar flow and after the basic flow pattern began to develop, a mixing length turbulence model was initiated. The calculations were run using a time-scaling technique along the lines suggested by McDonald and Briley [22] and previously used for cascade flows by Shamroth, Gibeling and McDonald [4]. This technique in conjunction with the existing LBI Navier-Stokes calculation procedure [9] leads to a very efficient numerical procedure which converged rapidly. Convergence was obtained from the initial start in approximately 150 time steps with convergence being determined by monitoring the time history of the flow at selected points in the field, the time history of the surface pressure distribution, and the time history of the flow field residuals. Convergence was assumed when the surface pressure distribution, the upstream velocity and pressure, and the downstream velocity showed no significant change with time. During this process, the maximum equation residuals dropped approximately three orders of magnitude from their initial values. No attempt was made to optimize convergence so it may be possible to converge the solution in less than 150 time steps. The calculation for this grid required approximately 18 s of CDC 7600 CPU time per time step. However, the code used to implement the algorithm is still a research code which has been constructed to have maximum flexibility in the choice of both dependent and independent variables, form of the equations, specification of boundary conditions, etc. The result is a highly general, versatile code which requires considerable computer overhead. Recently a similar code has been revised to limit some of the generality, and the run time after only a modest amount of recoding has been decreased by over 50 percent. It is anticipated that with some further more sophisticated code revisions, the computing time would decrease by an additional factor of between 2 and 3. This will result in a procedure requiring between 2.5 and 4.25 s per time step for these problems or requiring between 375 and 600 s per calculation.

Both calculations presented consider high Reynolds number flow and required a turbulence model. The results shown in the present report were obtained using a mixing length turbulence model in which

$$l = Mn\,[ky\,\mathfrak{D},\ .098\delta] \tag{7}$$

where k is the von-Karman constant, $\mathfrak{D}$ is the van Driest damping factor, and δ is the local boundary layer thickness. One major problem which arises concerns definition of the boundary layer thickness in the cascade flow field environment where no uniform core flow exists. In the present effort, δ was taken as twice the location where $U/U_{\max} = .95$ at each station. The quantity $U_{\max}$ is the local maximum velocity at each streamwise station in the region between the wall and a distance 0.1 chords from the wall. In addition, in the leading edge region, δ was obtained by fitting a parabolic curve between the value of the stagnation point and the 5 percent chord location. Although, as shall be shown, good results were obtained with this model, obviously it is a preliminary model and further work is needed in this area of turbulence modeling.

The first test case considered is the subsonic compressor cascade of Hobbs, Wagner, Dannenhoffer and Dring [21]. This compressor cascade shown in Fig. 3 was run at a Reynolds number based upon upstream conditions of 4.8×10^5, a Mach number based upon upstream conditions of approximately 0.10, and a ratio of upstream stagnation pressure to downstream static pressure of 1.0107. The flow was assumed to be at constant total temperature. The inlet

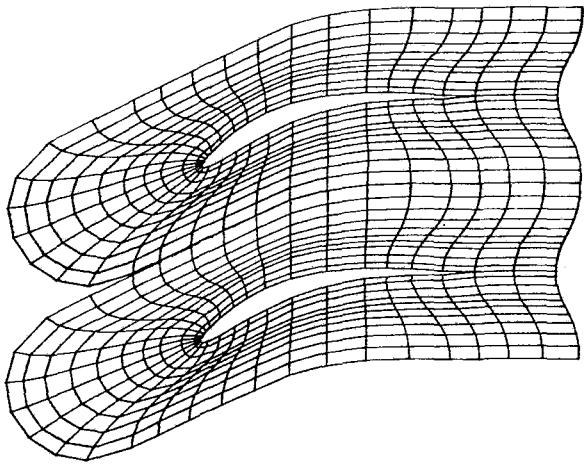


Fig. 3 Coordinate system for Stephens-Hobbs cascade

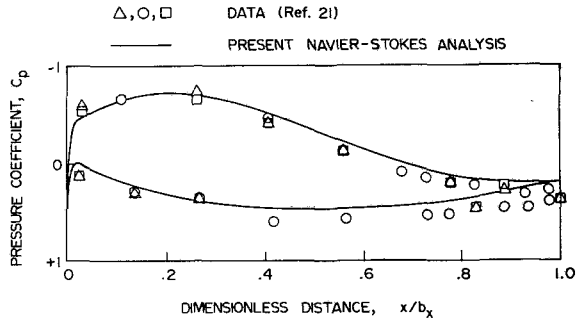


Fig. 4 Airfoil surface pressure distribution for Stephens – Hobbs cascade, $M_\infty \approx 0.1$

flow angle was specified as 52 deg. A mixing length turbulence model was used in the calculation with transition being forced at the 18 percent axial chord location as indicated by the experimental data. No correction in the calculation was made for endwall boundary layer growth, since endwall bleed was used in the experiment to minimize the effect. For clarity only selected coordinate lines are shown in Fig. 3; the actual grid spacing used was similar to that used for the Sanz calculation of Fig. 2.

A comparison of measured and predicted values for the surface pressure distribution are given in Fig. 4. The surface pressure coefficient is defined as $C_p = (p - p_\infty)/1/2\rho_\infty q_\infty^2$, where reference values are taken at the upstream boundary. As can be seen, the agreement between prediction and experiment is very good. Some discrepancies occur in the trailing edge region. These may be due to either lack of resolution in the trailing edge or near wake region, neglect of stream tube contraction, the assumption of uniform downstream static pressure, or experimental error. Comparisons of measured and predicted velocity profiles are shown in Figs. 5 and 6. The data was taken at the 97 percent chord and the predicted profiles at the 94 percent chord. These boundary layers are in regions where they have had an extensive history and may be developing rapidly and, therefore, represent a stringent test for a comparison. Although the plots are normalized as u/u_e, the predicted and measured edge velocity values agreed to within 2 percent. As can be seen in the figures, the comparisons are quite good. On the suction surface, both experiment and analysis clearly show a separating boundary layer profile with essentially the same thicknesses. The predicted thicknesses on the pressure side is slightly larger than that measured; however, the profile shapes are very similar. Although some discrepancies are apparent, the comparisons are considered to be good. A velocity vector plot is presented in Fig. 7. The general flow features such as

Downloaded 01 Jun 2010 to 171.66.16.70. Redistribution subject to ASME license or copyright; see http://www.asme.org/terms/Terms_Use.cfm

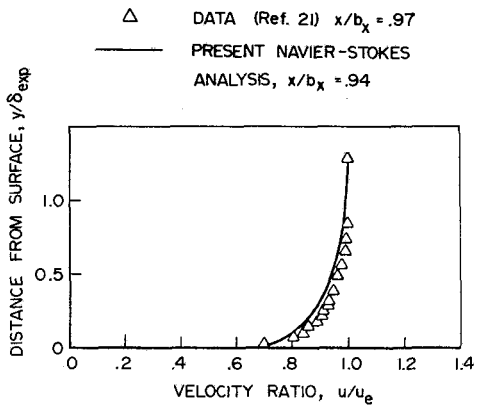


Fig. 5 Pressure surface boundary layer profile for Stephens-Hobbs airfoil

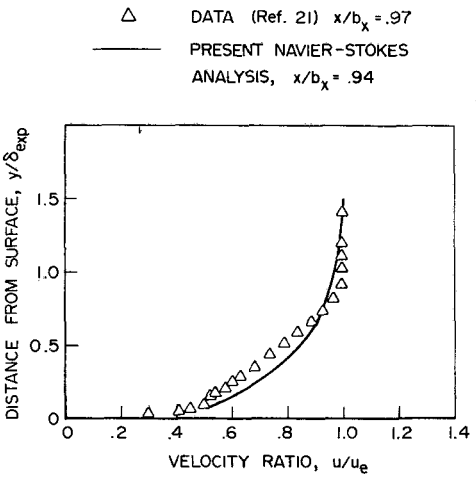


Fig. 6 Suction surface boundary layer profile for Stephens-Hobbs airfoil

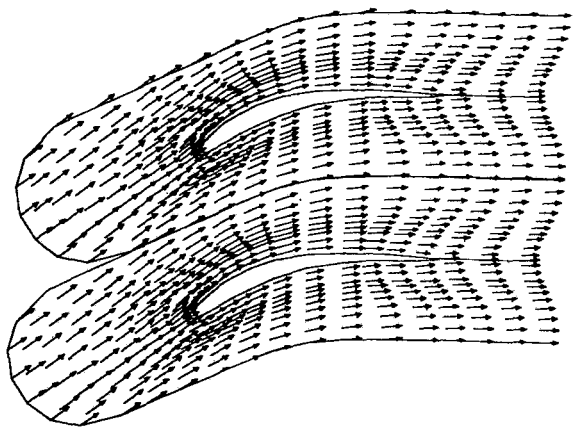


Fig. 7 Velocity field for Stephens-Hobbs cascade

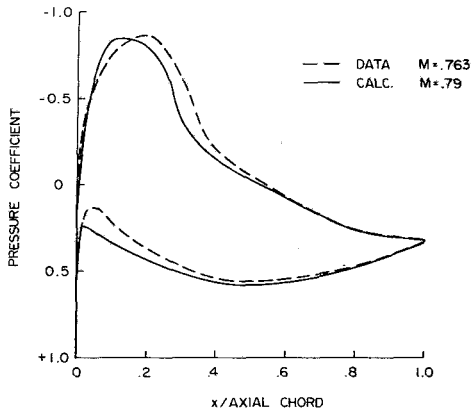


Fig. 8 Pressure distribution for Stephens-Hobbs cascade, transonic flow case

acceleration around the leading edge, boundary layer growth, flow turning, etc., are clearly visible.

The second case considered is the Hobbs-Stephens cascade configuration run in a transonic environment [20]. The calculation was run with a ratio of exit static pressure to inlet total pressure of 0.71. The resulting Reynolds number based upon axial chord and upstream conditions was approximately 0.88×10^6, and the inlet Mach number was approximately 0.785 compared to a measured value of .763. The inlet flow angle was taken as 46.8 deg. The experimental test was run with sidewall bleed to simulate streamtube contraction. Within the context of a two-dimensional analysis the most common manner of simulating three-dimensional effects due to endwall boundary layers or endwall contraction is to add a term to the continuity equation to simulate the change in stream tube width in the spanwise direction. If the momentum equations were written in conservation form, this leads to additional terms in the momentum equations. The magnitude of these terms is proportional to the ratio of the exit mass flux to the inlet mass flux along the centerplane normal to the spanwise direction with this ratio being termed the axial velocity density ratio. The correction procedure is discussed in detail in [23]. Based upon [20], an axial velocity density ratio (AVDR) of 1.12 was assumed to occur linearly through the cascade passage and a correction based upon this value was added to the equations. A comparison between the predicted and measured pressure distributions is shown in Fig. 8. The calculation shown was run for a value of $P_{\text{exit}}/P_{o_{\text{in}}} = 0.71$. The results of the calculation give good agreement with the data; however, a slight discrepancy in the shock location (the region of rapid pressure rise) and the leading edge pressure surface pressure distribution are evident. These differences could be due to the magnitude and/or distribution of the AVDR, and neglect of endwall contraction upstream of the casacde or experimental error. Although further comparisons may be required, the preliminary results here show a very encouraging degree of agreement for both the subsonic and transonic test cases.

Summary

This paper discusses application of a Navier-Stokes calculation procedure to turbulent high Reynolds number flow through a compressor cascade. Calculations were carried out on a highly stretched body-fitted coordinate system with highest resolution in the vicinity of the blade and in the blade leading edge region. Artificial dissipation was added to the equations to suppress spurious spatial oscillations associated with second order central differences. However, the amount of artificial dissipation used was such that a further decrease by a factor of 2 did not significantly affect the computed results. Calculations were initiated by assuming constant velocity magnitude with a boundary layer correction on the blade surface. Converged solutions were obtained in approximately 150 time steps. Comparisons of the results with existing experimental data showed good predictions of pressure distribution for both subsonic and transonic cases. Predictions of boundary layer velocity profiles also were good; however, further efforts in this area of turbulence modeling may be necessary.

Acknowledgment

This work was supported by the U.S. Department of the

Downloaded 01 Jun 2010 to 171.66.16.70. Redistribution subject to ASME license or copyright; see http://www.asme.org/terms/Terms_Use.cfm

Navy, Naval Air Systems Command under Contract N00019-81-C-0558.

References

1 Ecer, A. and Akay, H. U., "Investigation of Transonic Flow in a Cascade Using the Finite Element Method," *AIAA Journal*, Vol. 19, No. 9, 1981.

2 Hansen, E. C., Serovy, G. K., and Sockol, P. M., "Axial-Flow Compressor Turning Angle and Loss by Inviscid-Viscous Interaction Blade-to-Blade Computation," ASME JOURNAL OF ENGINEERING FOR POWER, Vol. 102, Jan. 1980.

3 McDonald, H., "Computation of Turbomachinery Boundary Layers," *The Aerothermodynamics of Aircraft Gas Turbine Engines*, AFAPL-TR-78-52, 1978.

4 Shamroth, S. J., Gibeling, H. J., and McDonald, H., "A Navier-Stokes Solution for Laminar and Turbulent Flow Through a Cascade of Airfoils," AIAA Paper No. 80-1426, 1980; (also see Rpt. R-920004-F, 1980).

5 Steger, J. L., Pulliam, T. H., and Chima, R. V., "An Implicit Finite Difference Code for Inviscid and Viscous Cascade Flow," AIAA Paper 80-1427, 1980.

6 Shamroth, S. J., and Gibeling, H. J., "A Compressible Solution of the Navier-Stokes Equations for Turbulent Flow about an Airfoil," NASA CR-3183, 1979; (also *AIAA Journal*, Vol. 18, Dec. 1980, pp. 1409–1410).

7 Shamroth, S. J., and Gibeling, H. J., "Analysis of Turbulent Flow About an Isolated Airfoil Using a Time-Dependent Navier-Stokes Procedure," paper presented at AGARD Specialists Meeting on Boundary Layer Effects on Unsteady Airloads, Aix-en-Provence, France, Sept. 1980.

8 Shamroth, S. J., "A Turbulent Flow Navier-Stokes Analysis for an Airfoil Oscillating in Pitch," paper presented at IUTAM Symposium on Unsteady Turbulent Shear Flow, Toulouse, 1981; (to be published by Springer-Verlag).

9 Briley, W. R., and McDonald, H., "Solution of the Multidimensional Compressible Navier-Stokes Equations by a Generalized Implicit Method," *J. Comp. Physics*, Vol. 24, No. 4, Aug. 1977, p. 372.

10 Lindemuth, I., and Killeen, J., "Alternating Direction Implicit Techniques for Two-Dimensional Magnetohydrodynamic Calculations," *Journal of Computational Physics*, Vol. 13, Oct. 1973, p. 181.

11 Briley, W. R., and McDonald, H., "On the Structure and Use of Linearized Block Implicit Schemes," *Journal of Computational Physics*, Vol. 34, 1980, pp. 54–73.

12 Douglas, J., and Gunn, J. E., "A General Formulation of Alternating Direction Methods," *Numerische Math.*, Vol. 6, 1964, pp. 428–453.

13 Thompson, J. F., Thames, F. C., and Mastin, C. W., "Boundary Fitted Curvilinear Coordinate Systems for Solution of Partial Differential Equations on Fields Containing Any Number of Arbitrary Two-Dimensional Bodies," NASA CR-2729, July 1977.

14 Gibeling, H. J. Shamroth, S. J., and Eiseman, P. R., "Analysis of Strong-Interaction Dynamic Stall for Laminar Flow on Airfoils," NASA CR-2969, Apr. 1978.

15 Eiseman, P. R., "A Coordinate System for a Viscous Transonic Cascade Analysis," *J. Comp. Physics*, Vol. 26, Mar. 1978, pp. 307–338.

16 Moretti, G., and Pandolfi, M., "Critical Study of Calculations of Subsonic Flows in Ducts," *AIAA Journal*, Vol. 19, No. 4, Apr. 1981.

17 Briley, W. R., McDonald, H., "Computation of Three-Dimensional Horseshoe Vortex Flow Using the Navier-Stokes Equations," Seventh International Conference on Numerical Methods in Fluid Dynamics, June 1980.

18 Shamroth, S. J., McDonald, H., and Briley, W. R., "A Navier-Stokes Solution for Transonic Flow Through a Cascade," SRA Rpt. 81-920007-F, 1982.

19 Shamroth, S. J., McDonald, H., Briley, W. R., "Application of a Navier-Stokes Analysis to Transonic Cascade Flow Fields," ASME Paper No. 82-GT-235.

20 Stephens, H. E., and Hobbs, D. E., "Design and Performance of Supercritical Airfoils for Axial Flow Compressors, Pratt and Whitney Aircraft Rpt. FR11455, 1979.

21 Hobbs, D. E., Wagner, J. H., Dan venhoffer, J. F., and Dring, R., P., 'Wake Experiment and Modeling for Fore and Aft-Loaded Compressor Cascade," Pratt and Whitney Aircraft Rpt. FR13514, 1980.

22 McDonald, H., and Briley, W. R., "Computational Fluid Mechanics Aspects of Internal Flows," AIAA Paper 79-1495, 1979.

23 Erdos, J. E., Alzner, E., and McNally, W., "Numerical Solution of Periodic Transonic Flow Through a Fan Stage," *AIAA Journal*, Vol. 15, Nov. 1977, pp. 1559–1568.

Downloaded 01 Jun 2010 to 171.66.16.70. Redistribution subject to ASME license or copyright; see http://www.asme.org/terms/Terms_Use.cfm

Boundary Layer and Loss Measurements on the Rotor of an Axial-Flow Turbine

H. P. Hodson
Whittle Laboratory,
University of Cambridge,
Cambridge, England CB3 0DS

The aerodynamic efficiency of an axial-flow turbine is significantly less than that predicted by measurements made on equivalent cascades which operate with steady inflow. This difference in efficiencies is strongly dependent upon the rotor-stator axial spacing. An experimental investigation of the rotor-stator interaction has therefore been conducted using a large-scale, low-speed turbine. The blade profile loss and surface shear stresses are presented for the midspan of the rotor and for a rectilinear cascade of identical geometry. Both wind tunnels were operated at a Reynolds number of 3.15×10^5. The turbine rotor midspan profile loss was approximately 50 percent higher than that of the rectilinear cascade. The shear stress measurements indicate that as a stator wake is convected through a rotor passage, the laminar boundary layers undergo transition in the vicinity of the wake. The 50 percent increase in loss is due to the time-dependent transitional nature of the boundary layers.

Introduction

The development of numerical methods for aerodynamic calculations has been very impressive in recent years. Not surprisingly, for flows of practical interest, the progress has been greatest in the field of steady-flow calculations. The designer, in using the results of steady-flow analyses or, indeed, cascade tests, assumes that the blade rows of an axial-flow turbomachine are sufficiently far apart that the flow is steady in both the stationary and the rotating frames of reference. However, the flow in a real machine is unsteady as a result of the relative motion of the blade rows. Indeed, Dean [1] has shown that in order to extract work from an inviscid turbine, the flow must be unsteady when viewed by a stationary observer. Currently, very little information is available concerning the relative importance of the unsteadiness on the aerodynamic and heat transfer characteristics of turbine blades.

The interaction of the rotating blades with the stationary blade rows can be divided into two parts. These are the effects of the potential and wake interactions. The potential influence of a blade extends both upstream and downstream and decays exponentially with a length scale typically of the order of the chord or pitch. In contrast, the wakes are convected downstream of the blade row and their rate of decay in the far field is much less than that of the potential influence. The wake effect will therefore persist even where the blade rows are spaced far apart. In modern machines, where the spacing between the blade rows is typically in the range of ¼ to ½ of a blade chord, it is likely that these effects will coexist. Furthermore, as machines become more compact and blade loadings are increased, then the levels of unsteadiness will increase.

The unsteadiness, which results from the rotor-stator interactions, affects the following aspects of turbomachine performance: blade loading, stage efficiency, heat transfer, flutter, noise generation and stall margin. This paper is concerned with the effects of rotor-stator interactions upon the aerodynamic efficiency of a single-stage, axial-flow turbine.

One of the first studies of the effects of unsteadiness upon turbine efficiency was carried out by Lopatitiskii et al. [2]. They reported that, depending upon the blade geometry and Reynolds number, the rotor profile loss in a single-stage machine was between two and four times greater than that for the same cascade operating with steady inlet conditions. Comparison of the efficiency and profile loss measurements showed that a large proportion of the "lost" efficiency was due to the increased profile loss. Kirillov et al. [3] found that the most important parameter in determining the increase in profile loss was the ratio of the maximum velocity in the wake to the convection speed of the wake. Yurinskiy and Shestachenko [4] showed that the level of increase of profile loss was largely independent on the nozzle blade profile loss. On inspection of the results of [2], [3], and [4], one can see that the effect of the unsteadiness on the profile loss was greater for the low Reynolds number, high reaction designs. This paper is concerned with the development of the blade-surface boundary layers under the influence of the unsteady flow, outside the regions of secondary flow. The ideas

Contributed by the Gas Turbine Division of THE AMERICAN SOCIETY OF MECHANICAL ENGINEERS and presented at the 28th International Gas Turbine Conference and Exhibit, Phoenix, Arizona, March 27-31, 1983. Manuscript received at ASME Headquarters November 24, 1982. Paper No. 83-GT-4.

Copyright © 1984 by ASME
Downloaded 01 Jun 2010 to 171.66.16.70. Redistribution subject to ASME license or copyright; see http://www.asme.org/terms/Terms_Use.cfm

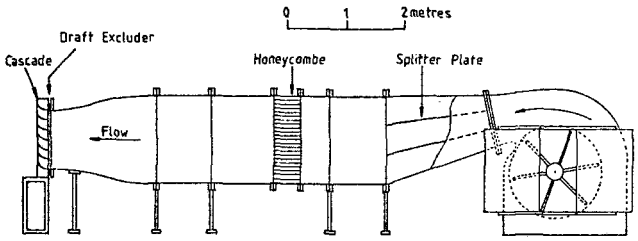


Fig. 1 Schematic diagram of the linear cascade

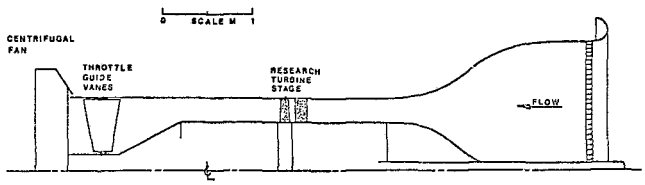


Fig. 2 Cambridge No. 2 rotating wind tunnel

presented are essentially two dimensional, but it is acknowledged that secondary flow effects and rotor tip leakage will contribute to the loss of efficiency.

The development of a boundary layer under the influence of an unsteady outer stream was first analyzed by Lighthill [5], who considered the response of a two-dimensional laminar boundary layer to a purely time-dependent oscillation of low amplitude in the free stream. Hill and Stenning [6] found by experiment that a laminar boundary layer, of the type analyzed by Lighthill, behaves linearly even for quite large amplitudes of the free-stream oscillations. Karlsson [7] showed that the same was true for turbulent boundary layers. Patel considered the influence of a convected disturbance on laminar [8] and turbulent [9] boundary layers. Again, the mean values, when compared with those for a steady outer stream, were unchanged. Despard and Miller [10], however, found that the mean separation point will move upstream of the steady state position as a result of unsteadiness in the outer flow. One possible implication of this is that where separation exists, the unsteadiness will result in either a more severe gross separation as in [11] or, should reattachment occur, a greater length of the blade-surface being covered by a turbulent boundary layer. This does not, of course, explain the results of many investigators.

The linear behavior of well-behaved laminar and turbulent boundary layers suggests that the mechanism for the increased loss lies elsewhere. Obremski and Fejer [12] found that the transition Reynolds number for a boundary layer subject to an oscillating outer stream was dependent upon an unsteady Reynolds number which was based upon the amplitude and frequency of the oscillation. Obremski and Morkovin [13] then provided a quasi-steady stability model in an attempt to explain the results of [12]. Walker [14] found that transition occurred on the stator blade of an axial-flow compressor much earlier than he would have expected. The transition was unsteady and was coupled to the passage of the rotor wakes over the blade surface. Walker presented a stability model, based upon that of [13] in order to explain his observations. In doing so, he assumed that the dominant factor in the process was the fluctuation in mean velocity caused by the wake.

Pfeil et al. [15] rotated a cascade of cylindrical bars in front of a flat plate boundary layer in an attempt to simulate the effect of rotor wakes upon stator blade boundary layers. They found that the Reynolds number for transition was much lower than that predicted by the measurements of [12]. The transition was unsteady, the boundary layer being turbulent in the vicinity of the wakes and laminar between them. The authors of [15] conclude that the stochastic fluctuations within the wake are probably the cause of the difference between their own observations and those of reference [12].

Evans [16] found that the stator-blade boundary layer of an axial-flow compressor oscillated between a characteristically laminar and turbulent condition in sympathy with the passing of the rotor wakes. Larguier et al. [17] used surface-mounted thermal anemometers to demonstrate the existence of unsteady transition of the type found by Evans [16]. Dring et al. [18] reported similar results for the rotor of an axial-flow turbine. Unfortunately, none of these publications make a comparison with measurements made on the same cascade operating with steady inflow, so the magnitude of the effect of the unsteady transition process is unknown.

Experimental Facilities

Two of the wind tunnels at the Whittle Laboratory of Cambridge University were used for the experiments in this paper. The first is a low-speed, single-stage, axial-flow turbine. The results from this will be compared with those from a linear cascade wind tunnel with a blade geometry identical to that of the midspan of the turbine rotor.

The scale of both wind tunnels makes them particularly suitable for making detailed flow measurements, including boundary-layer traverses [19]. The flow is incompressible and both wind tunnels were operated at a Reynolds number of 3.15×10^5 (based upon rotor midspan exit conditions).

Linear Cascade. The steady-state operation of the rotor midspan was determined using a linear cascade of identical geometry. The cascade is shown in Fig. 1. The seven blades have an aspect ratio of 3.0 and the center blade was provided with static pressure tappings at its midspan.

A traverse mechanism was fitted with a three-hole cobra probe at ½ of an axial chord downstream of the exit plane of the cascade. The inlet total pressure was measured using a conventional pitot tube.

The cascade was operated at the nominal design point of the turbine rotor. This involved a Reynolds number of 3.15×10^5 and axial inflow. The turbulence level at inlet to the cascade was 0.5 percent.

Single Stage Axial Flow Turbine. The Cambridge No. 2 rotating cascade wind tunnel, in the configuration of a single

Nomenclature

A = calibration constant
E = voltage
H = shape factor
h = static enthalpy
k = calibration constant
p = static pressure
p_0 = stagnation pressure
RMS = root-mean-square
s = surface distance
U = velocity
Y_c = loss coefficient
δ^* = displacement thickness
μ = dynamic viscosity
ρ = density
ν = μ/ρ
τ_w = wall shear stress
ψ = yaw angle
θ = momentum thickness

s = isentropic, surface
x = axial
overbar = mean value

Subscripts

1 = inlet
2 = exit
m = meridional, blade
rel = relative

Downloaded 01 Jun 2010 to 171.66.16.70. Redistribution subject to ASME license or copyright; see http://www.asme.org/terms/Terms_Use.cfm

stage turbine, was first investigated by Hunter [20] who reported on the secondary flow in the turbine as well as establishing the operating point. Denton and Usui [21] used a tracer gas technique in the turbine to determine the directions of fluid migration both at the midspan and near the end walls.

The wind tunnel is shown in Fig. 2. The large inlet contraction and honeycomb screens are followed by a parallel section which contains the single stage turbine. The speed of the rotor is regulated to within 1 rpm of a preset value. The airflow is provided by a centrifugal fan at the rear of the turbine and the throughput is controlled using throttle vanes at inlet to the fan. The turbulence level at the inlet to the stators was 0.25 percent.

The turbine was designed to be a free-vortex machine with zero swirl at the exit. Although a 50 percent reaction design of this type is conservative, the uniform and axial velocity at inlet to the stage [20] requires that the pressure gradients satisfy the conditions of radial equilibrium with no curvature in the meridional plane. References [20] and [21] have shown this to be the case. The stage consists of 36 stator blades followed by 51 rotor blades with aspect ratios of 1.5 and 2.0, respectively. The hub/tip ratio is 0.7. The thickness distributions of the blades are given in [22] and are fitted to parabolic camber lines with maximum thicknesses at 40 percent chord.

A rotating computer-controlled traverse mechanism has recently been fitted to the turbine [19]. The mechanism provides movement in a circumferential direction over 2½ blade passages at various spanwise locations within and downstream of the rotor passage. Information is transferred between the rotating and stationary frames of reference via a high quality 24-way slip ring unit.

The measurements described in this paper were all performed at the design condition of zero exit swirl. Further information can be found in Table 1.

Fast Response Instrumentation. Wall shear stress measurements have been made by many authors (e.g. [23]) using surface-mounted, hot-film anemometers. In the experiments described in this paper, DISA type 55R47 "Glue-On" hot films were used in conjunction with a DISA 56C16 anemometer bridge for the measurement of wall shear stress. The hot-film sensor is supplied as a film deposited on a piece of 50-μm thick mylar film. This film was glued to a larger piece of 25-μm thick acetate film upon which millimeter graduations had been marked. This facilitated the positioning of the film on the blade surface. The acetate film was fixed to the blade surface with self-adhesive tape. The total thickness of the sensor was insufficient to disturb the boundary layer.

The method of mounting made it possible to remove the sensor for calibration and to use the same hot film for all the measurements. The usual form of the calibration for constant-temperature, surface-mounted hot films is given by equation (1)

$$E^2 - A^2 = k\tau_w^{1/3} \tag{1}$$

The constants, A and k, were determined, for the operating range of the sensor, by calibrating the hot-film anemometer against a Preston Tube in the turbulent boundary layer of a flat plate. The calibration of Patel [24] was used for the Preston Tube. The constant, A, in equation (1) is nearly equal to the output voltage of the anemometer with zero flow. Most of the heat, at zero flow, is lost to the hot-film substrate, the flat plate was therefore manufactured from the same material as the turbine and cascade blades. It should be noted that errors of up to 10 percent can be expected if a hot film, which has been calibrated in a turbulent boundary layer, is used to make measurements in a laminar one (see, for example, [23]). In addition, the dynamic sensitivity of a hot film is less than the static value as a result of thermal feedback via the substrate which lies upstream of the heated element. The hot-film

Table 1 Physical description

	Stator	Rotor
Reynolds number, Re_2	4.20×10^5	3.15×10^5
Stage loading, $\Delta h/u_m^2$	–	1.0
Flow coefficient, u_x/u_m	–	0.49
Inlet angle (deg)	0.0	0.0
Exit angle (deg)	65.0	−65.0
Chord (mm)	152.4	114.3
Pitch-chord ratio	0.742	0.698
Aspect ratio	1.5	2.0
Blade number	36	51
Mean radius (m)	0.647	0.647

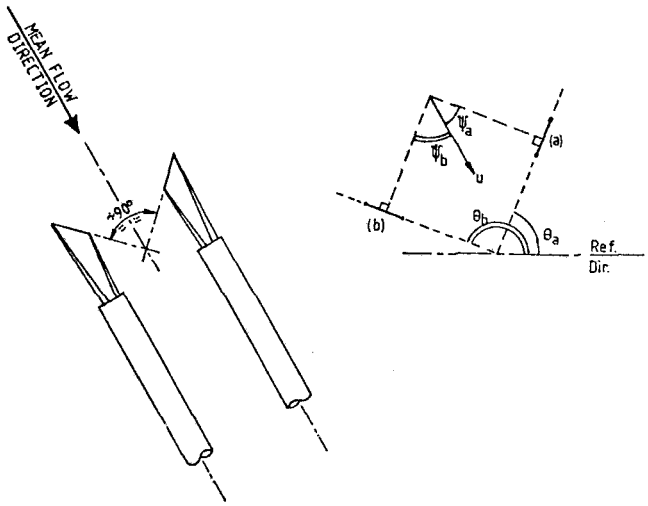


Fig. 3 Orientation of 45 deg hot-wire with respect to the mean flow

measurements have not been corrected for either of these "errors."

The rotor relative stagnation pressure loss was measured using a pitot tube, which contained a miniature pressure transducer, located at one half of an axial chord downstream of the rotor trailing edges at the mean radius. It was fitted to the rotor-relative traverse mechanism. The pitot was constructed from a small length of 1.5-mm bore steel tubing inside which a strain gage type pressure transducer was mounted. It was manufactured by Gaeltec of the U.K. The cut-off frequency of the pitot was greater than 10 kHz. A reference pressure was provided for the rear of the diaphragm by a conventional pitot tube which was also mounted on the rotor, upstream of the rotor blades at the mean radius. Allowance was made for the nonlinear response of the conventional pitot by exposing the fast response pitot to the same flow, upstream of the rotor blades, and measuring the voltage offset. Centrifugal loading on the diaphragm was also taken into account by this method.

In order to determine the mass-averaged loss coefficient it is of course necessary to know the relative velocity distribution at the exit of the rotor. This was determined using a two-dimensional adaptation of the single-sensor technique of Whitefield et al. [25]. The radial component of velocity was known to be small [21]. In the measurements, a DISA, 45-deg, hot-wire sensor, type 55P12, was mounted on the rotating frame traverse mechanism. It was positioned so that the probe support axis was approximately aligned with the mean flow direction (Fig. 3). The flow therefore bisected the two positions of the hot wire sensor. The corrected cosine law of Champagne et al. [26]

$$U_{\text{eff}}^2 = U_{\text{true}}^2(\cos^2\psi + k^2\sin^2\psi) \tag{2}$$

was used to describe the response of the wire to changes in the yaw angle, ψ. The wire was calibrated against an N.P.L. type pitot-static probe in a low turbulence wind tunnel. The general form of King's law

Downloaded 01 Jun 2010 to 171.66.16.70. Redistribution subject to ASME license or copyright; see http://www.asme.org/terms/Terms_Use.cfm

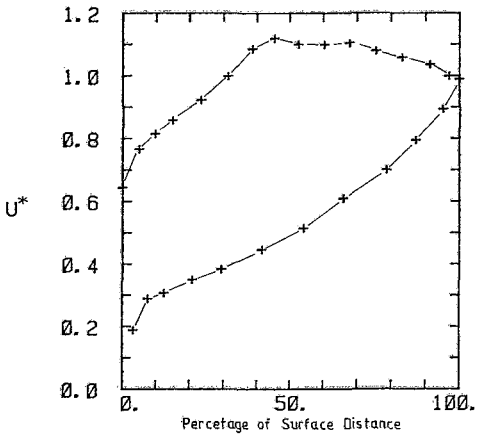


Fig. 4 Linear cascade velocity distribution

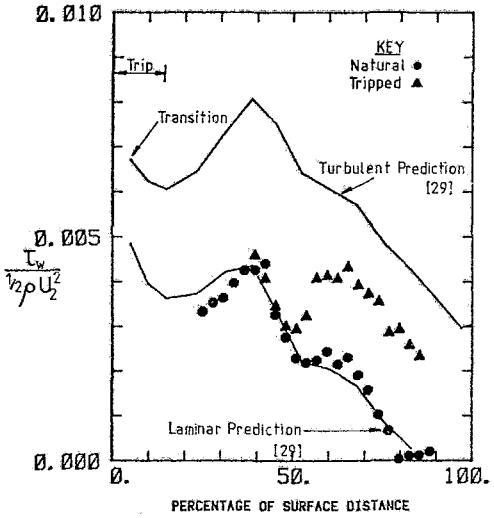


Fig. 5 Predicted and measured wall shear stresses on the suction surface of the linear cascade

$$E^2 - A^2 \simeq kU^2 \tag{3}$$

was considered to be sufficiently accurate for the measurements.

In all the measurements using the fast response instrumentation, phase-locked averaging [27] over 100 rotor revolutions was used to "clean up" the signal.

Results and Discussion

Linear Cascade. Two sets of measurements were obtained for the linear cascade, one with the natural blade-surface boundary layers and the second with the suction-surface boundary layer artificially tripped.

The nondimensional isentropic blade-surface velocity, as defined by

$$U^* = \sqrt{\frac{P_{01} - p}{P_{01} - p_2}} \tag{4}$$

is plotted against the distance along the blade surfaces in Fig. 4.

The results of the hot-film measurements on the suction-surface of the linear cascade are shown in Fig. 5. The shear stress is nondimensionalized with respect to the exit dynamic head, rather than the local value. The untripped boundary layer is laminar, with a separation occurring at 78 percent of the surface distance. An oil-and-dye flow visualization (Fig. 6) confirmed that a separation line exists at this location and showed no evidence of reattachment. The corresponding hot-film measurements showed that the laminar free-shear layer contains a growing Tollmein-Schlicting type of instability which coupled with the pressure-surface boundary layer fluid to produce a vortex street with a Strouhal number, based on exit velocity and trailing edge thickness, of 0.25.

In view of the observations made in [14–18] concerning the state of boundary layers in unsteady flow, further measurements were made with the suction-surface boundary layers artificially tripped near the leading edge. Several different trips were used in trying to form a turbulent boundary layer. However, the acceleration over the first half of the blade surface always produced either full or partial relaminarization, depending upon the position and severity of the trip. The acceleration parameter $\nu/u^2\ du/ds$ has a minimum value in this region of 2.6×10^{-6}, and it is known [28] that relaminarization can occur for values great than 3.0×10^{-6}. Thus, the difficulty in provoking a fully turbulent boundary layer is not surprising. It should be noted that the

Table 2 Mass-averaged loss coefficients, linear cascade

Natural boundary layers	$\bar{Y}_c = 0.0180$
Tripped suction surface	$\bar{Y}_c = 0.0339$

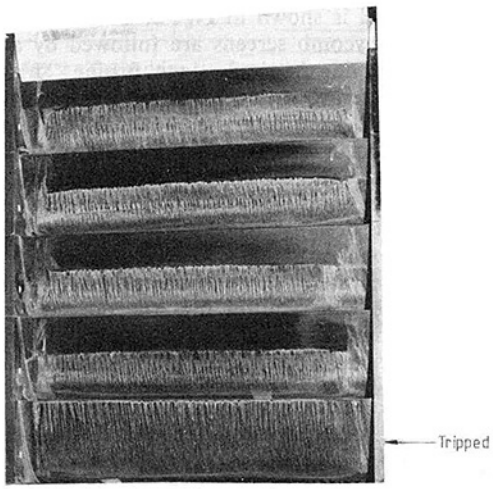


Fig. 6 Flow visualization on the suction surface of the linear cascade

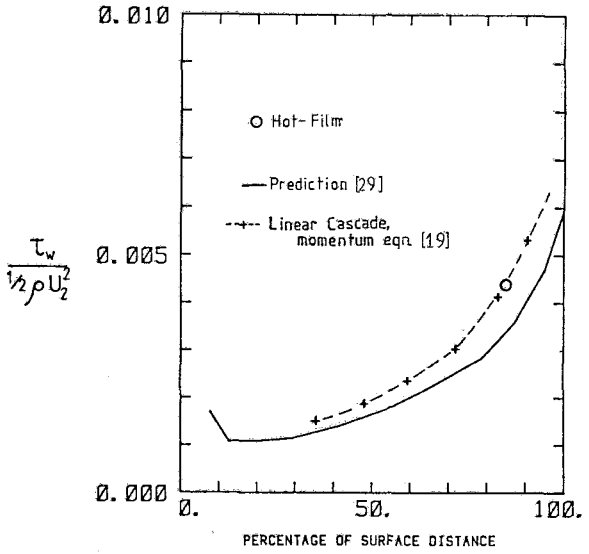


Fig. 7 Predicted and measured wall shear stresses on the pressure surface of the linear cascade

Downloaded 01 Jun 2010 to 171.66.16.70. Redistribution subject to ASME license or copyright; see http://www.asme.org/terms/Terms_Use.cfm

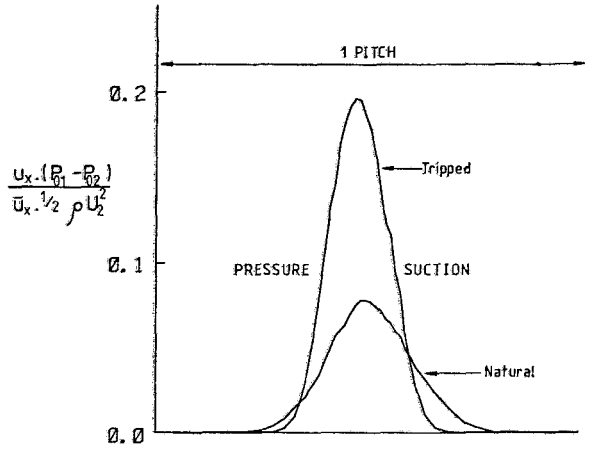


Fig. 8 Linear cascade loss coefficients

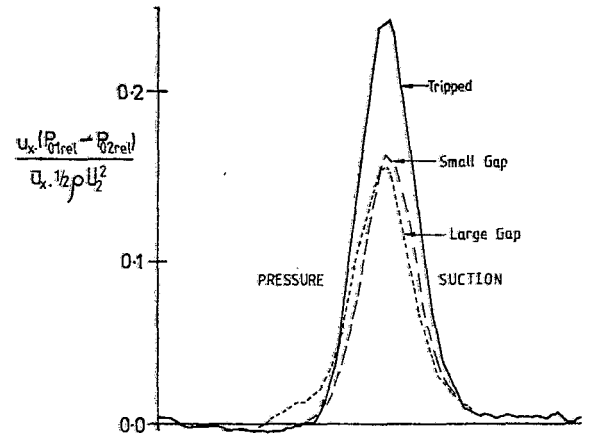


Fig. 9 Rotor relative loss coefficients

suction-surface acceleration is not particularly high for this blade, so similar results can be expected for most turbine blades operating at Reynolds numbers less than about 5×10^5.

The measurements presented in Fig. 5 show that relaminarization of the tripped boundary layer continues until peak suction is reached, even with the boundary layer trip finally selected. This trip was made from a 18-mm strip of 80 grade glass paper which was glued to the suction surface at the leading edge. Beyond peak suction, the transitional boundary layer rapidly moves towards a turbulent state.

The results of the blade static pressure measurements were used as input data for the boundary layer prediction scheme of Cebeci and Carr [29]. The predicted values of shear stress, superimposed upon the hot-film results, are shown in Fig. 5. The agreement between the predicted and measured values for the natural, laminar boundary layer is excellent. The prediction does not extend beyond the separation because of the singularity which then exists in the Prandtl boundary layer equations.

There is a difference between the predicted shear stress values for the fully turbulent boundary layer and the measured values in the transitional, tripped boundary layer, but it is larger than expected. This will be discussed together with the results of the exit traverse.

Figure 7 shows the predicted and measured values of wall shear stress, toegther with the values obtained by applying the momentum integral equation of von Karman to the boundary layer traverse data of [19]. In view of the excellent agreement between the predicted and measured values of the laminar

Table 3 Stator wake measurements

	43% Cx_s	117% Cx_s	
δ^*/stator pitch	0.0080	0.0084	} stationary frame
θ/stator pitch	0.0071	0.0070	
Shape factor, $H=\delta^*/\theta$	1.27	1.20	
Loss coefficient, $\bar{Y}_c$	0.014	–	
$(u_{max}-u_{min})/\bar{u}$	0.105	0.080	} rotating frame
Incidence variation (deg)	7.5	5.0	

suction surface boundary layer, it is surprising that the agreement is so poor on the pressure surface. However, the agreement between the measured value and the results of [19] is excellent. The reason for the poor prediction is not understood. The hot-film output signal and surface-flow visualization showed that Görtler vortices, one of the causes of discrepancies between measured and predicted boundary layers, did not exist.

The mass-flow weighted loss coefficient

$$Y_c = \frac{U_x(P_{01}-P_{02})}{\bar{U}_x \tfrac{1}{2}\rho U_2^2} \tag{5}$$

is plotted, in Fig. 8, for the linear cascade with its natural and tripped boundary layers. The mass-averaged values are presented in Table 2. The loss coefficients of both the tripped and the untripped blades are exceptionally low. This is a result of the large areas of favorable pressure gradients which exist on both surfaces and the low surface diffusion on the suction surface. The profile loss of the tripped cascade is 21 percent greater than the predicted value. This large discrepancy occurs because the trip is severe enough to generate a significant momentum loss as the boundary layer passes over it. The increased loss will result in a boundary layer which is thicker than predicted and, therefore, a wall shear stress which is less than that predicted.

Turbine Rotor. Three sets of data are presented for the turbine rotor at midspan. Two different axial spacings, equal to 75 and 150 percent of the stator axial chord, were investigated with the blade surface boundary layers in their natural state. A third series of measurements, at the smaller axial gap, were made with the rotor-blade suction surfaces fitted with boundary layer trips which were identical to those used on the linear cascade. At these values of rotor-stator gap, the level of unsteadiness which results from the interaction of the blade potential fields will be insignificant when compared to the unsteadiness which is caused by the relative motion of the stator wakes.

The results of the stator wake measurements, for two different traverse planes, are presented in Table 3. These traverse planes were located at 43 and 117 percent of the stator axial chord downstream of the stator trailing edges. The 117 percent Cx_s data were taken with the axial gap set to the large value. The measurements were made in the rotor-relative frame. They are presented in both frame of reference. Table 3 shows that the velocity defect in the relative frame reduces from 10.5 percent of the mean at 43 percent Cx_s to 8 percent at 117 percent Cx_s. Similarly, the variation in incidence reduces from 7.5 to 5.0 deg. It is acknowledged that these variations, while they are significant, are not necessarily as large as those which can occur in modern designs.

The mass-averaged profile loss coefficients of the turbine rotor blades are presented in Table 4. These show that while there is very little difference between losses of the two natural blades, tripping the suction surface boundary layer results in a significant increase. A comparison with the linear cascade values (Table 2) shows that the profile loss of the natural rotor is approximately 50 percent higher than that of the untripped blades of the linear cascade. It also shows that the profile loss of the tripped rotor is 40 percent greater than that of the tripped cascade.

Downloaded 01 Jun 2010 to 171.66.16.70. Redistribution subject to ASME license or copyright; see http://www.asme.org/terms/Terms_Use.cfm

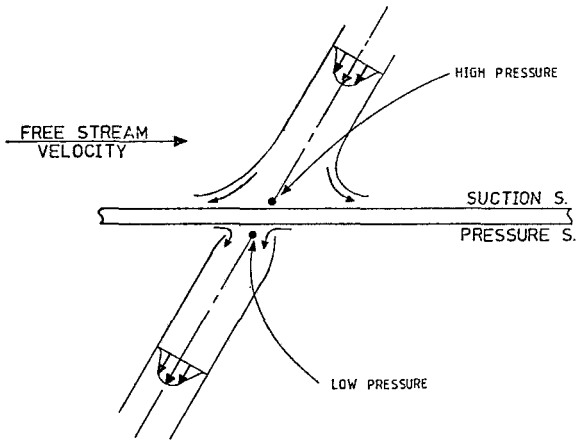


Fig. 10 Wake distortion on a turbine blade (Meyer, 1958)

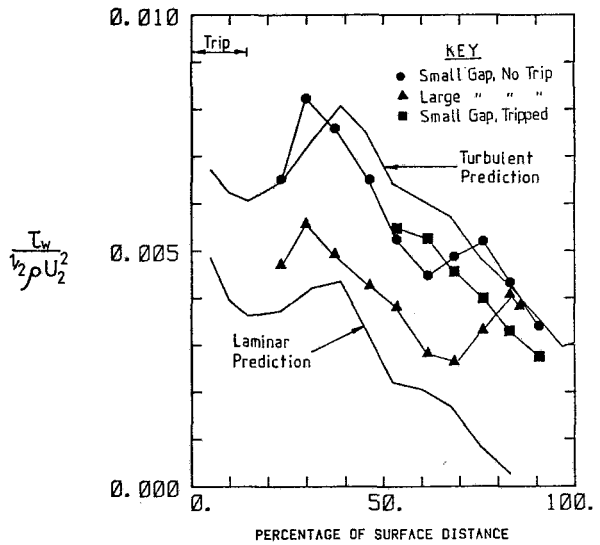


Fig. 11 Predicted and measured wall shear stresses on the suction surface of the turbine rotor blades

The profiles of the rotor-relative loss coefficients are shown in Fig. 9. The similarity between the measurements for the two axial gaps with natural boundary layers is apparent. In all three test cases, the profile loss is not zero between the wakes. Instead, it is positive on the suction-surface side of the wake and negative on the pressure side. This can be explained using the model of Meyer [30]. If the wake is considered to be a "negative" jet superimposed on the free stream (Fig. 10), then it is obvious that migration of the wake fluid occurs relative to the free-stream fluid in a direction which is aligned with the centerline of the wake. This will occur even when the wake has been chopped by the rotor blade. The wake fluid therefore moves towards the suction-surface as it is convected through the blade passage. On the pressure-surface, it is replaced by fluid from the free stream which has a higher relative stagnation pressure. Adachi and Murakami [31] have observed a similar phenomenon in the stator of an axial-flow compressor.

The time-averaged values of suction-surface wall the shear stress, measured by hot films on the turbine rotor, are shown in Fig. 11. The two-dimensional predictions are also shown. The use of a two-dimensional pressure distribution in the calculation of the boundary-layer growth is not unreasonable for this particular machine, since it is known [21] that the flow at midspan satisfies the design conditions of radial equilibrium with no curvature in the meridional plane. A two-

Table 4 Mass-averaged loss coefficients, turbine rotor

Small axial gap, natural boundary layers	$\bar{Y}_c = 0.0270$
Large axial gap, natural boundary layers	$\bar{Y}_c = 0.0263$
Small axial gap, tripped suction surface	$\bar{Y}_c = 0.0472$

dimensional boundary layer analysis does not, of course, take into account the effects of rotation on the blade-surface boundary layers.

The results in Figs. 5 and 11 show that over the first half of the blade suction surface the shear stresses of the natural boundary layer on the linear cascade correspond to the laminar values, whereas those on the turbine rotor are transitional. The untripped suction-surface boundary layer, with the smaller axial gap, exhibits a rapid increase in wall shear stress, starting just beyond the diffusion which follows peak suction. It therefore appears that this small amount of diffusion and subsequent constant pressure region are sufficient to promote a completion of the transition process. With the larger axial gap, the boundary layer is more laminar (i.e., lower mean shear stress) when it encounters this diffusion. Therefore, the transition process does not end until the relatively large, unfavorable pressure gradient is encountered beyond the pressure plateau. In contrast to the aforementioned, and to the results of the linear cascade, the tripped rotor suction-surface boundary layer shows no sign of relaminarization. The time-averaged shear stress for the tripped boundary layer is lower than the predicted value, presumably for the same reasons as on the linear cascade.

In Fig. 12, the phase-locked averages of the shear stress and its rotor-mean-square (as defined by equation (6)) are shown for various locations on the blade surface

$$RMS(\theta) = \sqrt{\frac{\sum_{n=1}^{N} \tau_w^2(\theta,n) - \sum_{n=1}^{N} \tau_w(\theta,n)^2}{N}} \quad :\theta = \text{Rotor position} \tag{6}$$

Equation (6) shows that the *RMS* is a measure of the level of the random fluctuations which occur at a particular rotor position. It contains no information regarding the periodic content of the anemometer signal. Therefore, by presenting the ensembled *RMS*, as well as the shear stress, it is possible to determine whether or not an increase in shear stress is accompanied by an increase in the local level of turbulence. The graphs in Fig. 12 are all plotted on the same scale. Only the fluctuating portion of the ensembled shear stress is shown for clarity. The reason for presenting the data in the form of phase-locked averages, rather than in its raw form ([17] and [18]) is that once the boundary-layer has lost its laminar character for all parts of the cycle of oscillation, the raw data are impossible to interpret by eye.

The observed differences in the time-averaged shear stresses of Fig. 11 are easily explained with reference to Fig. 12. With the smaller axial gap and no trip, (Fig. 12(*a*)) the boundary layer is indeed transitional over most of its length. At the first three locations shown, the boundary layer oscillates between a laminar (low shear stress and root-mean-square) and a near turbulent state (higher shear stress and root-mean-square). The nonzero root-mean-square in the laminar portion is caused by the cycle-to-cycle variations inherent in a turbomachine of this type. The amplitude of the signal is small, suggesting that the acceleration of the boundary layer over this section of the blade surface has a greater effect than that of the wake upon the transition process. Beyond peak suction, at 62 percent surface distance, the amplitudes of the signal and the root mean square have increased, suggesting that the boundary layer is undergoing a greater change of state during

Downloaded 01 Jun 2010 to 171.66.16.70. Redistribution subject to ASME license or copyright; see http://www.asme.org/terms/Terms_Use.cfm

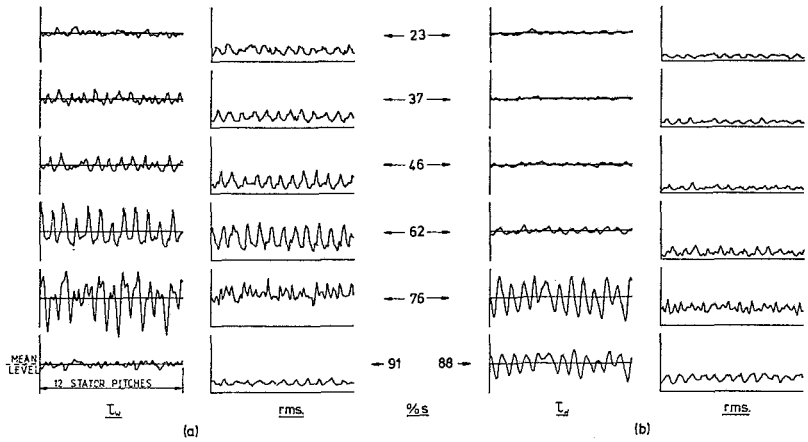


Fig. 12 Phase-locked averages of suction surface shear stresses (*a*) small axial gap, (*b*) large axial gap

the cycle. Also, at 62 percent *s* the minimum value of the root-mean-square is greater, implying that the boundary layer is never laminar, but the shape of the shear stress wave form does indicate that the boundary-layer is, on average, more laminar than turbulent whereas at 76 percent *s* the opposite is true. The minimum value of the *RMS* is also greater at 76 percent *s*, which supports the above observation. A feature of the shear-stress signal at 76 percent *s* is that the peak which existed at 62 percent *s* has become folded back so that there are two slightly smaller peaks instead of the one. This folding back continues as the boundary-layer develops so that by 92 percent *s* it is complete. The levels of the fluctuations are much smaller at this location, indicating that transition is almost complete. The records for 62 percent *s* show that the shear stress and turbulence quantities vary in phase with each other whereas at 91 percent *s*, they are in antiphase. Figure 12(*c*) shows that in the tripped boundary layer, the shear stress, and *RMS* are always in antiphase. Thus, the appearance of the double peaks at 76 percent *s* represents a change between the early, transitional boundary layer and the later, more turbulent, profile.

Figure 12(*b*) shows the shear stress and *RMS* records for the natural suction surface boundary layer with the larger axial gap. The trends are similar to those which occur in the case of the smaller axial gap. However, the transition from the early, mainly laminar state to the later, more turbulent state is delayed and more rapid. This was indicated in the time-averaged measurements of Fig. 11.

The results of the hot-film measurements on the suction surface of the tripped rotor blade are shown in Fig. 13. The levels of the fluctuations of both the shear stress and the *RMS* are much less than those which occur in the natural boundary layers. Also, the ratio of the *RMS* and the mean shear stress is approximately equal to the ratios of the maximum *RMS* value and the mean shear stress which occur in the natural boundary layers. The tripped boundary layer appears, therefore, to be completely turbulent over the entire length of the suction surface. This is in contrast to the tripped boundary layer of the linear cascade which undergoes partial relaminarization. It can only be concluded that this difference is due to the combined strengths of the boundary-layer trip and the wake-generated unsteadiness being greater than the relaminarizing effect of the acceleration of the suction surface. The lack of any relaminarization would account for the differences in the profile losses of tripped rotor and the tripped cascade.

Figure 14 compares the mean values of the shear stresses on the pressure-surface of the turbine rotor blade. The trends exhibited by the mean values are similar for both axial gaps, with the highest values existing in the case of the smaller axial

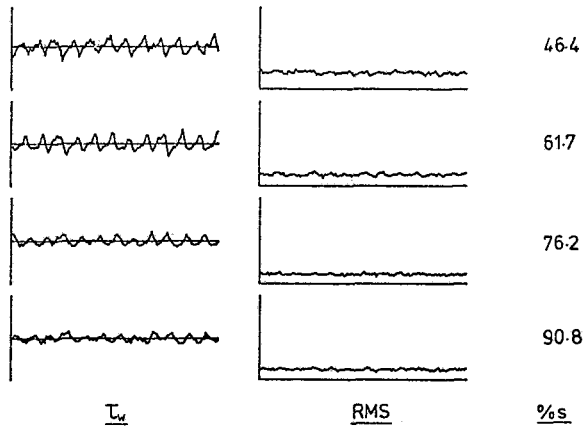


Fig. 13 Tripped rotor

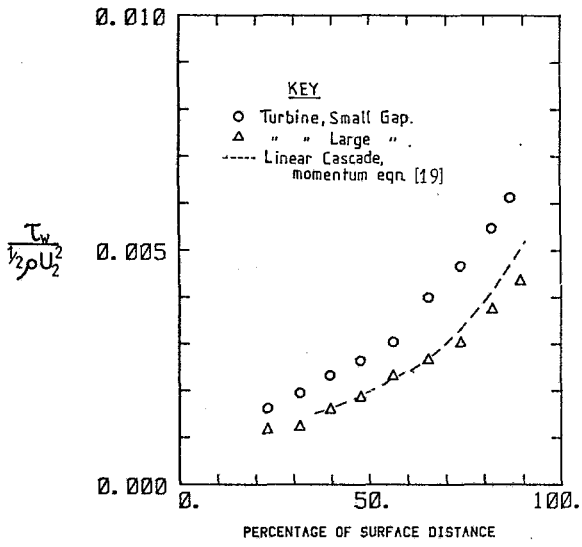


Fig. 14 Predicted and measured wall shear stresses on the pressure surface of the turbine rotor blades

gap. Neither boundary layer exhibits the rapid increases which have indicated transition on the suction surface.

The phase-locked averages of the rotor pressure-surface shear stress and the *RMS* are shown in Fig. 15 for both axial gaps. The vertical scale is five times that of Fig. 12. The most striking feature of Fig. 15 is the rapid attenuation of both the signal and its root mean square. This rapid attenuation is

Downloaded 01 Jun 2010 to 171.66.16.70. Redistribution subject to ASME license or copyright; see http://www.asme.org/terms/Terms_Use.cfm

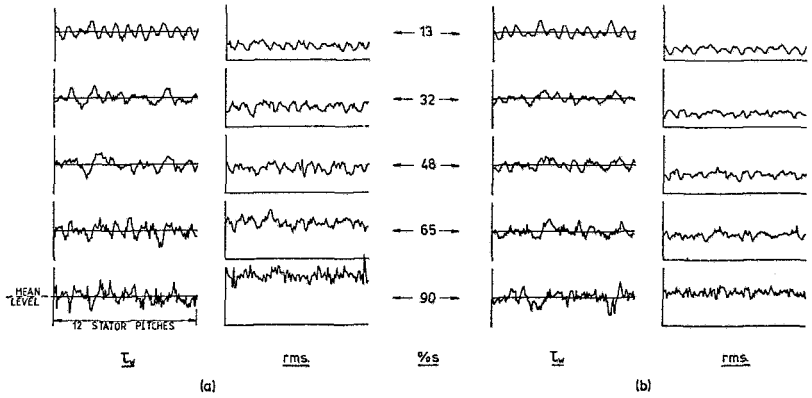


Fig. 15 *Phase-locked averages of pressure surface shear stresses: (a) small, (b) large axial gap*

thought to be a result of the wake fluid being replaced by low-turbulence, free-stream fluid as the wake migrates towards the suction surface during its passage through the blade row. The acceleration of the boundary layer along the pressure surface will also contribute to the attenuation, but the value of the parameter $\nu/u^2\ du/ds$ over the rear half of the pressure-surface is no greater than that on the leading half of the suction surface, where significant attenuation does not occur. Therefore, the acceleration cannot be the main cause of the attenuation. Although attenuation does occur, the boundary layer still appears to be transitional (nonzero *RMS*) over the entire pressure surface. This observation contradicts the observed similarity between the mean values of the boundary layer which occurs in the case of the larger axial gap and the laminar boundary layer of the linear cascade. The influence of secondary flow and tip leakage upon the pressure surface boundary layer cannot, therefore, be excluded.

Conclusions

The profile loss at the midspan of a turbine rotor is 50 percent higher than that of an equivalent linear cascade operating with steady inflow. The blade-surface boundary layers on the linear cascade were laminar, with a separation point on the suction surface close to the trailing edge. On the turbine rotor blades the unsteadiness generated by the stator wakes results in a time-dependent transitional boundary layer on most of the suction surface. There was no separation on the rotor blades. On the rotor pressure surface the boundary layer was mainly laminar and the fluctuations were much less than those on the suction surface. The 50 percent increase in profile loss is caused by the transitional nature of the rotor blade-surface boundary layers. This increase was largely independent of the rotor-stator gap for the range investigated.

The results in [2–4] show that the unsteady loss is greater in machines of high reaction and low Reynolds numbers. Such designs, under conditions of steady inflow, favor the presence of laminar boundary layers over a large portion of the blade suction surface. It is these blades, therefore, that will show the largest increase in profile loss as a result of the wake induced transition.

Acknowledgments

The author wishes to thank the staff of the Whittle Laboratory and in particular Dr. J. D. Denton for his supervision of the work which forms the basis of this paper. The financial support provided by the Central Electricity Generating Board is gratefully acknowledged.

References

1 Dean, R. C., "On the Necessity of Unsteady Flow in Fluid Machines," ASME *Journal of Basic Engineering*, Mar. 1959, pp. 24–28.

2 Lopatitskii, A. O., et al., "Energy Losses in the Transient State of an Incident Flow on the Moving Blades of Turbine Stages," *Energomashinostroenie*, Vol. 15, Aug. 1969.

3 Kirillov, I. I., Laskin, A. S., and Shpenzer, C. G., "Influence of Unsteadiness of the Flow on Efficiency of Turbine Stages," *Teploenergetika*, 1970, Vol. 17, No. 10, pp. 21–23.

4 Yurinskiy, V. T., and Shestachenko, I., Ya., "Losses in an Impulse Turbine Cascade in an Unsteady Flow," *Fluid Mechanics—Soviet Research*, Vol. 3, No. 1, Jan. 1974, pp. 22–27.

5 Lighthill, M. J., "The Response of Laminar Skin Friction and Heat Transfer to Fluctuations in the Stream Velocity," *Proc. R. Soc.*, 224A, 1954.

6 Hill, P. G., and Stenning, A. H., "Laminar Boundary Layers in Oscillating Flow," ASME *Journal of Basic Engineering*, Vol. 82, 1960.

7 Karlsson, S. K. F., "An Unsteady Turbulent Boundary Layer," *Journal of Fluid Mechanics*, Vol. 5, No. 4, 1959, pp. 622–636.

8 Patel, M. H., "On Laminar Boundary Layers in Oscillatory Flow," *Proc. R. Soc.*, 347A, 1977.

9 Patel, M. H., "On Turbulent Boundary Layers in Oscillatory Flow," *Proc. R. Soc.*, 353A, 1977.

10 Despard, R. A., and Miller, J. A., "Separation of Oscillatory Laminar Boundary Layers," *Journal of Fluid Mechanics*, Vol. 47, No. 1, 1971, pp. 21–23.

11 Samoilovich, G. S., Yablokov, V. G., and Rabotarev, V. G., "Profile Losses with Unsteady Flow Through Impulse Cascades of Moving Blades," *Teploenergetika*, Vol. 24, No. 2, 1977, pp. 40–42.

12 Obremski, H. J., and Fejer, A. A., "Transition in Oscillatory Boundary Layer Flows," *Journal of Fluid Mechanics*, Vol. 29, No. 1, 1967, pp. 93–111.

13 Obremski, H. J., and Morkovin, M. V., "Application of a Quasi-Steady Stability Model to Periodic Boundary Layer Flows," *AIAA Journal*, Vol. 7, No. 7, 1969, pp. 1298–1301.

14 Walker, G. J., "The Unsteady Nature of Boundary Layer Transition on an Axial-Flow Compressor Blade," ASME Paper No. 74-GT-135, 1974.

15 Pfeil, H., Herbst, R., and Schröder, T., "Investigation of the Laminar-Turbulent Transition of Boundary Layers Disturbed by Wakes," ASME Paper No. 82-GT-124, 1982.

16 Evans, R. L., "Boundary Layer Development on an Axial-Flow Compressor Stator Blade," ASME JOURNAL OF ENGINEERING FOR POWER, Vol. 100, Apr. 1978, pp. 287–293.

17 Larguier, R., and de Sievers, A., "Unsteady Flow Measurements in Turbomachines," Paper presented to Supersonic Tunnel Association, Toronto, Sept. 1975.

18 Dring, R. P., Joslyn, H. D., Hardin, L. W., and Wayner, J. H., "Turbine Rotor-Stator Interaction," ASME Paper No. 82-GT-3, 1982.

19 Hodson, H. P., "Unsteady Boundary Layers on an Axial-Flow Turbine Rotor Blade," Ph.D. thesis, Cambridge University, 1983.

20 Hunter, I. H., "Endwall Boundary Layer Flows and Losses in an Axial Turbine Stage," ASME JOURNAL OF ENGINEERING FOR POWER, Vol. 104, Jan. 1982, pp. 184–193.

21 Denton, J. D., and Usui, S., "Use of a Tracer Gas Technique to Study Mixing in a Low-Speed Turbine," ASME Paper No. 81-GT-86, 1981.

22 Smith, D. J. T., and Johnson, S. H., "Investigations on an Experimental Single-Stage Turbine of Conservative Design," A.R.C., R. & M. No. 3541, Jan. 1967.

23 Bellhouse, B. J., and Schultz, D. L., "Determination of Mean and Dynamic Skin Friction, Separation and Transition in Low-speed Flow With a Thin-Film Heated Element," *Journal of Fluid Mechanics*, Vol. 24, No. 2, 1966, pp. 379–400.

Downloaded 01 Jun 2010 to 171.66.16.70. Redistribution subject to ASME license or copyright; see http://www.asme.org/terms/Terms_Use.cfm

24 Patel, V. C., "Calibration of the Preston Tube and Limitations on Its Use in Pressure Gradients," *Journal of Fluid Mechanics*, Vol. 23, No. 1, pp. 185–208.

25 Whitfield, C. E., Kelly, J. C., and Barry, B., "A Three-Dimensional Analysis of Rotor Wakes," *Aero. Quart.*, Nov. 1972, pp. 285–300.

26 Champagne, F. H., Sleicher, C. A., and Wehrman, O. H., "Turbulent Measurements With Inclined Hot-Wires, Part I," *Journal of Fluid Mechanics*, Vol. 28, 1967, p. 153.

27 Gostelow, J. P., "A New Approach to the Experimental Study of Turbomachinery Flow Phenomena," ASME Paper No. 76-GT-47, 1976.

28 Jones, W. P., and Launder, B. E., "The Prediction of Laminarization With a Two-Equation Model of Turbulence," *Journal of Heat and Mass Transfer*, Vol. 15, 1972, pp. 301–315.

29 Cebeci, T., and Carr, W. C., "A Computer Program for Calculating Laminar and Turbulent Boundary Layers for Two Dimensional, Time-Dependent Flows," NASA, TM-78470, Mar. 1978.

30 Meyer, R. X., "The Effect of Wakes on the Transient Pressure and Velocity Distributions in Turbomachines," ASME *Journal of Basic Engineering*, Oct. 1958, pp. 1544–1552.

31 Adachi, T., and Murakami, Y., "Three-Dimensional Velocity Distribution Between Stator Blades and Unsteady Force due to Passing Wakes," JSME, Vol. 22, No. 170, Aug. 1979, pp. 1074–1082.

Downloaded 01 Jun 2010 to 171.66.16.70. Redistribution subject to ASME license or copyright; see http://www.asme.org/terms/Terms_Use.cfm

Flow in a Turbine Cascade: Part I—Losses and Leading-Edge Effects

J. Moore

A. Ransmayr

Department of Mechancial Engineering,
Virginia Polytechnic Institute
and State University,
Blacksburg, Va. 24061

An experimental investigation was conducted to study the effect of the leading-edge shape on the overall losses in a large-scale linear cascade of turbine blades. The leading-edge shapes used were a cylinder and a wedge. The cascade was designed to be geometrically similar to the cascade used by Langston et al. at United Technologies Research Center, with the same span/chord and pitch/chord ratios. Measurements of wall static pressure on the blades and of total pressure and flow direction downstream of the cascade showed only minor changes due to the alteration of the leading-edge shape. The measurements of the flow and loss distributions downstream of the cascade complement the results of Langston et al., which showed the flow development only within the cascade. The downstream flow is important, however, as apppoximately 50 percent of the losses occur downstream of the trailing edge. Regions of high loss were found near midspan at an axial location 40 percent of the axial chord downstream of the trailing edge. The sources of fluid in these regions are determined in Part 2.

Introduction

Improved understanding of three-dimensional flow and loss mechanisms in turbomachinery passages is leading to improved designs with higher efficiency and better performance [1–5]. Currently used design methods are mostly based on two-dimensional flow calculations for the blading. But, because the flow in a turbomachine is complex and three-dimensional, these methods are reaching the limit of their usefulness. To obtain further improvements, detailed investigations of the three-dimensional flow have been found to be necessary [6–13]. These are giving information about loss production mechanisms and about the differences between the actual flow and the two-dimensional, inviscid flow often assumed in blade design calculations.

In order to gain a better understanding of the flow it is usual to consider an ideal "primary" flow, which may, for example, be two-dimensional potential flow. The difference between this primary flow and the actual flow is then termed secondary flow.

There are two mechanisms which have a major influence on the generation of secondary flows in turbomachinery passages:

(*i*) Secondary flow due to rotation or curvature, which cause a flow with an initial distribution of normal vorticity to develop a streamwise component of vorticity. This mechanism has been used by Squire and Winter [14] and by Hawthorne [15, 16] to explain three-dimensional flows in curved ducts, pipe bends, and rotating channels. It also contributes strongly to the formation of so-called passage vortices in turbine cascades.

(*ii*) Horseshoe-vortex flow due to the interaction of endwall boundary layer flow with a blade leading edge. Upstream of the leading edge, a vortex line moves towards the leading edge within the boundary layer. This vortex line is then convected around the leading edge, causing vortex lines on each side of the blade. Hawthorne [17] used this mechanism to describe the scouring of river beds near the leading edges of bridge piers.

In the case of cascade flow, secondary flow is generated by the turning effect of the bend as well as by the horseshoe vortex phenomenon. These two effects are superposed as shown schematically in Fig. 1. The endwall boundary layer fluid within the passage follows a path of larger curvature towards the suction side and tends to form a passage vortex. The pressure-side leg of the horseshoe vortex rotates in the same direction as the passage vortex, whereas the other leg, in the suction-side/endwall corner region, turns in the opposite direction.

In modeling cascade flows, it is of interest to know the relative importance of these two effects in determining the three-dimensional flow in the passage. Therefore the factors which influence these mechanisms are briefly outlined:

(*a*) for a bend:

- the thickness of the inlet boundary layer
- the normal vorticity of the inlet flow
- the turning angle of the bend

(*b*) for the horseshoe vortex:

- the thickness and vorticity distribution of the inlet boundary layer
- the shape and radius of the leading edge
- and possibly incidence of the inlet flow and blade loading near the leading edge as well

Downstream of the passage a third effect, in addition to these two effects, can occur, i.e.:

(*iii*) Shed vorticity due to differences in spanwise velocities

Contributed by the Gas Turbine Division of THE AMERICAN SOCIETY OF MECHANICAL ENGINEERS and presented at the 28th International Gas Turbine Conference and Exhibit, Phoenix, Arizona, March 27–31, 1983. Manuscript received at ASME Headquarters December 21, 1981. Paper no. 83-GT-68.

Copyright © 1984 by ASME
Downloaded 01 Jun 2010 to 171.66.16.70. Redistribution subject to ASME license or copyright; see http://www.asme.org/terms/Terms_Use.cfm

near the pressure and suction surfaces of the blades at the trailing edge. This effect, shown schematically in Fig. 1, can also induce secondary velocities within the flow field.

As part of this study, the influence of the leading edge shape on the overall losses produced by a large-scale turbine cascade is investigated. The measurements employed are:

(*i*) Measurement of static pressures on the blade surfaces and on the end wall

(*ii*) Measurement of the flow distribution at cross sections upstream and downstream of the cascade; for example, a five-hole probe was traversed downstream of the cascade. Together these measurements provide information about the three-dimensionality of the flow.

In order to find the influence of the blade leading-edge shape on the cascade flow, two different shapes are used:

(*a*) A circular cylinder

(*b*) A wedge

The loss distributions downstream of the cascade show regions of high loss near midspan. In Part 2 of this paper [23], we reveal the sources of this high-loss fluid by measuring flow trajectories using an ethylene detection technique.

Five-Blade Replica of the Langston Turbine Cascade

Choice of the Langston Turbine Cascade. One of the most extensively documented turbine cascade flows in the literature is that reported by Langston, Nice, and Hooper [10], Graziani, Blair, Taylor, and Mayle [11], and Langston [13]. The geometry of the cascade used in the present investigation is the same as that used by Langston et al. and the results in these papers are therefore of most interest for this study.

Langston et al. [10] made comprehensive measurements of their cascade flow field using surface flow visualization, wall-static pressure tappings, hot wire anemometry, and traverses of a five-hole probe. With the five-hole probe they made detailed pressure measurements in twelve cross-sectional planes starting upstream of the leading edge, having eight planes within a cascade passage, and also having three planes downstream of the trailing edge. Contours of total pressure are presented on three planes within the passage; these clearly show the size of the horseshoe vortex and the secondary flow associated with the migration of the endwall boundary layer fluid to the suction side and the development of a passage vortex. The mass-averaged values of total pressure show the rate of loss production increasing through the blade row with *more than half* of the losses being created downstream of the trailing edge. No other data is presented downstream of the blade row, but clearly this region is of interest in studies of loss production and turbine inefficiency. In the present paper we show results of measurements in this region.

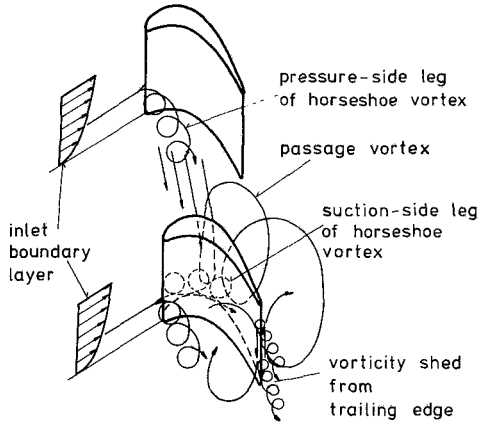


Fig. 1 Secondary flow mechanisms in a turbine passage

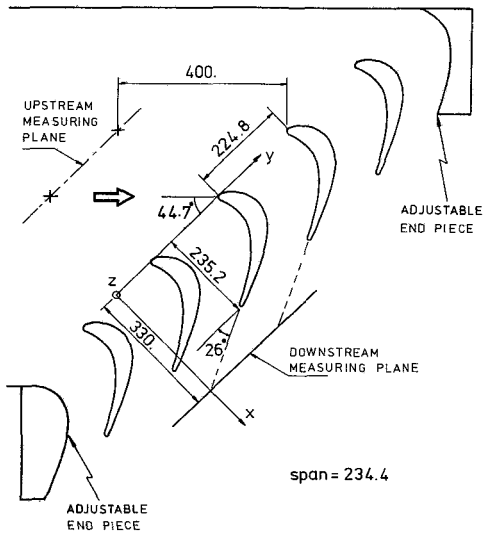


Fig 2 Cascade geometry and measurement planes. Linear dimensions in mm.

Langston Blade and Cascade Geometries. The Langston blade geometry is that of a reaction-turbine rotor section; the

Nomenclature

c = blade axial chord
c_f = skin friction coefficient
C_p = static pressure coefficient, equation 1
C_{pt} = total pressure loss coefficient, equation 4
$\bar{C}_{ptA}$ = representation of entropy flux, equation 7
$\bar{C}_{ptB}$ = pitchwise-mass-averaged entropy, equation (9)
H = $\equiv \delta^*/\theta$, shape factor
I, J = indices for grid matrix, Fig. 12
p = static pressure
p_t = total pressure
s = entropy
T = temperature
u,v,w = velocity components, Fig. 8
U = free-stream velocity
$\sqrt{\overline{u'^2}}/U$ = measure of turbulence intensity
V_n = velocity component normal to measuring plane, Fig. 8
x,y,z = Cartesian coordinates, Fig. 2
ΔY = blade pitch
ΔZ = blade span (measured from bottom wall)
β = mean camber line angle, measured from y-axis
δ^* = displacement thickness of boundary layer
δ_3 = mean kinetic energy thickness of boundary layer
δ_{99} = boundary layer thickness
η = mass flow coefficient, equation (5)
θ = momentum thickness of boundary layer
ρ = density
ϕ = flow angle, Fig. 8
ψ = flow angle, Fig. 8

Subscript

0 = stagnation
1 = upstream
2 = downstream

Overbar

$\bar{}$ = average
$=$ = mass average

Downloaded 01 Jun 2010 to 171.66.16.70. Redistribution subject to ASME license or copyright; see http://www.asme.org/terms/Terms_Use.cfm

airfoil mean camber line angles are $\beta_1 = 43.99$ deg and $\beta_2 = 25.98$ deg, respectively, giving a nominal turning angle of 110 deg and a velocity ratio of approximately 1.6. In the tests reported by Langston et al. [10, 11], the inlet air angle was 44.7 deg, close to zero incidence.

The blade camber line is close to being a double parabolic arc; and, based on the length of the camber line, the maximum blade thickness is approximately 16.7 percent and the leading and trailing edge radii are approximately 3.8 percent and 2.1 percent, respectively. The trailing edge is quite thick, presumably to accommodate cooling-air passages in the actual turbine.

The aspect ratio (span/axial chord) of the Langston cascade is low, 0.9888. But the pitch/axial chord ratio is large, 0.9555, giving the Zweifel loading parameter [19] a value of 1.124. The axial chord is 281.3 mm.

Choice of Scale and Cascade Geometry. The ratio of the radii of the leading and trailing edges of the Langston blade is approximately 0.56. This suggested the possibility of using 1-in.-dia stock for the leading edge and 9/16-in.-dia stock for the trailing edge of the scale model. With the cascade geometry and blade angles of Langston et al., the corresponding axial chord length is then 235.2 mm. The five-blade cascade, shown in Fig. 2, was constructed to this scale with a pitch of 224.8 mm and a span of 234.4 mm. The ratio of pitch/axial chord is 0.956, the same as used by Langston, and the ratio of span/axial chord is 0.997, approximately 1 percent larger.

Blade Construction. The main pieces used in the construction of the model blades are shown in Fig. 3. Side walls of 1/8-in. plexiglas are used for the pressure and suction surfaces; the leading edges are made from cylindrical plexiglas tubing of 1-in. o.d. and 3/4-in. i.d.; and the trailing edges are made from 9/16-in. dia aluminum rods. These pieces are screwed to three aluminum formers shaped to the blade profile with allowance made for the thickness of the plexiglas surfaces.

Reynolds Number and Trip Wires. The Reynolds number for this cascade, based on the blade axial chord and an exit velocity of 37.5 m/s, is 5.8×10^5. This is sufficiently low that the location of natural transition from a laminar to a turbulent boundary layer along the blade profile could significantly affect the profile losses. With the present method of blade construction, however, there are joints between the cylindrical leading-edge pieces and the plexiglas side walls. These joints are filled with plasticene and smoothed, but it is quite likely that they would influence transition, perhaps in a random manner. For this reason, a 0.020-in.-dia trip wire was epoxied to the plexiglas side walls on the pressure and suction surfaces of all the blades, approximately 3-mm downstream of the joints, as shown on Fig. 3.

Wedged-Shaped Leading Edges. The blades were tested with two leading-edge shapes. Firstly, the basic 1-in.-dia. cylindrical leading edge was used and then the cascade was tested with cast wedges added to modify the leading-edge shape. The blade geometry with the wedges, which were cast of casting resin, is shown in Fig 4. The wedges were aligned with the inlet flow direction, and with the wedges added the axial chord of the blade was 264.0 mm.

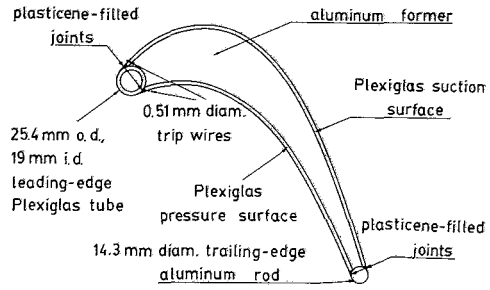


Fig. 3 Cross section of turbine blade showing details of the blade construction

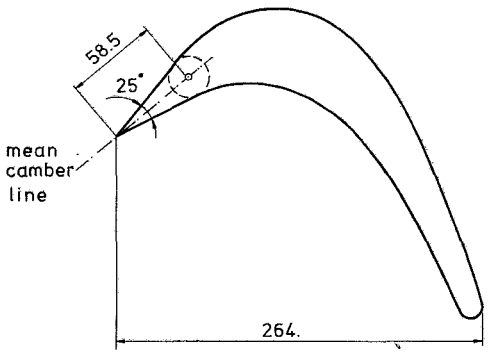


Fig. 4 Turbine blade with wedge-shaped leading edge. Linear dimensions in mm.

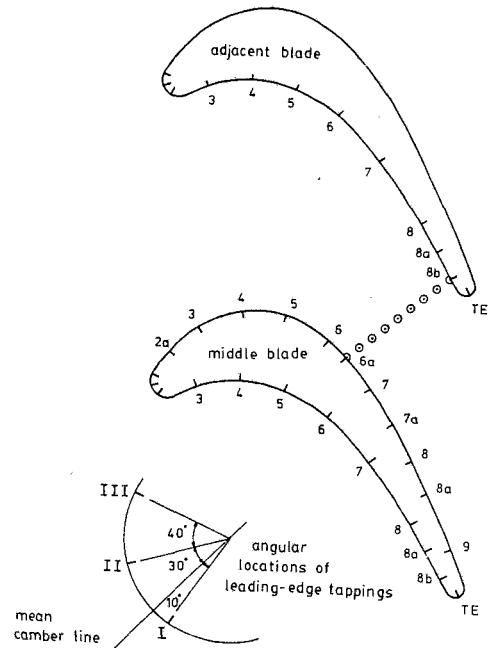


Fig. 5 Locations of static pressure tappings

Locations of Wall Static Pressure Tappings

Leading Edges—Cascade Repeatability. Three static pressure tappings are located in the leading-edge tube of each of the five blades. Figure 5 shows the angular locations of the tappings relative to the location of the mean camber line. These tappings are used for tests of cascade repeatability, which was achieved by adjustment of the end pieces, shown in Fig. 2. In the present tests the values of the static pressure coefficient, C_p, (equation 1) at points III near midspan were -1.90 ± 0.02 for all five blades.

Blade Surfaces and End Wall at Throat. Static pressure tappings are located on the suction and pressure surfaces of the middle blade, on the pressure surface of the blade adjacent to the middle blade, and on the end wall, as shown in Fig. 5. At each plane static pressure tappings are distributed

Downloaded 01 Jun 2010 to 171.66.16.70. Redistribution subject to ASME license or copyright; see http://www.asme.org/terms/Terms_Use.cfm

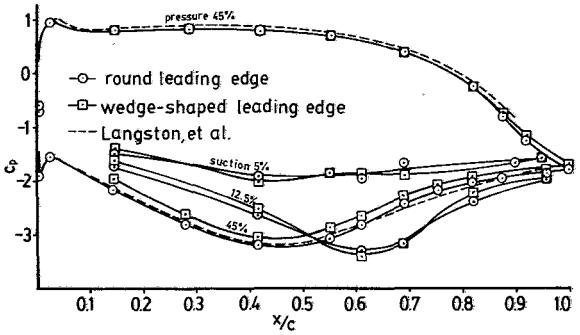


Fig. 6 Static pressure distributions around the middle blade at various spanwise locations (measured from the upper end wall). x measured from location of round leading edge in both cases; c = 235.2 mm.

along the blade span. The particular locations chosen are shown in Figs. 6 and 7.

Location of Downstream Measurement Plane. The five-hole probe was inserted through a slot in the end wall downstream of the cascade as shown in Fig. 2. Based on the axial chord of the cascade, the nondimensional distance of the probe downstream of the blade leading edge was $x/c = 1.4$. This location was chosen after considering the work of Came [8], who discussed the increase of losses downstream of a cascade. Came found that the losses in his cascade rose due to mixing until about $x/c = 1.7$ and then became relatively constant. On the other hand, Langston et al. [10] presented data showing the mass-averaged loss coefficient still rising at their last measurement plane, $x/c = 1.4$. It was desired to compare the present data with that of Langston et al. and therefore this plane was chosen.

Results

Upstream Boundary Layer. The inlet flow to the cascade was defined by performing boundary layer traverses with a hot-wire anemometer 400-mm upstream of the leading edges of the middle blade and of the adjacent blade. The boundary layer profiles were then integrated numerically to obtain the integral parameters displacement thickness, δ^*, momentum thickness, θ, kinetic energy thickness, δ_3, and shape factor, $H_{12} = \delta^*/\theta$. The values obtained are presented in Table 1. In addition, a measure of the turbulence intensity was obtained from the mean and root-mean-square values of the linearized hot wire signal, and the wall shear stress was measured using a Preston tube. These results, together with the free-stream velocity, $U = 23.5 \pm 0.4$ m/s, obtained with a Pitot probe, define the inlet flow condition for the present tests with both the round and the wedge-shaped leading edges.

This inlet flow, with a boundary layer thickness of 35–40 mm compared with a span of 235.2 mm, was chosen to correspond approximately with the Langston flow with a thick inlet boundary layer, 33 mm compared with a span of 281.3 mm. It should be noted however that the ratio of inlet displacement thickness to span for the present tests, which was approximately 0.023, was nearly twice the value of 0.0134 in the Langston test.

Wall Static Pressures. The static pressure results, obtained using a multitube inclined manometer, are presented in Figs. 6 and 7. Figure 6 shows the blade loading of the middle blade; static pressure measurements at 5, 12.5, and 45 percent of span are shown as a function of axial distance.

The static pressure coefficient, C_p, is defined as

$$C_p \equiv \frac{p - p_1}{\frac{1}{2}\rho U_1^2} \tag{1}$$

The dotted lines in Fig. 6 represent Langston's [10] results

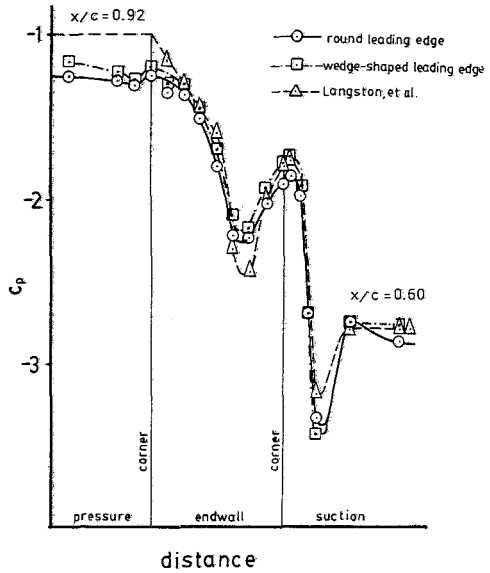


Fig. 7 Variations of wall static pressure around the throat of the blade passage

Table 1 Results of boundary layer measurements 400-mm upstream of the cascade

	Upstream of middle blade	Upstream of adjacent blade
δ_{99}	35. mm	40. mm
δ^*	5.03 mm	5.71 mm
θ	3.75 mm	4.25 mm
δ_3	6.71 mm	7.58 mm
H_{12}	1.34	1.34
c_f	0.0028	0.0027
$\left(\frac{\sqrt{\overline{u'^2}}}{U}\right)_{\text{free stream}}$	0.71%	0.71%

for comparison. The agreement is good for the round leading edge, and the present data reproduces quite closely the nonuniformity of the suction-side pressures due to the passage vortex. For the wedge-shaped leading edge, the pressure difference at any axial position is, of course, less since the wedges were just mounted in front of the round leading edges, thus increasing the chord length of the blades. The static pressure coefficients for both leading-edge shapes appear to be almost identical on the pressure side, except for a small deviation near the trailing edge. On the suction side for the wedge case, the static pressure near midspan is higher than for the round leading edge.

Figure 7 shows the static pressure distributions around the throat of the passage; the pressures are almost independent of the shape of the blade leading edge. The distributions are in agreement with the variations measured by Langston et al. [10] and Graziani et al. [11]. Stanitz et al. [21] who were investigating secondary flow in a duct, also reported a quantitatively similar static pressure distribution around the throat of their duct for the case with a 2.5-in. spoiler used to thicken the inlet boundary layer. For this flow, which had no horseshoe vortex at all, this variation in wall static pressure was calculated quite closely by Moore and Moore [22]. It appears, therefore, that the horseshoe vortex generated by the leading edge does not influence the passage vortex significantly in the present tests, at least as regards the local wall static pressure distribution.

This conclusion may seem somewhat surprising, but one interpretation of this is that the size of the horseshoe vortex is small compared with the thickness of the inlet boundary layer.

Downloaded 01 Jun 2010 to 171.66.16.70. Redistribution subject to ASME license or copyright; see http://www.asme.org/terms/Terms_Use.cfm

This interpretation is supported by the results of Sjolander [9], who performed a boundary layer traverse through the leg of the horseshoe vortex that separates from the pressure side. He found that near the wall to approximately 20–25 percent of the boundary layer thickness, the flow was very disorderly, with negligible dynamic pressure, but above this the outer portion of the boundary layer appeared largely undisturbed as it made its way over the separated region. Langston et al. [10] also presented data which showed the size of the horseshoe vortex to be small compared with the inlet boundary layer thickness. Contours of total pressure loss coefficient measured by Langston et al. (at their plane 3) just downstream of the blade leading edge showed the thickness of the pressure-side leg of the horseshoe vortex to be approximately 10 mm, which is about 30 percent of their inlet boundary layer thickness.

It is concluded that the nonuniform static pressure distribution especially on the suction side, as shown by Graziani et al. [11], is due to the turning of the thick inlet boundary layer and that the horseshoe vortex has only a small influence.

Five-Hole Probe Measurements. Five-hole probe measurements were made at the slot downstream of the cascade at $x/c = 1.4$, as shown in Fig. 2. The results are presented and analyzed using the two planes depicted in Fig. 8. The measurement plane is parallel to the plane containing the trailing edges of the blades; and a fictitious cross-sectional plane for the projection of secondary velocities and other data is defined to be perpendicular to the direction of the mean camber line at the trailing edges. Data taken in the measurement plane downstream of the cascade are projected onto this cross-sectional plane.

A nominal flow direction downstream of the blade row is defined in the direction of the mean camber line at the trailing edges of the blades ($\beta_2 = 26$ deg). The velocity component in this direction, which is defined to be the primary flow direction, is termed u. Thus secondary flow velocity components v and w are defined, which are contained within the cross-sectional plane. In the analysis of the five-hole probe data these three velocity components were calculated together with the component V_n, normal to the measuring plane, see Fig. 8. The flow angles, ψ and ϕ, connected with the velocity components are also shown in Fig. 8.

The upper half of the measuring plane was chosen for the flow field traverses. This was done for convenience and because the static pressure measurements within the blade passage were also taken in the upper half. Flow symmetry tests, upstream and downstream of the cascade, justified the taking of measurements in one-half only. Data were taken between locations 50 mm to the left and to the right of the two adjacent mean camber lines, as indicated in Fig. 8.

Averaged Properties. The mass-averaged total pressure loss coefficient is defined as

$$\overline{\overline{C}}_{pt} \equiv \frac{\int_0^{\Delta Y}\int_{\Delta Z/2}^{\Delta Z} \rho V_n C_{pt}\, dz dy}{\int_0^{\Delta Y}\int_{\Delta Z/2}^{\Delta Z} \rho V_n\, dz dy} \tag{2}$$

and the average normal velocity as

$$\overline{V}_n \equiv \frac{2}{\Delta Y \Delta Z}\int_0^{\Delta Y}\int_{\Delta Z/2}^{\Delta Z} V_n\, dz dy \tag{3}$$

where

$$C_{pt} \equiv \frac{p_{t1} - p_t}{\frac{1}{2}\rho U_1^2} \tag{4}$$

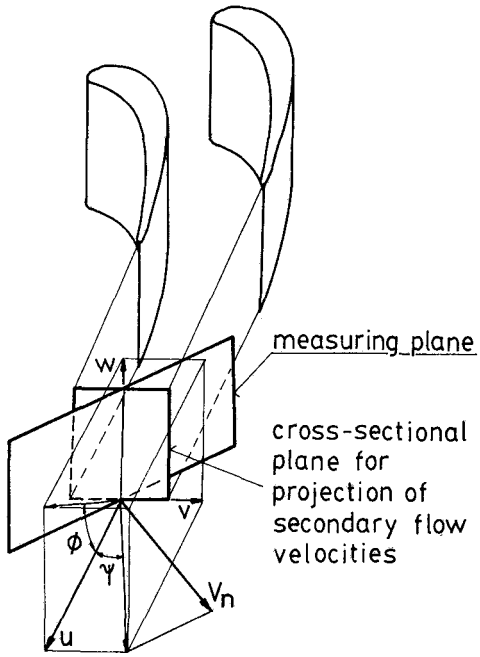


Fig. 8 Representation of downstream velocities using components v and w orthogonal to the velocity component, u, in the direction of the mean camber line at the trailing edge. V_n—velocity component normal to measuring plane.

The integrations are performed in the measuring plane over one blade pitch, from $y = 0$ to ΔY, and for the upper half of the plane from $z = \Delta Z/2$ at midspan to $z = \Delta Z$ at the upper end wall.

The results for the round and the wedge-shaped leading edges were

	Leading edge	
	Round	Wedge-shaped
$(\bar{\bar{C}}_{pt})_{x/c} = -1.2$	0.064 ± 0.004	0.064 ± 0.004
$(\bar{\bar{C}}_{pt})_{x/c} = 1.4$	0.38 ± 0.03	0.35 ± 0.03
$(\bar{V}_n)_{x/c} = 1.4$	14.33 ± 0.15 m/s	14.44 ± 0.15 m/s.

The net increase in $\bar{\bar{C}}_{pt} = 0.32$ for the round leading edge may be compared with a value of $0.31 - 0.04 = 0.27$ reported by Langston et al. for their plane 12, also at $x/c = 1.4$. The difference in the two results may be partly explained by the lower Reynolds number (based on axial chord and exit velocity) of the present cascade tests, $\mathrm{Re} = 5.8 \times 10^5$ compared with the Langston cascade tests of $\mathrm{Re} = 10 \times 10^5$. It would be expected that the lower Reynolds number would result in a higher loss. Also, in the present cascade the trip wires applied shortly downstream of the leading edges of the blades, as shown in Fig. 3, will probably have shifted the point of transition, between a laminar and a turbulent boundary layer, upstream. This would result in a higher skin friction around the blade than for the case of natural transition without trip wires and consequently in higher losses compared to the result obtained by Langston et al. Considering these two factors, the agreement between the losses measured in the present cascade and those measured by Langston et al. is reasonable.

The question of the significance of the difference between the measured values of $\bar{\bar{C}}_{pt}$ for the round and wedge-shaped leading edges was considered. Based on the accuracy achieved for the individual (local) total pressure loss coefficients, which solely depended on the accuracy of the pressure results from

Downloaded 01 Jun 2010 to 171.66.16.70. Redistribution subject to ASME license or copyright; see http://www.asme.org/terms/Terms_Use.cfm

the five-hole probe, a possible variation of ± 0.03 for $\overline{\overline{C_{pt}}}$ was estimated. With this level of accuracy the difference between the two values is thought to be within experimental error.

A mass flow coefficient, η, defined by

$$\eta \equiv \left(\int_0^{\Delta Y}\int_{\Delta Z/2}^{\Delta Z} \rho V_n \, dz dy\right)_2 \Big/ \left(\int_0^{\Delta Y}\int_{\Delta Z/2}^{\Delta Z} \rho V_n \, dz dy\right)_1 \quad (5)$$

gives a measure of the error in interpreting the mass flow rate through the cascade using the downstream flow measurements. The result was 91.4 percent versus approximately 95 percent obtained by Langston et al. This result is very sensitive to errors in measuring the downstream flow angle, ψ. For example, a systematic 1 deg error in flow angle could have caused a change in the measured mass flow rate of 4 percent. It is expected, however, that the inaccuracy of η is greater than the inaccuracy of $\overline{\overline{C_{pt}}}$, since any inaccuracy of V_n would have a self-cancelling effect in the integration to obtain $\overline{\overline{C_{pt}}}$.

Contour Plots and Secondary Flow Plots. Just as the averaged values of $\overline{\overline{C_{pt}}}$ and $\overline{V_n}$ agreed within experimental error for the two leading-edge shapes, so the distributions of C_{pt}, v, w, and V_n were also quite similar. For this reason, contour and secondary flow plots of these properties will only be presented for the case of the round leading edge, i.e. the basic profile tested by Langston et al.

Figure 9 shows contours of constant C_{pt} projected on the cross-sectional plane shown in Fig. 8 as seen by an observer looking upstream. The corresponding view of the secondary flow velocities is seen in Fig. 10. The highest values for C_{pt} appear in the endwall boundary layer and reach values of 2.7 at the wall for both leading-edge shapes. Values of C_{pt} greater than 1.0 also occur in the midspan region, which will be termed the "high-loss core" (for this measurement plane); this region has a significant area with C_{pt} greater than 0.5. A region of moderate loss ($0.1 < C_{pt} < 0.5$) extends from the high-loss core to the end wall in a location roughly downstream of the trailing edge. This represents fluid in the blade wake, which is bounded on both sides by relatively low loss fluid ($C_{pt} < 0.1$). The low-loss region extends from the edge of the endwall boundary layer, where there is a large "low-loss core," to midspan where it appears as a thin sheet between the high-loss core and the wake from the adjacent blade.

The secondary flow patterns in Fig. 10 are dominated by the passage vortex, which developed in the blade row upstream and, at this measurement plane, is centered near the peak value of C_{pt} ($\simeq$ 1.3) in the high-loss core. Seen in the cross-sectional plane at x/c = 1.4, the passage vortex has a core of solid body rotation with a diameter of the order of 10 percent of the span and streamwise vorticity of approximately 2000 rad/s; the maximum secondary velocities are of the order of 10 m/s in the passage vortex, and these may be compared with streamwise velocities of about 37.5 m/s.

Contours of Normal Velocity. Contours of constant normal velocity, V_n, are shown in Fig. 11 and are presented in the measuring plane. The values for these contours may be compared with the average normal velocity, $\overline{V_n}$ = 14.3 m/s. Large normal velocities occur near midspan; these are associated with the passage vortex observed in Fig. 10. The velocities shown at the endwall are not exactly zero because of the presence of the slot, which influenced the five-hole probe measurements close to the wall.

Contributions to the Overall Losses. In the discussion of the total pressure losses shown in Fig. 9, four areas were distinguished—the endwall boundary layer, the high-loss core, the blade wake, and the low-loss region. These areas are shown in Fig. 12, which gives the selected values of the indices, I and J, of the 50 × 50 grid matrix used to define the

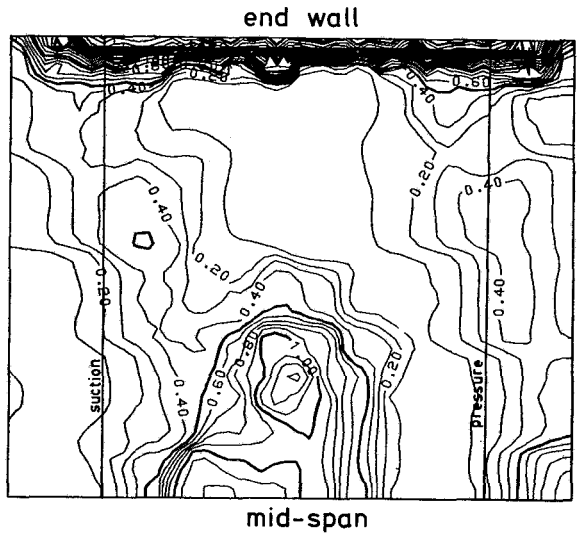


Fig. 9 Contours of total pressure loss coefficient, C_{pt}, for the round leading edge at x/c = 1.4: results projected in the cross-sectional plane; ___ projections downstream of blades in direction of mean camber lines at trailing edges; suction—downstream of middle blade; pressure—downstream of adjacent blade

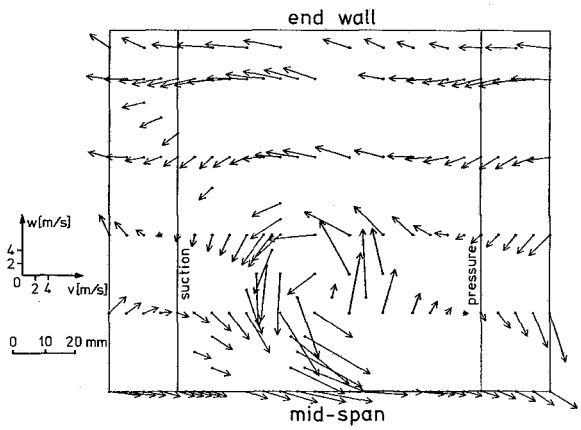


Fig. 10 Secondary flow vectors in the cross-sectional plane at x/c = 1.4 for the round leading edge: ___ Projections downstream of blades in direction of mean camber lines at trailing edges; suction—downstream of middle blade; pressure—downstream of adjacent blade

areas. The contribution of each area to the mass-averaged total pressure loss coefficient was found by integrating the numerator of equation (2), and the integration was performed over the same regions for both leading-edge shapes. The results are presented as percentages of contribution to the overall losses and are shown in Table 2.

The results for both leading-edge shapes agree within experimental error. Approximately 58 percent of the losses are found in the high-loss core near midspan. By contrast, the endwall boundary layer at this plane gives only about 12 percent, which is really surprisingly small. The area attributed to the blade wake accounts for 21 percent of the losses, and the low-loss region contains 9 percent.

The result for the endwall boundary layer is interesting. So a simple check of the magnitude of this value was made based on hot wire anemometer traverses of the boundary layer. These traverses were performed at the arrowed points of Fig. 9.

Assuming a uniform static pressure at the downstream measuring plane, the contributions of the boundary layer to the loss coefficient, $\overline{\overline{C_{pt}}}$, will be approximately

Downloaded 01 Jun 2010 to 171.66.16.70. Redistribution subject to ASME license or copyright; see http://www.asme.org/terms/Terms_Use.cfm

$$\left(\frac{U_2}{U_1}\right)^2 \frac{\delta_3}{\frac{\Delta Z}{2} - \delta^*}$$

where U_1 and U_2 are the free-stream velocities at the upstream and downstream measuring planes, respectively, δ_3 and δ^* are the energy and displacement thicknesses of the downstream boundary layer, and ΔZ is the span. Using this relation, the contribution of the endwall boundary layer to the overall losses was confirmed to be of the order of 10 percent at $x/c = 1.4$.

Total Pressure Losses and Entropy Fluxes. For flow of an ideal gas with small changes in total pressure compared with the absolute total pressure at the inlet and with small changes in total temperature, T_0, the mass-averaged entropy change is related to the mass-averaged total pressure loss coefficent by the approximation

$$\bar{s}_2 - s_1 \simeq \frac{U_1^2}{2T_0} \overline{\overline{C_{pt}}} \tag{6}$$

For example, in the present test with the round leading edge, $\overline{\overline{C_{pt}}} = 0.38$, $U_1 = 23.5$ m/s, and $T_0 = 298$ K, thus $\bar{s}_2 - s_1 = 0.35$ J/kgK.

The mass averaging of the total pressure losses in equation (2) may therefore be thought of as an integration of entropy fluxes, $\rho V_n (s - s_1)$, i.e.,

$$\overline{\overline{C_{pt}}} \cong \frac{2T_0}{U_1^2} \cdot \frac{\int_0^{\Delta Y} \int_{\Delta Z/2}^{\Delta Z} \rho V_n (s - s_1)\, dz dy}{\int_0^{\Delta Y} \int_{\Delta Z/2}^{\Delta Z} \rho V_n\, dz dy} \tag{2a}$$

The contributions to the overall losses shown in Table 2 represent contributions to the total flux of entropy at this plane. It is interesting that the highest flux of entropy occurs near midspan in the high-loss core.

Pitch-Averaged Losses. Further information about the distribution of entropy flux at the downstream measurement plane may be found by averaging the total pressure data in the pitchwise direction. Two distributions in the spanwise direction are considered, the distribution of entropy flux, or $\bar{C}_{ptA}$, and the distribution of pitchwise mass-averaged entropy, or $\bar{C}_{ptB}$. These are defined as

$$\bar{C}_{ptA} \equiv \frac{\int_0^{\Delta Y} \rho V_n C_{pt}\, dy}{\frac{2}{\Delta z} \int_0^{\Delta Y} \int_{\Delta Z/2}^{\Delta Z} \rho V_n\, dz dy} \tag{7}$$

such that

$$\overline{\overline{C_{pt}}} = \frac{2}{\Delta z} \int_{\Delta Z/2}^{\Delta Z} \overline{C_{ptA}}\, dz \tag{8}$$

and

$$\bar{C}_{ptB} \equiv \frac{\int_0^{\Delta Y} \rho V_n C_{pt}\, dy}{\int_0^{\Delta Y} \rho V_n\, dy} \tag{9}$$

The spanwise distributions of entropy flux, represented as $\bar{C}_{ptA}$ in the plots, are shown in Fig. 13. These confirm that the highest fluxes are associated with flow in the high-loss core. The distributions reach a peak at misdspan with higher levels than the maximum values recorded in the endwall boundary layers. In may also be confirmed that the areas under the curves yield, $\overline{\overline{C_{pt}}}$.

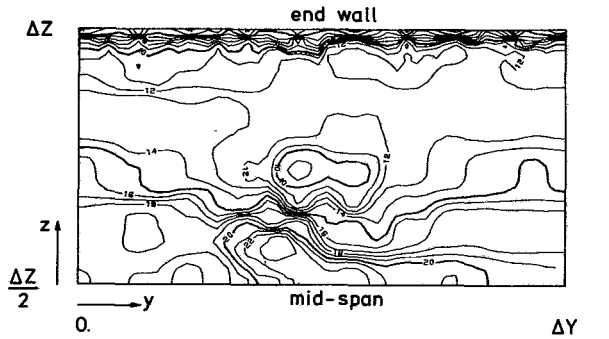


Fig. 11 Contours of velocity normal to the measuring plane (V_n, m/s) at $x/c = 1.4$ for the round leading edge. ΔY — blade pitch; ΔZ — blade span; $y = 0$—downstream of trailing edge of middle blade

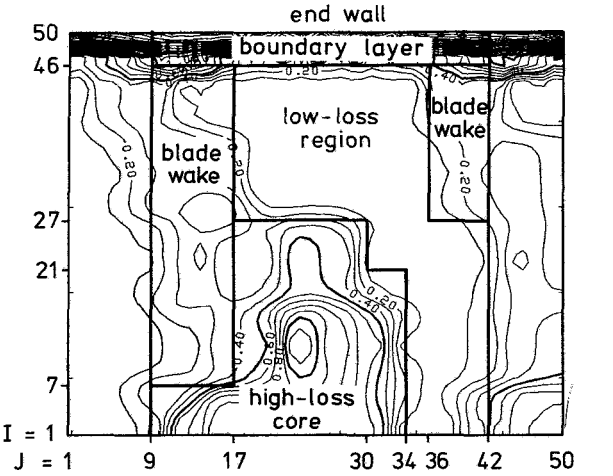


Fig. 12 Area chosen for numerical integration of total pressure losses at $x/c = 1.4$, see Table 2. *I, J*—indices of the 50 × 50 grid matrix used to define the areas. Note: these contours of total pressure loss are for the wedge-shaped leading edge.

Table 2 Loss contributions of significant regions to the overall losses at $x/c = 1.4$

	Leading edge	
	Round	Wedge-shaped
Endwall boundary layer	12.0%	12.6%
High-loss core	58.6%	58.2%
Blade wake	20.8%	20.5%
Loss-loss region	8.6%	8.7%

Pitchwise mass-averaged entropies, represented as $\bar{C}_{ptB}$, are shown in Fig. 14. The maximum values of entropy, corresponding to the maximum values of $C_{pt} = 2.7$, occur at the wall, while the minimum average entropies are found near the edge of the endwall boundary layer. The entropies then rise to another maximum at midspan.

Again it can be seen from Figs. 13 and 14 that there are only minor differences in the downstream flow attributable to the change in leading edge shape. This may perhaps be explained by the small incidence angle, the thick inlet boundary layer, the low aspect ratio, the high blade loading, or the thick trailing edge in the present tests. But it suggests that the leading edge shape and the details of the flow near the leading edge may have a relatively small influence on loss production in some cascade flows.

Downloaded 01 Jun 2010 to 171.66.16.70. Redistribution subject to ASME license or copyright; see http://www.asme.org/terms/Terms_Use.cfm

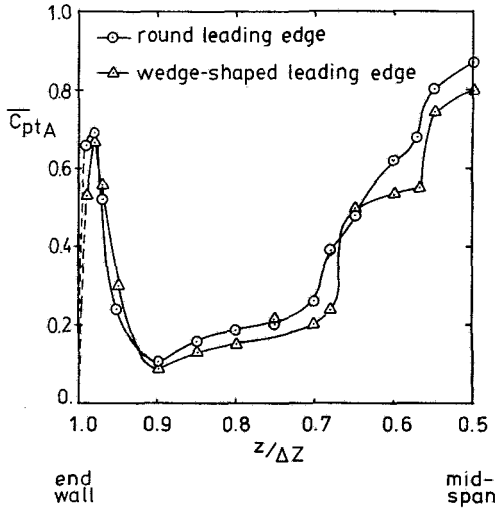


Fig. 13 Spanwise distributions of entropy flux, represented as $\bar{C}_{ptA}$, at $x/c = 1.4$

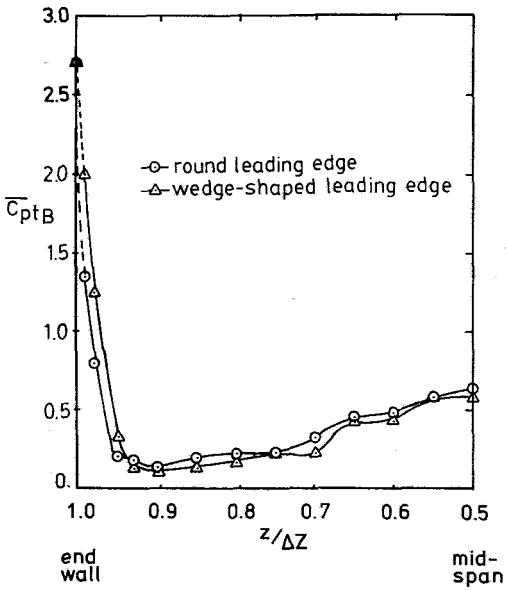


Fig. 14 Pitchwise mass-averaged entropies, represented as $\bar{C}_{ptB}$, at $x/c = 1.4$

Concluding Remarks

From a practical standpoint, the most significant result from the present tests is that the highest entropy fluxes downstream of this turbine cascade occur near midspan in a high-loss core and not near the endwalls. This result was independent of the leading-edge shape. The designer of a turbine using such blading ought to be warned that the next blade row could inherit a flow with a strongly nonuniform spanwise distribution of losses. He may, of course, already know that such flows do occur not only in stationary linear cascades but in rotating blade rows as well [24].

Acknowledgments

The authors wish to thank Rolls-Royce Limited, Aero Division, for supporting this work under a cooperative agreement with Virginia Polytechnic Institute and State University.

References

1 Dodge, P. R., "Numerical Method for Two-Dimensional and Three-Dimensional Viscous Flows," AIAA Paper No. 76-425, 1976.

2 Waterman, W. F., and Tall, W. A., "Measurement and Prediction of Three-Dimensional Viscous Flows in Low-Aspect-Ratio Turbine Nozzles," ASME Paper No. 76-GT-73, 1976.

3 Tall, W. A., "Understanding Turbine Secondary Flow," AGARD Conference on Secondary Flows in Turbomachines, Mar. 1977.

4 Schlegel, J. C., Liu, H. C., and Waterman, W., "Reduction of Endwall Effects in a Small, Low-Aspect-Ratio Turbine by Radial Work Redistribution," ASME JOURNAL OF ENGINEERING FOR POWER, Vol. 89, Jan. 1976, pp. 130–136.

5 Liu, H. C., Booth, T. C., and Tall, W. A., "An Application of Three-Dimensional Viscous Flow Analysis to the Design of a Low Aspect Ratio Turbine," ASME Paper No. 79-GT-53, 1979.

6 Herzig, H. Z., Hansen, A. G., and Costello, G. R., "A Visualization Study of Secondary Flows in Cascades," NACA TN 2947, Feb. 1953.

7 Dunham, J., "A Review of Cascade Data on Secondary Losses in Turbines," *Journal of Mechanical Engineering Science*, Vol. 12, No. 1, 1970, pp. 48–59.

8 Came, P. M., "Secondary Loss Measurements in a Cascade of Turbine Blades," Institution of Mechanical Engineers, Conf. Publ. 3, 1973, pp. 75–83.

9 Sjolander, S. A., "The Endwall Boundary Layer in an Annular Cascade of Turbine Nozzle Guide Vanes," M.E. thesis, Carleton Univ., Ottawa, Ontario, Canada, 1975.

10 Langston, L. S., Nice, M. L., and Hooper, R. M., "Three-Dimensional Flow Within a Turbine Cascade Passage," ASME JOURNAL OF ENGINEERING FOR POWER, Vol. 99, Jan. 1977, pp. 21–28.

11 Graziani, R. A., Blair, M. F., Taylor, J. R., and Mayle, R. E., "An Experimental Study of Endwall and Airfoil Surface Heat Transfer in a Large Scale Turbine Blade Cascade," ASME JOURNAL OF ENGINEERING FOR POWER, Vol. 102, Apr. 1980, pp. 257–267.

12 Barber, T. J., and Langston, L. S., "Three-Dimensional Modelling of Cascade Flows," AIAA Paper No. 79-0047, Jan. 1979.

13 Langston, L. S., "Crossflow in a Turbine Cascade Passage," ASME JOURNAL OF ENGINEERING FOR POWER, Vol. 102, Oct. 1980, pp. 866–874.

14 Squire, H. B., and Winter, K. G., "The Secondary Flow in Cascade of Aerofoils in a Nonuniform Stream," *J. of Aero. Sci.*, Vol. 18, No. 4., Apr. 1951.

15 Hawthorne, W. R., "Secondary Circulation in Fluid Flow," *Proc. Roy. Soc.*, 1951, A206, pp. 374–387.

16 Hawthorne, W. R., "Secondary Vorticity in Stratified Compressible Fluids in Rotating Systems," C.U.E.D./A-Turbo/TR63/1974.

17 Hawthorne, W. R., "A Theory of Struts in Boundary Layers," Gas Turbine Laboratory, MIT, 1951.

18 Johnston, J. P., "On the Three-Dimensional Turbulent Boundary Layer Generated by Secondary Flow," ASME *Journal of Basic Engineering*, Vol. 82, 1960, pp. 233–248.

19 Horlock, J. H., *Axial Flow Turbines*, Krieger, New York, 1973.

20 Klebanoff, P. S., "Characteristics of Turbulence in a Boundary Layer with Zero Pressure Gradient," NACA Rep. 1247, 1955.

21 Stanitz, J. D., Osborn, W. M., and Mizisin, J., "An Experimental Investigation of Secondary Flow in an Accelerating, Rectangular Elbow with 90 deg of Turning," NACA TN 3015, Oct. 1953.

22 Moore, J., and Moore, J. G., "A Calculation Procedure for Three-Dimensional, Viscous, Compressible Duct Flow—Part II: Stagnation Pressure Losses in a Rectangular Elbow," ASME *Journal of Fluids Engineering*, Vol. 101, Dec. 1979, pp. 423–428.

23 Moore, J., and Smith, B. L., "Flow in a Turbine Cascade—Part 2: Measurement of Flow Trajectories by Ethylene Detection," JOURNAL OF ENGINEERING FOR GAS TURBINES AND POWER, Vol. 106, April 1984, pp. 409–413.

24 Dring, R. P., and Joslyn, H. D., "Measurements of Turbine Rotor Blade Flows," in *Measurement Methods in Rotating Components of Turbomachinery*, ASME, 1980, pp. 51–58.

Downloaded 01 Jun 2010 to 171.66.16.70. Redistribution subject to ASME license or copyright; see http://www.asme.org/terms/Terms_Use.cfm

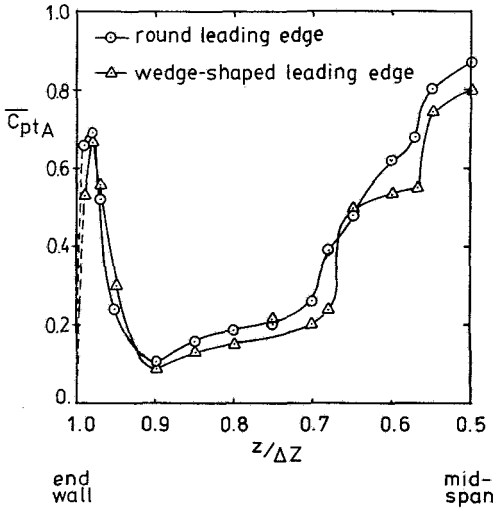


Fig. 13 Spanwise distributions of entropy flux, represented as $\bar{C}_{ptA}$, at $x/c = 1.4$

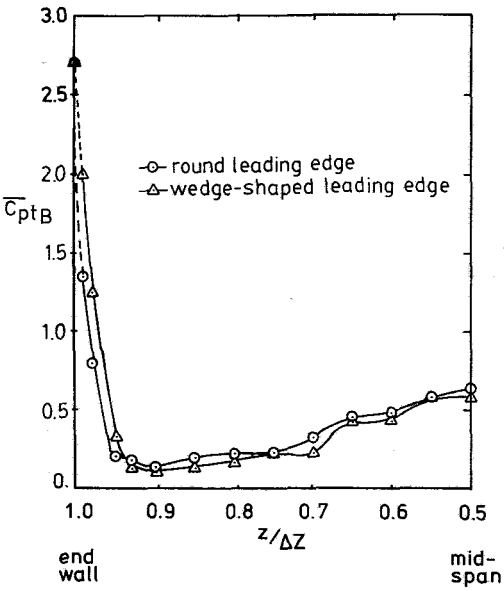


Fig. 14 Pitchwise mass-averaged entropies, represented as $\bar{C}_{ptB}$, at $x/c = 1.4$

Concluding Remarks

From a practical standpoint, the most significant result from the present tests is that the highest entropy fluxes downstream of this turbine cascade occur near midspan in a high-loss core and not near the endwalls. This result was independent of the leading-edge shape. The designer of a turbine using such blading ought to be warned that the next blade row could inherit a flow with a strongly nonuniform spanwise distribution of losses. He may, of course, already know that such flows do occur not only in stationary linear cascades but in rotating blade rows as well [24].

Acknowledgments

The authors wish to thank Rolls-Royce Limited, Aero Division, for supporting this work under a cooperative agreement with Virginia Polytechnic Institute and State University.

References

1 Dodge, P. R., "Numerical Method for Two-Dimensional and Three-Dimensional Viscous Flows," AIAA Paper No. 76-425, 1976.

2 Waterman, W. F., and Tall, W. A., "Measurement and Prediction of Three-Dimensional Viscous Flows in Low-Aspect-Ratio Turbine Nozzles," ASME Paper No. 76-GT-73, 1976.

3 Tall, W. A., "Understanding Turbine Secondary Flow," AGARD Conference on Secondary Flows in Turbomachines, Mar. 1977.

4 Schlegel, J. C., Liu, H. C., and Waterman, W., "Reduction of Endwall Effects in a Small, Low-Aspect-Ratio Turbine by Radial Work Redistribution," ASME JOURNAL OF ENGINEERING FOR POWER, Vol. 89, Jan. 1976, pp. 130–136.

5 Liu, H. C., Booth, T. C., and Tall, W. A., "An Application of Three-Dimensional Viscous Flow Analysis to the Design of a Low Aspect Ratio Turbine," ASME Paper No. 79-GT-53, 1979.

6 Herzig, H. Z., Hansen, A. G., and Costello, G. R., "A Visualization Study of Secondary Flows in Cascades," NACA TN 2947, Feb. 1953.

7 Dunham, J., "A Review of Cascade Data on Secondary Losses in Turbines," *Journal of Mechanical Engineering Science*, Vol. 12, No. 1, 1970, pp. 48–59.

8 Came, P. M., "Secondary Loss Measurements in a Cascade of Turbine Blades," Institution of Mechanical Engineers, Conf. Publ. 3, 1973, pp. 75–83.

9 Sjolander, S. A., "The Endwall Boundary Layer in an Annular Cascade of Turbine Nozzle Guide Vanes," M.E. thesis, Carleton Univ., Ottawa, Ontario, Canada, 1975.

10 Langston, L. S., Nice, M. L., and Hooper, R. M., "Three-Dimensional Flow Within a Turbine Cascade Passage," ASME JOURNAL OF ENGINEERING FOR POWER, Vol. 99, Jan. 1977, pp. 21–28.

11 Graziani, R. A., Blair, M. F., Taylor, J. R., and Mayle, R. E., "An Experimental Study of Endwall and Airfoil Surface Heat Transfer in a Large Scale Turbine Blade Cascade," ASME JOURNAL OF ENGINEERING FOR POWER, Vol. 102, Apr. 1980, pp. 257–267.

12 Barber, T. J., and Langston, L. S., "Three-Dimensional Modelling of Cascade Flows," AIAA Paper No. 79-0047, Jan. 1979.

13 Langston, L. S., "Crossflow in a Turbine Cascade Passage," ASME JOURNAL OF ENGINEERING FOR POWER, Vol. 102, Oct. 1980, pp. 866–874.

14 Squire, H. B., and Winter, K. G., "The Secondary Flow in Cascade of Aerofoils in a Nonuniform Stream," *J. of Aero. Sci.*, Vol. 18, No. 4., Apr. 1951.

15 Hawthorne, W. R., "Secondary Circulation in Fluid Flow," *Proc. Roy. Soc.*, 1951, A206, pp. 374–387.

16 Hawthorne, W. R., "Secondary Vorticity in Stratified Compressible Fluids in Rotating Systems," C.U.E.D./A-Turbo/TR63/1974.

17 Hawthorne, W. R., "A Theory of Struts in Boundary Layers," Gas Turbine Laboratory, MIT, 1951.

18 Johnston, J. P., "On the Three-Dimensional Turbulent Boundary Layer Generated by Secondary Flow," ASME *Journal of Basic Engineering*, Vol. 82, 1960, pp. 233–248.

19 Horlock, J. H., *Axial Flow Turbines*, Krieger, New York, 1973.

20 Klebanoff, P. S., "Characteristics of Turbulence in a Boundary Layer with Zero Pressure Gradient," NACA Rep. 1247, 1955.

21 Stanitz, J. D., Osborn, W. M., and Mizisin, J., "An Experimental Investigation of Secondary Flow in an Accelerating, Rectangular Elbow with 90 deg of Turning," NACA TN 3015, Oct. 1953.

22 Moore, J., and Moore, J. G., "A Calculation Procedure for Three-Dimensional, Viscous, Compressible Duct Flow—Part II: Stagnation Pressure Losses in a Rectangular Elbow," ASME *Journal of Fluids Engineering*, Vol. 101, Dec. 1979, pp. 423–428.

23 Moore, J., and Smith, B. L., "Flow in a Turbine Cascade—Part 2: Measurement of Flow Trajectories by Ethylene Detection," JOURNAL OF ENGINEERING FOR GAS TURBINES AND POWER, Vol. 106, April 1984, pp. 409–413.

24 Dring, R. P., and Joslyn, H. D., "Measurements of Turbine Rotor Blade Flows," in *Measurement Methods in Rotating Components of Turbomachinery*, ASME, 1980, pp. 51–58.

DISCUSSION

L. S. Langston[1]

I would like to compliment the authors on a fine piece of experimental work and on an insightful interpretation of their data. I will comment on two points that the authors raise in their paper:

1 The authors state that in [10], contours of total pressure coefficient measured just downstream of the leading edge

[1]Mechanical Engineering Department, University of Connecticut, Storrs, Conn. 06268.

Copyright © 1984 by ASME
Downloaded 01 Jun 2010 to 171.66.16.70. Redistribution subject to ASME license or copyright; see http://www.asme.org/terms/Terms_Use.cfm

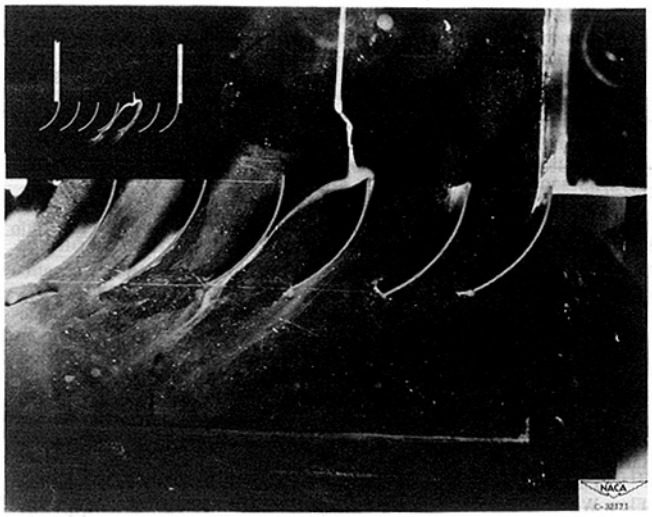


Fig. 15

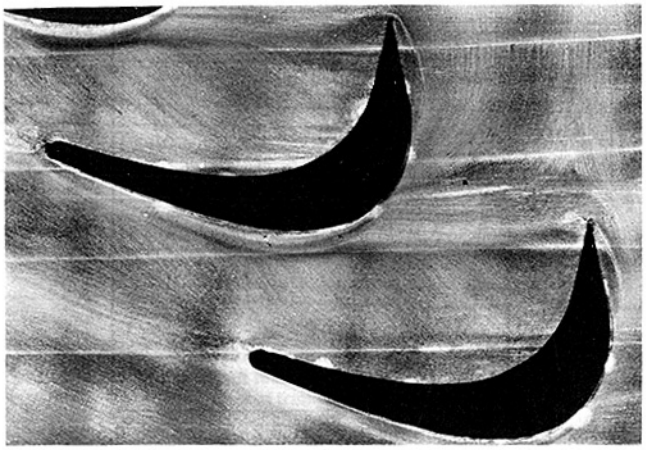


Fig. 16 Flow visualization of the limiting streamlines on the bottom wall of the cascade. Turbine blades with wedge-shaped leading edges.

(plane 3) showed the thickness of the pressure side leg of the horseshoe vortex to be about 30 percent of the inlet boundary layer thickness. The vortex was actually larger than this. An examination of the secondary flow velocity vectors (such as shown for plane 8 in Fig. 9 of [10]) for plane 3 (not presented in [10], because of space limitations) shows that the thickness of the region of vortical motion is about equal to the inlet boundary layer thickness, rather than 30 percent of it.

2 The authors' conclusion that the leading edge shape has little effect on loss production is in agreement with what we concluded [10]. We found that the position of the endwall saddle point of separation (i.e., the start of three-dimensional endwall loss production) was strongly dependent on the endwall pressure field. As the authors have shown in their study, the change in leading edge shape did little to change the airfoil pressure distribution (and by inference, did little to change the endwall pressure distribution) so that no appreciable change occurred in loss production.

As was pointed out previously [10], the small influence of leading edge geometry could also be inferred from the early NACA work of Herzig, Hansen, and Costello [6]. Figure 15 is a reproduction of their Fig. 29 (provided by L. J. Goldman of NASA Lewis Research Center and printed from the original negative) and shows a photo of the top view of low-speed air flow through a cascade of thin circular-arc airfoils. A smoke probe (the object with an offset tip at the top of Fig. 15) was positioned upstream of the cascade, and a smoke filament was injected into the endwall boundary layer. As shown in the figure, the smoke filament bifurcates at some distance from the relatively sharp leading edge of one of the airfoils, with one branch of the filament going into the suction side of the horseshoe vortex and the other branch going into the pressure side of the vortex.

The point of bifurcation (which should be just downstream of the saddle point of separation on the endwall) is clearly not dependent on the radius of curvature of the airfoil leading edge (which in this case is very small) but is dependent on the pressure field generated by the overall shape of pressure and suction surfaces of the cascade airfoils.

Thus, the result of this earlier experimental work supports the authors' conclusion on the influence of leading edge shape on loss.

Authors' Closure

The authors would like to thank Dr. Langston for his interesting discussion.

The secondary flow in the outer part of the boundary layer to which Dr. Langston refers can be simply explained by the turning of flow with an initial component of vorticity normal to the streamwise direction. Nearer the wall where the normal vorticity is larger, the streamwise vorticity generated is also larger. Eventually, it becomes so large that it results in flow separation, and near the wall there occur closed contours of total pressure loss. We took these closed contours as indicative of the size of the pressure-side leg of the horseshoe vortex. This size was approximately 30 percent of the inlet boundary layer thickness.

The smoke trace described by Dr. Langston is interesting, as he says, in that it shows that a horseshoe vortex can be generated by a cascade of thin plates at zero incidence. But the NACA study also contains the corresponding smoke trace for a cascade with the same turning angle (60 deg), but with the leading edge extended straight upstream to increase the axial chord by about 60 percent. In this case, no horseshoe vortex was observed.

It appears that this modification was *sufficient* to greatly reduce the influence of the horseshoe vortex phenomenon. There is, however, insufficient information in the NACA study to determine what was a *necessary* change. In our study, the wedge-shaped leading edge increased the axial chord by about 12 percent, and this resulted in the quite different endwall flow visualization picture shown in Fig. 16. (This may be compared with the trace shown in Fig. 2 of Part 2 of this paper [23]).

Downloaded 01 Jun 2010 to 171.66.16.70. Redistribution subject to ASME license or copyright; see http://www.asme.org/terms/Terms_Use.cfm

Flow in a Turbine Cascade: Part 2—Measurement of Flow Trajectories by Ethylene Detection

J. Moore

B. L. Smith

Department of Mechanical Engineering,
Virginia Polytechnic Institute
and State University,
Blacksburg, Va. 24061

In Part 1 of this paper, measurements of total pressure loss were described at an axial location 40 percent of the axial chord downstream of the trailing edge of a turbine cascade. These results revealed regions of high loss near midspan away from the walls and in the bulk of the flow. In this second part, the origins of fluid in these regions are traced using an ethylene detection technique. Ethylene injection near the blade leading edges and gas sampling downstream and near the blade trailing edges gives information about flow trajectories and mixing through the cascade. Details of the flame ionization detection system used to measure the ethylene concentrations are discussed.

Introduction

In Part 1 [1], we described some measurements of the overall flow development in a linear cascade of turbine blades designed to be geometrically similar to those of Langston et al. [2]. Flow with a relatively thick inlet boundary layer ($\delta^*/\Delta Z \cong 0.023$) on the end walls entered the cascade and a complex three-dimensional flow with large passage vortices developed. Downstream of the cascade, at $x/c = 1.4$, total pressure measurements in the top half of the passage showed a large region of high-loss fluid near midspan. The pitch-averaged losses were lowest at the edge of the endwall boundary layer, due to a low-loss region, and then rose towards midspan. The entropy fluxes (kW/Km^2) normal to the downstream measuring plane were higher at midspan than in the endwall boundary layer. In fact, only 12 percent of the total pressure losses was found in the endwall boundary layer while 58 percent was found in the "high-loss core" near midspan.

In this paper, we attempt to trace the sources of fluid in the high-loss core and in the low-loss region by ethylene injection and detection [3]. We locate fluid from the horseshoe vortices at the blade exit and at the downstream measuring plane, and we infer the flow trajectories of this fluid through the cascade.

Flame Ionization Detection System

A Gowmac model 12-800 flame ionization detector and model 40-700 electrometer were used as the basis of a detection system for ethylene. This system is shown schematically in Fig. 1.

A sample of air and ethylene is drawn isokinetically from the cascade flow field. A steady flow of 55 cc/min of sample is then fed to the flame ionization detector where it is mixed with a hydrogen flow of 20 cc/min. This mixture, with an equivalence ratio of 0.86 (fuel lean), burns as a laminar premixed flame in a surrounding air stream of 250 cc/min. The electrometer applies a potential between the flame holder and a collector downstream. The current flowing between

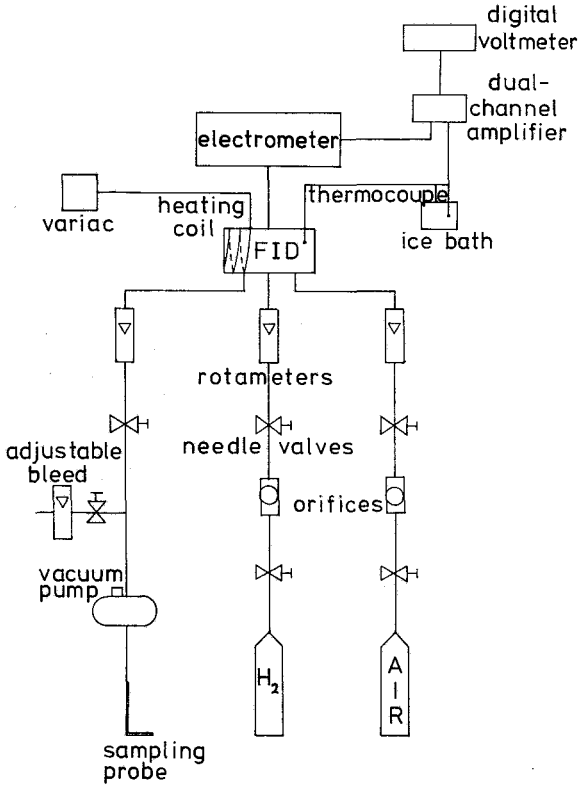


Fig. 1 Schematic of flame-ionization detection system for ethylene

Contributed by the Gas Turbine Division of THE AMERICAN SOCIETY OF MECHANICAL ENGINEERS and presented at the 28th International Gas Turbine Conference and Exhibit, Phoenix, Arizona, March 27-31, 1983. Manuscript received at ASME Headquarters, December 21, 1981. Paper No. 83-GT-69.

Copyright © 1984 by ASME
Downloaded 01 Jun 2010 to 171.66.16.70. Redistribution subject to ASME license or copyright; see http://www.asme.org/terms/Terms_Use.cfm



Fig. 2 Flow visualization of the limiting streamlines on the bottom wall of the cascade

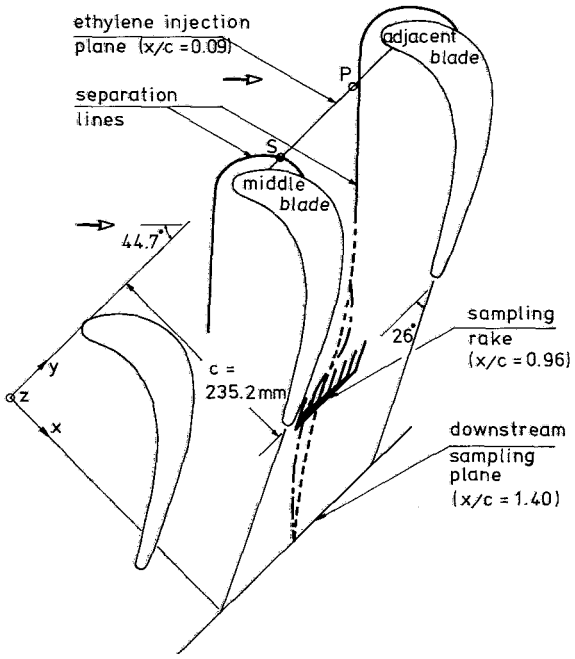


Fig. 3 Top view of test passage showing ethylene injection and sampling planes: 0, injection points for pressure-side (P) and suction-side (S) legs of horseshoe vortex; · · · , likely path of fluid from point P; — - — , likely path of fluid from point S

these two electrodes depends on the conductivity of the burned gas which in turn depends on the ionization of carbon in the sample. The electrometer then gives a millivolt signal proportional to the concentration of ethylene in the sample.

In the present system we further amplified the electrometer output by a factor of about 100 using a differential amplifier with an LM725 operational amplifier. Thus we obtained a signal which could be read directly on a digital voltmeter.

With this flame ionization detector it was important to maintain a very high resistance between the flame holder and the casing. The casing was therefore maintained at a temperature of 120–130° C using a tea-cup heater as an electrical heating coil. This prevented water condensation on the casing walls.

Over the period of the present tests the system response varied from 5 to 6 ppm of ethylene per volt. Care was taken to maintain the sample flow rate constant as the system was more sensitive to changes in this flow than to the hydrogen or air flow rates.

Ethylene injection rates of 150 cc/min were used and during the course of a test the ethylene concentration in the ambient air in the laboratory would vary by the order of 5 ppm. Zero levels were therefore measured by sampling the flow upstream of the cascade.

Tracing Horseshoe Vortex Flow

Figure 2 shows a flow visualization of the limiting streamlines on the endwall of the cascade for the case of the round leading edge which is considered in this paper. The visualization was achieved by rolling a mixture of diesel oil and titanium dioxide onto an aluminum sheet which was taped to the bottom wall; the thin lines on the picture were caused by the edges of the roller. The flow was then turned on for four minutes giving the picture shown. The middle blade of the picture is the middle blade of the five-blade cascade; the

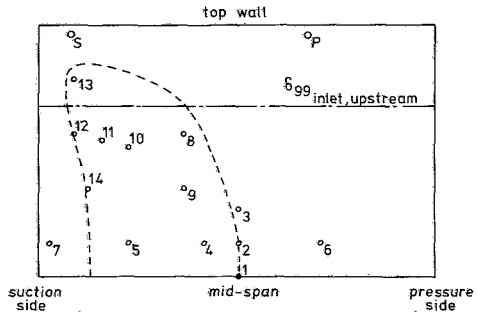


Fig. 4 View of ethylene injection plane (x/c = 0.09) looking upstream: 0, injection points for pressure-side (P) and suction-side (S) legs of horseshoe vortex; 1–14, injection points for tracing low-loss fluid, · · · , estimated locations of fluid with a downstream value of C_{pt} = 0.2

Nomenclature

c = blade axial chord
C_{pt} = total pressure loss coefficient, $\dfrac{p_{t1} - p_t}{\frac{1}{2}\rho U_1^2}$
p_t = total pressure
ppm = parts per million by volume
$\dot{Q}_{C_2H_4}$ = ethylene injection flow rate
U_1 = free stream velocity at inlet
V_n = velocity component normal to downstream measuring plane
x,y,z = cartesian coordinates, Fig. 3
$y_{C_2H_4}$ = mole fraction of ethylene
ΔY = blade pitch
ΔZ = blade span (measured from bottom wall)
δ^* = displacement thickness
ζ = ethylene detection efficiency, equation (1)
ρ = density

Subscript

1 = free stream at inlet

Downloaded 01 Jun 2010 to 171.66.16.70. Redistribution subject to ASME license or copyright; see http://www.asme.org/terms/Terms_Use.cfm

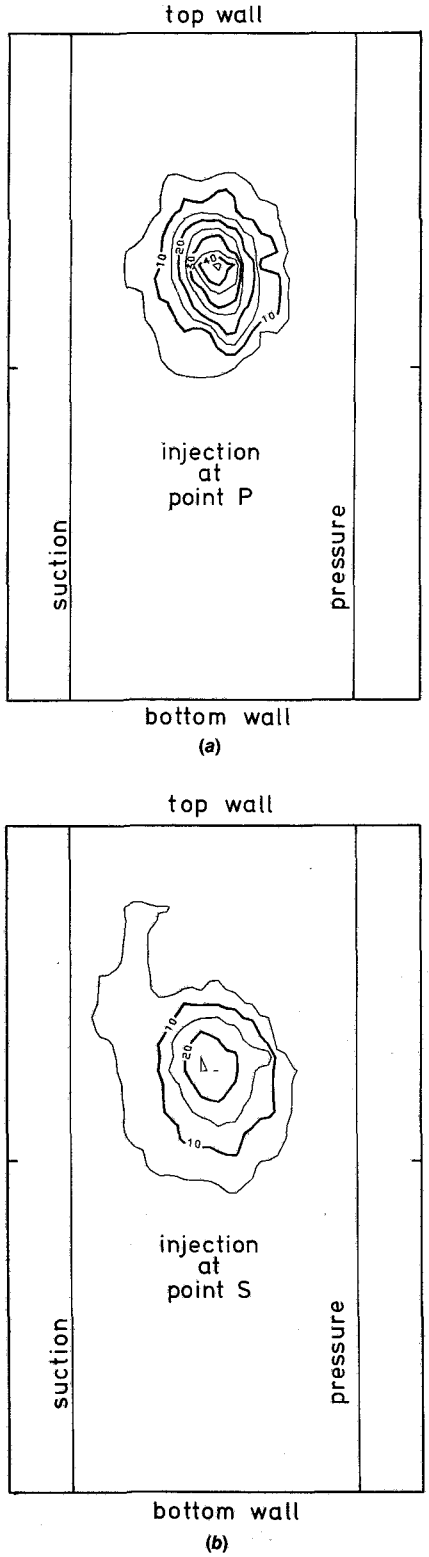


Fig. 5 Ethylene concentration contours at downstream measuring plane (x/c = 1.4). Concentrations in ppm. Contours plotted in cross-sectional plane (see Part 1 [1], Fig. 8) ——— projections downstream of blades in direction of mean camber lines at trailing edges; suction—downstream of middle blade; pressure—downstream of adjacent blade.

present studies were conducted in the flow between this blade and the adjacent blade on the suction side (i.e., the blade in the top right hand corner).

In Fig. 2, the separation of the endwall boundary layer and

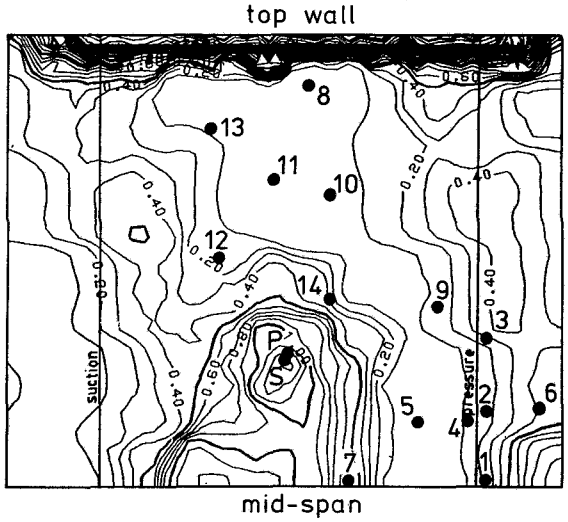


Fig. 6 Contours of total pressure loss coeffcient, C_{pt}, at the downstream measuring plane, x/c = 1.4. Results projected in the cross-sectional plane (see Part 1 [1], Fig 8). •, locations of peak concentrations for injection at the points shown in Fig. 4.

the formation of the horseshoe vortices near the blade leading edges are clearly defined by an accumulation of white titanium dioxide in a line which stretches across the passage to the suction side of the next blade. This almost straight line is associated with the pressure-side leg of the horseshoe vortex which reaches the suction side of the next blade at about midchord, just upstream of the throat. The other leg of the horseshoe vortex stretches around the leading edge and flows down the suction side, where it is clearly seen in the endwall corner region until about the quarter-chord position. At this point it appears to leave the endwall and move onto the suction surface.

The separation lines are also drawn on Fig. 3, which shows a top view of the test passage and sampling planes. The injection plane was at $x/c = 0.09$ just downstream of the leading edge and the two points, P and S, were chosen for injecting ethylene into the pressure-side and suction-side legs of the horseshoe vortex. The ethylene was injected at a rate of 150 cc/min through 3.1-mm dia tubes located 2.0 percent of the blade span (4.7 mm) from the top wall. Figure 4 shows a cross section of the injection plane viewed from downstream with the injection tubes drawn to scale. The injection was at a distance from the wall of approximately 12 percent of the inlet boundary layer thickness.

Sampling at Downstream Measuring Plane

The flow was sampled isokinetically with a probe of 1.0-mm i.d., which was traversed in the downstream measuring plane. The resulting concentration contours for points P and S are shown in Figs. 5(*a*) and 5(*b*), respectively. These plots may be compared with the corresponding contour plot of total pressure loss obtained in Part 1 [1] for the round leading edge, also at $x/c = 1.4$, and reproduced here in Fig. 6. The locations of the peak concentrations in Figs. 5(*a*) and 5(*b*) are marked as P and S in Fig. 6.

Figure 6 shows that the peak concentrations of ethylene from both legs of the horseshoe vortex are found in essentially the same location, at the downstream measuring plane, at a point corresponding very closely with the maximum total pressure loss ($C_{pt} \cong 1.3$) in the high-loss core. The maximum concentration of ethylene from the pressure-side leg of the horseshoe vortex is approximately 45 ppm while the peak from the suction-side leg is 25 ppm. The contours for the pressure-side leg in Fig. 5(*a*) are quite symmetrical about the peak with a reduction to one-half the peak concentration

Downloaded 01 Jun 2010 to 171.66.16.70. Redistribution subject to ASME license or copyright; see http://www.asme.org/terms/Terms_Use.cfm

Table 1 Distribution of ethylene flow between flow regions at $x/c = 1.4$

	Percentage of measured ethylene	
	Point P	Point S
High-loss core	81%	74%
Blade wake	8%	15%
Low-loss region	9%	8%
Endwall boundary layer	0%	0%

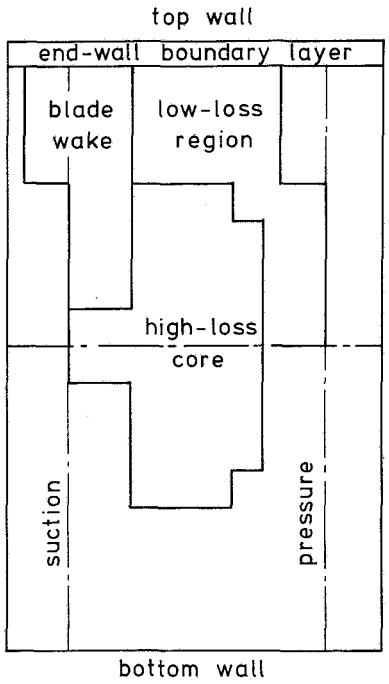


Fig. 7 Areas chosen for numerical integration of ethylene flow rates at $x/c = 1.4$ (see also Fig. 12 of Part 1 [1])

occurring at a radius of about 5 percent of the span. The mixing is somewhat more complete for the suction-side leg and the distribution shows a tail at concentration levels below 10 ppm, as seen in Fig. 5(*b*).

Efficiency of Ethylene Detection

The velocities, V_n, normal to the downstream measuring plane were presented in Part 1 in Fig. 11. These are combined with the measured ethylene mole fractions $y_{C_2H_4}$ to calculate measured ethylene flow rates at the downstream sampling plane. Thus, we define an efficiency of ethylene detection ζ as

$$\zeta = \frac{\int_0^{\Delta Z}\int_0^{\Delta Y} V_n y_{C_2H_4} dydz}{\dot{Q}_{C_2H_4}} \quad (1)$$

where $\dot{Q}_{C_2H_4}$ (= 150 cc/min) is the ethylene injection rate, and ΔY and ΔZ are the blade pitch and span, respectively.

For the two points, P and S, the efficiencies of ethylene detection were 83 and 88 percent, respectively.

Contributions to Ethylene Flow Rate

Comparing the shapes of the ethylene distributions at the downstream plane in Figs. 5(*a*) and 5(*b*), we find a major difference in the maximum concentration and in the tail for point S. The location of the 10 ppm contour is almost identical for both distributions but the maximum concentation for

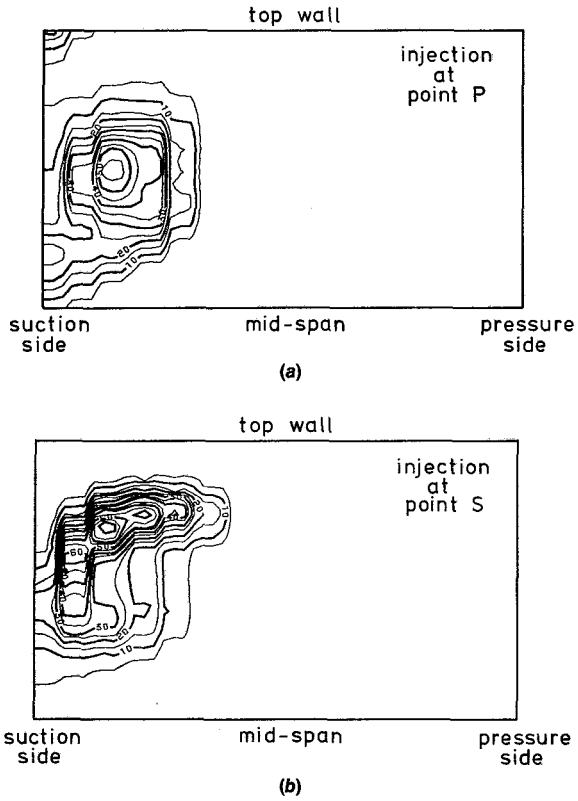


Fig. 8 Ethylene concentration contours near blade exit, $x/c = 0.96$ (concentrations in ppm)

point S is only 25 ppm compared with 45 ppm for point P. This means that less ethylene from point S flows within the high-loss core than from point P. Some of the ethylene from point S is presumably mixed out at concentration levels below 10 ppm in the tail in the blade wake.

In Part 1, we focused attention on four flow regions at the downstream plane. These were the endwall boundary layer, the high-loss core, the blade wake, and the low-loss region, and the corresponding areas of the downstream plane were defined in Fig. 12. Now we can integrate the numerator of equation (1) over these areas to find what fractions of the ethylene from points P and S pass through the high-loss core and what fractions through the other regions. But some of the ethylene measured at the downstream plane was found below midspan and some was found to have crossed the line projected downstream of the trailing edge of the middle blade. The areas for integration were therefore chosen to correspond with the areas shown in Fig. 12 of Part 1 but were modified to include these outside areas as shown in Fig. 7. The results are presented in Table 1 as percentages of the measured ethylene flow rate at the downstream plane.

The results in Table 1 show that the difference between the flow rates in the high-loss core is actually quite small for the two injection points. The percentage of ethylene from point P passing through the high-loss core is 81 percent compared with 74 percent from point S. The difference of 7 percentage points is made up by the blade wake as expected with 15 percent from point S compared with 8 percent from point P. In both cases, the low-loss region accounts for about 8 percent of the ethylene while the remainder was not found in the endwall boundary layer but in the next flow field on the suction side.

These results show that even in this complex flow the location of the peak concentration gives a good indication of the center of the ethylene distribution.

Downloaded 01 Jun 2010 to 171.66.16.70. Redistribution subject to ASME license or copyright; see http://www.asme.org/terms/Terms_Use.cfm

Sampling Near Trailing Edge

A seven-pronged rake was used for sampling just upstream of the blade exit at $x/c = 0.96$ (corresponding to Plane 9 of Langston et al. [2]). This was constructed using 1.6-mm dia tubing soldered in the configuration shown in Fig. 3. It was traversed vertically in the suction-side half of the passage. Figures 8(*a*) and 8(*b*) show the concentration contours at this plane for injection points P and S, respectively.

The contour shapes are quite different for the two injection points. Figure 8(*a*) shows the ethylene from the pressure-side leg of the horseshoe vortex in a relatively symmetrical distribution about a peak concentration of approximately 55 ppm. There is however a ridge of concentrations in excess of 20 ppm extending towards the suction side near midspan. This whole distribution is quite similar to the smoke trace obtained by Stanitz at al. and presented as Fig. 10 in [4]. There they showed the formation of a passage vortex in a 90 deg rectangular elbow by injecting smoke on the plane wall at the elbow inlet. It appears therefore that fluid from point P is distributed throughout the passage vortex just as the smoke in Stanitz's duct marked his passage vortex.

By contrast, Fig. 8(*b*) shows an entirely different distribution of ethylene. Here there is a band of high concentrations, between 50 and 70 ppm, across the top. If the interpretation of the results in Fig. 9 is that fluid from the pressure-side leg of the horseshoe vortex locates the center of the passage vortex at this plane, then the results in Fig. 8(*b*) indicate that fluid from the suction-side leg of the horseshoe vortex is being convected around the center of the passage vortex. Indeed it is already starting another sweep around the center. This could explain the band of high concentrations. In Fig. 3, we have drawn the likely paths of fluid from points P and S between the measured locations of maximum concentrations. These paths are consistent with the picture of fluid from point S being convected around fluid from point P which marks the passage vortex. In this top view, the path of fluid from point S appears like a sine wave, oscillating about the path of fluid from point P.

Consider the orientation of the rake in Fig. 3. A possible explanation of the band of high concentrations in Fig. 8(*b*) is that the path of fluid from point S actually takes it past several prongs of the rake each of which sees the *same* fluid with the same high concentrations.

Mixing Downstream of Blades

Some of the ethylene injected at point S has already diffused to the location of maximum concentration for point P by the blade exit. In Fig. 8(*b*), we find the concentration at this location is 27 ppm. Let us therefore consider the change along a trajectory following the maximum concentration for point P downstream of the blade. Along this trajectory, the change for ethylene from point S is from 27 to 25 ppm, similar to the change for point P, from 55 to 45 ppm. But along a trajectory around the edge of the passage vortex the concentration of ethylene from point S falls from 70 to less than 25 ppm. It appears that fluid at the edges of the passage vortex can mix out quite rapidly compared with fluid in its core. This explanation is consistent with the flow path of the fluid from point S shown in Fig. 3; this carries fluid from point S close to the blade surface at the trailing edge. It is also partly confirmed by the results of Table 1 where we found that 15 percent of the ethylene from point S mixed out at concentration levels below 10 ppm in the blade wake.

Tracing Fluid in the Low-Loss Region

In Part 1, Fig. 12, we defined a low-loss region based on total pressure measurements at the downstream measuring plane. The total pressure contours are reproduced here in Fig. 6 and the low-loss region is essentially that area with $C_{pt} < 0.2$. As discussed in Part 1, it consists of a large low-loss core near the endwall boundary layer with a thin ridge extending to midspan between the high-loss core and the adjacent blade wake. In this section we attempt to find the sources of this fluid in the ethylene injection plane shown in Fig. 3.

To do this, we injected ethylene through a 2.4-mm dia tube at the 14 locations shown numbered in Fig. 4. We then searched the downstream plane at $x/c = 1.4$ to find the peak concentrations. The locations of these we have marked with the corresponding numbers in Fig. 6. We have also estimated with the dotted line in Fig. 4 the location in the injection plane of fluid with a downstream value of C_{pt} equal to 0.2. Thus we see the source of fluid in the low-loss region. The source of this fluid is found in the suction-side half of the passage at the blade inlet where it accounts for approximately 27 percent of the flow area. This is consistent with the fact that fluid in the low-loss region represents about 36 percent of the mass flow through the cascade.

Conclusions

A high-loss core was observed near midspan at the downstream measuring plane ($x/c = 1.4$) in Part 1. Over 65 percent of the ethylene injected near the blade inlet at locations of horseshoe vortex flow was found downstream within this high-loss core. Flow from the pressure-side and suction-side legs of the horseshoe vortex appeared to be distributed around the location of maximum total pressure loss ($C_{pt} \cong 1.3$) in the high-loss core at the downstream plane.

Fluid from the pressure-side leg of the horseshoe vortex appeared to be distributed throughout the passage vortex at the blade exit. The distribution was similar to the distribution of smoke observed by Stanitz in a passage vortex in a rectangular elbow.

Ethylene injected at the location of the suction-side leg of the horseshoe vortex near the blade inlet was convected around the center of the passage vortex. Fluid at the edges of the passage vortex seemed to mix more rapidly downstream of the trailing edge than fluid near its core.

Fluid with low losses ($C_{pt} < 0.2$) at the downstream plane represented about 36 percent of the mass flow through the cascade. At the blade inlet this flow accounted for approximately 27 percent of the flow area.

Acknowledgment

The authors wish to thank Rolls-Royce Limited, Aero Division for supporting this work under a cooperative agreement with Virginia Polytechnic Institute and State University.

References

1 Moore, J., and Ransmayr, A., "Flow in a Turbine Cascade—Part 1: Losses and Leading-Edge Effects," JOURNAL OF ENGINEERING FOR GAS TURBINES AND POWER, Vol. 106, Apr. 1984, pp. 400-408.

2 Langston, L. S., Nice, M. L., and Hooper, R. M., "Three-Dimensional Flow Within a Turbine Cascade Passage," ASME JOURNAL OF ENGINEERING FOR POWER, Vol. 99, Jan. 1977, pp. 21-28.

3 Denton, J. D., and Usui, S., "Use of a Tracer Gas Technique to Study Mixing in a Low Speed Turbine," ASME Paper No. 81-GT-86.

4 Stanitz, J. D., Osborne, W. M., and Mizisin, J., "An Experimental Investigation of Secondary Flow in an Accelerating, Rectangular Elbow with 90 Deg of Turning," NACA TN 3015, Oct. 1953.

Downloaded 01 Jun 2010 to 171.66.16.70. Redistribution subject to ASME license or copyright; see http://www.asme.org/terms/Terms_Use.cfm

J.-J. Camus

J. D. Denton

J. V. Soulis
Whittle Laboratory,
Engineering Department,
Cambridge University,
Cambridge, England

C. T. J. Scrivener
Rolls Royce Limited,
Derby, England

An Experimental and Computational Study of Transonic Three-Dimensional Flow in a Turbine Cascade

Detailed experimental measurements of the flow in a cascade of turbine rotor blades with a nonplanar end wall are reported. The cascade geometry was chosen to model as closely as possible that of a H.P. gas turbine rotor blade. The blade section is designed for supersonic flow with an exit Mach number of 1.15 and the experiments covered a range of exit Mach numbers from 0.7–1.2. Significant three-dimensional effects were observed and the origin of these is discussed. The measurements are compared with data for the same blade section in a two-dimensional cascade and also with the predictions of two different fully three-dimensional inviscid flow calculation methods. It is found that both these calculations predict the major three-dimensional effects on the flow correctly.

Introduction

The development of efficient turbomachinery blading has always been associated with the systematic testing of blade profiles in two-dimensional cascade wind tunnels. There has been considerable debate about the relevance of such two-dimensional testing to the performance of blades which have to operate in the much more complex environment of a machine, but the fact that they are performed by most manufacturers implies that they still have value. Over the last decade the advent of reliable numerical methods of predicting two-dimensional flow in cascades has largely changed the function of cascade testing to that of verifying and calibrating the numerical methods rather than of developing new blade sections.

Three-dimensional cascade tests are an obvious halfway stage between the often unrealistic flow in a two-dimensional cascade and the complex, unsteady, three-dimensional, nonuniform flow in a real machine. In the past, such three-dimensional tests have been largely confined to studies of the secondary flow which arises from nonuniform inflow to cascades of two-dimensional geometry. However, a limited number of studies of the flow in cascades with three-dimensional geometry have been undertaken. Almost invariably, the three-dimensional geometry was imposed by the shape of the end walls rather than by twisted or tapered blading (e.g., Morris and Hoare [1], Kopper et al. [2]). Such tests may be performed on either annular or plane cascades. The former model the radial pressure gradients found in the machine correctly but are much more expensive and difficult to perform than the latter. However, it should be realized that three-dimensional cascade tests can only be realistically used to model the flow in high hub:tip ratio axial flow machines.

The need for three-dimensional cascade tests has increased recently because of the advent of new fully three-dimensional flow calculation methods (e.g., Denton [3], Moore and Moore [5], Laskaris [6]). These methods are already being used in design procedures and they require verification in the same way that two-dimensional methods are verified by two-dimensional cascade tests. The amount of published data on three-dimensional turbomachinery flows in known geometries is very limited indeed so there is considerable demand for good test data to verify the calculation methods. This is particularly true for transonic flows where the sensitivity of the flow pattern to three-dimensional effects is greatly increased. This sensitivity is well illustrated by the experiments of Dawes [7] who showed radical differences between the observed flow and two-dimensional predictions on extremely simple three-dimensional geometries. The only known transonic three-dimensional cascade tests are those of Spurr [8]. Although he modeled a realistic, very complex, three-dimensional geometry, only a limited amount of data was obtained because of the difficulty of performing accurate probe traverse measurements in a small annular cascade. The same problem, plus many others, makes it very difficult to obtain good test data from measurements in a real or model turbomachine where interpretation of the results is complicated by many factors (e.g., unsteadiness, tip leakage, nonuniform inflow) which are not under the control of the experimenter.

The present series of tests was therefore undertaken in order to provide information on three-dimensional effects in a planar cascade with geometry similar to that of a real H.P.

Contributed by the Gas Turbine Division of THE AMERICAN SOCIETY OF MECHANICAL ENGINEERS and presented at the 28th International Gas Turbine Conference and Exhibit, Phoenix, Arizona, March 27–31, 1983. Manuscript received at ASME Headquarters November 30, 1982. Paper No. 83-GT-12.

Copyright © 1984 by ASME
Downloaded 01 Jun 2010 to 171.66.16.70. Redistribution subject to ASME license or copyright; see http://www.asme.org/terms/Terms_Use.cfm

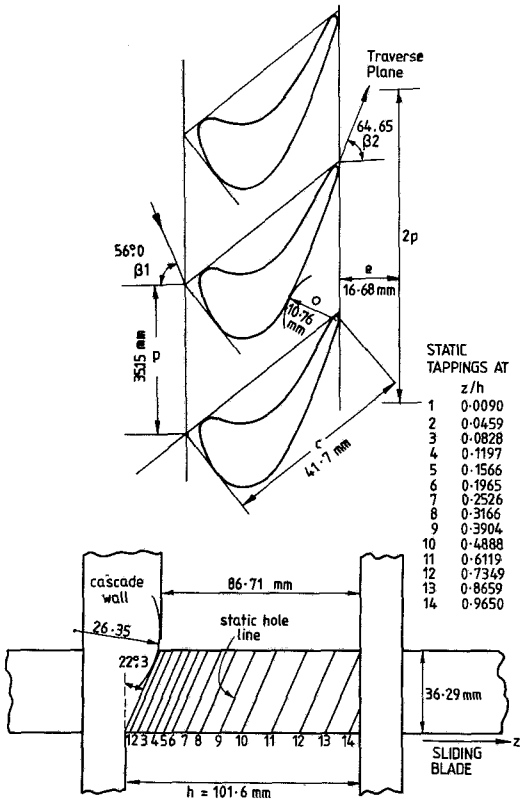


Fig. 1 Geometry and blade traversing positions for the flared RD turbine rotor cascade

Table 1 Details of the RD blade

No.	x cm	y cm	No.	x cm	y cm
1	3.4876	1.7627	27	0.0000	0.0000
2	3.3482	1.8339	28	0.1394	0.4191
3	3.2082	1.8910	29	0.2791	0.7760
4	3.0691	1.9355	30	0.4186	1.1356
5	2.9296	1.9682	31	0.5580	1.4849
6	2.7902	1.9901	32	0.6975	1.8186
7	2.6507	2.0012	33	0.8369	2.1262
8	2.5110	2.0020	34	0.9769	2.4044
9	2.3716	1.9914	35	1.1161	2.6479
10	2.2321	1.9700	36	1.2555	2.8590
11	2.0927	1.9370	37	1.3949	3.0343
12	1.9530	1.8928	38	1.5347	3.1760
13	1.8135	1.8367	39	1.6741	3.2870
14	1.6741	1.7683	40	1.8135	3.3690
15	1.5347	1.6878	41	1.9530	3.4259
16	1.3949	1.5948	42	2.0927	3.4587
17	1.2555	1.4887	43	2.2321	3.4690
18	1.1161	1.3691	44	2.3716	3.4567
19	0.9766	1.2354	45	2.5110	3.4216
20	0.8369	1.0876	46	2.6507	3.3609
21	0.6975	0.9248	47	2.7902	3.2741
22	0.5580	0.7460	48	2.9296	3.1592
23	0.4186	0.5507	49	3.0691	3.0109
24	0.2791	0.3378	50	3.2097	2.8778
25	0.1394	0.1087	51	3.3482	2.5758
26	0.0000	−0.1419	52	3.4876	2.0657

Leading edge radius 0.1836 cm at $x = 3.3243$ cm and $y = 2.0503$ cm
Trailing edge radius 0.05055 cm

Blade chord	41.7 mm
Pitch/chord	0.843
Stagger angle	28.5 deg
Inlet flow angle	56 deg
Opening/pitch ratio	0.382

gas turbine rotor. The blade section chosen was one which has been extensively tested and reported in two-dimensional flow (Haller [9]), so that three-dimensional effects could be identified and their importance assessed. The tests were carried out with both subsonic and supersonic exit flow so that any increased sensitivity of transonic flow to three-dimensional effects could be observed.

Test Geometry and Instrumentation

It was required to model the main three-dimensional features of the flow in a H.P. gas turbine rotor blade using a planar cascade. The amount of twist on such blades is not large and considerable simplification could be achieved by testing an untwisted blade with section identical to that at the midspan of the rotor. The outer annulus boundary of the machine was almost cylindrical whilst the inner boundary was flared inwards at 22.3 deg to the machine axis. The flare started close to the blade leading edge and ended close to the trailing edge, hence spanwise accelerations of the flow are induced and were expected to produce significant three-dimensional effects. In particular, the pressure on the flared end wall will be lowered at entry to the blade row and increased at exit, relative to the pressure on the plane end wall. The aspect ratio of the cascade was chosen to be the same as in the turbine so that the ratio of inlet to outlet flow area was very similar.

The resulting cascade geometry is shown in Fig. 1. It contained six blades, as experience with two-dimensional cascade testing has shown that this is sufficient to obtain reasonably periodic flow over the central passages. The cascade exhausted to a plenum as a free jet and no tailboards were used to control the flow downstream of the blades. The blade section coordinates and other relevant data are tabulated in Table 1.

The transonic cascade tunnel at the Whittle Laboratory has been described by Gostelow and Watson [10]. It is a closed circuit tunnel permitting independent variation of Reynolds and Mach numbers. The flow is sufficient to choke an 80 cm^2 throat at a pressure ratio of 2.5 corresponding to a cascade exit Mach number of 1.25. The facility is provided with a highly automated data acquisition system permitting very accurate location of the automatic traverse gear and remote monitoring of a large number of static pressures.

In order to obtain a complete three-dimensional pressure distribution on the blade surfaces, it was arranged that the central two blades of the cascade could slide through the end walls so that the complete span could be monitored by two rows of blade surface pressure tappings. These rows were in a plane parallel to the flared end wall. One on the suction surface contained 23 tappings and one on the pressure surface contained 11 tappings. In addition there were a total of 105 static pressure tappings on the two end walls.

The probe used to traverse downstream of the cascade was an AVA wedge probe of the type described by Sieverding et al. [11]; it was calibrated up to a Mach number of 2.0. The flow angle was obtained from the calibration rather than by nulling the probe as this greatly speeds up the traversing. In order to minimize disturbance to the flow the axis of the probe is aligned closely with the exit flow direction. The traverses were performed a distance 0.4 blade chords downstream from the trailing edge plane and on each a total of 100 points spread over two blade pitches were monitored. Traverses were performed at ten different spanwise locations, which were concentrated near to the flared end wall where larger three-dimensional effects, were expected.

A total of 16 different test conditions were investigated covering the ranges, Mach number $.7 < M < 1.2$, Reynolds number $3.6 \times 10^5 < Re < 10.6 \times 10^5$ and incidence $= -10$ deg to $+5$ deg. Processing and analysis of the vast amount of data obtained were only possible using a sophisticated

Downloaded 01 Jun 2010 to 171.66.16.70. Redistribution subject to ASME license or copyright; see http://www.asme.org/terms/Terms_Use.cfm

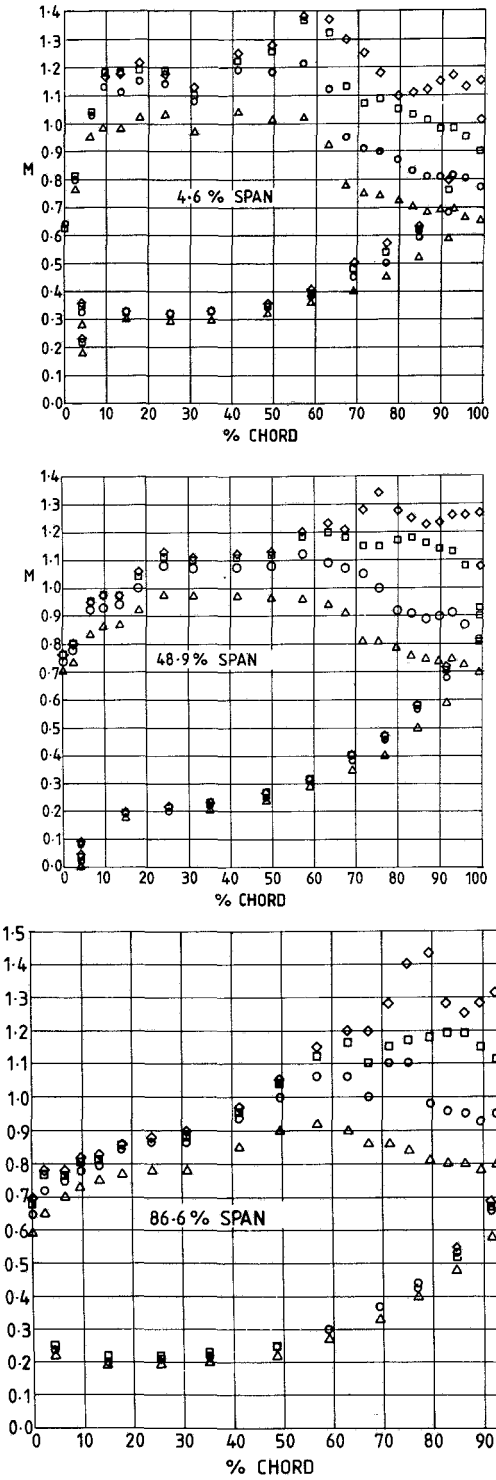


Fig. 2 Surface Mach numbers at zero incidence: ◇, $M_{2_{is}} = 1.2$; ⊙, $M_{2_{is}} = 0.85$; □, $M_{2_{is}} = 1.0$; △, $M_{2_{is}} = 0.7$

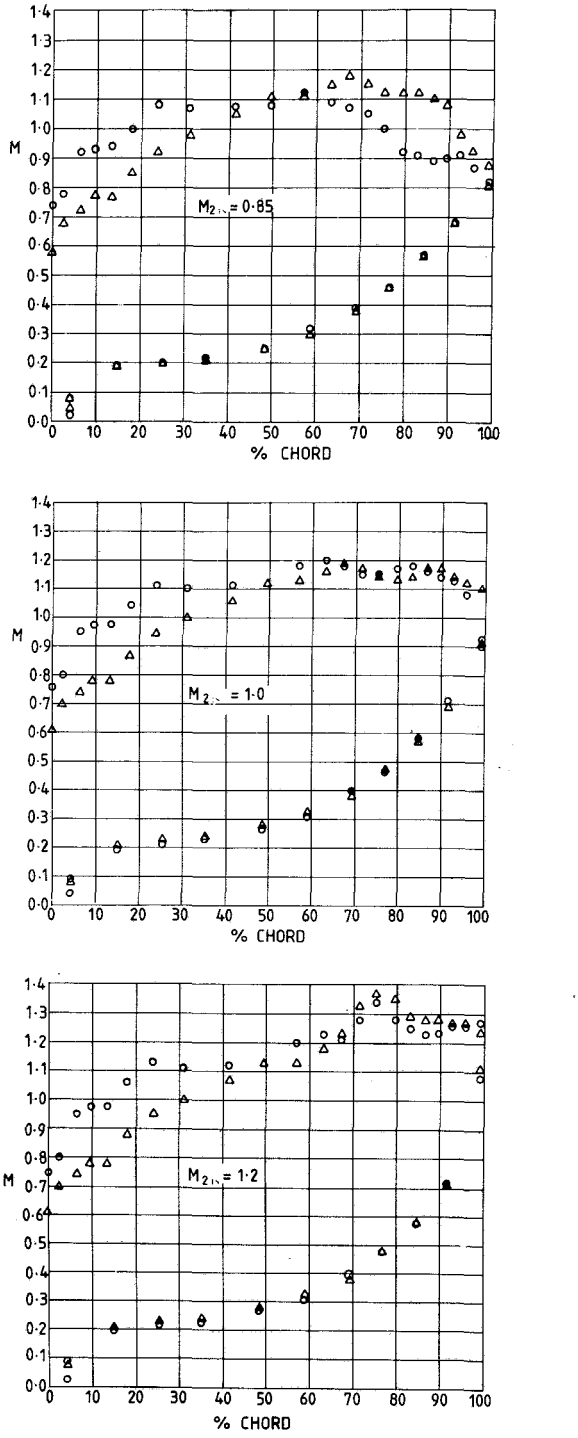


Fig. 3 Comparison of two-dimensional and three-dimensional surface Mach numbers at mid span: ○, three-dimensional cascade; △, linear cascade

computer based system which enabled plotted results to be available within 20 min of data acquisition.

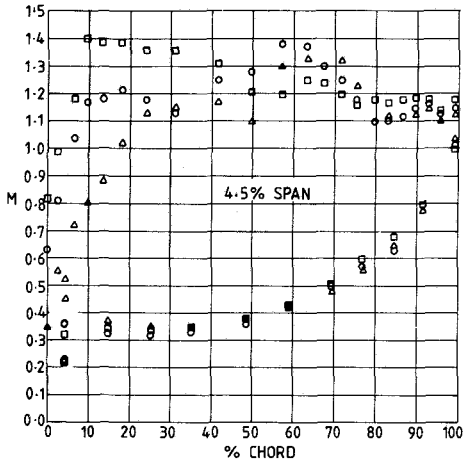
Flow visualization was obtained by using a mixture of fluorescent powder and oil painted onto the blade before starting the tunnel. The oil was carefully blended so that the surface dried only after several minutes of running at the required conditions. This method provided very clear details of the surface flow pattern, particularly of the end wall secondary flows. Schlieren photography was not attempted because it is not easy to adapt it to study three-dimensional flows.

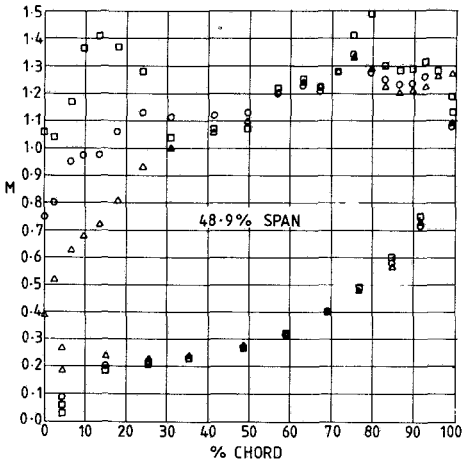
Experimental Results

Only a very limited selection of the results can be shown in this paper and the emphasis will be on illustrating inviscid three-dimensional flow effects which can be compared with the predictions of three-dimensional flow calculations. More details of the results obtained are given by Soulis [12].

Blade surface static pressures are presented as isentropic Mach numbers calculated from the surface static pressure and

Downloaded 01 Jun 2010 to 171.66.16.70. Redistribution subject to ASME license or copyright; see http://www.asme.org/terms/Terms_Use.cfm





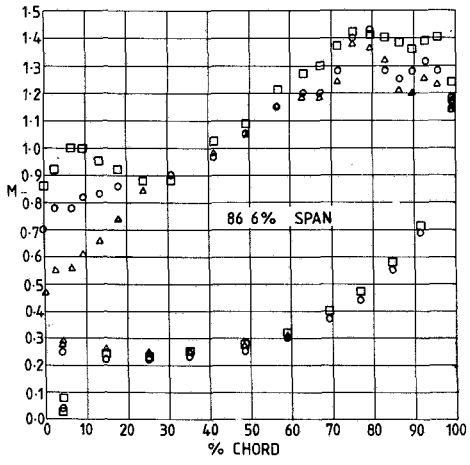


Fig. 4 Effect of incidence at $M_{2_{is}}$ = 1.2: □, + 5 deg incidence; ○, zero incidence (β_1 = 56 deg); △, − 10 deg incidence

the upstream stagnation pressure. When shock losses are present this isentropic Mach number is not the same as the true Mach number, but in practice differences are expected to be very small. Figure 2 shows the spanwise variation of this surface Mach number at zero incidence over a range of exit Mach numbers. Although shocks are present at the higher Mach numbers, they are considerably smeared by the shock wave-boundary layer interaction and do not show up clearly on the surface pressure tappings. However, experience from previous cascade tests in which Schlieren photography was used suggests that any region of decelerating supersonic flow on the blade surface is usually associated with a shock wave.

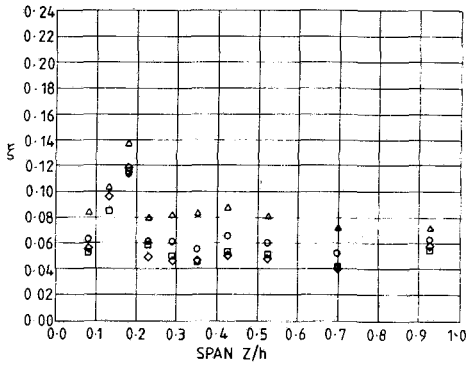


Fig. 5 Spanwise variation of energy loss coefficient, ξ: $M_{2_{is}}$ = 1.2, i = 0 deg. △▽, Re = 10.5 × 10^5; ○, Re = 5.3 × 10^5; □, Re = 8.0 × 10^5; △, Re = 3.5 × 10^5.

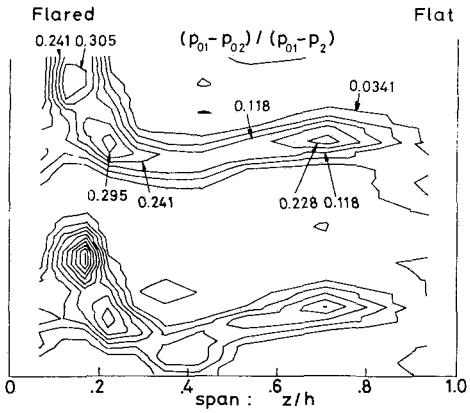


Fig. 6 Pressure loss coefficient contours: $M_{2_{is}}$ = 0.85 Re = 8 × 10^5

Such shocks are present on the suction surface near the trailing edge at all spanwise positions and at about 30 percent chord at 4.6 percent span.

The three-dimensional effects shown by Fig. 2 are qualitatively the same as expected. The surface Mach numbers are increased around the leading edge on the flared end wall because of the increased inlet Mach number induced by the wall curvature. This effect is reversed at the trailing edge where the Mach numbers are depressed near the flared end wall. As a result, the peak suction surface Mach number occurs much earlier on the flared wall and the amount of diffusion downstream of this peak is also increased. It is also clear that three-dimensional effects are not confined to the immediate vicinity of the flared end wall. In fact the changes between 50 and 100 percent span are just as great as those from 0–50 percent span. This is an illustration of the fact that three-dimensional effects are not localized in transonic flow.

Comparison of the three-dimensional results with those for the same blade in two-dimensional cascade are given at midspan only, in Fig. 3. This shows that the main differences occur around the leading edge where they are due to the higher inlet Mach number of the three-dimensional cascade for the same outlet Mach number. However, with subsonic outlet flow there are also differences on the suction surface near the trailing edge. These are probably due to differences in the outlet flow angle of the two cascades (see later).

The effects of incidence on the surface Mach numbers at an exit Mach number of 1.2 are illustrated in Fig. 4. As is usually found in two-dimensional cascades, incidence mainly affects the flow around the leading edge. The effects are, however, much greater than those found in two-dimensional flow

Downloaded 01 Jun 2010 to 171.66.16.70. Redistribution subject to ASME license or copyright; see http://www.asme.org/terms/Terms_Use.cfm

through the same cascade because of the higher inlet Mach number. This is particularly true near to the flared wall, where at + 5 deg incidence very high Mach numbers are reached close to the leading edge. It is possible that there is a shock-induced separation present in this region which would account for the comparatively uniform pressure over the forward part of the suction surface. A shock wave is clearly present at a similar location near midspan, where it does not cause a separation.

The effects of Reynolds number on the surface pressure distributions were very small over the range Re = 3.5×10^5 – 10.6×10^5 and consequently no results will be presented for this. The loss in the cascade did, however, vary with Reynolds number, and the spanwise variation of energy loss coefficient at an exit Mach number of 1.2 is shown in Fig. 5. As expected the loss decreases as Re is increased.

Although there were insufficient traverse planes to enable the secondary loss to be separated from the profile loss, especially near the plane end wall, it is clear that the secondary loss is much greater on the flared wall and that the center 50 percent of span is unaffected by secondary loss. This is confirmed by Fig. 6, which shows contours of stagnation pressure loss coefficient at the traverse plane. Although the detail available is not as great as would be desirable for a study of secondary loss, the contours illustrate dramatically the very large loss increase on the flared end wall. The origin of this high secondary loss is not immediately clear as there is no obvious separation present at zero incidence. However, the much higher diffusion present on the flared wall will lead to more rapid boundary layer growth and the surface flow visualization showed stronger crossflow onto the suction surface downstream of the shock on this wall.

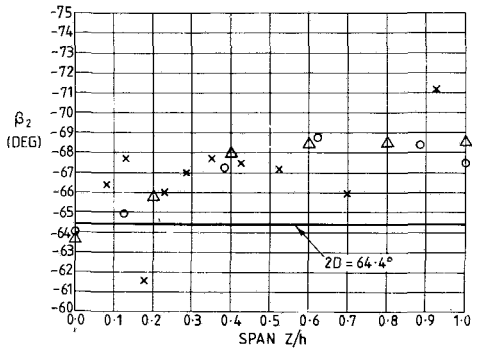


Fig. 7 Spanwise variation in exit flow angle $M_{2_{is}}$ = 1.2: X, measurement; △, three-dimensional time marching calculation; ○, three-dimensional potential flow calculation

The two-dimensional coefficient of the blade was 3.99 percent at Re = 8.1×10^5 and M_2 = 1.2. This is slightly less than the minimum loss achieved by the three-dimensional cascade and some 20 percent less than the midspan loss. The increase in loss can be attributed to the increased surface velocities around the leading edge of the three-dimensional cascade at the same exit Mach number as the two-dimensional cascade.

The spanwise variation of exit flow angle at M_2 = 1.2 and zero incidence is shown in Fig. 7, where it is compared to the two-dimensional value and to the results of three-dimensional calculations. The secondary loss region appears as an area of underturning as is usual in the outer part of a secondary flow passage vortex. It is likely that the angles close to the flared wall, although similar to those at midspan, represent over-turning relative to the angle which would have been achieved with a uniform inlet flow. This would be expected from secondary flow theory and is probably also the reason for the high turning close to the flat endwall. Over most of the span the exit angle is about 2 deg greater than the two-dimensional value. This increase in turning can be attributed to the increase in flow area downstream of the throat which results from the flare. A simple continuity analysis shows that provided the area change does not significantly alter the loss, it must increase the turning.

Figure 8 illustrates the remarkable detail which was obtained from the surface flow visualization. It shows the rear suction surface of the blades with the flared end wall on the left. The shock-boundary layer interaction is shown clearly extending across the whole span and the end wall. It can be seen how the shock curves upstream toward the flared wall. The secondary flow regions are also clearly visible with that on the flared wall being more extensive and having stronger spanwise flows than that on the plane wall. Near the leading edge the visualization showed the classic secondary flow pattern with saddle points of separation on both endwalls.

Comparison With Three-Dimensional Calculations

Two completely different three-dimensional inviscid calculation methods were used to predict the flow in the flared

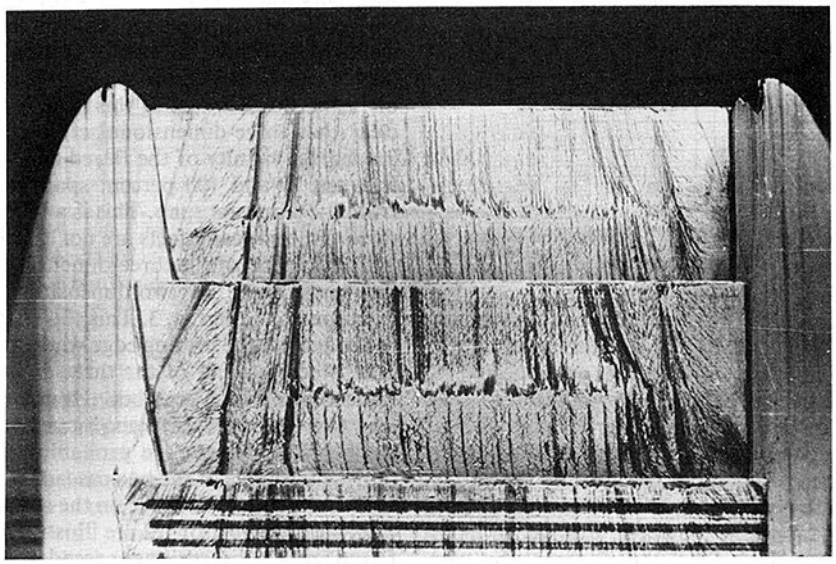


Fig. 8 Surface flow visualization: $M_{2_{is}}$ = 1.20, Re = 8×10^5. Rear suction surface with flared end wall on left.

Downloaded 01 Jun 2010 to 171.66.16.70. Redistribution subject to ASME license or copyright; see http://www.asme.org/terms/Terms_Use.cfm

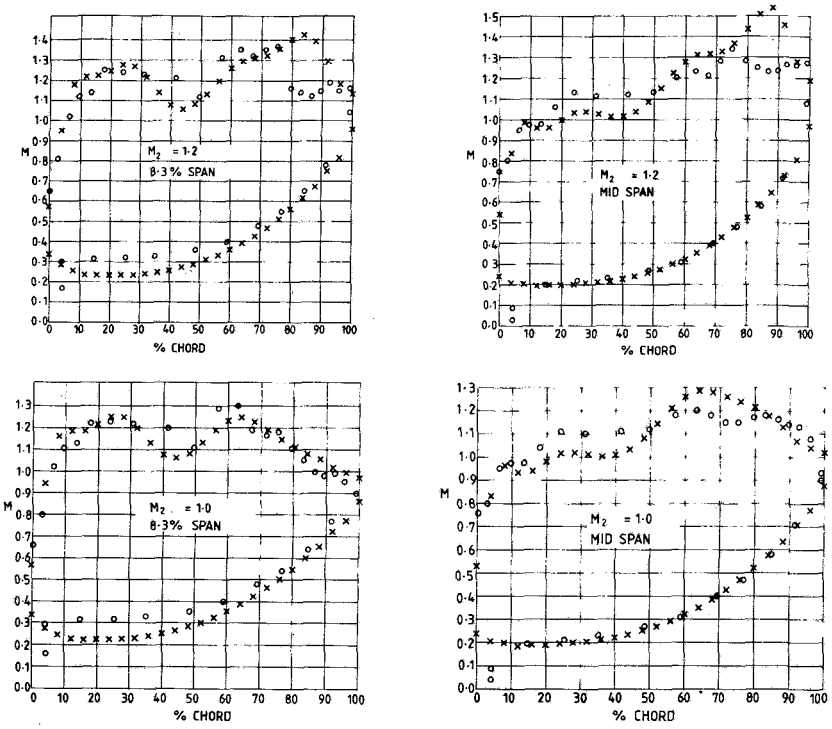


Fig. 9 Comparison with time marching calculation: o, measurements; X, calculation

cascade. Denton's [3] three-dimensional time marching solution of the Euler equations is well documented (Denton and Singh [4]) and will not be described further. Calculations with this method were performed before any experimental results were available and it should be noted that the method used was Denton's original one not the new scheme described *in [15]*.

In addition a newly developed three-dimensional potential flow calculation (Soulis [12]) was used. This method solves the full potential equation in conservative finite volume form using a method similar to that of Jameson [13]. Supersonic flow and shock capturing are included, using the artificial compressibility concept of Hafez and Murman [14]. The assumption of potential flow limits the method to cases where only weak shock waves occur (i.e., $M < 1.3$ for normal shocks) since momentum is not exactly conserved across shock waves although mass flux is conserved. Vorticity may be shed from the trailing edge of blades, but it is assumed that this remains on the grid boundaries. The position of these vortex sheets is guessed and held fixed, but experience suggests that this approximation is not a serious limitation on the accuracy of the method. Because only a single variable (the potential) is used, the method should be computationally more efficient than are solutions of the three-dimensional Euler equations.

The potential method can use any convenient grid system; however, for the present calculations both methods used an identical $8 \times 49 \times 6$ point mesh. This is a comparatively coarse grid for three-dimensional calculations, especially when shocks are present, since both methods smear shocks over several grid points, but was enforced by limitations on computer storage. Calculation times on an IBM 370-165 were of the order of 4 min for the time marching method and 3 min for the potential flow method.

Figure 9 compares the time marching solution and experiment at exit Mach numbers of 1.0 and 1.2 and at zero incidence. Agreement is good over most of the surface with the major discrepancy being on the suction surface near the trailing edge at the higher Mach number. This error is

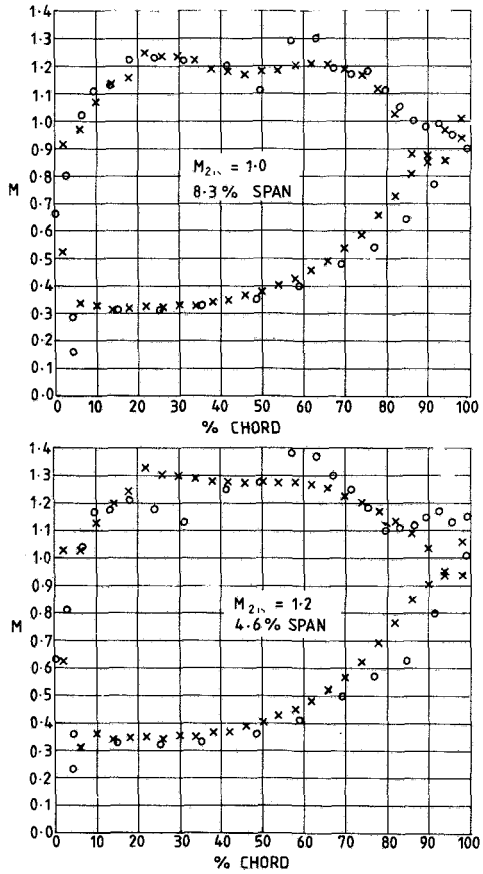


Fig. 10 Comparison with three-dimensional potential flow calculations

probably associated with the inability of the coarse grid to capture details of the trailing edge shock system and its intersection with the suction surface. The high Mach numbers

Downloaded 01 Jun 2010 to 171.66.16.70. Redistribution subject to ASME license or copyright; see http://www.asme.org/terms/Terms_Use.cfm

around the leading edge on the flared endwall are well predicted.

Solutions using this method at positive incidence predicted a strong shock in the suction surface leading edge region near the flared end wall. This shock was not observed near the endwall but was presented at midspan (Fig. 4) thus lending support to the idea that there may be separated flow in the region of the intersection of the suction surface leading edge with the flared end wall under these conditions.

Comparison of the potential flow method with measurements are shown in Fig. 10 for the same conditions as Fig. 9. The level of agreement is on the whole rather better than that of the time marching method, especially near the trailing edge. It seems that the Kutta condition of equal velocity on the two surfaces at the trailing edge, as used by the potential method, is more realistic than that of equal pressures used by the time marching method in this particular case.

Comparisons of measured and predicted exit flow angles are shown in Fig. 7. The two three-dimensional methods agree very well between themselves and with the measurements around midspan. The time marching method could have been used to predict inviscid details of the secondary flows but because no inlet boundary layer profile was available this was not attempted. Hence, neither method will give the correct exit angle near the end walls. The general trend of the predicted exit angles to increase from flared to flat end wall can be explained by the increase in meridional velocity from trailing edge to traverse plane along the flared wall. Since tangential velocity is conserved downstream of the blade, this results in a decrease of exit angle with distance downstream of the cascade on this wall. Hence the measured exit angles near to the flared wall may represent overturning in the inner region of the passage vortex, relative to the angle which would occur with uniform, inviscid inlet flow.

Conclusions

Detailed measurements of three-dimensional transonic flow have been obtained in a planar cascade with geometry similar to that of a H.P. gas turbine rotor. The quality of measurements obtained is considered much higher than would have been possible in a real turbine and so they permit a more systematic study of three-dimensional effects uncomplicated by such factors as unsteadiness, tip leakage, and nonuniform inlet flow. The measurements provide a good test of the validity of current three-dimensional inviscid flow calculations methods.

The qualitative effect of the three-dimensional geometry on the blade surface pressures is predictable by simple physical arguments. The increased leading edge loading on an end wall with convex outwards curvature is an undesirable feature as is the increased diffusion upstream of a trailing edge on an endwall with concave inwards curvature. Both these features are undesirable in a turbine design. A significant result from the present measurements is the greatly increased secondary loss on the flared endwall. The exact mechanism of this increase was not revealed by the experiments but it is probably in part associated with the increased diffusion on the endwall and suction surface.

Three-dimensional inviscid calculation methods are able to predict the main features of the flow reasonably well, even using comparatively coarse grids. However, much finer grids would be needed to resolve details of the complex trailing edge shock system or for any method which attempts to compute the viscous effects in the cascade.

Acknowledgments

The authors wish to thank the Ministry of Defence (P.E.) and Rolls Royce Limited for financial support of the experimental work and Rolls Royce Limited for permission to publish the results in this paper.

References

1 Morris, A. W. H., and Hoare, R. G., "Secondary Loss Measurements in a Cascade of Turbine Blades With Meridional Wall Profiling," ASME Paper No. 75-WA/GT-13.

2 Kopper, F. G., Milano, R., and Vanco, M., "Experimental Investigation of Endwall Profiling in a Turbine Vane Cascade," *AIAA Journal*, Vol. 19, No. 8, Aug. 1981.

3 Denton, J. D., "A Time-Marching Method for Two- and Three-Dimensional Blade-to-Blade Flows," Aeronautical Research Council, R. & M. 3775, 1975.

4 Denton, J. D., and Singh, V. K., "Time-Marching Methods for Turbomachinery Flow Calculation: Part I, Basic Principles and Two-Dimensional Applications; Part II: Three-Dimensional Flows in Turbomachines," V.K.I. LS 1979-7. Apr. 1979.

5 Moore, J., and Moore, J. G., "A Calculation Procedure for Three-Dimensional, Viscous Compressible Duct Flow, Parts I and II" ASME *Journal of Engineering for Fluids*, Vol. 101, Dec. 1979.

6 Laskaris, T. E., "Finite Element Analysis of Three-Dimensional Potential Flow in Turbomachines," *AIAA Journal*, Vol. 16, No. 7, July 1978.

7 Dawes, W. N., "A Study of Shock Waves in Three-Dimensional Transonic Flow," Ph.D. thesis, Cambridge University, Sept. 1979.

8 Spurr, A., "A Computational and Experimental Study of Fully Three-Dimensional Transonic Flow in Turbomachinery," Ph.D. thesis, University of Southampton, Mar. 1980.

9 Haller, B. R., "The Effects of Film Cooling Upon the Aerodynamic Performance of Transonic Turbine Blades," Ph.D. thesis, Cambridge University, Sept. 1980.

10 Gostelow, J. P., and Watson, P. J., "A Closed Circuit Variable Density Air Supply for Turbomachinery Research," ASME Paper No. 76-GT-62, 1976.

11 Sieverding, C., Maretto, L., Lehthaus, F., and Lawaczeck, O., "Design and Calibration of Four Probes for Use in Transonic Turbine Cascade Testing," V.K.I. Tech. Note 100, 1974.

12 Soulis, J. V., "Calculation of Transonic Potential Flow Through Turbomachinery Blade Rows," Ph.D. thesis, Cambridge University, Sept. 1981.

13 Jameson, A., and Caughey, D. A., "A Finite Volume Method for Transonic Potential Flow Equations," AIAA Paper No. 77-635, Oct. 1977.

14 Hafez, M. M., Murman, E. M., and South, J. C., "Artificial Compressibility Methods for Numerical Solution of Transonic Full Potential Equation," AIAA Paper No. 78-1148, July 1978.

15 Denton, J. D., "An Improved Time Marching Method for Turbomachinery Flow Calculation," ASME Paper No. 82-GT-239.

Downloaded 01 Jun 2010 to 171.66.16.70. Redistribution subject to ASME license or copyright; see http://www.asme.org/terms/Terms_Use.cfm

A Navier-Stokes Analysis of Three-Dimensional Turbulent Flows Inside Turbine Blade Rows at Design and Off-Design Conditions

C. Hah
Fluid Mechanics Engineer,
Fluid Mechanics and Combustion Branch,
Corporate Research and Development,
General Electric Company,
Schenectady, N.Y. 12301

A numerical scheme based on the compressible Navier-Stokes equation has been developed for three-dimensional turbulent flows inside turbine blade rows. The numerical scheme is based on a fully conservative control volume formulation and solves the governing equations in fully elliptic form. Higher order discretizations are used for the convection term to reduce the numerical diffusion. An algebraic Reynolds stress model modified for the effects of the streamline curvature and the rotation is used for the closure of the governing equations. General coordinate transformations are used to represent the complex blade geometry accurately, and a grid generation technique based on elliptic partial differential equations is employed. Comparisons with the experimental data show that various complex three-dimensional viscous flow phenomena (three-dimensional flow separation near the leading edge, formation of the horseshoe vortex, etc.) are well predicted with the present method.

Introduction

The reliable prediction of the three-dimensional viscous flows inside the blade passage in a turbomachine is crucial in estimating and improving the performance of modern turbofan engines. The aerodynamic loss mechanism inside the blade row is directly related to the various viscous flow phenomena. Among the important three-dimensional viscous flow phenomena existing in blade passages are boundary layers on the blade surface and endwalls, the horseshoe vortex at the junction of the blunt leading edge and the endwalls, tip clearance flows and wakes. With advancement in the design of turbomachines, the blade loading has been increased to reduce the number of blades and stages, for which reason the effect of viscous flow becomes more dominant. The prediction or even the description of the three-dimensional viscous flow inside a turbine blade passage has been a very difficult problem in fluid mechanics because of the extremely complex nature of the flow.

There have been numerous experimental studies to understand and describe the flow fields inside a turbine blade passage. Salvage [1] reviewed various works prior to 1974 on cascade secondary flow behavior and its effect on aerodynamic losses. The complex nature of the endwall flow and the three-dimensional passage vortex were shown by Herzig et al. [2] through flow visualization. Came [3] obtained inlet and exit plane total pressure surveys of a large-scale cascade with varying inlet and outlet boundary layer thickness and incidence. Goldman and McLallin [4] investigated the aerodynamic performance of annular cascades. More recently Waterman and Tall [5] performed total pressure surveys at various axial locations for large-scale, low-aspect-ratio turbine nozzles. Langston et al. [6] performed a more comprehensive and detailed study of the flow field within a large-scale turbine cascade and showed clearly various aspects of the complex three-dimensional flow field.

Although significant developments of computational fluid mechanics have been achieved along with increasing computer capabilities, many three-dimensional viscous flow phenomena have not been predicted successfully. Patankar and Spalding [7], Brilley [8], and Dodge [9] proposed numerical methods based on the three-dimensional differential equations. However, various assumptions employed with these methods result in parabolic and partially parabolic solutions of the flow fields. Adequate representation of the turbine geometry with these methods has been one of the major difficulties. Various recent developments in two- and three-dimensional viscous flow calculations in turbomachinery are extensively reviewed by McNally and Sockol [10] and Moore and Moore [11].

The present study is aimed at developing and testing a

Contributed by the Gas Turbine Division of THE AMERICAN SOCIETY OF MECHANICAL ENGINEERS and presented at the 28th International Gas Turbine Conference and Exhibit, Phoenix, Arizona, March 27-31, 1983. Manuscript received at ASME Headquarters December 16, 1982. Paper No. 83-GT-40.

Copyright © 1984 by ASME
Downloaded 01 Jun 2010 to 171.66.16.70. Redistribution subject to ASME license or copyright; see http://www.asme.org/terms/Terms_Use.cfm

numerical method to calculate three-dimensional turbulent flows with large flow separation inside the turbine blade passage. It can be applied to both incompressible and compressible flows.

To obtain useful numerical predictions for complex turbulent flows, the problem of reducing numerical diffusion and using the proper turbulence closure model should be carefully examined. Various previous studies (for example, [12]) have shown that the upwinding discretization scheme of the convection terms leads to significant error in the solution. Often the excessive numerical diffusion obscures important physical processes. Higher order discretization schemes, which have been developed and tested extensively for simpler flows, are used for the present study.

It is well known that the turbulent flow with large amounts of flow separation is very strongly affected by the streamline curvature and rotation. Various studies [13, 14] have indicated that an improper turbulence closure scheme introduces additional error in the prediction, which is comparable to numerical diffusion in many practical situations. For the present study, an algebraic Reynolds stress model with tensor-invariant correction for the streamline curvature and rotation is applied.

In the next section, the governing equations and turbulence closure modeling are described. The numerical scheme and higher order discretization scheme to reduce numerical diffusion are discussed in the following section, and numerical results are then compared with the experimental data. The conclusions drawn from this study are given in the last section.

Governing Equations and Turbulence Closure Modeling

Various conservation equations for the turbulent flow inside turbine blade passages can be written as follows

- Mass:

$$\frac{1}{\rho}\frac{D\rho}{Dt}+U_{i,i}=0 \tag{1}$$

- Momentum:

$$\rho\frac{DU_i}{Dt}+2\epsilon_{ijk}\Omega_j U_k=\rho F_i-\frac{\partial p}{\partial x_i}+\frac{\partial}{\partial x_j}\left(\mu\frac{\partial U_i}{\partial x_j}-\rho\overline{u_i u_j}\right) \tag{2}$$

- Energy:

$$c_p\frac{DC}{Dt}-\frac{\beta C}{\rho}\frac{Dp}{Dt}=\theta+\frac{1}{\rho}\frac{\partial}{\partial x_i}\left(k_c\frac{\partial C}{\partial x_i}-\overline{u_i c}\right) \tag{3}$$

- Gas State:

$$P=\rho RC \tag{4}$$

where U_i = mean velocity, u_i = fluctuating velocity, C = mean temperature, c = fluctuating temperature, ϵ_{ijk} = permutation tensor, θ = dissipation due to viscosity, β = coefficient of thermal expansion, Fi = additional body force, R = gas constant, and Ω_i = rotation speed.

To evaluate the stress terms, the following two transport equations are solved.

$$U^i\frac{\partial k}{\partial x^i}=\frac{\partial}{\partial x^i}\left(\frac{\nu_{\text{eff}}}{\sigma_k}\frac{\partial k}{\partial x^i}\right)+P-\epsilon \tag{5}$$

$$U^i\frac{\partial \epsilon}{\partial x^i}=\frac{\partial}{\partial x^i}\left(\frac{\nu_{\text{eff}}}{\sigma_\epsilon}\frac{\partial \epsilon}{\partial x^i}\right)+S-C_{\epsilon 2}\frac{\epsilon^2}{k} \tag{6}$$

where

$$\nu_{\text{eff}}=C_\mu\frac{k^2}{\epsilon},\quad k=\frac{1}{2}g_{ij}\overline{u^i u^j}$$

Nomenclature

$C_S, C_1, C_\epsilon, C_{\epsilon 1}, C_{\epsilon 2}, \gamma, D_6$ = constants in turbulence closure models
C = mean temperature
c = fluctuating temperature
c_p = specific heat
C_p = static pressure coefficient, $(P-P_0)\Big/\frac{1}{2}\rho_0 U_0^2$
C_{pt} = total pressure coefficient $(P_{t0}-P_t)\Big/\frac{1}{2}\rho_0 U_0^2$
$\bar{C}_{pt}$ = mass averaged total pressure coefficient, equation (21)
Fi = additional body force in equation (2)
g_{ij}, g^{ij} = metric tensor
k = turbulence kinetic energy
k_c = thermal conductivity
P = $-\overline{u_i u_j}U^i_{,j}$
p = static pressure
p' = fluctuating component of static pressure
P_c = Peclet number based on the grid spacing ($U\delta_k/\nu$)
R = gas constant
U, V, W = axial, normal, and spanwise mean velocities
u, v, w = axial, normal, and spanwise fluctuating velocities
U^i, u^i = contravariant mean and fluctuating velocity component
U_s = streamwise velocity
U_n = normal velocity
β = coefficient of thermal expansion
Ω_i = angular velocity of rotor
η = mass flow coefficient, equation (22)
δ_{ij} = Kronecker delta
$\epsilon_{ijk}, \epsilon^{ijk}$ = permutation tensor
ν = kinematic viscosity
ρ = density
θ = dissipation due to viscosity, equation (3)
τ_w = wall shear stress
Γ^i_{jk} = Christoffel symbol of second kind

Subscripts

p = pressure side
s = suction side
t = total
o = upstream
ms = midspan
1 = first mode near the wall
w = value at the wall

Superscripts

$-$ = average value
$*$ = intermediate value
$'$ = corrective value

Downloaded 01 Jun 2010 to 171.66.16.70. Redistribution subject to ASME license or copyright; see http://www.asme.org/terms/Terms_Use.cfm

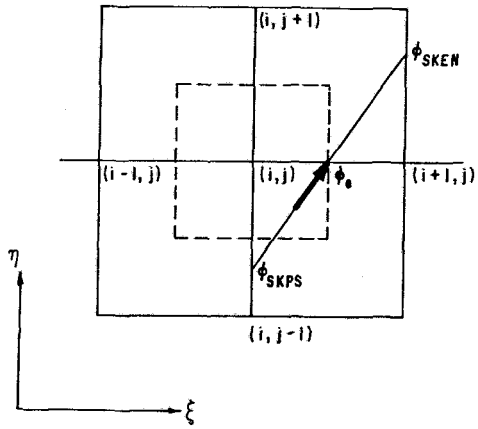


Fig. 1 Grid notation on control volume surface

and

$$S = C_S \frac{\epsilon^2}{k^3} (\overline{u^i u^j} - 2/3\ k\delta_{ij})(\overline{u^j u^i} - 2/3\ k\delta_{ji}) \tag{7}$$

The individual Reynolds stress components are obtained with the following algebraic equations.

$$0 = (1 + C_1)(-\overline{u_k u^j} U^i_{,k} - \overline{u_k u^i} U^j_{,k})(1 - \gamma) - 2(\epsilon^{ilm}\Omega_l \overline{u_m u^j} + \epsilon^{jlm}\Omega_l \overline{u_m u^i}) - 2/3 g^{ij}(1 - \gamma) - C_{\phi 1}\frac{\epsilon}{k}(\overline{u^i u^j} - 2/3 g^{ij}) + D_6 \Omega_n (\epsilon^{lnj}\overline{u_l u^j} + \epsilon^{lnj}\overline{u_l u^i}) \tag{8}$$

where γ, $C_{\phi 1}$ are constants in the modeling and C_1 is a variable which represents the collective effects of the convection and the diffusion terms in the exact transportation equation of the Reynolds stresses. The physical basis of equation (8) is explained in [15, 16] and the model was successfully applied for the prediction of curved flows inside various diffusers with the inlet swirl [14]. Various constants in the turbulence modeling are not optimized for the present study and the values are: $C_\mu = 0.09$, $C_{\phi 1} = 1.5$, $C_S = 1.8$, $C_{\epsilon 2} = 1.44$, $D_6 = 0.7$, $\delta_k = 1.0$, $\delta_\epsilon = 1.22$, and $\gamma = 0.6$.

Numerical Scheme and Boundary Conditions

Numerical Algorithm. The governing conservation equations are solved using a fully conservative control volume approach along with turbulence closure equations. The governing equations can be expressed in the following general form for the convenience of the formulation.

$$(\rho U_i \phi)_{,i} = (\Gamma \phi_{,i})_{,i} + S_\phi \tag{9}$$

where ϕ is any of the dependent variables (U, V, W, k or ϵ), Γ is the diffusion coefficient, and S_ϕ encompasses all remaining terms. The finite difference equations are formulated by integrating the above differential equations over arbitrarily shaped control volume. The mean velocity, temperature, and turbulence quantities are solved simultaneously with the assumed pressure field. The pressure field is adjusted to satisfy the mass conservation and the mean velocity components, and density is corrected based on the corrected pressure field. The overall procedure is an iterative line-by-line procedure and can be applied to both steady and unsteady problems. With the divergence theorem, equation (9) can be represented as follows for the arbitrarily shaped control volume.

$$\int_A \rho\ \phi\ U_i n_i dA = \int_A \frac{\Gamma_{\text{eff}}}{\sigma_\phi} \phi_{,i} n_i dA + \int_R S_\phi dR \tag{10}$$

where A is the boundary surface of the control volume R.

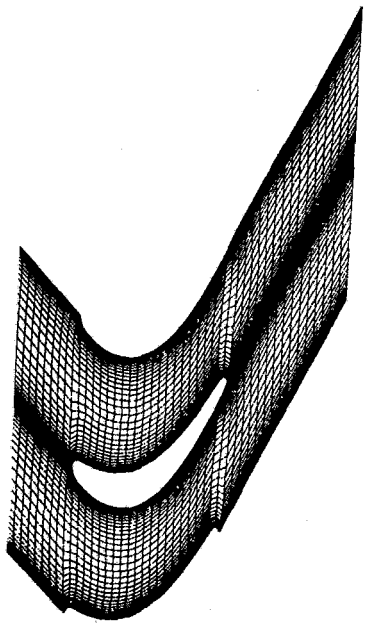


Fig. 2 Blade-to-blade grid

Various integrations in equation (10) are approximated by interpolating the values at nodal points of the computational grid. For the integration of the convection term [left-hand side of equation (10)], the value of the unknown variable should be estimated at the control volume surface. A simple two-dimensional grid on a computational plane is given in Fig. 1 for the convenience of the explanation. The most desirable way to specify the value of ϕ_e is by averaging the values at P and E (central differencing). However, the central differencing of the convection term causes instability in the solution when the cell Peclet number ($U\delta x/\nu$) exceeds two when the viscosity effect is neglected and alternate discretization of the convection term is required. The widely used upwind differencing assumes the value of ϕ_P or ϕ_E for ϕ_e, depending on the flow direction at e. Although the upwind differencing provides a stable solution regardless of the cell Reynolds number, significant amounts of "false" or numerical diffusion arise with the practical size of the grid because of the high truncation error. The numerical scheme for the incompressible flow using rectangular grids with the central upwind discretization is explained in detail by Gosman and Pun [17]. Therefore, the higher order discretization scheme and extension to the general nonorthogonal grids and compressible flow will be described in detail. The quadratic upstream interpolation scheme by Leonard [18] and the skew upwinding scheme by Raithby [19] have been properly extended and modified. The details of the modification and applications of the above schemes to the prediction of various diffuser flows with inlet swirl and inlet distortion are given in [14]. With the modified quick scheme, the following expression is used to estimate the unknown variables at the control volume surface.

$$\text{if } U_e \geq 0;\ \phi_e = \frac{6}{8}\phi_i + \frac{2}{8}\phi_{i+1} + \frac{1}{8}(\phi_{i+1} - \phi_{i-1}) \tag{11a}$$

$$\text{if } U_e < 0;\ \phi_e = \frac{6}{8}\phi_{i+1} + \frac{2}{8}\phi_i + \frac{1}{8}(\phi_i - \phi_{i+2}) \tag{11b}$$

where the first two terms in the right hand of the equation are programmed implicitly and the third and fourth terms are handled as extra source terms whose values are evaluated based on the results of the previous iteration. With the above formulae, the solution converges when the Peclet number is

Downloaded 01 Jun 2010 to 171.66.16.70. Redistribution subject to ASME license or copyright; see http://www.asme.org/terms/Terms_Use.cfm

less than four without any possible wiggles in the solution. When the Peclet number exceeds four and local instability is observed, upwind differencing is used for the local cells.

The skew upwinding scheme is aimed primarily at reducing the error due to the streamline-to-grid skewness. The value of dependent variables at the control volume surface is assessed by performing upwind differencing on the true streamline. The surface momentum flux at the point e is represented as follows with the modified skew upwinding scheme.

$$(U\phi)_e = \alpha_e(\phi_E[-[-U_e,0]] + \phi_P[[U_e,0]]) + \beta_e(\phi_{SE}[-[-U_e,0]] + \phi_S[[-U_e,0]]) \text{if } U_e \geq 0$$

or

$$\alpha_e(\phi_E[-[-U_e,0]] + \phi_P[[U_e,0]]) + \beta_e(\phi_{NE}[-[-U_e,0]] + \phi_N[[U_e,0]]) \text{if } U_e < 0 \qquad (12)$$

where $\alpha_e + \beta_e = 1$, α_e is a function of the angle between the streamline and the grid line, and the symbol $[[A,B]]$ denotes the greater of A and B. The first part of equation (12) is programmed implicitly and the second part is handled as additional source terms. With the above scheme, unknown values at 27 adjacent nodal points are used for formulation instead of seven points in the pure upwinding scheme.

Computational Grid. To represent the complex geometry of the turbine blade accurately and distribute the computational meshes in an optimum fashion, a nonorthogonal body-fitted coordinate system is used, and the governing equations are transformed accordingly. For the present study, the grid is generated by solving a set of Poisson equations, and mesh-point clustering is performed near the boundary with the method proposed by Steger and Sorenson [20].

The computational grid for the present study is given in Fig. 2 where two blade passages are shown to illustrate the grid distribution on the turbine blade. The computation is performed on the one blade-to-blade passage. Second-order forward or backward finite differences are used at the cells adjacent to the boundaries and the governing equations are integrated over the finite control volumes. No special treatments for the control volumes at the leading edge and the trailing edge have been performed.

The governing equation (10) can be written as follows on simple Cartesian coordinates.

$$\frac{\partial}{\partial x}(\rho U\phi) + \frac{\partial}{\partial y}(\rho V\phi) + \frac{\partial}{\partial z}(\rho W\phi) = \frac{\partial}{\partial x}\left(\Gamma^\phi \frac{\partial\phi}{\partial x}\right) + \frac{\partial}{\partial y}\left(\Gamma^\phi \frac{\partial\phi}{\partial y}\right) + \frac{\partial}{\partial z}\left(\Gamma^\phi \frac{\partial\phi}{\partial z}\right) + S^\phi \qquad (13)$$

As the blade geometry does not change in the spanwise direction (z-direction) for the test problems of the present study, coordinate transformation is performed only on the blade-to-blade surface. Then the above equation can be written in (ξ,η,z) coordinates as follows.

$$\frac{1}{J}\frac{\partial}{\partial\xi}(\rho G_1\phi) + \frac{1}{J}\frac{\partial}{\partial\eta}(\rho G_2\phi) + \frac{\partial}{\partial z}(\rho W\phi) = \frac{1}{J}\frac{\partial}{\partial\xi}\left[\frac{\Gamma^\phi}{J}(\alpha\phi_\xi - \beta\phi_\eta)\right] + \frac{1}{J}\frac{\partial}{\partial\eta}\left[\frac{\Gamma^\phi}{J}(\gamma\phi_\eta - \beta\phi_\xi)\right] + \frac{\partial}{\partial z}\left(\Gamma^\phi \frac{\partial\phi}{\partial z}\right) + S^\phi \qquad (14)$$

where

$$G_1 = Uy_\eta - Vx_\eta$$
$$G_2 = Vx_\xi - Uy_\xi$$
$$\alpha = x_\eta^2 + y_\eta^2$$
$$\beta = x_\xi x_\eta + y_\xi y_\eta$$
$$\gamma = x_\xi^2 + y_\xi^2$$

and J is the transformation Jacobian, $J = x_\xi y_\eta - x_\eta y_\xi$.

A fully staggered arrangement is employed for the velocities and pressures in order to avoid decoupling effects between velocity and pressure which are frequently observed with the normal grid arrangement. Wachpress [21] and Rhie and Chow [22] derived a similar formulation on nonorthogonal curvilinear coordinates for the two-dimensional case with different grid arrangements (partially-staggered or normal grid). Their validity and relative merits should be further assessed for a wide range of problems. With the staggered grid, an axial velocity component node is located at the leading edge of the blade. The values of pressure on the boundary are extrapolated from the inner solution.

Boundary Conditions and Solution Procedure. The inlet boundary conditions were taken from the measurement where possible. The distribution of the turbulence kinetic energy at inlet was estimated using the equilibrium theory. The rate of energy dissipation at the inlet section was obtained from

$$\epsilon = C_\mu k^{3/2}/L \qquad (15)$$

where L is the characteristic length scale and $L = 0.01\,L_1$ (L_1 is the pitch of the cascade). At the exit plane, the asymptotic boundary condition (the second-order streamwise derivation of unknown variables is zero) is used and the overall mass conservation through the cascade flow passage is strictly imposed by correcting the outlet velocity components with the calculated velocity profiles on the plane next to the outlet and the inlet flow mass during iteration. The wall function for the velocity vector is used to reduce the grid points near the wall. At nodes nearest to the solid walls, the velocity vector is assumed to be on the plane parallel to the solid walls, and wall function is applied for the velocity vector. With the assumption of local equilibrium and the wall function, the following relationships are obtained at the node next to the wall

$$\tau_w = \frac{\rho C_\mu^{1/4} k_1^{1/2} U_1}{A\,ln(y_1 C_\mu^{1/4} k_1^{1/2}/\nu) + B} \qquad (16a)$$

$$\epsilon_1 = A\frac{C_\mu^{3/4} k_1^{3/2}}{y_1} \qquad (16b)$$

where $A = 2.40$, $B = 5.45$, and y_1 is the distance from the wall. The value of k_1 is estimated from the transport equation of the turbulence kinetic energy by neglecting the convective and diffusive effects through the wall. The first node is located 0.003 chords away from the wall, and the node is located inside the inertial sublayer ($30 < y_1\sqrt{\tau_w/\rho}/\nu < 400$). The periodicity conditions are also strictly imposed on the corresponding nodes. All velocity components, pressure, density, and corrective values of all the variables are the same on the periodic boundary nodes. The fluctuations of the mass flow rate at each axial plane are monitored during iteration and when the total mass flow residual divided by the inlet mass flow rate is less than 10^{-3}, the solution is assumed to be converged. About 75 s is required per iteration on a VAX 11/780 with $53\times31\times20$ nodes, and the solution converges with 850 iterations.

The sequence of solution is as follows. The three momentum equations are first solved to get three velocity components with the intermediate pressure field. In solving the momentum equations, the values of ρG_1, ρG_2, and ρW at the control volume surface are updated after each complete sweep of the flow domain. As the new velocity and density fields obtained with the intermediate pressure field do not satisfy the mass conservation, the pressure field is adjusted toward the satisfaction of the continuity equation. For this purpose, the following expressions are used for corrections.

Downloaded 01 Jun 2010 to 171.66.16.70. Redistribution subject to ASME license or copyright; see http://www.asme.org/terms/Terms_Use.cfm

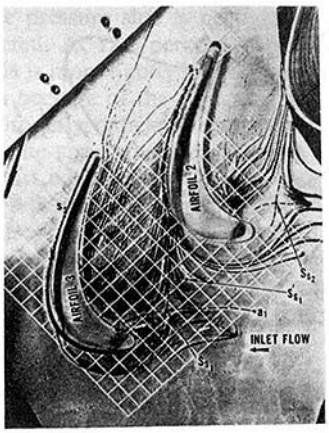


Fig. 3 Experimentally obtained limiting streamlines on the endwall (experiment by Langston et al. [6])

$$G_1 = G_1^* + G_1' \tag{17a}$$

$$G_2 = G_2^* + G_2' \tag{17b}$$

$$W = W^* + W' \tag{17c}$$

$$p = p^* + p' \tag{17d}$$

$$\rho = \rho^* + \rho' \tag{17e}$$

where the superscript * denotes values with intermediate pressure field and ′ denotes the corrective values. The corrective values should be estimated based on the continuity equation. For this purpose, G_1', G_2', W' and ρ' should be related to p'. The following relationships are obtained based on the momentum equations and gas state equation

$$G_1' = (B_\xi y_\eta - C_\xi x_\eta) p_\xi' + (B_\eta y_\eta - C_\eta x_\eta) p_\eta' \tag{18a}$$

$$G_2' = (C_\eta x_\xi - B_\eta y_\xi) p_\eta' + (C_\xi x_\xi - B_\xi y_\xi) p_\xi' \tag{18b}$$

$$W' = D p_z' \tag{18c}$$

$$\rho' = \frac{p'}{RT} \tag{18d}$$

where the terms B_ξ, B_η, C_ξ, and C_η are from the following discretized momentum equations

$$U_p^* = B_\xi p_\xi^* = B_\eta p_\eta^* + \text{ other terms} \tag{19a}$$

$$V_p^* = C_\xi p_\xi^* = C_\eta p_\eta^* + \text{ other terms} \tag{19b}$$

$$W' = D p_z' + \text{ other terms} \tag{19c}$$

To obtain the simplified relationships shown in equation (18), all the other terms on the right-hand side of equation (19) are neglected.

Equations (17) are combined into the continuity equation (1) to obtain the corrective pressure field p', and the corrective values of G_1', G_2', W', and ρ' are estimated using equation (18). From the values of G_1' and G_2', the corrections for the velocity components U' and V' are further obtained by using similar arguments for U and V

$$U = U^* + U' \tag{20a}$$

$$V = V^* + V' \tag{20b}$$

and combining equations (20) and (17) and (18).

The pressure corrections on the present nonorthogonal coordinates are strict extensions of the pressure corrections on rectangular coordinates with the staggered grid arrangement. The second terms in equations (19*a*) and (19*b*) are due to the nonorthogonality of the grid, and these additional terms vanish when the coordinate becomes orthogonal and all the formulation automatically becomes the formulation on the orthogonal grid system. For nonorthogonal grids used for the present problem, the second terms in equations (19*a*) and (19*b*) are not negligibly small and should be properly included in the estimation of G_1' and G_2' for the converged solution. Although the simultaneous correction for the velocity and density is found to be necessary for fast convergence when the local Mach number is relatively high, the procedure is not important for the present test problem because the flow is nearly incompressible.

After solving the momentum and continuity equations, the energy and the turbulence equations are solved with updated correction terms. The above procedures have been suc-

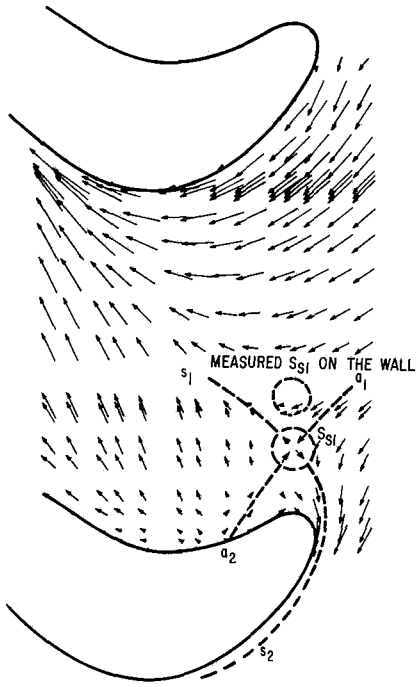


Fig. 4(*a*) Predicted velocity vector inside the wall boundary layer (1 percent span) with the inlet angle at 44.6 deg

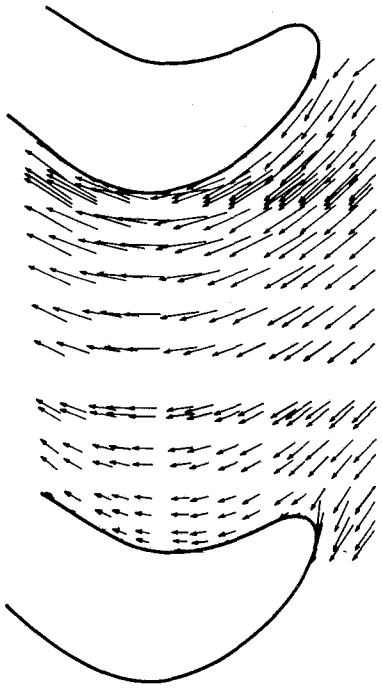


Fig. 4(*b*) Predicted velocity vector at the midspan with the inlet angle of 44.6 deg

Downloaded 01 Jun 2010 to 171.66.16.70. Redistribution subject to ASME license or copyright; see http://www.asme.org/terms/Terms_Use.cfm

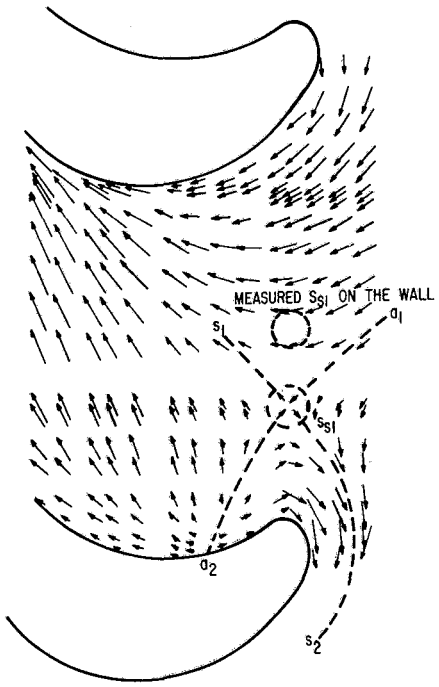


Fig. 5 Predicted velocity vector inside the wall boundary layer (1 percent span) with decreased inlet angle

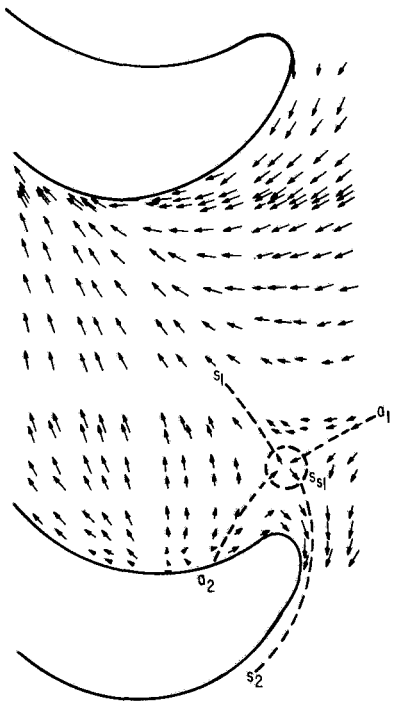


Fig. 6 Predicted velocity vector inside the wall boundary layer (1 percent span) with the fully developed inlet boundary layer

cessfully applied for the prediction of various diffuser flows with the inlet swirl [14].

Comparison Between the Numerical Prediction and the Experimental Data. The experimental data on three-dimensional flows within a turbine cascade passage reported by Langston et al. [6] are used for comparison purposes. The experimental study includes a detailed survey of the velocity and the static pressure across the whole flow domain and flow visualization at the endwall in a large-scale, plane turbine cascade. More detailed interpretations of the cross flows are also given by Langston [23]. Some of the important parameters of the cascade geometry are

- Axial chord: 0.2813 M
- Pitch/axial chord: 0.9555
- Aspect ratio: 0.9888

The inlet flow condition is a uniform velocity profile at 0.66 M upstream of the leading edge with an equilibrium boundary layer. The inlet Reynolds number based on the blade axial chord is 5.9×10^5 and Mach number around 0.1. The boundary layer thickness is 0.033 M with a shape factor of 1.35. Detailed measurements with an inlet angle of 44.6 deg are reported along with additional flow visualization results for a lower inlet angle.

Mean Velocity. The inlet wall boundary layer separates and forms a horseshoe vortex near the leading edge with one leg of the vortex in one airfoil passage and the other leg in the adjacent passage. Large amounts of crossflow are generated because of the vortex motion in this passage and the secondary flows from various origins (pressure-driven, turbulence-driven, etc.). One of the most important and interesting features of the limiting streamline is the separation saddle point, S_{s1} between two airfoils. This saddle point occurs where the horseshoe vortex is formed and the two attachment lines ($S_{s1}a_1$ and $S_{s1}a_2$) and two separation lines ($S_{s1}s_1$ and $S_{s2}s_2$) divide the entire flow field near the endwall into distinct regions of three-dimensional flows. Langston et al. [6] argued that the location of the separation saddle point is mainly decided by the pressure field and took another measurement with a higher inlet flow angle. The points S'_{s1} in Fig. 3 represent the new saddle point with a decreased inlet angle (from 44.6 deg to 32.2 deg). The computed velocity vector at 1 percent span from the endwall is shown in Fig. 4 and at midspan in Fig. 5. The computation uses a grid of $53\times31\times20$ nodes in axial, pitchwise, and spanwise directions. The computational domain is one complete flow passage from the 50 percent axial chord upstream of the leading edge and 50 percent axial chord downstream of the trailing edge of the blade. As shown in Fig. 4, the numerical results also confirm the separation saddle point and the details of the separation lines and the reattachment lines around the three-dimensional singular point. The experimentally obtained saddle point on the wall is also shown in Fig. 4. The computed saddle point is based on the velocity on the plane which is away from the wall (1 percent span) and better agreement is obtained if extrapolation of the velocity component is used. The numerical results in Fig. 5 also indicate that the separation point is further moved toward the suction side of the passage and upstream of the leading edge, and the crossflow field becomes more severe. The location of the saddle point and its surrounding attachment and separation lines are a function of the cascade geometry and inlet flow conditions (inlet angle and the character of the inlet wall boundary layer). To examine the effect of the inlet boundary layer thickness, the flow field is calculated with fully developed inlet boundary layer, and the resulting velocity field near the leading edge is shown in Fig. 6. Comparison of Figs. 4 and 6 indicates that when the inlet flow has thicker boundary layer, the separation saddle point is moved toward the pressure side of the passage and upstream of the airfoil. Also the crossflow becomes more severe. The overall effect of thicker inlet boundary layer is similar to that due to decreasing the inlet flow angle although the magnitude of the effect is much smaller.

Static Pressure Distribution. The static pressure distributions on the blade surface are compared in Figs. 7, 8, and 9. The experimental spanwise variation of the static

Downloaded 01 Jun 2010 to 171.66.16.70. Redistribution subject to ASME license or copyright; see http://www.asme.org/terms/Terms_Use.cfm

pressure on the pressure side is negligible and this trend is properly predicted. At 12.5 percent of the span, the suction side of the blade is more lightly loaded compared to the value of the midspan because of the flow separation on the blade, which is also properly indicated by the numerical result. At 2.3 percent of the span, the measurement shows the static pressure is almost constant on the suction side of the blade due to the flow separation. The numerical result at 2.3 percent of the span also indicates much flattened static pressure distribution on the suction side, although some deviations are observed near the trailing edge of the blade. The static pressure distributions on the endwall are compared in Fig. 10.

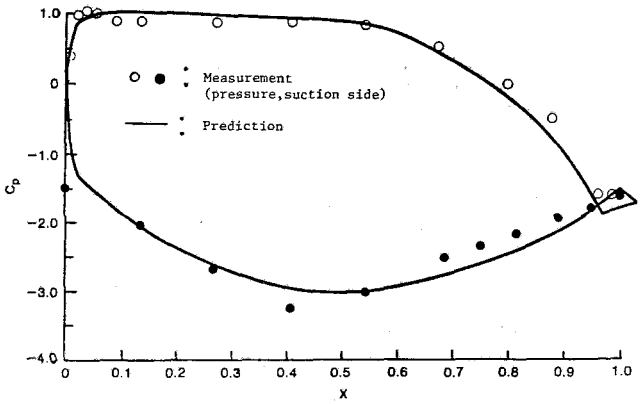


Fig. 7 Comparison of static pressure distribution on blade surface at midspan (experiment by Langston et al. [6])

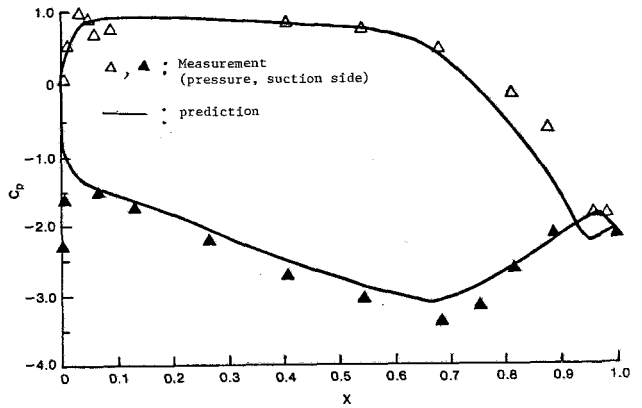


Fig. 8 Comparison of static pressure distribution on blade surface at 12.5 percent span (experiment by Langston et al. [6])

Due to the strong secondary flow activity, the minimum pressure occurs in the passage off the blade surface. Local maximum static pressure is also observed near the separation saddle point. These two distinctive physical features are also clearly shown by the numerical prediction although there is some quantitative disagreement.

Secondary Flow Velocity. Figure 11 shows the comparison of the streamwise and the normal velocity components inside the endwall boundary layer at 69.2 percent chord and 23 percent passage height from the suction side. Although the prediction indicates milder secondary velocity profiles compared to the measurements [23], the qualitative trend is well predicted for this very complex flow field. The velocity vector plots of the secondary flow in the plane of constant axial distance (82.1 percent of the axial chord) are compared in Figs. 12 and 13. The velocity vector shown in Figs. 12 and 13 is obtained by subtracting vectorally the midspan component from the local velocity and it approximately represents the secondary flow field. The predicted center of the vortical motion is located further from the blade suction surface compared to the flow measurement.

Aerodynamic Loss Coefficient. Figure 14 shows the comparison of the mass-averaged loss coefficient as a function of axial distance. The mass-averaged aerodynamic loss coefficient at each axial plane is defined as follows.

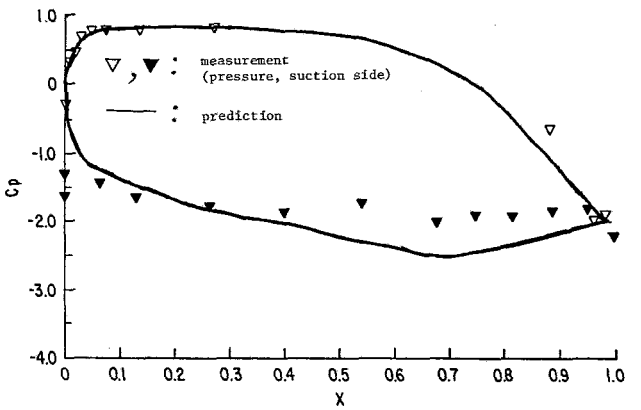


Fig. 9 Comparison of static pressure distribution on blade surface at 2.3 percent span (experiment by Langston et al. [6])

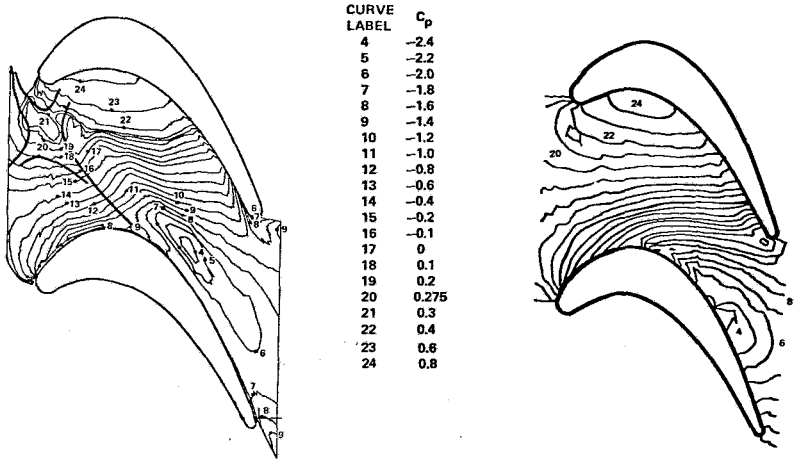


Fig. 10 Comparison of the static pressure distribution on the endwall

Downloaded 01 Jun 2010 to 171.66.16.70. Redistribution subject to ASME license or copyright; see http://www.asme.org/terms/Terms_Use.cfm

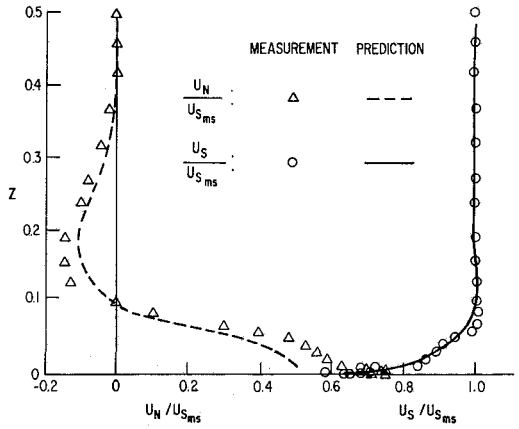


Fig. 11 Comparison of the streamwise and the normal velocity components inside wall boundary layer at 69 percent axial chord and 23 percent passage height away from the suction side

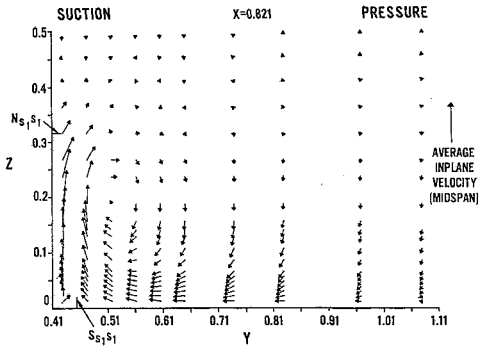


Fig. 12 Measured secondary flow velocity vector in plane of 82.1 percent axial chord (experiment by Langston et al. [6])

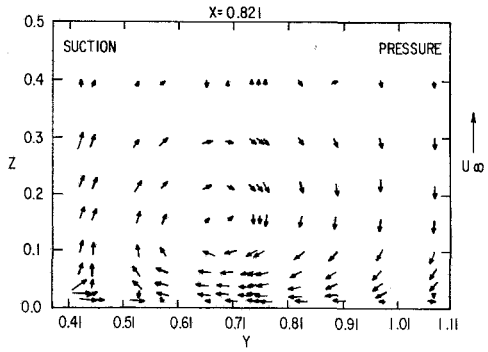


Fig. 13 Predicted secondary flow velocity vector in plane of 82.1 percent axial chord

$$\bar{C}_{pt} = \frac{\int_{y_s}^{y_p} \int_0^{MS} C_{pt} U_x dz dy}{\int_{y_s}^{y_p} \int_0^{MS} U_x dz dy} \tag{21}$$

where the integration is from the endwall to the midspan of the blade passage. Also the following mass flow coefficient based on the experimental data is shown on the figure.

$$\eta = \frac{\int_{y_s}^{y_p} \int_0^{MS} U_x dz dy}{\left[\int_{y_1}^{y_2} \int_0^{MS} U_x dz dy\right]_{\text{Plane 1}}} \tag{22}$$

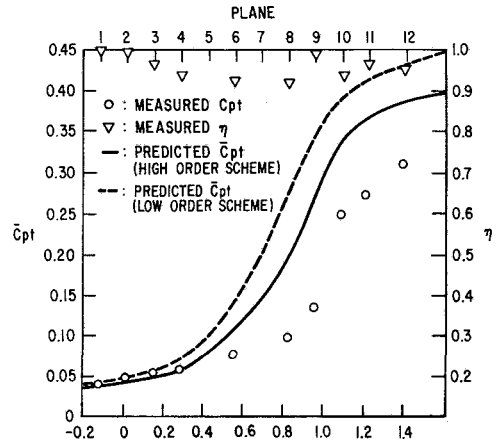


Fig. 14 Comparison of the mass-averaged loss coefficient (experiment by Langston et al. [6])

Third-order polynomials are used between nodes to perform the integrations. The results with the pure upwind differencing scheme for the convection term are also compared in Fig. 14. With the present prediction method, the total mass at each axial plane is almost absolutely preserved, and the fluctuation of the total mass flow rate is less than 0.1 percent. Although the numerical solution predicts higher growth of the aerodynamic loss than the experimentally observed one, the overall trends (sudden jump near the trailing edge and more gradual increase downstream of the trailing edge region) are well predicted. Finer computational meshes near the wall and more sophisticated turbulence closure model may produce better predictions.

Conclusions

A numerical model is developed for calculation of the three-dimensional turbulent flows inside a turbine blade passage. The governing equations are solved in nonorthogonal curvilinear coordinates. Higher-order discretization schemes for the convection term are applied to reduce the numerical diffusion, and an algebraic Reynolds stress model modified for the streamline curvature effect is used. The important conclusions drawn from this study are as follows:

1 The developed numerical scheme is fully elliptic and is based on the fully conservative control volume approach, and is applied using numerically generated nonorthogonal curvilinear coordinates. This method predicts most of the three-dimensional viscous phenomena inside a turbine blade passage with accuracy satisfactory for the engineering practice.

2 The effects of inlet angle and inlet boundary layer thickness on the location of the separation saddle point and associated separation and reattachment lines are correctly simulated, and the importance of these effects on the entire flow field is confirmed numerically.

3 The qualitative characteristics of the secondary flow field is reasonably well predicted in spite of the extreme complexity of the flow field.

4 The local pressure loss and the trends of mass-averaged total aerodynamic losses are qualitatively predicted.

5 The presently developed numerical method can be used to study the effects of endwall contouring, optimum geometry, and other design parameters. Efforts are now being made in this direction.

References

1 Salvage, J. W., "A Review of the Current Concept of Cascade Secondary Flow Effects," von Karman Institute for Dynamics Technical Note 95, Mar. 1974.

Downloaded 01 Jun 2010 to 171.66.16.70. Redistribution subject to ASME license or copyright; see http://www.asme.org/terms/Terms_Use.cfm

2 Herzig, H. Z., Hansen, A. G., and Costello, G. R., "A Visualization Study of Secondary Flows in Cascades," NACA Report 1163, 1953.

3 Came, P. M., "Secondary Loss Measurements in a Cascade of Turbine Blades," Institution of Mechanical Engineers, Conference Publ. 3, 1973, pp. 75–83.

4 Waterman, W. F., and Tall, W. A., "Measurement and Prediction of Three-Dimensional Viscous Flows in Low Aspect Ratio Turbine Nozzles," ASME Paper 76-GT-73, 1976.

5 Goldman, L. J., and McLallin, K. L., "Cold Air Annular Cascade Investigation of Aerodynamic Performance of Cooled Turbine Vanes," NASA TM X-3006, 1974.

6 Langston, L. S., Nice, M. L., and Hooper, R. M., "Three-Dimensional Flow Within a Turbine Cascade Passage," ASME JOURNAL OF ENGINEERING FOR POWER, Vol. 99, No. 1, Jan. 1977.

7 Patankar, S. V., and Spalding, D. B., "A Calculation Procedure for Heat, Mass and Momentum Transfer in Three-Dimensional Parabolic Flows," *International Journal of Heat and Mass Transfer*, Vol. 15, 1972, pp. 1787–1806.

8 Briley, W. R., "Numerical Method for Predicting Three-Dimensional Steady Viscous Flows in Ducts," *Journal of Computational Physics*, Vol. 14, No. 1, 1974, pp. 8–28.

9 Dodge, R. P., "A Numerical Method for Two-Dimensional and Three-Dimensional Viscous Flows," AIAA Ninth Fluid and Plasma Dynamics Conference, AIAA Paper No. 76-425, July 1976.

10 McNally, W. D., and Sockol, P. M., "Computational Methods for Internal Flows with Emphasis on Turbomachinery," NASA Technical Memorandum X-2764, 1981.

11 Moore, J., and Moore, J. G., "Viscous Flow Calculations in Turbomachinery," *VKI Lecture Series 1982–05*, Vol. 2, 1982.

12 Raithby, G. D., "A Critical Evaluation of Upstream Differencing Applied to Problems Involving Fluid Flow," *Computer Methods in Applied Mechanics and Engineering*, Vol. 9, 1976, pp. 75–103.

13 Leschziner, M. A., and Rodi, W., "Calculation of Annular and Twin Parallel Jets Using Various Discretization Schemes and Turbulence Model Variations," ASME *Journal of Fluids Engineering*, June 1981, pp. 352–360.

14 Hah, C., "Calculation of Planar, Conical, and Annular Diffuser Flows with Inlet Swirl and Inlet Distortion Effects," to appear in *AIAA Journal*.

15 Hah, C., and Lakshminarayana, B., "Prediction of Two- and Three-Dimensional Asymmetric Turbulent Wakes, Including the Comparison of Turbulence Models," *AIAA Journal*, Vol. 18, Oct. 1980, pp. 1196–1204.

16 Hah, C., "Three-Dimensional Structure and Turbulence Closure of the Wake Developing in a Wall Shear Layer," *AIAA Journal*, Vol. 20, Nov. 1982, pp. 1599–1605.

17 Gosman, A. D., and Pun, W. M., "Calculation of Recirculating Flows," (Lecture Notes), Department of Mechanical Engineering, Imperial College, London, Rep. No. HTS/74/2, 1974.

18 Leonard, B. P., "A Stable and Accurate Convective Modeling Procedure Based on Quadratic Upstream Interpolation," *Computer Methods in Applied Mechanics and Engineering*, Vol. 19, 1979, pp. 59–98.

19 Raithby, G. D., "Skew-Upwind Differencing Schemes for Problems Involving Fluid Flow," *Computer Methods in Applied Mechanics and Engineering*, Vol. 9, 1976, pp. 153–164.

20 Sorenson, R. L., and Steger, J. L., "Numerical Generation of Two-Dimensional Grids by the Use of Poisson's Equations with Grid Control at Boundaries," *Proceedings of Workshop on Numerical Grid Generation*, NASA Langley Research Center, Oct. 1980.

21 Wachpress, E. L., "The Numerical Solution of Turbulent Flow Problems in General Geometry," General Electric Company Report KAPL-4116, 1979.

22 Rhie, C. M., and Chow, W. L., "A Numerical Study of the Turbulent Flow Past an Isolated Airfoil with Trailing Edge Separation," AIAA Paper 82-0998, 1982.

23 Langston, L. S., "Crossflows in a Turbine Cascade Passage," ASME Paper No. 80-GT-5, 1980.

Downloaded 01 Jun 2010 to 171.66.16.70. Redistribution subject to ASME license or copyright; see http://www.asme.org/terms/Terms_Use.cfm

Calculation of Three-Dimensional, Inviscid, Rotational Flow in Axial Turbine Blade Rows

W. Van Hove
von Karman Institute for Fluid Dynamics,
B-1640 Rhode Saint Genese, Belgium
and
Rijksuniversiteit Gent, Belgium

This paper describes a fully explicit, time marching, corrected viscosity, finite volume method to solve the Euler equations in a cylindrical coordinate system. The rotational character of the incoming flow can be taken into account. On the outflow boundary, a generalized radial equilibrium condition is imposed. Blade rows of complex geometry can be handled. At present, the method has been used to calculate the flow through the nozzle vanes of the VKI low-speed turbine facility. The calculated results show good agreement with the experimental data for the spatial distribution of both the static pressure and the flow angle.

Introduction

This paper describes a method to calculate three-dimensional, inviscid, rotational flow in axial turbomachinery blade rows of complex geometry. The equations solved are the Euler equations with respect to a cylindrical coordinate system fixed to the blade row. The centrifugal and coriolis forces are taken into account. On the inflow boundary, radial gradients of the flow can be introduced, allowing the calculation of rotational flow. On the outlet boundary, a generalized radial equilibrium condition is used. The back pressure is imposed only at one radius and the radial outlet pressure distribution is part of the solution.

All calculation methods presented in the literature to solve the three-dimensional Euler equations in a turbomachinery blade passage are explicit time marching methods. Two approaches can be distinguished. The first one uses the MacCormack explicit discretization scheme, either in finite difference form in a rectangular computational domain obtained after a coordinate transformation [16, 20, 21] or directly in finite volume formulation in the physical domain [4]. The MacCormack scheme is second-order accurate in time and additional artificial viscosity is usually required to correctly capture shock waves. Other authors prefer to use schemes that are only first-order accurate in time but introduce an important dissipative effect during the time marching procedure to increase the convergence speed [2, 3, 8, 9, 10, 17]. The corrected viscosity scheme presented in this paper belongs to the latter group of methods. It is a single step, explicit discretization scheme derived from the original Lax scheme. The scheme is quite easy to program, is computer memory efficient and needs a minimum computational effort per iteration.

The blade passage of a turbomachine can have a very complex shape. Some authors prefer to transform the blade passage into a rectangular domain [16, 20, 21] and discretize the transformed equations with the MacCormack scheme which is also second-order accurate in space in a rectangular grid. The conservative form of the transformed equations is not easy to obtain. The simple stretching functions used for the transformation will lead to precision problems in highly cambered turbine blades with rounded leading and trailing edge. In this paper the finite volume or control volume method is used, discretizing directly the physical domain. This method, first used by McDonald for blade-to-blade flow calculations [15], is now widely used for turbomachinery calculations. Applications to three-dimensional, invisicid flow in turbomachinery bladings are reported in [2, 3, 4, 8, 9, 10, 17]. The control volume proposed in this paper, like the one used by Denton [8, 9, 10, 17], involves only six surrounding points to approximate the fluxes through the surface of the control volume, thus minimizing the computational effort per control volume. The resultant discretization is conditionally consistent and generally first order accurate.

The aim of the present paper is not to propose an improved method showing better accuracy and/or shorter calculation time than existing ones, but to demonstrate the possibilities and limitations of such a method to calculate three-dimensional, rotational flow. To this purpose the calculation method was applied to calculate the flow through the nozzle vanes of the VKI low-speed turbine facility. Detailed measurements of the three-dimensional flow field inside and downstream of the blade passage are available [19] for comparison with the calculated flow field. The geometry is fairly simple and the flow is incompressible, but important secondary flows are present. To the author's knowledge, such a comparison between measured and calculated secondary flows in an annular turbine cascade has not yet been published in the literature.

Equations

For turbomachinery blade row calculations it is convenient

Contributed by the Gas Turbine Division of THE AMERICAN SOCIETY OF MECHANICAL ENGINEERS and presented at the 28th International Gas Turbine Conference and Exhibit, Phoenix, Arizona, March 27-31, 1983. Manuscript received at ASME Headquarters, December 27, 1982. Paper No. 83-GT-119.

Copyright © 1984 by ASME
Downloaded 01 Jun 2010 to 171.66.16.70. Redistribution subject to ASME license or copyright; see http://www.asme.org/terms/Terms_Use.cfm

to express the Euler equations in a cylindrical coordinate system fixed to the blade row, rotating with constant angular velocity Ω around the z-axis which coincides with the machine axis.

The integral form of the equations is used. Suitably nondimensionalized and written in matrix form for convenience, the basic equations are

$$\frac{\partial \sigma}{\partial t} + \nabla \cdot F(\sigma) = b(\sigma) \frac{\partial \sigma}{\partial t} \tag{1}$$

$$+ \frac{1}{r}\frac{\partial r f_r(\sigma)}{\partial r} + \frac{1}{r}\frac{\partial f_\theta(\sigma)}{\partial \theta} + \frac{\partial f_z(\sigma)}{\partial z} = b(\sigma)$$

$$\sigma = \begin{pmatrix} \rho \\ \rho w_r \\ \rho w_\theta \\ \rho w_z \\ \rho e_R \end{pmatrix} \qquad b(\sigma) = \begin{pmatrix} 0 \\ \rho w_\theta^2/r + p/r + \rho r\Omega^2 + 2\rho\Omega w_\theta \\ -\rho w_r w_\theta/r - 2\rho\Omega w_r \\ 0 \\ 0 \end{pmatrix}$$

$$f_r(\sigma) = \begin{pmatrix} \rho w_r \\ \rho w_r^2 + p \\ \rho w_r w_\theta \\ \rho w_r w_z \\ \rho h_R w_r \end{pmatrix}$$

$$f_\theta(\sigma) = \begin{pmatrix} \rho w_\theta \\ \rho w_r w_\theta \\ \rho w_\theta^2 + p \\ \rho w_\theta w_z \\ \rho h_R w_\theta \end{pmatrix} \qquad f_z(\sigma) = \begin{pmatrix} \rho w_z \\ \rho w_r w_z \\ \rho w_\theta w_z \\ \rho w_z^2 + p \\ \rho h_R w_z \end{pmatrix}$$

Using the ideal gas law, the following closure relation expressing the pressure in terms of the basic unknowns is obtained

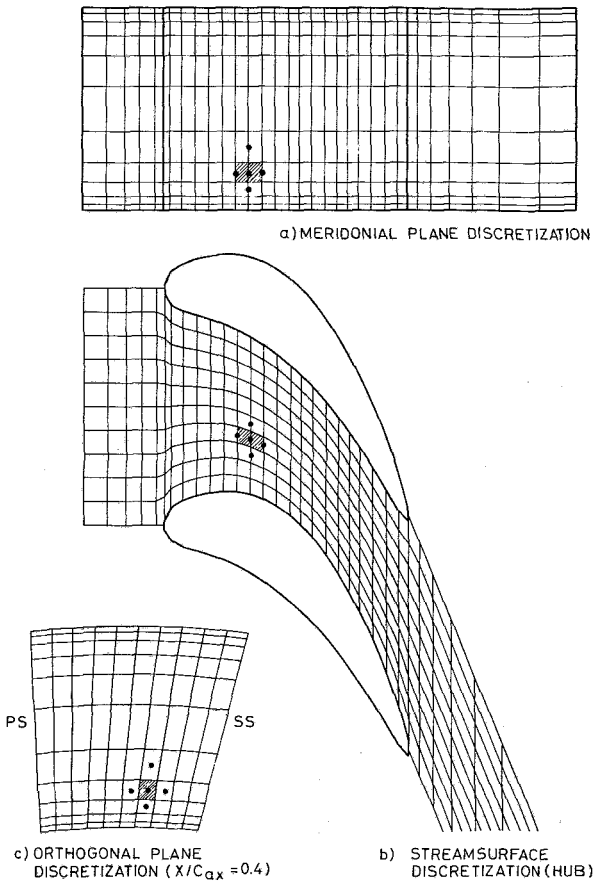


Fig. 1 Blade passage discretization (coarse grid)

$$p = (\kappa - 1)\rho\left(e_R - \frac{w^2}{2} + \frac{\Omega^2 r^2}{2}\right) \tag{2}$$

Grid

The computational domain consists of one blade passage with up- and downstream periodic extensions approximately along the flow direction. These extensions permit the in-

Nomenclature

c_{ax} = axial chord length
c_p, c_v = specific heats, $\kappa = c_p/c_v$
CP_s = static pressure coefficient, $CP_s = \underline{\underline{(p_{01,FS} - p_s)}} / (p_{01,FS} - p_{s2})$
e = internal energy, $e = c_v T$
e_R = $e + \frac{W^2}{2} - \frac{\Omega^2 r^2}{2}$
h = blade height
h_R = rothalpy, $h_R = e_R + \frac{p}{\rho}$
N = number of blades
$\mathbf{n}$ = unity vector normal to a surface
p = pressure
r,θ,z = cylindrical coordinates
S = closed surface around the control volume
t = time
T = temperature
V = volume of the control volume
w = relative velocity, $w = |\mathbf{w}|$
x = axial coordinate, $x = 0$ at leading edge
y = radial coordinate, $y = 0$ at hub
α = viscosity coefficient
β = pitchwise flow angle, $\beta = \text{atg}(w_\theta/w_z)$
γ = radial flow angle, $\gamma = \text{atg}(w_r/w_z)$
Δ = typical grid dimension
Δt = time step
ω = loss coefficient, $\omega = (p_{01,FS} - p_0)/(p_{01,FS} - p_{s2})$
Ω = angular velocity of the blade
ρ = density

Subscripts

FS = free stream
i, j, k = r,θ,z coordinate index
irr = irrotational flow
l = time index
l_0 = updating time index
m = relative to one side surface of the control volume
r,θ,z = components in coordinate direction
s = static quantity
sec = secondary flow
u = outward
0 = total quantity
1 = inlet
2 = outlet

Superscripts

$\overline{}$ = pitchwise averaged
$\underline{\underline{}}$ = pitch- and spanwise averaged

Downloaded 01 Jun 2010 to 171.66.16.70. Redistribution subject to ASME license or copyright; see http://www.asme.org/terms/Terms_Use.cfm

troduction of pitchwise uniform in- and outlet boundary conditions. The domain is divided into elementary grid cells using three families of surfaces (Fig. 1):

— streamwise surfaces, variably spaced between hub and tip, which are the two limiting surfaces;

— orthogonal surfaces, variably spaced between inlet, leading edge, trailing edge and outlet. The in- and outlet planes are chosen perpendicular to the z-axis. Both the leading and trailing edge define an orthogonal surface;

— bladewise surfaces, evenly spaced over the blade passage. The suction side of one blade and the pressure side of the next blade, both with their up- and downstream periodic extensions, are the two limiting surfaces.

The points at which the equations are solved, are located in the center of the orthogonal side surfaces of the grid cells. This location of the calculation points not only reduces the number of points by one in the radial and circumferential directions, but it also greatly simplifies the treatment of the solid wall boundary condition.

Two consecutive grid cells in the axial direction constitute the control volume used to discretize the equations around the central calculation point. Figure 2 shows the control volume in its most general geometric configuration.

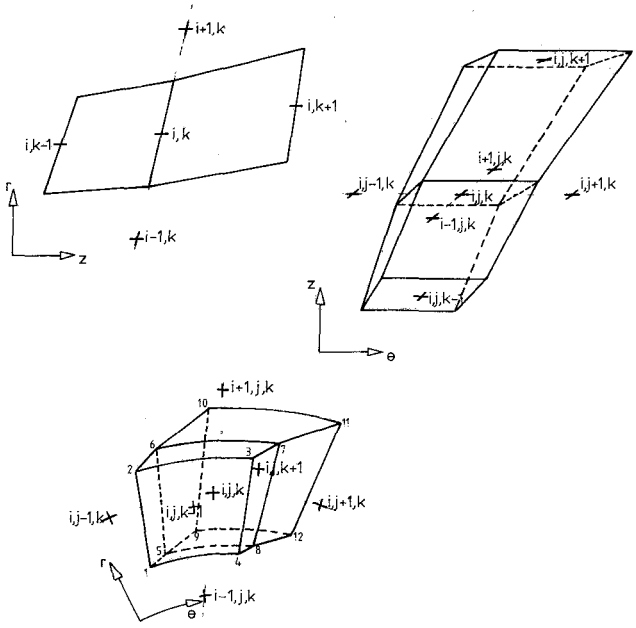


Fig. 2 Control volume

Corrected Viscosity Scheme

This one step explicit discretization scheme was first introduced by McDonald [5] in an attempt to increase the accuracy of his calculation method [15]. It was subsequently used for blade-to-blade flow calculations, with a time marching finite volume method with different types of control volumes [1, 6, 7, 14]. Stability, accuracy and convergence speed have been investigated by several authors [5, 6, 7, 12, 13, 14, 22].

For a point in the flow field, the discretized equations become

$$\sigma^{l+1}_{i,j,k} = -\frac{\Delta t}{V}\left[\iiint_S F \cdot \mathbf{n}_u dS\right]^l + \Delta t\, b^l_{i,j,k}$$

$$+\frac{1}{6}\left(\sigma^l_{i-1,j,k}+\sigma^l_{i+1,j,k}+\sigma^l_{i,j-1,k}+\sigma^l_{i,j+1,k}+\sigma^{l+1}_{i,j,k-1}+\sigma^l_{i,j,k+1}\right)$$

$$-\frac{\alpha}{6}\left(\sigma^{l0}_{i-1,j,k}+\sigma^{l0}_{i+1,j,k}+\sigma^{l0}_{i,j-1,k}+\sigma^{l0}_{i,j+1,k}+\sigma^{l0}_{i,j,k-1}\right.$$

$$\left.+\sigma^{l0}_{i,j,k+1}-6\sigma^{l0}_{i,j,k}\right) \qquad (3)$$

(Note that in the third term on the right-hand side the updated value $l+1$ is used at $k-1$.)

Integrating (1) over the control volume and approximating the time derivative with a forward discretization in which the term at time level l is replaced by an average value over the surrounding points, yields (3), with the exception of the last term on the right-hand side. This is in fact the original Lax scheme which was used by McDonald [15] in his time marching finite area blade-to-blade flow calculation and which has a high convergence speed but a poor accuracy due to the introduction of an important numerical viscosity (the third term on the right-hand side of (3) introduces second order derivatives with coefficients of order Δ). The last term on the right-hand side of (3) is a correction term for this numerical viscosity. The correction term remains constant during IT iterations and is then updated for the next IT iterations. The updating rate IT should be chosen as small as possible to increase convergence speed, but below a certain limit the calculation becomes unstable. The resultant corrected viscosity scheme (3) is stable for the Courant-Friedrichs-Lewy condition (provided IT is large enough), which limits the time step for all explicit discretization schemes, and it has good convergence speed properties. The accuracy at convergence is determined by the accuracy of the approximation used for the surface integral in (3). The time history of the calculation is completely artificial. The viscosity coefficient $\alpha = 1-\epsilon$, where ϵ is a small positive number, permits the retention of some viscosity in the scheme to capture shock waves.

Finite Volume Discretization

The surface integral in (3) is replaced by a sum of surface integrals over the six side surfaces of the control volume. The values of the unknown functions F are then considered constant over each side surface and equal to (see Fig. 2):

— orthogonal surfaces: value at the center point;

— bladewise surfaces: mean value between adjacent points;

— streamwise surfaces: geometrically weighted mean value between adjacent points.

The surface integral is then approximated as

$$\iint_S F \cdot \mathbf{n}_u dS \cong \sum_{m=1}^{6}\left[f_{r,m}\iint_{S_m} n_r dS\right.$$

$$\left.+f_{\theta,m}\iint_{S_m} n_\theta dS + f_{z,m}\iint_{S_m} n_z dS\right] \qquad (4)$$

where $\Sigma_{m=1}^{6}\, S_m = S$, i.e., closed surface around the control volume, and where

$$\sum_{m=1}^{6}\iint_{S_m} n_r dS = \sum_{m=1}^{6}\iint_{S_m} n_\theta dS = \sum_{m=1}^{6}\iint_{S_m} n_z dS = 0$$

The 18 surface integrals on the right-hand side of (4) contain only geometrical information. They are calculated once for each grid and stored for subsequent use in the time marching procedure. Fortunately not all 18 values have to be stored for each calculation point. For the streamwise and orthogonal surfaces (which are conical surfaces) n_θ is zero and n_r and n_z are independent of θ. For the bladewise surfaces n_θ is independent of θ.

Downloaded 01 Jun 2010 to 171.66.16.70. Redistribution subject to ASME license or copyright; see http://www.asme.org/terms/Terms_Use.cfm

To evaluate the volume V in (3) and the surface integrals in (4), each elementary grid cell is transformed into a cube with unit side length using an isoparametric transformation. Details are given in [23]. Note that for one control volume the contributions of the two composing grid cells must be summed.

The consistency and accuracy of finite volume discretizations in two-dimensional applications and for several types of control surfaces is investigated in [1]. Based on the results obtained in [1] for the discretization of two-dimensional flow fields with analog elements, one can conclude that the finite volume discretization (4) is conditionally consistent and, if consistent, generally first-order accurate. A consistency error occurs when first-order derivatives not present in the original partial differential equations are introduced by the discretization with a coefficient of order Δ^n. First- or second-order accuracy means that higher-order derivatives are introduced with coefficients of order Δ, respectively Δ^2. The consistency condition for the discretization (4) is only influenced by the orthogonal surfaces and states that only small variations are allowed between the corresponding surface integrals of the three orthogonal surfaces 1-2-3-4-1, 5-6-7-8-5, 9-10-11-12-9 (Fig. 2) of one control volume. The accuracy of the discretization is mostly influenced by the variations of the direction of $\mathbf{n}$ over the bladewise and streamwise side surfaces of one control volume. Second-order accuracy is achieved when the corresponding families of grid surfaces are nearly parallel. Note that consistency errors and poor accuracy only occur when important grid distortions are present within one control volume and that highly skewed grids as often encountered in turbomachinery bladings (see Fig. 1 as an example) are not necessarily inaccurate. The discretization (4) applied to the grid of Fig. 1 is therefore consistent and practically second-order accurate in most of the computational domain except around the leading and trailing edge.

Boundary Conditions

Periodic Boundary. The missing calculation points outside the computational domain are replaced by the corresponding points at the other periodic boundary.

Wall. The impermeability condition is achieved by setting mass and energy fluxes through the wall to zero and by reducing the momentum flow to a pressure force perpendicular to the wall. The pressure on the wall is obtained by extrapolation from the inner calculation points. As there are no calculation points on the wall itself, no further condition or special treatment is needed. This makes the wall boundary condition very simple, but reduces somewhat the precision of wall pressure and velocity distributions.

Leading Edge. Around a blunt leading edge the grid is highly distorted and discretization errors are important. This is especially the case when a conditionally consistent first-order discretization scheme is used. In order to reduce these errors, the leading edge is discretized as shown in Fig. 3(*a*). Two distinct points are used for the leading edge reducing grid distortion but introducing a special leading edge control volume with an extra wall boundary surface.

Trailing Edge. An inviscid flow calculation always shows an unrealistically strong overexpansion around a rounded trailing edge. To overcome this to some extent and at the same time to reduce grid distortion, a small triangle is added to the blade trailing edge (Fig. 3(*b*)). The length of this triangle is of the order of two times the trailing edge thickness, which seems to be a good compromise between reducing the overexpansion and influencing the blade loading. To avoid too small an axial grid spacing, the suction part of the triangle is chosen in circumferential direction, introducing the same special control volume already used for the leading edge.

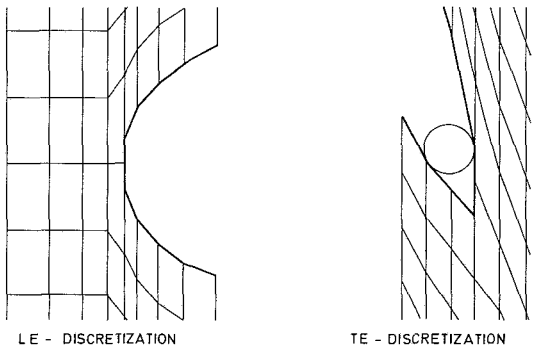


Fig. 3 Leading and trailing edge discretization

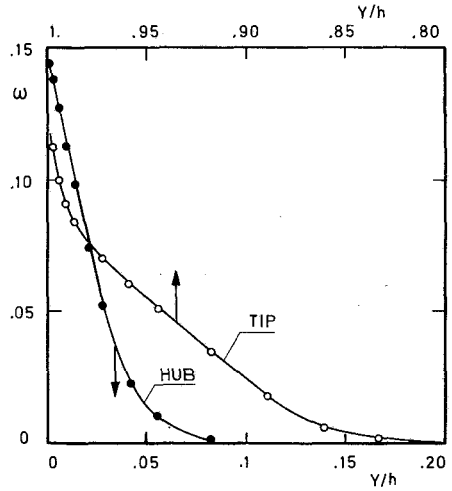


Fig. 4 Measured upstream total pressure loss distribution

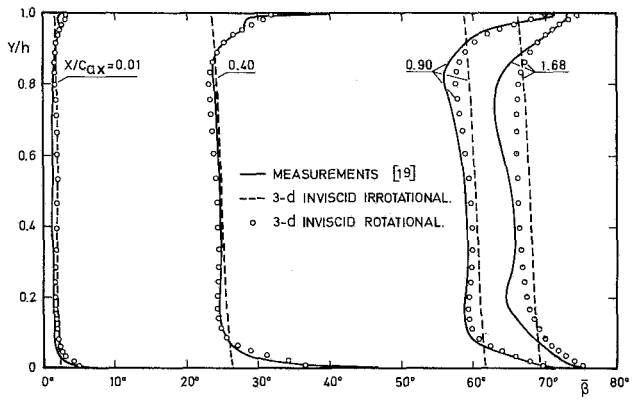


Fig. 5 Radial distribution of the pitchwise mass-averaged flow angle

Inlet. The physical boundary conditions are the flow angles $\beta_1(r)$ and $\gamma_1(r)$, the total pressure $p_{01}(r)$ and the total temperature $T_{01}(r)$. Only the radial distribution is given and it is assumed that these four quantities are uniform in pitchwise direction. As a numerical boundary condition the axial momentum equation is solved over a half control volume (one grid cell) for every calculation point in the inlet plane.

Outlet. At the outlet a generalized radial equilibrium

Downloaded 01 Jun 2010 to 171.66.16.70. Redistribution subject to ASME license or copyright; see http://www.asme.org/terms/Terms_Use.cfm

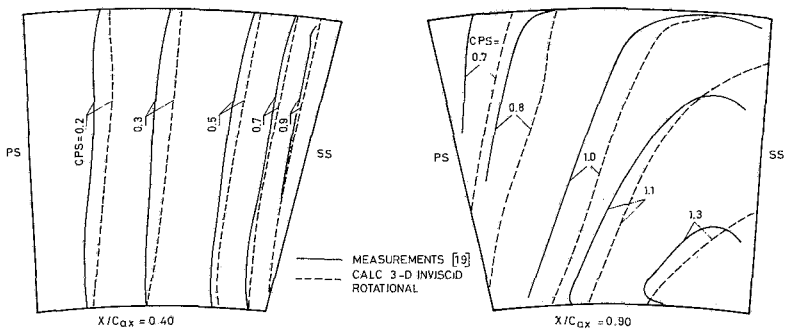


Fig. 6 Static pressure contours

condition is imposed. Consider the stationary radial momentum equation (which has to be fulfilled at convergence)

$$\frac{1}{r}\frac{\partial r\rho w_r}{\partial r}+\frac{1}{r}\frac{\partial \rho w_r w_\theta}{\partial \theta}+\frac{\partial \rho w_r w_z}{\partial z}$$

$$-\frac{\rho w_\theta^2}{r}-\rho r\Omega^2-2\Omega\rho w+\frac{\partial p}{\partial r}=0 \qquad (5)$$

This equation is integrated in the pitchwise direction at constant radius over one blade pitch in the outlet plane. Using the following notation for the averaged value of a quantity q (area average)

$$\bar{q}=\frac{N}{2\pi}\int_0^{2\pi/N} q\,d\theta \cong \frac{1}{J-1}\sum_{j=1}^{J-1} q_j \quad (J\text{: number of bladewise surfaces})$$

the result is

$$\frac{\partial p_2}{\partial r}=\frac{1}{r}\overline{\rho w_\theta^2}-\frac{1}{r}\overline{\rho w_r^2}+r\Omega^2\bar{\rho}+2\Omega\overline{\rho w_\theta}-\frac{\partial \overline{\rho w_r^2}}{\partial r}-\frac{\partial \overline{\rho w_r w_z}}{\partial z} \qquad (6)$$

where the θ derivative cancels due to the periodicity condition and the outlet static pressure p_2 is uniform in pitchwise direction. Integration of (6) in radial direction between two radii r_A and r_B with a trapezoidal integration rule yields

$$p_{2_B}=P_{2_A}+\frac{1}{2}(r_B-r_A)\left[\left(\frac{1}{r}\overline{\rho w_\theta^2}-\frac{1}{r}\overline{\rho w_r^2}+r\Omega^2\bar{\rho}+2\Omega\overline{\rho w_\theta}\right)_B+\left(\frac{1}{r}\overline{\rho w_\theta^2}-\frac{1}{r}\overline{\rho w_r^2}+r\Omega^2\bar{\rho}+2\Omega\overline{\rho w_\theta}\right)_A\right]$$

$$-\left[(\overline{\rho w_r^2})_B-(\overline{\rho w_r^2})_A\right]$$

$$-\frac{1}{2}(r_B-r_A)\left[\left(\frac{\partial \overline{\rho w_r w_z}}{\partial z}\right)_B-\left(\frac{\partial \overline{\rho w_r w_z}}{\partial z}\right)_A\right] \qquad (7)$$

If the static pressure is known at one radial position the static pressure can be calculated at any other radial position using (7) (the z derivatives are approximated by a backward finite difference scheme using information from the last two orthogonal planes). This calculation is performed each time the viscosity correction term is updated and the resultant pressure distribution is used as an outlet boundary condition until the next updating. The outlet boundary condition then reduces to imposing the static pressure at one fixed radius. As numerical boundary conditions, the continuity and the three momentum equations are solved over a half control volume for every calculation point in the outlet plane.

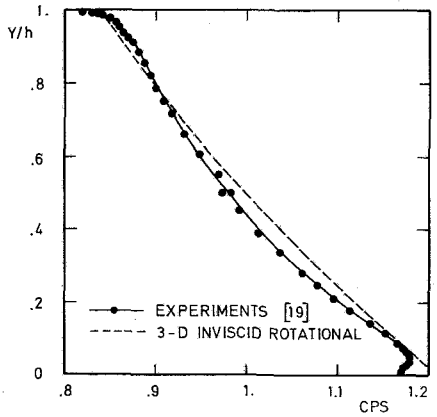


Fig. 7 Downstream radial static pressure distribution

Low Aspect Ratio Turbine Nozzle

Calculations are performed for the low aspect ratio turbine nozzle guide vane tested at the von Karman Institute under incompressible flow conditions. The geometry is fairly simple, but the flow is highly three-dimensional due to the presence of secondary flows. Geometry, test conditions, and measurements are presented in [19]. It is the only test case available in the literature giving detailed measurements of the three-dimensional flow inside and downstream of an axial turbine blade passage. The present paper deals with the computational aspects and the comparison between calculation and experiment.

The inlet conditions are axial flow ($\beta_1=\gamma_1=0$), constant total temperature, and a radial total pressure distribution determined from the total pressure loss distribution measured upstream of the blade (Fig. 4). At the outlet the static pressure is fixed at midheight to a value corresponding with an isentropic outlet Mach number of 0.3. A lower Mach number is difficult to achieve with a time marching calculation solving the compressible Euler equations. A higher Mach number would show a noticeable influence of compressibility on the secondary flows [18]. The ratio of specific heats is $\kappa = 1.4$.

The coarse grid of Fig. 1 was used to start the calculation. The final results presented in this paper are obtained with a grid of 65 orthogonal, 31 streamwise and 21 bladewise surfaces ($65\times30\times20$ calculation points). The following numbers indicate the degree of convergence: the maximum difference between the mass flow through an orthogonal surface and the mean mass flow was 0.25 percent of the latter; the maximum relative change in density $\Delta\rho/\rho$ over one step was $2\cdot10^{-4}$; the pitchwise mass averaged outlet flow angle β_2 at midheight was stabilized within ±0.1 deg.

Calculations were performed on a VAX 11/780 computer. The computer memory required for a $65\times31\times21$ grid (in-

Downloaded 01 Jun 2010 to 171.66.16.70. Redistribution subject to ASME license or copyright; see http://www.asme.org/terms/Terms_Use.cfm

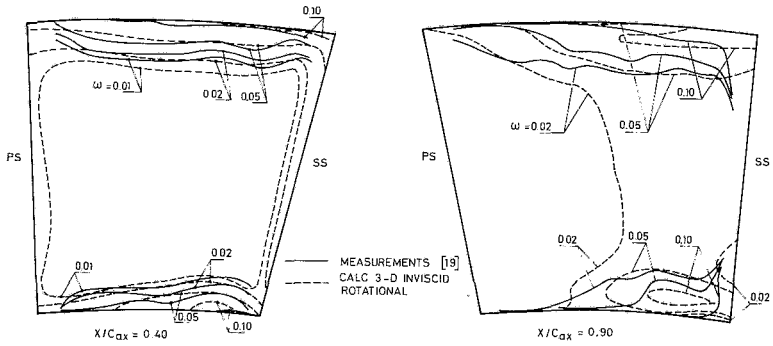


Fig. 8 Total pressure loss contours

cluding the time marching program) is ca 2.5 Mbytes and the CPU time per point and per time step is 0.0024 s. Some 100 h of CPU time were totalized to obtain the results shown.

Pitchwise Mass-Averaged Flow Angles. The evolution of the pitchwise mass-averaged flow angles β over the blade height is compared with measurements in Fig. 5 for four axial positions $x/c_{ax} = 0.01$, 0.4, 0.9, 1.7. Inside the blade passage the underturning and overturning of the flow are quite well predicted both in magnitude and in position. Downstream of the blade passage, however, a uniformization of the flow occurs affecting mostly the underturning. A possible explanation for this uniformization is the pitchwise constant outlet static pressure and the periodicity condition downstream of the blades. In the inviscid model, the passage vortices of adjacent blade passages can interact through the periodicity boundary and cancel each other, while in the real flow situation the passage vortices are separated by the blade wakes. Replacing the outlet periodic boundary by a slip line or a vortex sheet simulating the trailing shed vorticity could perhaps improve the downstream secondary flow prediction.

Static Pressure. Measured and calculated lines of constant static pressure coefficient CP_s are compared in Fig. 6 for $x/c_{ax} = 0.4$, 0.9. Although some discrepancies exist, the general trend is well predicted. Figure 7 compares measured and calculated radial outlet static pressure distributions.

Total Pressure Loss. Measured and calculated lines of constant total pressure loss coefficient ω are compared in Fig. 8 for $x/c_{ax} = 0.4$, 0.9. The inviscid model follows the physics of the flow by accumulating the losses (already present in the inlet boundary layer) in the suction side endwall corner. Large differences exist, however, between measured and calculated 1 and 2 percent loss lines. These differences may be attributed to the influence of numerical viscosity. Every discretization scheme inevitably introduces discretization errors under the form of higher-order derivatives with coefficients depending on the grid dimensions. These higher-order derivatives usually behave like a viscous term. Simple first-order discretizations like the one presented in this paper limit the computational effort per point but are more subject to discretization errors than more accurate discretizations involving more surrounding points. Regions of important grid distorsion around leading and trailing edge introduce large discretization errors. Denton [11] also reports on the influence of discretization errors introducing entropy losses and thus stagnation pressure losses convected downstream and influencing the whole flow region.

Note that this dissipative property of discretization schemes is a necessary condition to insure stability and to capture correctly shock waves. Calculation methods presented in the literature to calculate transonic flows explicitly introduce a numerical or artificial viscosity often more important than the physical viscosity, to avoid nonlinear oscillations in regions of large flow gradients.

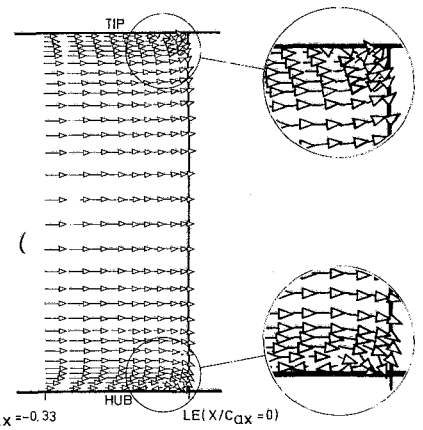


Fig. 9 Calculated velocities approaching leading edge

Secondary Flows. (In Figs. 9 and 10 the tail of the vector represents the magnitude of the velocity and the triangle shows the direction).

The velocity vectors in the calculation points next to the inlet periodic boundary (the "suction side" of it) are represented in Fig. 9. The vectors shown are constructed with the axial and radial velocity components. The onset of the horseshoe vortex is clearly visible, demonstrating the ability of the method to calculate reverse flow.

The actual secondary velocity components are shown in Fig. 10 for $x/c_{ax} = 0.01$, 0.4, 0.9. To be able to define the secondary velocities, a second calculation was performed with uniform total pressure at the inlet. The result of this calculation will be referred to as the irrotational flow. For comparison the pitchwise mass-averaged flow angles for the irrotational flow are also indicated on Fig. 5.. The secondary velocity is then defined as $\mathbf{w}_{sec} = \mathbf{w} - \mathbf{w}_{irr}$. The vectors in Fig. 10 are constructed with the radial and tangential component of $\mathbf{w}_{sec}$. The inlet free stream velocity is also represented. For the interpretation of Fig. 10 one should keep in mind that the streamwise velocity is much larger than the secondary velocity and that the secondary flows shown are not closed vortices but spirallike fluid motions.

In the result for $x/c_{ax} = 0.01$, the two legs of the horseshoe vortex can be distinguished. The pressure side leg rapidly moves to the middle of the passage, the suction side leg remains in the corner. At $x/c_{ax} = 0.4$, the pressure side leg fully developed in the passage vortex while some trace is left of the suction side leg in the corner. Close to the trailing edge ($x/c_{ax} = 0.9$) the suction side leg has disappeared and the passage vortex occupies most of the section. The predicted

Downloaded 01 Jun 2010 to 171.66.16.70. Redistribution subject to ASME license or copyright; see http://www.asme.org/terms/Terms_Use.cfm

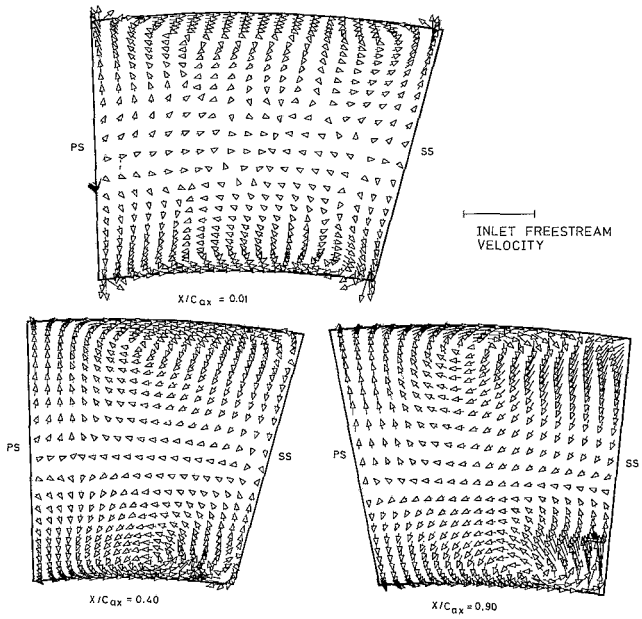


Fig. 10 Calculated secondary velocities

secondary velocities compare quite well with the measured ones [19] although the core of the calculated passage vortex is somewhat closer to the suction side than in the measurements.

Conclusion

The results presented show that it is possible to calculate secondary flows with an inviscid, rotational calculation method, provided the grid resolution is high enough in the secondary flow region. This supports the hypothesis that the main secondary flows (the horseshoe vortex and the passage vortex) are mainly an inviscid phenomenon caused by the existence of vorticity in the incoming flow, although the origin of this vorticity is the viscous end wall boundary layer. Inside the blade passage the secondary flows are quite well predicted. Far downstream of the blades the calculated flow tends towards uniformity due to the boundary conditions, but the predicted outlet flow angle is still closer to reality than an irrotational flow calculation. Discretization errors and numerical viscosity do represent a problem when calculating the redistribution of the inlet end wall boundary layer losses.

The test case of [19] has a fairly simple geometry and the flow is completely subsonic. Therefore, the ability to discretize more complex geometries and to calculate transonic shocked flow could unfortunately not be demonstrated. However, the capability of the method to calculate transonic flow with shocks has been sufficiently demonstrated in two-dimensional blade-to-blade flow [1, 6, 7, 14]. At present the calculation method is applied to more complex geometries and transonic flow.

Acknowledgments

Part of this work has been supported by a grant from the "Instituut tot aanmoediging van het Wetenschappelijk Onderzoek in Nijverheid en Landbouw" (IWONL). The author is very grateful to Professor C. H. Sieverding and A. Arts for the many informative discussions.

References

1 Arts, A., and Van Hove, W., "Cascade Flow Calculations Using a Finite Volume Method," VKI TN 146, Oct. 1982.

2 Bosman, C., and Highton, J., "A Calculation Procedure for Three-Dimensional Time Dependent, Inviscid, Compressible Flow Through Turbomachine Blades of any Geometry," *J. Mech. Engrg. Sc.*, Vol. 21, No. 1, 1979, pp. 39–49.

3 Bosman, C., "Inviscid Three-Dimensional Flow Calculation in Blade Rows and Stages (Finite Volume Method)," in *Numerical Methods for Flows in Turbomachinery Bladings*, VKI LS 1982–05.

4 Brochet, J., et al., "Calcul de l'ecoulement 3D dans une roue mobile de soufflante, Mise en oeuvre sur un calculateur parallele," ONERA TP 1981–120.

5 Couston, M., McDonald, P. W., and Smolderen, J. J., "The Damping Surface Technique for Time Dependent Solutions to Fluid Dynamic Problems," VKI TN 109, Mar. 1975.

6 Couston, M., "Time Marching Finite Area Method," in *Transonic Flows in Axial Turbomachinery*, VKI LS 84, 1976.

7 Couston, M., "Méthode de calcul de l'ecoulement interaube pseudo-tridimensionnel en regime transsonique," Ph.D. thesis, U. Libre de Bruxelles, Sept. 1976.

8 Denton, J. D., "A Time Marching Method for Two-Dimensional and Three-Dimensional Blade-to-Blade Flows," ARC R&M 3775, 1974.

9 Denton, J. D., "Extension of the Finite Area Time Marching Method to Three Dimensions," in *Transonic Flows in Axial Turbomachinery*, VKI LS 84, 1976.

10 Denton, J. D., and Singh, U. K., "Time Marching Methods for Turbomachinery Calculations," in *Application of Numerical Methods to Flow Calculations in Turbomachinery*, VKI LS 1979–07.

11 Denton, J. D., "An Improved Time Marching Method for Turbomachinery Flow Calculation," ASME P 82 GT 236.

12 Essers, J-A., "Méthodes nouvelles pour le calcul numérique d'écoulements stationnaires de fluides parfaits compressibles," Ph.D. thesis, U. de Liege, 1977.

13 Essers, J-A., "Artificial Evolution Techniques for Transonic Flows," in *Numerical Methods for Flow in Turbomachinery Bladings*, VKI LS 1982–05.

14 Lehthaus, F., "Anwendung eines Zeit-Schritt-Verfahrens zur Berechnung der transsonischen Durchstromung ebener Turbinegitter und experimentelle Uberprufung," DFVLR-AVA Bericht 251 77 A 01, Feb. 1977.

15 McDonald, P. W., "The Computation of Transonic Flow Through Two-Dimensional Gas Turbine Cascades," ASME P 71 GT 89.

16 Oliver, D. A., and Sparis, P., "Computational Aspects of the Prediction of Multidimensional Transonic Flows in Turbomachinery. Part 1 — Aerodynamic Analyses Requiring Advanced Computers," NASA CP 347, 1975, pp. 567–585.

17 Sarathy, K. P., "Computation of Three-Dimensional Flow Fields Through Rotating Blade Rows and Comparison With Experiment," ASME JOURNAL OF ENGINEERING FOR POWER, Vol. 104, No. 2, Apr. 1982, pp. 394–402.

18 Sieverding, C. H., and Wilputte, Ph., "Influence of Mach Number and End Wall Cooling on Secondary Flows in a Straight Nozzle Cascade," ASME JOURNAL OF ENGINEERING FOR POWER, Vol. 103, No. 2, Apr. 1981, pp. 257–264; also a VKI Preprint 1980–02.

19 Sieverding, C. H., Van Hove, W., Boletis, E., "Experimental Study of the Three-Dimensional Flow Field in an Annular Turbine Nozzle Guide Vane," Paper presented at 28th ASME Int. Gas Turbine Conference, 1983.

20 Thompkins, W. T., and Oliver, D. A., "Three-Dimensional Flow Calculation for a Transonic Compressor Rotor," in *Through Flow Calculations in Axial Turbomachinery*, AGARD CP 195, May 1976.

21 Thompkins, W. T., "A FORTRAN Program for Calculating Three-Dimensional, Inviscid, Rotational Flows with Shock Waves in Axial Compressor Blade Rows," NASA CR 3560, June 1982.

22 Van Hove, W., and Arts, A., "Comparison of Several Finite Differende Schemes for Time Marching Methods as Applied to One Dimensional Nozzle Flow," VKI TN 132, June 1979.

23 Van Hove, W., "Workshop on Two-Dimensional and Three-Dimensional Flow Calculations in Turbine Bladings—Test Case 3-Calculation B," in *Numerical Methods for Flows in Turbomachinery Bladings*, VKI LS 1982–05.

Downloaded 01 Jun 2010 to 171.66.16.70. Redistribution subject to ASME license or copyright; see http://www.asme.org/terms/Terms_Use.cfm

Experimental Study of the Three-Dimensional Flow Field in an Annular Turbine Nozzle Guidevane

C. H. Sieverding

W. Van Hove[1]

E. Boletis

von Karman Institute for Fluid Dynamics,
B-1640 Rhode Saint Genese, Belgium

The paper describes the experimental investigation of the three-dimensional flow through a low-speed, low aspect ratio, high turning annular turbine nozzel guide vane. The flow is explored by means of double-head, four-hole pressure probes in twelve axial planes from upstream to far downstream of the blade row. The results are presented under the form of contour plots and spanwise pitch-averaged distributions of losses, flow angles, and static pressure distributions. The concept of presenting the evolution of the endwall boundary layer under the form of streamwise and crossflow velocity components is discussed in detail.

Introduction

Since the mid-seventies research on secondary flows in turbine cascades has undergone a remarkable reorientation. At that time it was recognized that the usual practice of compiling data from flow measurements consisting merely of surveys of the flow conditions in up- and downstream planes was unsatisfactory. This approach proved unable to produce a sound basis for evaluating both the magnitude and the spanwise distribution of secondary losses and flow angles. It became clear that real progress could only be made by exploring the entire flow field to try to better understand the evolution of the three-dimensional flow field throughout the cascade. As a matter of fact, this change ended the era of systematic parametric studies because of the tremendous amount of work involved to carry out a full survey of even a single complete flow field. Hence, the experimental programs should now be conceived to provide a limited number of well documented test cases which can contribute to a better view of the complex flow structures occurring in turbine blade passages and serve for comparison with advanced theoretical calculation methods. Examples of such test cases for the flow in straight cascades were published by Langston [1], Marchal and Sieverding [2], and Carrick [3].

The present paper describes the complete three-dimensional flow field in an annular low-speed turbine cascade. Sjolander [4] conducted a similar experiment but his measurements were done on a low turning cascade with blades which are not representative of actual blade design philosophy.

Experimental Facilities

Test Facility. The tests were carried out in the VKI open loop low-speed turbine test rig. The main purpose of this rig is the investigation of secondary flows in annular cascades. The rig has been designed to study the following configurations:

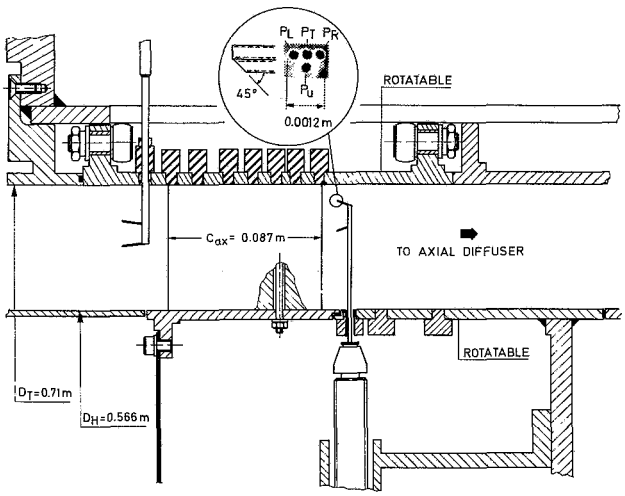


Fig. 1 Test section

(*i*) guidevane alone with collateral inlet end wall boundary layer; (*ii*) guidevane alone with skewed inlet boundary layer generated by a rotating hub end wall upstream of the cascade; (*iii*) guidevane with down-stream rotor; (*iv*) guidevane with preceding complete stage.

The test section for configuration (*i*), which is the subject of this paper, is shown in Fig. 1. The guidevane is a low aspect ratio blade ($H/C=0.6$) with tip and hub diameters of 0.71 m and 0.566 m, respectively. The constant diameter inlet duct of 0.57 m length is sufficiently long to generate a representative inlet endwall boundary layer thickness. The air is supplied from a radial blower which discharges the air into a cylindrical settling chamber equipped with flow straighteners and equalizers providing uniform flow conditions at the entrance to the inlet duct. The high swirling flow leaving the guide vane is exhausted to atmosphere via a cylindrical duct of 0.44 m length and a conical diffuser of 0.38 m length.

Figure 1 shows also some details of the experimental

[1] Presently, Ryksuniversiteit Gent, Belgium

Contributed by the Gas Turbine Division of THE AMERICAN SOCIETY OF MECHANICAL ENGINEERS and presented at the 28th International Gas Turbine Conference and Exhibit, Phoenix, Arizona, March 27-31, 1982. Manuscript received at ASME Headquarters, December 27, 1982. Paper No. 83-GT-120.

Copyright © 1984 by ASME
Downloaded 01 Jun 2010 to 171.66.16.70. Redistribution subject to ASME license or copyright; see http://www.asme.org/terms/Terms_Use.cfm

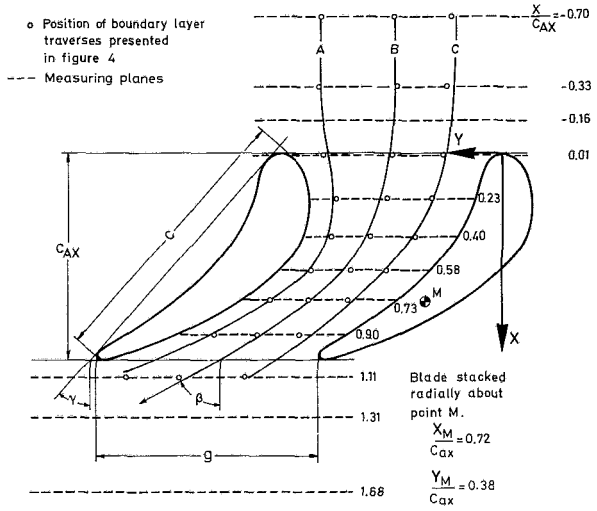


Fig. 2 Cascade geometry at midblade height

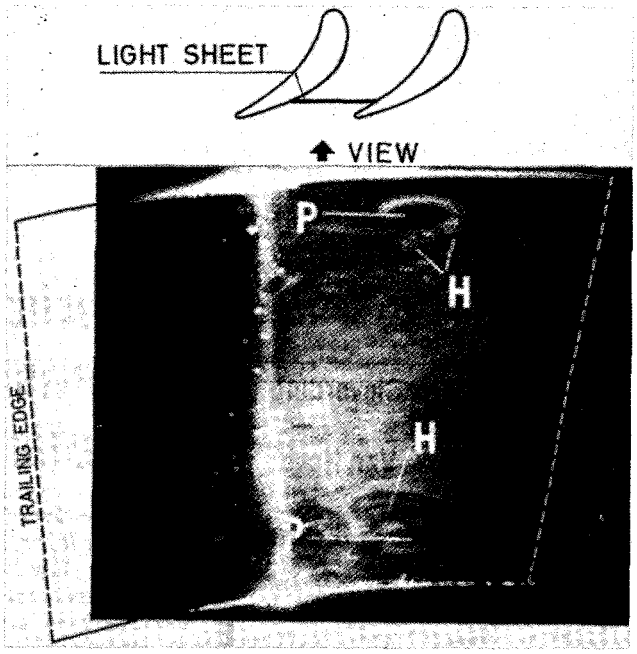


Fig. 3 Smoke visualization

procedure for measuring the three-dimensional flow development through the blading. The flow is surveyed with double-headed, four-hole pressure probes which are introduced through the outer casing upstream of the cascade exit. The probes execute radial traverses in a fixed circumferential position. A circumferential displacement of the probe shaft with respect to the blade is obtained by rotating the guide vane. T-shaped inserts are used to close perfectly the slot except for the passage of the probe shaft. The downstream flow is surveyed with a probe introduced through the hub endwall which is made partly rotatable. This arrangement allows not only an easy change of the position of the radial traverses but also a quick control of the downstream flow periodicity over several blade passages.

Blade and Cascade Geometry. The nozzle guide vane investigated has a constant profile over the blade height and is untwisted. This profile (Fig. 2) was used in fact for the stator hub section of a turbine designed and tested at NASA [5]. The blade coordinates are given in the appendix. The same blade section has previously been used for 3D flow measuremnts in straight cascades [2]. The most important geometrical characteristics of the nozzle row are summarized below:

– tip diameter, D_T	0.71 m
– hub diameter, D_H	0.566 m
– chord length, C	0.12 m
– axial chord length, C_{ax}	0.087 m
– aspect ratio, H/C	0.6
– number of blades, N	21

Nomenclature

C = chord
CP = local total pressure coefficient, $(P_{01,MS} - P_{0,l}) / (P_{01,MS} - \overline{\overline{P}}_{s,2})$
$\overline{\overline{CP_0}}$ = total pressure loss, $(P_{01,MS} - \overline{\overline{P}}_{02}) / (P_{01,MS} - \overline{\overline{P}}_{s,2})$
CP_s = local static pressure coefficient, $(P_{01,MS} - P_{s,l}) / (P_{01,MS} - \overline{\overline{P}}_{s,2})$
D = diameter
g = pitch
H = blade height
$H_{1,2}$ = boundary layer form factor
0 = throat
P = pressure
Re = Reynolds number, $\mathrm{Re} = \frac{c \cdot V_1}{\nu}$
T = temperature
Tu = turbulence level, $Tu = \sqrt{\overline{v'^2}_{ax}} / V_{MS}$
V = velocity
v' = velocity fluctuation
x,y = coordinates (see Fig. 2)
β = flow angle in blade-to-blade plane (referred to axial direction)
β' = blade angle (angle between tangent to camberline and axial direction)
γ = radial flow angle, $\gamma = \mathrm{arctg}\left(\frac{V_r}{V_{ax}}\right)$
δ = boundary layer thickness
δ^* = boundary layer displacement thickness
θ = boundary layer momentum thickness
ν = kinematic viscosity

Subscripts

1 = upstream conditions, defined in plane $x/c_{ax} = -0.70$
2 = downstream conditions, defined in plane $x/c_{ax} = 1.68$
atm = atmospheric conditions
ax = axial direction
H = hub
l = local
M,MS = midspan
n = crossflow
0 = total conditions
r = radial direction
s = static conditions, streamwise direction
T = tip

Superscripts

— = pitchwise mass-averaged value or time-averaged value
= = pitch- and spanwise mass-averaged values

Downloaded 01 Jun 2010 to 171.66.16.70. Redistribution subject to ASME license or copyright; see http://www.asme.org/terms/Terms_Use.cfm



Fig. 4 Evolution of streamwise and crossflow velocity profiles

- pitch to chord ratio at hub, mean and tip: 0.705; 0.795; 0.885
- inlet blade angle, β_1': −7 deg
- arc cos (0/g) at hub, mean and tip (measured values)[2]: 69.0; 67.8; 66.8 deg

The blade is stacked radially about point M in Fig. 2. The blade is made from araldite.

Test Program and Test Conditions. There are a total of 12 measuring planes. Their position is indicated in Fig. 2. In each plane 12 to 18 radial traverses were made, each full traverse from tip to hub containing 35 (from upstream to trailing edge plane) or 50 (downstream planes) measuring points. Due to the nonradial blade surfaces, it is not always possible to explore sufficiently close to the endwall-blade surface corners with radially moving probes. Hence, some care has to be taken in presenting radial distributions of pitchwise-averaged flow values. The data were recorded on magnetic tape and processes on a PDP 11/34 computer.

The test conditions are summarized in the following table:

upstream: $X/C_{ax} = -0.7$, midspan

- total temperature, T_{01}: 288°
- total pressure, P_{01}: Patm + 70 mm H_20
- flow angle in blade-to-blade plane, β_1: 0.7°
- radial flow angle, β_1: 0°
- velocity, V_1: 12.5 m/s
- Reynolds number, Re_1: 0.98×10^5
- turbulence, Tu: 0.8%

Downstream: $X/C_{ax} = 1.68$

- static pressure at hub, P_{s2}: Patm-7 mm H_20

[2] Note: angles are given with respect to axial direction.

Downloaded 01 Jun 2010 to 171.66.16.70. Redistribution subject to ASME license or copyright; see http://www.asme.org/terms/Terms_Use.cfm

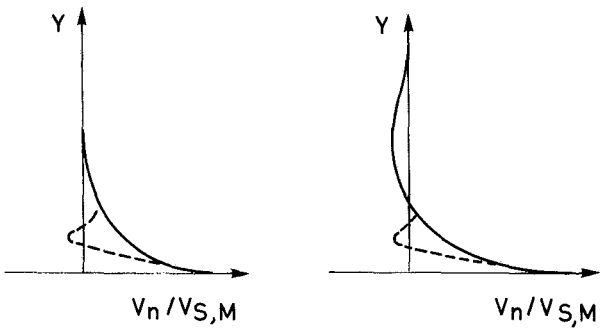


Fig. 5 Crossflow profiles in blade passage with zero (—) and negative (· -) initial crossflow components

Details of the inlet endwall boundary layer are given later.

Note that a tripping wire of 0.2 mm ϕ was placed on the blade suction side at $X/C=0.35$ (chordwise position). It was used to allow comparison with straight cascade results using the same blade at similar flow conditions [2]. In the latter case the tripping wire served to stabilize the flow on the rear blade suction side where random laminar boundary layer separations were observed.

Measuring Accuracy. The experimental accuracies associated with the four hole probes are as follows

– radial position of probe	±0.1 mm
– axial and tangential position of probe	±0.5 mm
– total pressure coefficent, CP_0	±0.01
– static pressure coefficient, CP_s	±0.02
– flow angle in blade-to-blade plane, β	±0.8 deg
– radial flow angle in streamwise direction	±1 deg

Note that the measuring accuracy for the radial flow angle deteriorates for wall distances smaller than 2 mm.

Experimental Results

Smoke Visualization. Before starting the measurements, smoke visualizations were done using the laser light sheet technique. This technique has already been successfully applied in straight cascade [2] and does not need further description. In the present case, the light sheet enters the blade passage through the top wall and the observer (camera) is positioned downstream of the blade row as indicated in Fig. 3. The photograph in Fig. 3 shows as an example the smoke patterns inside the blade passage in an axial plane at X/C_{ax} = 0.8. The outlet velocity of 2 to 3 m/s is about one order smaller than for the three dimensional flow measurements. The photograph is a montage of two pictures taken at different times. The reason is a nonuniform spatial distribution of the smoke at the inlet to the blading resulting in a very uneven quality of the photographs at hub and tip. The bright line to the left is the intersection of the light sheet with the suction surface. The position of the trailing edges is added by hand to indicate more clearly the position of the light sheet plane with respect to the sector formed by the end walls and the trailing edges.

The picture shows the existence of vortex structures in both the hub and the tip regions. The dissimilarites in the vortex structures are probably due to differences in the endwall boundary layer characteristics and the blade loading. In analogy to smoke visualizations in straight cascades [2] we can distinguish two types of vortices: vortex "*P*" is the so-called passage vortex and vortex "*H*" the continuation of the suction side leg of the leading edge horseshoe vortex (the pressure side leg of the horseshoe vortex rotates in the same direction as the passage vortex and cannot be distinguished from this one). At the tip, two vortices of type *H* are seen. The position of these vortices was, however, not stable, indicating a cyclic variation of the tip leading edge flow with one or two cyclic moving horseshoe vortices. Such cyclic varying vortex structures at very low speed are also reported by Peake et al. [6] for the flow around obstacles on a flat wall with a laminar end wall boundary layer. This unsteady phenomenon does not seem to occur for turbulent end wall boundary layers. The lower endwall vortex structure presents probably quite well the actual flow patterns at normal test conditions, i.e., at $Re_1 = 0.98 \times 10^5$. By this we do not intend to imply that the Reynolds number does not affect size and intensity of the vortices.

"Boundary Layer" Profiles. From the many traverse data we have chosen to present the evolution of the boundary layer profiles along the three stream surfaces, A, B, and C, from $X/C_{ax} = -0.70$ to 1.11 (see Fig. 2). Referred to the channel width the streamlines at midblade height are positioned at approximately 1/4, 1/2, and 3/4 distance from the pressure side. The exact positions of the boundary layer traverses at midblade height are given below (for definition of X and Y see Fig. 2):

X/C_{ax}	-0.70	-0.33	0.01	0.23	0.40	0.58	0.73	0.90	1.11
Y_A/c_{ax}	0.90	0.90	0.89	0.82	0.86	0.94	1.14	1.42	1.87
Y_B/c_{ax}	0.54	0.51	0.54	0.57	0.65	0.74	0.96	1.22	1.60
Y_C/c_{ax}	0.23	0.26	0.29	0.34	0.43	0.57	0.76	1.01	1.27

It should be noted that the pitchwise position of the radial traverses with respect to the blade changes slightly from hub to tip since the blade surfaces are nonradial surfaces.

The boundary layer profiles are presented in the form of streamwise and crossflow profiles in Fig. 4. The streamwise direction in a given field point is defined as the flow direction of the corresponding inviscid two dimensional flow field. Since the authors did not yet dispose of a three dimensional flow calculation computer code, the flow angles were calculated with a two dimensional singularity method by Martensen [7] applied to the flow in blade-to-blade planes at different blade heights. A comparison of the calculated and measured flow angles at midblade height along the stream lines, A, B, and C, is given below.

X/C_{ax}		-0.70	-0.33	0.01	0.23	0.40	0.58	0.73	0.90	1.11
A	Theor.	0.7	-3.0	-9.6	3.8	21.0	43.3	55.9	66.0	
	Exp.	1.0	-3.3	-8.7	2.9	20.3	42.7	54.7	65.5	
B	Theor.	0.7	1.7	7.2	16.3	25.7	40.1	51.3	61.6	66.3
	Exp.	0.6	1.4	6.1	16.1	24.5	39.9	50.6	60.0	67.6
C	Theor.	0.7	2.3	12.8	21.5	30.3	42.4	50.0	56.3	
	Exp.	0.5	2.5	12.1	21.0	29.8	41.7	51.2	55.0	

The discrepancies between calculated and measured angles are in general quite small, $\Delta\beta_{max} = 1.5$ deg, and do not exceed the experimental angle error band of ±0.8 deg in 60 percent of the cases. Since the discrepancies exceeding the error band are random, it was concluded that the flow angle β at midspan was indeed not significantly influenced by secondary flows and that little error was made by putting the crossflow component everywhere at midspan to zero. This implied in practice that the calculated inviscid flow angles β_{theor} along each radial traverse line were corrected by the corresponding angle difference $\beta_{meas} - \beta_{theor}$ at midspan. It is recognized that

Downloaded 01 Jun 2010 to 171.66.16.70. Redistribution subject to ASME license or copyright; see http://www.asme.org/terms/Terms_Use.cfm

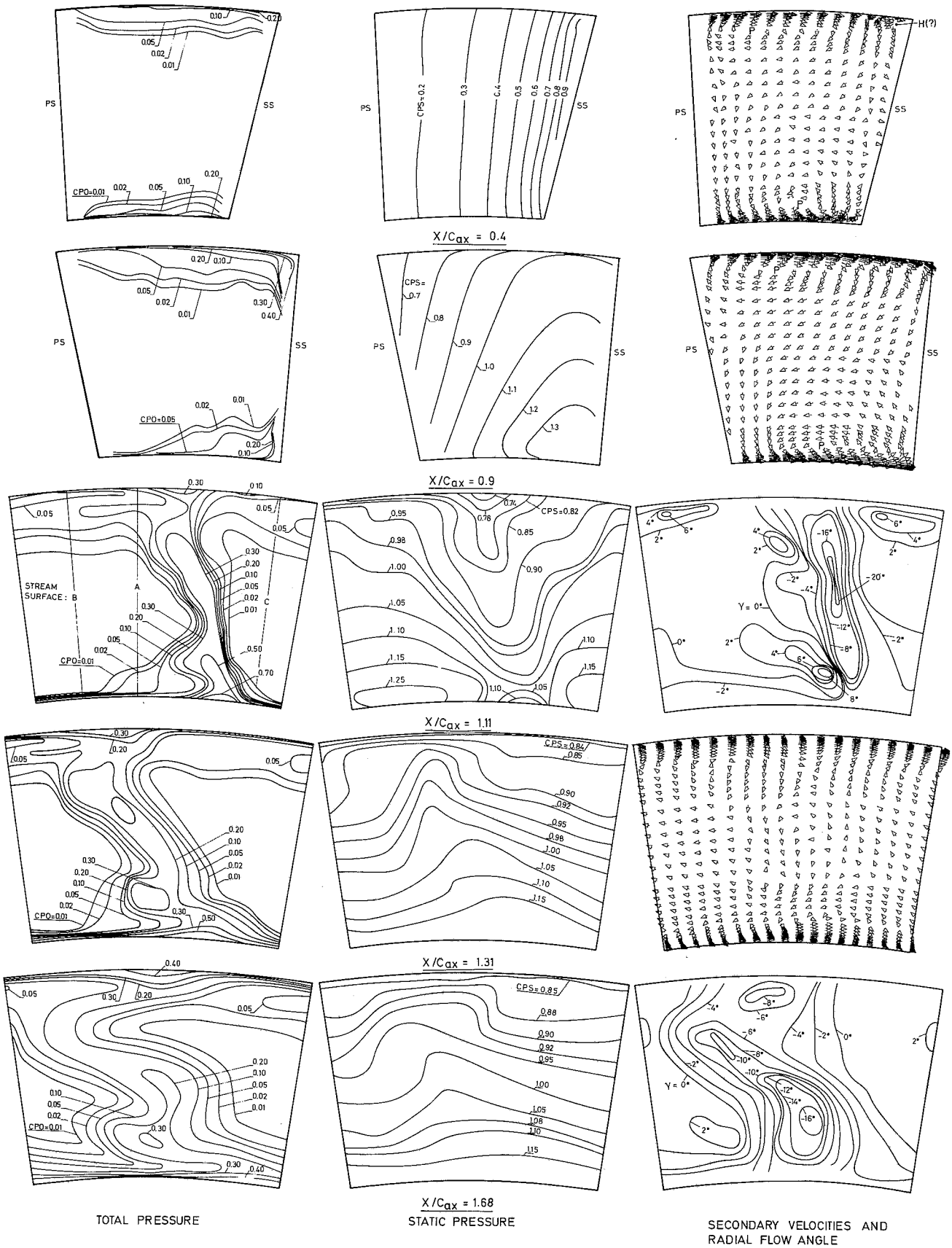


Fig. 6 Secondary velocity and contour plots of losses, static pressure, and radial flow angle distribution at different axial planes

Downloaded 01 Jun 2010 to 171.66.16.70. Redistribution subject to ASME license or copyright; see http://www.asme.org/terms/Terms_Use.cfm

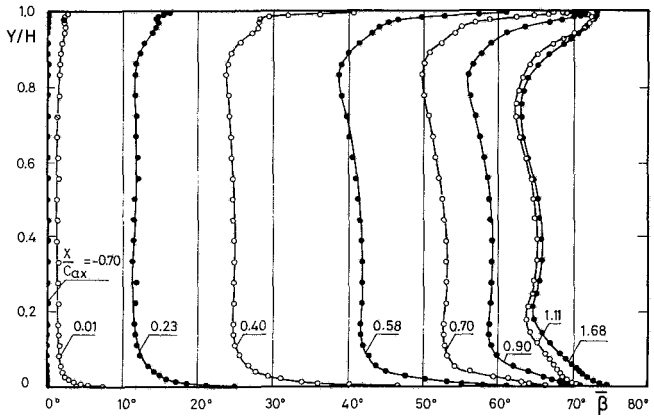


Fig. 7 Axial evolution of radial distribution of pitchwise-averaged flow angle β

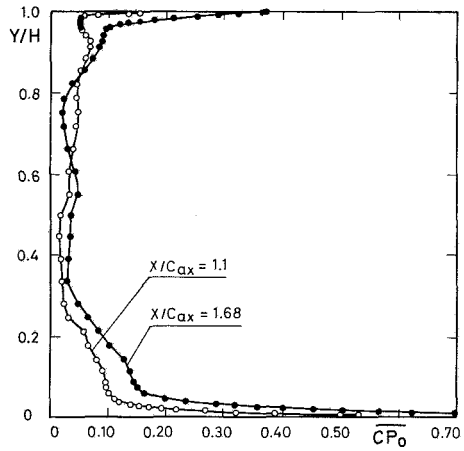


Fig. 8 Spanwise total pressure loss distribution in two downstream planes

the calculation of the inviscid flow field near the endwalls with a two dimensional method will be less satisfactory than at midspan.

At $X/C_{ax} = -0.70$, all stream surfaces are collateral. However, there are noticeable differencs at hub and tip. The table below shows the main inlet end wall boundary layer characteristics:

	$Y/H=0$(hub)	$Y/H=1$(tip)
δ/H	0.11	0.15
δ^*/H	0.017	0.025
θ/H	0.010	0.019
$H_{1,2}$	1.67	1.33

The tip boundary layer is fully turbulent, while the hub boundary layer which develops over a shorter distance than the tip boundary layer is still in a transitional state. Boundary layer traverses at different times showed invariably the same profile.

Streamwise Profile. The most striking aspect is the general decrease of the radial extension of the velocity deficiency of the streamwise component of the boundary layer profile throughout the blade passage apart from the leading edge region at the hub where a local increase is observed. Beyond this general statement a further interpretation of the boundary layer profiles proves rather difficult. To start with, it seems to be appropriate to use the more general term "velocity profile" rather than "boundary layer profile." Indeed, the profiles are the result of a superposition of several effects which make it difficult to apply the usual boundary layer concept. The normal growth of the inlet endwall boundary layer is fundamentally modified under the influence of horseshoe and passage vortices on one side and the radial pressure gradient on the other side. The vortices act as transport agents for low momentum boundary layer material in both tangential and radial directions which leads to the formation of a low energy region near the rear blade suction side. The radial pressure gradient is both consequence and cause of three dimensional flow effects. First, the radial pressure gradient is a consequence of the requirement of radial equilibrium in the meridional flow plane. This pressure gradient derives from the radial velocity gradient which in turn proceeds from the blade design. This fact is expressed by the general slope of the velocity curves which becomes evident for $X/C_{ax} \geq 0.4$. Within the blade passage the radial pressure gradient increases from the pressure side to the suction side as will be shown later. Secondly, the radial pressure gradient is the driving force for a radial displacement of the end wall boundary layer material. Depending on the location, the pressure gradient may amplify (e.g., in the corner formed by the suction side and the outer end wall) or counteract (e.g., in the corner formed by the suction side and the inner end wall) the effect of the passage vortex on the radial transport of boundary layer material. These various influences are reflected in the velocity profiles but it is difficult to distinguish them clearly.

Downstream of the cascade the interpretation of the velocity profiles is even more hazardous due to the presence of the wake which tends to spread out rather quickly in the tangential direction. The position of the radial traverses at $X/C_{ax} = 1.11$, corresponding to the streamlines A, B, and C, are indicated on the total pressure contour plot in Fig. 6.

Crossflow Profiles. Crossflow velocity components will be defined positive when pointing from the pressure side to the suction side. The development of the crossflow profile is very different for the stream surfaces A, B, and C. The reason is to look for in the upstream effect of the cascade causing a streamline curvature ahead of the airfoil leading edge. Associated with this streamline curvature are transverse pressure gradients which impose in the near end wall region a negative cross flow component on stream surface A and a positive component on stream surface C. This is very important for the further development of the crossflow profiles through the cascade.

Let us look first at the crossflow profile along stream surface C near the blade pressure side. Inside the blade passage the transverse pressure gradient reinforces the already positive crossflow component leading to maximum values at the wall in the region of the maximum transverse pressure gradient ($X/C_{ax} = 0.3$ to 0.6). The differences at hub and tip can be attributed, in decreasing order, to (*a*) different thicknesses of the inlet end wall boundary layers at hub and tip; (*b*) differences in blade loading; and (c) differences in the position of the traverses with respect to the pressure side. The hub and tip profiles differ further by the magnitude of the crossover crossflow profile (examples of crossflow and crossover flow profiles are shown in Fig. 5) which is to be attributed to the action of the passage vortex. This feature of the crossflow profile is very strongly developed at the tip but almost nonexistent at the hub. In the tip region the crossover point is almost invariably situated at $Y/H = 0.9$. The radial extension of the crossover crossflow profile increases throughout the cascade and extends at $X/C_{ax} = 0.9$ almost to midspan.

The evolution of the crossflow profile along stream surface A (near blade suction side) differs entirely from that of the pressure side stream surface C. The transverse pressure gradient counteracts the upstream effect of the cacade which imposed a negative crossflow component at the cascade inlet. This influence becomes evident at $X/C_{ax} = 0.23$. The initial

Downloaded 01 Jun 2010 to 171.66.16.70. Redistribution subject to ASME license or copyright; see http://www.asme.org/terms/Terms_Use.cfm

cross flow profile is gradually inverted but inside the blade passage there always remains a slight local negative crossflow region limiting the extension of the positive part of the crossflow profile near the wall to 5 percent of the blade height. This quite straightforward interpretation, however, does not explain the entire shape of the crossflow profiles even though the value of the crossflow component hardly exceeds $V_n/V_{s,M}=0.03$ to 0.04 between 5 and 95 percent of the blade height. A possible explanation is given in Fig. 5. The continuous curves present the basic cases of a simple crossflow profile and a crossover crossflow profile, both originating from an initial zero crossflow profile, while the dashed curves indicate possible deformations of the basic curves due to an initial negative crossflow profile. This illustrates clearly the possibility of two or even three crossover points seen in Fig. 4.

Due to its position at about midpitch, stream surface B exhibits only small crossflow components in the upstream flow field (see $X/C_{ax}=-0.33$ in Fig. 4). Hence, the crossflow profiles are of the two basic types in Fig. 5. The only exception is the tip profiles for $X/C_{ax}=0.90$ which is similar to the equivalent profile of stream surface A.

The presentation of the velocity profiles in the form of streamwise and crossflow boundary layer profiles was done to check whether this boundary layer concept is a valid approach for a theoretical description of viscous flows in typical turbine passages. In view of the complexity and variety of the measured profiles, it is hard to believe that it is really worthwhile to persue this approach. Let us mention for example Langston's crossover crossflow profile [8] which seems to be the most appropriate profile published so far for the description of flows in straight turbine cascades. Langston's profile is determined by three parameters which depend on the blade loading and need to be correlated on the basis of experimental evidence. But even if this could be done, Langston's profile cannot deal with the upstream effect of the blading on the incoming cross flow profile. The application to annular cascades is even more problematic due to the additional effect of the radial pressure gradient.

Contour Plots and Secondary Flow Charts. Figure 6 presents a combination of secondary flow charts and contour plots of total pressure, static pressure, and radial flow angle for the flow inside and downstream of the blade passage. The evolution of the blade-to-blade angle through the cascade will be presented later under the form of pitchwise-averaged values. The total and static pressures are presented in the form of pressure coefficients, CP_0 and CP_s.

The radial flow angle γ is calculated from the ratio of radial and axial velocity component

$$\gamma=\text{arc } tg\frac{V_r}{V_{ax}}$$

Due to the high values of the flow angle β downstream of the cascade, $\beta=60$ to 75 deg, the absolute value of the radial angle γ is considerably bigger than the flow inclination measured in the streamwise direction. An error of 1 deg in the radial angle in the streamwise direction amounts to about 2–3 deg error after projection into the meridional plane.

The secondary velocity vector is obtained by decomposing the actual flow vector into a streamwise vector and a vector normal to it. The streamwise direction in the whole flow field is calculated with a singularity method by Martensen [7] applied to the flow in blade-to-blade planes at different blade heights.

Flow Inside the Blade Passage. Due to space limitations the flow conditions inside the blade passage are presented only in two axial planes, situated at $X/C_{ax}=0.4$ to 0.9.

The secondary flow charts indicate clearly in both planes the existence of the passage vortex (indicated as "*P*" in Fig. 6), which is the main driving force for the tangential and, near the suction side, the radial displacement of the endwalls boundary layer material. The differences at hub and tip are considerable and have to be attributed to (*a*) the difference in vortex strength at hub and tip; (*b*) the radial pressure gradient, and (*c*) the leaning of the blade surfaces. The radial pressure gradient which is still extremely weak at $X/C_{ax}=0.4$ has taken important proportions at $X/C_{ax}=0.9$, in particular near the suction side where the pressure difference reaches 30 percent of the outlet dynamic head. The big difference in the pitchwise position of the vortex centers at hub and tip is somewhat surprising and it seems unlikely that it can be attributed entirely to the different blade loading. The difference might in fact point to the inability of a two dimensional method to predict correctly the streamwise direction of the inviscid flow field near the endwalls.

The measurements reveal little about the horseshoe vortex and its significance outside the entrance region of the blade passage. There is still some evidence in plane $X/C_{ax}=0.4$ for the existence of the suction side leg of the horseshoe vortex (indicated by *H* in upper right figure) but this is about as far as one can go. As for the pressure side leg of the horseshoe vortex, we do not expect it to appear as a distinct vortex except in the immediate vicinity of the leading edge plane, since its sense of rotation coincides with that of the passage vortex.

Flow Downstream of Blade Passages. The influence of the radial pressure gradient on the outlet flow field is the most striking aspect in all three downstream planes. The first plane is situated abut 10 percent of the axial chord away from the trailing edges ($X/C_{ax}=1.11$). Outside the wake region the constant total pressure lines are wide spaced at tip and closely spaced at the hub with considerably higher losses at hub than at tip. Within the wake region one observes a radial transport of low momentum material from the endwall and possibly also from the blade boundary layer. This radial migration from tip to hub is confirmed by the distribution of the radial flow angle γ. Values of up to -20 deg are recorded for γ in the center of the wake slightly above midspan. Also, the wake region is characterized by significant tangential pressure variations which contriute probably to the dissipation of the losses in pitchwise direction when proceeding further downstream.

The radial convection of losses continues in the measuring plane $X/C_{ax}=1.31$. The corresponding secondary velocity chart is chosen to underline this feature. A superposition of loss contour plot and secondary velocity chart contributes also to a better understanding of the pitchwise shift of the constant loss lines at hub and tip.

In the last plane ($X/C_{ax}=1.68$) the endwall boundary layers have grown significantly at both hub and tip and the width of the wake is almost twice that in the preceding plane. The radial pressure gradient is nearly the same as before and keeps the migration of low momentum material through the wake going. The radial flow angles are still very significant although somewhat less than before. Compared to plane $X/C_{ax}=1.11$, the position of the maximum negative angle has shifted towards the hub.

Spanwise Distribution of Pitch-Averaged Flow Angles and Losses. The axial evolution of the spanwise distribution of the pitchwise integrated flow angle $\bar{\beta}$ is presented in Fig. 7. The early evolution of $\bar{\beta}$ at hub and tip is influenced considerably by the differences of the upstream boundary layer profiles at hub and tip. It is noteworthy that the sensitivity of the angle distribution to the shape of the upstream boundary layer profile is confirmed by three dimensional inviscid rotational flow calculations [9]. Further downstream, $X/C_{ax}\geq 0.58$, the distribution of $\bar{\beta}$ is dominated by the presence of the passage vortices. The different radial evolutions of $\bar{\beta}$ at hub and tip

Downloaded 01 Jun 2010 to 171.66.16.70. Redistribution subject to ASME license or copyright; see http://www.asme.org/terms/Terms_Use.cfm

are a clear sign for the different vortex strength, i.e., the different blade loading at hub and tip. Downstream of the blade the angle distribution varies rather little with increasing distance from the trailing edge plane except close to the hub where a further increase of $\bar{\beta}$ is observed. The reason for this local angle increase is probably to look for in a reduction of the axial velocity component due to the appreciable rise of losses.

Spanwise loss distributions are presented only for the downstream measurements at $X/C_{ax} = 1.11$ and 1.68 (Fig. 8). There is a general increase of losses between the two planes except for a local region between 60 and 80 percent of the span. The local decrease is certainly related to the radial migration of losses. The overall losses between the two planes increase from $\overline{\overline{CP}}_0 = 5.4$ to 7.2 percent. These values include an inlet endwall loss of 0.7 percent. The increase of $\overline{\overline{CP}}_0$ presents both mixing losses and end wall boundary losses.

Conclusions

1 The upstream influence of the cascade on the inlet cross flow profile is of primary importance for the further development of the crossflow profile through the cascade. Streamlines near the blade suction side exhibit a negative inlet cross flow profile resulting in very complicated profiles inside the blade passage.

2 The passage flow field is under the strong influence of the radial pressure gradient. The direct effect of the pressure gradient is amplified through the creation of passage vortices of different strength at hub and tip. The combined effect of radial pressure gradient and different passage vortex strength causes significant differences of the loss and flow angle distribution at hub and tip inside the passage.

3 The outlet flow field is characterized by an important radial migration of low momentum material from tip to hub. The radial transport through the wake region is confirmed by the measurement of the radial flow angle distribution.

4 The flow structure in annular cascades is so complex that boundary layer methods will only be of little use. Progress can be expected only from the solution of the Navier-Stokes equations.

References

1 Langston, L. S., Nice, M. L., and Hooper, R. M., "Three Dimensional Flow Within a Turbine Cascade Passage," ASME *Journal of Engineering for Power*, Vol. 99, No. 1, 1977, pp. 21–28.

2 Marchal, Ph., and Sieverding, C. H., "Secondary Flows Within Turbomachinery Bladings, AGARD CP 214," Secondary Flows in Turbomachines," 1977, paper 11.

3 Carrick, M. A., "Secondary Flow and Losses in Turbine Cascade With Inlet Skew, "AGARD CP 214 "Secondary Flows in Turbomachines," 1977, paper 9.

4 Sjolander, S. A., "The End Wall Boundary Layer in an Annular Cascade of Turbine Nozzle Guide Vanes," Carleton U., TR ME/A 75-4, Dec. 1975.

5 Whitney, W. J., Szamza, E. M., Moffit, T. P., and Monroe, D. E., "Cold-Air Investigation of a Turbine for High Temperature Engine Application," NASA TN D 3751, Jan. 1967.

6 Peake, D. J., and Tobak, M., "Three Dimensional Interactions and Vortical Flows with Emphasis on High Speeds," AGARD-ograph 252, 1980.

7 Martensen, E., "Berechnung der Druckverteilung an Gitterprofilen in ebener Potentialstromung mit einer Fredholmschen Integralgleichung," *Arch. Rat. Mech. & Analysis*, Vol. 3, No. 3, 1959, p. 235.

8 Langston, L. S., "Cross Flows in a Turbine Cascade Passage," ASME Paper 80-GT-5, 1980.

9 Van Hove, W., "Calculation of Three Dimensional, Inviscid, Rotational Flow in Axial Turbine Blade Rows," JOURNAL OF ENGINEERING FOR GAS TURBINES AND POWER, Vol. 106, Apr. 1984, pp. 430–436.

APPENDIX

Blade Profile Coordinates

X	$Y_{suct.s}$	$Y_{press.s}$
0	0	0
1.08	−4.08	4.08
2.40	−5.76	5.76
4.20	−7.14	7.14
6.60	−8.40	8.04
9.00	−9.36	8.64
11.40	−10.20	9.36
13.80	−10.80	10.08
16.20	−11.22	10.92
19.02	−11.58	11.94
21.00	−11.70	12.72
23.40	−11.64	13.80
25.80	−11.46	14.88
28.20	−11.16	16.14
30.60	−10.56	17.52
33.00	−9.84	18.96
35.40	−8.88	20.52
37.80	−7.74	22.20
40.20	−6.36	23.94
42.60	−4.68	25.80
45.00	−2.88	27.84
46.80	−1.26	29.40
48.60	0.48	31.15
50.82	2.76	33.36
52.80	5.10	35.46
55.20	8.22	38.10
57.60	11.58	40.92
60.00	15.24	44.04
62.04	18.36	46.74
64.08	21.66	49.62
66.00	24.90	52.32
67.80	28.08	55.02
69.60	31.44	57.72
72.00	36.24	61.44
74.40	41.40	65.16
77.10	47.70	69.48
79.20	52.92	72.96
81.60	59.58	76.92
83.40	65.10	80.04
85.20	71.46	80.88
86.88	78.96	78.96

The table presents the coordinates of the blade section in a flat plane perpendicular to the blade stacking line (Fig. 2) at the proper stagger angle of 42.5 deg (referred to axial direction). The corresponding coordinates on cylindrical surfaces can easily be derived. Trailing and leading edges are rounded.

Downloaded 01 Jun 2010 to 171.66.16.70. Redistribution subject to ASME license or copyright; see http://www.asme.org/terms/Terms_Use.cfm

Journal of Engineering for Gas Turbines and Power

Technical Briefs

Modifications of the Ives-Liutermoza Conformal-Mapping Procedure for Turbomachinery Cascades

W. J. Rae[1]

A conformal mapping technique, appicable to compressor and turbine cascades, is presented. The technique can be used to map the field surrounding the cascade into a rectangle, in which the image of the blade surface lies along one side of the rectangle, the image of the trailing edge is at two corners of the rectangle, and the image of downstream infinity lies at the other two corners. These features make it possible to use the mapping in several contemporary flow field analysis codes, which carry out their calculations in such a rectangular plane. The mapping produces an O-type grid in the cascade plane.

1 Introduction

Modern turbomachinery flow field codes perform their calculations in a transformed space, in which the blade surfaces and other boundary surfaces are conveniently located. The requirement for coordinate transformations having certain convenient features is especially important for codes which use the strong conservation law forms of the equations of motion (see, for example, [1, 2]. Both of these codes employ a transformation of the cascade plane into a rectangle, in which the image of the blade surface lies on the lower boundary, with the trailing edge located at the two lower corners. The images of downstream infinity lie at the two upper corners, while the image of upstream infinity is at the midpoint of the upper boundary. The isolation of these singular points (images of the trailing edge and of downstream infinity) at the corners of the computational plane is a key step in implementing an implicit time-marching method of solution.

Dulikravich [1] has presented a sequence of transformations which map a given cascade into such a rectangle. The present paper is a comparable sequence, which is a modification of the conformal-mapping technique presented by Ives and Liutermoza [3]. Section 2 below presents a brief review of the mapping steps used in [3]. The principal modification made here is to introduce an additional shearing of the coordinates, such that one of the coordinate lines in the physical plane extends from the trailing edge to downstream infinity. In the transformed plane, the images of this line are the two vertical sides of the rectangle. This modification is described in Section 3.

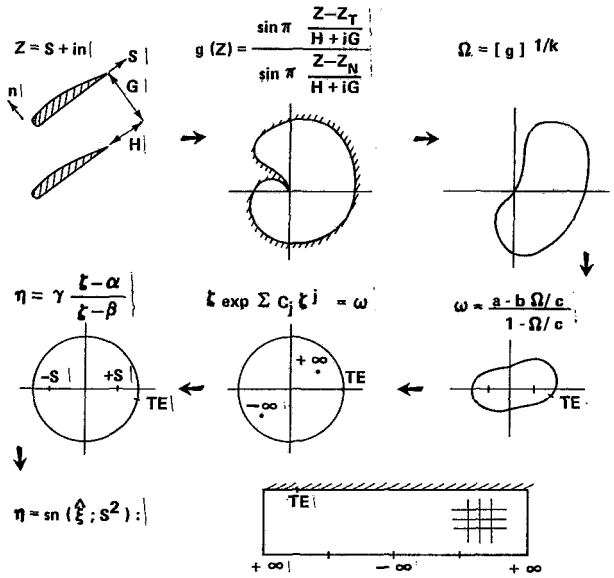


Fig. 1 Steps in the Ives transformation

A second modification, reported in Section 4, is a method for mapping blades having a rounded trailing edge. The original publication of Ives and Liutermoza [3] contained results for such blades, but did not disclose the additional steps that were used to handle the rounded trailing edge.

The technique described in this paper has been applied to a number of cascades, having gap/chord ratios down to around 0.8. For lower values (i.e., higher solidities), one of the key steps in the method fails to converge. Some details of this experience are described in Section 5 along with a number of suggestions for overcoming this problem.

2 The Ives Transformation

The transformation presented in [3] is a series of six steps, which are sketched in Fig. 1. The blade geometry and cascade parameters (G and H) are given in the physical, or z-plane. The first step is a ratio-of-sines transformation, which maps the region exterior to the blades into a region enclosed by a curve in the g-plane. The sharp corner at the origin in the g-plane is the image of the trailing edge; it is opened up by an exponentiation, which produces the figure in the Ω-plane. A bilinear transformation is then used to obtain an oval-shaped

[1] Aerodynamic Research Department, Arvin/Calspan Advanced Technology Center, Buffalo, N.Y. 14225; present address: Department of Mechanical Engineering, State University of New York at Buffalo, Buffalo, NY 14260.

Contributed by the Gas Turbine Division of THE AMERICAN SOCIETY OF MECHANICAL ENGINEERS and presented at the 28th International Gas Turbine Conference and Exhibit, Phoenix, Arizona, March 27-31, 1983. Manuscript received at ASME Headquarters December 27, 1982. Paper No. 83-GT-116.

Copyright © 1984 by ASME
Downloaded 01 Jun 2010 to 171.66.16.70. Redistribution subject to ASME license or copyright; see http://www.asme.org/terms/Terms_Use.cfm

figure in the ω-plane, which is roughly centered about the origin, and has the images of upstream and downstream infinity at $\omega = -1$ and $+1$. This oval is then mapped into a unit circle in the ζ-plane, with the trailing edge at $\zeta = 1$, by a variant of the Theodorsen-Garrick transformation [4]. A bilinear transformation is applied next, in order to locate the images of infinity at $\pm S$. Finally, an elliptic sine transformation is used to map the unit circle into a rectangle in the $\hat{\xi}$-plane, in which the images of downstream infinity lie at two corners and the blade surface lies along one of the long sides.

While the equations used to carry out this mapping are straightforward, their numerical evaluation for practical shapes introduces a number of specific questions. In particular, these include the branches used for the complex sine and for the exponentiation, the algorithm used for determining the parameters a, b, and c in the Ω, ω mapping, and the Fast Fourier Transform methods used for evaluating the complex coefficients in the Theodorsen-Garrick step. One of the key steps required in the application of this step is an underrelaxation of the adjustments called for at each iteration (see, for example, [5], section 2.5). These questions are addressed in [6], which also contains the listing of a computer program applicable to compressor cascades with sharp trailing edges.[2] Typical CPU times for these calculations,

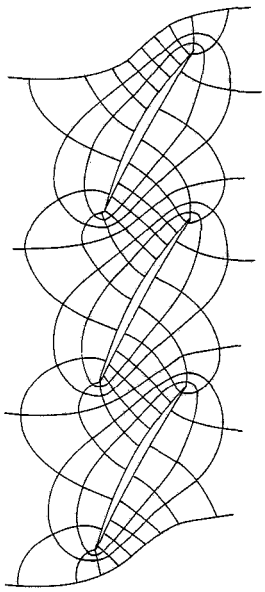


Fig. 2 Coordinate grid in Z-plane

done on an IBM 370/3031, are in the range of 50 to 100 ms per grid point, depending on the number of iterations required in various steps.

Flow field computations can now be carried out in the $\hat{\xi}$-plane, using a rectangular grid. This grid, when mapped back into the physical plane, has the appearance shown in Fig. 2. The blade row chosen for illustration in Fig. 2 has sharp leading and trailing edges and a cambered double-circular-arc profile. It should be noted that the coordinate line which extends to infinity downstream does not originate at the trailing edge.

3 Modification of the Mapping: Sheared Grid

The locations of the grid lines extending to downstream infinity are incompatible with a number of contemporary flowfield-analysis codes, since the image of the trailing edge does not lie at a corner of the rectangle in the computational plane. The methods presented in [1] and [2] have found it more convenient to work with a grid in the $\hat{\xi}$-plane, in which the trailing-edge image is located in the corners.

It is possible to achieve a grid of this type by using a sheared grid in the $\hat{\xi}$-plane and by invoking the periodicity of the elliptic sine function. One such grid, shown in Fig. 3, was used in [2]. It is found by connecting a parabola between the images of the trailing edge and downstream infinity, perpendicular to the blade surface, and by using parabolas parallel to this one to define the grid. This maps back to the physical plane as shown in Fig. 4. The blade row shown here is composed of NACA 65(12) 10 airfoils, with a slant gap/chord ratio of 1.0 and was used in the Euler-code calculations descibed in [2].

The mesh cells resulting from this shearing are rectangular at the blade surfaces and are parallelograms far from the surface. The codes described in [1] and [2] are capable of handling a moderate amount of this type of grid distortion, but the precise tolerance limits are not known.

4 Modification of the Mapping: Rounded Trailing Edge

The original publication of Ives and Liutermoza [3] contained results for turbine blades having rounded trailing edges, but did not disclose the additional mapping steps that were needed to handle such shapes; the formulas presented in their paper and applied in [6] were valid only for the case of a sharp trailing edge.

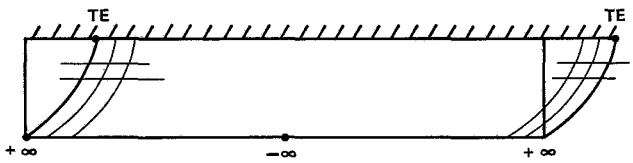


Fig. 3 Sheared grid in the $\hat{\xi}$-plane

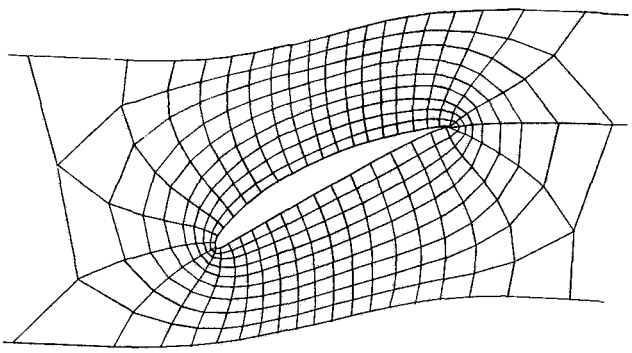


Fig. 4 Coordinate mapping for NACA 65 (12) 10 cascade

The method can be extended so as to handle a rounded trailing edge, by recognizing that the complex parameter ZT appearing in the transformation to the g-plane lies inside the blade and that the value of the parameter k is no longer related to the included angle at the trailing edge. A generalized notation for the coordinates is shown in Fig. 5. The coordinate x is parallel to the axis of rotation, and the s, n coordinates can be located arbitrarily, since their rotation relative to x and y is given by $\gamma = \tan^{-1}(H/G)$. A new parameter, ZTE, locates the point that will be joined to

[2] A list of errata for [6] is available from the author.

Downloaded 01 Jun 2010 to 171.66.16.70. Redistribution subject to ASME license or copyright; see http://www.asme.org/terms/Terms_Use.cfm

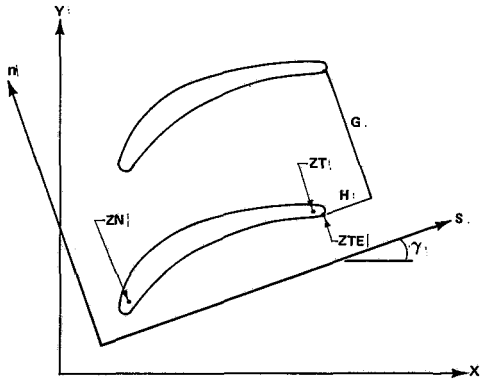


Fig. 5 Coordinate system

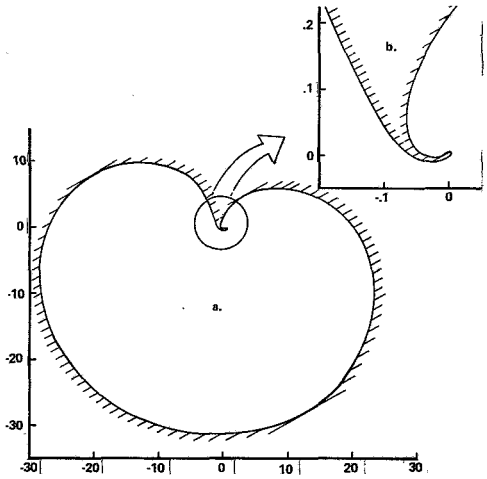


Fig. 7 Turbine cascade: *g*-plane

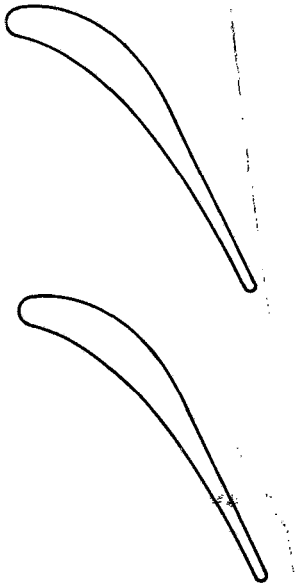


Fig. 6 Turbine cascade

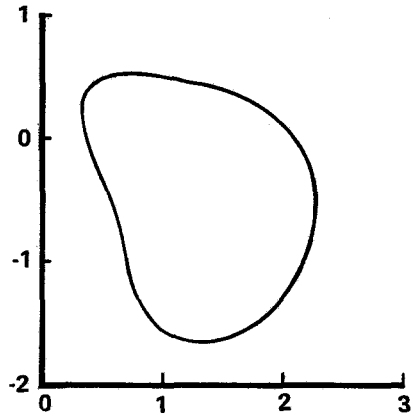


Fig. 8 Turbine cascade: Ω-plane

downstream infinity. Note that H is negative for a turbine cascade.

The modifications made for the rounded-trailing-edge case can best be illustrated by an example: Fig. 6 shows a turbine cascade, with gap/chord ratio 1.25. Figure 7(*a*) shows the *g*-plane corresponding to this cascade, and Fig. 7(*b*) is a magnified view of the region near the origin. The exponent k is now used to open up this region; a value $k = 4.0$ produces the Ω-plane shown in Fig. 8. All of the subsequent steps in the mapping have the same qualitative appearance as shown in Fig. 1. The final grid generated is shown in Fig. 9.

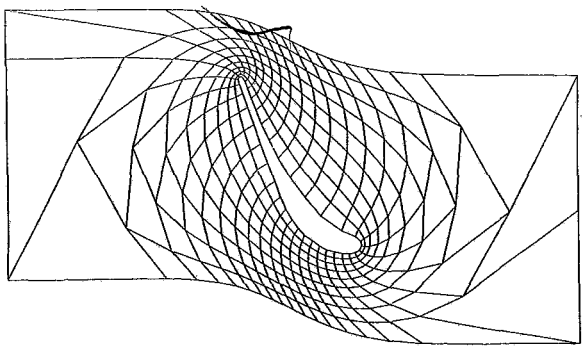


Fig. 9 Modified Ives grid for turbine cascade

5 High-Solidity Problems

The steps described above continue to be valid as the blade-row solidity is increased. Numerical difficulties are encountered when the gap/chord ratio falls below approximately 0.8, however, because the oval in the ω-plane becomes quite elongated. Figure 10 shows the relation between the angular variables in the ω and ζ planes for a gap/chord ratio of 0.6; the abscissa is proportional to arg ζ, which is assigned 128 equally spaced points for the Fast-Fourier-Transform evaluations of the Theodorsen-Garrick transformation. The ordinate shows the corresponding polar angle in the ω-plane. The steep gradients in this curve lead to a loss of accuracy in the locations of grid points near the leading and trailing edges of the blades, and the resulting grid is not usable.

Downloaded 01 Jun 2010 to 171.66.16.70. Redistribution subject to ASME license or copyright; see http://www.asme.org/terms/Terms_Use.cfm

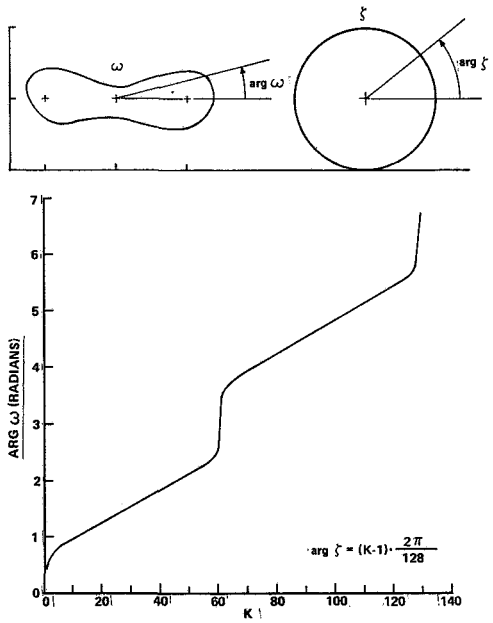


Fig. 10 Relation of angular mapping variables for high-solidity blading

A possible remedy for this problem might be the insertion of an additional step, designed to reduce the elongation of the oval in the ω-plane. One such step is a transformation that maps an ellipse into a circle [7]; with a suitable choice of parameters, it should be possible to map the oval into a more nearly circular shape. The remaining mapping steps would then be completed as before.

Conclusions

The modifications reported above make available a coordinate-mapping technique that can be used for blade rows of moderate solidity that have rounded trailing edges. The final grid is sheared, in such a way as to produce grid cells which are rectangles at the blade surfaces and parallelograms away from the blades. The corresponding cells in the computational plane have the images of the trailing edges and of downstream infinity located at the corners of the grid, a feature that is used in certain contemporary flow field-analysis codes.

The methods presented are applicable for a gap/chord ratio down to about 0.8; further work is required, in order to extend this range.

Acknowledgments

The author has had the benefit of many discussions of this work with Joseph P. Nenni, John R. Moselle, and George S. Dulikravich. This work was supported by the Air Force Aero Propulsion Laboratory, Wright-Patterson AFB, Ohio, and by the Internal Research Program of the Calspan Corporation.

References

1 Dulikravich, D. S., "CAS2D—FORTRAN Program for Nonrotating Blade-to-Blade, Steady, Potential Transonic Cascade Flows," NASA TP 1705, July 1980.

2 Nenni, J. P., and Rae, W. J., "Experience With the Development of an Euler Code for Rotor Rows," ASME Paper No. 83-GT-36, Mar. 1983.

3 Ives, D. C., and Liutermoza, J. F., "Analysis of Transonic Cascade Flow Using Conformal Mapping and Relaxation Techniques," *AIAA Journal*, Vol. 15, 1977, pp. 647–652.

4 Theodorsen, T., and Garrick, I. E., "General Potential Theory of Arbitrary Wing Sections," NACA Technical Report 452, 1934; Garrick, I. E., "On the Plane Potential Flow Past a Lattice of Arbitrary Airfoils," NACA Report 788, 1944.

5 Henrici, P., "Fast Fourier Methods in Computational Complex Analysis," *SIAM Review*, Vol. 21, Oct. 1979, pp. 481–527.

6 Rae, W. J., "A Computer Program for the Ives Transformation in Turbomachinery Cascades," Calspan Report No. 6275-A-3, ADA 096416, Nov. 1980.

7 Kober, H., *Dictionary of Conformal Transformations*, Dover Publications, 1957.

Downloaded 01 Jun 2010 to 171.66.16.70. Redistribution subject to ASME license or copyright; see http://www.asme.org/terms/Terms_Use.cfm

Matrix Solution of Compressible Flow on S_1 Surface Through a Turbomachine Blade Row With Splitter Vanes or Tandem Blades

Wu Chung-Hua
Professor and Director.

Wang Baoguo
Research Associate.

Institute of Engineering Thermophysics,
Academia Sinica,
Beijing, People's Republic of China

The basic aerothermodynamic equations of turbomachine flow expressed with respect to nonorthogonal curvilinear coordinates and corresponding nonorthogonal velocity components are used to solve the compressible flow S_1 surface in a turbomachine blade row with splitter vanes or tandem blades. The equation of stream function is solved by matrix technique, and the mass flow ratio and outlet flow angle are determined by applying the Kutta-Joukowsky condition to the trailing edges of the main blade and the splitter vane. Typical examples are given to illustrate the effectiveness of the present method.

Introduction

In order to solve the three-dimensional turbomachine flow in a relatively simple manner, an approach was taken to obtain the three-dimensional solution by an appropriate combination of mathematically two-dimensional flows on two kinds of relative stream surface, S_1 and S_2 [1]. This approach may also be used individually to give approximate three-dimensional flow on assumed S_1 and S_2 surfaces as first reported in [2–5].

However, in the 1950s, after performing a number of typical calculations it became evident that in order to improve the relatively poor accuracy of numerical differentiation at grid points near a curved boundary, the coordinate lines should coincide with the curved blade, casing and hub profiles, and, thus, general nonorthogonal curvilinear coordinates could be used to advantage. Consequently, a new set of basic aerothermodynamic equations employing general nonorthogonal curvilinear coordinates and corresponding nonorthogonal velocity components was developed in the early 1960s [6, 7] and have been used to solve the individual flow on S_1 and S_2 surfaces [8, 9] or to solve the three-dimensional flow through a turbomachine by iterative calculation of the flows on S_1 and S_2 surfaces [10, 11]. In this paper these basic equations are used to investigate the flow on the S_1 surface in a turbomachine blade row with splitter vanes or tandem blades.

For incompressible flow, Spraglin [12] obtained a solution for flow through cascades in tandem by the use of conformal mapping technique, and Kramer, Stockman, and Bean [13] obtained a solution for flow through a pump rotor with splitter vanes by the stream-function equation given in [1, 3] and by matrix technique. The same equation was used by Katsanis and McNally [14] to calculate the flow through a tandem blade turbomachine by relaxation technique. In both [13] and [14] the mass-flow ratio and the outlet flow angle are given. Nakase and Senoo [15] and Liu, Ribaud, and Abdelrahman [16] extended the method of singularity to compute the S_1 flow with splitter vanes.

In this paper, the new set of basic equations presented in [7] is solved by a matrix technique in which both the mass flow ratio and outlet flow angle are determined by applying the Kutta-Joukowsky condition to the trailing edge of the main blade and of the splitter vane. A typical example is given to illustrate the effectiveness of the present method.

Basic Equations

Basic aerothermodynamic equations governing the flow of a viscous gas in a turbomachine were given by Wu in [17] and [18]. One-dimensional approximate equations consistent with two-dimensional or three-dimensional equations, and the use of entropy to account for the major viscous effects in an engineering manner were suggested. The latter was adopted in [8, 19] and by others and is also used in this paper.

The basic aerothermodynamic equations for relative flow of a viscous gas passing through a turbomachine blade row rotating at constant angular speed, ω, are [18]

Continuity:

$$\frac{\partial \rho}{\partial t} + \nabla \cdot (\rho \mathbf{W}) = 0 \tag{1}$$

Motion:

$$-\frac{1}{\rho}\nabla p + \frac{1}{\rho}\nabla \cdot \Pi' = \frac{d'\mathbf{W}}{dt} - \omega' r + 2\omega \times \mathbf{W} \tag{2}$$

1st Law of Thermodynamics:

$$\frac{dI}{dt} = \frac{1}{\rho}\frac{\partial p}{\partial t} + \dot{q} + \frac{1}{\rho}\nabla \cdot (\Pi' \cdot \mathbf{W}) \tag{3}$$

Contributed by the Gas Turbine Division of THE AMERICAN SOCIETY OF MECHANICAL ENGINEERS and presented at the 28th International Gas Turbine Conference and Exhibit, Phoenix, Arizona, March 27–31, 1983. Manuscript received at ASME Headquarters November 30, 1982. Paper No. 83-GT-10.

Copyright © 1984 by ASME
Downloaded 01 Jun 2010 to 171.66.16.70. Redistribution subject to ASME license or copyright; see http://www.asme.org/terms/Terms_Use.cfm

2nd Law of Thermodynamics:

$$T\frac{ds}{dt}=\dot{q}+\frac{\Phi}{\rho} \tag{4}$$

in which the first term on the right-hand side of equation (2) denotes the acceleration of relative flow.

For engineering calculations, it is usually assumed that the relative flow is steady and adiabatic, then the unsteady terms of p,ρ, and $\dot{q}$ drop out from the preceding equations. One should, however, be careful with the heat transfer term. It usually has a sign opposite to that of the viscous term, and in the special case of laminar boundary layer flow for a gas whose Prandtl number is equal to unity, these two terms cancel each other, resulting in a constant value of I along the relative streamline (see, for instance, [18] for a detailed analysis). With regard to the gas viscosity, its effect on flow cannot be entirely neglected in the design of turbomachines, but we are as yet unable to include the viscous terms in design calculations. An approximate engineering treatment now widely used consists of the following: (*a*) instead of equation (4), the increase of entropy along a streamline is computed from appropriate polytropic relation, as first suggested in [17], or from experimental the stagnation-pressure-loss coefficient [19]; (*b*) the entropy gradient value so obtained is then used in the following form of equation of motion for nonviscous gas [1]

$$\mathbf{W}\times(\nabla\times\mathbf{V})=\nabla I-T\nabla s \tag{2a}$$

In essence, this engineering model means that the accumulated effect of upstream viscous action in increasing entropy is considered while the local viscous stresses are neglected. A typical effect of applying this model to S_2 calculation is shown in Fig. 1. It is seen that the radial entropy gradient term in the equation tends to decrease the flow velocity toward the inner and outer walls, approximating the actual flow much better than the case where the entropy term is neglected. Therefore, this model has been widely used for S_2 calculations.

For S_1 surface flow, the results obtained for the velocity distribution along the the blade surface under inviscid assumption usually agree very well with experimental data. Thus, for the S_1 calculation alone, it does not seem necessary to consider the increase of entropy along streamlines. But in the solution of three-dimensional flow through iterative calculation of flow on S_1 and S_2 surface, it is necessary to consider consistent value of entropy at each point for the calculation on S_1 surface and on S_2 surfaces. So, in general,

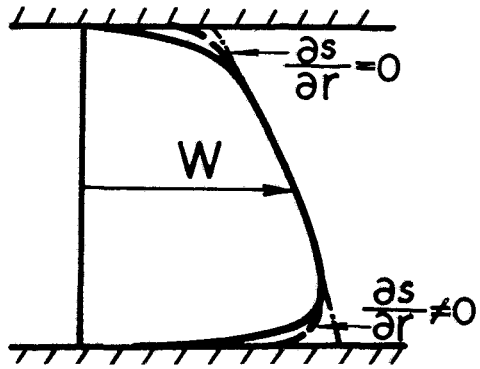


Fig. 1 Velocity variation considering and neglecting entropy gradient

the following set of basic equations is considered for S_1 calculation

$$\nabla\cdot(\rho\mathbf{W})=0 \tag{1a}$$

$$\mathbf{W}\times(\nabla\times\mathbf{V})=\nabla I-T\nabla s \tag{2a}$$

$$\frac{dI}{dt}=0 \tag{3a}$$

$$\frac{ds}{dt}>0 \tag{4a}$$

Equations Governing Fluid Flow on General S_1 Surface

Let (y^1, y^2, y^3) be the usual orthogonal Cartesian coordinates of a point, P, and (x^1, x^2, x^3) be its nonorthogonal curvilinear coordinates (see Fig. 2) with its base vector

$$\mathbf{e}_i=\partial\mathbf{R}/\partial x^i \tag{5}$$

where $\mathbf{R}$ is the radius vector from origin. The square of the distance between P and a neighboring point is

$$(ds)^2=g_{ij}dx^i dx^j (i,j=1,2,3) \tag{6}$$

where g_{ij} is the covariant metric tensor of the three-dimensional space

$$g_{ij}=(\partial y^k/\partial x^i)\cdot(\partial y^k/\partial x^j)=\mathbf{e}_i\cdot\mathbf{e}_j=g_{ji} \tag{7}$$

The length of the element of arc measured along a curvilinear coordinate line is

$$ds_{(i)}=\sqrt{g_{ii}}dx^i \text{ (not summed for } i) \tag{8}$$

Nomenclature

a = velocity of sound or Jacobian of matrix, $a_{\alpha\beta}$
c_p, c_v = specific heat of gas at constant pressure and constant volume, respectively
$\mathbf{e}_i$ = base vector of x^i coordinate system
$\mathbf{e}^i$ = reciprocal base vector of x^i coordinate system
g = Jacobian of matrix g_{ij}
g_{ij} = covariant metric tensor of x^i coordinate system
g^{ij} = contravariant metric tensor of x^i coordinate system
H = absolute stagnation ethalpy per unit mass of gas, $h + V^2/2$
I = relative stagnation rothalpy per unit mass of gas, $h + (\mathbf{W})^2/2-(\omega r)^2/2$
$\dot{q}$ = heat transfer to unit mass of gas per unit time
s = entropy per unit mass of gas
T = absolute temperature of gas
t = time
w^i = contravariant component of relative velocity of gas
w_i = covariant component of relative velocity of gas
W^i = physical component of relative velocity along the x^i-direction
x^i = general nonorthogonal curvilinear coordinate system
σ = angle between tangent of generator of S_1 stream surface of revolution in the meridional plane and axial direction, $\tan^{-1}(Wr/Wz)$
Ψ = stream function defined on S_1 relative stream surface
Ψ_s = the value of stream function along the splitter vane or tandem blade surface
Π' = viscous stress tensor
Φ = dissipation function

Superscripts

$^{\circ\prime}$ = relative stagnation state
* = non-dimensional variable
(ν) = νth iteration

Subscript

i = inlet station

Downloaded 01 Jun 2010 to 171.66.16.70. Redistribution subject to ASME license or copyright; see http://www.asme.org/terms/Terms_Use.cfm

The reciprocal vector, $\mathbf{e}^i$, is defined by

$$\mathbf{e}^i = (\mathbf{e}_j \times \mathbf{e}_j)/\sqrt{g} \tag{9}$$

A vector, $\mathbf{W}$, in the three-dimensional space is expressed in terms of either base vector, $\mathbf{e}_i$, or the reciprocal vector, $\mathbf{e}^i$, as follows (see Fig. 3):

$$\mathbf{W} = w^i \mathbf{e}_i \tag{10}$$

$$\mathbf{W} = w_i \mathbf{e}^i \tag{11}$$

the contravariant component, w^i, is directly related to the physical component by

$$W^i = \sqrt{g_{ii}}\, w^i \tag{12}$$

and the convariant component is related to the physical component by

$$w_i = \mathbf{W} \cdot \mathbf{e}_i = g_{ij} w^j \tag{13}$$

The following differential operators in general curvilinear coordinate are useful in expressing the basic equations (1*a*–4*a*) in terms of physical components of velocity:

$$\nabla \cdot \mathbf{W} = \frac{1}{\sqrt{g}} \frac{\partial(\sqrt{g} w^i)}{\partial x^i} \tag{14}$$

$$\nabla I = \mathbf{e}^i \frac{\partial I}{\partial x^i} \tag{15}$$

and the contravariant components ξ^i of a vector

$$\nabla \times \mathbf{V} = \xi^i \mathbf{e}_i \tag{16}$$

are

$$\xi^i = \frac{1}{\sqrt{g}} \left(\frac{\partial v_k}{\partial x^j} - \frac{\partial v_j}{\partial x^k} \right) \tag{17}$$

To calculate the flow along a given S_1 surface, it is most convenient to take nonorthogonal curvilinear coordinates x^1 and x^2 on the S_1 surface and x^3 normal to it. Then

$$W^3 = w^3 = w_3 = 0 \tag{18}$$

When the normal distance between two adjacent S_1 surfaces with $dx^3 = 1$ be denoted by τ

$$\sqrt{g_{33}} = \tau \tag{19}$$

The square of the distance between two neighboring points on the (x^1, x^2) coordinate surface may be written as

$$(ds)^2 = a_{\alpha\beta} dx^\alpha dx^\beta (a, \beta = 1,2) \tag{20}$$

where $a_{\alpha\beta}$ is the covariant metric tensor of the surface:

$$a_{\alpha\beta} = \frac{\partial y^\kappa}{\partial x^\alpha} \cdot \frac{\partial y^\kappa}{\partial x^\beta} = \mathbf{e}_\alpha \cdot \mathbf{e}_\beta = a_{\beta\alpha} \tag{21}$$

Let the angle between the x^1 and x^2 coordinate lines be denoted by θ_{12}, then

$$g_{12} = g_{21} = a_{12} = a_{21} = \sqrt{a_{11}}\sqrt{a_{22}} \cos\theta_{12} \tag{22}$$

$$g_{i3} = g_{3i} = 0 \qquad (i = 1,2) \tag{23}$$

$$g = g_{33} a = \tau^2 a_{11} a_{22} \sin^2 \theta_{12} \tag{24}$$

$$w_1 = a_{11} w^1 + a_{12} w^2 = \sqrt{a_{11}}(W^1 + W^2 \cos\theta_{12}) \tag{25}$$

$$w_2 = a_{21} w^1 + a_{22} w^2 = \sqrt{a_{22}}(W^1 \cos\theta_{12} + W^2) \tag{26}$$

Substituting equations (12), (14), (18), and (24) into equation (1*a*) results in

$$\frac{\partial(\tau\rho W^1 \sqrt{a_{22}} \sin\theta_{12})}{\partial x^1} + \frac{\partial(\tau\rho W^2 \sqrt{a_{11}} \sin\theta_{12})}{\partial x^2} = 0 \tag{1b}$$

Substituting equations (10), (15), (16) into equation (2*a*) results in

$$w^i \mathbf{e}_i \times \xi^i \mathbf{e}_i = \left(\frac{\partial I}{\partial x^i} - T \frac{\partial s}{\partial x^i} \right) \mathbf{e}^i \tag{27}$$

When equations (9) and (17) and the following relation between the absolute and relative vorticity is used

$$\nabla \times \mathbf{V} = \nabla \times \mathbf{W} + 2\omega \tag{28}$$

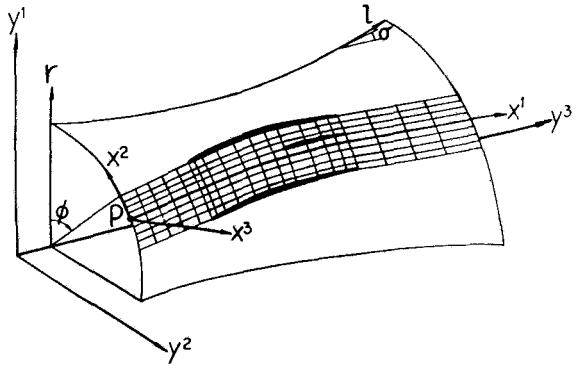


Fig. 2 Nonorthogonal curvilinear coordinates

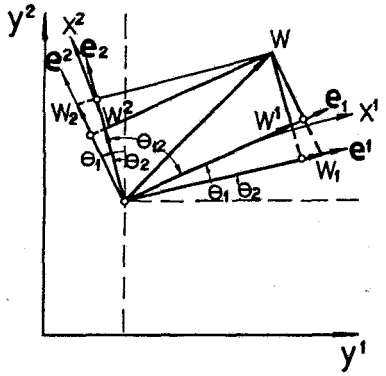


Fig. 3 General nonorthogonal curvilinear coordinates x^1 and x^2, base vectors $\mathbf{e}_1$ and $\mathbf{e}_2$, reciprocal vectors $\mathbf{e}^1$ and $\mathbf{e}^2$, and corresponding velocity components

equation of motion (2*a*) in the $\mathbf{e}^2$ direction is

$$-w^1 \left[\left(\frac{\partial w_2}{\partial x^1} - \frac{\partial w_1}{\partial x^2} \right) + 2\omega^3 \sqrt{a_{11} a_{22} \tau^2 \sin^2 \theta_{12}} \right] = \frac{\partial I}{\partial x^2} - T \frac{\partial s}{\partial x^2} \tag{29}$$

By using equations (26) and (25), equation (29) becomes

$$\frac{\partial}{\partial x^2}[(W^1 + W^2 \cos\theta_{12})\sqrt{a_{11}}] - \frac{\partial}{\partial x^1}[(W^1 \cos\theta_{12} + W^2)\sqrt{a_{22}}] = 2\tau\sqrt{a_{11} a_{22}}\,\omega^3 \sin\theta_{12} + \frac{\sqrt{a_{11}}}{W^1}\left(\frac{\partial I}{\partial x^2} - T \frac{\partial s}{\partial x^2} \right) \tag{2b}$$

Principal Equation

Equation (1*b*) is the necessary and sufficient condition that there exists a function, Ψ, with

$$\frac{\partial \psi}{\partial x^1} = -\tau\rho W^2 \sqrt{a_{11}} \sin\theta_{12}$$

$$\frac{\partial \psi}{\partial x^2} = \tau\rho W^1 \sqrt{a_{22}} \sin\theta_{12} \tag{30}$$

Substituting equations (30) into equation (2*b*) results in the following principal equation

$$\frac{1}{a_{11}} \frac{\partial^2 \psi}{\partial (x^1)^2} - 2\frac{\cos\theta_{12}}{\sqrt{a_{11} a_{22}}} \frac{\partial^2 \psi}{\partial x^1 \partial x^2} + \frac{1}{a_{22}} \frac{\partial^2 \psi}{\partial (x^2)^2} + \frac{J}{\sqrt{a_{11}}} \frac{\partial \psi}{\partial x^1} + \frac{K}{\sqrt{a_{22}}} \cdot \frac{\partial \psi}{\partial x^2} = M \tag{31}$$

where

$$M = \frac{\tau\rho \sin\theta_{12}}{W^1 \sqrt{g_{22}}} \left(\frac{\partial I}{\partial x^2} - T \frac{\partial S}{\partial x^2} \right) + N \tag{32}$$

Downloaded 01 Jun 2010 to 171.66.16.70. Redistribution subject to ASME license or copyright; see http://www.asme.org/terms/Terms_Use.cfm

$$N=\left(\frac{\partial ln\rho}{\sqrt{g_{11}}\partial x^1}-\cos\theta_{12}\frac{\partial ln\rho}{\sqrt{g_{22}}\partial x^2}\right)\frac{\partial\psi}{\sqrt{g_{11}}\partial x^1}+\left(\frac{\partial ln\rho}{\sqrt{g_{22}}\partial x^2}\right.$$

$$\left.-\cos\theta_{12}\frac{\partial ln\rho}{\sqrt{g_{11}}\partial x^1}\right)\frac{\partial\psi}{\sqrt{g_{22}}\partial x^2}+2\tau^2\rho\omega^3\sin^2\theta_{12} \tag{33}$$

Equation (2*b*) can be put into the following form

$$C_1\frac{\partial^2\psi}{\partial(x^1)^2}+C_2\frac{\partial^2\psi}{\partial x^1\partial x^2}+C_3\frac{\partial^2\psi}{\partial(x^2)^2}=C_4 \tag{34a}$$

or

$$\frac{\partial}{\partial x^1}\left(\frac{A_{21}}{\rho}\frac{\partial\Psi}{\partial x^1}+\frac{A}{\rho}\frac{\partial\Psi}{\partial x^2}\right)+\frac{\partial}{\partial x^2}\left(\frac{A_{12}}{\rho}\frac{\partial\Psi}{\partial x^2}+\frac{A}{\rho}\frac{\partial\Psi}{\partial x^1}\right)$$

$$=2\sqrt{g}\omega^3+\frac{\sqrt{g_{11}}}{W^1}\left(\frac{\partial I}{\partial x^2}-T\frac{\partial s}{\partial x^2}\right) \tag{34b}$$

This form of equation is convenient to use for judging the type of the quasi-linear differential equation (34*a*). Its equation of characteristics is

$$(C_2)^2-4C_1C_3=4(a)^2[(W)^2-(a)^2]\sin^2\theta_{12} \tag{35}$$

The partial differential equation (34) is then of the hyperbolic type when $W>a$ and characteristics exist. It is of the elliptic type when $W<a$ and the characteristics are imaginary.

The nondimensionalized form of equation (31) is [8]

$$\frac{1}{g_{11}^*}\frac{\partial^2\psi^*}{\partial(x^1)^2}-2\frac{\cos\theta_{12}}{\sqrt{g_{11}^*}\sqrt{g_{22}^*}}\frac{\partial^2\psi^*}{\partial x^1\partial x^2}+\frac{1}{g_{22}^*}\frac{\partial^2\psi^*}{\partial(x^2)^2}+\frac{J^*}{\sqrt{g_{11}^*}}\frac{\partial\psi^*}{\partial x^1}$$

$$+\frac{K^*}{\sqrt{g_{22}^*}}\frac{\partial\psi^*}{\partial x^2}=\left(\frac{\partial ln\rho^*}{\sqrt{g_{11}^*}\partial x^1}-\cos\theta_{12}\frac{\partial ln\rho^*}{\sqrt{g_{22}^*}\partial x^2}\right)\frac{\partial\psi^*}{\sqrt{g_{11}^*}\partial x^1}$$

$$+\left(\frac{\partial ln\rho^*}{\sqrt{g_{22}^*}\partial x^2}-\cos\theta_{12}\frac{\partial ln\rho^*}{\sqrt{g_{11}^*}\partial x^1}\right)\frac{\partial\psi^*}{\sqrt{g_{22}^*}\partial x^2}+\left[2\rho^*\tau^{*2}\omega^{3*}\sin^2\theta_{12}\right.$$

$$\left.+\frac{\tau^*\rho^*\sin\theta_{12}}{\sqrt{g_{22}^*}W^{1*}}\left(\frac{\partial I^*}{\partial x^2}-T^*\frac{R}{U_i^2}T_i^{\circ\prime}\frac{\partial S^*}{\partial x^2}\right)\right]\Gamma \tag{36}$$

In axial-flow turbomachines, the departure of S_1 surface from a surface of revolution has been generally estimated to be small. Recent detailed three-dimensional calculations [20] and an order-of-magnitude analysis [21] validate this estimation. For a surface of revolution

$$\omega^3=-\omega\frac{\sin\sigma}{\sqrt{g^{33}}} \tag{37}$$

and equation (2*b*) becomes

$$\frac{\partial}{\partial x^2}[(W^1+W^2\cos\theta_{12})\sqrt{g_{11}}]-\frac{\partial}{\partial x^1}[(W^1\cos\theta_{12}+W^2)\sqrt{g_{22}}]$$

$$=-2\sqrt{g_{11}g_{22}}\tau\omega\sin\sigma\sin\theta_{12}+\frac{\sqrt{g_{11}}}{W^1}\left(\frac{\partial I}{\partial x^2}-T\frac{\partial S}{\partial x^2}\right) \tag{2c}$$

The density of gas is related to the relative velocity and entropy by the following equation [1]

$$\frac{\rho}{\rho_i^{\circ\prime}}=\left[1-\frac{k-1}{2}\frac{(\rho W)^2}{(\rho_i^{\circ\prime}a_i^{\circ\prime})^2(\rho/\rho_i^{\circ\prime})}\right]^{\frac{1}{k-1}}e^{-\frac{S_i^{\circ\prime}}{R}} \tag{38}$$

The value of ρ and W can be determined from their product by rewritting equation (38) as

$$\Sigma^2=\left(1-\frac{\phi}{\Sigma^2}\right)^{\frac{2}{k-1}} \tag{39}$$

and

$$\Sigma=\rho^*\left(\frac{H_i^*}{I^*+\frac{(\gamma^*)^2}{2}}\right)^{\frac{1}{k-1}}e^{(S^*-S_i^{*\circ\prime})} \tag{40}$$

and

$$\phi=\frac{1}{2(\Gamma\tau^*\sin\theta_{12})^2H_i^*}\left(\frac{H_i^*}{I^*+(\gamma^*)^2/2}\right)^{\frac{k+1}{k-1}}\left[\frac{1}{g_{22}^*}\left(\frac{\partial\psi^*}{\partial x^2}\right)^2\right.$$

$$\left.-\frac{2\cos\theta_{12}}{\sqrt{g_{11}^*g_{22}^*}}\frac{\partial\psi^*}{\partial x^1}\frac{\partial\psi^*}{\partial x^2}+\frac{1}{g_{11}}\left(\frac{\partial\psi^*}{\partial x^1}\right)^2\right]e^{2(S^*-S_i^{*\circ\prime})} \tag{41}$$

The table in [1] can then be used to find Σ (i.e., ρ) from known value of ϕ (i.e., ρw). W is then computed from ρw after ρ is obtained.

Boundary Conditions and Method of Solution

Steady, subsonic flow on the S_1 surface through a turbomachine blade row with splitter vanes or tandem blades is considered in this section. It is obvious that solution of this problem is somewhat more difficult, because boundary shape and boundary conditions are more complex than ordinary S_1 flow problems.

Boundary Conditions. Equation (36) is to be solved over the region bounded by $A_1B_1B_2A_2$ and FK_1GK_2F (Fig. 4). The periodic conditions at inlet and outlet have to be satisfied. At the internal boundary,

$$\psi_s=\text{const} \tag{42}$$

At the station A_1A_2 sufficiently far upstream of the blades, the flow condition is taken to be uniform and the flow angle equal to the given inlet flow angle.

At the exit station B_1B_2 far downstream of the blade, the flow condition is also taken to be uniform, but the outlet flow angle is unknown.

For a blade having a sharp trailing edge, the Kutta-Joukowsky condition may be applied and the correct exit angle far downstream is the one that gives the flow at the trailing edge satisfying that condition. But in actual engineering problems, the blade usually has a round trailing edge. For round trailing edge, some available empirical rule for the outlet flow angle may be used. On the basis of a large number of experiments, a criterion is proposed in [22] by M.I. Joukowsky, namely, the velocities are equal at the blade cutoff points

$$|W_p|=|W_s| \tag{43}$$

where W_p and W_s are velocities at the blade cutoff points on the pressure and suction surfaces, respectively. V. S. Joukowsky and S. S. Kutateladze further pointed out that this flow model gives an outlet flow angle in good agreement with experimental data [23]. This criterion is used in this paper for both main blade and splitter blade and is herein referred to as trailing edge condition.

Iteration Between ψ-Field and ρ-Field. Iterative process between $\{\psi\}$ and $\{\rho\}$ is carried out with assumed values of mass-flow ratio and outlet flow angle. ψ_s and β_2 satisfying trailing edge condition are then obtained.

When every partial derivative in equation (36) is replaced by a second-order, central-difference expression the following matrix equation [24] is obtained

$$[M]\{\psi\}^{(n+1)}=\{P\}^{(n)} \tag{44}$$

or

$$[M]\{\Delta\psi\}^{(n+1)}=\{R\}^{(n)} \tag{45}$$

where $\{P\}$, $\{\Delta\psi\}$ and $\{R\}$ are column matrices formed by ψ and ρ at each grid point and $[M]$ is the matrix composed of the coefficients. $\{\Delta\psi\}^{(n+1)}\equiv\{\psi\}^{(n+1)}-\{\psi\}^{(n)}$ and $\{R\}$ is the residual. In this paper, the $[L]$ $[U]$ decomposition method is chosen for fast convergence. For subsonic flow, this method is very stable numerically. To solve equation (36), two relaxation factors, α_ψ and α_ρ, are selected to iterate $\{\psi\}$ and $\{\rho\}$ on the right-hand side of the equation. Thus

Downloaded 01 Jun 2010 to 171.66.16.70. Redistribution subject to ASME license or copyright; see http://www.asme.org/terms/Terms_Use.cfm

$$\psi^{*(\nu)} = \psi^{*(\nu-1)} + \alpha_\psi(\tilde{\psi}^{*(\nu)} - \psi^{*(\nu-1)}) \quad (46)$$

$$\rho^{*(\nu+1)} = \rho^{*(\nu)} + \alpha_\rho(\tilde{\rho}^{*(\nu+1)} - \rho^{*(\nu)}) \quad (47)$$

where

$\psi^{*(\nu)}$ is value taken for the νth iteration.

$\tilde{\psi}^{*(\nu)}$ is calculated value of the νth iteration.

Additional stability was further obtained for compressible flow by increasing the inlet Mach number gradually to the required value.

It is interesting to note that ψ_s^* value is an initial estimate in the process of solving $\{\psi^*\}$. Correct ψ_s^* value is obtained in the manner discussed in the next section.

Determination of β_2 and ψ_s^* Value. Let the velocity difference at the blade cutoff point be denoted by

$$\Delta W \equiv W_s - W_p \quad (48)$$

ΔW-value for main-blade and splitter-vane are denoted by ΔW_1 and ΔW_2, respectively. The following auxiliary functions are introduced.

$$F_1(\beta_2,\psi_s) = \sum_{j=1}^{n}\sum_{i=1}^{m}\prod_{\substack{k=1\\k\neq 1}}^{m}\frac{\beta_2-(\beta_2)_k}{(\beta_2)_i-(\beta_2)_k}\prod_{\substack{l=1\\l\neq j}}^{n}\frac{\psi_s-(\psi_s)_l}{(\psi_s)_j-(\psi_s)_l}(\Delta W_1)_{ij} \quad (49)$$

$$F_2(\beta_2,\psi_s) = \sum_{j=1}^{n}\sum_{i=1}^{m}\prod_{\substack{k=1\\k\neq i}}^{m}\frac{\beta_2-(\beta_2)_k}{(\beta_2)_i-(\beta_2)_k}\prod_{\substack{l=j\\l\neq j}}^{n}\frac{\psi_s-(\psi_s)_l}{(\psi_s)_j-(\psi_s)_l}(\Delta W_2)_{ij} \quad (50)$$

where $(\Delta W_\alpha)_{ij}$ denotes ΔW_α obtained from $(\beta_2)_i$ and $(\psi_s)_j$. Then, the values of β_2 and ψ_s obtained by solving the following equation will satisfy the trailing edge condition

$$\left.\begin{aligned}F_1(\beta_2,\psi_s)&=0\\F_2(\beta_2,\psi_s)&=0\end{aligned}\right\} \quad (51)$$

The solution is obtained by the use of a combination of Newton iterative method and steepest descent method. Convergence rate of the former is faster than the latter, but choice of initial value is difficult. Therefore the latter is employed first until the solution is converged to a specified tolerance. Then the former is used. Actual computation shows that numerical stability is very good.

Iterative Scheme. The iterative scheme for direct problem of flow along S_1 stream surface with a splitter vane is as follows

$$\begin{matrix}(\beta_2)_i & \{\psi^*\}_{ij} & (\Delta W_1)_{ij} & \left\{\begin{matrix}F_1(\beta_2,\psi_s)=0 & \psi_s & \{\psi^*\}\\ F_2(\beta_2,\psi_s)=0 & \beta_2 & \{\rho^*\}\end{matrix}\right. & \\ (\psi_s)_j & \{\rho^*\}_{ij} & (\Delta W_2)_{ij} & \end{matrix} \quad \text{stop}$$

When there are two splitter vanes placed in the passage of the main cascade, equation (51) becomes

$$\left.\begin{aligned}F_1(\beta_2,\psi_{s,1},\psi_{s,2})&=0\\F_2(\beta_2,\psi_{s,1},\psi_{s,2})&=0\\F_3(\beta_2,\psi_{s,1},\psi_{s,2})&=0\end{aligned}\right\} \quad (52)$$

where $\psi_{s,1}$ and $\psi_{s,2}$ are ψ_s-values at the two splitter vanes, respectively. Solution of this case can be carryed out in the same way as described previously.

It may be mentioned that a very similar problem exists in the case of flow along a S_2 surface [25], i.e. flow at the exit of a fan passing through a splitter ring. The same approach described in this paper may be used to solve that problem.

Numerical Examples

In order to investigate the possibility of improving the performance of the cascade computed in [8], the first half of every other blade of that cascade is cut off, resulting in splitter vanes having the same shape as the latter half of the main blade. For the purpose of checking the present computer code, a calculation is first made for the main cascade with an inlet Mach number of 0.658, inlet air angle of 30 deg. The velocity distribution obtained is compared with the experimental data [26] in Fig. 5. The agreement is seen to be quite good. Then solution is obtained for the same inlet Mach number of 0.658 and inlet angle of 30 deg for the cascade with splitter blades. Two hundred and fifty six grid points are used in the calculation of the main cascade, with 12×8 points in the cascade channel. Five hundred and seventy grid points are used in the calculation of the cascade with splitter vanes, with 7×15 points in the front part of the channel and 11×15 points in the rear part of the channel.

In the calculation of the cascade with splitter vanes, calculation for the following four sets of β_2 and ψ_s^* values are first made

ψ_s^*	52.4	55.6	52.4	55.6
β_2	13.70°	13.70°	22.60°	22.60°

Interpolation by equation (51) gives the following values of β_2 and ψ_s^*, satisfying the trailing edge condition:

$$\beta_2 = 11.8 \text{ deg}, \quad \psi_s^* = 47.3$$

The distributions of Mach numbers along the blade surfaces obtained in these two cases are compared in Fig. 6. It is seen that the blade arrangement in the latter case, having the effect of reducing the solidity of the cascade in the front part of the channel, gives significantly lower velocities on the suction surface of the main blade in the front part of channel. However, the turning angle is 1.2 deg smaller than that in the former.

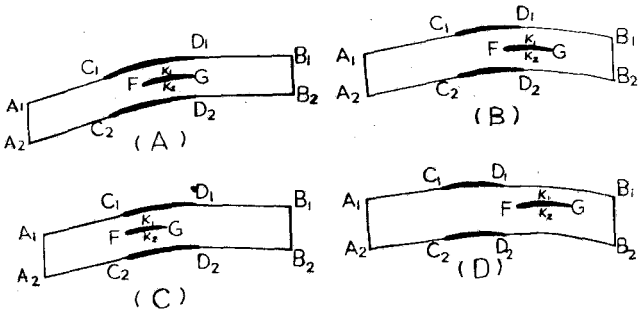


Fig. 4 Cascades with splitter vanes or tandem blades

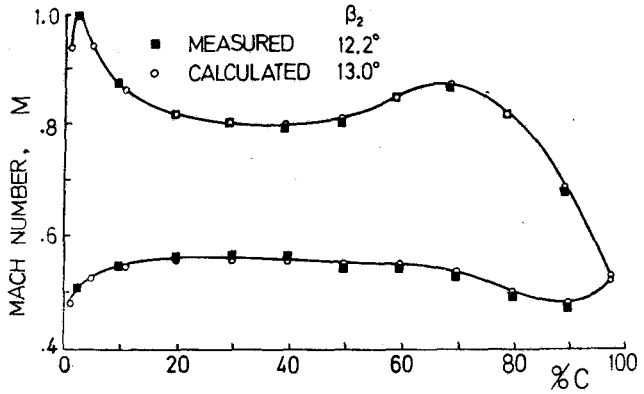


Fig. 5 Comparison of calculated Mach number distribution and experimental data

Downloaded 01 Jun 2010 to 171.66.16.70. Redistribution subject to ASME license or copyright; see http://www.asme.org/terms/Terms_Use.cfm

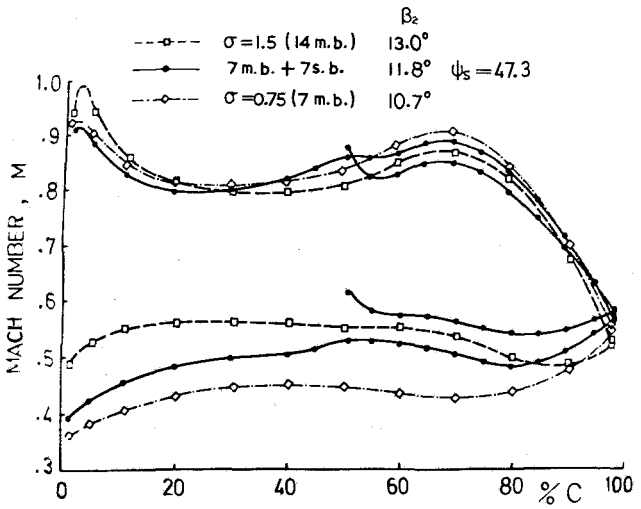


Fig. 6 Mach number variation along the blade surface for three cascades

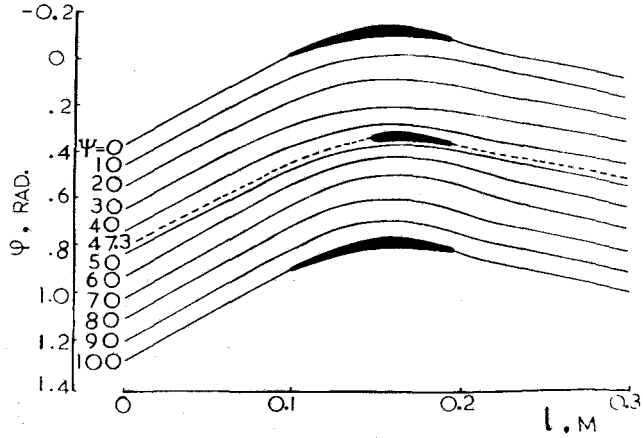


Fig. 7 Distribution of streamlines in the cascade with splitter vanes

Figure 7 shows the distribution of streamlines in the latter case. For purpose of comparison, the main cascade with a reduced solidity of 0.75 is also calculated. The result is shown in Fig. 6. It is noticed during the calculation, that the velocity distributions are very sensitive to location in the channel of the leading and trailing edge of the splitter vane.

Concluding Remarks

The compressible flow along a S_1 surface in a turbomachine blade row with splitter vanes is obtained by a matrix solution of the recently developed basic aerothermodynamic equations employing nonorthogonal velocity components and the application of the Kutta-Joukowsky condition at the trailing edges of the main blade and splitter blade. The computation is stable; the correct mass flow ratio and outlet flow angle are determined after computing four sets of assumed values.

The method can be easily extended in S_1 cascades having two splitter vanes or cascades in tandem. The flow along a S_2 surface having a splitter ring downstream of a fan can also be solved in a similar manner.

References

1 Wu Chung-hua, "A General Theory of Three-Dimensional Flow in Subsonic and Supersonic Turbomachines of Axial, Radial, and Mixed-Flow Types," ASME Paper No. 50-A-79, ASME *Transactions*, Nov. 1952.

2 Wu Chung-hua, "A General Through-Flow Theory of Fluid Flow With Subsonic or Supersonic Velocity in Turbomachines Having Arbitrary Hub and Casing Shapes," NACA TN 2302, 1951.

3 Wu Chung-hua, and Brown, C. A., "Method of Analysis for Compressible Flow Past Arbitrary Turbomachine Blades on General Surface of Revolution," NACA TN 2407, 1951.

4 Wu Chung-hua, "Matrix and Relaxation Solutions That Determine Subsonic Through-Flow in an Axial-Flow Gas Turbine," NACA TN 2750, 1952.

5 Wu Chung-hua, "Subsonic Flow of Air Through a Single-Stage and a Seven Stage Compressor," NACA TN 2961, 1953.

6 Wu Chung-hua, "Basic Aerothermodynamic Equations Governing Fluid Flow in Turbomachines Expressed in Terms of Nonorthogonal Curvilinear Coordinates," Research Note, Institute of Mechanics, 1963; and Lecture Notes, China University of Science and Technology, 1975.

7 Wu Chung-hua, "Three-Dimensional Turbomachines Flow Equations Expressed with Respect to Nonorthogonal Curvilinear Coordinates and Methods of Solution," *Proceedings of the 3rd International Symposium on Air-Breathing Engines*, 1976, pp. 233–252; or *Engineering Thermophysics in China*, Vol. 1, No. 2, 1980, Rumford Pub. Co., U.S.A.

8 Wu Wen-quan, and Liu Cui-e, "Flow-Field Matrix Solution for Direct Problem of Flow Along S_1 Relative Stream Surface Employing Nonorthogonal Velocity Components," *Journal of Engineering Thermophysics*, Vol. 1, No. 1, 1980, pp. 18–27 (in Chinese); or *Engineering Thermophysics in China*, Vol. 1, No. 3, pp. 307–322, (Rumford Pub. Co., U.S.A.).

9 Zhu Rong-guo, "Flow Field Line-Relaxation Solution for Inverse Problem of Flow Along S_2 Relative Stream Surface Employing Nonorthogonal Curvilinear Coordinates and Corresponding Nonorthogonal Velocity Components," *Journal of Engineering Thermophysics*, Vol. 1, No. 1, 1980, pp. 28–35.

10 Academia Sinica and Shenyang Aeroengine Company; "Theory, Method and Application of Three-Dimensional Flow Design of Transonic Axial-Flow Compressor," *Journal of Engineering Thermophysics*, Vol. 1, No. 1, 1980, pp. 44–54. (in Chinese).

11 Wu Wen-quan, Zhu Rong-guo, and Liu Cui-e, "Computer Programs of Flow Calculations on Relative Stream Surfaces S_1 and S_2 Employing Nonorthogonal Curvilinear Coordinates and Nonorthogonal Velocity Components and Their Application to the Design of Turbomachine Blades Based on Three-Dimensional Flow," *Proceedings of 4th ISABE*, 1979, pp. 277–287; or *Journal of Aircraft*, Vol. 17, No. 5, 1980, pp. 319–325.

12 Spraglin, W. E., "Flow Through Cascades in Tandem," NACA TN 2393, 1951.

13 Kramer, J. J., Stockman, N. O., and Bean, R. J., "Incompressible Nonviscous Blade-to-Blade Flow Through a Pump Rotor With Splitter Vanes," NASA TN D-1186, 1962.

14 Katsanis, T., and McNally, W. D., "Fortran Program for Calculating Velocities and Streamlines on a Blade-to-Blade Stream Surface of a Tandem Blade Turbomachine," NASA TN D-5044, 1969.

15 Nakase, Yoshiyuki, and Senoo, Yasutoshi, "The Theory of Inviscid Flow Through a Turbomachine (3rd Report, Blade-to-Blade Solution with Splitter Vanes)," *Transactions JSME*, Vol. 39, No. 322, 1973, pp. 1855–1862 (in Japanese).

16 Luu, T. S., Ribaud, Y., and Abdelrahman, M. M., "Transonic Flow Analysis in an Impeller Equipped with Splitter Blades," in *Performance Prediction of Centrifugal Pumps and Compressors*, 1980.

17 Wu Chung-hua, and Wolfenstein, L., "Application of Radial-Equilibrium-Condition to Axial-Flow Compressor and Turbine Design," N.A.C.A. T.R. 955, 1950.

18 Wu Chung-hua, "Fundamental Aerothermodynamic Equations for Stationary and Moving Coordinate Systems: Action of Viscous Forces and Physical Significance of Viscous Terms," *Journal of Mechanical Engineering*, Vol. 13, No. 4, Dec. 1965 (in Chinese) or *Engineering Thermophysics in China*, Vol. 1, No. 1, 1980, Rumford Pub. Co., U.S.A.

19 Members of the Compressor and Turbine Research Division, "Aerodynamic Design of Axial-Flow Compressors," N.A.C.A. RM E56B03, 1956.

20 Zhu Gen-xing, Ge Man-chu, and Wu Chung-hua, "Three-Dimensional Design of a Subsonic Stator Based on Successive Calculations of S_1 and S_2 Surface Flows," Paper No-822051, 3rd Symposium of Chinese Society of Engineering Thermophysics, 1982.

21 Cai Rui-xian, "Constraint on the Independent Design Parameters of Turbomachines at Hub and Casing and Estimation of the Twist of S_1 Surface in Axial-Flow Turbomachine," Research Report No. 81-46, Inst. of Engg. Thermophysics, Chinese Academy of Sciences, 1981 (to be published in *Scientia Sinica*).

22 Joukowsky, M. I., "Calculation of Flow Through a Cascade of Blades and Design of Cascades From a Given Velocity Distribution," (in Russian) *CKTI*, Vol. 27, 1954.

23 Joukowsky, V. C., and Kutateladze, S. S., "Improvement in Aerodynamic Performance of Blades for Steam and Gas Turbines" (in Russian).

24 Wu Chung-hua, "Formulas and Tables of Coefficients for Numerical Differentiation with Function Value Given at Unequally Spaced Points and Application to the Solution of Partial Differential Equation," NACA TN 2214, 1950.

25 Zhu Rong-guo, "Flow-Field Line Relaxation Solution for S_2 Relative Stream Surface with Splitter-Ring Boundary Condition," *Journal of Engineering Thermophysics*, Vol. 2, No. 3, 1981, pp. 253–255, (in Chinese).

26 Savage, M., Felix, R., and Emery, J., "High-Speed Cascade Tests of a Blade Section Designed for Typical Hub Conditions of High-Flow Transonic Rotors," NACA RM L55F07, 1955.

Downloaded 01 Jun 2010 to 171.66.16.70. Redistribution subject to ASME license or copyright; see http://www.asme.org/terms/Terms_Use.cfm

Experimental Study of Centrifugal Impeller Discharge Flow in Vaneless and Vaned Diffusers

M. Inoue[1]
Komatsu Ltd.,
Hiratsuka, Kanagawa, Japan

N. A. Cumpsty
Whittle Laboratory,
University of Cambridge,
England

The flow discharged from centrifugal impellers is highly distorted and its behavior in the diffuser could be expected to have a determining effect on the performance of the compressor. The present work sets out to investigate this. The experimental work reported in this paper was designed to investigate the interaction between the vaned diffuser and the impeller. Unsteady measurements of velocity and wall static pressure were made at numerous positions in a vaned diffuser using an on-line data logging system. Experiments were carried out at a range of flow coefficients for three diffusers with 10, 20, and 30 vanes set at each of three different radius ratios, 1.04, 1.1, and 1.2. A limited number of experiments were also carried out with restaggered diffuser vanes and as a reference case extensive measurements were made in a vaneless diffuser build. The impeller, which was designed for a pressure ratio of 4.6, was run at low speed (3000 rpm) after modification to make its overall diffusion equivalent to that at the high speed for which it was designed. The circumferential distortion from the impeller was attenuated very rapidly in the entrance region of the diffuser vanes and suprisingly had only minor effects on the flow inside the vaned diffuser passage. The effect of the diffuser vanes on the flow discharged from the impeller was evident and reversal of flow back into the impeller was detected when the diffuser vanes were close to the impeller and the flow rate was not very high. The time-mean total and static pressure at impeller outlet were found to vary over the pitch of a diffuser vane, and a variation in the strength of the impeller wake was also observed.

Introduction

The behavior of the distorted flow discharged from a centrifugal impeller into a vaneless diffuser has been fairly extensively studied experimentally [1, 2] and theoretically [3, 4] since Dean and Senoo's [5] original work published in 1960. The performance of the vaneless diffuser can be predicted with reasonable accuracy at the design point, provided the flow profile entering the diffuser is either known or can be estimated.

By contrast the study of the vaned diffuser has been rather neglected, even though it is the normal choice for medium or high-pressure ratio machines. This has happened perhaps because it is more complicated both to model theoretically and to investigate experimentally. The nonuniform flow from the impeller is sensed as an unsteady flow by the diffuser vanes, while the presence of the diffuser vanes is seen as an unsteady disturbance by the impeller; it is not possible to choose a frame of reference which will produce only steady processes, and this makes even the consideration of the problem confusing. It is the purpose of this paper to investigate these unsteady interactions with the aim of being able to predict, albeit rather approximately, what takes place.

The phenomenon of nonuniform flow leaving an impeller has been extensively considered both in connection with the study of the behavior of the impeller itself and the behavior of vaneless diffusers. The relative flow leaving the impeller is normally highly nonuniform and has given rise to the jet-wake description coined by Dean and Senoo [5]. Dean and Senoo envisaged the flow as uniform in the axial direction and abruptly nonuniform in the circumferential direction. As more measurements have become available, the neatness of this original description has come to seem less satisfactory, mainly because the flow varies so strongly in the axial direction at outlet, but also because the gradient between the high and low relative velocity regions is not invariably very steep. Nevertheless, the flow leaving an impeller is generally highly distorted with significant patches of low relative velocity. At first sight, it would seem impossible for any downstream diffuser to produce a large pressure recovery with such a flow entering it.

Baghdadi and MacDonald [6] reported tests of vaned diffusers using a vortex nozzle in which the appropriate swirl and radial velocities at entry to the radial diffuser vanes were established in a stationary rig. The flow entering the diffuser vanes was therefore steady and uniform. In discussion of this paper, it was pointed out that the flow into a diffuser around an impeller would be highly nonuniform and unsteady. In a subsequent paper, Baghdadi [7] described measurements of time mean performance obtained with the same shape of

[1] Formerly in the Whittle Laboratory, University of Cambridge, England

Contributed by the Gas Turbine Division for publication in the JOURNAL OF ENGINEERING FOR GAS TURBINES AND POWER. Manuscript received by the Gas Turbine Division November 9, 1982.

Copyright © 1984 by ASME
Downloaded 01 Jun 2010 to 171.66.16.70. Redistribution subject to ASME license or copyright; see http://www.asme.org/terms/Terms_Use.cfm

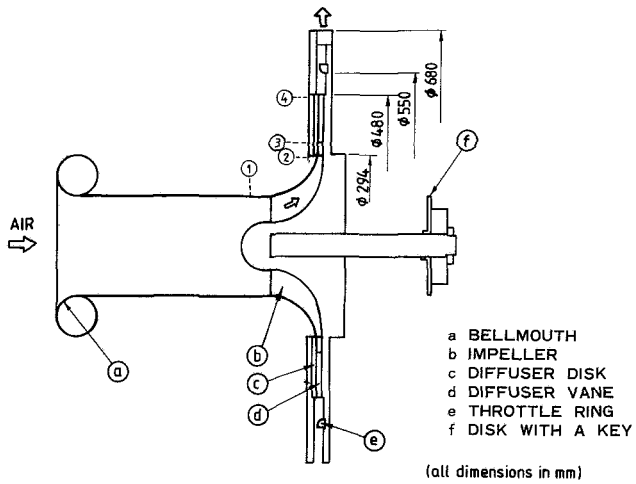


Fig. 1 Schematic cross section through the test rig (measurement stations shown by encircled numbers)

vanes in the stationary rig and in a compressor. The performance was very nearly identical, indicating that the diffusers were well able to cope with the flow nonuniformity and unsteadiness from the impeller. This result begs the question as to how the diffuser is able to tolerate these wide local excursions in flow, and the present paper is an attempt toward providing the information to answer such a question.

The interaction between the impeller and the diffuser vanes is a strong source of vibrational excitation. To produce predictions for this beyond correlations also requires an understanding of the interaction process.

High-pressure rise compressors produce supersonic velocities into the diffuser. This produces a rather complicated flow with shock waves whose gradients are sufficiently steep to be difficult to measure satisfactorily. Furthermore, the temperature variations in such a high-speed flow render the hot-wire a difficult instrument for anything but qualitative measurements. There is, therefore, a place for measurements at low speed, provided the flow from the impeller is qualitatively similar to that found at high speed. By machining down the inducer of an impeller intended for high-speed operation, it is possible to retain the same overall diffusion inside the impeller at low speeds. Measurements of the outlet flow from the impeller modified in this way for the present experiments show very similar behavior to that observed or expected at high speed.

It is unfortunate that no similar modification is possible to accurately simulate at low speed the supersonic flow around the diffuser vane leading edges. Nevertheless, some approximation to the effect can be achieved by having a significant mean flow incidence onto the diffuser vanes, as was the case for most of the measurements performed here.

The bulk of the work summarized in this paper is concerned with the interaction between the impeller and the diffuser. Early in the investigation, it was found that the unsteadiness from the impeller, which was very strong at the diffuser passage entrance, decayed so rapidly as to be undetectable only a short distance along the passage. (No explanation has been found for this, and it remains a subject of investigation.) The investigation therefore concentrated on the behavior close to the vane leading edge region and on the effect of the vanes on the impeller. Before describing the results obtained with the vaned diffuser, some results obtained with the vaneless diffuser are shown. These vaneless results serve to show the "unperturbed" impeller outlet flow as well as some interesting effects of flow in vaneless diffusers.

Test Rig

An outline of the test rig is shown in Fig. 1 in a cross-sectional view. The impeller, with a tip diameter of 294 mm and radial vanes at outlet, had a design pressure ratio of 4.6:1 and a specific speed of 76. The impeller has 26 blades, half of which are splitter blades. The rotational speed at the design point was 31500 rev/min, but for the present tests this was reduced to 3000 rev/min. At this speed the air is essentially incompressible, and if no steps are taken to allow for this, the volume flow rate at impeller outlet is too great, and the fluid processes in the impeller are altered. The details of the impeller design are proprietary, but at the design point, the one-dimensional mean flow has a diffusion ratio of 1.58 between inlet and outlet. By machining down the inducer tip diameter from the original value of 187 to 167 mm (with a curve blending into the original well before the tip), it was possible to produce the same overall level of diffusion in the impeller at 3000 rev/min as that at design speed. This modification reduced the specific speed of the impeller and modified the shroud contour slightly, but for a radial outlet impeller such as this the blade curvature and overall diffusion ratio were expected to be of primary importance in determining the outlet flow. It was therefore expected that even at this low speed there would be a wide wake developed at the impeller exit similar to that at design speed.

The exit radius from the diffuser was 240 mm, giving a radius ratio from impeller tip to diffuser outlet of 1.632. For the vaned and the vaneless diffuser, the axial width was constant and equal to the impeller passage width at outlet, 12.3 mm.

Nomenclature

N = number of diffuser vanes
P_T = total pressure (N/m^2)
P_s = static pressure (N/m^2)
Q = volumetric flow rate (m^3/s)
R = dimensionless radius based on impeller outlet radius, r_2
Ro = Rossby number, $W/\Omega r_c$
r = radius (mm)
r_c = radius of curvature of impeller bend from radial to axial direction (m)
S_{rev} = strength of reversed flow from diffuser into impeller
t = time (s)
U_2 = impeller tip speed (m/s)
V = absolute velocity (m/s)
W = relative velocity (m/s)
X = instantaneous flow quantity
z = axial distance from front wall (shroud side) nondimensionalized by the passage width
δ^* = wake displacement width (mm)
ϵ = wake width (mm)
θ = angular coordinate in direction of impeller rotation
θ_{rel} = relative angle between a specified impeller full blade and a diffuser vane
ρ = density of fluid (kg/m^3)
ϕ = flow coefficient = $Q/\pi r_2^2 U_2$
ψ = static head coefficient made dimensionless by ρU_2^2
Ω = angular velocity of impeller

Subscripts

1 = at inlet to impeller
2 = at outlet from impeller
3 = at leading edge radius of diffuser vanes
4 = at outlet from diffuser
j = component related to jet
r = radial component
w = component related to wake
θ = tangential component

Superscripts

$'$ = unsteady part of the flow quantity
$-$ = mass flow average quantity in circumferential direction

Downloaded 01 Jun 2010 to 171.66.16.70. Redistribution subject to ASME license or copyright; see http://www.asme.org/terms/Terms_Use.cfm

The air discharged from the diffuser into a radial passage, and thence through a throttle ring into the atmosphere. The throttle ring not only controlled the flow rate, but also imposed an axisymmetric outlet pressure on the diffuser.

Construction of Vaned Diffusers

Because the tests were to be performed at low Mach numbers, it was decided that curvature could be tolerated in the diffuser vanes and that thin circular arc aerofoils with rounded leading edges would be a satisfactory and simple design. The vanes were all circular arc in shape, with the curvatures specified to give a mean divergence angle equivalent to a two-dimensional diffuser of 8 deg. The majority of the tests were performed with the diffuser vane inlet angle inclined at 60 deg to the radial direction, this being judged from the vaneless diffuser tests to be the optimum angle. Toward the end of the program, some tests were also carried out with the vane angle of 70 deg, but except where otherwise started, results may be assumed to have been obtained at 60 deg.

In order to avoid the trouble of moving the traverse gear circumferentially from one measuring position to another, it was decided to rotate the disk carrying the diffuser vanes, with measurements made through only a single hole in the stationary back plate at each radius. The diffuser disk was rotated by moving three protruding studs fixed on the diffuser disk through the front wall.

Each of the diffuser vanes was made of 2-mm brass sheet with a semicircular rounded leading edge. These are fixed on the diffuser disks with three pins near the leading edge, middle, and trailing edge. The vanes had some flexibility, and the curvature was not required to vary much with vaneless space ratio for a constant vane number. The same vanes could therefore be used to construct diffusers of various vaneless space ratios by merely changing three pin hole positions on the disk. Four diffuser configuration are shown in outline in Fig. 2. Changing the vaneless space ratio also led to a change in the outlet radius and to a small change in the overall area ratio. Measurements have indicated that most of the pressure rise occurs near the inlet to the diffuser and the variation in area ratio was insignificant.

Instrumentation

At 3000 rev/min the blade passing frequency was 1.3 kHz, and a system capable of measuring at least 20 kHz was necessary for the instantaneous measurement systems. This frequency was well within the range of conventional hot-wire probes and pressure transducers.

A subminature, single hot-wire, was used to measure instantaneous velocities and flow directions in the diffuser. The wire was approximately 1-mm long and 5μm in diameter welded onto two 12-mm-long needles. The hot wire was calibrated for velocity magnitude and direction. The orientation of the wire was in the $r-\theta$ plane; only the velocity components in the radial and circumferential directions were measured because the component in axial direction was negligible in comparison. The range of instantaneous flow angle was expected within -30 deg $\sim$ $+$ 60 deg from the circumferential direction. For the measurements the hot wire probe was rotated about its axis in 30 deg increments from 60 to 150 deg. Comparing the outputs in each of the four directions, the computer program decided for each measurement which pair to use to ensure that only well-conditioned equations were solved to obtain velocity magnitude and direction.

The accuracy of the hot-wire measurements was estimated to be about 3.5 percent in magnitude and 1.5 deg in direction (20:1 odds). The time-average flow rates, calculted from the instantaneous measurements, were compared with those

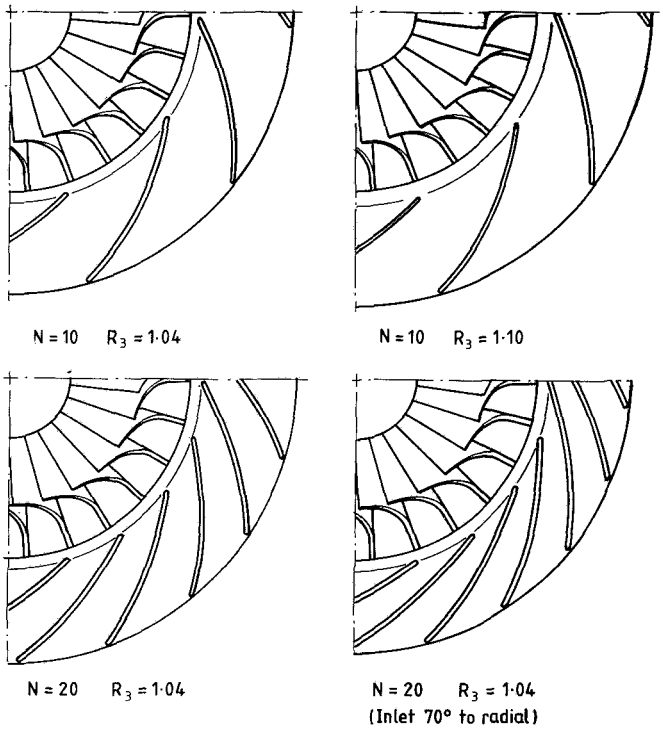


Fig. 2 Four vaned diffuser configurations: vane inlet at 60 deg to radial except where stated

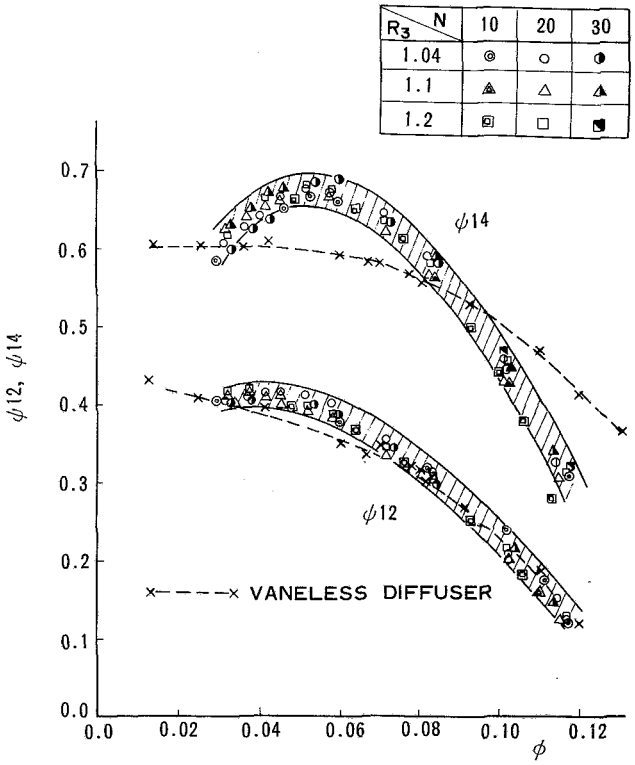


Fig. 3 Impeller and compressor stage pressue rise for vaned and vaneless diffusers

obtained with the aid of the bellmouth inlet ((*a*) of Fig. 1). The flow rates measured by the hot wire deviated less than 6 percent at maximum from those obtained from the bellmouth, which were estimated to be accurate within 2 percent. (Since the radial velocity was typically only about 1/3 that of the tangential velocity, the accuracy of the resultant velocity needed to be good to about 2 percent to achieve this.)

Downloaded 01 Jun 2010 to 171.66.16.70. Redistribution subject to ASME license or copyright; see http://www.asme.org/terms/Terms_Use.cfm

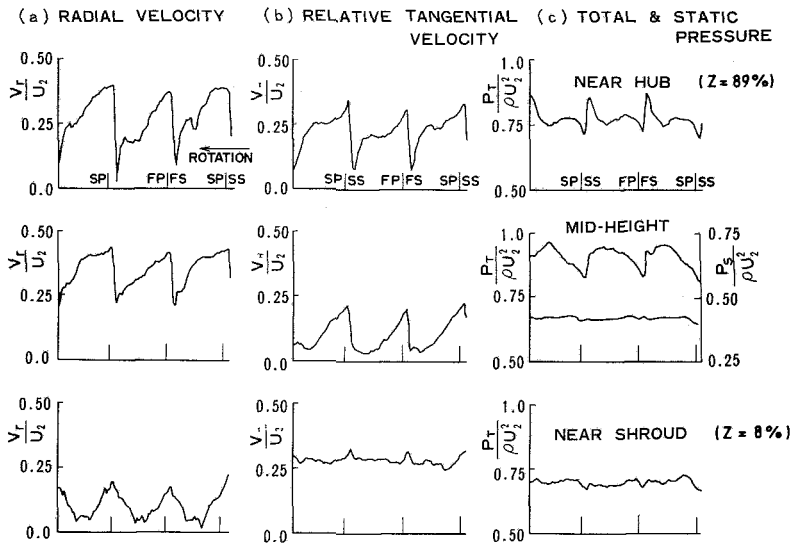


Fig. 4(*a*) Ensemble-averaged instantaneous flow measured at inlet to vaneless diffuser (R = 1.024) at three axial stations ϕ = 0.035

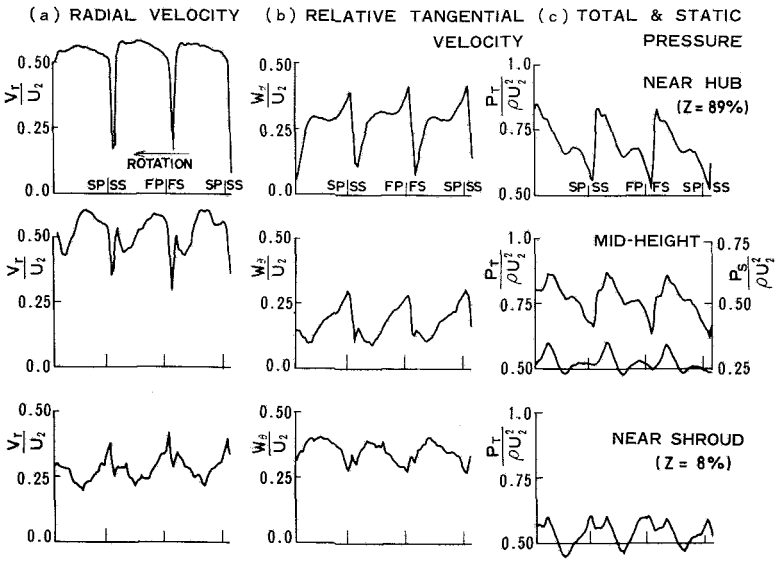


Fig. 4(*b*) Ensemble-averaged instantaneous flow measured at inlet to vaneless diffuser (R = 1.024) at three axial stations (ϕ = 0.085)

A miniature pressure transducer manufactured by Gaeltec Ltd. was used for wall static pressure measurements. The transducer was of a half-bridge, strain-gauge type with a resonant frequency of approximately 50 kHz. The sensitivity of the probe was hardly affected by temperature change, but the zero drift was large. Therefore, only the fluctuating part of the static pressure was measured, with an estimated accuracy of 2 percent by this transducer. By adding the time-averaged static pressure measured through a conventional static pressure tap and transducer (with an estimated accuracy of 2 percent), the absolute instantaneous pressure was obtained.

Static pressures were measured on the hub side diffuser wall. Because the axial width of the diffuser was only 12.3 mm and the diffuser walls were flat, it is believed that the wall static pressures will be a good measure of the pressure over the whole diffuser width. The instantaneous total pressure was calculated from the instantaneous static pressure and velocity.

The output from a hot wire or a pressure transducer was fed to a computer through a built-in A-D converter. The sampling and conversion rate of the system was chosen as 40 kHz, so that 30 measurements were made over one blade-to-blade passage of the impeller running at a rotational speed of 3000 rpm. Since the flow at the inlet to the diffuser was highly turbulent, a phase-locked sampling and ensemble averaging technique was used. Fifty sets of data were sampled and averaged to obtain each set of data presented here.

Overall Performance

The overall performance of the compressor was measured with both a vaneless diffuser and a variety of vaned diffusers in order to determine the flow conditions for detailed measurements. The results are shown in Fig. 3, where time mean static pressure rises through the entire compressor stage, ψ_{14}, and through the impeller, ψ_{12} are plotted against throughflow rate, ϕ. The results for the vaned diffuser were all obtained with a vane inlet angle of 60 deg to the radial; at 70 deg to the radial, ψ_{14} is about 2 percent higher at the peak which occurs at about ϕ = 0.033.

It is found from Fig. 3 that the overall performance curves ψ_{14} for all nine configurations of vaned diffusers have a similar trend to each other, falling in the shaded area shown on the characteristic graph, but the trend for the vaneless

Downloaded 01 Jun 2010 to 171.66.16.70. Redistribution subject to ASME license or copyright; see http://www.asme.org/terms/Terms_Use.cfm

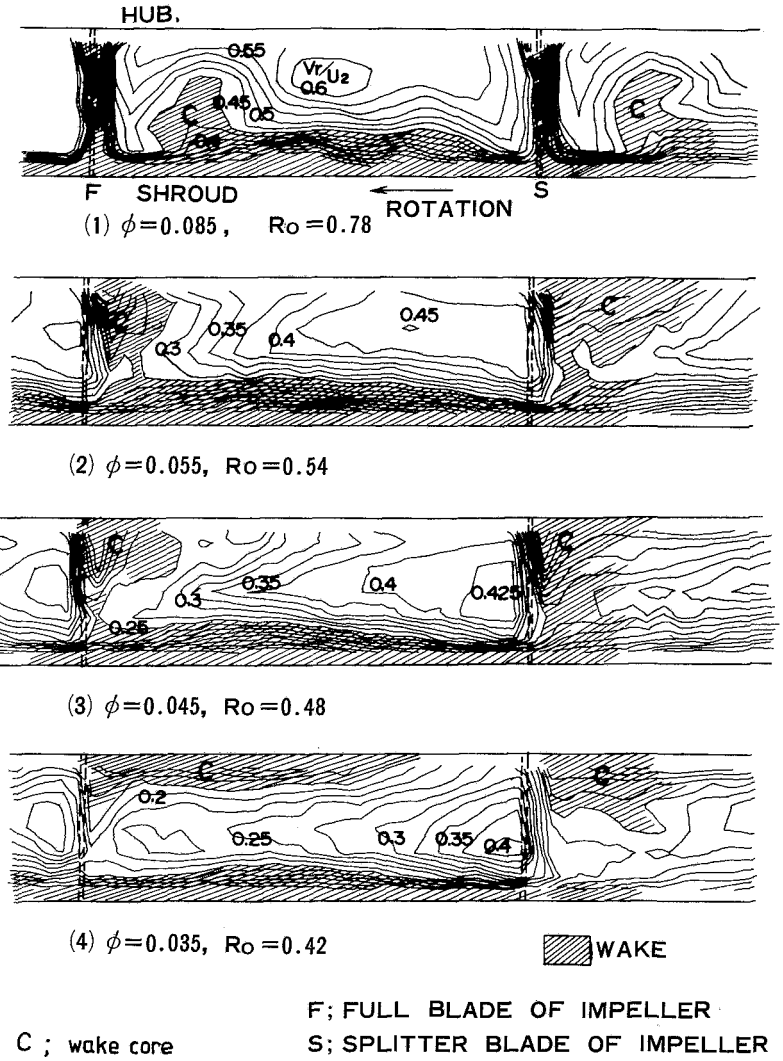


Fig. 5 Contours of radial velocity at inlet to vaneless diffuser (R = 1.024)

diffuser is very different. The performance curves for the vaned diffusers have clear peaks around a flow rate, ϕ, of 0.055, and the peaks in ψ_{14} are raised more than 10 percent above the value for the vaneless diffuser.

The static pressure rise characteristics through the impeller for builds with vaned diffusers are also up to 6 percent larger than that for the vaneless diffuser at flow rates, ϕ, from 0.04 to 0.07. This difference suggests that some change occurred to the flow through the impeller by interaction between the impeller and vaned diffuser.

By referring to the overall performance data, the flow conditions for detailed measurements were chosen to be ϕ = 0.045, 0.055, and 0.085. These correspond to flow rates below, equal to, and above that required for maximum pressure rise of the vaned build. The highest flow rate, ϕ = 0.085, corresponds to a predicted incidence of zero into the diffuser vanes based on an assumed impeller slip factor of 0.85.

Detailed Measurements for the Vaneless Diffuser

Instantaneous Velocity Measurement. Instantaneous measurements of velocity were made over the axial width of the vaneless diffuser at various radii, with particular detail at the inlet, in order to get reference data for studying the interaction between the impeller and the vaned diffuser.

Figure 4(a) and (b) show measurements at a radius ratio of 1.024 just outside the impeller. For flow rates of ϕ = 0.085 and 0.045, these figures show ensemble-averaged circumferential distributions of radial and tangential velocities, and total and static pressures at three different axial positions (near hub, z = 89 percent, middle, z = 49 percent and near shroud, z = 8 percent). The positions of impeller blades are indicated by FS and FP for the suction and pressure faces of the full vanes and by SS and SP for the equivalent faces of the splitter vanes. The flow passages in the impeller were different, depending on whether a full or splitter vane functioned as the suction or pressure surface, but the measurements showed no discernible difference in the flow patterns discharged from these two types of channels.

The change in flow rate had the most noticeable effect on the radial velocity pattern. For a flow rate of ϕ = 0.085 the radial flow pattern at the middle of the passage plainly showed the existence of a dip, or wake, which was located a little apart from the suction surface. Near the hub wall the radial velocity decreased from suction to pressure side, and this trend is similar in direction to the potential flow pattern, but near the shroud there appears to be an extensive wake over most of the passage. In contrast to this, when the flow rate was reduced to 0.045, a distinct large wake region developed near the hub adjacent to the suction surface. That this is not merely an increase in wake size will be apparent from discussions of Fig. 5 that follow.

Downloaded 01 Jun 2010 to 171.66.16.70. Redistribution subject to ASME license or copyright; see http://www.asme.org/terms/Terms_Use.cfm

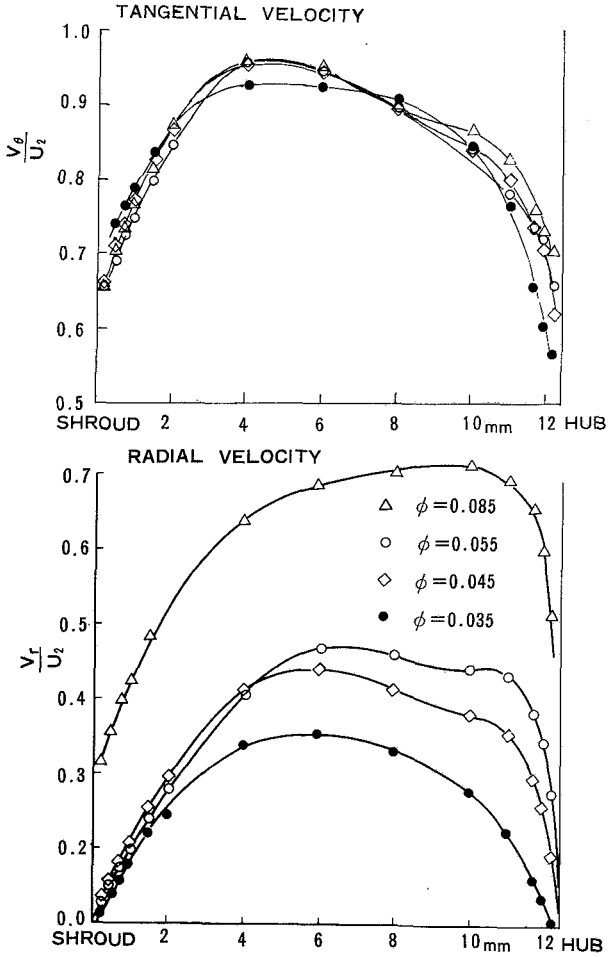


Fig. 6 Mean velocity variations in the axial direction at inlet to vaneless diffuser (R = 1.024) for various flow rates

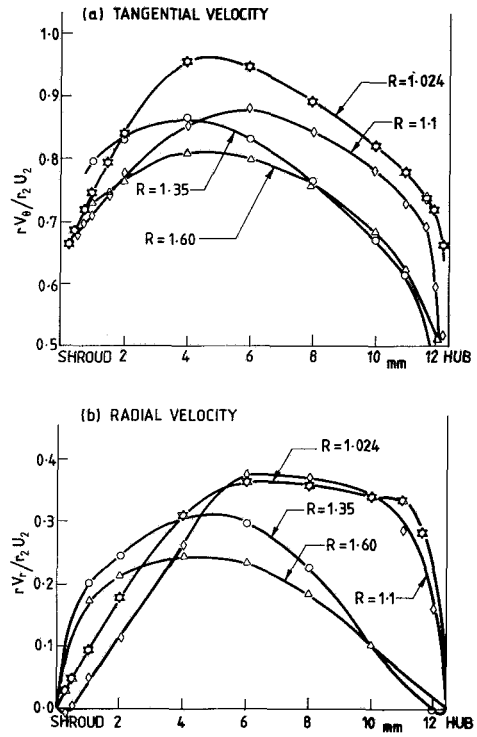


Fig. 7 Time mean velocity variation in the axial direction in the vaneless diffuser at various radii (ϕ = 0.055)

The relative tangential velocity, $W_\theta = V_\theta - r\Omega$, showed a steep rise toward the pressure surface at midpassage and near the hub for both flow rates. Since the blades of the impeller were radial at outlet, the radial velocity does not have a direct influence on the tangential velocity. The distortion in the radial velocity can therefore have had only a weak influence on the circumferential variation in tangential velocity and the secondary flow was believed to have had the major effect on the tangential velocity pattern.

The total pressure distributions showed similar trends, differing only in detail, to those of absolute tangential velocity, which were inverted shapes of the relative tangential velocity patterns. The static pressure distortion is shown for convenience on the midpassage trace, although it was measured on the hub wall. It is the static pressure which determines the energy transfer between jet and wake in the diffuser [5], and this pattern changed greatly in shape and amplitude with flow rate. The amplitude of the static pressure variation at ϕ = 0.045 decreased to only 1/5 of the value at ϕ = 0.085, which is at first surprising since blade loading is normally assumed to increase as flow rate decreases. With a radial outlet impeller, however, the blade loading near the outlet is predominantly produced by Coriolis acceleration of the flow and is therefore proprotional to flow rate. The decrease in static pressure variation was, however, even larger than this would suggest.

Figure 5 illustrates the ensemble-averaged radial velocity distributions by constant velocity contours over the cross section at the inlet to the diffuser (R_3 = 1.024) for four flow rates. The shaded areas show where the radial velocity was smaller than the averaged radial velocity of the corresponding impeller passage. One can see more clearly from this figure that the core of the wake, shown by a C on Fig. 5, altered its location and area with flow rate. (Here wake core means the low velocity region, excluding 20 to 30 percent of the passage width at the shroud side where the velocity was low irrespective of flow rate, probably as a result of clearance flow between the impeller vanes and the shroud walls.) At a flow rate of 0.085, the wake core was located near the suction side/shroud side corner, and its circumferential position was about 20 percent of the impeller blade pitch out from the suction surface. A similar flow pattern was presented by Eckardt in Fig. 12 of [1].

When the flow rate was reduced to ϕ = 0.055, the wake core was confined to the suction surface, and the wake front reached the hub side wall. Further decrease of the flow rate to 0.045 caused a movement of the wake to the hub side. The wake on the side wall continued to grow to fill the passage with decreasing flow rate; at ϕ = 0.035, it filled about 80 percent of the impeller blade pitch.

This movement of the wake was caused by the secondary flow generated through the effects of curvature in the impeller and rotation. Johnson and Moore [8] have analyzed the behavior of the wake in the impeller and concluded that the position of the wake is influenced by the Rossby Number, $W/\Omega r_c$, and also by the magnitude of total pressure defect. They showed that when the wake is strong, so that a large secondary vorticity is produced, the inertia would carry the wake beyond its stable location. The Rossby number represents the ratio of the effects of the axial to radial curvature and the rotation on the secondary flow in the impeller. In the present case, it was 0.48 at ϕ = 0.045, the flow rate at which the wake on the hub began to grow rapidly. The strong Coriolis force moved the stable location of the wake onto the suction surface from the shroud wall but then the inertia of the strong secondary flow has carried the wake further around onto the hub side wall.

In the impeller tested by Eckardt [9], the wake core

Downloaded 01 Jun 2010 to 171.66.16.70. Redistribution subject to ASME license or copyright; see http://www.asme.org/terms/Terms_Use.cfm

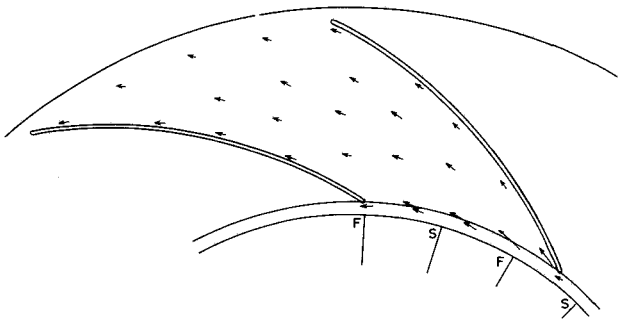


Fig. 8 Velocity vector pattern inside vaned diffuser near the shroud, N = 10, vaneless ratio R_3 = 1.04, ϕ = .055

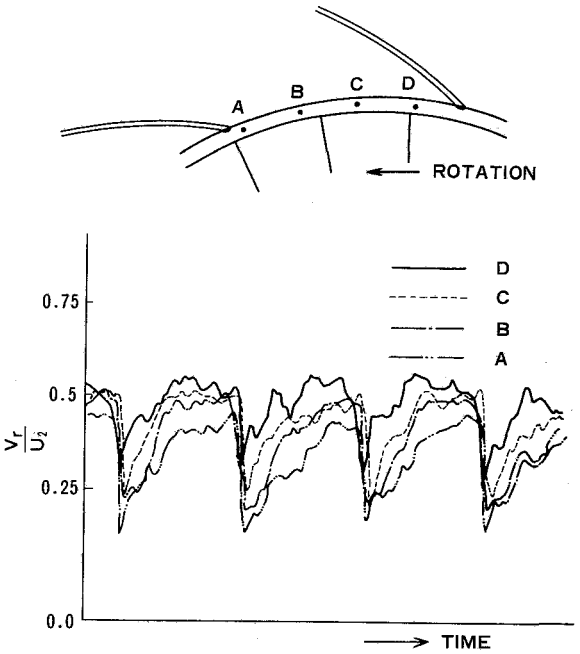


Fig. 9 Variations with respect to time in the radial velocity between the vaned diffuser leading edge for various circumferential positions: passage midheight (Z = 49 percent), R = 1.024, N = 10, R_3 = 1.04

remained near the shroud between 50 and 20 percent of the blade pitch out from the suction surface, depending on mass flow and rotational speed. The transfer of the wake on to the hub side was not observed. Eckardt's impeller had been designed for a pressure ratio of 7:1 at 27,000 rpm, but he tested it at 10,000 ~ 18,000 rpm, without any modification of the impeller passage to correct for density change such as that carried out on the present impeller. The Rossby number therefore became large, because of large relative velocity in the impeller, and the stable location of the wake on the shroud wall was maintained.

Time-Averaged Velocities. The change of the wake core position with flow rate significantly affected the mean radial velocity profile in the axial direction at the inlet to the diffuser. This profile is one of the important factors determining the behavior of the flow in the vaneless diffuser, as was recently shown by Senoo et al [4]. Figure 6 shows the variation of the mean velocity profiles with flow rate. At a flow rate of 0.085, the radial velocity increased from the shroud to the hub side, with a large deficit region at the shroud side and a very thin boundary layer on the hub wall. As the flow rate was reduced, the time mean boundary layer at the hub side grew considerably in response to penetration of the wake onto the hub wall, resulting in a nearly symmetric time mean pattern of radial velocity at ϕ = 0.035. Figure 6 also shows the average value of absolute whirl velocity out of the impeller, indicating only small changes with flow rate.

Figure 7 shows the variation with radius of the radial velocity and the angular momentum for one flow rate. The angular velocity profile does vary significantly with radius, but the most interesting effect is in the radial velocity. At R = 1.1, reversed flow is seen on the shroud wall of the diffuser. The profile on the shroud side then fills out and separation appears on the hub side at R = 1.35. At this radius ratio, the boundary layers on both sides are effectively merged and there is no longer a "potential" core. This curious switching of the reversed flow has been explained by the work of Seno and Kinoshita [12].

The instantaneous measurements of radial velocity at various radii in the vaneless diffuser indicated that the circumferential distortion of the flow did not disappear even at R = 1.3. The distortion patterns of tangential velocity and total pressure decreased rapidly with radius, a trend attributable to the existence of energy transfer between jet and wake described by Senoo and Ishida [2].

Detailed Measurements for the Vaned Diffuser

Instantaneous Measurements. Instantaneous velocity patterns in the vaned diffuser channels of various configurations were measured in order to investigate the behavior of the disturbance discharged from the impeller. One example of the results is shown in Fig. 8, which presents the velocity vector pattern near the shroud for a build with 10 vanes and a vaneless space ratio = r_3/r_2 = 1.04. The pattern is shown for the instant when a full impeller blade is aligned with the leading edge of the diffuser vane forming the pressure side of the diffuser channel under measurement. It was found from the measurements that the periodic fluctuation from the impeller attenuated so rapidly at the inlet to the diffuser vanes that the changes in the instantaneous flow in the diffuser channel with the relative position of the impeller were barely detectable. This was more marked for the diffusers with larger numbers of vanes and for lower flow rates, but virtually no periodic component in the velocity could be detected at R = 1.1 for a diffuser with 10 vanes and the vane leading edge at R_3 = 1.04.

The effect was surprising and no explanation for it has been obtained. As the arrows in Fig. 8 indicate, the diffuser decelerates the flow without major separation at the diffuser exit and therefore appears to be working satisfactorily. Detailed measurements were made at the diffuser inlet, R = 1.024, to clarify the effect of the diffuser vanes on the flow discharged from the impeller. Data were acquired by rotating the diffuser disks over one diffuser vane pitch in increments of 3 deg for 10 vanes, 1.5 deg for 20 vanes, and 1 deg for 30 vanes.

Figure 9 displays a typical example of radial velocity fluctuations at midpassage, Z = 49 percent, for various circumferential positions between a pair of diffuser vanes. The profile, as well as the averaged value, varied markedly with the circumferential position. (For the vaneless diffuser, the velocity distribution has the same profile, irrespective of circumferential position.) It is, however, possible to calculate the time-mean, nonuniform velocity pattern from time-dependent velocity fluctuations at several circumferential positions using the technique described in [10].

Figure 10 shows in a three-dimensional plot the instantaneous radial velocity patterns at the impeller outlet for three relative positions between the impeller blades and the diffuser vanes. These results were obtained at a flow rate of 0.055 for the diffuser with 10 vanes and a vaneless space ratio R_3 = 1.04. The circumferential positions of the full and

Downloaded 01 Jun 2010 to 171.66.16.70. Redistribution subject to ASME license or copyright; see http://www.asme.org/terms/Terms_Use.cfm

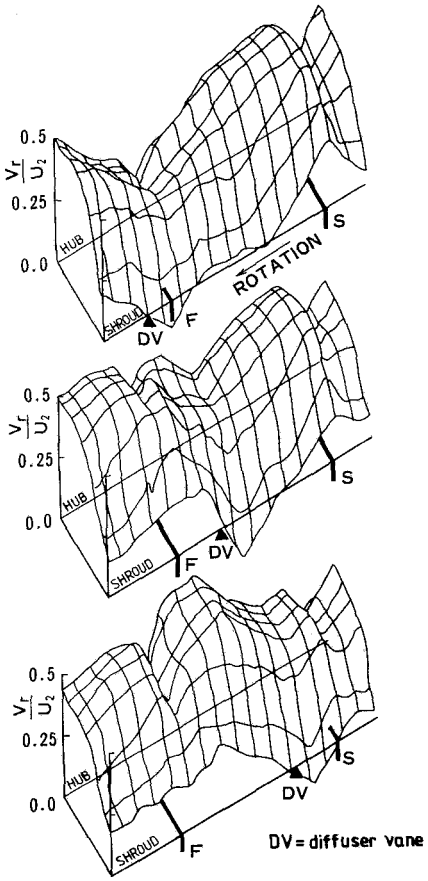


Fig. 10 The radial velocity measured in vaneless space between impeller and diffuser vanes leading edge for three relative positions: $R = 1.024, N = 10, R_3 = 1.04, \phi = 0.055$

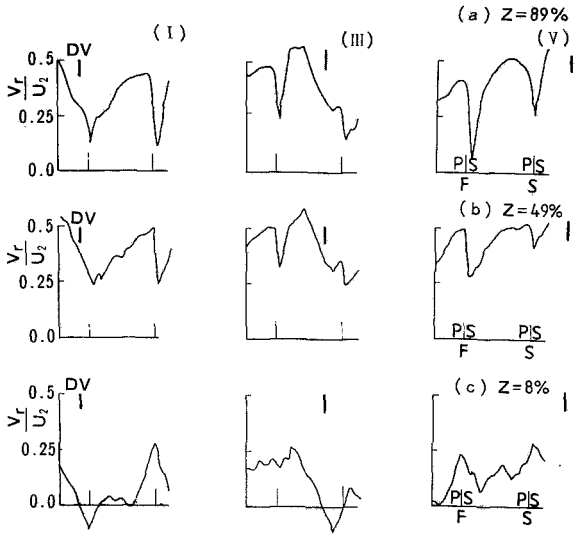


Fig. 11 The instantaneous ensemble average *radial* velocity for the axial positions and three relative circumferential positions measured between impeller and diffuser vane leading edge $R = 1.024, N = 10, R_3 = 1.04, \phi = 0.055$

splitter impeller blades and the diffuser vane leading edge are indicated by F, S, and DV, respectively. The plots are fixed relative to the impeller, and "valleys" can be seen corresponding to wakes off the impeller vanes. A pronounced

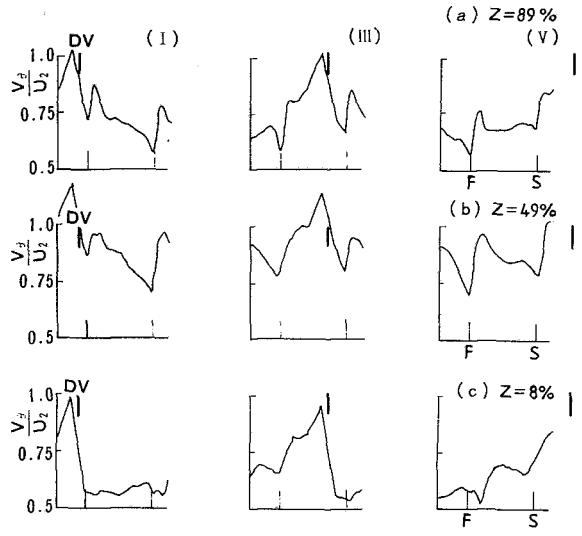


Fig. 12 The instantaneous ensemble average *tangential* velocity for three axial positions and three relative circumferential positions measured between the impeller and diffuser vane leading edge: $R = 1.024, N = 10, R_3 = 1.04, \phi = 0.055$

change in profile occurred as the impeller rotated, with a strong depression in velocity observed near the diffuser leading edge location. This depression forced the flow to reverse near the shroud in places where no reversed flow existed for the vaneless diffuser at this flow rate. As the diffuser vane leading edge moved away from the suction surface of the impeller passage, the radial velocity near the impeller suction side was increased and in the bottom trace in Fig. 10 was larger than the radial velocity at the pressure side. The wake, which had been observed at the suction side in the vaneless diffuser, seemed to change its position to the pressure side, but this interpretation is incorrect, for the moving deficit from the vanes is not a wake, as shown below.

These three-dimensional plots of the flow provided a qualitative outline of the influence of the diffuser vanes on the flow leaving the impeller. For the detailed investigation, it is more appropriate to divide the three-dimensional flow pattern into two parts which are the circumferential distortion and the nonuniform pattern in axial direction.

The variations in the circumferential distortion of radial velocity are shown in Fig. 11 at three representative axial positions for the same conditions as Fig. 10. Again the impeller blades are shown to be stationary in the figure and the diffuser vanes appear to move past. Two of the positions shown coincide with the relative positions between impeller and diffuser vane in Fig. 10.

The absolute tangential velocity patterns, corresponding to the radial velocity patterns in Fig. 11, are shown in Fig. 12. The tangential velocity profiles were also strongly affected by the diffuser vanes, with conspicuous peaks exceeding the impeller tip speed observed in the profiles near the suction side of the diffuser vane leading edge. It should be noted that the position of the peaks in tangential velocity did not coincide with that of the valleys in radial velocity patterns, which was near the pressure side of the diffuser vane leading edge.

The variation in total pressure patterns at impeller outlet was less remarkable than expected from the tangential velocity patterns because the peak of the tangential velocity occurred near the low static pressure region of the diffuser vane suction side. The impeller blade wakes formed the peak in the total pressure pattern, as might be expected since the absolute tangential velocity is highest there.

Downloaded 01 Jun 2010 to 171.66.16.70. Redistribution subject to ASME license or copyright; see http://www.asme.org/terms/Terms_Use.cfm

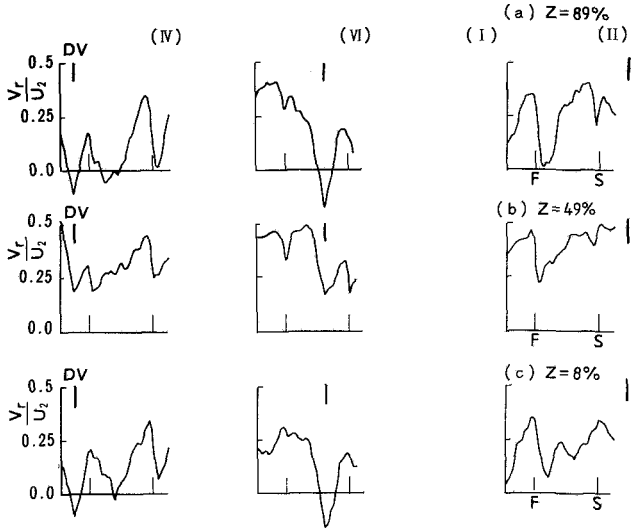


Fig. 13 The instantaneous ensemble average *radial* velocity for the axial positions and three relative circumferential positions measured between impeller and diffuser vane leading edge: $R = 1.024$, $N = 10$, $R_3 = 1.04$, $\phi = 0.045$

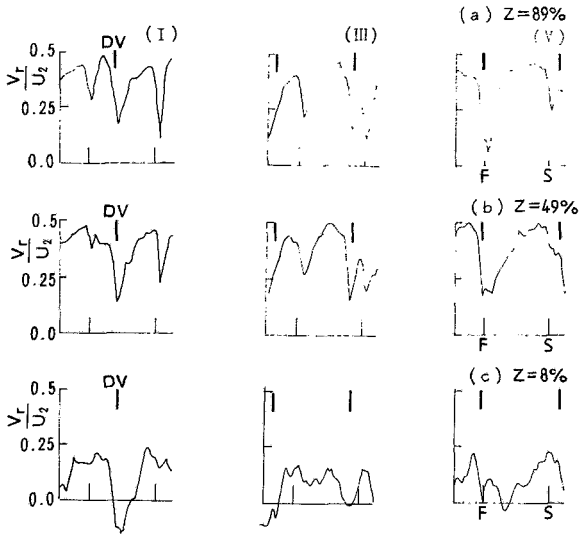


Fig. 15 The instantaneous ensemble average *radial* velocity for the axial positions and three relative circumferential positions measured between impeller and diffuser vane leading edge: $R = 1.024$, $N = 20$, $R_3 = 1.04$, $\phi = 0.055$

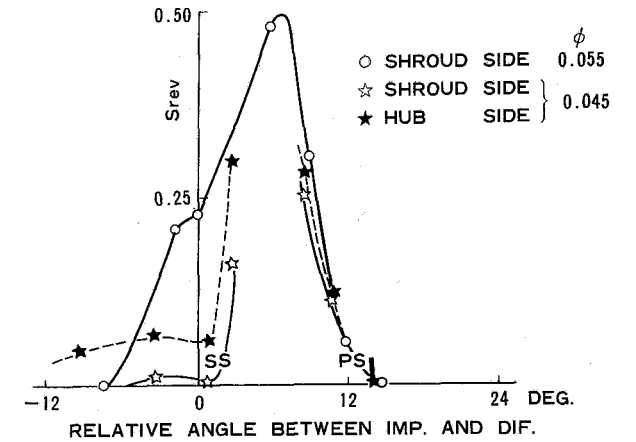


Fig. 14 The variation in reversed flow strength, S_{rev}, with relative angle between impeller vanes and diffuser vane leading edge for two flow rates: $R = 1.024$, $N = 10$, $R_3 = 1.04$

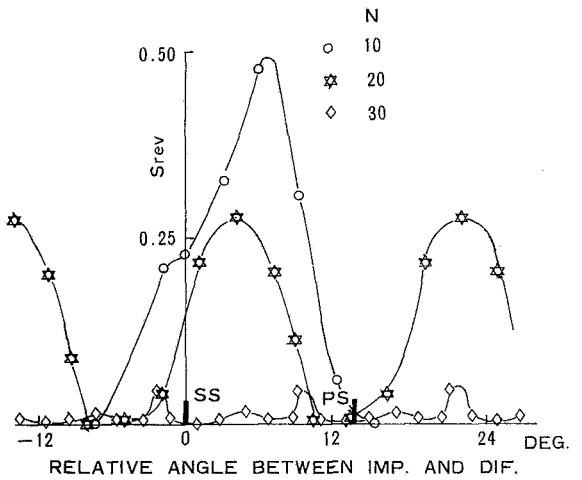


Fig. 16 The variation in reversed flow strength, S_{rev}, with relative angle between impeller vanes and diffuser vane leading edge for different numbers of vanes: $R = 1.024$, $R_3 = 1.04$

The radial velocity patterns for the same diffuser are shown in Fig. 13 when the flow rate was reduced to $\phi = 0.045$. The influence of the diffuser vanes was noticeably greater in the flow near the hub compared with the results for $\phi = 0.055$, and the reversed flow there was comparable in magnitude to that near the shroud. It should be noted, however, that the effect of the diffuser vanes on the radial velocity near the shroud was perhaps smaller at the lower flow rate. The mean radial velocity at the hub decreased drastically when the flow rate was decreased from $\phi = 0.055$ to 0.045 but still remained larger than that near the shroud. The fact that the diffuser vanes had an effect of similar magnitude on the radial velocity patterns near the hub and the shroud in spite of the larger average velocity near the hub suggests some influence of the wake configuration on the interaction between the impeller and the diffuser. As the vaneless diffuser tests had shown, the character of the low velocity regions at the shroud and the hub for $\phi = 0.045$ were quite different, being concentrated near the suction side of the passage on the hub side but spread over most of the width of the passage near the shroud.

A comparison of the reversed flow strength, S_{rev}, which is defined as the area of the radial velocity profile below the zero velocity line, is made in Fig. 14. The abscissa indicates the relative angle between a specified impeller full blade and a diffuser vane, θ_{rel}. The magnitude of S_{rev} on the shroud side at $\phi = 0.045$ was about half that a $\phi = 0.055$, while the newly apparent reversed flow at the hub side had a similar strength to the value at the shroud side. One therefore expects that the total amount of the reversed flow changed comparatively little when the flow rate reduced from $\phi = 0.055$ to 0.045. One of the reasons for the reduction of the reversed flow strength near the shroud is that the mean radial velocity near the shroud is actually increased at the lower flow rate, as had been observed in the case of a vaneless diffuser.

Figure 15 shows the radial velocity distribution for a 20 vaned diffuser with flow rate, radius ratio, and inlet angle the same as that in Fig. 11. The pattern is more complicated but the size of the disturbance produced by the diffuser vanes and the amount of reversed flow are significantly less. For 30

Downloaded 01 Jun 2010 to 171.66.16.70. Redistribution subject to ASME license or copyright; see http://www.asme.org/terms/Terms_Use.cfm

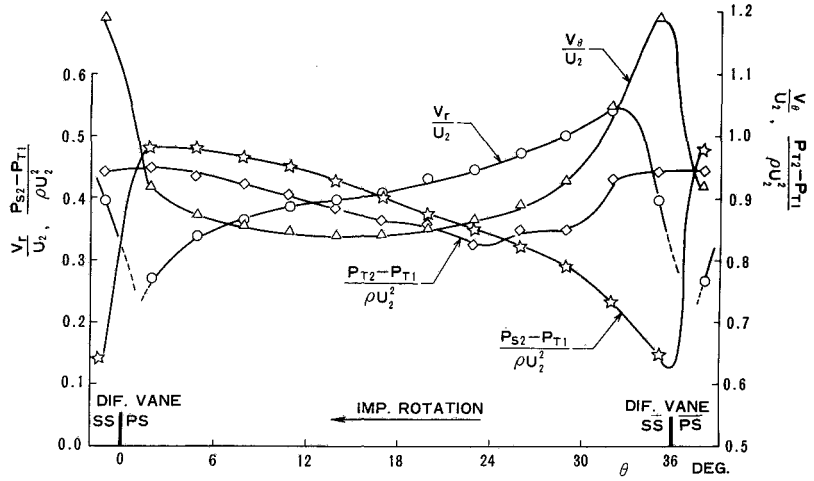


Fig. 17 The steady parts of instantaneous flow properties at midheight of passage (Z = 49 percent) between impeller and diffuser vane leading edge: R = 1.024, N = 10, R_3 = 1.04, ϕ = 0.055

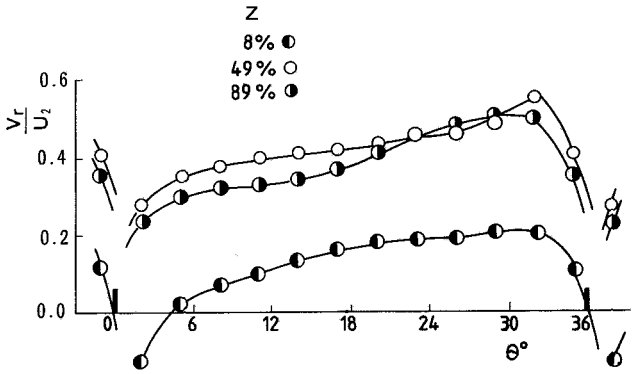


Fig. 18 The time-mean radial velocity distribution between impeller and diffuser vane leading edge at three axial positions: R = 1.024, N = 10, R_3 = 1.04, ϕ = 0.055

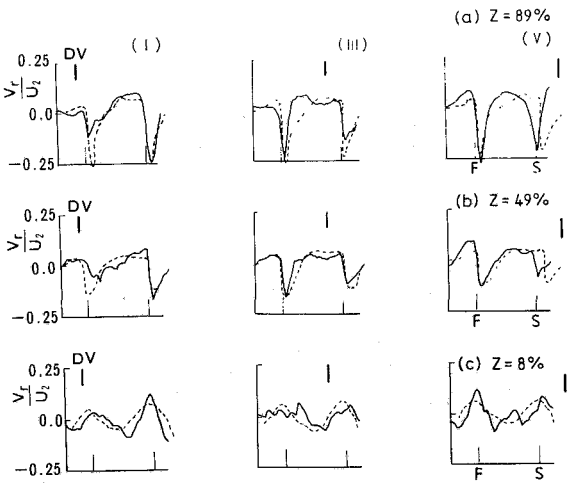


Fig. 19 The unsteady part of the instantaneous radial velocity between impeller and diffuser vane leading edge for the axial position and three relative circumferential positions: R = 1.024, N = 10, R_3 = 1.04, ϕ = 0.055 (vaneless diffuser results shown by broken line)

vanes, the effect is still smaller, and the effect of vane number on the reversed flow strength S_{rev} is summarized by Fig. 16.

The tangential velocity and total pressure disturbances are also smaller as the vane number is increased and the disturbance to the impeller outlet flow decreases rapidly as the diffuser inlet radius R_3 is increased. These effects are all illustrated in [10].

The Unsteady and Steady Flow Field. It became clear, as previously mentioned, that the low velocity regions observed near the diffuser vane leading edges were different in nature to the wakes (consisting of an accumulation of high loss fluid) generated in the impeller. The deep depressions in velocity near the vane leading edges were believed to be induced by the circulation around the diffuser vanes. In analyzing the interaction between the impeller and the diffuser, it is therefore appropriate to divide the instantaneous flow patterns of some property $X(\theta, t)$, into steady and unsteady parts

$$X(\theta, t) = \bar{X}(\theta) + X'(\theta, t)$$

The steady part, $\bar{X}(\theta)$, was calculated by mass-averaging the instantaneous values at each circumferential position. The unsteady part, $X'(\theta, t)$, was obtained by subtracting the steady part from the instantaneous flow distribution. This unsteady part can be considered as the nonuniform flow pattern generated in the impeller outlet flow under the influence of the diffuser vanes. (The instantaneous pattern is an ensemble average.)

Figure 17 presents circumferential distributions of the steady components at midheight in the diffuser derived from the instantaneous radial and tangential velocities which were shown in Fig. 11 and Fig. 12. The steady parts of the corresponding static and total pressure patterns are also shown in the figure. These distributions show that the circumferential variations of the steady components are significant and are the main cause of the peculiar distortions of the instantaneous flow patterns at the outlet from the impeller shown in Figs. 11 and 12, for example. Figure 17 also shows that the total pressure varied circumferentially by more than 10 percent of the mean value, presumably because the work input from the impeller varied circumferentially due to the interaction between the impeller and the vaned diffuser. An alternative explanation is that the loss generation in the impeller varies circumferentially, but it is rather hard to imagine the mechanism for this which would lead to high total pressure near the diffuser vane leading edge. The circumferential variation in total pressure makes clear the inadequacy of treating the total pressure measured at a single circumferential position as an adequately representative total pressure of the impeller discharge flow.

The steady patterns near the shroud and hub side walls, z = 8 percent and 89 percent are illustrated for the same con-

Downloaded 01 Jun 2010 to 171.66.16.70. Redistribution subject to ASME license or copyright; see http://www.asme.org/terms/Terms_Use.cfm

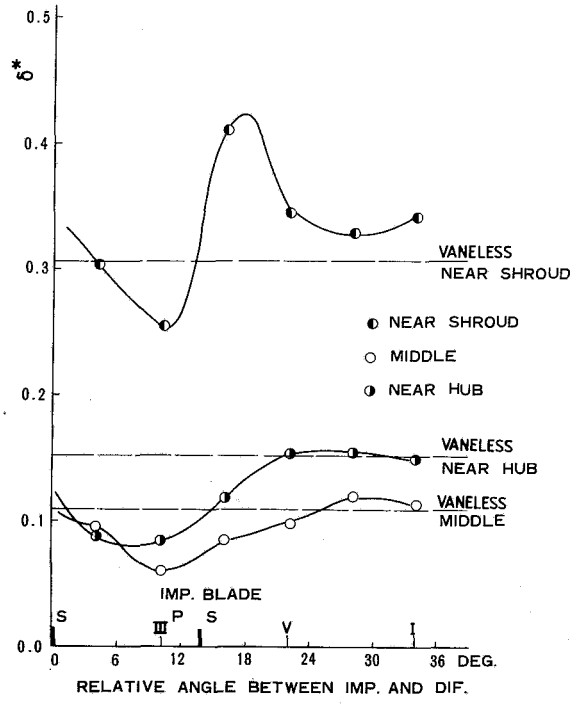


Fig. 20 Variation in the wake displacement width measured between impeller and diffuser vane leading edge with relative circumferential position: R = 1.024, N = 10, R_3 = 1.04, ϕ = 0.055 (vaneless results shown by straight broken lines)

ditions in Fig. 18, where the result for midheight is shown again for comparison. The profiles are very similar in shape but the amplitude of the circumferential variation in radial velocity was about 15 percent greater near the shroud than at the center or near the hub, resulting in the extensive region of reversed flow.

These periodic flow patterns in circumferential direction were associated with the blade loading, or circulation, of the diffuser vanes, and it has been demonstrated in [10] and [11] that a singularity method assuming inviscid irrorational flow could predict these steady flow patterns at the inlet to the vaned diffuser, particularly near the middle of the passage.

The unsteady radial velocity patterns, which were obtained by subtracting the steady parts in Fig. 17 from the instantaneous velocity patterns in Fig. 11, are shown in Fig. 19. Superimposed on the traces with dotted lines are the flow patterns for the vaneless diffuser. There is a striking similarity between these unsteady patterns and those for the vaneless diffuser, showing that the principal source of variation in Fig. 11 is evidently the steady pattern from the diffuser vanes which has been removed. Some deviations were, however, noticed between the two patterns indicating an influence of the diffuser vanes on the flow in the impeller.

This similarity between the vaneless and the unsteady velocities provides a useful insight into the processes. It seems that, as a working approximation, the resultant flow can be regarded as the linear addition of the undisturbed flow from the impeller (as measured at inlet to a vaneless diffuser) and the steady disturbance produced by the diffuser vanes. As the flow rate was reduced the agreement between the unsteady velocity and the velocity into the vaneless diffuser became less good, indicating that the addition of effects was no longer adequate.

Effect of Diffuser Vanes on Impeller Wake Displacement Width. In order to investigate the influence of the diffuser vane on the impeller flow quantitatively, the wake displacement widths[2] were calculated and compared with the value for the vaneless diffuser in Fig. 20. The wake was defined for this purpose as the region where the local velocity was below the mean velocity at each axial position for one blade pitch of the impeller. The wake displacement widths for the vaneless diffuser build are shown by horizontal lines in Fig. 20. Since the patterns shown in Fig. 20 were obtained from the fluctuating parts of the instantaneous velocity patterns, constant velocities were added to each pattern from the vaned diffusers so that the mean velocities were the same as those for the vaneless diffuser, and the wake displacement widths for the vaned and vaneless diffusers could be compared on the same basis.

The wake displacement width, δ^*, for the vaned diffuser varied around the value for the vaneless case, depending on the relative position between the diffuser vanes and the impeller blades. The numbers in Roman numerals on the abscissa indicate the relative positions corresponding to those with the same numbers in Fig. 19. The averaged value of δ^* was reduced by about 15 percent from the value for the vaneless diffuser over most of the passage except near the shroud as follows

Axial position	Hub	Mid	Shroud
Vaneless	0.15	0.11	0.31
Vaned (N = 10, R_3 = 1.04)	0.13	0.09	0.33

When the flow rate was increased to ϕ = 0.085, the unsteady part of the instantaneous radial velocity distribution was so little influenced by the diffuser vanes that the radial velocity plots were nearly identical to those for the vaneless build. This may be attributable to the small incidence into the vanes and correspondingly small circulation around the vane leading edge.

When the flow rate was reduced to ϕ = 0.045, the influence of the diffuser vanes was particularly augmented near the hub; the unsteady velocity patterns were distinctly different from those of the vaneless diffuser, with the shapes of the patterns depending quite strongly on the diffuser vane position relative to the impeller blades. At relative position such as (V) the wake was located away from the suction side and near the center of the passage, indicating that the core of the wake near the hub was forced to change its location due to some effect to the diffuser vane. At this flow coefficient, ϕ = 0.045, the variation in the wake displacement width, δ^*, near the hub with the relative position between the diffuser and impeller was amplified by a factor of about three compared with the case for ϕ = 0.055, while the mean value changed but little from that for the vaneless diffuser.

Figure 21 illustrates the effect of the vane number on the mean wake displacement widths at three axial positions and at a flow rate of 0.045. With large numbers of diffuser vanes the mean values of δ^* near hub and at midheight were reduced by about 50 and 25 percent, respectively, from those for the vaneless diffuser, whereas a small increase was observed near the shroud. The decrease in the wake displacement width with the vaned diffuser seems to be one of the reasons for an increase in static pressure rise through the impeller compared with the value for the vaneless diffuser (Fig. 3).

Mean Radial Velocity Profile. Nonuniformity of the flow in the axial direction is another factor in determining the distortion of the flow discharged from the impeller. Figure 22

[2] The wake displacement width is defined as

$$\delta^* = \epsilon(1 - W_w/W_j)$$

where ϵ is the wake width, and W_w and W_j are the mean velocity of the wake and jet.

Downloaded 01 Jun 2010 to 171.66.16.70. Redistribution subject to ASME license or copyright; see http://www.asme.org/terms/Terms_Use.cfm

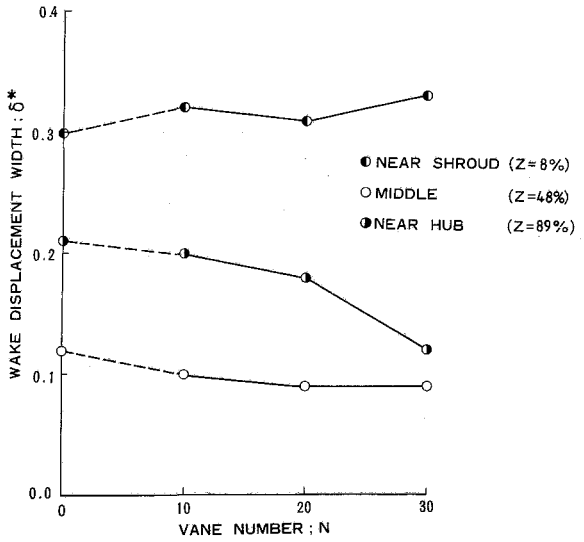


Fig. 21 Variation in the mean wake displacement width measured between impeller and diffuser vane leading edge with number of diffuser vanes: $R = 1.024, R_3 = 1.04, \phi = 0.055$

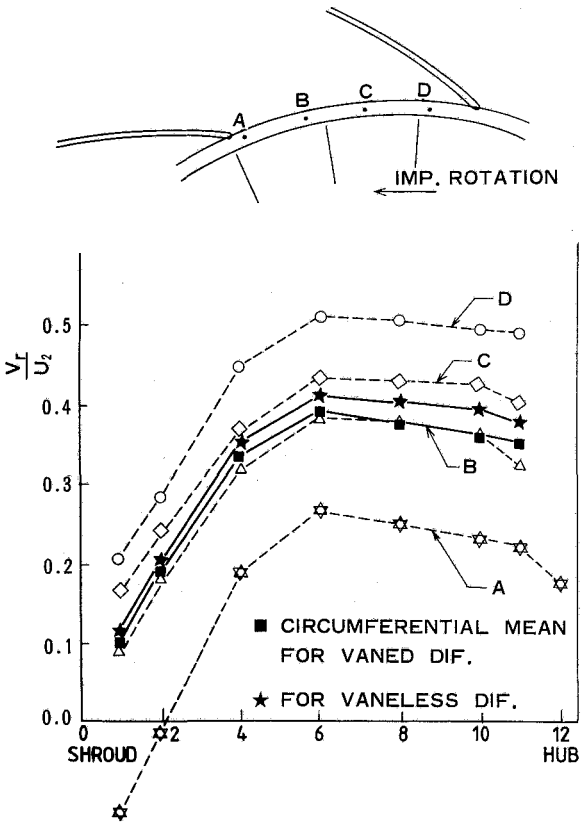


Fig. 22 Mass averaged radial velocity distribution in axial direction: $R = 1.024, N = 10, R_3 = 1.04, \phi = 0.055$

shows the mass-averaged radial velocity distributions in the axial direction at several circumferential positions between a pair of diffuser vanes for the same condition as Fig. 11. The shapes of the distributions were very similar, but the magnitudes were significantly different, depending on the circumferential positions. The radial velocity was strongly depressed at the pressure side of the diffuser vane leading edge, position A, which resulted in an appearance of strong reversed flow region near the shroud. Nevertheless, when the circumferentially averaged profile, represented by a symbol "■" in the graph, is compared to the mean radial velocity distribution in the vaneless diffuser, denoted by a symbol of "★," the two profiles are found to be similar in shape and magnitude. For other configurations of the vaned diffuser or for other flow rates, good agreement between the mean radial and tangential velocity distributions and total pressure distributions for the vaned and vaneless diffusers was also observed.

Concluding Remarks

The majority of the test program was carried out with diffuser vanes having an inlet angle of 60 deg to the radial. At $\phi = 0.055$, this produced a mean incidence angle onto the vanes of about 10 deg at the midaxial position ($z = 6$ mm), rising to over 25 deg near the shroud. The impeller pressure rise peaks at rather lower values than this, suggesting that better overall performance could be obtained with diffuser vanes staggered at 70 deg. This has been experimentally confirmed, and it was also found that compared with the 60 deg inlet vanes, the steady nonuniformity in the flow was greatly reduced at $\phi = 0.045$. This diffuser configuration has now been investigated further and will be reported on later.

In high-speed machines, there are strong pressure gradients produced by the diffuser vane leading edge shocks. The high incidence onto the diffuser vanes for the low-speed tests reported in the present paper makes the tests more relevant to high-speed machines, as the incidence produces strong radial and tangential pressure gradients. The circumferential direction of the rapid pressure rise in the present tests is reversed, compared with the shock, and the radial decay will be more rapid. Nevertheless, the effect on the flow in the impeller is likely to have similarities and be useful as a means for gaining insight into the flow.

From a detailed instantaneous measurement of the distorted flow discharged from a radial bladed impeller into a vaneless diffuser, it appears that the core of the wake at the impeller outlet changed its position from the shroud to the hub past the suction surface as the throughflow rate was decreased. As a result the circumferentially averaged radial flow near the hub was reduced drastically at low flow rates when the wake reached the hub side. The wake on the hub wall continued to expand with decreasing flow rate until it finally filled most of the impeller blade pitch. The movement of the wake is predictably by secondary flow theory.

The amount of reversed flow for vaned diffusers with small vaneless ratio was significantly greater than that for the vaneless diffuser, but the strength of the reversed flow was weakened as the vane number increased. As the flow rate was decreased, strong reversed flow appeared at the diffuser vane leading edge position, first near the shroud and then, at still lower flow, near the hub.

The circumferential nonuniformity from the impeller was clearly evident at large radii in the vaneless diffuser. However, when the vaned diffusers were installed, the periodic unsteadiness of the flow diminished rapidly in the diffuser vane channels and clear variation of the velocity pattern with the rotation of the impeller was restricted to the inlet region of the diffuser vanes.

The instantaneous flow patterns in the vaned diffusers could be divided into the unsteady and steady parts. At entry to the diffuser, just outside the impeller, the unsteady part showed the distorted flow pattern discharged from the impeller, and this was generally similar to the instantaneous flow pattern in the vaneless diffuser. On the other hand, the steady part indicated the nonuniform flow pattern produced by the circulation about the diffuser vanes and corresponded to the flow pattern in the radial cascade test rig such as used by Bagdadhi and McDonald [6]. The steady pattern is strongly affected by the mean incidence onto the blades, as confirmed

Downloaded 01 Jun 2010 to 171.66.16.70. Redistribution subject to ASME license or copyright; see http://www.asme.org/terms/Terms_Use.cfm

by operation with the 70 and 60 deg inlet vanes at the same flow rate.

Although the unsteady part of the pattern at inlet to the vaned diffuser was generally similar to the instantaneous pattern in the vaneless diffuser, it was affected to some extent by the diffuser vanes. Except near the shroud, the mean wake displacement width was reduced in comparison with the value for the vaneless diffuser, and the reduction became larger as the vane number was increased. This suggests that the mixing of jet and wake was stimulated in the impeller by the presence of the vanes.

The mass-averaged, total pressure distributions were not uniform circumferentially, and the variation was more than 15 percent of the mean rise across the impeller.

The circumferential mean radial velocity profile in the axial direction at the vaned diffuser inlet was almost identical with that for the vaneless diffuser. Nevertheless, reversed flow appeared in the low radial velocity region near the diffuser vane leading edge when the flow rate was small, and this led to an increase of loss near the side walls.

Acknowledgment

The authors would like to thank Mr. K. Bryant for his great help in building the rig and in carrying out many measurements and Mr. E. C. Deverson for his invaluable assistance and suggestion in the experimental work.

Grateful acknowledgment is made to the Ministry of Defence, Procurement Executive for their support of the research project and to Mr. P. M. Came for his advice and encouragement.

References

1 Eckardt, D., "Instantaneous Measurements in the Jet and Wake Discharge Flow of a Centrifugal Compressor Impeller," ASME JOURNAL OF ENGINEERING FOR POWER, Vol. 97, 1975, pp. 337–346.

2 Senoo, Y., and Ishida, M., "Behavior of Severely Asymmetric Flow in a Vaneless Diffuser," ASME JOURNAL OF ENGINEERING FOR POWER, Vol. 97, 1975, pp. 375–387.

3 Johnston, J. P., and Dean, R. C., "Losses in Vaneless Diffusers of Centrifugal Compressors and Pumps," ASME JOURNAL OF ENGINEERING FOR POWER, Vol. 82, 1966, pp. 49–60.

4 Senoo, Y., Kinoshita Y., and Ishida, M., "Asymmetric Flow in Vaneless Diffusers of Centrifugal Blowers," ASME *Journal of Fluids Engineering*, Vol. 99, 1977, pp. 104–113.

5 Dean R. C., and Senoo, Y., "Rotating Wakes in Vaneless Diffusers," ASME *Journal of Basic Engineering*, Vol. 82, 1960, pp. 563–574.

6 Baghdadi, S., and McDonald, A. T., "Performance of Three Vaned Radial Diffusers with Swirling Transonic Flow," ASME *Journal of Fluids Engineering*, Vol. 97, No. 2, 1975, pp. 155–170.

7 Baghdadi, S., "The Effect of Rotor Blade Wakes on Centrifugal Compressor Diffuser Performance—A Comparative Experiment," ASME *Journal of Fluids Engineering*, Vol. 99, 1977, p. 45.

8 Johnson, M. W., and Moore, J., "The Development of Wake Flow in a Centrifugal Impeller," ASME JOURNAL OF ENGINEERING FOR POWER, Vol. 102, 1980, pp. 382–399.

9 Eckardt, D., "Detailed Flow Investigation Within a High-Speed Centrifugal Impeller," ASME *Journal of Fluids Engineering*, Vol. 98, 1976, pp. 390–402.

10 Inoue, M., "Centrifugal Compressor Diffuser Studies," Ph.D. thesis, University of Cambridge, 1980.

11 Fisher, E. H., and Inoue, M., "A Study of Diffuser Rotor Interaction in a Centrifugal Compressor." *Jnl. of Mech. Eng. Sci.*, Vol. 23, No. 3, 1981, pp. 149–156.

12 Senoo, Y., and Kinoshita, Y., "Influence of Inlet Flow Conditions and Geometries of Centrifugal Vaneless Diffusers on Critical Flow Angles for Reverse Flow," ASME Conference on "Centrifugal Compressor and Pump Stability," New Orleans, 1976.

Downloaded 01 Jun 2010 to 171.66.16.70. Redistribution subject to ASME license or copyright; see http://www.asme.org/terms/Terms_Use.cfm

Distinction Between Different Types of Impeller and Diffuser Rotating Stall in a Centrifugal Compressor With Vaneless Diffuser

P. Frigne[1]

R. Van Den Braembussche

von Karman Institute for Fluid Dynamics,
Chaussée de Waterloo, 72
1640 Rhode Saint Genèse, Belgium

This paper describes the results of an experimental investigation of the subsynchronous rotating flow patterns in a centrifugal compressor with vaneless diffuser. Several compressor configurations have been examined by means of hot wire anemometry. Fourier analysis allowed one to distinguish between the different modes of unstable operation. For both impeller and diffuser rotating stall, comparison is made between the amplitude, frequency, and periodicity of the induced velocity fluctuations. The results are further cross-checked with other experimental data.

Introduction

At reduced flow rates, the stable operation of centrifugal compressors can be perturbed by the occurrence of self-excited flow oscillations, which may result in a significant drop in aerodynamic performances. Moreover, these constitute a source of mechanical excitation, which may limit the range of operation because of vibrational problems. This becomes very critical at high pressure levels, where the corresponding forces are much larger, due to the increased density of the working fluid.

The best known unsteady flow phenomenon is surge. It is characterized by the occurrence of large low frequent velocity and pressure fluctuations, which are synchronous through the complete compression system. Some authors [1, 2] have also reported a mild type of surge, which occurs just before the onset of full surge. It has the same characteristics, but the amplitude of the oscillations is much lower.

The unsteady flow phenomenon which gives rise to the occurrence of subsynchronous rotating velocity fluctuations is commonly referred to as "rotating stall." In contrast with surge and mild surge, the net flow rate through the compressor remains constant. Rotating stall can be generated by a destabilization of the impeller flow [3, 4, 5] or for radial compressors with a vaneless diffuser, rotating stall can also be triggered by a destabilization of the diffuser flow [6, 7, 8]. The operating points where this instability occurs are not limited to the positive slope of the compressor characteristic, but they have also been observed on the negative slope side [11], where normally stable operation is expected.

This paper describes a series of tests in which the unstable operating range of centrifugal compressors with vaneless diffusers has been explored. Three stator configurations have been combined with one impeller, in order to generate different types of unsteady flow. In each observed flow instability, the origin of the destabilization and unsteady flow characteristics have carefully been determined.

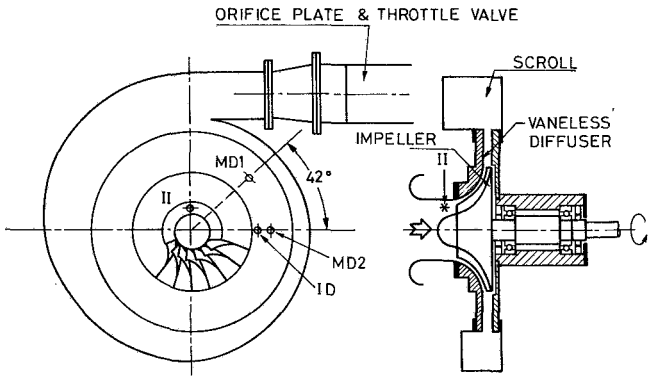


Fig. 1 Experimental facility

Experimental Facility, Instrumentation and Techniques

The experiments have been performed in an open loop centrifugal compressor test facility of the Rijksuniversiteit Gent. Figure 1 shows the basic configuration A. The compressor inlet is at atmospheric conditions. At the outlet of the diffuser, the flow is collected by a scroll and fed into a nor-

[1] Presently at Institut CERAC, CH-Ecublens

Contributed by the Gas Turbine Division of THE AMERICAN SOCIETY OF MECHANICAL ENGINEERS and presented at the 28th International Gas Turbine Conference and Exhibit, Phoenix, Arizona, March 27-31, 1983. Manuscript received at ASME Headquarters December 21, 1982. Paper No. 83-GT-61.

Copyright © 1984 by ASME
Downloaded 01 Jun 2010 to 171.66.16.70. Redistribution subject to ASME license or copyright; see http://www.asme.org/terms/Terms_Use.cfm

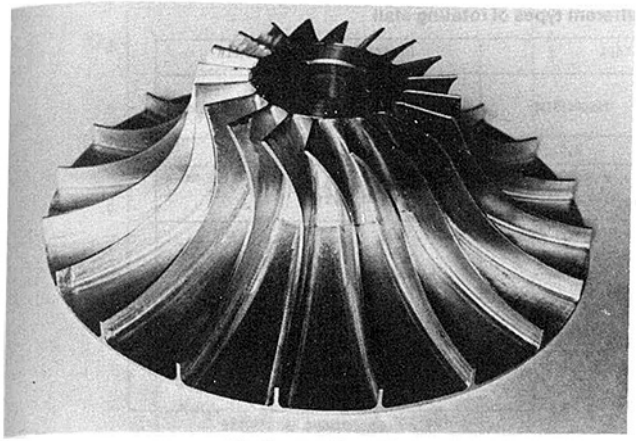


Fig. 2 Test impeller

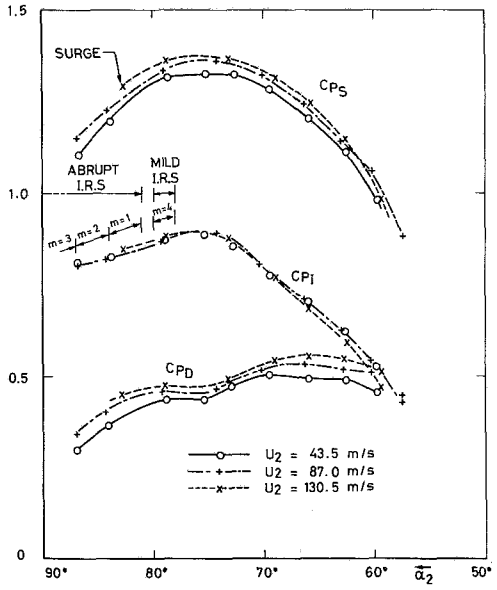


Fig. 3 Performance map of configuration A

malized tube, which allows for flow control and measurement. The unshrouded impeller (Fig. 2) has 20 radial blades and an exit diameter of .416 m.

The compressor is equipped with a vaneless diffuser with a radius ratio of 1.62, and a width to rotor outlet radius ratio of .077.

Besides the classic pressure and temperature probes required for the overall performance measurements, four hot

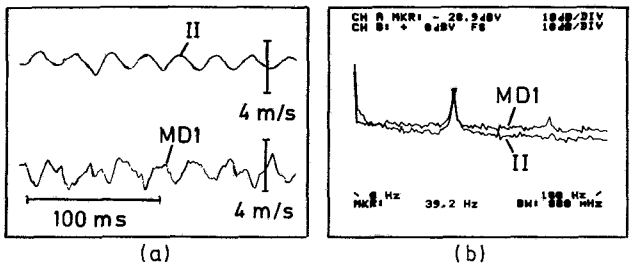


Fig. 4 Mild IRS (m = 4); U_2 = 43.5 m/s; α_2 = 79 deg

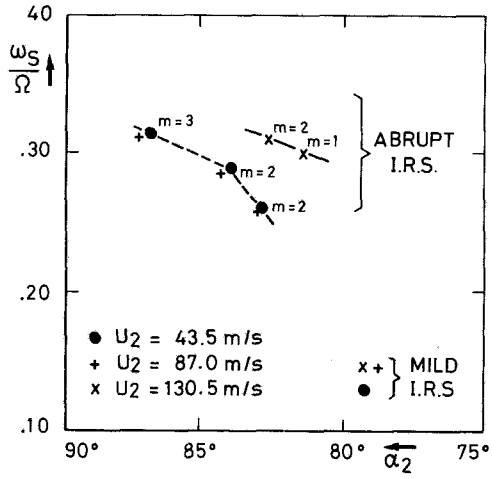


Fig. 5 Influence of the diffuser inlet absolute flow angle α_2 on the relative propagation speed of mild and abrupt IRS

wire probes are also installed. They are mounted perpendicular to the mean flow direction: one at the impeller inlet (II), one at the diffuser inlet (ID) and two at $R/R_2 = 1.3$ inside the diffuser (MD1 and MD2) at 42 deg circumferential distance (Fig. 1).

The linearized anemometer signals are visualized on an oscilloscope and processed with an HP 3582A two-channel spectrum analyzer to determine the frequency spectrum of each channel and the coherence and phase shift between two different locations.

The steady performance of the impeller, the vaneless diffuser, and the compressor stage are measured at three different rotational speeds and expressed in terms of a static pressure rise coefficient

$$C_p = \frac{\Delta p}{\frac{1}{2}\rho_0 U_2^2}$$

Nomenclature

A = relative amplitude of the velocity fluctuations
b = diffuser axial width (m)
C_p = static pressure rise coefficient
m = number of rotating stall cells
N = number of impeller blades
p = static pressure (N/m^2)
R = radius (m)
U = circumferential velocity (m/s)
V = absolute flow velocity (m/s)
α = absolute flow angle measured from meridional
β = relative flow angle measured from meridional
ρ = density (kg/m^3)
Φ = flow coefficient at the impeller outlet (V_{r2}/U_2)
ω_s = angular speed of the rotating stall cells (radians/s)
Ω = angular speed of the impeller (radian/s)

Subscripts

0 = inlet plenum
1 = inducer inlet
2 = impeller outlet or diffuser inlet
3 = diffuser outlet
u = circumferential direction
r = radial direction

Abbreviations

IRS = impeller rotating stall
DRS = diffuser rotating stall
IGV = inlet guide vane
I = impeller
D = diffuser
S = stage
II = inducer inlet
ID = diffuser inlet
MD = middle of the diffuser

Downloaded 01 Jun 2010 to 171.66.16.70. Redistribution subject to ASME license or copyright; see http://www.asme.org/terms/Terms_Use.cfm

Table 1 Characteristics of the different types of rotating stall

	IMPELLER ROTATING STALL			DIFFUSER ROTATING STALL	
TYPE / CHARACTERISTIC	MILD	ABRUPT	PROGRESSIVE	HIGH FREQUENCY	LOW FREQUENCY
Configuration	A	A	B,C	C	C
Relative amplitude, A, in the diffuser	$\alpha_2 \nearrow \Rightarrow A \nearrow$ MAX $\searrow$ A_{MAX}=.065 (U_2=43.5 m/s)	$\alpha_2 \nearrow \Rightarrow A \nearrow$ MAX $\searrow$ $A_{MAX} \cong$.30 (U_2=43.5m/s)	$\alpha_2 \nearrow \Rightarrow A \nearrow$ MAX $\searrow$ A_{MAX}=.10 (U_2=43.5 m/s)	$\alpha_2 \nearrow \Rightarrow A \nearrow$ MAX $\searrow$ A_{MAX}=.10 (U_2=43.5 m/s)	$\alpha_2 \nearrow \Rightarrow A \nearrow$ MAX $\searrow$
Cell number m	m=5 (U_2=43.5 m/s) m=4 (U_2=87 m/s) m=4 (U_2=130.5m/s) No harmonics	$81° < \alpha_2 < 84°$: m=1 $84° < \alpha_2 < 87°$: m=2 $87° < \alpha_2$ = m=3 m=1 only at $U_2 \geq 130.5$ m/s	m = 1 : always dominant m = 2, m = 3 } harmonics	m=3 No harmonics	m=2 No harmonics
Relative propagation speed ω_s/Ω	ω_s/Ω = .14 $\alpha_2 \nearrow \Rightarrow \omega_s/\Omega$ = ct.	$.26 < \omega_s/\Omega < .31$ $\alpha_2 \nearrow \Rightarrow \omega_s/\Omega \nearrow$	$.82 > \omega_s/\Omega > .67$ $\alpha_2 \nearrow \Rightarrow \omega_s/\Omega \searrow$ MIN $\nearrow$	$.17 < \omega_s/\Omega < .21$ $\alpha_2 \nearrow \Rightarrow \omega_s/\Omega \nearrow$	$.13 < \omega_s/\Omega < .16$ $\alpha_2 \nearrow \Rightarrow \omega_s/\Omega \nearrow$

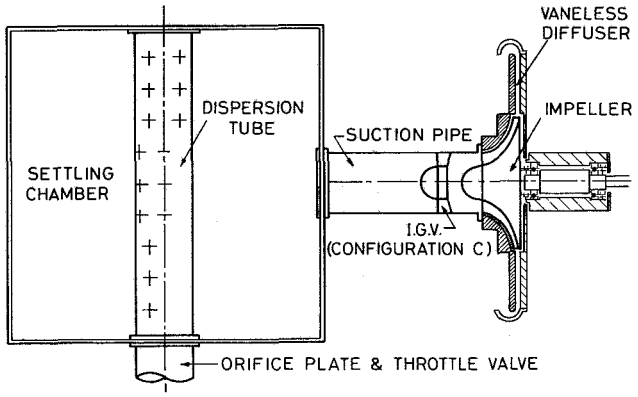


Fig. 6 Compressor configuration B (without IGV); compressor configuration C (with IGV)

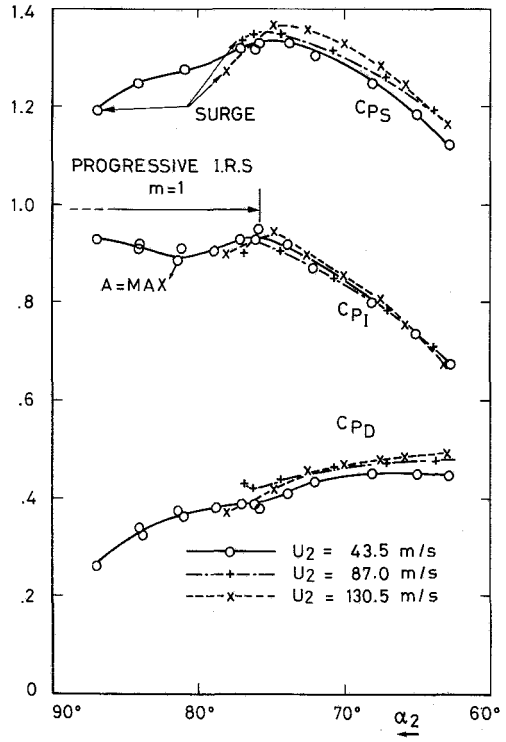


Fig. 7 Performance map of compressor configuration B

The mass flow rate is related to the diffuser inlet flow angle, α_2, because of the important influence of this parameter on the diffuser stability. It is calculated from slip factor correlations and checked against the measured impeller temperature rise. Increasing values of α_2 correspond to decreasing mass flow.

Flow perturbations rotating in the diffuser will generate periodic signals at MD1 and MD2 with period, τ_2. Due to the 42 deg difference in circumferential position, there will be a time lag, τ_1, between the signals MD1 and MD2 which allows for the determination of the angular propagation speed, ω_s, of the pattern and the number of cells, m

$$m = \frac{360 \text{ deg}}{42 \text{ deg}} \cdot \frac{\tau_1}{\tau_2} \qquad (m \text{ must be integer})$$

$$\omega_s = \frac{2\pi}{m \cdot \tau_2} \qquad \text{(radians/s)}$$

The relative amplitude of the velocity oscillations is defined as

$$A = \frac{V_{\max} - V_{\min}}{2 \cdot V_{\text{RMS}}}$$

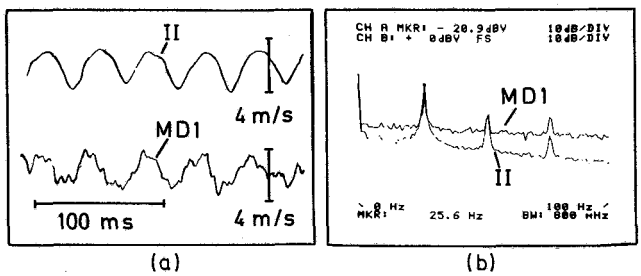


Fig. 8 Progressive IRS (m = 1), U_2 = 43.5 m/s, α_2 = 78 deg

Test Results With the Basic Configuration A

The performances of the different compressor components are shown in Fig. 3.

The impeller characteristic reaches a maximum for α_2 = 76 deg. The diffuser characteristic has a maximum at α_2 = 65 deg and a minimum at α_2 = 77 deg.

At U_2 = 130.5 m/s, the flow rate is limited to α_2 = 83 deg due to the occurrence of surge. At lower speed, no surge was detected.

When decreasing the flow rate, first destabilization occurs at α_2 = 78 deg at the left of the maximum of the impeller characteristic.

Figure 4 shows, respectively, the hot wire signals II and

Downloaded 01 Jun 2010 to 171.66.16.70. Redistribution subject to ASME license or copyright; see http://www.asme.org/terms/Terms_Use.cfm

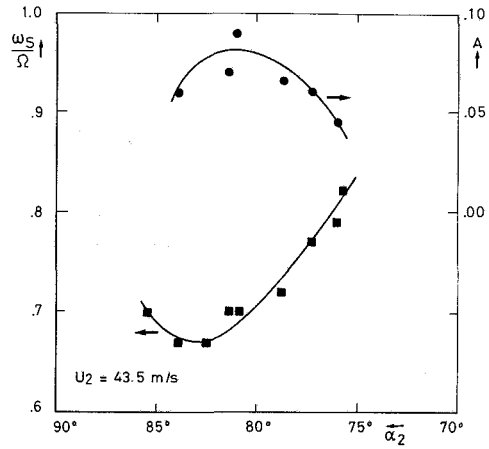


Fig. 9 Influence of the diffuser inlet absolute flow angle, α_2, on the relative amplitude and propagation speed for progressive IRS

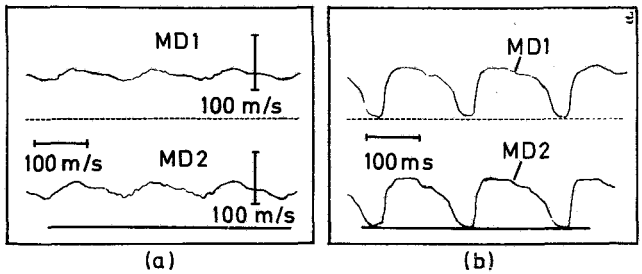


Fig. 10 Mild surge and surge, U_2 = 130.5 m/s

MD1 and the corresponding frequency spectra. As the flow oscillations can be detected both upstream and downstream of the impeller, this instability is very likely to be attributed to a destabilization of the impeller flow.

There are four stall cells, which rotate at a relative propagation speed ω_s/Ω = .15. The relative amplitude of the oscillations reaches 6 percent at U_2 = 43.5 m/s.

This instability, which can be considered as a mild type of IRS, disappears at α_2 = 80 deg, and the flow becomes stable again. At α_2 = 81.5 deg, impeller rotating stall reappears suddenly at U_2 = 43.5 m/s with a high amplitude of 25 percent which remains independent of the flow rate.

Initially, the number of stall cells is m = 1 but increases to m = 2 as the flow rate is reduced below α_2 = 82.7 deg. At α_2 = 87 deg, there is a transition to m = 3. The propagation speed ω_s/Ω is about .30 and increases as the flow rate is reduced (Fig. 5). Within the accuracy of the measurements, this relative propagation speed was found to be independent of impeller rpm.

Because of its sudden appearance and high amplitude, this impeller flow instability is considered as an abrupt type of IRS. The characteristics of both types of IRS are listed in Table 1.

At U_2 = 130.5 m/s, surge occurs at α_2 = 83 deg. The frequency of the induced flow oscillations is 11 Hz and the amplitude reaches 100 percent in the diffuser.

Test Results With Configuration B

Only impeller induced rotating stall has been observed on the basic configuration A. In order to also generate diffuser rotating stall, the compressor rig has been modified to make the vaneless diffuser more critical.

In the literature, there exists a general agreement concerning the destabilizing influence of an increased diffuser radius ratio. However, this parameter could not be changed on the basic configuration without redesigning the scroll. To

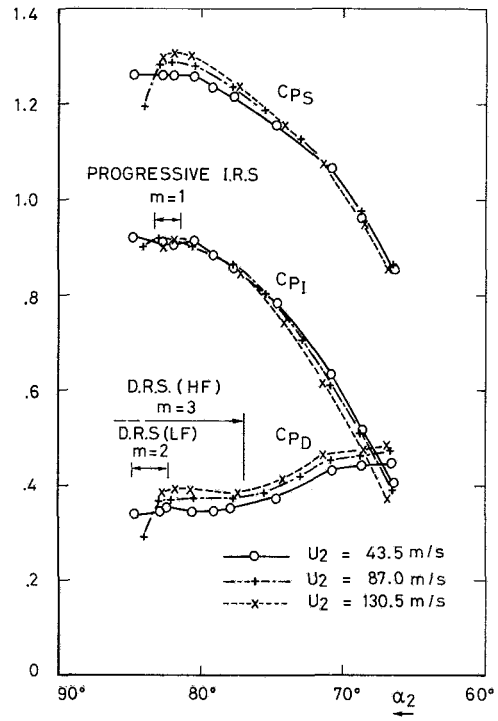


Fig. 11 Performance characteristics of compressor configuration C

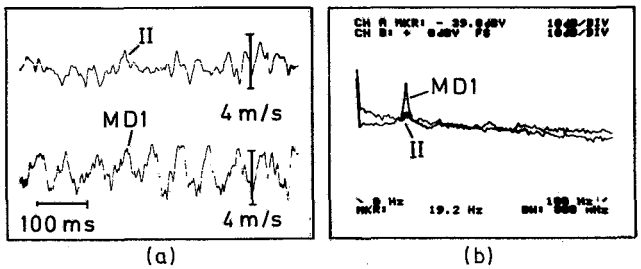


Fig. 12 DRS (HF) (m = 3); U_2 = 43.5 m/s; α_2 = 80.5 deg

avoid this problem, an alternative compressor configuration has been installed (Fig. 6).

The vaneless diffuser has the same width, but the radius ratio is increased to 1.92. Flow is discharged at atmospheric pressure after 180 deg turning at the diffuser exit. The mass flow is now controlled at the compressor inlet. In order to obtain sufficient flow uniformity, a large settling chamber has been installed at compressor inlet.

The overall performance curves (Fig. 7) are very similar to those of the previous configuration except that the impeller characteristic exhibits a minimum for α_2 = 81 deg. The inlet settling chamber constitutes a large aerodynamic capacity which is responsible for the occurrence of surge for U_2 higher or equal to 87.0 m/s as soon as the flow rate is decreased below the maximum pressure rise of the compressor.

At U_2 = 43.5 m/s, first instabilities occur at α_2 = 76 deg close to the maximum of the impeller characteristic. Figures 8 (a) and 8(b) show the hot wire signals II and MD1 and the corresponding frequency spectra. This type of rotating stall is also caused by a destabilization of the impeller flow, but its characteristics are quite different from test series A. The amplitude of the velocity fluctuations in the diffuser increases gradually towards a maximum of 10 percent at α_1 = 81 deg, which corresponds to the minimum of the impeller static pressure rise (Fig. 9).

The relative propagation speed ω_s/Ω is between .65 and .8

Downloaded 01 Jun 2010 to 171.66.16.70. Redistribution subject to ASME license or copyright; see http://www.asme.org/terms/Terms_Use.cfm

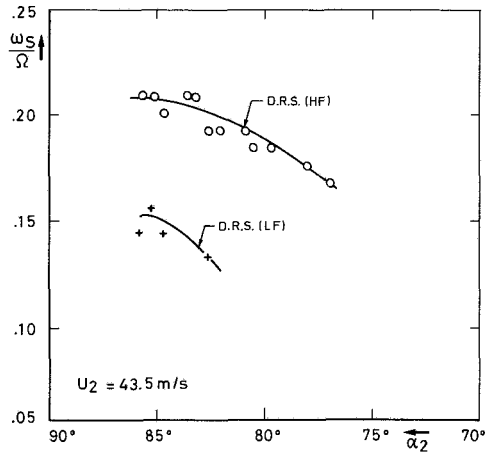


Fig. 13 Influence of the diffuser inlet absolute flow angle, α_2, on the relative propagation speed of DRS (HF) and DRS (LF)

and decreases towards a minimum when the flow rate is decreased. These values are independent of RPM. There is only one stall cell at all mass flows. However, as one can see from Figs. 8(*a*) and 8(*b*), the velocity fluctuations are not sinusoidal. This means that higher harmonics, representative for the modes $m = 2$ and $m = 3$ are rotating at the same relative propagation speed as the first mode $m = 1$. Because of its smooth amplitude variation with flow rate, this instability is believed to be triggered by a "progressive" boundary layer stall [12] on the impeller blades. It is therefore considered as a progressive type of IRS. Its main characteristics are listed in Table 1.

At higher rpm, as a precursor of surge, also mild surge or limit cycles have been detected [1, 2]. Figures 10(*a*) and 10(*b*) compare the hot wire traces MD1 and MD2, respectively, during mild surge and full surge. The frequency of mild surge (8 Hz) is slightly higher than the surge frequency (6 Hz), but the amplitude of the flow oscillations reaches only 10 percent and is thus about one order of magnitude lower than for full surge (100 percent).

Rotating stall could not be observed at higher rpm because the flow rate is limited by surge. According to [13], the initiation of surge can be delayed towards lower flow rates if the aerodynamic capacity of the compression system can be decreased.

In order to verify this hypothesis and to examine rotating stall at higher peripheral speeds, an aerodynamic resistance has been inserted in the suction pipe, between settling chamber and compressor inlet. As a result, the performance curve could be extended to $\alpha_2 = 82$ deg for $U_2 = 87$ m/s. It was also observed that progressive IRS was independent of peripheral speed and not affected by the close coupled resistance. Surge frequency has increased from 6 Hz to 20 Hz and the amplitude A has reduced from 100 percent to 20 percent.

Test Results With Configuration C

In configuration A and B no instability due to diffuser flow destabilization has been registered. However, according to the corrected Senoo-criterium [11], diffuser rotating stall should be generated at $\alpha_2 = 77$ deg. A possible explanation for this is that diffuser rotating stall is suppressed by the occurrence of impeller rotating stall. In order to verify this, inlet guide vanes have been installed in the suction pipe, which create a 60 deg positive prerotation at the inducer tip. Based on the hypothesis that impeller rotating stall is triggered when a critical incidence is reached at the inducer inlet, this instability should be delayed from $\alpha_2 = 76$ deg to $\alpha_2 = 82$ deg. In this

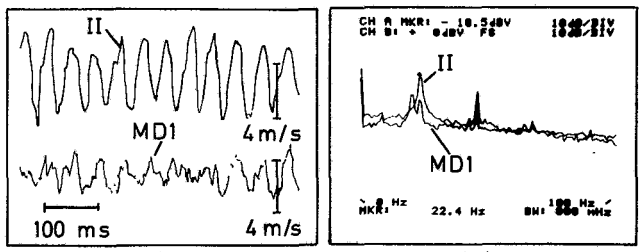


Fig. 14 $U_2 = 43.5$ m/s; $\alpha_2 = 82.6$ deg

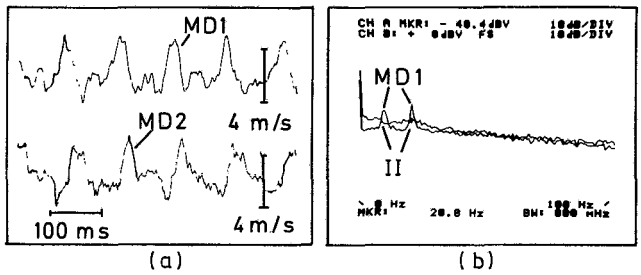


Fig. 15 $U_2 = 87$ m/s; $\alpha_2 = 8.36$ deg (DRS (HF) ($m = 3$) DRS (LF) ($m = 2$)

way, a sufficiently broad margin for diffuser rotating stall would be created.

The overall compressor performances are shown on Fig. 11. Compared to the previous configuration B (Fig. 7) one can observe a 6 deg shift to the left of the impeller characteristic. The maximum compressor pressure rise has decreased because of the prerotation. The diffuser characteristic is almost unchanged.

First instabilities appear in the diffuser at $\alpha_2 = 77$ deg. This corresponds to a minimum in the diffuser characteristic. Figures 12(*a*) and 12(*b*) show the hot wire signals II and MD1 and their power spectra at $\alpha_2 = 80$ deg. As the frequency peak of 19.2 Hz is not observed at the inducer inlet, one can conclude that it is due to diffuser rotating stall. From the phase shift between MD1 and MD2 one can calculate that three stall cells are rotating with a relative propagation speed $\omega_s/\Omega = .20$. This propagation speed increases when the flow rate is further reduced (Fig. 13), but it does not depend on rpm. The relative amplitude of the induced velocity oscillations amounts to 10 percent and is almost independent of the flow rate. A remarkable feature of this type of instability is that no harmonics are induced. This means that the shape of the velocity fluctuations is very sinusoidal.

With the achieved prerotation, the critical flow angle for impeller rotating stall is predicted at $\alpha_2 = 82$ deg. This is experimentally confirmed by the hot wire signals and spectra II and MD1 obtained at $\alpha_2 = 82.6$ deg (Fig. 14(*a*) and 14(*b*)). The frequency peak at 23.2 Hz is measured at the rotor inlet and inside the diffuser. It corresponds to one stall cell which rotates at $\omega_s/\Omega = .67$. These results are very similar to the progressive IRS observed without prerotation.

The frequency peak at 19.2 Hz corresponds to diffuser rotating stall and cannot be detected at the inducer inlet. When closing the throttle valve further to $\alpha_2 = 83.1$ deg, diffuser rotating stall remains unaffected, but impeller rotating stall disappears completely.

At $\alpha_2 = 83.6$ deg, a new type of unstable flow with a frequency of 8.8 Hz occurs (Fig. 15(*a*) and 15(*b*)). As it is not detected at the inducer inlet, it should correspond to a second type of diffuser rotating stall. From the phase shift between MD1 and MD2, one can deduce that two stall cells are rotating at $\omega_s/\Omega = .13$ (Fig. 13).

Downloaded 01 Jun 2010 to 171.66.16.70. Redistribution subject to ASME license or copyright; see http://www.asme.org/terms/Terms_Use.cfm

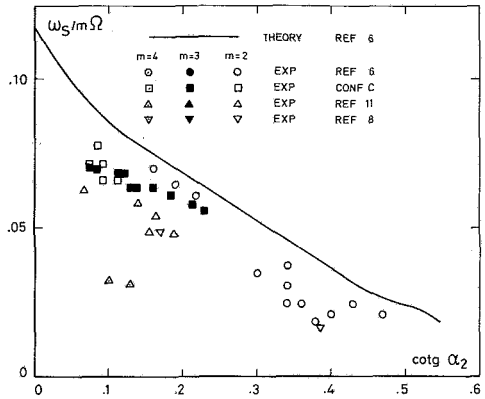


Fig. 16 Variation of rotational speed in function of inlet air angle

Table 1 gives the most important characteristics of the different types of diffuser rotating stall. Both types do not really occur simultaneously but rather in an intermittent mode. At $\alpha_2 = 86$ deg, the surge limit is reached. The frequency of the flow oscillations is still 6 Hz and is thus unaffected by the inlet guide vanes.

From the comparison of the test results with and without prerotation, the following conclusions can be drawn:

- Diffuser rotating stall can be suppressed completely if impeller rotating stall is initiated first;
- On the contrary, if diffuser rotating stall is first triggered, impeller rotating stall may occur at critical inducer incidence conditions.

Discussion of the Results

The five types of rotating stall observed in these three compressor configurations show a large variety in terms of propagation speed, amplitude, and number of stall cells as shown in Table 1. In this chapter, one will try to obtain a better insight by comparing these results with other experimental data and theoretical predictions from the literature.

Several theoretical studies about diffuser rotating stall have been published. Based on a stability analysis of the linearized inviscid and compressible flow equations in a radial vaneless diffuser, Jansen [6] has concluded that diffuser rotating stall is generated when a local flow reversal occurs ($V_r < 0$). By combining this criterion with a steady axisymmetric calculation of the three-dimensional boundary layers along the diffuser walls, Jansen [6, 14] and later Senoo [7, 15, 16] have determined the influence of the diffuser geometry and flow conditions on the stability limit for diffuser rotating stall.

Present authors have shown [11] that Senoo's prediction of the critical diffuser inlet flow angle agrees well with experimental data if a Reynolds number correction is applied. This is also valid for configuration C.

The theory of Jansen also predicts the relations between rotational speed ω_s/Ω, the diffuser inlet flow angle α_2 and the number of stall cells, m (Fig. 16). This relation agrees very well with the experimental data of [6, 8, 11] and with both types of diffuser rotating stall of configuration C. These last ones can therefore be considered as two different modes of the same diffuser flow instability.

For all the abovementioned cases of diffuser rotating stall, the measured velocity fluctuations are very sinusoidal and no harmonics have been observed in the frequency spectra. One of the authors [19] has shown, by means of a nonlinear, time-evolutive calculation that diffuser rotating stall can be generated by a strong interaction between the boundary layers along the diffuser walls and the inviscid flow core. In this theory, the unsteady boundary layers constitute a source of viscous excitation and the flow field acts as a response system.

Abdelhamid [17] has developed a linearized stability analysis for the inviscid flow field in a radial vaneless diffuser taking into account the interaction with the upstream impeller. Depending on the parameter

$$Z_u = \frac{dV_u}{dV_r}$$

two different types of rotating stall are predicted. For $Z_u < 0$, the characteristics of the instabilities are similar to those of diffuser rotating stall as discussed before. However, for $Z_u > 0$, a new type of rotating stall is predicted with a rotational speed varying between .30 and .50. The onset of this instability does not depend on the diffuser inlet flow angle but is still influenced by the diffuser radius ratio. In terms of rotational speed, this is very similar to the results of [9], the high frequent flow oscillations of [10], and the abrupt impeller rotating stall observed in configuration A. Comparing in more detail all these experimental data, it appears that similarity exists also in terms of amplitude of the velocity oscillations ($A \cong 30$ percent) and number of stall cells ($m = 1, 2, 3, 4$). The frequency spectra of the velocity signals show the presence of harmonics.

For an impeller with radial or backward bended blades, positive Z_u values are only possible if the impeller flow becomes very unstable. The flow oscillations are then likely to propagate also upstream of the impeller. This phenomenon is very similar to rotating stall in axial flow compressors. Takata and Nagano [18] have shown that rotating stall can be explained as a resonant interaction between an axial rotor blade row and a downstream flow field. As the destabilization process is strongly related to the unsteady behavior of the impeller flow, this second group of isntabilities are therefore interpreted by the authors as impeller rotating stall.

A further analysis of the experimental data reveals that the rotating stall with high rotational speed ($.50 < \omega_s/\Omega < .80$), observed in configurations B and C is similar to the ones reported in [3, 4, 5]. However, the variation of the propagation speed with the flow rate shows an opposite trend. This third group of instabilities should also be considered as impeller rotating stall. In contrast with group 2, which seems to be due to an abrupt destabilization of the impeller flow, the instabilities of group 3 are more likely to be generated by a progressive boundary layer stall on the impeller blades.

Some analogy exists between the mild type of impeller rotating stall observed in configuration A and the small stall state observed in an axial flow compressor [20] just before the onset of deep stall. These instabilities are both characterized by a high number of stall cells and a low amplitude of velocity fluctuations. However, additional experimental confirmation is required here before any further conclusion can be drawn.

Conclusions

An experimental investigation has been presented of the unsteady flow characteristics of a centrifugal compressor with vaneless diffuser for several stator configurations. Different types of rotating flow patterns have been observed and their characteristics were compared mutually and cross-checked with other experimental data and theoretical approaches. From the analysis it has become clear that almost all rotating instabilities can be subdivided into three distinct groups:

Group I: diffuser rotating stall due to a strong interaction between boundary layer and inviscid core flow in the vaneless diffuser. Typical for this instability is the low relative propagation speed ($\omega_s/\Omega \leq .20$) and the moderate amplitude of the velocity fluctuations ($A \cong .10$). Different modes of this

Downloaded 01 Jun 2010 to 171.66.16.70. Redistribution subject to ASME license or copyright; see http://www.asme.org/terms/Terms_Use.cfm

instability can occur intermittently, but they all satisfy the relation shown in Fig. 16.

Group II: abrupt impeller rotating stall due to a strong interaction between impeller and diffuser. This instability is characterized by a high amplitude of velocity fluctuations ($A \cong .30$). The propagation speed varies between .20 and .40 and the number of stall cells increases when the flow rate is reduced.

Group III: progressive impeller rotating stall due to flow separation in the impeller. The propagation speed is very high and varies between .50 and .80. The amplitude of the velocity oscillations in the diffuser is moderate ($A \cong .10$). From the available experimental data, the number of stall cells seems to remain constant.

It is worth mentioning that in contrast to progressive or abrupt impeller rotating stall no harmonics have been observed during diffuser rotating stall. This criterion is of course rather weak but it may be an indication for the origin of the rotating stall if the available experimental information is not sufficient to determine the propagation speed and the number of stall cells.

References

1 Toyama, K., Runstadler, P. W., Dean, R. C., "An Experimental Study of Centrifugal Compressor Surge," ASME *Transactions*, Vol. 99, No. 1, Mar. 1977, pp. 115–131.

2 Dean, R. C., and Young, L. R., "The Time Domain of Centrifugal Compressor and Pump Stability and Surge," ASME *Transactions*, Vol. 99, No. 1, Mar. 1977, pp. 53–63.

3 Lenneman, E., and Howard, J. H. G., "Unsteady Flow Phenomena in Rotating Centrifugal Impeller Passages," ASME *Transactions*, Vol. 92, No. 2, Jan. 1970, pp. 65–72.

4 Kubo, T., and Murata, S., "Unsteady Flow Phenomena in Centrifugal Fans," *Bulletin JSME*, Vol. 19, No. 135, Sept. 1976, pp. 1039–1046.

5 Mizuki, S., Ariga, I., and Kawashima, Y., "Investigation Concerning Rotating Stall and Surge Phenomena Within Centrifugal Compressor Channels," ASME Paper No. 78-GT-9.

6 Jansen, W., "Rotating Stall in Radial Vaneless Diffusers," ASME *Transactions*, Vol. 86, No. 4, Dec. 1964, pp. 750–758.

7 Senoo, Y., and Kinoshita, Y., "Limits of Rotating Stall and Stall in Vaneless Diffusers of Centrifugal Compressors," ASME Paper No. 78-GT-19.

8 Abdelhamid, A. N., Colwill, W. H., and Barrows, J. F., "Experimental Investigation of Unsteady Phenomena in Vaneless Radial Diffusers," ASME *Transactions*, Vol. 101, No. 1, 1979, pp. 52–60.

9 Abdelhamid, A. N., and Bertrand, J., "Distinctions Between Two Types of Self-Excited Gas Oscillations in Vaneless Radial Diffusers," ASME Paper No. 79-GT-58.

10 Abdelhamid, A. N., "Effects of Vaneless Diffuser Geometry on Flow Instability in Centrifugal Compression Systems," ASME Paper No. 81-GT-10.

11 Van Den Braembussche, R., Frigne, P., and Roustan, M., "Rotating Nonuniform Flow in Radial Compressors," in *Centrifugal Compressors, Flow Phenomena and Performance*, AGARD CP 282, Paper 12, May 1980.

12 Aerodynamic Design of Axial Flow Compressors," NASA SP 36, 1965.

13 Dussourd, J. L., Pfannenbecker, G., and Singhania, S. K., "Considerations for the Control of Surge in Dynamic Compressors Using Close Coupled Resistances," ASME *Transactions*, Vol. 99, No. 1, Mar. 1977, pp. 64–75.

14 Jansen, W., "Steady Fluid Flow in Radial Vaneless Diffusers," ASME *Transactions*, Vol. 86, No. 3, Sept. 1964, pp. 607–619.

15 Senoo, Y., Kinoshita, Y., and Ishida, M., "Asymmetric Flow in Vaneless Diffusers of Centrifugal Blowers," ASME *Transactions*, Vol. 99, No. 1, Mar. 1977, pp. 104–114.

16 Senoo, Y., and Kinoshita, Y., "Influence of the Inlet Flow Conditions and Geometries of Centrifugal Vaneless Diffusers on Critical Flow Angle for Reverse Flow," ASME *Transactions*, Vol. 99, No. 3, Mar. 1977, pp. 98–103.

17 Abdelhamid, A. N., "Analysis of Rotating Stall in Vaneless Diffusers of Centrifugal Compressors," ASME Paper No. 80-GT-184.

18 Takata, H., and Nagano, S., "Nonlinear Analysis of Rotating Stall," ASME Paper No. 72-GT-3.

19 Frigne, P., "Theoretische en experimentele studie van de subsynchrone zelfgeexciteerde stromingsoscillaties in radiale turbocompressoren," Ph.D. thesis, Rijksuniversiteit Gent, June 1982.

20 Breugelmans, F. A. E., Mathioudakis, K., and Casalini, F., "Flow in Rotating Stall Cells of a Low-Speed Axial Flow Compressor," paper to be presented at the 6th ISABE Meeting Paris, June 1983.

Downloaded 01 Jun 2010 to 171.66.16.70. Redistribution subject to ASME license or copyright; see http://www.asme.org/terms/Terms_Use.cfm

J. Moore

J. G. Moore

Department of Mechanical Engineering,
Virginia Polytechnic Institute and
State University,
Blacksburg, Va. 24061

P. H. Timmis

Rolls-Royce Ltd., Aero Division,
Leavesden, Watford, England

Performance Evaluation of Centrifugal Compressor Impellers Using Three-Dimensional Viscous Flow Calculations

Calculations of three-dimensional viscous flow in the impeller of a centrifugal compressor are used as the basis of a study of the thermodynamics of the compression process. Flow in a high hub-tip ratio low specific speed impeller of approximately 3.4:1 pressure ratio is considered. Results are presented showing the work and loss production processes in the impeller. A strong influence of tip-leakage flow on the performance of this unshrouded wheel is found.

Introduction

There are, perhaps, three categories of flow calculation methods:

(*a*) those that give results which we don't believe,
(*b*) those that give results which we do believe, but we knew already, and
(*c*) those that give results we do believe *and* results which
  (*i*) we cannot obtain by measurement,
  (*ii*) we could not previously quantitatively predict, and
  (*iii*) we did not foresee.

In the development of three-dimensional viscous flow calculation methods for turbomachinery design, we have been attempting to reach category (*b*), in the hope of progressing to category (*c*).

We have been refining our method by comparison with high-quality data from well-documented experiments. In the case of Eckardt's centrifugal compressor, we reproduced [1, 2] those features of the flow and performance which can be measured, i.e.,

(*i*) the work done, the pressure ratios, and the efficiencies,
(*ii*) the shroud static pressure distribution,
(*iii*) the three-dimensional flow and wake formation, and
(*iv*) the wake mixing in the vaneless diffuser.

But the full potential of viscous flow methods for impellers involves the calculation and study of details of impeller performance which cannot presently be measured, for example:

(*a*) blade surface pressures,
(*b*) tip leakage flows,
(*c*) shear work at the shroud, and
(*d*) entropy production rates.

In the present paper, the potential of viscous flow calculations for revealing such details of impeller flow is explored. Use is made of a recently developed procedure [3, 4] for obtaining entropy production rates from the calculated flow field.

The impeller considered is a high hub-tip ratio low specific speed wheel which gives approximately 3.4:1 total pressure ratio at 32,000 rpm with an air mass flow rate of 1.0 kg/s. Results are presented showing the work and loss production processes in the impeller. The factors contributing to the work, including shear work at the shroud, are considered separately. Impeller efficiencies are calculated and discussed; these include the wheel efficiency which measures the performance of the impeller as a diffuser. Information about loss production is sought in entropy production rates. A strong influence of tip leakage flow on the performance of this unshrouded impeller is found.

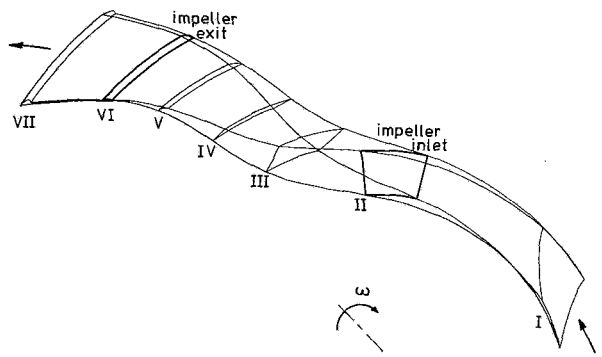


Fig. 1 Flow field for the impeller

Contributed by the Gas Turbine Division of THE AMERICAN SOCIETY OF MECHANICAL ENGINEERS and presented at the the 28th International Gas Turbine Conference and Exhibit, Phoenix, Arizona, March 27-31, 1983. Manuscript received at ASME Headquarters December 21, 1982. Paper No. 83-GT-62.

Copyright © 1984 by ASME
Downloaded 01 Jun 2010 to 171.66.16.70. Redistribution subject to ASME license or copyright; see http://www.asme.org/terms/Terms_Use.cfm

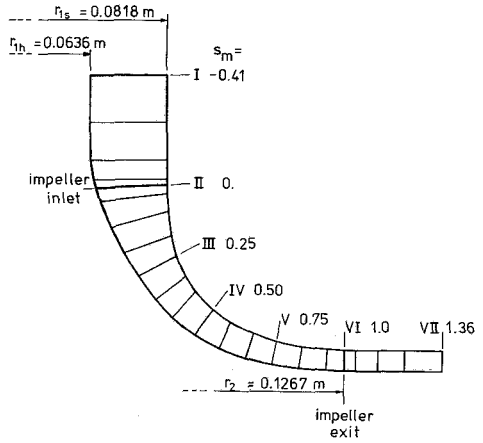


Fig. 2 Meridional view of calculation planes for impeller flow

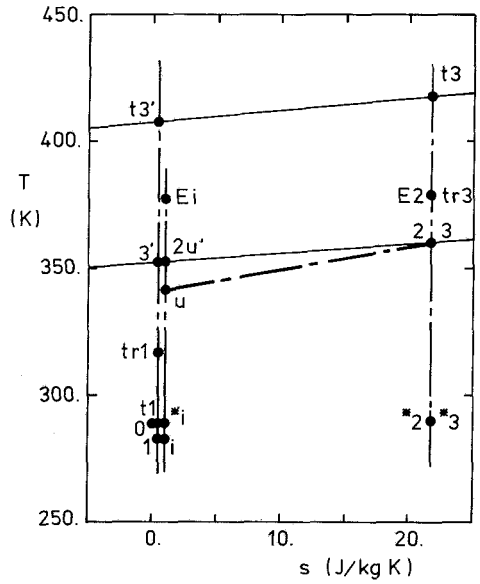


Fig. 3 Thermodynamic state points for the impeller at 31895 RPM and 1.01 kg/s. *T*, mass-averaged temperature; *s*, mass-averaged entropy; —— lines of constant pressure.

Flow Field Geometry

A schematic of the flow domain used for the calculations is shown in Fig. 1. Figure 2 gives a meridional section of the impeller and shows the parallel-walled inlet section and the constant-height vaneless diffuser. Steady flow calculations were performed in this rotating flow field between the quasi-orthogonal calculation planes shown in Fig. 2.

Figures 1 and 2 identify seven cross-sectional planes from I at the inlet to the flow field to VII at the end of the vaneless diffuser. The leading edge of the impeller is at plane II and the trailing edge at plane VI. A dimensionless meridional distance s_m along the impeller shroud is defined such that $s_m = 0$ at the leading edge and $s_m = 1.0$ at the trailing edge. Calculated flow results within the impeller will be presented at planes III, IV, and V for which $s_m = 0.25$, 0.50, and 0.75, respectively.

The overall impeller dimensions are shown in Fig. 2. The tip radius is 0.1267 m and the hub and shroud radii at the impeller inlet are 0.0636 m and 0.0818 m, respectively. The hub-to-shroud height at the impeller exit is 0.0053 m. For the calculations discussed here the impeller rotated at 31895 RPM and the air mass flow rate was 1.01 kg/s. The impeller has 19 blades.

The flow at the inlet plane (I) was in the axial direction with a uniform free stream and a turbulent boundary layer with thickness equal to 7 percent of the local hub-to-shroud height on both the hub and shroud walls. The total conditions in the free stream were 288.15 K and 101,325 N/m^2, and this state is used as the datum state for entropy.

The tip-clearance gap for the impeller was specified as a percentage of the local hub-to-shroud height. This varied linearly from 1.0 percent at the leading edge to 3.3 percent at $s_m = 0.40$ to 4.3 percent at the trailing edge.

Thermodynamic Performance

The overall performance calculated for the impeller at these conditions is described by the state points in Table 1 and Fig. 3, and by the efficiencies and work parameters in Table 2. Four cross-sectional planes are used for these results. Plane 1 is the inlet to the flow domain, 28.5 mm upstream of Plane *i* at the leading edge of the impeller blades. Plane 2 is at the impeller tip and Plane 3 is a plane used in the calculations just downstream of the impeller exit at $r_3/r_2 = 1.001$. The states shown are static states (1, *i*, 2, 3), total states (*t*1, *t*3), relative total states (*tr*1, *tr*3), and rotary stagnation states (*1 = *t*1, **i*, *2, *3). Also shown are state *u*, reached by isentropic cen-

Nomenclature

c_p = specific heat capacity at constant pressure
H^* = rothalpy
ΔH = change in stagnation enthalpy, $c_p (T_{t2} - T_{t1})$
ΔH^* = change in rothalpy, $c_p (T_2^* - T_1^*)$
$\dot{m}$ = mass flow rate
p = pressure
r = radius
s = entropy
s_m = dimensionless meridional distance along impeller shroud, Fig. 2
T = temperature
u_1, u_2, u_3 = calculated relative velocity components
U = ωr tangential velocity
V = absolute velocity
W = relative velocity
η = efficiency
ρ = density
ρu = convective mass flux
ω = angular velocity of the impeller
I–VII = calculation planes, Figs. 1 and 2

Subscript

θ = tangential
r = reduced

Plane Subscripts

1 = flow inlet
i = impeller inlet
2 = impeller exit
3 = downstream of impeller exit, $r_3/r_2 = 1.001$

State Subscripts

E = relative stagnation, Eq. 5 and 6
0 = reference stagnation, free stream at inlet
t = absolute stagnation
tr = relative stagnation
u = reached isentropically from i, Fig. 3 and Eq. 3

Efficiency Subscripts

p = polytropic
s-s = static-to-static
t-t = total-to-total
w = wheel

Superscripts

* = rotary stagnation
′ = reached isentropically, Fig. 3

Downloaded 01 Jun 2010 to 171.66.16.70. Redistribution subject to ASME license or copyright; see http://www.asme.org/terms/Terms_Use.cfm

Table 1 Thermodynamic state points for the impeller at 31895 rpm, 1.01 kg/s

State	p/p_0[a]	T(K)	s(J/kgK)
0	1.000	288.15	0
1	(0.9409)	283.3	0.51
*t*1,*1	(0.9983)	288.2	0.51
*tr*1	(1.398)	317.2	0.51
i	(0.9341)	282.89	1.05
**i*	(0.9964)	288.16	1.05
u	1.813	341.88	1.05
Ei	2.556	377.14	1.05
2	(2.026)	360.31	21.75
*E*2,*tr*2	(2.410)	378.65	21.75
*2	(0.9437)	289.66	21.75
2*u*′	(2.026)	352.91	1.05
3	(2.029)	360.5	21.81
*t*3	(3.379)	417.1	21.81
*tr*3	(2.414)	378.85	21.81
*3	(0.9436)	289.67	21.81
3′	(2.029)	352.86	0.51
*t*3′	(3.379)	408.31	0.51

[a]Note: the slight inconsistency of these values arises because the pressures were independently mass averaged.

Table 2 Efficiencies and work parameters for the impeller at 31895 rpm, 1.01 kg/s

$$\eta_{s-s13} = \frac{T_3' - T_1}{T_3 - T_1} = 0.901$$

$$\eta_{t-t13} = \frac{T_{t3}' - T_{t1}}{T_{t3} - T_{t1}} = 0.932$$

$$\eta_{wi2} = \frac{T_{2u}' - T_u}{T_2 - T_u} = 0.599$$

$$\eta_{p13} = \frac{1n(T_3'/T_1)}{1n(T_3/T_1)} = 0.911$$

$$\frac{\Delta H}{U^2} = \frac{c_p(T_{t2} - T_{t1})}{\omega^2 r_2^2} = 0.7234$$

$$\frac{\Delta H^*}{U^2} = \frac{c_p(T_2^* - T_1^*)}{\omega^2 r_2^2} = 0.0086$$

$$\frac{\Delta H - \Delta H^*}{U^2} = 0.7148$$

$$\frac{V_{\theta 2}}{\omega r_2} = 0.7159$$

trifugal pressure rise from state *i*, and the additional states *Ei* and *E*2 = *tr*2, used to describe the impeller performance as a diffuser. The remaining states (3′, *t*3′, 2*u*′) are used in calculating the isentropic impeller efficiencies defined in Table 2. The values given are mass-averaged properties at each plane, with a zero level for entropy defined at the reference state (0).

Impeller Efficiencies

The total-to-total, static-to-static, and polytropic efficiencies for the impeller between states 1 and 3 are calculated to be 93.2, 90.1, and 91.1 percent, respectively. These values seem reasonable for an impeller with a high hub/tip ratio at inlet and a low specific speed. As usual with centrifugal impellers they are high partly because they include the centrifugal pressure rise which in a sense is obtained isentropically.

Wheel Efficiency

The static temperature rise in the impeller is due to

1 Reduction of the relative kinetic energy

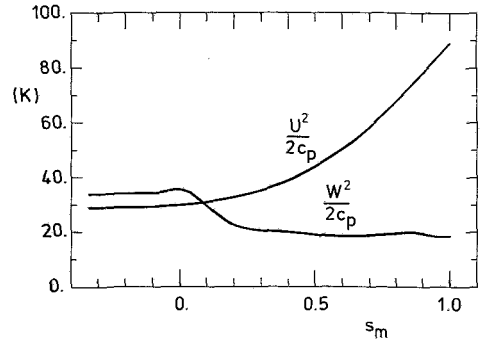


Fig. 4 Contributions of centrifugal effects and relative kinetic energy to temperature changes and work in the impeller

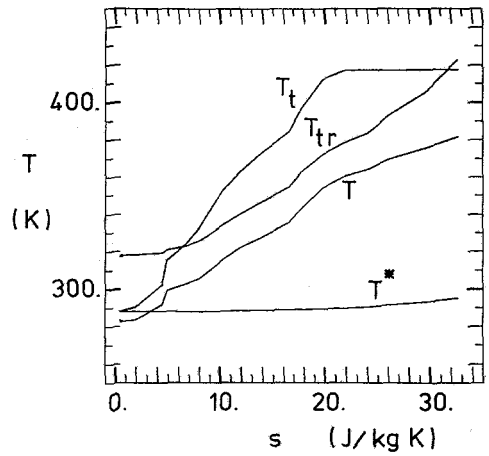


Fig. 5 *T-s* diagram for impeller compression process showing development of four mass-averaged temperatures.

2 Centrifugal effects

3 A rothalpy increase due to shear work at the shroud

This may be written

$$T_2 - T_i = \underbrace{\frac{W_i^2 - \bar{W}_2^2}{2c_p}}_{\substack{\text{relative kinetic energy change}}} + \underbrace{\frac{U_2^2 - U_i^2}{2c_p}}_{\substack{\text{centrifugal effects}}} + \underbrace{T_2^* - T_i^*}_{\substack{\text{rothalpy increase}}} \quad (1)$$

and in the present calculations

$$T_2 - T_i = (35.26 - 18.34) + (88.99 - 29.99) + (289.66 - 288.16)$$
$$= 16.92 + 59.00 + 1.50$$
$$= 77.42\,\text{K} \quad (2)$$

The largest contribution is clearly the temperature change of 59 K due to centrifugal effects and this accounts for 76.2 percent of the rise. The diffusion of the relative kinetic energy accounts for 21.9 percent of the rise, and the shear work at the shroud the other 1.9 percent.

The relative kinetic energy and the kinetic energy associated with the local wheel speed are also presented as mass-averaged properties in Fig. 4, where their development through the impeller may be followed. As expected, the centrifugal temperature rise increases in a roughly parabolic way. The relative kinetic energy on the other hand remains nearly constant after giving a temperature rise in the first 20 percent of the passage. A quick diffusion of velocity early in the passage is often associated with high performance in diffusers; larger adverse pressure gradients are imposed while the wall boundary layers are still relatively thin and able to

Downloaded 01 Jun 2010 to 171.66.16.70. Redistribution subject to ASME license or copyright; see http://www.asme.org/terms/Terms_Use.cfm

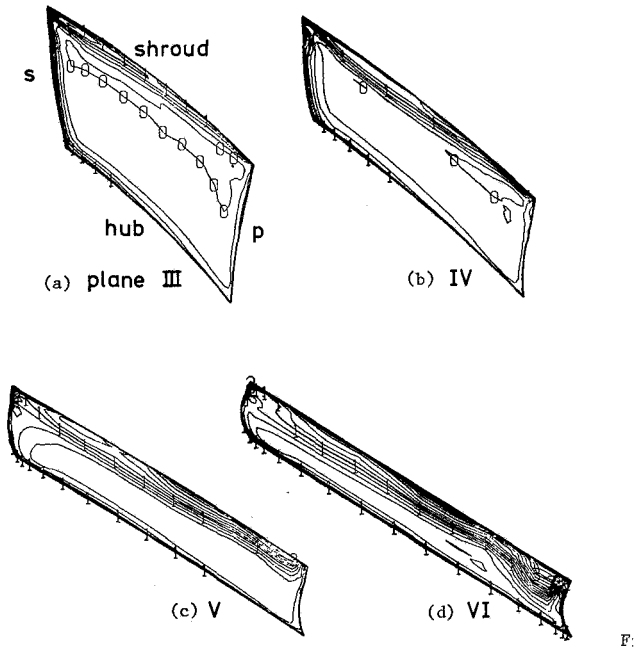


Fig. 6 Distributions of entropy on four calculation planes through the impeller. Contour interval = 10 J/kgK; contour label = entropy/40; s, suction side; p, pressure side.

withstand the pressure rise without stalling; this was the philosophy behind the design of this impeller passage.

The irreversibilities of the impeller flow process are due to friction and mixing and are associated with the relative kinetic energy and the shear work at the shroud, while the centrifugal effects may be considered to be a reversible contribution. Thus it is appropriate when considering the efficiency of the impeller to remove the centrifugal temperature rise from consideration by defining an intermediate state and a wheel efficiency η_w such that

$$T_u - T_i = \frac{U_2^2 - U_i^2}{2c_p} \tag{3}$$

and

$$\eta_w = \frac{T_{2u'} - T_u}{T_2 - T_u} \tag{4}$$

The process between the static states u and 2 then represents the performance of the impeller as a rotating curved diffuser with a stationary shroud wall. The relative kinetic energy of the flow at the inlet to the impeller is given by

$$T_{Ei} - T_u = T_{tri} - T_i = \frac{W_i^2}{2c_p} = 35.26\,\text{K} \tag{5}$$

and at the impeller exit it is given by

$$T_{E2} - T_2 = T_{tr2} - T_2 = \frac{W_2^2}{2c_p} = 18.34\,\text{K} \tag{6}$$

These are mass-averaged kinetic energies, and it is important to recognize that u is also defined in Equation (3) using mass-averaged values. The centrifugal temperature rise only occurs in the impeller so it must be evaluated between the impeller inlet plane i and the impeller exit plane 2. Furthermore it depends on the flow distribution at inlet and so mass-averaged properties are used. (It may be noted that this procedure for evaluating state u and the present calculations of wheel efficiency differ from those used by Vavra [5], who evaluated $U_i^2/2c_p$ using the inducer tip speed instead of mass-averaging the wheel speed.)

Equation (4) for wheel efficiency may be rewritten as

$$\eta_w = \frac{T_{2u'} - T_2}{\dfrac{W_i^2 - W_2^2}{2c_p} + T_2^* - T_i^*} \tag{7}$$

and in these calculations

$$\eta_w = \frac{11.03}{16.92 + 1.50} = 0.599 \tag{8}$$

This relatively low efficiency for the impeller acting as a diffuser may be explained in part due to the shear work at the shroud and friction on the walls, but mainly it is due to losses created directly and indirectly by tip-leakage flow from passage to passage. This is discussed in more detail below.

Rothalpy Changes and the Contribution of Shear Work to the Total Temperature Rise

The rise in absolute total temperature through the impeller involves a change in the absolute kinetic energy as well as the three contributions described above. Thus

$$T_{t2} - T_{t1} = \frac{W_1^2 - W_2^2}{2c_p} + \frac{U_2^2 - U_1^2}{2c_p} + T_2^* - T_1^* + \frac{V_2^2 - V_1^2}{2c_p} \tag{9}$$

and in the present calculations

$$\begin{aligned} T_{t2} - T_{t1} &= (33.90 - 18.34) + (88.99 - 29.07) + (289.66 - 288.15) \\ &\quad + (56.64 - 4.83) \\ &= 15.56 + 59.92 + 1.51 \\ &\quad + 51.81 \\ &= 128.80\,\text{K} \end{aligned} \tag{10}$$

The four contributions to the work input of the impeller may be seen in Fig. 5, which shows the development of four temperatures through the impeller. These are:

1 The static temperature, T
2 The absolute total temperature, T_t
3 The relative total temperature, T_{tr}
4 The rotary stagnation temperature, T^*

The relationships between these temperatures are

$$T_t = T + V^2/2c_p \tag{11}$$

$$T_{tr} = T + W^2/2c_p = T^* + U^2/2c_p \tag{12}$$

and

$$T^* = T + W^2/2c_p - U^2/2c_p = H^*/c_p \tag{13}$$

where H^* is the rothalpy. Thus, the changes in relative kinetic energy may be seen by following $T_{tr} - T$, the changes in the centrifugal effects by following $T_{tr} - T^*$, and the changes in absolute kinetic energy by following $T_t - T$. T^* increases due to shear work as shown, especially in the stationary vaneless diffuser downstream of the impeller where the calculation proceeds with the assumption of steady relative flow.

Table 2 gives the work input parameter $\Delta H/U^2 = 0.7234$. Also shown is a (new) shear work parameter $\Delta H^*/U^2 = 0.0086$. The difference between these two values represents the work input due to changes in moment of momentum (Euler work). The calculated value of 0.7148 is in close agreement with the normalized, mass-averaged, absolute tangential velocity $V_{\theta 2}/\omega r_2 = 0.7159$, with which it should be identical.

The shear work at the impeller shroud accounts for 1.17 percent of the total work input. It is, of course, of the same order as the work due to disk friction on the back face of the

Downloaded 01 Jun 2010 to 171.66.16.70. Redistribution subject to ASME license or copyright; see http://www.asme.org/terms/Terms_Use.cfm

impeller. Disk friction is ignored in the present calculations; this is equivalent to assuming that the energy due to disk friction is conducted away from the impeller casing as fast as it is produced. On the other hand, the casing could be taken to be insulated, in which case the work due to disk friction would also result in a total temperature rise of the flow.[1] In practice, some combination of these two extremes will probably occur and we can say that the error in our calculated total temperature rise due to our neglect of disk friction is probably less than 1 percent.

Eliminating the shear work contribution in equation (8) would give, with all other things remaining unchanged, $\eta_w = 11.03/16.92 = 0.652$ compared with the earlier value of $\eta_w = 0.599$. Certainly, with no shear work at the shroud wall, the impeller efficiency would be higher. But this is probably not a correct way of estimating the whole effect of the stationary shroud wall on the diffusion in the impeller. To gain more insight, we must study the tip leakage flow in detail.

[1] To incorporate this in the flow calculations would require an increase in the temperature in the impeller and a relaxation of the currently used boundary condition of adiabatic walls.

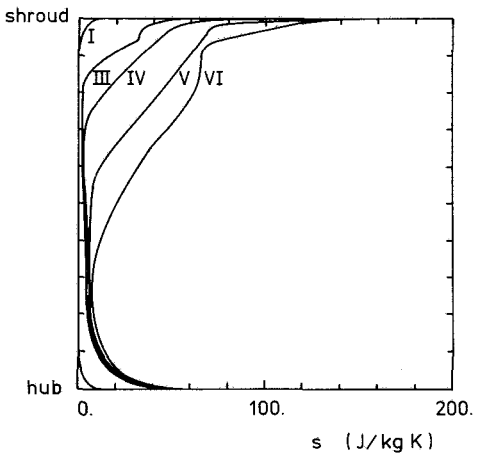


Fig. 7 Development of blade-to-blade, mass-averaged entropies

Entropy Distributions in the Impeller Passage

The mass-averaged entropy at the impeller exit is 21.8 J/kgK, but of course the flow contains regions with much higher and lower values than this mean. Figure 6 shows the distributions of entropy on four of the calculation planes through the compressor. In Fig. 6(*d*), we see the distribution at the impeller exit. All across the shroud wall and especially in the shroud/pressure-side corner region, the entropies are a factor of 3 to 8 times the mean value with some fluid locally even higher. This is a picture typical of the exit of a low specific speed impeller (see, for example, [6]) in which the passage height becomes much smaller than the tangential width and the tip clearance gap becomes a significant fraction, here 4.3 percent, of the blade height.

The development of this loss pattern may be followed in Fig. 6 and in Fig. 7, which shows the distribution of blade-to-blade mass-averaged entropies between the hub wall and the shroud. In the first 25 percent of the impeller passage, up to plane III, shown in Fig. 6(*a*), the blade-to-blade average indicates similar magnitudes of entropy production on the

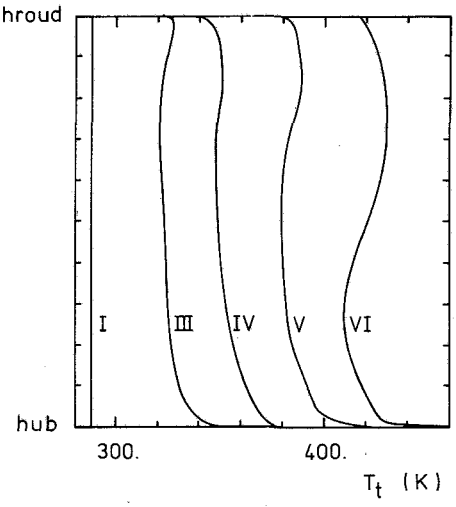


Fig. 8 Development of blade-to-blade, mass-averaged total temperatures

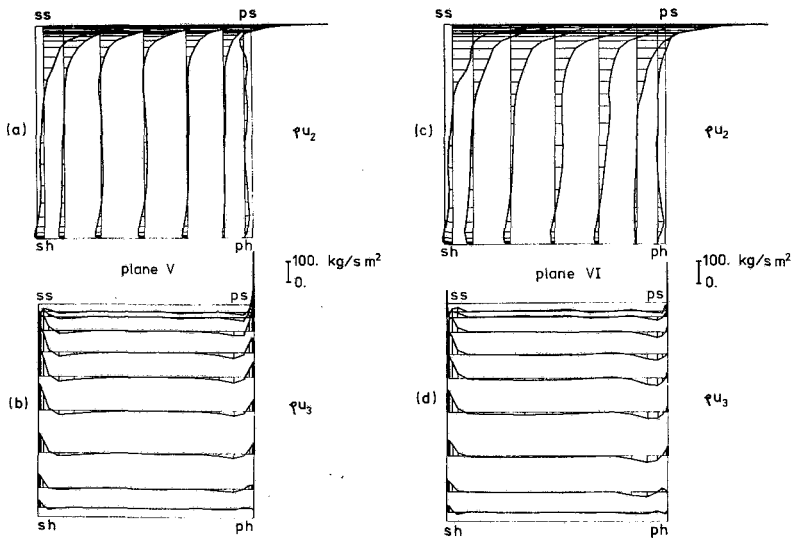


Fig. 9 Convective fluxes perpendicular to the bulk flow direction from blade-to-blade (ρu_2) and hub-to-shroud (ρu_3). ss, suction/shroud corner; sh, suction/hub corner; ps, pressure/shroud corner; ph, pressure/hub corner.

Downloaded 01 Jun 2010 to 171.66.16.70. Redistribution subject to ASME license or copyright; see http://www.asme.org/terms/Terms_Use.cfm

hub and shroud walls. Figure 6(*a*) shows a more rapid production of entropy in the suction side boundary layer than on the pressure side, and peaks of high entropy are found in the shroud/suction-side corner region where tip-leakage flow is mixing with the bulk throughflow.

Figure 8 shows blade-to-blade mass-averaged values of absolute total temperature which measure the work done on the fluid; we see that more work is done at the hub in the inducer section of the impeller. This trend to more losses at the shroud and more work at the hub is continued through the midsection of the impeller as shown in Figs. 7 and 8.

In Fig. 9, the convective fluxes, ρu_2 and ρu_3, perpendicular to the bulk flow direction from blade-to-blade and hub-to-shroud, are drawn on a square representation of the flow cross-section. A strong secondary flow (ρu_3) from the hub to the shroud near the suction side wall develops between planes IV and V, as shown in Fig. 9(*b*). This convects the high entropy fluid in the suction side boundary layer to the shroud wall where it is entrained and mixed with tip-leakage flow.

Towards the exit of the impeller, between planes V and VI, the large secondary velocities due to tip leakage dominate the flow near the shroud wall and the high entropy fluid moves towards the pressure side as seen in Fig. 6(*c*) and 6(*d*). A component of velocity from the shroud to the hub also develops near the pressure side as the impeller exit is approached, and this is shown in Fig. 9(*d*).

Blade Loading and Tip Leakage Flow

The blade loading which governs the work input to the fluid is shown in Fig. 10. The distribution is relatively uniform throughout the impeller and the loading at the hub is similar in magnitude to that at the shroud as expected for a low specific speed impeller. The pressure difference at the shroud drives fluid through the tip-clearance gap. In the present calculations the flow passed uniformly through the tip gap, giving the linear distribution of cumulative mass fraction shown in Fig. 11. By the exit of the impeller the flow through, the tip gap has reached 12 percent of the mass flow.

The tip-leakage fluid, driven by a pressure difference of the order of 0.2 p_0, will pass through the tip gap with a relative Mach number of the order of 0.6. The kinetic energy of this component of the velocity will likely be dissipated and produce entropy downstream of the tip gap.

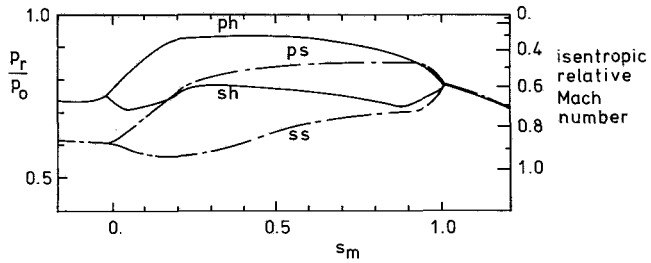


Fig. 10 Blade loading of the impeller. Reduced static pressure in or near the corners of the impeller passage. sh, suction side hub corner; ph, pressure side hub corner; ps, maximum along the shroud; ss, minimum along the shroud.

Blade Surface Pressure Distributions

The static pressure distribution throughout the impeller has been converted to a distribution of reduced static pressure following the procedure described in [2]. This in turn has been converted to a distribution of isentropic relative Mach number for an ideal flow with uniform rotary stagnation conditions, $p^* = p_0$ and $T^* = T_0$. These relative Mach numbers on the impeller surfaces are shown in Fig. 12.

In the inducer on the suction surface, Fig. 12(*a*) shows the Mach number locally as high as 0.9, with a large region higher than 0.8. Following the suction surface, the Mach number then falls slowly to 0.6 at the trailing edge. More rapid deceleration occurs in the inducer near the other three walls, as seen in Figs. 12(*b*), 12(*c*), and 12(*d*); this explains the calculated decrease in mass-averaged relative kinetic energy early in the impeller passage, observed in Fig. 4.

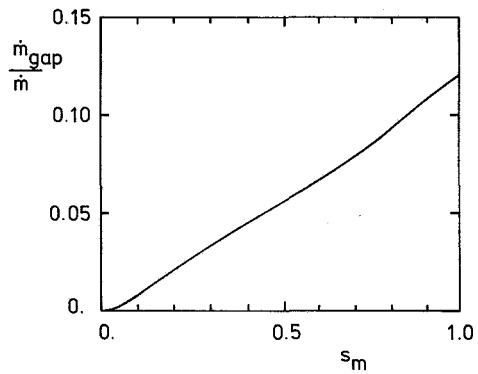


Fig. 11 The cumulative fraction of the mass flow that passed through the tip gap

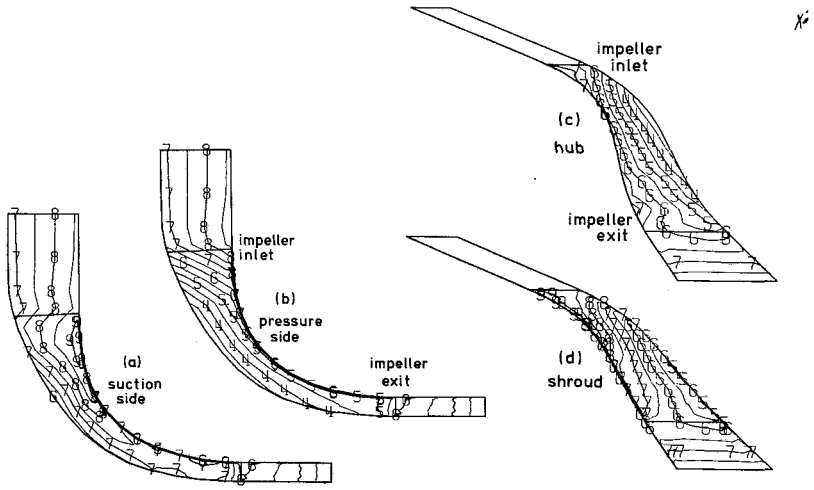


Fig. 12 The static pressure distribution expressed as isentropic relative Mach number contours. Scale: Mach number = 0.1 times the contour label

Downloaded 01 Jun 2010 to 171.66.16.70. Redistribution subject to ASME license or copyright; see http://www.asme.org/terms/Terms_Use.cfm

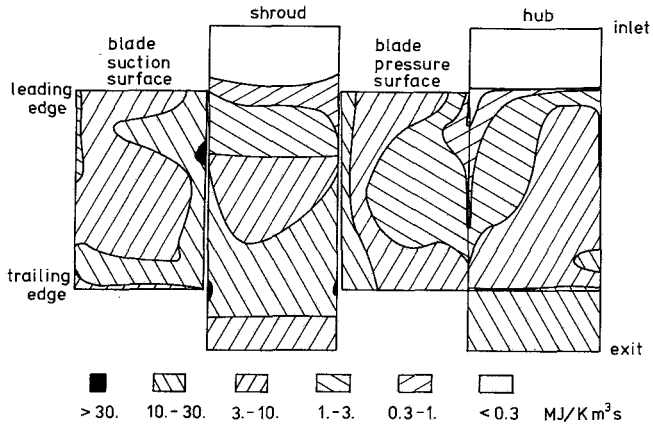


Fig. 13 Entropy production rates at the walls of the impeller passage

On the suction surface, the Mach number reduction from 0.9 to 0.6 is equivalent to a relative velocity ratio $W_2/W_{max} = 0.59$.

Distributions of Entropy Production

Entropy production rates were calculated throughout the flow field using the procedure described in [3] and [4]. These distributions give a complete picture of where losses are produced in the present flow calculations. As such they contain far more information about the inefficiency of an impeller than has been hitherto available.

Several trends appear in the calculated results. Entropy production rates rise near the walls due to the increased dissipation in the boundary layers as the walls are approached. The production rates increase in both the suction and pressure surface boundary layers towards the shroud wall, i.e., towards the tip clearance gap. A region of high entropy production rates occurs near the shroud/suction-side corner in a region where the relative kinetic energy of the tip-leakage flow is being dissipated.

Some idea of the particular areas of the passage walls where entropy production is highest may be obtained by plotting the values at the wall on a graph showing each surface developed. Such a plot is shown in Fig. 13. High losses occur near the suction surface in the inducer and towards the trailing edge. All along the pressure and suction surfaces near the shroud wall the losses are high. Shear work probably accounts for the high losses near the shroud wall as the impeller exit is approached and near the stationary hub wall in the vaneless diffuser.

The regions of highest loss adjacent to the walls occur near the shroud wall at the impeller exit and on the suction surface again near the shroud at the end of the inducer. The areas of lowest loss are found mostly on the hub and pressure surfaces and on the shroud in the inducer.

For reference, the mean rate of entropy production for the impeller is approximately 0.04 MJ/Km^{3}s. This may be compared with local values greater than 30. MJ/Km^{3}s in Fig. 13.

The region just downstream of the tip gap near the shroud/suction-side corner has local values of entropy production rate of approximately 40. MJ/Km^{3}s all along the impeller from $s_m = 0.08$ near the inlet to $s_m = 0.94$ near the exit. This rate is 1000 times the mean rate, and although it occurs over a very small volume, it may account for approximately one-quarter of the losses in the present calculations. With an impeller total-to-total efficiency of 93 percent, this region then gives about 2 percent of the inefficiency. If the mean tip gap/height ratio is also about 2 percent, then this calculation suggests very roughly a 1 percent degradation of efficiency for each 1 percent increase in mean tip gap. Values of this order can be found in the literature [7].

More work is needed to integrate the entropy production rates over specific volumes in the flow passage, and we are continuing this study.

Conclusions

Calculations of viscous flow in the impeller of a centrifugal compressor have been used as the basis of a study of the thermodynamics of the compression process. The study focussed on the potential of three-dimensional viscous flow methods to reveal details which cannot presently be measured. It attempted to demonstrate the future uses of such methods to the designer. For the operating point considered, the calculations showed:

(*a*) the relatively uniform blade loading of the impeller;

(*b*) blade surface pressure distributions with sustained high Mach numbers on the suction surface and more rapid deceleration on the other three walls;

(*c*) a decrease in mass-averaged relative kinetic energy in the first 20 percent of the impeller passage followed by nearly constant values;

(*d*) the contributions to the static temperature rise as 76.2 percent due to centrifugal effects, 21.9 percent due to the reduction in relative kinetic energy, and 1.9 percent due to shear work at the shroud wall;

(*e*) the efficiency of the impeller passage as a diffuser, i.e., the wheel efficiency, to be 59.9 percent;

(*f*) the shear work at the shroud to be 1.2 percent of the total work input;

(*g*) a uniform rate of tip-leakage flow with 12 percent of the mass flow passing through the tip gap by the impeller exit;

(*h*) the rapid production of entropy in the shroud/suction-side corner region where tip-leakage flow is mixing with the bulk throughflow;

(*i*) the distributions of entropy in the passage with high values near the shroud wall all across the passage at the impeller exit;

(*j*) high rates of entropy production in the suction surface boundary layer in the inducer, near the shroud wall as the impeller exit is approached, and near the stationary walls of the vaneless diffuser.

It appears that there is a real opportunity to quantitatively explain the inefficiency of centrifugal compressors using viscous flow methods. More work is needed to interpret the loss production rates inherent in the results of viscous flow calculations.

References

1 Moore, J., and Moore, J. G., "Lecture Notes on Viscous Flow Calculations in Turbomachinery," von Karman Institute for Fluid Dynamics Lecture Series on Numerical Methods for Flows in Turbomachinery Bladings, Apr. 26-30, 1982.

2 Moore, J., and Moore, J. G., "Three-Dimensional, Viscous Flow Calculations for Assessing the Thermodynamic Performance of Centrifugal Compressors—Study of the Eckardt Compressor," AGARD Conference Proceedings No. 282 of the AGARD Meeting on Centrifugal Compressors, Flow Phenomena and Performance, Brussels, May 1980.

3 Moore, J., and Moore, J. G., "Entropy Production Rates from Viscous Flow Calculations: Part I—A Turbulent Boundary Layer Flow," 83-GT-70, submitted for presentation at the 1983 ASME Gas Turbine Conference, Phoenix, Ariz.

4 Moore, J., and Moore, J. G., "Entropy Production Rates from Viscous Flow Calculations: Part II—Flow in a Rectangular Elbow," 83-GT-71, submitted for presentation at the 1983 ASME Gas Turbine Conference, Phoenix, Ariz.

5 Vavra, M. H., "Basic Elements for Advanced Design of Radial-Flow Compressors," AGARD Lecture Series No. 89 on "Advanced Compressors," 1970.

6 Hamrick, J. T., Mizisin, J., and Michel, D. J., "Study of Three-Dimensional Flow Distribution Based on Measurements in a 48-Inch Radial-Inlet Centrifugal Impeller," NACA TN 3101, 1954.

7 Balje, O. E., *Turbomachines. A Guide to Design, Selection and Theory*, John Wiley, New York, 1981.

Downloaded 01 Jun 2010 to 171.66.16.70. Redistribution subject to ASME license or copyright; see http://www.asme.org/terms/Terms_Use.cfm

A CAD Method for Centrifugal Compressor Impellers

H. Krain
Research Engineer, DFVLR,
Institut fur Antriebstechnik,
Cologne, West Germany

A computer-aided design method (CAD) has been developed for radially ending and backswept centrifugal compressor impellers. The geometrical concept introduced for generating the impeller geometry takes care of numerical, manufacturing, as well as aerodynamic aspects. The fluid dynamic calculation method applied is based on a quasi-three-dimensional approach coupled with a boundary layer calculation method. Detailed quantitative comparisons between theoretical data and laser measurements taken within a radially ending impeller revealed predominantly good agreement. Backswept impellers of different size and shape have been designed by the approach presented.

Introduction

Surge and efficiency of centrifugal compressors are known to be significantly influenced by the impeller discharge flow characteristics. Generally, a highly distorted, unsteady jet/wake pattern is expected within the impeller exit/diffuser inlet area, which additionally complicates a reliable prediction of throat blockage and channel diffuser recovery [1, 2, 3]. Extensive laser measurements carried out at DFVLR, Cologne, revealed strong effects of the separated impeller discharge flow on the vaned diffuser inlet conditions [1]. Unsteady flow angle fluctuations up to 17 deg superimposed by a considerable flow angle difference between hub and shroud have been analyzed within the vaned diffuser inlet area. Furthermore, noticeable impeller reactions occured even far downstream of the diffuser throat where usually steady-state conditions are presumed [4]. In this area unsteady flow angle fluctuations up to 10 deg were still present, proving that a channel diffuser design based on a steady-state approach is doubtful, as far as the diffuser is coupled with a heavily separated impeller [3, 5, 17]. Therefore, a steady impeller discharge flow is desirable not only in regard to flow range and efficiency improvements but also with respect to a reliable and simplified diffuser design.

Aiming at this goal, today's advanced aerodynamic calculation methods should become quick and reliable impeller design tools capable of generating smooth impeller discharge flows. But, due to the three-dimensional flow effects, such theories are difficult to apply in the centrifugal compressor aerodynamics. Nevertheless, significant improvements have been obtained during the last years [6, 7, 8, 9]. Presently, even three-dimensional viscous theories are treated, and reasonable results have been presented [10, 11]. However, since an impelller design optimization generally is an iterative process, storage and central processor unit time are important quantities even in view of high-speed digital computers. Additionally, a simple input data preparation as well as an easily understandable output preparation are necessary for such a design approach. Last but not least, the design procedure should withstand a quantitative check with reliable measurements taken within centrifugal compressor impellers running under realistic operating conditions. An impeller design method meeting the requirements indicated has been developed at DFVLR.

Design Approach

A block diagram illustrating the design procedure is shown in Fig. 1. The overall design package has a modular structure, thus ensuring a time efficient operation. Initially, the impeller geometry is generated and the geometrical quantities necessary for the fluid dynamic calculation are prepared. Based on Wu's streamsheet approach [12] the fluid dynamic quantities are calculated on hub-to-shroud and blade-to-blade stream surfaces introduced to simplify the three-dimensional flow problem. In addition, a boundary layer calculation is involved providing information on the tolerable deceleration of the relative flow [13]. The results obtained may be analyzed

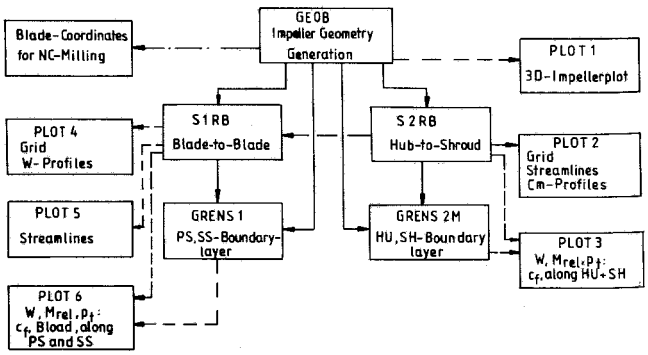


Fig. 1 Block diagram of the impeller design procedure

Contributed by the Gas Turbine Division of THE AMERICAN SOCIETY OF MECHANICAL ENGINEERS and presented at the 28th International Gas Turbine Conference and Exhibit, Phoenix, Arizona, March 27–31, 1983. Manuscript received at ASME Headquarters December 21, 1981. Paper No. 83-GT-65.

Copyright © 1984 by ASME
Downloaded 01 Jun 2010 to 171.66.16.70. Redistribution subject to ASME license or copyright; see http://www.asme.org/terms/Terms_Use.cfm

on a graphic terminal by means of the six plot-modules available. Figure 1 displays a coupling between the hub-to-shroud and blade-to-blade solution. The blade-to-blade calculation can be carried out independently for different radial positions. The input data for these calculations are prepared by the geometrical program (GEOB) as well as by the hub-to-shroud solution (S2RB). Thus the results obtained by the blade-to-blade calculations are directly dependent on the hub-to-shroud solution; reactions of the blade-to-blade solutions on the hub-to-shroud solution are neglected. Similarly, a direct interaction between the boundary layer calculation and the flow field solutions have not yet been taken into account, because this would only be an appropriate approach if an unseparated flow could be ensured during the whole iterative design process. Thus the results of the boundary layer calculations are primarily taken as a criterion for flow stability. Additionally, the local displacement thickness is taken from these results to account for the aerodynamic blockage during the final design. The input for the plot-modules (PLOT2 ÷ PLOT6) is taken from the flow field and boundary layer calculations. The grids used for the flow field calculations as well as the velocity, Mach number, and total pressure distributions are plotted. These quantities are results of the flow field calculations. Additionally, the skin friction coefficient, c_f, which is a result of the boundary layer calculation, is plotted versus flow path length.

Regarding a quick and reliable input data handling, the meridional contours as well as the blade geometry are described by analytical functions, thus avoiding a time consuming point by point generation [14]. This approach reduces the necessary input data set for the overall design procedure to only 16 geometrical parameters (see Table 1) that are used for a successive variation of the complex impeller geometry.

The influence of the various parameters listed in Table 1 on the impeller geometry is illustrated in Fig. 2. Figure 3 shows three different types of impellers generated and analyzed by the design procedure described. Obviously, the input data set is easy to handle and nevertheless capable of creating a variety of impeller types which is most advantageous to the iterative design process. The blade geometry generated meets the requirements of today's numerically controlled five axis milling machines. The blade surfaces are always provided in such a way that flank milling is appropriate. Additionally, the use of analytical functions for generating the blade geometry ensures continuous partial derivatives up to the second order, which are required for the succeeding aerodynamic calculation method.

Figure 2 additionally illustrates the location of the splitter blade leading edge, which can be shifted in the axial direction, thus ensuring a sufficient blade loading control ahead of the splitter blade. Presently, the geometrical concept applied

Table 1 Geometrical input data set

Parameter	Description
r_2	impeller tip radius
r_{1i}	leading edge hub radius
r_{1t}	leading edge shroud radius
b_{2s}	exit width
l	impeller length
Δr_2	hub contour parameter
γ_N	hub exit parameter $\gamma_N = 0 \rightarrow$ radial, $\gamma_N \neq 0 \rightarrow$ diagonal
α	shroud contour parameter
γ_G	shroud exit parameter, $\gamma_G = 0 \rightarrow$ radial, $\gamma_G \neq 0 \rightarrow$ diagonal
β_{1t}	leading edge blade angle
β_{1sa}	angle for influencing backsweep
β_{2a}	blade exit angle
h	blade curvature parameter
Z_R	blade number
Z_{split}	splitter blade location
l_{indu}	inducer length

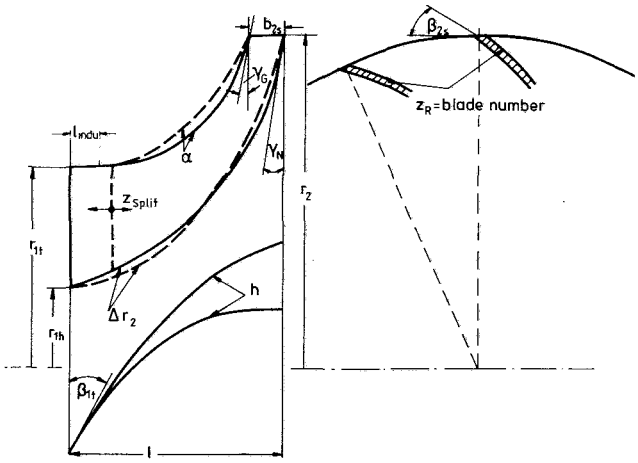


Fig. 2 Influence of the geometrical parameters on the impeller geometry

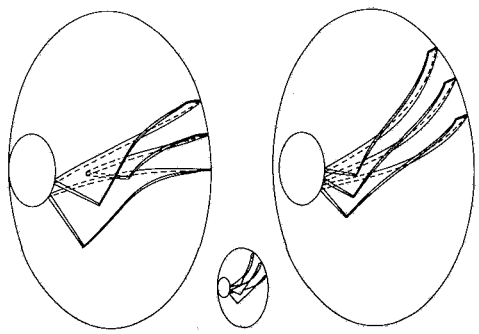


Fig. 3 Examples for impeller types generated and analyzed by the design procedure

Nomenclature

B = streamsheet thickness (hub-to-shroud)
b = streamsheet thickness (blade-to-blade)
c_f = skin friction coefficient
c_{mL} = component of meridional velocity perpendicular to laser beam axis
h_t = total enthalpy
k = ratio of specific heats
M = Mach number
$\dot{m}$ = mass flow rate
N_s = specific speed
$\mathbf{n}$ = normal unit vector of streamsurface
PS = pressure side
p = pressure
R = gas constant
r = radial coordinate
SS = suction side
s = entropy
T = temperature
u = circumferential velocity
$\mathbf{w}$ = relative velocity vector
x/s_m = dimensionless meridional shroud length
y/t = dimensionless blade pitch
z = axial coordinate
z/b = dimensionless meridional channel depth
Θ = circumferential coordinate
π_t = total pressure ratio
ψ = streamfunction
ω = angular velocity

Subscripts

0 = ambient condition
1 = impeller inlet
2 = impeller exit
m = meridional
rel = relative
t = total

Downloaded 01 Jun 2010 to 171.66.16.70. Redistribution subject to ASME license or copyright; see http://www.asme.org/terms/Terms_Use.cfm

assumes that the splitter geometry is the same as the main blade geometry and that the splitter is located midpitch between the main blades. Furthermore, the blade leading edges are assumed to coincide with lines of constant, z. However, if required, these assumptions may be changed.

Basic Aerodynamic Equations

The following basic flow equations are to be solved for the quasi-three-dimensional approach

Continuity:

$$\nabla \cdot (\rho \cdot \mathbf{w}) = 0 \tag{1}$$

Motion:

$$-\mathbf{w} x (\nabla x \mathbf{w}) + 2\omega x \mathbf{w} = -\nabla h_{t,\mathrm{rel}} + T\nabla s \tag{2}$$

Energy (no preswirl):

$$\nabla h_{t,\mathrm{rel}} = 0 \tag{3}$$

State of gas:

$$\rho/\rho_0 = (T/T_0)^{1/(k-1)} \cdot e^{-(s-s_0)/R} \tag{4}$$

Geometric conditions:

$$\mathbf{n} \cdot \mathbf{w} = 0 \tag{5}$$

If a streamfunction, ψ, is introduced into equations (1-5), two governing nonlinear partial differential equations of the second order are obtained describing the flow development on blade-to-blade and hub-to-shroud streamsurfaces:

Blade-to-Blade Calculation

$$A(z,\Theta)\frac{\partial^2\psi}{\partial z^2} + B(z,\Theta)\frac{\partial^2\psi}{\partial z \partial \Theta} + C(z,\Theta)\frac{\partial^2\psi}{\partial \Theta^2} + D(z,\Theta,\rho,b)\frac{\partial\psi}{\partial z} + E(z,\Theta,\rho,b)\frac{\partial\psi}{\partial\Theta} + F(z,\Theta,\rho,b,\omega,s,\partial\psi/\partial\Theta) = 0 \tag{6}$$

Hub-to-Shroud-Calculation

$$A(r,z)\frac{\partial^2\psi}{\partial r^2} + B(r,z)\frac{\partial^2\psi}{\partial r \partial z} + C(r,z)\frac{\partial^2\psi}{\partial z^2} + D(r,z,\rho,B)\frac{\partial\psi}{\partial r} + E(r,z,\rho,B)\frac{\partial\psi}{\partial z} + F(r,z,\rho,B,\omega,s,\partial\psi/\partial r) = 0 \tag{7}$$

Condition for Elliptic Equation

$$\delta = A \cdot C = (B/2)^2 > 0 \tag{8}$$

As indicated by equation (3), the aerodynamic calculation presently is limited to flows without inlet swirl although the incorporation of this effect principally is possible [15]. The condition for elliptic partial differential equations (8) is satisfied by both the blade-to-blade and hub-to-shroud equations which basically restricts the aerodynamic calculation to subsonic flows. This is a severe restriction with respect to high pressure ratio centrifugal impellers ($\pi_{t12} > 6$) which are operating with supersonic inlet conditions. For such impellers the calculation method presented momentary is only applicable if a normal shock is assumed at the tip of the impeller leading edge. With this assumption, the design procedure has been applied for a backswept impeller of pressure ratio $\pi_{t12} = 11$. Reasonable results were obtained; a comparison with measured flow field data, however, couldn't be carried out, since such data are not yet available.

A comprehensive derivative of equations (1-8) and detailed information about the numerical solution procedure are given in [9, 15]. The coefficients A – F in equations (6) and (7) are

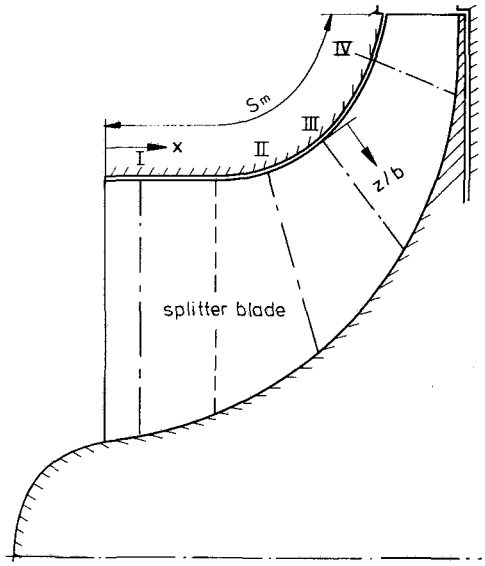


Fig. 4 Arrangement of optical measurement planes within the impeller

Table 2 Positions of laser measurement planes within the impeller [1]

Measurement plane	Location x/s_m
I	0.08
II	0.43
III	0.59
IV	0.87

functions of the impeller geometry indicated by the cylindrical coordinates, r, z and Θ. A fast and exact determination of these quantities is necessary for a satisfactory numerical solution process. However, the numerical reduction is very complex since these coefficients are complicated functions of the first and second streamsurface derivatives [15]. Therefore, it is most advantageous to describe the stream surface by a continuous mathematical function. This procedure considerably simplifies a fast and exact determination of the coefficients A – F. Primarily the hub-to-shroud surface, which for advanced centrifugal impellers usually is twisted and completely three dimensional, should be created in this way. The analytic surface generated by the 16 geometrical input parameters meets these requirements. Thus the goemetrical concept introduced simultaneously takes care of numerical, manufacturing and aerodynamic aspects. Nevertheless it should be noted that the design procedure described is restricted to impeller types compatible with the geometrical background concept. But, if required, a prescribed advanced impeller geometry can be approximated by the geometrical input parameters listed in Table 1. Such an approximation had to be carried out when the design procedure was checked with measured data.

Comparisons of Theoretical and Experimental Results

The design procedure was primarily proved with laser measurements taken within a radial discharge impeller running at 300 m/s tip speed that has 28 blades in total and 14 splitter blades. Details of the impeller geometry and of the experimental flow field analysis within this type of impeller are presented in [1]. Figure 4 illustrates the arrangement of the optical measurement planes from the inducer inlet to the impeller exit. All measurement planes are perpendicular to the shroud contour, and their correct position is submitted in Table 2.

Downloaded 01 Jun 2010 to 171.66.16.70. Redistribution subject to ASME license or copyright; see http://www.asme.org/terms/Terms_Use.cfm

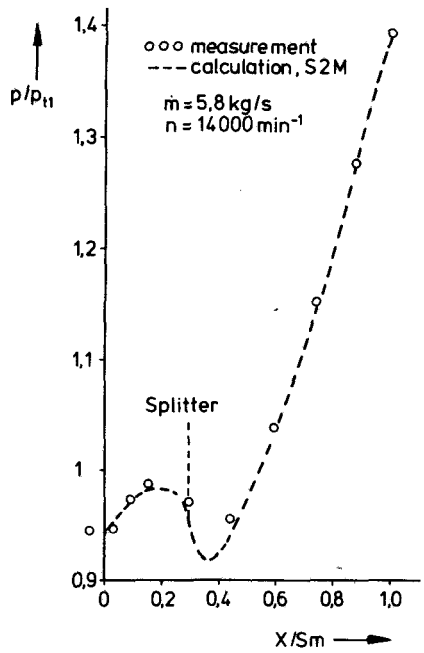


Fig. 5 Comparison of measured and calculated shroud statics: n = 14,000 min^{-1}, $\dot{m}$ = 5.8 kg/s

At first, Fig. 5 shows a comparison between calculated and measured static pressures taken along the shroud contour. Obviously an excellent agreement is obtained primarily in that area where the flow is turned to the radial direction ($x/s_m > 0.4$). This is predominantly due to the centrifugal forces which isentropically generate about 75 percent of the static pressure rise within an ordinary centrifugal impeller ($w_2/w_1 \cong 0.7$). Consequently, the comparison of calculated and measured shroud statics usually will result in a fairly good agreement which nevertheless gives only little information about the quality of the relative flow prediction. More evidence, however, is obtained by a detailed quantitative comparison with laser measurements taken within the rotating system since this approach excludes the dominating influence of the centrifugal forces. In addition, such a comparison is not only limited to the shroud region but can also be carried out within the entire flow channel.

Figure 6 shows such a comparison for measurement plane I (Fig. 4). The calculated and measured meridional velocities, referred to the rotor tip speed, are plotted against the dimensionless blade pitch for five different meridional positions (z/b = 0.1, 0.3, 0.5, 0.7, 0.9). Measurements have been carried out by means of an advanced, automated laser velocimeter [16]. The theoretical results are interpolated data taken from ten blade-to-blade solutions which were connected with the hub-to-shroud solution (Fig. 1). A pronounced boundary layer shape doesn't occur because detailed wall friction effects are neglected in this part of the aerodynamic calculation method (equations (2) and (6)).

Effects of the blade-to-blade solutions on the hub-to-shroud solution have been neglected. In spite of that, the measured data throughout properly fit the theoretical results obtained. This is mainly due to the blade-congruous flow observed in this area [1] which doesn't claim for an additional interaction between both types of stream surfaces, if the initial hub-to-shroud surface is chosen blade-congruent. Towards the impeller exit, of course, this surface deviates from the blade geometry thus taking care of slip effects.

Figure 7 shows a comparison between measurement and calculation for plane II (Fig. 4). Since plane II is located aft of the splitter blade leading edge, measurements as well as

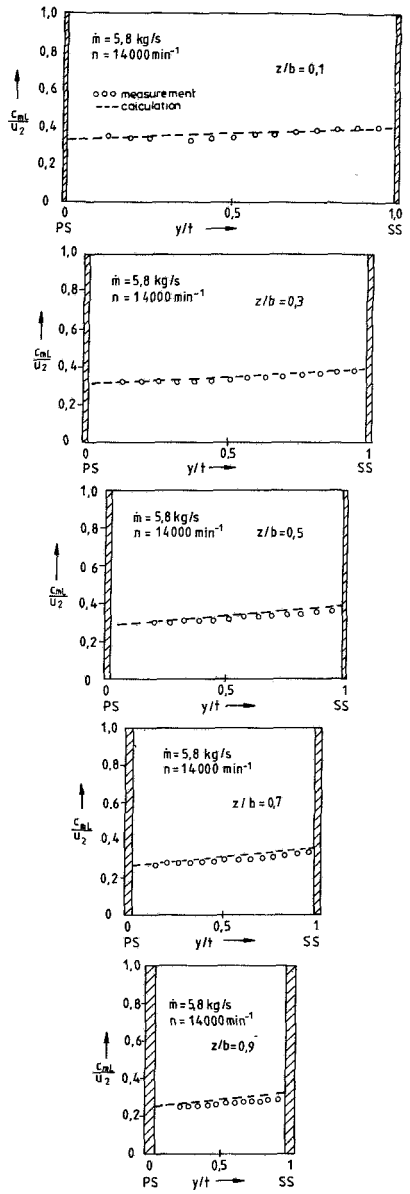


Fig. 6 Comparison of theoretical data with laser measurements at measurement plane I: n = 14,000 min^{-1}, $\dot{m}$ = 5.8 kg/s

calculations have been carried out within adjacent channels. The two channels shown are divided by the splitter blade. Again the measured data are confirmed by the theoretical results. A good agreement is obtained for all meridional positions (z/b = 0.1–0.9) and within both channels.

Figure 8 shows a similar comparison for plane III. Noticeable deviations between measured and calculated data are only observed within the shroud area of the right flow channel (z/b = 0.1), whereas in the remaining part measurements are properly fitted by the theoretical data. But even in the shroud area of the right channel, where the flow obviously tends towards a premature separation, the blade-to-blade solution reveals the correct results at the middle of the flow channel.

Measured and calculated meridional velocities of plane IV are compared to each other in Fig. 9. Significant deviations are observed in the shroud area (z/b = 0.1–0.3) within both channels where the actual flow now reveals a pronounced wake character. This deviation was to be expected since the

Downloaded 01 Jun 2010 to 171.66.16.70. Redistribution subject to ASME license or copyright; see http://www.asme.org/terms/Terms_Use.cfm

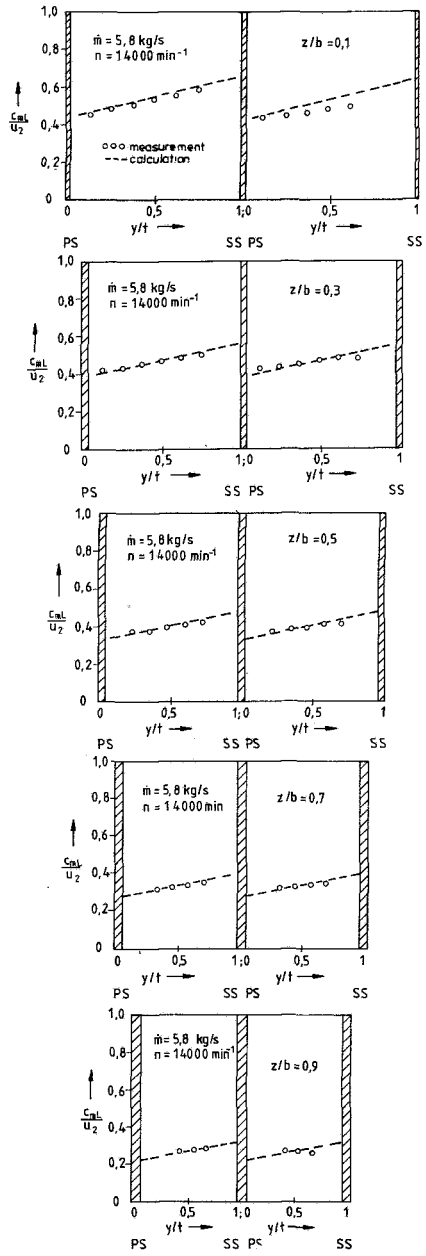


Fig. 7 Comparison of theoretical data with laser measurements at measurement plane II: $n = 14{,}000\ \text{min}^{-1}$, $\dot{m} = 5.8$ kg/s

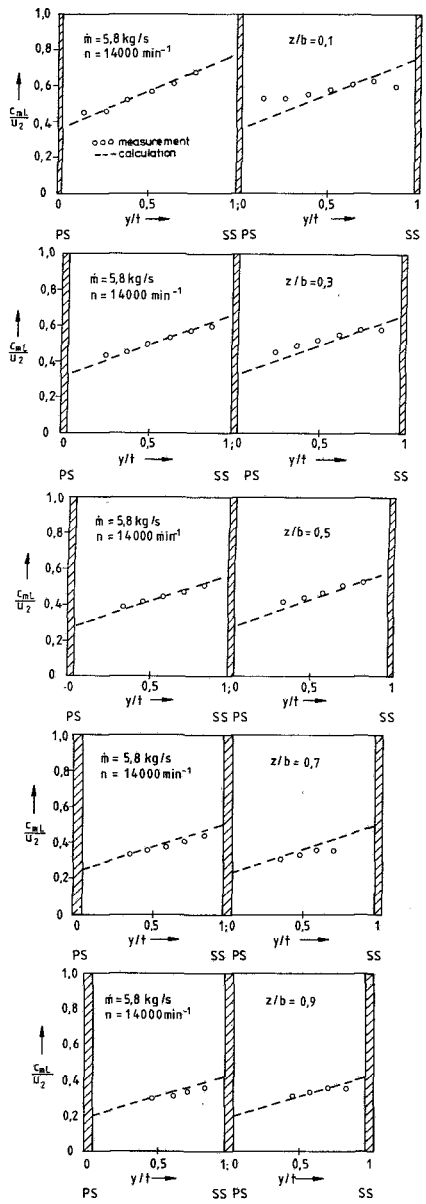


Fig. 8 Comparison of theoretical data with laser measurements at measurement plane III: $n = 14{,}000\ \text{min}^{-1}$, $\dot{m} = 5.8$ kg/s

theoretical model applied doesn't take care of detailed skin friction effects (equation (2)). Only a global entropy rise derived by assuming a constant polytropic impeller efficiency is taken into account. But even close to the impeller exit this simplified assumption is appropriate to achieve a fairly good agreement between measured and calculated data, at least in the hub region ($z/b = 0.7$–0.9). At midchannel ($z/b = 0.5$) measured data are slightly higher than the calculated which is certainly due to the wake area's displacement effect that has not been taken into account in the calculation.

Thus, the quasi-three-dimensional approach expectantly fails to predict the correct wake shape, whereas otherwise it results in a good agreement with measured data within the predominantly unseparated area. Above all, the designer of centrifugal impellers is interested in unseparated impellers, and therefore the correct prediction of a wake area's shape will not necessarily attract his utmost attention. Rather a simple but reliable information whether separation has to be expected or not is important. In this context, the boundary layer calculation method involved (Fig. 1) is believed to be a useful design tool. Figure 10 shows the result of a boundary layer calculation carried out along the shroud. The calculated local skin friction coefficient, c_f, is plotted against the dimensionless meridional length. Separation is to be expected if c_f tends toward zero. According to the results obtained separation occurs at $x/s_m \cong 0.78$ which qualitatively corresponds with the measurements. For this analysis the mean relative velocities along the shroud contour obtained by the hub-to-shroud solution have been taken as input data for the boundary layer calculations.

Design Procedure's Application

The comparison between calculated and measured data of a radially ending impeller resulted in a predominantly good agreement. In order to prove the procedure's capability for the design of advanced backswept rotors, similar comparisons

Downloaded 01 Jun 2010 to 171.66.16.70. Redistribution subject to ASME license or copyright; see http://www.asme.org/terms/Terms_Use.cfm

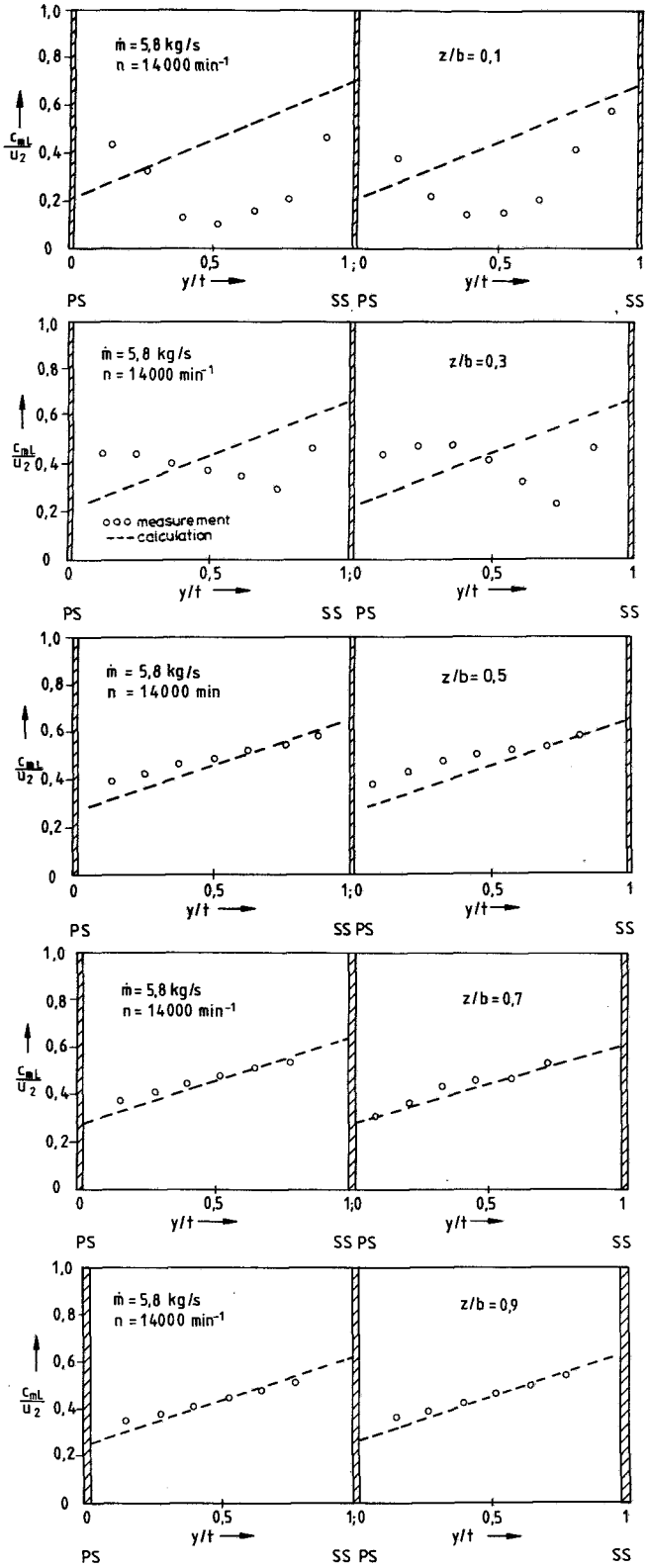


Fig. 9 Comparison of theoretical data with laser measurements at measurement plane IV: n = 14,000 min^{-1}, $\dot{m}$ = 5.8 kg/s

between theory and measurements are planned for this type of machine. The design package has been used for the design of two different types of backward leaning rotors adapted to the conditions of the DFVLR test rigs. A low specific-speed, 30-deg backswept impeller (N_s = 80) and a high specific-speed, 30-deg backswept small turbocharger impeller (N_s = 115,

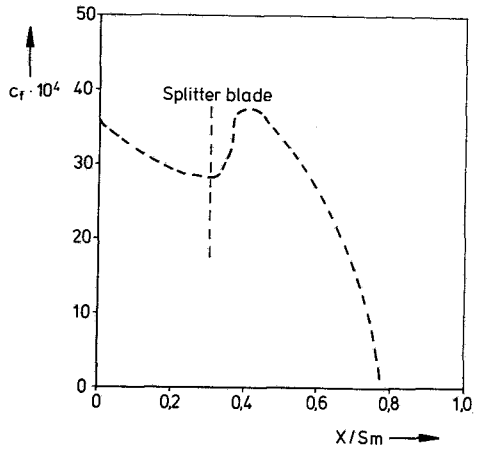


Fig. 10 Development of the local skinfriction coefficient along the shroud contour: n = 14,000 min^{-1}, $\dot{m}$ = 5.8 kg/s

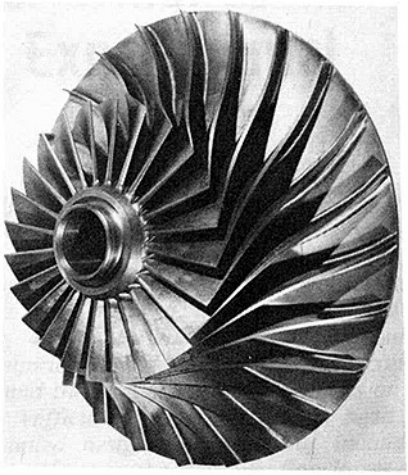


Fig. 11 Newly designed low specific speed 30-deg backswept impeller

Fig. 3) have been designed. Figure 11 shows a photograph of the low specific-speed rotor. The flow field within both types of impellers will be experimentally analyzed within the near future, thus giving additional evidence on the design procedure's reliability and applicability.

Conclusions

A computer-aided design method for centrifugal impellers has been developed with particular respect to a quick and easy input/output handling. Based on a geometrical concept, describing the impeller geometry by analytical functions a coherent design procedure is obtained that simultaneously takes care of numerical, manufacturing and aerodynamic aspects. Detailed comparisons between calculated data and laser measurements taken within a radially ending impeller resulted in a predominantly good agreement. A boundary layer calculation method involved indicated the onset of the separation and wake area. Thus the design procedure developed obviously is a useful design tool with regard to a reliable relative flow field prediction and may be used to reduce the wake area's size.

References

1 Krain, H., "A Study on Centrifugal Impeller and Diffuser Flow," ASME JOURNAL OF ENGINEERING FOR POWER, Vol. 103, No. 4, Oct. 1981, pp. 688-697.

2 Johnson, M. W., and Moore, J., "Secondary Flow Mixing Losses in a Centrifugal Impeller," ASME Paper No. 82-GT-44.

3 Runstadler, P. W., Jr., Dolan, F. X., and Dean, R. C. Jr., *Diffuser Data Book*, Creare, TN-186, 1975, p. 88.

4 Krain, H., "Experimental and Theoretical Investigation on the Fluid

Downloaded 01 Jun 2010 to 171.66.16.70. Redistribution subject to ASME license or copyright; see http://www.asme.org/terms/Terms_Use.cfm

Dynamics of a Centrifugal Compressor Stage," *Proceedings of the CASI Centrifugal Compressor Symposium*, Toronto, May 1982, p. 33.

5 Waitman, B. A., Reneau, L. R., and Kline, S. J., "Effects of Inlet Conditions on Performance of Two-Dimensional Subsonic Diffusers," ASME *Journal of Basic Engineering*, Sept. 1961, pp. 349–360.

6 Hirsch, Ch., and Warzee, G., "A Finite Element Method for Through-Flow Calculations in Turbomachines," ASME Paper No. 76-FE-12.

7 Howard, J. H. G., and Osborne, C., "A Centrifugal Compressor Flow Analysis Employing a Jet-Wake Passage Flow Model," ASME *Journal of Fluids Engineering*, 1977, pp. 141–147.

8 Bosman, C., and El-Shaarawi, M. A. I., "Quasi-Three-Dimensional Numerical Solution of Flow in Turbomachines," ASME *Journal of Fluids Engineering*, Vol. 99, 1977, pp. 132–140.

9 Krain, H., and Eckard, D., "The Flow Field in a High-Speed Centrifugal Impeller: A Comparison of Experimental and Theoretical Results," *Proceedings of the First International Conference on Centrifugal Compressor Technology*, Madras, Feb. 1978, B1-25.

10 Moore, J., and Moore, J. G., "Calculations of Three-Dimensional, Viscous Flow and Wake Development in a Centrifugal Impeller," in *Performance Prediction of Centrifugal Pumps and Compressors*, 1980, pp. 61–67.

11 Walitt, L., "Numerical Analysis of the Three Dimensional Viscous Flow Field in a Centrifugal Impeller," AGARD-CP-282, 1980, p. 28.

12 Wu, C. H., " A General Theory of Three-Dimensional Flow in Subsonic and Supersonic Turbomachines of Axial, Radial and Mixed-Flow Types," NACA TN-2604, 1952, p. 92.

13 Bradshaw, P., and Unsworth, K., "An Improved Fortran Program for the Bradshaw-Ferriss-Atwell Method of Calculating Turbulent Shear Layers," I. C. Aero Report 74-02, Feb. 1974, p. 51.

14 Casey, M. V., "A Computational Geometry for the Blades and Internal Flow Channels of Centrifugal Compressors," ASME Paper No. 82-GT-155, p. 10.

15 Krain, H. "Contribution to the Quasi-Three-Dimensional Calculation Within Centrifugal Compressor Impellers," (in German), Doctoral thesis, Technische Hochschule Aachen, Dec. 1975, p. 185.

16 Schodl, R., "A Laser-Two-Focus (L2F) Velocimeter for Automatic Flow Vector Measurements in the Rotating Components of Turbomachines," ASME Paper No. 1980, In *Measurement Methods in Rotating Components of Turbomachinery*, pp. 139–147.

17 Rodgers, C., "The Performance of Centrifugal Compressor Channel Diffusers," ASME Paper No. 82-GT-10, p. 13.

Downloaded 01 Jun 2010 to 171.66.16.70. Redistribution subject to ASME license or copyright; see http://www.asme.org/terms/Terms_Use.cfm

On the Evaluation of Reynolds Number and Relative Surface Roughness Effects on Centrifugal Compressor Performance Based on Systematic Experimental Investigations

H. Simon
Head of Aero-Thermodynamics Research and Development.

A. Bülskämper
Research and Development Engineer.

Mannesmann Demag, Compressors and Pneumatic Equipment, Duisburg, Germany

This paper summarizes the results of systematic investigations into the Reynolds number effects. It is based on performance map measurements carried out on a compressor test rig which was constructed primarily for this purpose. The measurements were performed for stages with different flow coefficients ($0.004 \leqq \phi_l \leqq 0.05$), with different gases (air, nitrogen, helium, freon) and in the inlet pressure range 0.2 bar $\leqq p_l \leqq$ 40 bar. By analogy with the turbulent flow in technically rough pipes, semi-empirical correlations are derived concerning the effects of the Reynolds number and the relative surface roughness on the characteristic performance parameters (efficiency, flow coefficient, head coefficient, work coefficient). For the detailed design calculation of individual stages, provision is made for the different effects on the hydraulic flow losses and the disk friction losses. Simplified correlations are given for the conversion of characteristics measured during thermodynamic performance tests. The correlations are applied to various single and multistage compressors, and the results compared with measured performance characteristics in the Reynolds number range $6 \times 10^3 \leqq Re_l \leqq 1.1 \times 10^7$. The good correspondence obtained forms the basis for recommending the application of these simplified relationships for the improvement of centrifugal compressor performance test codes (e.g. ASME PTC-10 and ISO TC 118).

Introduction

The growth of fields of application for centrifugal compressors, particularly in chemical and petrochemical processes, requires reliable advance calculation of compressor performance, taking into account extreme operating conditions, e.g., very low volume flow rates and very high pressures. In general, it is only possible to transfer model results to various applications if dynamic flow similarity is maintained in the compressor, i.e., if the decisive similarity parameters (including the Reynolds number) are the same. Exact knowledge of the effects of the Reynolds number on the performance characteristics of centrifugal compressor stages is therefore an essential requirement for the correct and dependable design of a centrifugal compressor.

Considering the time and cost involved, it is not always possible, or even meaningful, to realize the specified Reynolds number during the performance test in the manufacturer's shop. The more reliable the conversion of the measured performance parameters, the greater can be the permissible deviations (Re_t/Re_{sp}). Although a large number of valuable contributions have been published on this subject (see bibliography), there is as yet no one commonly accepted procedure (accepted by compressor manufacturers and users) for converting measured compressor performance maps from test to guarantee conditions.

The method proposed in the ASME Power Test Code (PTC 10) [1] does not make proper allowance for the variations in hydraulic conditions encountered in different applications (relative impeller tip width, flow coefficient, Reynolds number, relative surface roughness). No differentiation is made in its correction formula between Re-dependent and Re-independent flow losses. Following this formula the change in flow losses with changing Reynolds number is independent of the level of the Reynolds number. As a result, the correction

Contributed by the Gas Turbine Division of THE AMERICAN SOCIETY OF MECHANICAL ENGINEERS and presented at the 28th International Gas Turbine Conference and Exhibit, Phoenix, Arizona, March 27-31, 1983. Manuscript received at ASME Headquarters, December 27, 1982. Paper No. 83-GT-118.

Copyright © 1984 by ASME
Downloaded 01 Jun 2010 to 171.66.16.70. Redistribution subject to ASME license or copyright; see http://www.asme.org/terms/Terms_Use.cfm

of efficiencies especially for high Reynolds numbers is unrealistically high, whereas it can be too low with small Reynolds numbers (Figs. 12, 13, 15, 16, 19). In addition, the shape of the efficiency versus Reynolds number curve depends on the Reynolds number (Re_t) at which measurements were taken.

Based on theoretical considerations, the loss gradient should decrease continuously as the Reynolds number increases, with the efficiency approaching a limit value asymptotically. This is confirmed by the results of carefully conducted experimental investigations (Figs. 9, 10).

Wiesner [2] and Osterwalder [3] give a good general survey of the various approaches [4–16] used for efficiency conversion.

The following type of equation is applied in almost all papers

$$\frac{1-\eta}{1-\eta_{\mathrm{Ref}}} = a + (1-a)\left[\frac{\mathrm{Re}_{\mathrm{Ref}}}{\mathrm{Re}}\right]^n \qquad (1)$$

The various authors give values between $0 \leqq a \leqq 0.57$ for the proportion "a" of Re-independent losses, and values between $0.1 \leqq n \leqq 0.5$ for the exponent n.

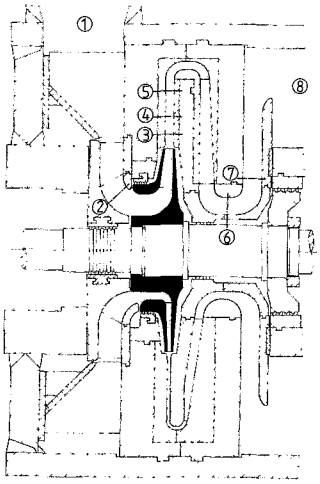
As a result of these different values, widely varying efficiency corrections are obtained, particularly in the case of low flow coefficient stages with hydraulically unfavorable flow passages in which the influence of the relative surface roughness is also very large. Generally, a comparison with experimental results is only meaningful and possible if the conditions prevailing during measurement, including the relative surface roughness of the flow channels are well known. That this is not the case in the majority of the published measurements is one of the reasons for the large variations in the results of the different correction formulas.

Because of these considerable uncertainties in the evaluation of the effects of the Reynolds number and the relative roughness on flow losses in the compressor stage, a test rig was built especially for the purposes of these investigations. On this rig, extensive measurements of performance maps have been carried out, in the course of which the main parameters were varied systematically. A method was developed of making correct provision in compressor design calculation for the effects of the Reynolds number and of the relative roughness. Deduced from this, a relatively simple procedure was worked out for converting measured compressor performance characteristics, taking into account the Reynolds number effects.

Experimental Investigations

Test Bed. For the systematical investigations into Reynolds number effects, a single-stage test compressor was built which was connected to a closed loop. The closed loop permits operation of the stages at different pressure levels ($0.2 \leqq p_1 \leqq 40$ bar) and with different gases (air, nitrogen, helium, freon).

The investigated stages consisted of the following flow-conducting components (Figs. 1, 2): inlet casing, impeller, diffuser (vaneless or vaned), return channel, and outlet collector.



Pos.	No.	Meas. value
①	4	pressure, temperature (suction conditions)
②	4	pressure, temperature, flow direction
③	1	dynamic pressure
④	2	pressure, temperature, flow direction (movable)
⑤	2	pressure, temperature, flow direction (movable)
	8	static pressure
⑥	2	pressure, flow direction
⑦	12	static pressure
⑧	4	pressure, temperature (discharge conditions)

Fig. 1 Cross section of the test arrangement

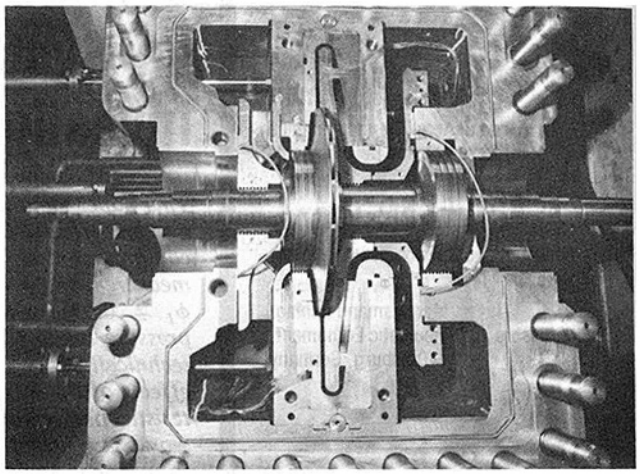


Fig. 2 Test compressor

Nomenclature

a = Re-independent part of losses
b = width
c = velocity
c_M = torque coefficient
d = diameter
Δh = work
Δh_L = hydraulic losses
Δh_s = isentropic head
k_s = equivalent sand roughness
$\dot{m}$ = mass flow rate
n = exponent
P = gas power
P_{DF} = disk friction losses
p = pressure
Ra = mean surface roughness
Re = Reynolds number $u_2\, b_2/\nu_1$
Re_{DF} = disk friction Re-number $u_2\, 0.005\, d_2/\nu_1$
u_2 = impeller tip speed
$\dot{V}$ = volume flow rate
β = blade angle, with circumferential direction
η = efficiency
η_{DF} = disk friction efficiency
η_h = hydraulic efficiency
η_{Leak} = leakage efficiency
η = dynamic viscosity
λ = friction factor
μ = work coefficient
ν = kinematic viscosity
ρ = density
ϕ = volume flow coefficient $\dot{V}/(u_2\, d_2^2)$
ψ = head coefficient

Subscripts

h = hydraulic
Leak = leakage
m = meridional direction
max = maximum
p = polytropic
Ref = reference condition
s = isentropic
sp = specified condition
t = test condition
u = circumferential direction
1 = impeller inlet condition
2 = impeller/stage discharge condition
∞ = value for Re $\rightarrow \infty$

Downloaded 01 Jun 2010 to 171.66.16.70. Redistribution subject to ASME license or copyright; see http://www.asme.org/terms/Terms_Use.cfm

The top half of Fig. 1 shows a stage with a medium flow coefficient, whereas the bottom half depicts a stage with an extremely low flow coefficient. Extensive pressure and temperature measurements at inlet and discharge of the compressor and between the individual components enable the flow losses of the entire stage to be allocated to the individual components. The entire data acquisition (Fig. 3) is computer controlled. Results are evaluated even as the tests are being conducted. Five impellers have been intensively investigated on this test rig, partly with different diffuser and return channel configurations. The stages and their diffuser configurations were selected to allow variation of the main parameters of conventional centrifugal compressor stages (flow coefficient, impeller blade angle). The main parameters of these stages are shown in Table 1.

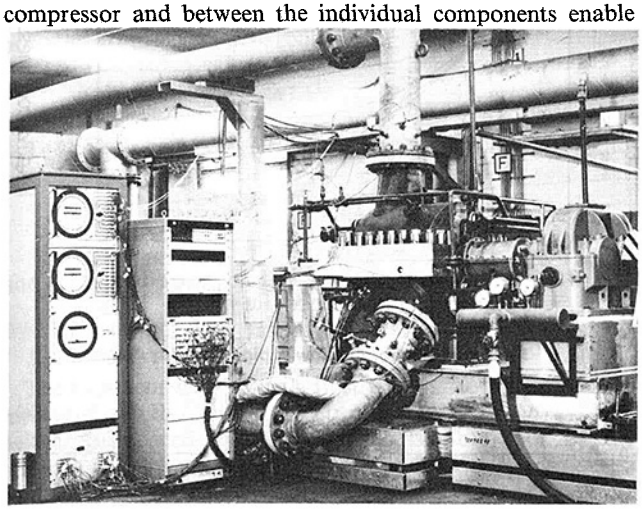


Fig. 3 Test bed and data acquisition system

Test Readings. Figures 4 and 5 show for two selected examples (Stages 1 and 4) a number of results in the form of referred stage performance characteristics. The reference values are the head and flow coefficient and the efficiency, measured with nitrogen at an inlet pressure of $p_1 = 1$ bar.

The Reynolds number was varied primarily by altering the inlet pressure. In the 1 bar $\leqq p_1 \leqq$ 40 bar range, nitrogen was used, whereas air was used in the subatmospheric range 0.2 bar $\leqq p_1 < 1$ bar. Measurements using freon 12 and helium provided additional informations about the influence of Reynolds number. In this case, however, the different compressibility effects must be considered. Using freon 12, the same Mach number as with nitrogen was present, whereas with helium, the same tip speed was present. This is clearly

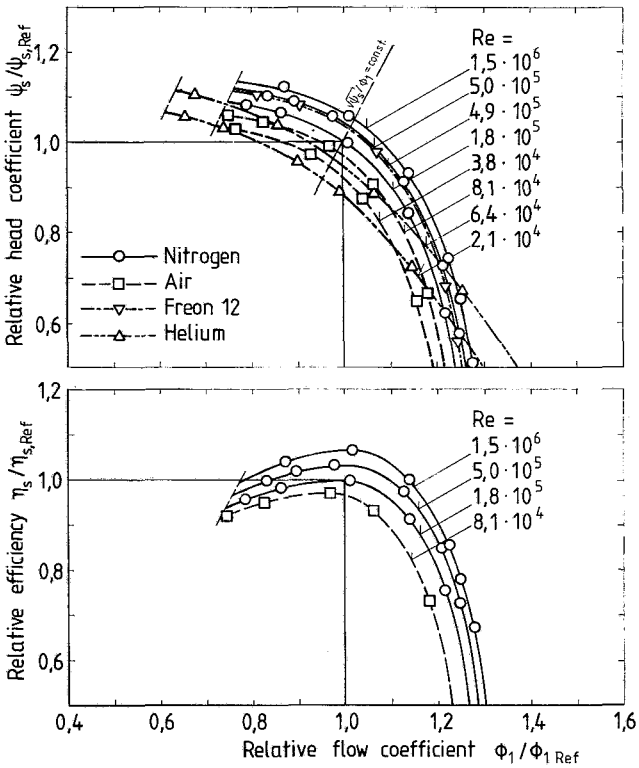


Fig. 4 Measured performance characteristics of stage 1 (ϕ_{1Ref} = 0.031)

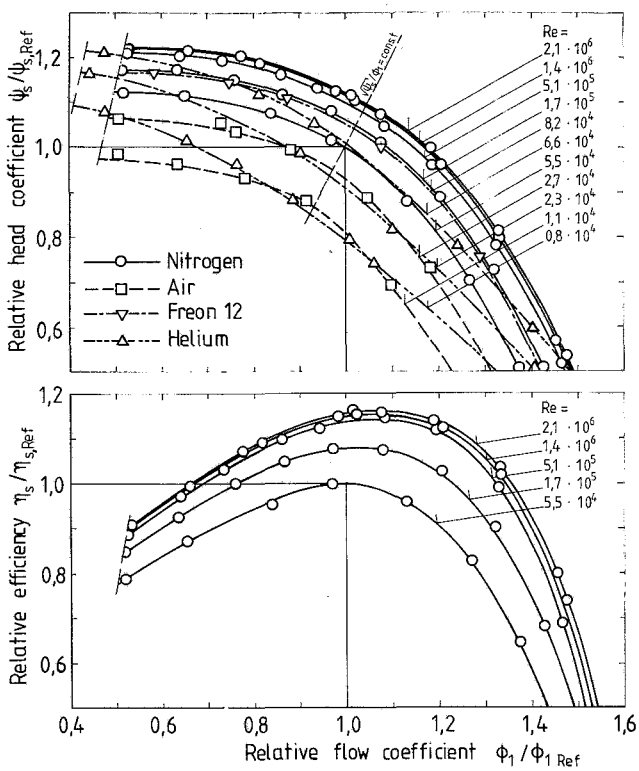


Fig. 5 Measured performance characteristics of stage 4 (ϕ_{1Ref} = 0.007)

Table 1 Data of tested stages

Stage	1	2	3	4	5
ϕ_{1Ref}	0.031	0.014	0.007	0.007	0.004
d_2(m)	0.35	0.35	0.35	0.35	0.35
b_2(m)	0.0098	0.006	0.0033	0.004	0.0025
β_2(°)	50	50	50	35	35
d_{hub}/d_2	0.4	0.4	0.4	0.4	0.4
Diff.-type	VLD	VLD	VLD	VLD + VD	VLD
Gas	N_2,Air, He,F12	N_2,Air, He,F12	N_2,Air, He,F12	N_2,Air, He,F12	N_2,Air, He
Range of Re	$40\,10^3$ – $1.5\,10^6$	$8\,10^3$ – $2\,10^6$	$6\,10^3$ – $1.7\,10^6$	$8\,10^3$ – $2.1\,10^6$	$7\,10^3$ – $1.3\,10^6$

Downloaded 01 Jun 2010 to 171.66.16.70. Redistribution subject to ASME license or copyright; see http://www.asme.org/terms/Terms_Use.cfm

reflected in the shape of the corresponding performance characteristics.

The results show a very marked effect of the Reynolds number on efficiency, head coefficient, and position of the performance characteristic related to the optimum efficiency (flow coefficient correction). A comparison of the two figures shows that the effect of the Reynolds number increases as the flow coefficient of the stage decreases. These results positively confirm the fact that very precise allowance must be made for changes of this nature already in the calculation of compressor performance, and particularly so in the case of multistage compressors.

The determination of the stage efficiencies was based on temperature measurements (traversing probes), performed both in the nozzles, immediately ahead of the impeller, and in the diffuser. Although the machine was effectively heat-insulated, even these temperature measurements were insufficient to reliably determine efficiencies in the case of very small mass flows. It was for this reason that no efficiencies were represented in the extreme subatmospheric range and when measuring with helium. Contrastingly, very reliable measurements of head performance characteristics were made thanks to optimum selection of the ranges of the pressure transducers. The latter exhibited maximum measuring errors of around ± 0.06 percent. A variety of values (temperature, static pressure, total pressure, direction of flow) is available for all depicted measuring points, which means that analyses can be carried out for all flow-conducting compressor components. In conjunction with suitable loss models and by means of a meaningful subdivision into Re-independent and Re-dependent losses, this permits almost universally valid evaluation of the effect of the Reynolds number on compressor performance characteristics.

Flow Loss Conversion Model

The aim of this investigation is not to develop models for the precise advance calculation of flow losses occurring in individual flow-conducting components or in complete compressor stages. Its main subject is rather to calculate changes in flow losses as a function of the Reynolds number and of relative roughness. It is thereby assumed that the flow losses for a given reference condition are known. The complexity of the flow conditions, which can also differ widely depending on the application of the centrifugal compressor stage (e.g. large and small flow coefficients) excludes a purely theoretical solution. This is obvious when one considers that we are dealing with the loss behavior of a three-dimensional, quasi-stationary, locally separated flow in part-stationary, part-rotating flow passages with irregular cross-section patterns.

It is undoubtedly meaningful to divide total losses into Re-independent (a) and Re-dependent ($1-a$) losses. This approach has already been used by many authors. It is important that the effects of the relative roughness on flow losses should also be considered.

Very detailed investigations on the influence of the Reynolds number and the relative roughness on flow losses have been conducted for flows in hydraulically smooth and hydraulically rough pipes. These results lend themselves, as proposed for example by Woehrl [16], to use in the conversion of Re-dependent flow losses in compressor stages. A comparison with measured results then permits adaptation of the loss model by means of corresponding calibration of meaningfully selected coefficients. Before this can be done, precise knowledge of the surface roughness of the compressor stages under measurement must be available.

The diagram for the pipe friction factor λ, published by Nikuradse [17], was obtained from pressure loss

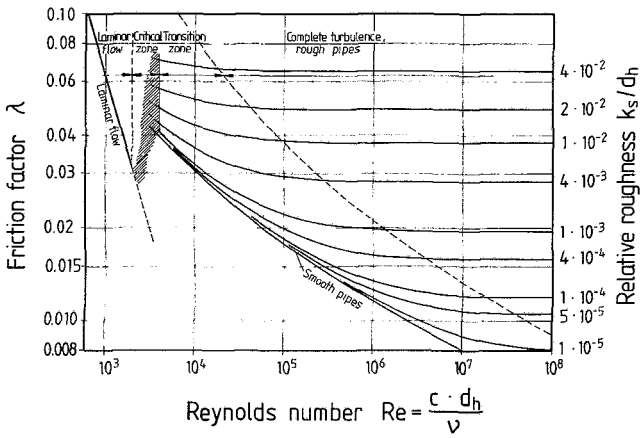


Fig. 6 Friction factor for the flow in pipes (Moody diagram)

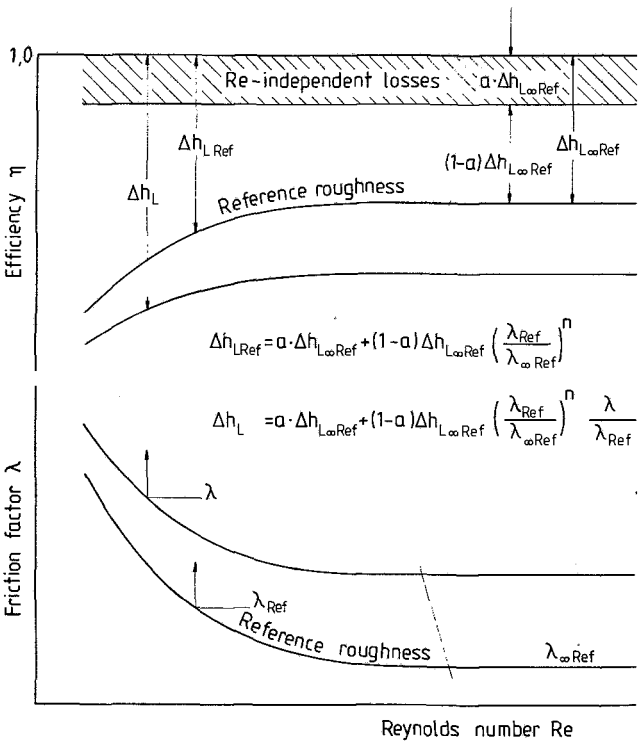


Fig. 7 Model for the conversion of hydraulic losses by analogy with flow in rough pipes

measurements made in pipes whose surfaces had been roughened by grains of sand. Colebrook and White [18] have investigated pipes with technical roughness and arrived at a deviation in the pipe friction factor in the transition area between hydraulically smooth and hydraulically completely rough surfaces. Moody [19] has summarized their results diagramatically (Fig. 6). Instead of the sand roughness defined by Nikuradse, an equivalent sand roughness k_s is introduced here. For technical roughness, the mean surface roughness value Ra according to DIN 4768 [20] is taken; this may also be replaced by the frequently used RMS value. The authors [21, 22, 23] give differing values for the relationship between technical roughness and equivalent sand roughness. To simplify matters,

$$k_s = 2\,\mathrm{Ra} \tag{2}$$

shall be used.

The change of the flow losses associated with the Reynolds number and the relative roughness will, by analogy with the

Downloaded 01 Jun 2010 to 171.66.16.70. Redistribution subject to ASME license or copyright; see http://www.asme.org/terms/Terms_Use.cfm

turbulent flow in technically rough pipes, be considered in accordance with the Moody diagram (Fig. 7)

$$\Delta h_{L\mathrm{Ref}} = a\ \Delta h_{L\infty\mathrm{Ref}} + (1-a)\,\Delta h_{L\infty\mathrm{Ref}} \left[\frac{\lambda_{\mathrm{Ref}}}{\lambda_{\infty\mathrm{Ref}}}\right]^n \tag{3}$$

or for an arbitrary relative roughness

$$\Delta h_L = a\ \Delta h_{L\infty\mathrm{Ref}}(1-a)\,\Delta h_{L\infty\mathrm{Ref}} + \left[\frac{\lambda_{\mathrm{Ref}}}{\lambda_{\infty\mathrm{Ref}}}\right]^n \frac{\lambda}{\lambda_{\mathrm{Ref}}} \tag{4}$$

The pipe friction coefficients λ can be calculated according to Colebrook

$$\frac{1}{\sqrt{\lambda}} = 1.74 - 2\log_{10}\left[\frac{2k_s}{d_h} + \frac{18.7}{\mathrm{Re}\sqrt{\lambda}}\right] \tag{5}$$

and λ_∞ according to von Karman

$$\frac{1}{\sqrt{\lambda_\infty}} = 1.74 - 2\log_{10}\left[\frac{2k_s}{d_h}\right] \tag{6}$$

The exponent n serves to adjust the loss conversion to the measured results. The Re-independent losses a $\Delta h_{L\infty\mathrm{Ref}}$ are neither influenced by the Reynolds number, nor by the relative roughness. Their magnitude is determined at a reference roughness. The other losses $(1-a)\ \Delta h_{L\infty\mathrm{Ref}}$ are converted in accordance with the λ-values in the Moody diagram by the Colebrook or von Karman equations.

The flow loss conversion model described by equations (3) and (4) can be applied to every flow-conducting compressor component. The proportion "a" must in each case be determined by means of a loss analysis at relative reference roughness.

A loss analysis of such detail contributes well to the optimization of individual components within the compressor stage, and also to precise prediction of the performance characteristics of individual stages. However, a more global approach is more feasible for the performance prediction of multistage centrifugal compressors, and above all, for the conversion of measured compressor performance characteristics for different Reynolds numbers and roughnesses.

Consideration of Reynolds Number and Roughness Effects in Stage Design Calculation

In stage design calculation it is not necessary to consider all the individual flow-conducting components separately. It is, however, necessary to divide the losses into

— hydraulic losses (η_h)
— disk friction losses (η_{DF})
— leakage losses (η_{Leak})

Isentropic efficiency

$$\eta_s = \frac{\Delta h_s}{\Delta h} = \eta_h \eta_{DF} \eta_{\mathrm{Leak}} \tag{7}$$

Isentropic head coefficient

$$\psi_s = \frac{\Delta h_s}{u_2^2/2} = \eta_h \frac{c_{2u}}{u_2} \tag{8}$$

Work coefficient

$$\mu = \frac{\Delta h}{u_2^2/2} = \frac{c_{2u}/u_2}{\eta_{DF}\eta_{\mathrm{Leak}}} = \frac{\psi_s}{\eta_h \eta_{DF} \eta_{\mathrm{Leak}}} \tag{9}$$

Hydraulic efficiency

$$\eta_h = \frac{\Delta h_s}{u_2 c_{2u}} = \frac{\psi_s}{c_{2u}/u_2} \tag{10}$$

Disk friction efficiency

$$\eta_{DF} = \frac{P - P_{DF}}{P} \tag{11}$$

Labyrinth seal efficiency

$$\eta_{\mathrm{Leak}} = \frac{\dot{m}}{\dot{m} + \dot{m}_{\mathrm{Leak}}} \tag{12}$$

Equations (7) and (8) illustrate that, when considering the change in isentropic efficiency, the Re and Ra dependence of the hydraulic losses (η_h), disk friction losses (η_{DF}), and leakage losses (η_{Leak}) must be taken into account, whereas only the hydraulic losses (η_h), and possibly the referred circumferential component of the impeller discharge flow (c_{2u}/u_2), enter into the change in the head coefficient. This demonstrates already that differing effects on isentropic efficiency and head coefficient are to be expected.

Hydraulic Losses. To allow global consideration of the hydraulic losses of the entire stage, a representative Reynolds number and a representative relative roughness must first be defined. They must be defined for the area in which the majority of the Re-dependent losses occurs (impeller and diffuser). A rough analysis gives us for the mean flow velocity $c = u_2/2$ and for the mean hydraulic diameter $d_h = 2\ b_2$. Taking the kinematic viscosity at stage inlet as representative, we arrive at a Reynolds number, which is also used in the ASME Power Test Code (PTC 10) and some other publications.

$$\mathrm{Re} = \frac{u_2 b_2}{\nu_1} = \frac{u_2 b_2}{\eta_1}\rho_1 \tag{13}$$

For the equivalent relative roughness, application of equation (2) gives

$$\frac{k_s}{d_h} = \frac{Ra}{b_2} \tag{14}$$

with a representative value for impeller passage and diffuser being introduced for the roughness Ra.

By analogy with equation (3) the hydraulic losses $(1 - \eta_{h\infty})_{\mathrm{Ref}}$ for a fixed reference roughness can be converted for various Re numbers

$$(1-\eta_h)_{\mathrm{Ref}} = a(1-\eta_{h\infty})_{\mathrm{Ref}} + \\ + (1-a)(1-\eta_{h\infty})_{\mathrm{Ref}}\left[\frac{\lambda_{\mathrm{Ref}}}{\lambda_{\infty\mathrm{Ref}}}\right]^n \tag{15}$$

and by analogy with equation (4) for an arbitrary roughness and Re number

$$(1-\eta_h) = a(1-\eta_{h\infty})_{\mathrm{Ref}} + \\ + (1-a)(1-\eta_{h\infty})_{\mathrm{Ref}}\left[\frac{\lambda_{\mathrm{Ref}}}{\lambda_{\infty\mathrm{Ref}}}\right]^n \frac{\lambda}{\lambda_{\mathrm{Ref}}} \tag{16}$$

A known or measured hydraulic efficiency (index t) at an arbitrary Reynolds number and arbitrary roughness can then be converted to arbitrarily specified conditions (index sp) by applying equation (16)

$$\frac{(1-\eta_h)_{sp}}{(1-\eta_h)_t} = \frac{a + (1-a)\left[\frac{\lambda_{sp\ \mathrm{Ref}}}{\lambda_{\infty\ \mathrm{Ref}}}\right]^n \frac{\lambda_{sp}}{\lambda_{sp\ \mathrm{Ref}}}}{a + (1-a)\left[\frac{\lambda_{t\ \mathrm{Ref}}}{\lambda_{\infty\ \mathrm{Ref}}}\right]^n \frac{\lambda_t}{\lambda_{t\ \mathrm{Ref}}}} \tag{17}$$

For the proportion "a" of the Re-independent hydraulic losses, the following dependence on the flow coefficient can be derived by analyzing the individual losses for different stages ($d_{2\mathrm{Ref}} = 0.4$ m, $Ra_{\mathrm{Ref}} = 2.5\ \mu$m)

$$a = 0.38 + 0.08\log_{10}(\phi_1) \tag{18}$$

A detailed comparison with measured results for the stages listed in Table 1 yields a good correspondence with the exponent $n = 1$, which means that a direct analogy with pipe flow is given.

Downloaded 01 Jun 2010 to 171.66.16.70. Redistribution subject to ASME license or copyright; see http://www.asme.org/terms/Terms_Use.cfm

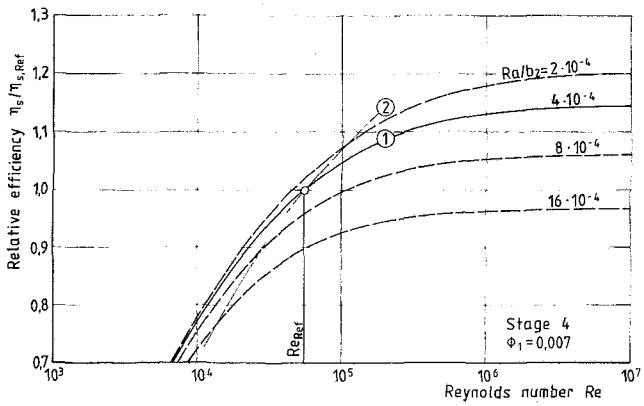


Fig. 8 Applications of the correction procedure

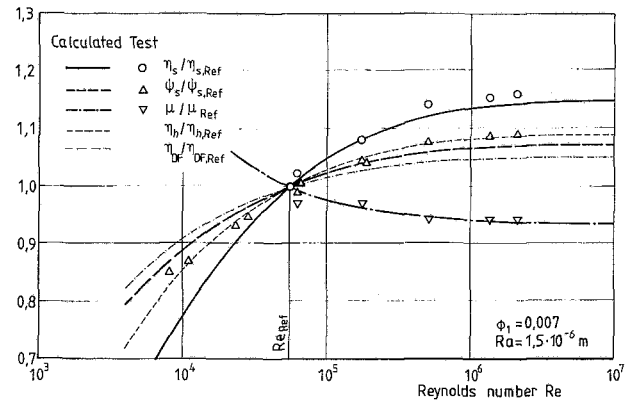


Fig. 9 Comparison of calculated results with test values (stage 4)

Disk Friction Losses. Besides flow losses, impeller disk friction losses are also important, particularly at small flow coefficients. Many investigations have been carried out on the ideal case of a disk rotating in a casing [24–31]. However, their findings, and particularly the relationships they give for the effects of the Reynolds number and the surface roughness, are not directly transferable to the friction losses in the spaces between impeller and casing, because:

- Similarity of the flow conditions is not given (pre-whirl, throughflow, different boundary layers)
- Investigations with technical roughness were only carried out for hydraulically smooth surfaces
- The effect of the relative roughness was only investigated for sand-rough surfaces with sand grain diameters considerably greater than the equivalent sand roughness corresponding to the technical roughness
- The region of high Reynolds numbers, which is of particular relevance for centrifugal compressors, is not dealt with
- The proposed relationships for the change in the torque coefficient with changing Reynolds number contain a constant exponent, which means that, even for very high Reynolds numbers, still considerable loss changes are calculated
- For rough surfaces the hydraulic length, representative of the loss mechanism in the boundary layers, does not seem to be the disk radius

In his investigations, Fukuda [28] comes to the following results:

- The torque coefficient (c_M) changes with changing Reynolds number in a similar way to the pipe friction factor
- In the transition from sand grain to technical roughness, changes in the torque coefficient occur similar to the pipe friction factor (Nikuradse - Colebrook)

Our own investigations confirm this basic similarity of the torque coefficient and the pipe friction factor.

Based on the measured c_M-curves at a known technical roughness, a hydraulic diameter was so determined that the relationships practically correspond with those of the Moody diagram ($d_h = 0.01\ d_2$). Assuming fully developed core rotation, the half of the impeller tip speed may be regarded as the representative velocity for the Reynolds number.

As the disk friction losses may be regarded as completely Re-dependent, we arrive at the simple relationship

$$\frac{1-\eta_{DF}}{1-\eta_{DF\infty}} = \frac{\lambda}{\lambda_\infty} \tag{19}$$

The following quantities are used for the calculation of the λ-values according to equations (5) and (6)

$$\mathrm{Re}_{DF} = \frac{u_2 d_h}{2\,\nu_1} = \frac{u_2 0.01\ d_2}{2\,\eta_1}\rho_1 \tag{20}$$

$$\frac{k_s}{d_h} = \frac{2\ Ra}{0.01\ d_2} \tag{21}$$

Ra is a representative mean value for the roughness at the outer faces of the impeller in the region of the outer diameter and the opposite casing walls. A known disk friction efficiency (index *t*) may then be converted to arbitrary conditions (index *sp*) by applying equation (19)

$$\frac{(1-\eta_{DF})_{sp}}{(1-\eta_{DF})_t} = \frac{\lambda_{sp}}{\lambda_t} \tag{22}$$

Assuming that the change in labyrinth seal efficiency with changing Re is negligible, relationships (17) and (22) permit calculation of the change in the isentropic efficiency η_s.

Head Coefficient and Work Coefficient. Following equation (8), the effects of Re and *Ra* on the head coefficient result from the change in the hydraulic efficiency and possibly from a change of c_{2u}/u_2. With the aid of detail measurements in the vaneless diffusers, in depth calculations were performed for all the measuring points of the different stage configurations given in Table 1 in order to determine the data at the impeller discharge. For none of the stages clear and evident changes in the $c_{2u}/u_2 = f\ (c_{2m}/u_2)$ functions with changing Reynolds number could be found. This means that the head coefficient, considered at the same flow coefficient, changes primarily in the same way as the hydraulic efficiency, and that an additional marginal change is only brought about by the different compressibility.

For the work coefficient, the dependence direct from equation (9) results mainly from the change in the disk friction efficiency.

Flow Coefficient Correction. The Re-dependent flow losses in a compressor stage increase—referred to c_{2u}/u_2—with increasing volume flow rate from surge to choke. The Re effect reduces these referred flow losses at the choke limit to a greater extent than at the surge limit. The result of this is a shift in the position of the optimum efficiency towards a larger volume flow as the Reynolds number increases. A good correspondence is obtained for the stages under investigation and through comparison with measurements taken on multistage compressors if the reference point (point for η_{max}) for the head performance characteristic is shifted along a parabola.

$$\left(\frac{\psi_{sp}}{\psi_t}\right)_{\eta_{max}} = \left(\frac{\phi_{sp}}{\phi_t}\right)^2_{\eta_{max}} \tag{23}$$

Change of Performance Characteristics. If the condition of equation (23) is fulfilled, the shape of the performance characteristics $\psi\ (\phi)$ and $\eta\ (\phi)$ can be retained as dimen-

Downloaded 01 Jun 2010 to 171.66.16.70. Redistribution subject to ASME license or copyright; see http://www.asme.org/terms/Terms_Use.cfm

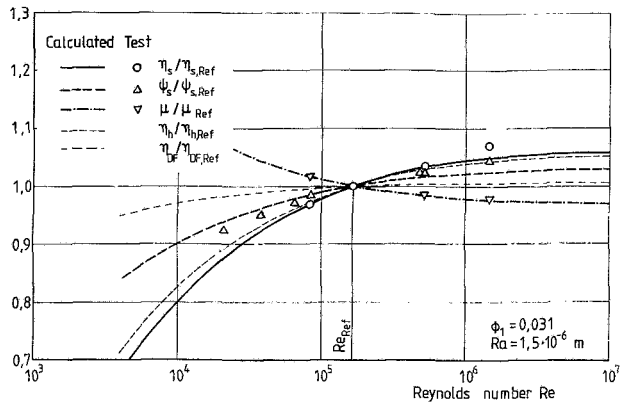


Fig. 10 Comparison of calculated results with test values (stage 1)

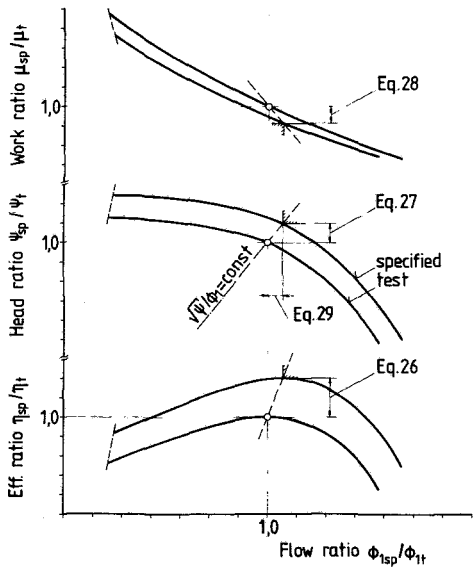


Fig. 11 Conversion of reference points and performance characteristics

sionless characteristics and transferred into the new reference values ϕ_{sp}, ψ_{sp}, and η_{sp}, calculated with the aid of equations (8), (17), and (22) for the volume flow rate $\dot{V}_{sp}$.

Applications and Comparison With Test Results. The flow loss conversion model is based on investigations of compressor stages, as are generally used in the process industry. These compressor stages are usually designed with backward-leaned impeller blades and not too extreme loading with regard to the Mach number. For these stages, the proposed model permits consistent efficiency conversion in the entire Re and *Ra* range of practical relevance, irrespective of the combination of the starting values (η_t, Re, Ra/b_2). The illustrations below show different possibilities of application and comparison with test results.

Figure 8 shows the effects of the Reynolds number and the relative roughness on the isentropic efficiency of a stage (stage 4, $\phi_1 = 0.007$) referred to a measured value selected as reference value. The extended line (1) shows the efficiency as a function of Re at a relative roughness Ra/b_2 held constant. The change in the Reynolds number can be obtained by varying arbitrarily one or more parameters (u_2, b_2, η_2, ρ_1). This curve is therefore also valid for the purely geometrical reduction or enlargement of the stage (scaling effect). The second line (2) shows the change in the efficiency for the scaled reduction or enlargement of the stage at a constant absolute roughness *Ra*. The considerable changes for different Reynolds numbers and relative roughnesses confirm that in any conversion of flow losses, both parameters must be observed. This applies particularly to stages with small flow coefficients. To achieve maximum efficiencies, stages such as are used frequently in high-pressure compressors with large Reynolds numbers must be manufactured with correspondingly high surface quality (Figs. 14, 17).

For the abovementioned stage, Fig. 9 shows a comparison of the calculated relative stage efficiencies, head coefficients and work coefficients with the measured values. The calculated curves for hydraulic efficiencies and disk friction efficiencies are also shown. Figure 10 gives the same relationships for a stage with a higher flow coefficient (stage 1, $\phi_1 = 0.031$). Note that the head coefficient changes are not considered in these illustrations in relation to the same volume flow rate or the same flow coefficient, but for the points of *maximum efficiencies*, i.e., *along a parabola* (Figs. 4, 5).

The effect of the roughness was checked during the investigation of the return channels by means of measurements on the same blading using three grades of roughness [32]. Further confirmation was provided by the measurements of various impellers with two different flow coefficients which were enlarged geometrically, but had identical absolute roughness *Ra*.

Simplified Procedure for the Conversion of Measured Characteristics for Process Stages

The aforementioned model for the conversion of measured individual stage characteristics is, in principle, also applicable to multistage compressors. For this, however, each individual stage must be analyzed before the machine characteristic can be calculated on the basis of the different stage characteristics. This procedure, however, is too involved, particularly when converting the measured characteristics of multistage process compressor stages. For this reason, a method was developed to permit very simple conversion of measured characteristics. In this method, the Re-dependent losses of the entire process stage direct are converted in order to obtain conversion of the measured process stage efficiency.

$$\frac{(1-\eta)_{sp}}{(1-\eta)_t} = \frac{a+(1-a)\left[\frac{\lambda_{sp\,\mathrm{Ref}}}{\lambda_{\infty\,\mathrm{Ref}}}\right]^n \frac{\lambda_{sp}}{\lambda_{sp\,\mathrm{Ref}}}}{a+(1-a)\left[\frac{\lambda_{t\,\mathrm{Ref}}}{\lambda_{\infty\,\mathrm{Ref}}}\right]^n \frac{\lambda_t}{\lambda_{t\,\mathrm{Ref}}}} \tag{24}$$

As we are dealing here with the conversion of the process stage efficiency, the proportion of Re-independent losses "*a*" must first be determined anew. Additional leakage losses, e.g., across the axial thrust balancing drum, and also mechanical losses, are not considered in these analyses. They must be dealt with specifically from case to case. Allowing for disk friction losses and leakage losses through the impeller labyrinths, which percentages decrease rapidly with increasing flow coefficient, the analysis of individual losses yields the simple relationship (compared with equation (18)).

$$a = 0.3 \neq f(\phi_1) \tag{25}$$

In this form, equation (24) still permits the conversion of flow losses from test to specified conditions for different relative roughnesses.

A further simplification is obtained by dispensing with the conversion of the measured values for different roughnesses and, at the same time, omitting the reference to the reference roughness. The latter means that, strictly speaking, "Re-independent" flow losses are no longer completely independent of Re and *Ra* because they are calculated with the efficiency η_t, which is measured with the specific Reynolds number and roughness prevailing during the test. The

Downloaded 01 Jun 2010 to 171.66.16.70. Redistribution subject to ASME license or copyright; see http://www.asme.org/terms/Terms_Use.cfm

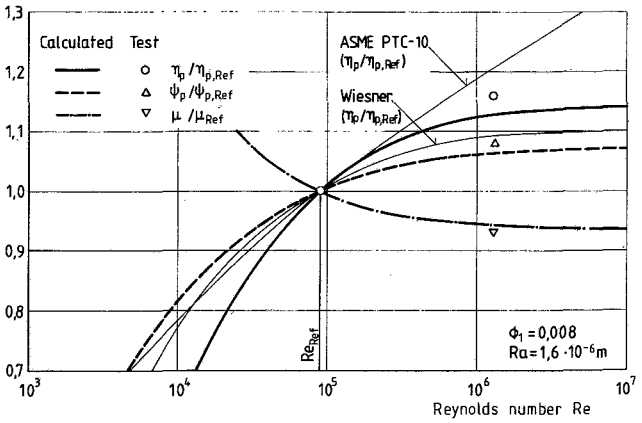


Fig. 12 Comparison of calculated results with test values for a natural gas compressor (test inlet pressures p_1 = 1/15 bar)

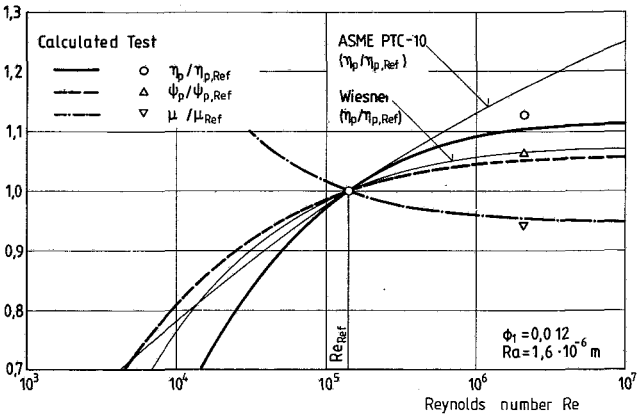


Fig. 13 Comparison of calculated results with test values for a natural gas compressor (test inlet pressures p_1 = 1/15 bar)

deviations brought about by this simplification are negligible in the case of application in acceptance test measurements and guarantee comparisons.

Equation (24) yields for the process stage efficiencies

$$\frac{1-\eta_{sp}}{1-\eta_t}=\frac{a+(1-a)\left[\frac{\lambda_{sp}}{\lambda_\infty}\right]^n}{a+(1-a)\left[\frac{\lambda_t}{\lambda_\infty}\right]^n} \tag{26}$$

where $a=0.3$ = constant

$n=1$

λ = equation (5) or equation (6).

Equation (23) applies for the conversion of the performance characteristics reference points; the change in the head coefficient along the parabola can be approximated generally as follows

$$\frac{\psi_{sp}}{\psi_t}=0.5+0.5\,\frac{\eta_{sp}}{\eta_t} \tag{27}$$

With equation (9), this gives the conversion for the work coefficient

$$\frac{\mu_{sp}}{\mu_t}=0.5+0.5\,\frac{\eta_t}{\eta_{sp}} \tag{28}$$

The corresponding flow coefficient correction is obtained using equation (23)

$$\frac{\phi_{sp}}{\phi_t}=\sqrt{\frac{\psi_{sp}}{\psi_t}}=\sqrt{0.5+0.5\,\frac{\eta_{sp}}{\eta_t}} \tag{29}$$

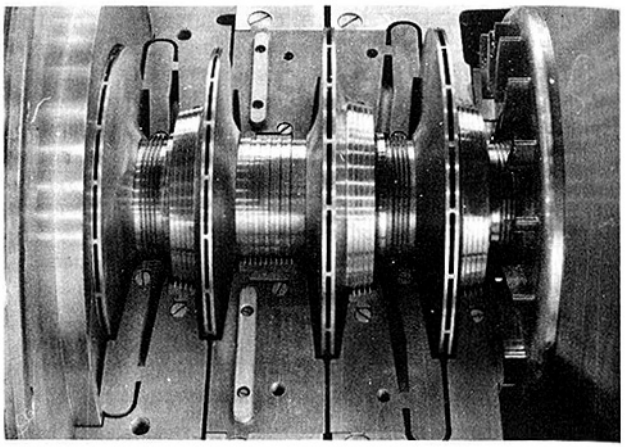


Fig. 14 Inner casing with rotor of the high-pressure oxygen compressor (p_2/p_1 = 125 bar/52 bar)

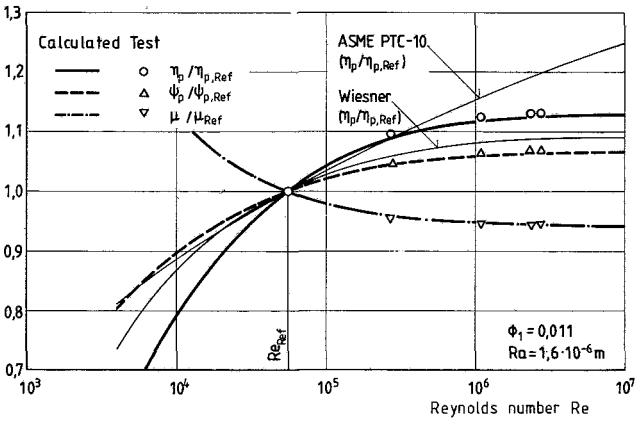


Fig. 15 First section of the high-pressure oxygen compressor (test inlet pressures p_1 = 1/5/20/45/52 bar)

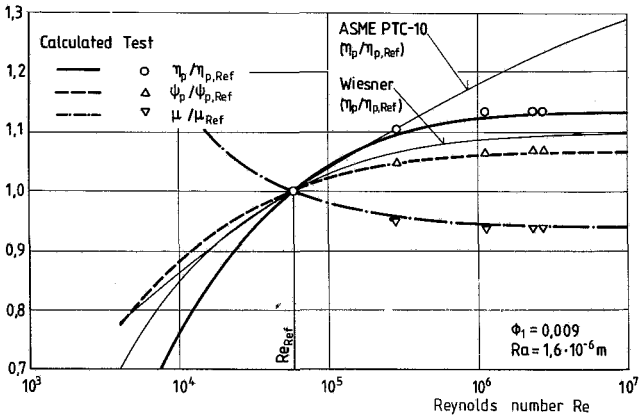


Fig. 16 Second section of the high-pressure oxygen compressor

The shape of the measured performance characteristic of the process stage can be retained as a dimensionless characteristic and transferred into the converted reference points. The application of the conversion procedure is depicted in Fig. 11.

In the case of multistage process compressors, the Reynolds number, according to equation (13), should be introduced for the first stage of each process stage, and the roughness as a representative value for the process stage.

For the conversion of measured process stage performance characteristics, these relationships should be applied to polytropic efficiencies and head coefficients. Compared to

Downloaded 01 Jun 2010 to 171.66.16.70. Redistribution subject to ASME license or copyright; see http://www.asme.org/terms/Terms_Use.cfm

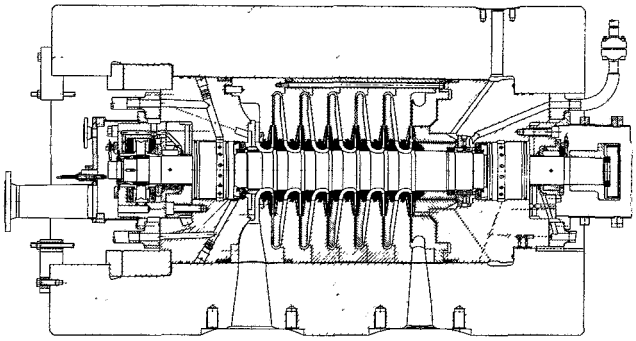


Fig. 17 Sectional drawing of the ultra high pressure compressor (max. discharge pressure > 900 bar)

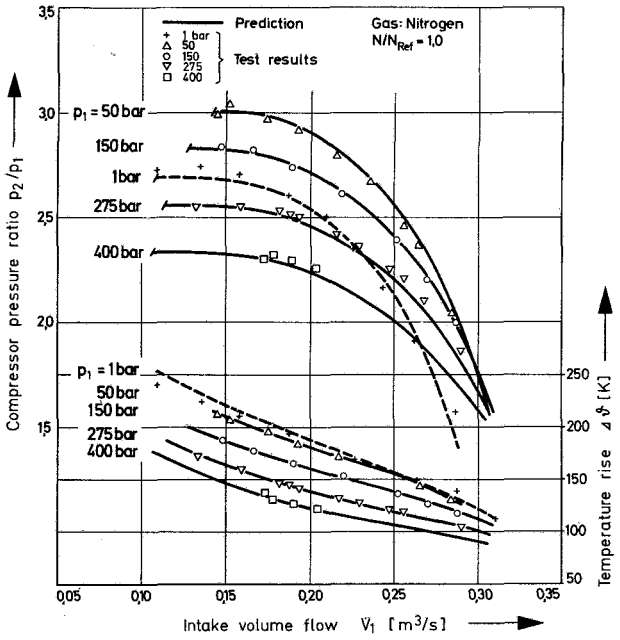


Fig. 18 Performance characteristics of the ultra high pressure compressor

use with isentropic values, marginally smaller corrections are obtained.

Applying this simplified procedure to individual stages provides practically the same results as were already presented for the more detailed analysis in Figs. 9 and 10. In the following Figs. (12, 13, 15, 16, 18, 19), for five examples, comparisons are made between process stage measurements and calculated results. The representative roughness to be introduced was determined for each stage on the basis of roughness measurements. To facilitate comparison, the curves for the efficiency changes, as calculated according to ASME PTC-10 [1] and Wiesner [2], are also shown.

— Two six-stage natural gas compressors for a design pressure ratio of p_2/p_1 = 110 bar/35 bar were designed for different flow rates (ϕ_1 = 0.008 resp. 0.012) and tested in each case using a CO_2/He mixture at inlet pressures of 1 and 15 bar. Figures 12 and 13 show a comparison of the calculated polytropic efficiency and head coefficient curves with the test results. The efficiencies for the inlet pressure of 1 bar were determined on the basis of the measured efficiencies for the inlet pressure of 15 bar from the measured head coefficient changes.

— A high-pressure oxygen compressor (Fig. 14) for a design pressure ratio of p_2/p_1 = 125 bar/52 bar was tested under design conditions using oxygen up to a discharge pressure of 135 bar. Besides the test under design conditions, closed loop measurements with nitrogen were taken for the inlet pressures p_1 = 1/5/20 bar. Figures 15 and 16 show comparisons between measurement and calculation for both compressor sections.

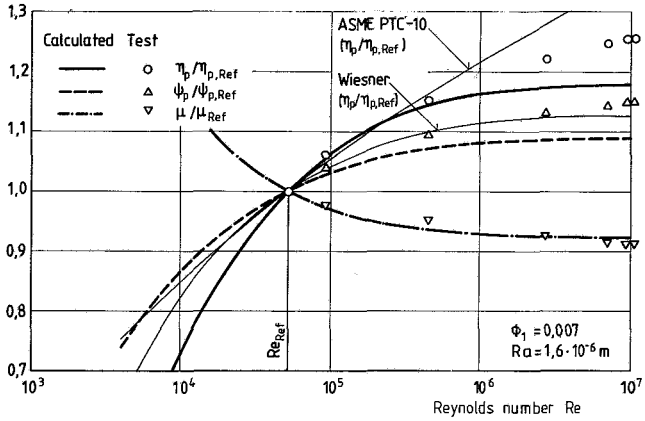


Fig. 19 Comparison of calculated results with test values for the ultra high pressure compressor (test pressures p_1 = 1/9/50/150/275/400 bar)

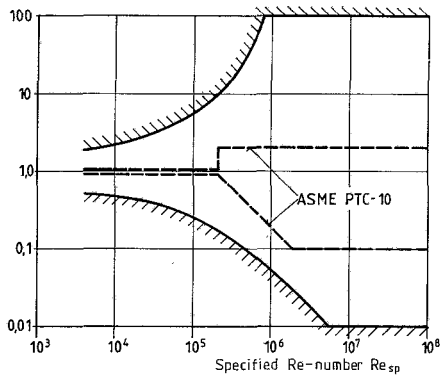


Fig. 20 Allowable range of application for the correction procedure

— A six-stage centrifugal compressor (Fig. 17) for ultra high pressures (maximum discharge pressure $p_{2\,max}$ > 900 bar) with the design performance data

Inlet pressure	350 bar
Discharge pressure	800 bar

was developed and subjected to extensive testing. Thermodynamic tests were run with nitrogen at the inlet pressures p_1 = 1/9/50/150/275/400 bar. Figure 18 shows a comparison between calculated performance curves and test results. The rise in the pressure ratio and the change in the temperature rise results in the lower inlet pressure range ($1 \leqq p_1 \leqq 50$ bar) above all from the Reynolds number effect. In the upper pressure range ($p_1 > 50$ bar), the characteristics are influenced primarily by the change in the gas properties. Figure 19 contrasts the Reynolds number effects on efficiency and head coefficient, calculated by the simplified method, with the test results. In these tests, a Re range of

$$5\,10^4 \leqq \mathrm{Re}_t \leqq 1.1\,10^7$$

was covered.

In all the comparisons performed to date between calculated and test results, a good correspondence was also obtained using this simplified method. The test results for efficiency and head coefficient for $\mathrm{Re} > \mathrm{Re}_{\mathrm{Ref}}$ are generally above the calculated curves, which means that an excessive upward correction can be practically excluded.

The comparison of the ASME PTC-10 [1] conversion method with the test results shows, particularly for high Reynolds numbers, a too large improvement in efficiency and

Downloaded 01 Jun 2010 to 171.66.16.70. Redistribution subject to ASME license or copyright; see http://www.asme.org/terms/Terms_Use.cfm

hence also in the head coefficient. The Wiesner formulae [2] on the other hand give a change corresponding to the Reynolds number which is too low. The PTC-10 method suffers additionally because it does take into account neither the effect of the relative roughness nor the flow correction.

The simplified method, described herein for converting measured performance characteristics from test to guarantee conditions, was also compared with other test results by a working group of the ICAAMC (International Compressed Air and Allied Machinery Committee), investigating the subject "Workshop Performance Tests on Turbocompressors" [33]. All comparisons confirm that this model represents a considerable improvement over all previously published methods. The good correspondence with test results permits an expansion of the application range beyond the limits allowed by ASME PTC-10. The proposed range of application is shown in Fig. 20. It was determined working on the assumption that a conversion of the losses of around ± 20 percent will be permitted. To allow comparison, the limits permitted by ASME PTC-10 are also shown.

Conclusions and Recommendations

The investigations, performed into the effects of the Reynolds number and the relative surface roughness on the operating behavior of centrifugal compressors, lead to the following conclusions and recommendations:

— Proper calculation of the Reynolds number effect can only be carried out if at the same time allowance is made for the effect of the relative surface roughness on the flow losses. Even if the conversion of flow losses is only to be carried out for the particular roughness in question, this roughness must be known and must be considered in the conversion model (Figs. 6, 8).

— The loss model, based on an analogy with the turbulent flow in technically rough pipes, is suitable for the conversion of flow losses in centrifugal compressors with respect to different Reynolds numbers and roughnesses.

— For the analysis of single stages and their components (optimization, performance prediction), the model permits calculation of the effects of both the Reynolds number and the surface roughness.

— For the design calculation of centrifugal compressors, the effects of the Reynolds number and the relative roughness on the hydraulic flow losses (η_h) and the disk friction losses (η_{DF}) are determined separately, allowing calculation of the effects on the efficiency and the head coefficient. At the same time, allowance can easily be made for the stage characteristic change associated with the flow correction at maximum efficiency (equation (23)).

— The conversion of measured multistage compressor section characteristics from test to guarantee conditions is permitted reliably by the simplified model introduced in this paper. The method takes into account the relative roughness existing in the test (equations (26) to (29)).

— The good correspondence obtained between these model calculations and the test results forms the basis for recommending the application of the simple relationships presented herein for the improvement of centrifugal compressor performance test codes (e.g. ASME PTC-10 and ISO TC 118 [34]).

References

1 ASME, "Power Test Codes, Compressors and Exhausters," PTC-10, 1965, Reaffirmed 1973.

2 Wiesner, F. J., "A New Appraisal of Reynolds Number Effects on Centrifugal Compressor Performance," ASME Paper 78-GT-149.

3 Osterwalder, J., and Hippe, L., "Betrachtungen zur Aufwertung bei Serienpumpen," VDI-Berichte Nr. 424, 1981, pp. 1–17.

4 Ippen, A. T., "The Influence of Viscosity on Centrifugal-Pump Performance," *ASME Trans.*, Vol. 68, Nov. 1946, pp. 823–848.

5 Mühlemann, E., "Zur Aufwertung des Wirkungsgrades von Überdruck-Wasserturbinen," Schweizerische Bauzeitung, 66. Jahrgang, No. 24, June 1948, pp. 331–333.

6 Davis, H., Kottas, H., and Moody, A. M. G., "The Influence of Reynolds Number on the Performance of Turbomachinery," *ASME Transactions*, Vol. 73, July 1951, pp. 499–509.

7 Davis, H., and Harrison, N. J., "Equivalent Performance Parameters for Turboblowers and Compressors," *ASME Trans.*, Vol. 80, Jan. 1958, pp. 108–116.

8 Rotzoll, R., "Untersuchungen an einer langsamlaufenden Kreiselpumpe bei verschiedenen Reynoldszahlen," Konstruktion, 10. Jahrgang, Heft 4, 1958, pp. 121–130.

9 Rütschi, K., "Zur Wirkungsgradaufwertung von Strömungsmaschinen, Verhalten einer Einzelmaschine und einer Reihe von Maschinen verschiedener Größe," *Schweizerische Bauzeitung*, 76. Jahrgang, Heft 41, Oct. 1958, pp. 603–606.

10 Balje, O. E., "A Study on Reynolds Number Effects in Turbomachines," *ASME Transactions*, Vol. 86, No. 3, July 1964.

11 Schmidt-Theuner, P., and Mattern, J., "Reynolds- und Spieleinfluß beim Turbolader-Radialverdichter," Brown-Boveri-Mitteilungen, Band 55, Aug. 1968, pp. 453–456.

12 Heidelberg, L. J., Ball, C. L., and Weigel, C., "Effects of Reynolds Number on Overall Performance of a 6-inch Radial Bladed Centrifugal Compressor," NASA TN D-5761, Apr. 1970.

13 Mashimo, T., Suefsa, H., Ariga, I., and Watanabe, I., "Effects of Reynolds Number on Performance Characteristics of a Centrifugal Compressor," ASME Paper 71-GT-25, Mar. 1971.

14 Weigel, C., and Ball, C. L., "Reynolds Number Effects on Overall Performance of a 10, 8 Centimeter (4, 25 in.) Sweptback Bladed Centrifugal Compressor," NASA TN D-6440, Jan. 1972.

15 Mashimo, T., Watanabe, I., and Ariga, I., "Effects of Reynolds Number on Performance Characteristics of a Centrifugal Compressor, with Special Reference to Configurations of Impellers," ASME Paper 74-GT-59.

16 Wöhrl, B., "Analyse der hydraulischen Verluste in einer Radialverdichterstufe und Abschätzung des Reynoldszahleinflusses auf die Wirkungsgradkennlinien," Dissertation am Institut für Thermische Strömungsmaschinen und Maschinenlaboratorium der Universität Stuttgart, Dec. 1980.

17 Nikuradse, J., "Strömungsgesetze in rauhen Rohren," VDI-Forschungsheft 361, 1933.

18 Colebrook, C. F., "Turbulent Flow in Pipes, with Particular Reference to the Transition Region between the Smooth and Rough Pipe Laws," *Journal of the Institution of Civil Engineers*, Vol. 11, 1939, pp. 133–156.

19 Moody, L. F., and Princeton, N. Y., "Friction Factors for Pipe Flow," *ASME Transactions*, 1944, pp. 671–684.

20 DIN 4768, "Ermittlung der Rauheitsmeßgrößen Ra, Rz, R_{max} mit elektrischen Tastschnittgeräten," Aug. 1974.

21 Young, A. D., "The Drag Effects of Roughness at High Subcritical Speeds," *J. Roy. Aeron. Soc.*, Vol. 54, 1950, pp. 534–540.

22 Speidel, L., "Ermittlung der notwendigen Oberflächengüte and eventueller Rauhigkeitsverluste bei Dampfturbinen," Elektrizitätswirtschaft, Jg. 61, H. 21, 1962.

23 Woelk, G. U., "Einflüsse der Fertigungsgenauigkeiten und Profilrauheit auf das strömungstechnishe Verhalten von Verdichtergittern," Atomkernenergie (ATKE), Bd. 32, 1978.

24 Schultz-Grunow, F., "Der Reibungswiderstand rotierender Scheiben in Gehäusen," Zeitschrift für angew. Math. und Mech., Bd. 15, Heft 4, 1935, pp. 191–204.

25 Pantell, K., "Versuche über Scheibenreibung," Zeitschrift für angew. Mathematik und Mechanik, Bd. 16, Heft 4, 1949/1950, pp. 97–108.

26 Daily, J. W., and Nece, R. E., "Chamber Dimension Effects on Induced Flow and Frictional Resistance of Enclosed Rotating Disks," ASME *Journal of Basic Engineering*, Vol. 82, 1960, pp. 217–232.

27 Nece, R. E., and Daily, J. W., "Roughness Effects on Frictional Resistance of Enclosed Rotating Disks," ASME *Journal of Basic Engineering*, Vol. 82, 1960, pp. 553–561.

28 Fukuda, H., "The Effects of Runner Surface Roughness on the Performance of a Francis Turbine," *Bulletin of JSME*, Vol. 7, No. 26, 1964, pp. 346–356.

29 Watabe, K., "On Fluid Resistance of Enclosed Rotating Rough Disks," *Bulletin of JSME*, Vol. 8, No. 32, 1965, pp. 609–619.

30 Kurokawa, J., and Toyokura, T., "Study on Axial Thrust of Radial Flow Turbomachinery," *Proc. 2nd International JSME Symposium*, Tokyo, 1972, pp. 31–40.

31 Kurokawa, J., Toyokura, T., Shinjo, M., and Matsuo, K., "Roughness Effects on the Flow along an Enclosed Rotating Disk," *Bulletin of the JSME*, Vol. 21, No. 162, Dec. 1978, pp. 1725–1732.

32 Simon, H., and Rothstein, E., "On the Development of Return Passages of Multistage Centrifugal Compressors," (To be published at the ASME Spring Conf., Houston, 83).

33 ICAAMC, Minutes of Meeting "Reynolds Number Correction Method," Zürich, Oct. 19th, 1981.

34 International Organization for Standardization, Technical Committee ISO/TC 118 "Compressors, Pneumatic Tools and Pneumatic Machines," Sub-Committee ISO/TC 118/SC 1 "Turbocompressors," "Turbocompressors-Performance Test Code," Guidance for Work to TC 118/SC 1, Stockholm, June 26th, 1979.

Downloaded 01 Jun 2010 to 171.66.16.70. Redistribution subject to ASME license or copyright; see http://www.asme.org/terms/Terms_Use.cfm

DISCUSSION

R. A. Strub[1]

The paper by Dr. Simon and Mr. Bülskämper mentions a working group of the ICAAMC investigating "Workshop Performance Tests on Turbocompressors." This discussion provides some supplementary information about the work of this group.

In 1979 the Process Compressor Subcommittee of the International Compressed Air and Allied Machinery Committee (ICAAMC) decided to investigate the problem of Reynolds number correction between workshop tests and specified process conditions. A working group under my chairmanship was formed to examine the available correction methods and to select the most suitable formulae that could be recommended for incorporation in the appropriate international standards. The following companies agreed to participate on the working group:

- Dresser Industries Inc., Dresser Clark Division
- United Technologies, Elliott Company
- Ingersoll Rand Company
- Transamerica Delaval
- Mannesmann Demag
- MAN-GHH Sterkrade
- Nuovo Pignone S.p.A.
- Sulzer Brothers Limited

The ICAAMC correction equations (given in [35] and included as equations (26), (27), (28), and (29) of the present paper) were the results of many meetings and discussions between the members of this working group. Many different equations were proposed by members of the committee and the best ideas were incorporated into a simple formula that was finally accepted by all participants. Dr. Simon was present at all of our meetings and made many useful contributions.

The paper under discussion, however, gives the misleading impression that the ICAAMC equations were proposed to the ICAAMC working group by Dr. Simon and directly adopted by the working group for comparison purposes with measurements. The fact that the ICAAMC equations can be obtained by simplification of equation (17) of Dr. Simon's paper strengthens this impression, and the reader could be forgiven for believing that they were derived in this way. In fact, the original proposals made by Dr. Simon to this working group were very different from the equations presented in his paper. Discussions within the working group have certainly influenced the development of the ideas and formulae presented by Dr. Simon and Mr. Bulskamper. I therefore regret that the present paper was published by Dr. Simon without informing the working group of the ICAAMC and that no credit has been given to the debt he owes to discussion at its meetings.

The working group of the ICAAMC has compared the predictions of the ICAAMC correction equations with test data supplied by the participating companies. Test data for 31 compressors (17 multistage and 14 single-stage compressors) leading to about 120 test points were submitted by various manufacturers. The deviation of the measured efficiency ratio from the calculated efficiency ratio given by the curve for all of the tests results is plotted in Fig. 21. This figure demonstrates an almost equal distribution of the deviation (scatter) for all sets of data, thus showing that the proposed formula is acceptable for practical purposes. This figure also shows that

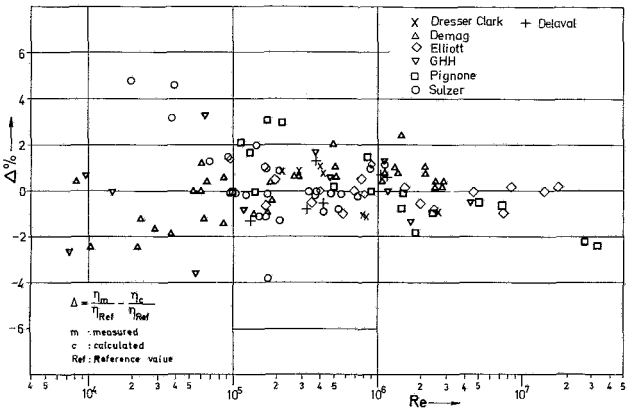


Fig. 21 Comparison between measurements and calculation using the ICAAMC correction equation (equation (26) of Dr. Simon's paper; taken from reference (35).

the scatter for tests at low Reynolds numbers is greater than that at high Reynolds numbers. A large scatter can be expected when performing tests at low pressure or at low peripheral speed, which leads to low driving power.

It was agreed by the participating companies at the beginning of their collaboration on this work that the recommendation of the working group would be jointly presented to ASME and other organizations for incorporation in a revision of existing test codes.

Further References

35 "Influence of the Reynolds Number on the Performance of Centrifugal Compressors," Report of the working group of the Process Compressor Subcommittee of the International Compressed Air and Allied Machinery Committee, finalized Oct. 5, 1982 and issued May 6, 1983, Zurich, Switzerland.

F. J. Wiesner[2]

The authors are to be commended for their valuable addition to the literature on this subject. Although there are a number of questions which should be answered in further clarification of the material presented in this paper, this discusser would appreciate a response to only one in particular. How were the curves labeled "Wiesner" in Figs. 12, 13, 15, 16 and 19 obtained? By starting with the ASME PTC-10 curves shown on these same plots (from which reasonable average values for the "reference" efficiencies can be obtained), this writer has been unable to closely reproduce the trends on these plots which are attributed to the methods of [2]. For the most part, efficiency ratios were arrived at which were higher than shown by the thin solid lines – tending toward the levels of the heavier solid lines which represent the authors' method. With respect to Figs. 12, 13 and 16, in particular, there would appear to be much better agreement between these methods than is implied on the plots.

L. Sapiro[3]

The authors have made an interesting contribution to a subject which still continues to be debatable. However, I do have some reservations regarding their recommendations for incorporating the simplified relationships of this paper into the ASME PTC-10 and ISO TC 118.

My concern stems from the questionable validity of applying conclusions derived from single-stage analytical and actual test models to correct the overall performance of any

[1] Sulzer Escher Wyss Ltd., CH-8023, Zurich, Switzerland, Mem. ASME

[2] Chief Aerodynamicist, United Technologies Elliott, Jeannette, Pa. 15644

[3] Senior Technical Consultant, Solar Turbines, Inc., San Diego, Calif. 92138 Mem. ASME

Copyright © 1984 by ASME
Downloaded 01 Jun 2010 to 171.66.16.70. Redistribution subject to ASME license or copyright; see http://www.asme.org/terms/Terms_Use.cfm

multistage compressor. As I mentioned during the discussion of Wiesner's paper in the Transactions of the ASME [36], high pressure ratio compressors, especially those handling heavy hydrocarbons, present good examples for the study of this questionable validity. They are critically dependent upon individual stage matching. Thus, a single Reynolds number correction on the overall performance will not be adequate.

A straightforward way to predict performance that accounts for Reynolds number effects as well as Mach number effects consists of correcting each stage individually and working up progressively until arriving at the overall performance. On the other hand, usually it is not possible to arrive at the same overall design performance by applying a single correction to the overall test results.

The formulas for Re number correction, such as the ones presented by this paper and previous ones, are very valuable and should be used for the prediction of performance by applying them to each of the individual stages making up the multistage compressor. However, their suitability for directly correcting the test results is uncertain.

In the majority of cases, test conditions can be selected in such a way as to reduce to a minimum the differences between the friction factor on test and the one at design conditions. This nullifies the need for Reynolds number corrections. However, in those cases where multistage compressors can only be tested at conditions which produce appreciable different Reynolds number effects than at design conditions, the correction should be applied stage by stage.

The correction method for multistage compressors requires a good knowledge of the individual stage characteristics of the configuration being tested, and their matching. Having completed the test, the overall performance has to be compared with its prediction. If there are differences, the individual stage characteristics would have to be adjusted until producing an acceptable agreement with the overall results. Once this laborious task is completed, the individual stages should be corrected for the Re number and used for predicting the overall performance at design conditions.

Regarding the ASME PTC-10 allowable deviations of Reynolds number, it is generally agreed that the present ones are not appropriate and should be revised. The tolerance curves proposed by the authors on Fig. 20 indicate similar trends as the ones of Davis [7] and Wiesner, shown on Fig. 8 of Wiesner's paper. When converting Davis's definition of Re number to the ASME's one, his curves agree very well with Wiesner's, and they are more conservative than the ones of the authors.

Regarding the stages investigated by the authors, it should be noted that they had an inlet flow coefficient ranging from 0.004 to 0.031 (or in the nomenclature of others [37], from 0.005 to 0.039). Those values correspond to a specific speed range of 27 to 76. However, even the stage of the highest value (NS of 76) is smaller than the optimum design value for centrifugal compressors (NS of 90 to 110). Unfortunately, no tests were conducted in the region covering optimum to high specific speed stages to prove the validity of the author's conclusions for any type of single stage.

Also, the authors state that the percentage of losses which are independent of Reynolds number is essentially constant for any value of flow coefficient (specific speed). Thus, stages with extremely narrow impeller and vaneless diffuser passages (NS of 27), where the friction losses predominate, and stages with wide passages of very small radii of curvature (NS of 120), where separation and recirculation losses predominate, would have the same 30 percent of losses independent of Re number (formula (25)). Using the more accurate formula (18), those values would be 19 percent and 29 percent, for NS of 27 and 120, respectively. Those values contradict my studies (formula (5) [37] or Table 1 of [36], and others, which indicated a much higher variation. For the same specific speed extremes my studies would indicate 0 percent and 54 percent, respectively (100 percent and 46 percent due to friction losses, respectively). For the author's stages 3 and 4, they would indicate 5 percent, while for stage 1 they would indicate 41 percent. Other references (Table 1 of [36], indicate extreme values of 15 percent and 57 percent. It is difficult to understand why there is such a small effect of specific speed (inlet flow coefficient) on the percentage losses as indicated by the authors.

References

36 Wiesner, F. J., "A New Appraisal of Reynolds Number Effects on Centrifugal Compressor Performance," ASME JOURNAL OF ENGINEERING FOR POWER, Vol. 101, July 1979, pp. 384–396.

37 Sapiro, L., "Preliminary Staging Selection for Gas Turbine Driven Centrifugal Compressor," ASME Paper No. 73-GT-31, Apr. 1973.

Authors' Closure

The authors appreciate the contributions to this discussion and would like to take this opportunity to clear up certain misunderstandings and answer questions concerning the content of the paper.

Dr. Strub's comments only refer to part of our publication—the simplified conversion of measured characteristics from test to specified conditions. In the ICAAMC working group, various conversion methods have been discussed. While the proposals of other members of the working group were derived from the well-known methods of Rütschi [9], Wöhrl [16], and Wiesner [2], we have formulated our own model for the conversion of flow losses (see Fig. 7) which, compared with the others, is the only one which permits physically meaningful conversions free of contradiction. Our model, which provides equation (24) for the conversion of process stage efficiency, has been discussed in detail in the working group. If the conversion of measured characteristics for various roughnesses is waived, the result is the simplified equation (26) which was finally accepted by all participants. The other parts of the conversion method (Fig. 11) were also introduced by us and adopted by the working group without modification, in particular:

- Equation (25), for the Re-independent part of losses
- Equations (27), (28), and (29), for the conversion of head coefficient and work coefficient with a corresponding volume flow coefficient correction
- The transfer of dimensionless characteristics to the new reference points
- The allowable range of application of the conversion method (Fig. 20).

As the members of the ICAAMC working group are well aware, the entire conversion method in all its detail has been determined to a decisive degree by our contributions as is duly documented by the aforementioned facts. We therefore have to reject the objections raised by Dr. Strub. However, we welcome the confirmation of this method which the additionally quoted measurements have provided.

Wiesner's conversion method for efficiency [2] is based on "nominal conditions," which neither coincide with our "reference conditions" nor with the "specified conditions." For this reason, the change in losses must first be converted from Wiesner's nominal conditions to the reference conditions and then from the nominal conditions to the assumed specified conditions. The calculation procedure can be explained in an example with reference to the Wiesner curve shown in Fig. 16. For this compressor, the nominal conditions are as follows: $Re_{NOM} = 52{,}635$; $Ra_{NOM} = 125\ \mu\text{in.} \hat{=} 3.18\ \mu\text{m}$. For our reference conditions, the following data apply:

Downloaded 01 Jun 2010 to 171.66.16.70. Redistribution subject to ASME license or copyright; see http://www.asme.org/terms/Terms_Use.cfm

$Re_{Ref} = 58{,}200$, $Ra_{Ref} = 62.9$ μin. $= 1.6$ μm. If one inserts these values in the equation for efficiency conversion (equation (4) in [2]), the result (including a roughness influence $f_{Ref}/f_{NOM} = 0.9767$) is the ratio $(1 - \eta_{Ref})/(1 - \eta_{NOM}) = 0.9704$. For an assumed specified Re number of $Re_{sp} = 10^6$ and the given roughness $Ra_{sp} = 62.9$ μin. $\hat{=} 1.6$ μm, the result (including a roughness effect of $f_{sp}/f_{NOM} = 0.9373$) is the ratio $(1 - \eta_{sp})/(1 - \eta_{NOM}) = 0.8533$. Division of the changes in loss thus calculated produces $(1 - \eta_{sp})/(1 - \eta_{Ref}) = 0.8793$, which, given the reference efficiency $\eta_{Ref} = 0.5782$, finally results in the efficiency ratio $\eta_{sp}/\eta_{Ref} = 1.0880$. This value is entered in Fig. 16 at $Re_{sp} = 10^6$. The efficiency ratios, plotted in Fig. 12, 13, 15, 16, and 19, can be determined in the same way for any Re number.

In his paper, Wiesner also quotes a range of allowable deviations between the test and the specified Re number which are permitted in the efficiency conversions. The drawn limits are ascertained for a permissible efficiency change of 1 percent. If one applied this principle to our stages 1–5, the result would be a considerable shift of the limits, owing to the flow coefficient. The limits adopted by Davis [6] represent the range in which, according to Davis, the influence of the Re number can be dismissed as negligible. The limits suggested by us imply that for a mean relative roughness, the change in the losses does not exceed 20 percent within the allowable range of application. Within these limits, our method for the conversion of measured characteristics produces for practical purposes sufficient accuracy which corresponds to the usual measurement tolerances.

For stage 5, Sapiro suggests a Re-independent part of losses of $a = 0$ instead of $a = 0.3$ (equation (25)). According to equation (7), the isentropic stage efficiency also includes the leakage losses at the impeller shroud. These losses, which we assume to be independent of the Reynolds number and roughness, constitute for stage 5 alone 22 percent of the total losses. If only the hydraulic losses in this individual stage are considered, the Re-independent part of losses is 19 percent (equation (18)). Apart from low Re-independent losses in the impeller, this percentage is mainly a result of the fact that increasing wall friction and dissipation lead to an increase in the flow angle in the vaneless diffuser and thus to a shorter flow path. An analysis of the diffuser flow shows that for this stage the increase in flow losses only constitutes approximately 60 percent of the increase in the wall friction and dissipation coefficients. For this reason, $a = 0$ cannot be accepted for those stages. In the region of maximum efficiency stages ($0.045 \leq \phi_1 \leq 0.065$), Heidelberg [12] and Weigel [14] have published test results which were taken into account when determining the Re-independent part of losses. Figure 22 shows a comparison of their test results with our calculated curves. The authors themselves describe their efficiency evaluation as unreliable; thus, only the change in the head coefficient was considered. The test results of Weigel correspond well to our calculated curve. The change in head coefficient measured by Heidelberg for a decreasing Re number is greater than the result of the calculation. An increase in the Re-independent part of the losses, as proposed by Sapiro, would further enlarge the deviations between measurement and calculation.

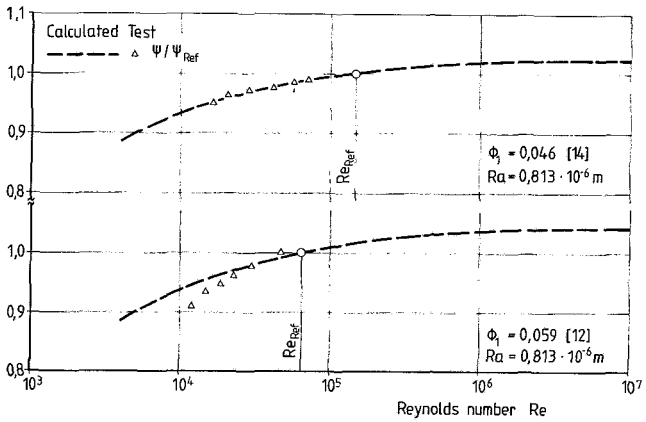


Fig. 22 Comparison of calculated results with test values of Heidelberg [12] and Weigel [14]

The conversion of measured process stage characteristics from test to specified Reynolds numbers can be conducted with the method described in the paper given the prerequisite that all stages are properly matched together. In addition, the acceptance test has to be conducted in strict accordance with the other allowable deviations given in the test codes (e.g., ASME PTC-10 Class II or Class III). Under these conditions the conversion of the test results should produce satisfactory correlation with the results to be expected under the specified conditions (see Figs. 12, 13, 15, 16). If the decisive similarity parameters (e.g., volume ratios, Mach numbers) cannot be maintained during the test, a detailed analysis of the measured process stage performance map is necessary with the aid of the individual stage characteristics, as has also been mentioned by Sapiro. This method has, for example, been applied to the ultra-high-pressure compressor (Fig. 17) because, during the tests, the volume ratios could not be adequately maintained in the inlet pressure range 1 bar $\leq p_1 \leq$ 400 bar.

Downloaded 01 Jun 2010 to 171.66.16.70. Redistribution subject to ASME license or copyright; see http://www.asme.org/terms/Terms_Use.cfm

An Investigation of the Flow Characteristics and of Losses in Radial Nozzle Cascades

S. G. R. Hashemi
Graduate Student,
Lehigh University,
Bethlehem, Pa.

R. J. Lemak
Senior Aerodynamic Design Engineer,
Air Products and Chemicals, Inc.
Mem. ASME

J. A. Owczarek
Professor,
Department of Mechanical Engineering and Mechanics,
Lehigh University,
Bethlehem, Pa.
Mem. ASME

A study was made of the flow in radial nozzle cascades using an air test rig and a water test rig. In the air test rig, three cobra probes were used in circumferential and spanwise traverses to determine the total pressure variations in the flow field at three radii downstream of the nozzles at which static pressure was also measured. The tests were made on two sets of nozzle blades having heights of 0.148 in. (0.376 cm) and 0.200 in. (0.508 cm), at trailing edge angles (measured from circumferential direction) of 15, 20, and 25 deg, and at two flow Mach numbers of approximately 0.2 and 0.35. The test results presented in this paper, in the form of loss coefficients and flow angles, were flow-weighted and averaged. Flow visualization in the air test rig was made on the walls bounding the nozzle blades using the graphite power-oil mixture technique. Additional tests were made on the water test rig using dye injection technique. Photographs were obtained showing clearly formation of secondary flow around each nozzle blade in the form of the leading edge vortex. The test results confirm the existence of the leading edge vortices reported peviously, and extend their study to the radial nozzle cascades.

Introduction

The major losses in radial turbines can be divided into nozzle passage loss, rotor incidence loss, rotor passage loss, rotor discharge loss, and wheel disk friction loss. The purpose of this investigation was to study the nozzle passage loss and the flow angle variation downstream of a typical cascade of radial nozzle blades used in industrial turbines. The objective was also to study the secondary flow pattern around the nozzles and in the vaneless space following them. The tests were made on an air rig and on a water rig.

Compared to our understanding of the flow through nozzles of axial cascades, little is known on the flow through radial nozzle cascades. In 1952, Balje made an attempt to calculate the nozzle loss using friction coefficient for a flat plate in a paper discussing a method of computing performance characteristics of radial-inflow turbines [1]. In 1960, Mizumachi presented results of a detailed experimental and analytical study of flow in radial-inflow turbines [2]. His tests on the flow in the nozzles were made in an air test rig which had an inlet scroll leading to a radial-inflow nozzle cascade. This cascade was followed by another radial cascade of blades whose purpose was to remove most of the swirl from the flow. This second cascade was followed by a flow straightener located in an axial exit duct. The rig was so designed that it permitted direct measurement of the angular momentum of the air leaving the nozzle. The nozzle flow exit angle was determined from the flow rate, calculated nozzle exit velocity, and the angular momentum of the air. Six straight nozzle cascades having 16 or 20 blades were tested. (Some test results on a special curved nozzle cascade were also reported.) The nozzles had a height, H, of 26 mm and a chord, c, of 67.5 mm. Thus their aspect ratio $H/c = 0.385$. The trailing edge radii of the nozzles were in the range of 135 to 144.2 mm, and the throat widths were in the 7.30 to 15.09 mm range.

Mizumachi's test results indicate that the nozzle exit flow angles, θ_{TE}, can be determined from equation

$$\theta_{TE} = 0.92 \sin^{-1}(t/s) \quad (1)$$

where t denotes the throat width, and s represents the pitch of a two-dimensional axial nozzle cascade obtained by transformation of the nozzle tested. The range of the angle $\sin^{-1}(t/s)$ of the nozzles tested was 5.8 to 15.8 deg. The nozzle total loss coefficient, ζ, which includes the end wall, profile friction, and the secondary flow losses as well as the scroll loss, was found to decrease from about 0.12 to 0.07 as the Reynolds number based on chord and nozzle exit velocity, Re_c, increased from 1.5×10^5 to 4×10^5. (This corresponds to the range of the Reynolds number based on nozzle height of 5.8×10^4 to 1.5×10^5.) The only exception was a nozzle cascade having very small trailing edge angle, $\sin^{-1}(t/s) = 5.8$ deg, for which the loss coefficient ζ was about 0.15 in the Reynolds number range $2.5 \times 10^5 \leq Re_c \leq 5 \times 10^5$. It dropped to 0.11 in the range $5 \times 10^5 \leq Re_c \leq 6 \times 10^5$.

Hiett and Johnston, in 1963, reported on tests run on three radial-inflow air turbines whose tip widths were 3/16 in. (4.76 mm), 5/16 in. (7.94 mm), and 1/2 in. (12.7 mm) [3]. There

Contributed by the Gas Turbine Division of THE AMERICAN SOCIETY OF MECHANICAL ENGINEERS and presented at the 28th International Gas Turbine Conference and Exhibit, Phoenix, Arizona, March 27-31, 1983. Manuscript received at ASME Headquarters December 27, 1982. Paper No. 83-GT-126.

Copyright © 1984 by ASME
Downloaded 01 Jun 2010 to 171.66.16.70. Redistribution subject to ASME license or copyright; see http://www.asme.org/terms/Terms_Use.cfm

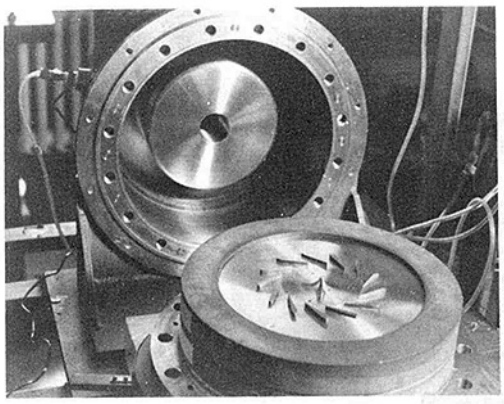


Fig. 1 View of opened air test rig showing adjustable nozzle blades attached to probe holder walls, shroud wall, and inlet collector

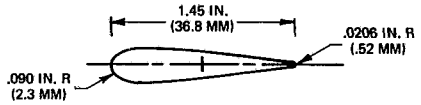


Fig. 2 Nozzle blade used in tests

were 17 blades having aspect ratios of 0.38, 0.24, and 0.14. The blade trailing edge radius was, approximately, 5.5 in. (140 mm) with a trailing edge pitch to chord ratio of 0.75. The nozzle trailing edge angle could be set at 10, 20, and 30 deg. The flow angles from the nozzles were obtained by calculation of the area requied to satisfy the measured mass flow rate and the temperature and total and static pressures in the air stream at the nozzle outlet measuring plane. In order to investigate the effect of incidence angle on nozzle performance, two tests were run with the inlet scroll of one turbine and with another turbine wheel. The Reynolds number based on the flow speed at nozzle exit and on the turbine tip widths was in the range of 0.75×10^5 to 2.0×10^5 depending on the width. The Mach number at nozzle exits was 0.3. The results indicated that the nozzle pressure loss coefficient, which was in the range of 0.03 to 0.07, is dependent on the incidence angle to the cascade and on the nozzle trailing edge angle. The inlet scrolls, which may be responsible for the incidence effects, were found to produce losses of the same magnitude as the nozzles. The flow angles 0.5 in. (12.7 mm) downstream of the nozzles were found to be 1.3 to 3.1 deg larger than the nozzle trailing edge angles.

Hiett and Johnston concluded that the flow angles at nozzle exit corresponded closely to those obtained from the sine rule of a transformed two-dimensional cascade for the 20 deg and 30 deg nozzle trailing edge angles. In addition, they concluded from the radial turbine performance results that for small trailing edge angles the sine rule can be used with acceptable accuracy for radial nozzles without a transformation.

In 1966, Rodgers [4] gave the following equation for the total nozzle loss coefficient at small incidence angles for $1.0 > r/r_{TE} > 0.91$:

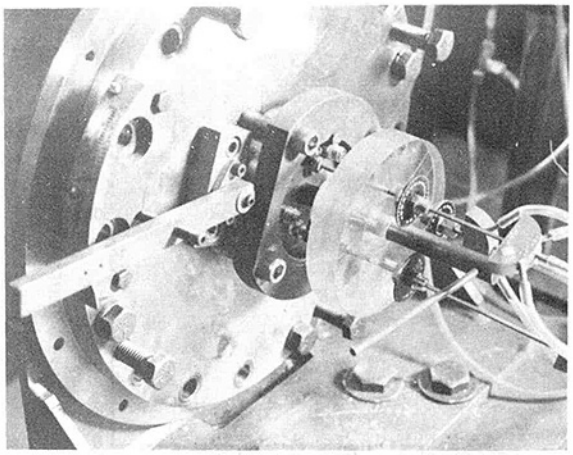


Fig. 3 Front view of air test rig showing center body, pressure probes, and actuator arm

$$\zeta_N = \frac{0.05}{(\mathrm{Re}_H)^{0.2}}\left[\frac{3\cot\alpha}{s/c} + \frac{s\sin\alpha}{H}\right] \tag{2}$$

where α denotes the nozzle blade angle, the nozzle pitch, s, corresponds to the nozzle throat diameter, and the Reynolds number is based on the nozzle height and exit velocity.

Benson and Jackson [5] in 1973 reported on studies of flow in the interspace between nozzles and rotors of a radial-inflow water turbine model. The flow was observed by photographing the paths of polystyrene particles having unit specific gravity. They found that the turbine rotor speed, in addition to the flow rate, has an effect on the flow angle at nozzle exit. Their tests have shown that the flow angle downstream of flat, straight nozzle blades having trailing edge angle of 15.4 deg in general at first decreased with decreasing radius and subsequently started to increase. At a radius ratio rl/r_{TE} of 0.95 the flow angle was, depending on the test condition, between 43 deg and 30 deg. It remained approximately constant in the radius ratio range of about 0.88 to 0.75. Subsequently, it started to increase.

In 1976 Khalil, Tabakoff, and Hamed reported on their experimental and theoretical studies of losses in nozzles of radial-inflow turbines [6]. The experiments were made on an air test rig having relatively thin, long, curved nozzle blades. The results are shown in the form of total pressure, Mach number, and flow angle maps at the inlet and exit of the nozzle cascade for one test condition. The analytical predictions are presented in the form of graphs showing the effect on the total nozzle loss coefficient of the flow angle, Mach number, nozzle blade height, and the boundary layer profile parameters. The characteristics of the skewed end wall boundary layers were determined using a mean loading between the suction and pressure nozzle sufaces. Although their analytical model does not recognize the existence of the leading edge vortices it comes quite close (to within 20 percent) in predicting the nozzle total pressure loss coefficient for two flow rates.

Nomenclature

c = blade chord
C = flow speed
H = blade height
r = radius
Re = Reynolds number
s = pitch of blades at trailing edge radius
t = throat width
α = nozzle angle measured from tangential direction
ζ = nozzle loss coefficient $[=(C_{2,\mathrm{is}}^2 - C_2^2)/C_2^2]$
θ = flow angle measured from tangential direction

Subscripts

c = blade chord
H = blade height
is = isentropic condition
IN = inlet
M = result based on mass flow rate
r = radial component
SUP = supply conditions
TE = trailing edge
θ = tangential component
2 = nozzle exit conditions
2D = transformed two-dimensional axial cascade

Downloaded 01 Jun 2010 to 171.66.16.70. Redistribution subject to ASME license or copyright; see http://www.asme.org/terms/Terms_Use.cfm

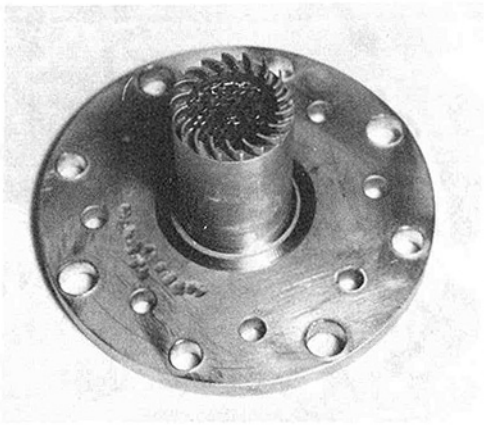


Fig. 4 Cascade of vanes for removal of swirl and flow straightener

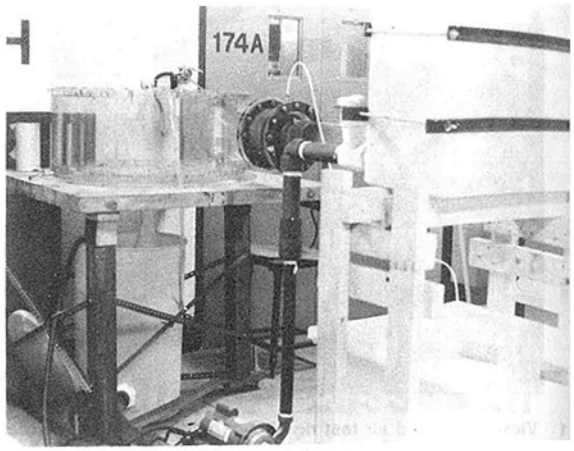


Fig. 5 View of water test rig

In 1980, Fairbanks presented results of experiments and analysis of the deviation angles at the exit of radial nozzle cascades [7]. In the tests, a turbocharger rig was used with a vaneless dummy replacing the rotor. The nozzles were straight with very thin trailing edges. Their apsect ratio $H/c \approx 0.26$. The flow angle at the exit from the nozzles was determined using total pressure probes located at various angles. The mean flow angle at nozzle exit was found to be 30 deg for the nozzle trailing edge angle of 27 deg. The mass-flow averaged nozzle total loss coefficient ζ ranged from 0.033 at the lowest mass flow rate to 0.0414 at the highest mass flow rate. No values of the Reynolds number are given.

This investigation is concerned with the flow through adjustable radial nozzle cascades of low aspect ratio (H/c = 0.102 and 0.138) tested at various trailing edge angles.

Description of the Test Rigs

Air Test Rig. The air test rig, designed and built by the Cryogenic Machinery Department of the Air Products and Chemicals Inc., consisted of a radial cascade of 13 straight nozzle blades spaced uniformly on a radius in a space formed between two parallel flat walls, as shown in Fig. 1. Inlet to the cascade was through a large annular, constant cross-sectional area collector. A simple, straight nozzle blade profile, shown in Fig. 2, was chosen for the cascade, of the type used in many current industrial radial-inflow tubines. Two sets of interchangeable blades of chord length 1.45 in. (36.83 mm) and heights of 0.148 in. (3.76 mm) and 0.200 in. (5.08 mm) were used. Thus the aspect ratios H/c of the nozzles used were 0.102 and 0.138. The ratio of the pitch at the trailing edge to the chord, s/c, was about 0.62. The axes of rotation, located half-way along the lengths of the blades, were on a radius of 2.25 in. (57.15 mm). The blades, which were in contact with the bounding walls, could be backed away from the shroud wall and have their angles adjusted with the aid of an actuator arm. At the exit of the test rig a 6-in. (152.4-mm) flexible duct was provided, discharging to the atmosphere.

A center body located immediately downstream of the nozzle cascade, which could be rotated, housed three cobra total pressure probes and three static pressure wall taps. The probes and the taps were at the radii of 1.44 in. (36.6 mm), 1.28 in. (32.5 mm), and 1.03 in. (26.2 mm). The total pressure probes could themselves be rotated and, by rotation of the center body, circumferential traverses could be made downstream of the vanes. In addition, the total pressure probes could be moved in and out to various spanwise locations in the space between the shroud and the probe-holder walls. Small protractors were provided on each probe accurate to ± 1 deg. The diameter of the tubes forming the cobra probes was 0.04 in. (1.06 mm); as a result, probe interference effect on the total pressure readings was very small. Figure 3 shows the total pressure probes mounted in the center body, and the actuator arm used to set the nozzle angles. All pressures, including the differences between the supply pressure and the total pressures, were measured using a manometer bank.

Dry, filtered air was supplied to the test apparatus by two reciprocating compressors each with a maximum delivery pressure of 110 psig (757 kPa) and a capacity of 500 scfm (0.236 m^3/s). An upstream pressure regulator was used to provide a controllable constant pressure at the inlet to the cascade.

Appearance of very loud high-pitch noise at moderate supply pressures necessitated addition of a set of vanes downstream of the nozzle cascade. These vanes, whose purpose was to remove most of the swirl from the flow were placed, together with a flow straightener, in the exit opening in the shroud wall. They are shown in Fig. 4. No meaningful test data could be collected when the loud noise, or "vortex whistle," was present.

The flow rate through the nozzle cascade was measured using an ASME flanged tap, square-edged orifice located in the inlet piping. The pressure drop across the orifice was measured with the aid of a water manometer. The air temperature was measured with thermocouples.

Water Test Rig. A water test rig, 2.75 times larger than the air test rig, was built out of clear plastic to allow visualization of the flow field and to provide a check on the flow angles. The length of the nozzles was 4.0 in. (101.6 mm). Their height was 0.55 in. (13.97 mm), and their trailing edge angle was 28 deg. A photograph of this rig is shown in Fig. 5.

Water at ambient temperature was pumped to an overflow tank from which it entered the test rig through a duct of progressively increasing cross-sectional area provided with flow straighteners. After flowing through the radial nozzle cascade, the water was collected in a tank supplying the pump. Flow visualization was accomplished using the dye injection technique. The dye velocity was close to that of the flowing water. This was accomplished by adjustment of the height of the dye dispenser. In the tests whose purpose was to determine the flow angle downstream of the nozzle cascade, the dye injector was placed between the nozzles at midplane between the bounding walls. In the visualization tests of the leading edge vortex, the dye injector was touching either the top or the bottom wall bounding the nozzles and was placed upstream of the blades.

Test Results

The tests in the air rig were made for the two nozzle blade

Downloaded 01 Jun 2010 to 171.66.16.70. Redistribution subject to ASME license or copyright; see http://www.asme.org/terms/Terms_Use.cfm

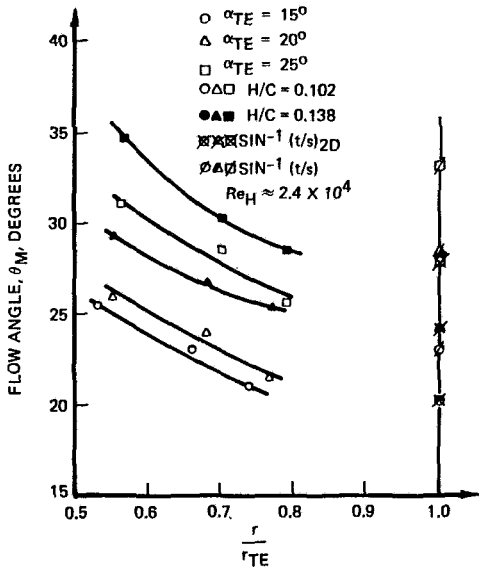


Fig. 6 Variation of the flow angle with radius ratio for the low pressure test

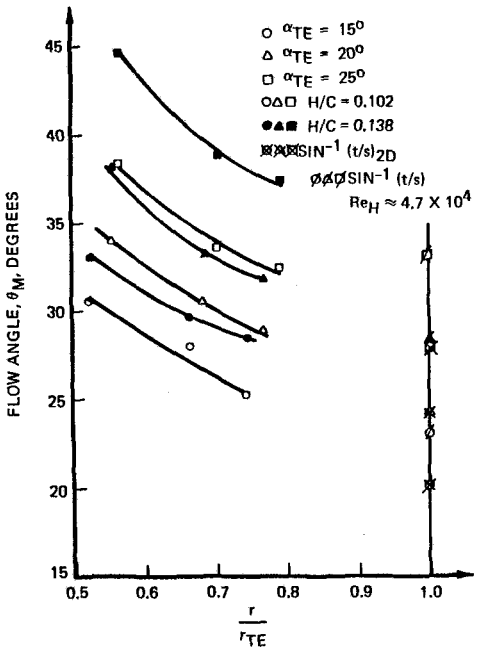


Fig. 7 Variation of the flow angle with radius ratio for the high pressure test

sets of different height (0.148 in. (3.76 mm) and 0.200 in. (5.08 mm)) at three nozzle trailing edge angles of 15, 20, and 25 deg, and two supply pressures of 9.3 and 20.0 in. (236 and 508 mm) of mercury. These conditions corresponded to Mach numbers at nozzle exits of, approximately, 0.20 and 0.34 for the smaller nozzle height and 0.14 and 0.24 for the larger nozzle height. Each probe reading was made at eight evenly spaced angular positions of the center body covering 40-deg arcs. In addition, for each center body position, readings were taken at six locations in the spanwise-direction between the probe-holder and shroud walls. Subsequently, the results were flow-weighted. This way average values of the flow speed, Mach number, and total pressure at each probe radius were determined.

The tests at the lower supply pressure were made without the swirl-removing vanes shown in Fig. 4, but only with a flow

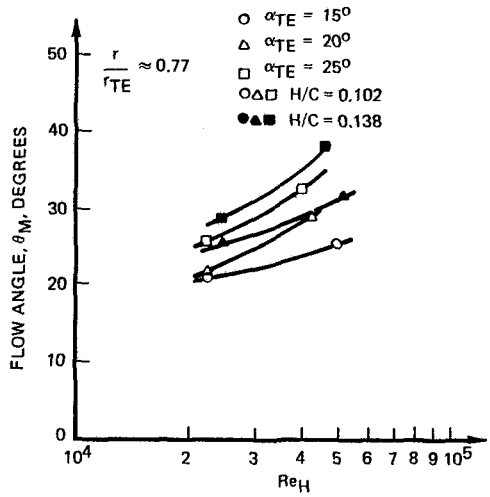


Fig. 8 Variation of the flow angle with the Reynolds number Re_H for $r/r_{TE} \approx 0.77$

straightener and a screen placed in the shroud exit. At that pressure, however, no tests could be run at nozzle angles smaller than 15 deg because of appearance of a high-pitch, high-intensity noise. This phenomenon, known as the "vortex whistle," is discussed in recent publications by M. Kurosaka ([8] and [9]). When the noise was present, the total pressure reading of the probes was higher than the supply pressure. (At a supply gage pressure of 30 in. (762 mm) of mercury, this pressure difference was about 6 in. (152 mm) of mercury.) To the writers' knowledge, this has never been reported previously. The measured noise frequency was about 6500 Hz. The highest supply gage pressure at which the noise was absent, with the swirl-removing vanes and flow straightener in place was about 22 in. (559 mm) of mercury for the nozzle angle of 15 deg. It was the appearance of this noise-producing phenomenon that put a limit on the flow Mach number and the lowest nozzle angle at which tests could be run.

Flow Angles. At first it was thought that the flow angles could be measured using cobra probes by introducing a correction for the measured radial static pressure variation and for the, also measured, dependency of the probe side holes pressure readings on the flow angle. This approach, however, proved to be unsuccessful.

As a result, it was decided to determine flow angles at the radii corresponding to the probe locations using the mass flow rates from the orifice meter and the flow-weighted average flow velocities [10]. Figures 6 and 7 show the variation of the average flow angle determined this way with the radius ratio r/r_{TE}. The results show that the average flow angle in the vaneless space increases as the radius decreases from that of the first probe to that of the third probe. In addition, they show that the average flow angles are higher for the nozzle height of 0.200 in. (5.08 mm) than for 0.148 in. (3.76 mm). The flow angles for $\alpha_{TE} = 15$ deg are smaller than those reported by Benson and Jackson for their nozzles. Indicated in Figs. 6 and 7 are the trailing edge angles determined for transformed two-dimensional axial cascades corresponding to the nozzles used, and for not transformed, radial nozzles using the sine rule

$$\theta = \sin^{-1}(s/t) \tag{3}$$

The results show that at $Re_H \approx 2.4 \times 10^4$ corresponding to the lower supply pressure and the larger aspect ratio ($H/c = 0.138$) the sine rule applied to a transformed two-dimensional cascade gives a reasonable estimate of the average nozzle exit flow angle. The sine rule applied to the radial cascade gives reasonably nozzle exit flow angle estimate at the higher

Downloaded 01 Jun 2010 to 171.66.16.70. Redistribution subject to ASME license or copyright; see http://www.asme.org/terms/Terms_Use.cfm

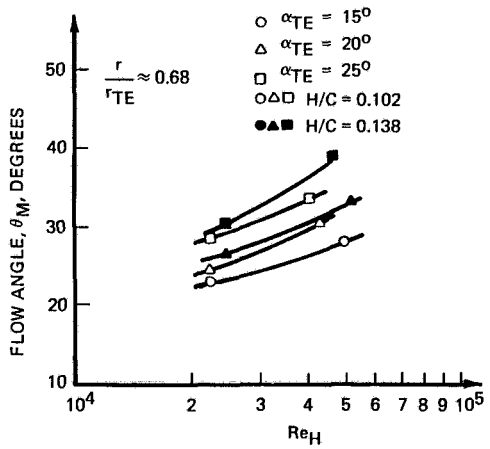


Fig. 9 Variation of the flow angle with the Reynolds number Re_H for $r/r_{TE} \approx 0.68$

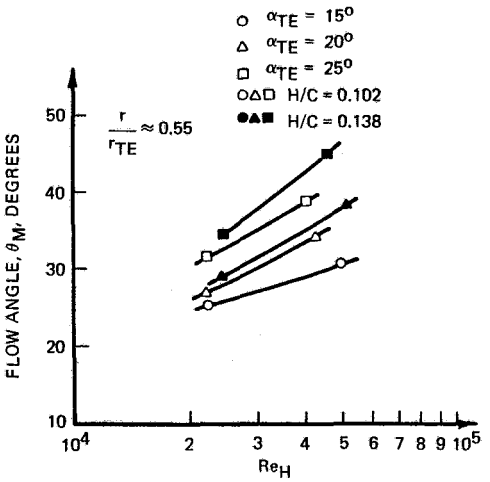


Fig. 10 Variation of the flow angle with the Reynolds number Re_H for $r/r_{TE} \approx 0.55$

Reynolds number ($Re_H \approx 4.7 \times 10^4$). The (extrapolated) nozzle exit flow angles are larger than those reported by Mizumachi. They agree with Mizumachi's value for the trailing edge angle, as given by equation (1), only for $Re_H \approx 2.4 \times 10^4$, $\alpha_{TE} = 15$ deg, and aspect ratio $H/c = 0.102$. The values of the average nozzle exit flow angles obtained by extrapolation of the flow angles in the vaneless space, correspond to nozzles having zero trailing edge thickness. The actual nozzle exit angles should be larger.

The flow angles shown in Figs. 6 and 7 have been replotted in Figs. 8, 9, and 10 as functions of the Reynolds number based on the blade height and nozzle exit velocity for three radii corresponding to the probe locations. (The radius ratios r/r_{TE} for these locations were, approximately, 0.77, 0.68, and 0.55 for the three nozzle angles investigated.) The results show that the flow angle in the vaneless space downstream of the nozzles increases as the Reynolds number increases. This indicates that, in the range tested, as the Reynolds number increases the effect of the radial pressure gradient on the flow also increases.

The flow angle was also determined by dye injection in midposition between bounding walls on the water test rig. The nozzle blade aspect ratio was 0.138, the nozzle trailing edge angle was 28 deg and the Reynolds number $Re_H = 1.4 \times 10^4$. The flow angle at the nozzle exit and at the radii corresponding to the three probe locations in the air test rig was about 31 deg. This midplane flow angle should be somewhat smaller than the average flow angle because, as a

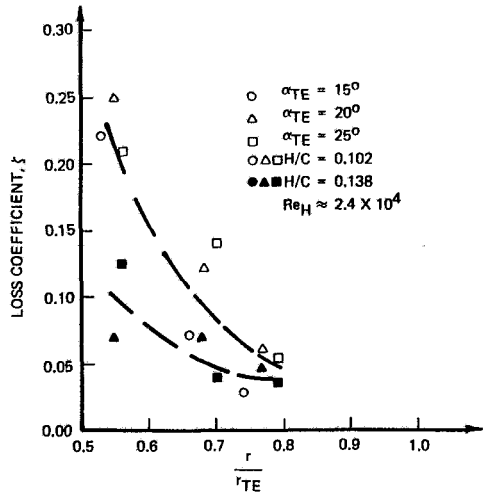


Fig. 11 Variation of the loss coefficient ζ with radius ratio for the low pressure test

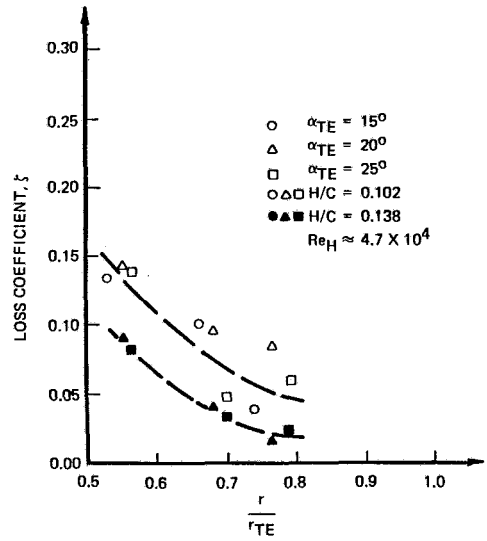


Fig. 12 Variation of the loss coefficient ζ with radius ratio for the high pressure test

result of the radial pressure gradient, the flow angle in the boundary layer at the bounding walls is larger. (Graphite powder and oil flow visualization studies showed that at the walls this angle was close to 46 deg at probe No. 2 location for the nozzle angle of 15 deg.) The values of the flow angle at the trailing edge radius determined from the sine rule was 30.7 deg for a transformed two-dimensional cascade, and 35 deg for a nontransformed cascade. The water-rig result is in reasonable agreement with the flow angle shown in Fig. 6 for $\alpha_{TE} = 25$ deg and $H/c = 0.138$.

Loss Coefficient. Figures 11 and 12 show variation of the nozzle (plus vaneless space) loss coefficient, ζ, with the radius ratio r/r_{TE} for the low pressure and the high pressure test, respectively. The results show that, as expected, the loss coefficient increases as the radius ratio decreases. It is higher for the low-aspect ratio nozzles than for the high-aspect ratio nozzles. The effect of increasing the nozzle trailing edge radius with decreasing exit angle is clearly visible.

Figures 13, 14, and 15 show variations of the nozzle (plus vaneless space) loss coefficient, ζ, with the Reynolds number Re_H corresponding to the three radial positions of the probes. The loss coefficient is, in general, found to decrease with increasing Reynolds number, being much higher for the lower

Downloaded 01 Jun 2010 to 171.66.16.70. Redistribution subject to ASME license or copyright; see http://www.asme.org/terms/Terms_Use.cfm

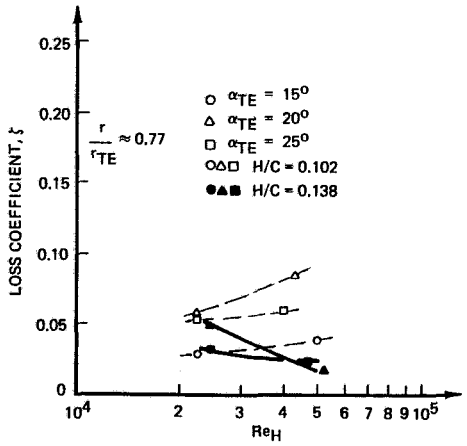


Fig. 13 Variation of the loss coefficient ζ with the Reynolds number Re_H for $r/r_{TE} \approx 0.77$

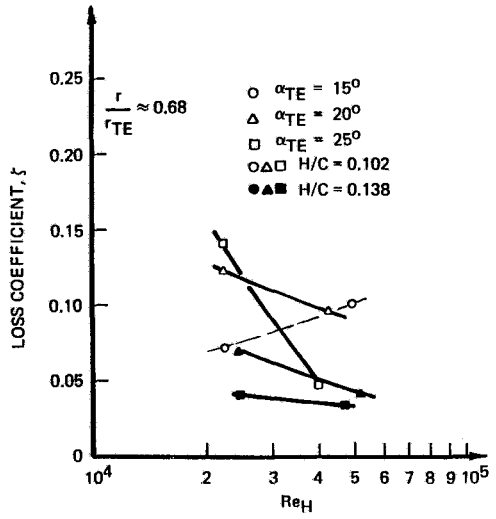


Fig. 14 Variation of the loss coefficient ζ with the Reynolds number Re_H for $r/r_{TE} \approx 0.68$

aspect ratio nozzles than for the higher aspect ratio nozzles. In the nozzle angle range investigated (α_{TE} = 15 to 25 deg), the dependency of the loss coefficient on the nozzle angle does not show a well-defined trend.

The loss coefficients shown in Fig. 13 are lower than those reported by Mizumachi, although they include part of the vaneless space loss and correspond to somewhat lower Reynolds numbers Re_H. This is surprising because, in addition, the aspect ratio of the nozzles used in these tests was much smaller than the aspect ratio of the nozzles used by Mizumachi, and the trailing edge thickness was larger. Although in these tests the supply pressure was measured in a large, low-velocity collector which caused small losses, as will be shown in the section on flow visualization, some of our nozzles had incoming flow at large incidence angles.

The nozzle loss correlation of Rodgers, given by equation (2), also predicts higher losses than those determined in this investigation for r/r_{TE} = 0.77 although this correlation applies only to the vicinity of the nozzle trailing edge radius ($1.0 > r/r_{TE} > 0.91$). For $Re_H = 2.5 \times 10^4$, s/c = 0.625, and s/H = 4.5, and α_{TE} = 20 deg, $\zeta_{Rodgers}$ = 0.097 while from Fig. 13 ζ = 0.05.

No comparisons were made with the predictions of various effects on the loss coefficient given by Khalil, Tabahoff, and Hamed because their graphs apply to high Mach number flows (M = 0.8) and larger radius ratio.

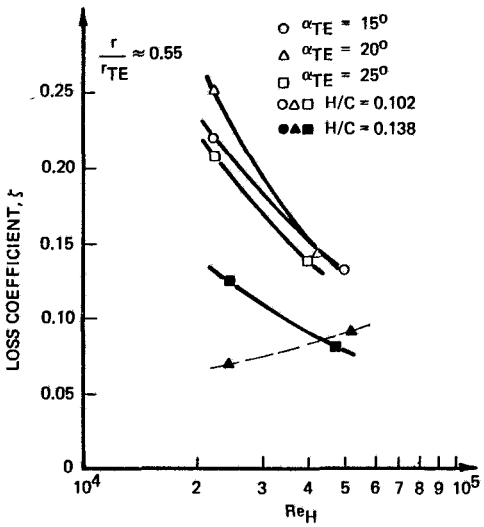


Fig. 15 Variation of the loss coefficient ζ with the Reynolds number Re_H for $r/r_{TE} \approx 0.55$

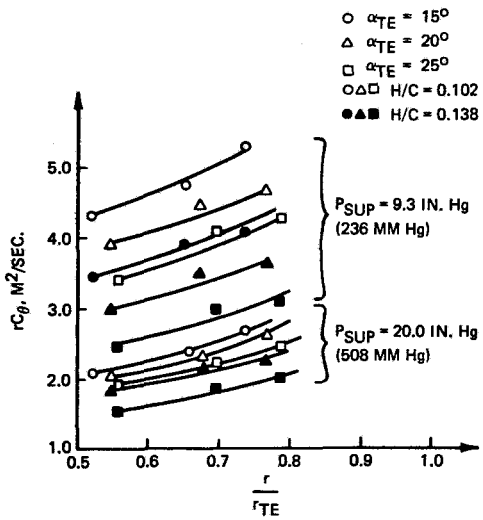


Fig. 16 Variation of rC_θ with radius ratio

Figure 16 shows variation of the specific angular momentum, rC_θ, with radius for both supply pressures used. The results indicate that, for the conditions of the test, the variaton of the angular momentum ratio with radius can be approximated by equation

$$\frac{r_1 C_{\theta 1}}{r_2 C_{\theta 2}} = \left(\frac{r_1}{r_2}\right)^{0.7} \tag{5}$$

Uncertainties. The values of the average flow angles have uncertainties of ± 0.017 rad = ± 0.97 deg. The uncertainty of the loss coefficient ζ for the low pressure test and 0.138 aspect ratio nozzle having 20 deg setting angle was ± 0.005. For the high pressure test and 0.102 aspect ratio nozzle having 20 deg setting angle, the uncertainty of ζ was determined to be ± 0.002.

The fact that the uncertainty values are low while the test points exhibit noticeable scatter can be explained by large variation of the incidence angles from nozzle to nozzle while the circumferential traverses were made only over 40 deg arcs.

Secondary Flow Visualization

A series of flow visualization tests were run on the air and water rigs. In the air rig, drawing paper was attached to the

Downloaded 01 Jun 2010 to 171.66.16.70. Redistribution subject to ASME license or copyright; see http://www.asme.org/terms/Terms_Use.cfm

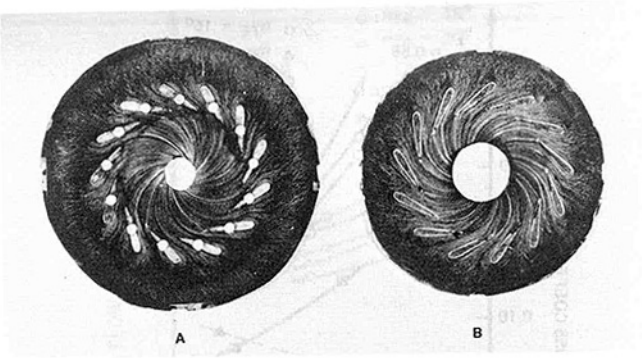


Fig. 17 Flow patterns in the air test rig: nozzle trailing edge angle 15 deg, nozzle height 0.20 in. (5.08 mm), supply pressure 9.3 in. (236 mm) of mercury; A—probe holder wall; B—shroud wall



Fig. 18 Flow pattern on the shroud wall of the air test rig: nozzle trailing edge angle 10 deg, nozzle height 0.20 in. (5.08 mm), supply pressure 9.3 in. (236 mm) of mercury

shroud and the probe holder walls and covered with a mixture of oil and fine graphite powder. Subsequently, air was allowed to flow through the nozzle cascade for five minutes. Then, the paper was removed and photographed. In the water test rig, dye was injected to visualize the flow. Typical results are shown in Figs. 17 and 22. The flow patterns show clearly the secondary flows in form of leading edge vortices, and the direction of the incoming flow to the cascade (in the oil and graphite air test patterns).

The leading edge vortices in *axial flow cascades* received attention since 1972 [11]. In 1977, Langston, Nice, and Hooper [12], and Marchal and Sieverding, [13], reported results of extensive investigations of the leading edge vortices in such cascades. Additional information on them can be found in references [14] and [15]. The common description of this phenomenon, which corresponds to the horse-shoe vortex in a flow along a wall past a cylinder, refers to the two legs of the vortex. One leg wraps itself along the suction side of the blade and rotates in direction opposite to that of the secondary flow generated by the cross-channel pressure gradient, or the passage vortex. It is referred to as the counter vortex. Its size decreases as it moves into the blade passage, while at the same time its separation line moves toward midspan of the blade. The other leg, referred to as the pressure side leg, merges and becomes part of the passage vortex and meets the suction surface of the adjacent blade. Its separation line usually moves a little away from the end wall up the suction surface of the blade. The flow angle at cascade exit is strongly affected by the passage vortex.

Figures 17 to 22 show the flow patterns of the leading edge vortices in the *radial inflow cascade* tested. The wall traces show that the inlet angle to the cascade varied circumferentially and, as a result, some leading edge vortex traces differed considerably from each other. The photographs show that in radial inflow cascades with incoming flow direction varying from radial to that of zero incidence angle, as a result of a strong radial pressure gradient, the passage vortices are either very weak or entirely absent and the upstream-facing (pressure side) legs of the leading edge vortices in general do not meet the suction sides of the adjacent blades.



Fig. 19 Flow pattern on the shroud wall of the air test rig: nozzle trailing edge angle 25 deg, nozzle height 0.148 in. (3.76 mm), supply pressure 9.3 in. (236 mm) of mercury

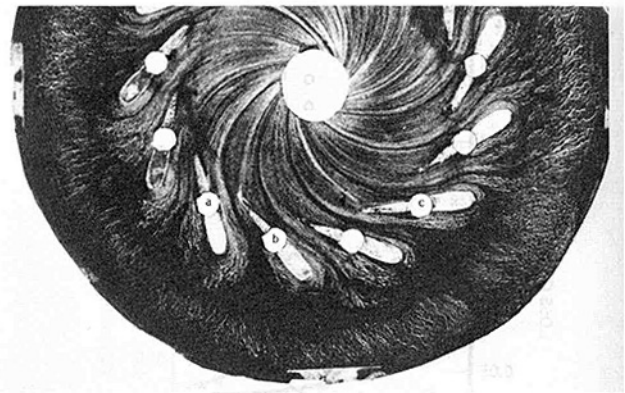


Fig. 20 Enlargement of the bottom part of Fig. 17(*A*)

Figure 18 shows clearly that the vortex legs forming on the suction (downstream-facing) side of the blades are swept by the radial pressure gradient away from the blades. At the same time the vortex legs forming on the pressure (upstream-facing) side of the blades are pressed against the blade side walls and leave the blades at the trailing edges. Thus they form a spiral of well-defined traces (of counter-rotating vortices) which converge to the small exit radius. Their angle at $r/r_{TE} = 0.77$ is approximately 42 deg.

Figure 19 shows the leading edge vortex traces at relatively large nozzle angle ($\alpha_{TE} = 25$ deg). The flow angle at the walls is close to 48 deg at $r/r_{TE} = 0.77$. An unusual disturbance of the paths of the vortices in the vaneless space can be seen in the 270 to 360 deg quadrant.

Figure 20 shows enlargement of the bottom part of photograph A shown in Fig. 17. The flow patterns around blade *a* to which the incoming flow was almost radial, shows that at large incidence angles and relatively small trailing edge blade angles, the leading edge vortex is large with the pressure side (upstream-facing) leg being swept toward the trailing edge of the blade around which it forms, while the suction side (downstream-facing) leg at nozzle exit is located midway in the interblade space. The flow around blade *b* is at almost zero incidence. It produces a leading edge vortex whose both legs converge towards the sides of blade *b* at midchord

Downloaded 01 Jun 2010 to 171.66.16.70. Redistribution subject to ASME license or copyright; see http://www.asme.org/terms/Terms_Use.cfm

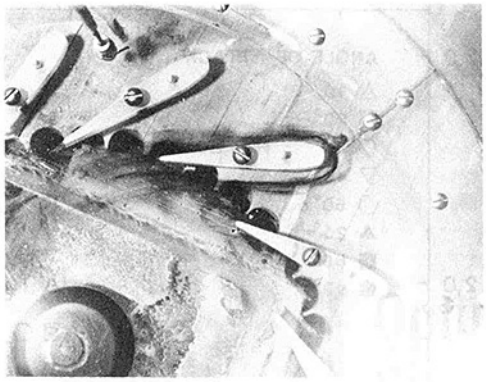


Fig. 21 Leading edge vortex in the water test rig

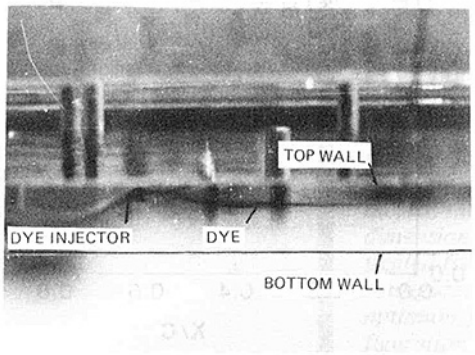


Fig. 22 Side view of the separation streamline of the upstream-facing leg of the leading edge vortex shown in Fig. 21

location. The vortex leg on the downstream-facing blade side is subsequently swept in the radial direction by the pressure gradient, while the vortex leg on the upstream-facing blade side stays attached up to the trailing edge. The flow around blade *c*, which is at an incidence angle somewhere between that of blades *a* and *b*, has a downstream-facing leg which wraps itself along the suction side of the blade before being deflected in the radial direction by the pressure gradient. Its upstream-facing (pressure side) leg is well separated from the adjacent blade. Figure 20 shows clearly that the shape of the leading edge vortices in a radial inflow cascade depends strongly on the incidence angle.

Figure 21 shows the leading edge vortex made visible by injection of dye at the top end wall in the water test rig. The blade corresponds to the blade shown in Fig. 17(B) whose trailing edge is at 90 deg location measured from the top. The shape and location of the vortex corresponds well to the oil and graphite wall traces. There is a back-flow of dye along the needle near the stagnation region indicating possible presence of more than one vortex filaments. Figure 22 shows separation line of the upstream-facing leg of the leading edge vortex shown in Fig. 21 which migrates from the vicinity of the end wall toward the midspan of the blade. Similar flow pattern in axial-flow cascades on the suction sides of blades was reported in references [12] and [13].

Conclusions

A study was made of the flow characteristics downstream of straight low-aspect ratio radial-inflow nozzle cascades (H/c = 0.102 and 0.138), having trailing edge angles of 15, 20, and 25 deg. The average flow angle was found to be higher for the higher aspect ratio nozzles than for the lower aspect ratio nozzles. In addition, in the range investigated, it was found to increase with increasing Reynolds number based on nozzle height, Re_H.

The sine rule applied to a transformed two-dimensional cascade corresponding to the cascade tested gave reasonable estimate of the average flow exit angle of nozzles having very thin trailing edges for $\mathrm{Re}_H \approx 2.4 \times 10^4$ and $H/c = 0.138$. When applied to the radial cascade, the sine rule gave reasonable estimate of the average exit flow angle of nozzles having very thin trailing edges at the higher Reynolds number, $\mathrm{Re}_H \approx 4.7 \times 10^4$ for both aspect ratios nozzles.

The nozzle (and vaneless space) loss coefficient was found, in general, to decrease with increasing Reynolds number Re_H, being much higher for the lower aspect ratio nozzles than for the higher aspect ratio nozzles. In the nozzle angle range investigated, the loss coefficient did not show a well-defined dependency on the nozzle angle.

The nozzle angle and loss results reported in this study are affected by the fact that the incidence angles varied from nozzle to nozzle while circumferential traverses were made over 40 deg arcs only.

The flow visualization study has shown that the shape of the leading edge vortex in a radial-inflow cascade depends strongly on the incidence angle of the incoming flow. The upstream-facing vortex leg, in general, does not meet the adjacent blade. Its separation line migrates toward the midspan of the blade. The downstream-facing vortex leg is swept by the radial pressure gradient in the radial direction away from the blade.

Acknowledgment

The writers express their gratitude to the Air Products and Chemicals, Inc. which supported this study through their research Contract No. 060-020-8.

References

1 Balje, O. E., "A Contribution to the Problem of Designing Radial Turbomachines," *Trans. ASME*, Vol. 74, May 1952, pp. 451–472.

2 Mizumachi, N., "A Study of Radial Gas Turbine," The University of Michigan, Translation IP-476, 1960.

3 Hiett, G. F., and Johnston, I. H., "Experiments Concerning the Aerodynamic Performance of Inward-Flow Radial Turbines," *Proceedings, Inst. of Mechanical Engineers*, Vol. 178, Part 3, I, 1963, pp. 29–42.

4 Rodgers, C., "Efficiency and Performance Characteristics of Radial Turbines," SAE paper No. 660754, 1966.

5 Benson, R. S., and Jackson, D. C., "Flow Studies in Radial Inflow Turbines Interspace Between Nozzles and Rotors," Inst. of Mech. Engrs., *Conference on Heat and Fluid Flow in Steam and Gas Turbine Plant*, 1973, pp. 213–223.

6 Khalil, I. B., Tabakoff, W., and Hamed, A., "Losses in Radial Inflow Turbines," ASME *Journal of Fluids Engineering*, Vol. 98, Sept. 1976, pp. 364–371.

7 Fairbanks, F., "The Determination of Deviation Angles at Exit From the Nozzles of an Inward Flow Radial Turbine," ASME paper 80-GT-147, 1980.

8 Kurosaka, M., "Vortex Whistle: An Unsteady Phenomenon in Swirling Flow and its Effect on Steady Flow Field," AIAA paper 81-0212, 1981.

9 Kurosaka, M., Chu, J. Q., and Goodman, J. R., "Ranque-Hilsch Effect Revisited: Temperature Separation Traced to Orderly Spinning Waves or 'Vortex Whistle'," AIAA paper 82-0952, 1982.

10 Hashemi, S. G. R., "An Investigation of Flow Charactersitics in Radial Nozzle Cascades," M.Sc. thesis, Lehigh University, Mechanical Engineering Department, 1983.

11 Belik, L., "Secondary Flow in Blade Cascade of Axial Turbomachines and the Possibility of Reducing its Unfavorable Effects," *Second International JSME Symposium, Fluid Machinery and Fluidics*, Tokyo, Sept. 1972, pp. 41–49.

12 Langston, L. S., Nice, M. L., and Hooper, R. M., "Three-Dimensional Flow Within a Turbine Cascade Passage," ASME JOURNAL OF ENGINEERING FOR POWER, Vol. 99, No. 1, Jan. 1977, pp. 21–28.

13 Marchal, P. L., and Sieverding, C. H., "Secondary Flows Within Turbomachinery Bladings," in *Secondary Flows in Turbomachines*, AGARD-CP-214, Paper 11, 1977.

14 Langston, L. S., "Crossflows in a Turbine Cascade Passage," ASME JOURNAL OF ENGINEERING FOR POWER, Vol. 102, Oct. 1980, pp. 866–874.

15 Gregory-Smith, D. G., "Secondary Flows and Losses in Axial Flow Turbines," ASME Paper 82-GT-19, 1982.

16 Benson, R. S., "A Review of Methods for Assessing Loss Coefficients in Radial Gas Turbines," *International Journal of Mechanical Sciences*, Vol. 12, 1970, pp. 905–932.

Downloaded 01 Jun 2010 to 171.66.16.70. Redistribution subject to ASME license or copyright; see http://www.asme.org/terms/Terms_Use.cfm

DISCUSSION

M. Kurosaka[1]. The authors' encounter with the "vortex whistle" appears to remind us, once again, that, whenever swirling in-flow is involved, one has to be always on the lookout for the possible contamination of flow field induced by these vigorous unsteady dynamic disturbances.

As reported in the authors' references [8, 9], in at least three instances of the radial flow test rigs known to the discusser, a loud screech sound, or the "vortex whistle," emerged when the swirl became sufficiently large; the frequency spectrum revealed the presence of spiky peaks of a pure tone and its harmonics, the frequency of which increased proportionately to swirl. As soon as the "vortex whistle" appeared, the time-averaged, steady flow became distorted: the swirl angle distribution became drastically different from the one before the emergence of the whistle. At the same time, the total pressure near the outer casing exceeded its value upstream of the vanes(!), in exactly the same manner as reported by the authors, and this was compensated by the decrease of total pressure near the inner casing. Furthermore, the total temperature became separated in the radial direction, with hotter air found near the outer casing and colder air found near the inner wall, a phenomenon evocative of the Ranque-Hilsch effect. The degree of temperature separation was such that, in one instance, the outer casing became noticeably warm to the touch, while icing was observed on the inner casing.

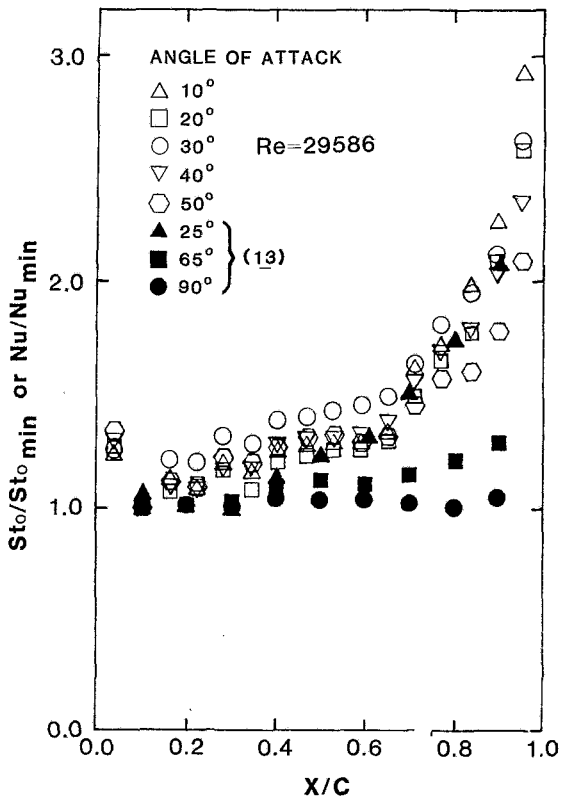
What is intriguing is the fact that once the vortex whistle is eliminated by the installation of acoustic suppressors, this distortion in the flow field disappears at once. This implies that the distortion in the steady flow is caused by none other than unsteady disturbances, through the mechanism of acoustic streaming. In fact, these observations led us to demonstrate ([17, 18] that the dominant cause of the Ranque-Hilsch effect, so far a little-understood phenomenon, is precisely this dimly foreseen mechanism of acoustic streaming.

To all of this may be added a caveat: some of the "steady" flow data taken in the presence of intense disturbances in swirling flows of gas turbines may be suspect – they may be highly contaminated by the unsteady disturbances, as found by the authors.

Parenthetically, the data showing the excess total pressure over its incoming value appear to have been measured also in [19]; although the author did not state any connection with the whistling sound and the subsequent discussions are not clear, the measurements taken downstream of vanes (Figure 26) unmistakably show a distribution similar to the one obtained in the presence of the vortex whistle.

Authors' Closure

The authors appreciate very much the comments of Professor Kurosaka on the "vortex whistle" phenomenon



and thank him for providing other examples of swirling flow test results in which an increase in the total pressure over that of the incoming flow was measured. In our tests, the acoustic streaming associated with this unsteady flow almost eliminated the leading edge vortices from the graphite powder-oil traces, and in one case it even tore the paper attached to the walls.

There is one possible explanation of the total pressure rise observed during the presence of the "vortex whistle" in our tests. In the exit pipe from our test rig, near the rig itself, we observed a high-frequency transient backflow caused by pressure falling below atmospheric. It appears possible, therefore, that at least in our tests, the observed total pressure increase was caused by the atmosphere doing work on the oscillating core flow at the exit from the test rig.

Additional References

17 Kurosaka, M., "Acoustic Streaming in Swirling Flow and the Ranque-Hilsch (Vortex-Tube) Effect," *Journal of Fluid Mechanics*, Vol. 124, 1982, pp. 139-172.

18 Kurosaka, M., Goodman, J. R., Kuroda, H., and Chu, J. Q., "An Interplay Between Acoustic Waves And Steady Vortical Flow," AIAA Paper 83-0740, 1983.

19 Beshoven, R. L., "An Investigation of Compressible Flows with Large Whirl Components," Aeronautical Engineers thesis, Naval Postgraduate School, 1967.

[1] Kurosaka, M., Professor, Department of Aerospace and Mechanical Engineering, The University of Tennessee Space Institute, Tullahoma, Tenn. 37388. Mem. ASME

Copyright © 1984 by ASME
Downloaded 01 Jun 2010 to 171.66.16.70. Redistribution subject to ASME license or copyright; see http://www.asme.org/terms/Terms_Use.cfm

Optimization of the Three-Dimensional Flow Path in the Scroll-Nozzle System of a Radial Inflow Turbine

E. A. Baskharone
Garrett Turbine Engine Company,
A Division of the Garrett Corporation,
Phoenix, Ariz. 85010
Mem. ASME

A three-dimensional inviscid flow analysis in the combined scroll-nozzle system of a radial inflow turbine is presented. The coupling of the two turbine components leads to a geometrically complicated, multiply-connected flow domain. Nevertheless, this coupling accounts for the mutual effects of both elements on the three-dimensional flow pattern throughout the entire system. Compressibility effects are treated for an accurate prediction of the nozzle performance. Different geometrical configurations of both the scroll passage and the nozzle region are investigated for optimum performance. The results corresponding to a sample scroll-nozzle configuration are verified by experimental measurements.

Introduction

Many radial turbines are designed with varying-area scrolls to provide uniform flow conditions through the nozzle channels and at the rotor tip station. The conventional approach has been to independently design the scroll and nozzle. In this paper, an approach is described in which the scroll and nozzle guide vane assembly is designed as one unit using a three-dimensional compressible flow analysis.

A moderate amount of experimental data concerning the radial turbine scroll and nozzle is found in the literature [1, 2]. In [1], extensive flow measurements in the scroll passage were reported. An equivalent set of experimental data for both the vaned and unvaned nozzle regions was presented by Khalil et al. [2]. In addition to the boundary layer characteristics across the nozzle, it was indicated that the losses are highly dependent on the vane loading and the flow exit angle. These two parameters can be obtained through the inviscid flow analysis presented here for a fairly accurate loss prediction in the nozzle region.

Early designs of radial turbines were based on simplified, one-dimensional flow models in the scroll and vaneless nozzle [3–6]. Later, a two-dimensional blade-to-blade flow analysis in the nozzle was presented [7], using the stream function formulation of Katsanis [8]. The cross flow in the scroll passage was also analyzed by Hamed, et al. [9] for different through-flow velocity profiles and scroll cross-section configurations. However, the accuracy of simulating the scroll flow in this manner is directly dependent on a prior knowledge of the scroll through-flow pattern to be introduced in the flow-governing equation as a source term.

Contributed by the Gas Turbine Division of THE AMERICAN SOCIETY OF MECHANICAL ENGINEERS and presented at the 28th International Gas Turbine Conference and Exhibit, Phoenix, Arizona, March 27–31, 1983. Manuscript received at ASME Headquarters, December 27, 1982. Paper No. 83-GT-127.

The first flow analysis of the combined scroll-nozzle assembly of a radial turbine was presented [10, 11] assuming an inviscid and incompressible flow field. Several geometrical details were not treated in this two-dimensional analysis such as the shape of the scroll cross-section and the nozzle end-walls. The results of this analysis showed that the scroll-nozzle coupling can lead to circumferentially nonuniform stator flow rates. The analysis was next extended to a three-dimensional flow solution in a strictly unvaned scroll-nozzle unit [12].

With the given geometry and operating conditions in the unvaned scroll study of [12], a maximum exit critical Mach number (V/a_{cr}) of as low as 0.445 was obtained. The entire flow field in this study was therefore incompressible for all practical purposes although the linearization approach for handling the flow compressibility was outlined in the same reference. The results of the present study, where an average exit Mach number of 0.986 was achieved, represent a numerical extension to those of [12]. The difference in the Mach number level between the two studies is partially due to the relatively large flow turning across the stator guide vanes as part of the solution domain in the present analysis.

Compared to the flow study of [12], the present study applies the concept of including the circulation as a field variable to the case where lifting bodies exist in the solution domain. This problem was handled by Baskharone et al. [11] except that the latter was a two-dimensional flow analysis compared to the current three-dimensional approach.

The flow analyses of [10–12] are considered significant contributions to the study of flow behavior in nonrotating components of radial turbines. A common factor in these references is the use of the finite-element method in solving the flow-governing equations. This method is particularly suitable for geometrically complicated solution domains. Another attractive feature of this method is the ease of in-

Copyright © 1984 by ASME
Downloaded 01 Jun 2010 to 171.66.16.70. Redistribution subject to ASME license or copyright; see http://www.asme.org/terms/Terms_Use.cfm

troducing natural boundary conditions [15], which is the case along solid boundaries in the present study.

In the present study, the three-dimensional inviscid flow in the vaned scroll-nozzle system of a radial turbine is analyzed using the finite-element method. The coupling of both turbine components in this manner leads to a geometrically complicated, multiply-connected flow domain. Nevertheless, this coupling accounts for the mutual effects of both elements on the three-dimensional flow pattern throughout the entire system. Compressibility effects are treated for an accurate prediction of the nozzle performance.

The current inviscid flow analysis provides the designer with a detailed picture of the flow behavior in the scroll and nozzle of a radial turbine on a first-order basis. The solution may also be used as a pressure solver for a Navier-Stokes solution using the equation-splitting technique of Dodge [13].

The analysis is applied to the scroll-nozzle assembly of a Garrett radial inflow turbine. Static pressure distributions which were measured in the scroll, are compared to the predictions. Performance variations are presented for variations in the scroll and nozzle geometries.

Analysis

Governing Equations. With the velocity potential ϕ as the primary field variable, the principle of mass conservation is expressed as follows.

$$\nabla \cdot (\rho \nabla \phi) = 0 \tag{1}$$

where the static density ρ is calculated using the isentropic flow relation

$$\rho = \rho_0 \left\{ 1 - \frac{\gamma - 1}{2} \left(\frac{\nabla \phi \cdot \nabla \phi}{a_0} \right)^2 \right\}^{1/(\gamma-1)} \tag{2}$$

In the present analysis, the quasi-harmonic equation (1) is linearized using a known density field, that may either be the result of a preceding iteration or an initial guess.

The iteration solution of equation (1) is generally represented by equation (3).

$$\nabla \cdot \{ \rho^{(n)} \nabla \phi^{(n+1)} \} = 0 \tag{3}$$

where the superscripts (n) and $(n+1)$ refer to the nth and $(n+1)$th iterations, respectively. The conservative form of equation (3) is preserved in the finite-element formulation for the numerical stability it offers.

Boundary Conditions. Both homogeneous and nonhomogeneous Neumann-type boundary conditions are associated with the velocity-potential formulation of the problem. A generalized boundary condition may be written as follows.

$$\mathbf{n} \cdot (\rho \nabla \phi) = f \tag{4}$$

where

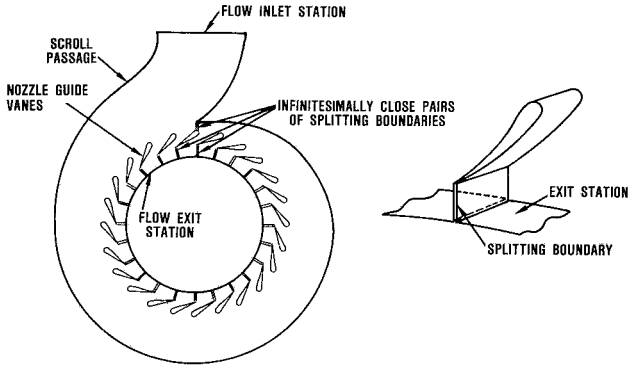


Fig. 1 Arrangement of splitting boundaries to convert the flow region to a simply-connected domain

$f = 0$ across a solid boundary, including the scroll wall and the vane surfaces;

$f = f_i$ the inlet mass flux at the scroll inlet station; and

$f = f_e$ the exit mass flux at the nozzle exit station (Fig. 1).

Knowledge of the turbine operating conditions leads to fixed values for both f_i and f_e. The general boundary condition represented by equation (4) is sufficient as long as the stator is not totally choked.

Domain Multiconnectivity

The inclusion of nozzle vanes in the flow region leads to a multiply-connected domain. A unique flow field in such a domain is attainable through a special procedure described by Baskharone, et al. [14] for a doubly-connected two-dimensional flow domain. A generalized form of this procedure is applied here by splitting the flow region at the tangential locations shown in Fig. 1. Each splitting boundary in this figure consists of a pair of fictitious infinitesimally-close planes. The derivatives of ϕ across each of these boundaries are continuous. However, a jump in ϕ across each boundary exists and represents the circulation around the nozzle vane. These discontinuities are recognized as discrete field variables to be determined in the finite-element solution, as described in [14].

Finite-Element Formulation

Figure 2 shows the finite-element discretization model used in the present analysis. This is an array of small nonoverlapping tetrahedral elements with different sizes to reflect an anticipated pattern of gradients in the flow region. In a typical element e, the potential is linearly interpolated as follows.

Nomenclature

a = local sonic speed (m/s)
N_i = element shape function associated with the ith corner node
$\mathbf{n}$ = local normal unit vector
R = gas constant (Joules/kg-K)
T = temperature (K)
V = velocity (m/s)
x, y, and z = Cartesian coordinates (m)
γ = ratio of specific heats
ρ = flow density (kg/m^3)
Ω = area (m^2)
τ = volume (m^3)
ϕ = velocity potential (m^2/s)
ϕ_i = value of ϕ at the ith nodal point

Subscripts

cr = refers to critical flow conditions
e = refers to the nozzle exit station
i = refers to the scroll inlet station
o = refers to stagnation conditions
r = refers to a radial velocity component

Superscripts

(e) = refers to a typical finite element
(n) = refers to the nth iteration

Downloaded 01 Jun 2010 to 171.66.16.70. Redistribution subject to ASME license or copyright; see http://www.asme.org/terms/Terms_Use.cfm

$$\phi^{(e)} = \sum_{i=1}^{4} N_i(x,y,z)\phi_i \tag{5}$$

where the summation extends over the four corner nodes of the element.

The substitution of equation (5) in the flow-governing equation (3) results in a residual which is made orthogonal to the shape functions N_i in accordance with Galerkin's principle [15]. This leads to the following set of equations corresponding to the typical element e.

$$\int_{\tau^{(e)}} \rho[\nabla N_i \cdot \nabla N_j]\phi_j \cdot d\tau = \int_{\Omega^{(e)}} N_i \rho[\mathbf{n} \cdot \nabla \phi] d\Omega,$$

$$i = 1,2,3,4$$

$$j = 1,2,3,4 \tag{6}$$

Summing up all element contributions at a typical node α shared by a total of E_α elements, the global form of the finite-element equation at this node assumes the following form.

$$\sum_{e=1}^{E_\alpha} \int_{\tau^{(e)}} \rho[\nabla N_i \cdot \nabla N_j]\phi_j d\tau = \sum_{e=1}^{E_\alpha} \int_{\Omega^{(e)}} N_i \rho[\mathbf{n} \cdot \nabla \phi] d\Omega \tag{7}$$

The boundary-condition term on the right-hand side of equation (7) is evaluated for nodes on the flow inlet and exit stations using the general expression of mass flux, equation (4).

Another set of finite-element equations is added to treat the domain multiconnectivity. In these equations, the discontinuities in ϕ across the splitting boundaries are introduced as nodeless degrees of freedom. The final form of these equations as well as a detailed derivation are found in [16].

Solution of the Finite-Element Equations

A linear system of algebraic equations is obtained upon the substitution of the density, ρ, from a known solution or an initial guess. The unknowns in this system are the nodal potential values as well as the potential jump across each splitting boundary in Fig. 1.

A modified version of the frontal equation solver by Hood [17] was used to invert the matrix of influence coefficients in each iteration. The modifications in Hood's procedure were made to allow the introduction of potential discontinuities across the splitting boundaries (Fig. 1) as nodeless degrees of freedom for a subgroup of elements in the finite-element model, as described in [16]. They also make it possible to define flow constraints in the global frame of reference. An example of such constraints in the present analysis is the continuity of mass flux across each of these boundaries. The density changes between iterations were damped using an under-relaxation factor to assure steady convergence of the compressible-flow solution.

Code Verification

Based on the present analysis, a FORTRAN code was developed and used to investigate the inviscid flow field in the scroll-nozzle system of a Garrett radial turbine. The finite-element discretization model of the system is shown in Fig. 2 for the baseline configuration (Figs. 6 and 7). In this model, a total of 6621 nodal points and 20,853 solid tetrahedral elements were generated. This is as many as 8.0 times the number of nodes and 7.5 times the number of elements in the scroll flow analysis of [12]. The increase was necessary because of the high velocity gradients from one guide vane to another in the present study. All elements generated in the geometry phase of the code were linear tetrahedral solid elements. This element type is the simplest for three-dimensional applications from a computational viewpoint.

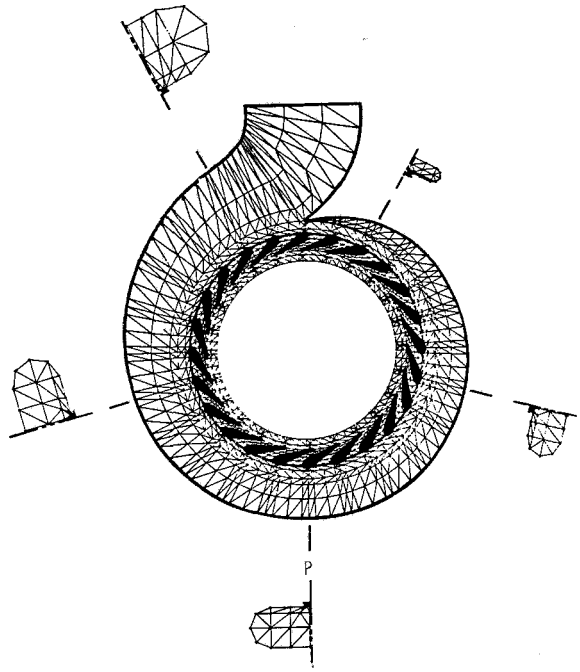


Fig. 2 Scroll-nozzle assembly finite-element discretization model with cross sections in the scroll passage

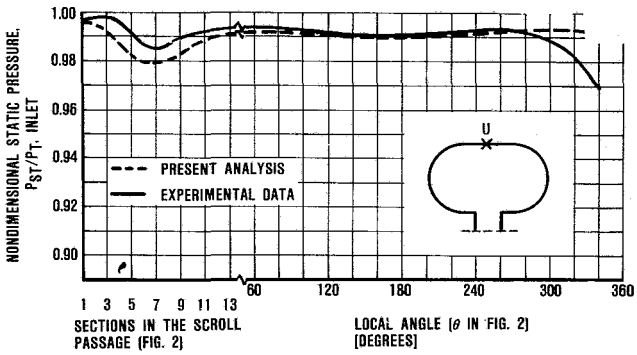


Fig. 3 Comparison of the analytical and experimental static pressure at the extreme outer point (*U*) in the scroll passage

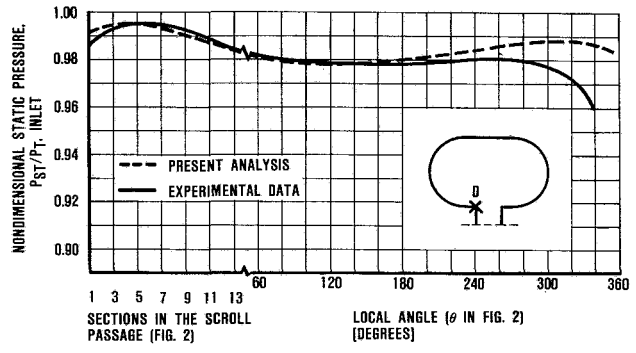


Fig. 4 Comparison of the analytical and experimental static pressure at the extreme inner point (*D*) in the scroll passage

Besides, the utilization of this element leads to a substantially low CPU time consumption.

The advantages offered by the linear element were numerically illustrated by the author in [16] for a similar, but two-dimensional flow study. In this reference, the two-dimensional version of the current element, namely the three-node triangular element, was compared to a parabolic element

Downloaded 01 Jun 2010 to 171.66.16.70. Redistribution subject to ASME license or copyright; see http://www.asme.org/terms/Terms_Use.cfm

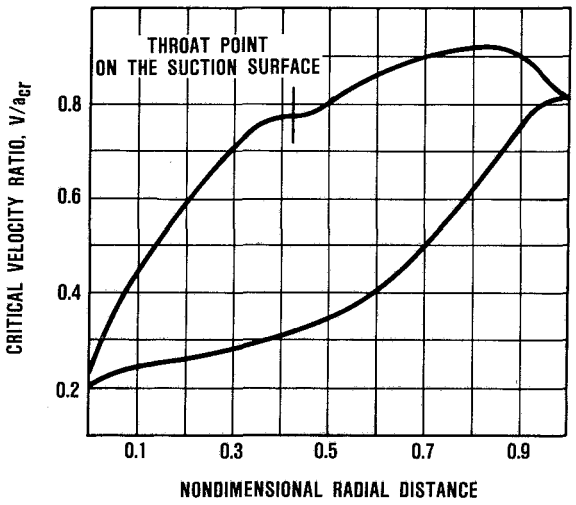


Fig. 5 Vane loading for the straight endwall configuration

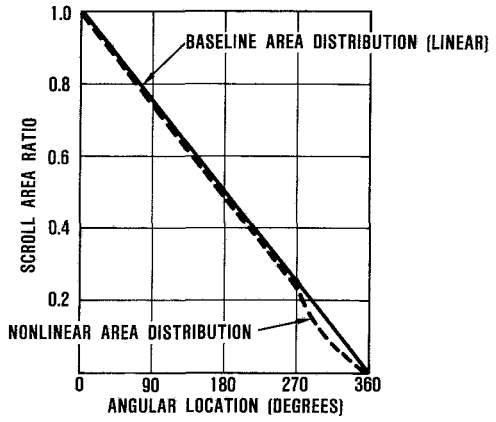


Fig. 6 Circumferential distribution of the scroll cross-sectional area

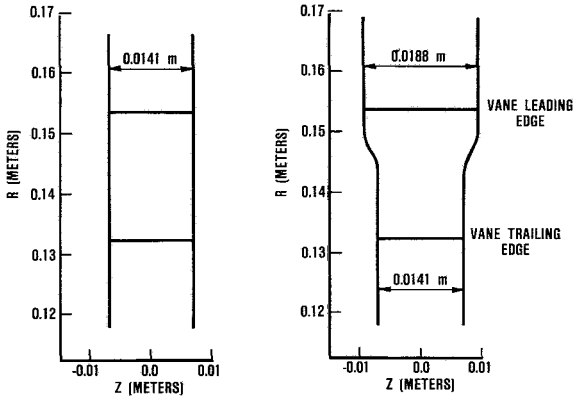


Fig. 7 Stator flowpath for the straight baseline and contoured endwall configurations

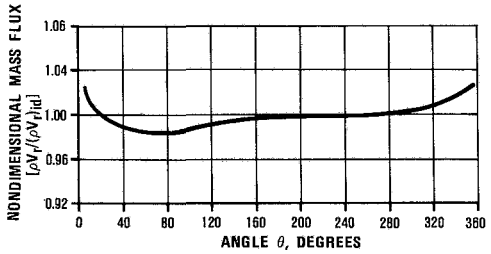


Fig. 8 Circumferential distribution of mass flux through the stator at the leading edge for the linear scroll-area distribution

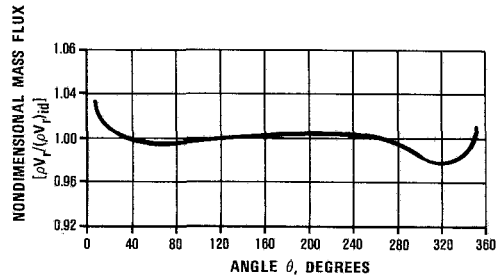


Fig. 9 Circumferential distribution of mass flux through the stator at the leading edge for the nonlinear scroll-area distribution

in a discretization model keeping the same total number of nodes in each case. It was found that the linear-element model consumed only 2.5 percent of the CPU time relative to the model with parabolic elements. The sacrifice in the solution precision in the linear-element case is recovered by using a larger number of nodes, which allows a solution with less CPU time and accuracy comparable to the parabolic element. This comparison was the basis for selecting the type of finite element as well as the size of the discretization model for the present flow analysis.

The iterative solution of the compressible flow field consumed an average of 3500 CPU seconds per each scroll-nozzle configuration on a CDC-835 computer system.

A comparison between the numerical results and the experimental data is shown in Figs. 3 and 4. In these figures, the static pressure distribution at the extreme outer and inner points of the scroll cross-section are plotted against the angular location along the scroll passage. Good agreement between the two sets of data is observed over a major part of the scroll including the inlet portion. The boundary-layer buildup along the scroll wall and the continuous loss of total pressure around the circumference are believed to be responsible for the deviation between the experimental data and the analytical solution in the last portion of the scroll passage.

During the iterative solution of the compressible flow field, the vane surface velocity distribution downstream of the throat point on the suction side developed from nearly flat to the accelerating diffusing character shown in Fig. 5. This characteristic is due to the flow compressibility which dominates this region.

Design Optimization Applications

The finite-element code was used to redesign the baseline geometry of the scroll-nozzle system of a Garrett radial turbine (Fig. 2). The baseline configuration of this system consisted of a linearly varying scroll cross-sectional area (Fig. 6) and straight nozzle endwalls (Fig. 7). The predicted circumferential distribution of mass flow through the nozzle channels and the vane loading at the angular location P (Fig. 2) are shown in Figs. 5 and 8 for this configuration. The mass flow distribution in Fig. 8 is plotted as the ratio between the mass flux-per-unit area through the stator (ρV_r) and the ideal value if the total mass flow is discharged uniformly at the leading-edge station through the stator.

Note that the nonuniformities in the mass-flow distribution arise from the scroll-nozzle interaction. In addition, the higher passage mass flows adjacent to the scroll tongue are due to a displacement of the scroll flow by the flow in the inlet portion (Fig. 1). Since the exit boundary condition implies a

Downloaded 01 Jun 2010 to 171.66.16.70. Redistribution subject to ASME license or copyright; see http://www.asme.org/terms/Terms_Use.cfm

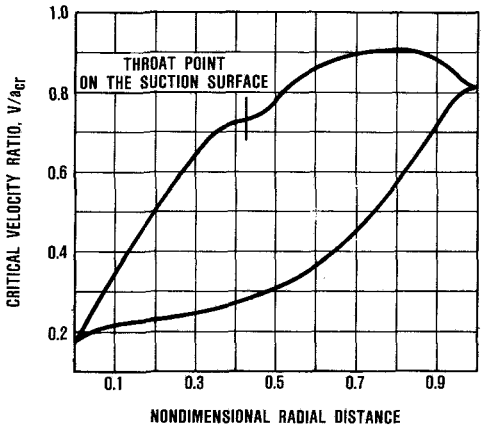


Fig. 10 Vane loading corresponding to the contoured nozzle endwall configuration

circumferentially-uniform mass flux, small adjustments in flow distribution occur downstream of the nozzle vanes. These adjustments are believed to induce minor variations in the suction-surface loading downstream of the throat, depending on the radial distance between the trailing edge and the flow-exit station where this condition is specified.

In order to reduce the circumferential irregularity of mass flow through the nozzle channels, a slightly nonlinear distribution of the scroll cross-sectional area was introduced (Fig. 6). The resulting distribution of mass flow is shown in Fig. 9. Comparison of Figs. 8 and 9 reveals that the effect of varying the scroll flow area is not restricted to the tangential location where the area changes are made. This is a result of the elliptic nature of the flow-governing equation (1) and, in the present case, the gap upstream the extreme upper vane (Fig. 1). Comparison of Figs. 8 and 9 shows that the favorable adjustments in mass flow occur in the first half of the nozzle channels. However, the larger difference in mass flow between the last two channels resulting from the nonlinear area distribution (Fig. 9) may have an unfavorable impact on the rotor performance.

Next, the aerodynamic effects of contouring the nozzle endwalls were evaluated using the same nonlinear scroll cross-sectional area distribution of Fig. 6. The contoured-endwall configuration (Fig. 7) was designed to improve the nozzle performance by reducing the potential for cross-flow in the nozzle channels and achieving a continuously accelerating flow in this region.

The vane loading at the tangential location P (Fig. 2) is shown in Fig. 10 for this nozzle-endwall geometry. Comparison of this velocity distribution with that in Fig. 5 reveals that a better vane loading is achieved in the contoured-endwall configuration. The contouring of endwalls, which was confined to approximately 40 percent of the radial chord (Fig. 6), results in a noticeable reduction of the vane loading over this interval. This is typically a design objective since the blade-to-blade static pressure difference acts as the driving force for secondary flow in the stator passsage. It was found that this pressure difference in the contoured-endwall design was 21 percent less than that corresponding to straight endwalls. This favorable effect decays at lower radii within the stator up to 50 percent of the radial chord. Beyond this point, an opposite trend takes place where the straight endwalls result in less pressure difference. However, the difference in this pressure increment between the two configurations in this region is not as significant (less than 11 percent). Figure 10 also shows that the contoured-endwall nozzle results in a continuously accelerating flow over the vane suction surface in the vicinity of the throat point.

Conclusion

The aerodynamic performance of the vaned scroll-nozzle system in a radial turbine was investigated using a three-dimensional finite-element approach. Several geometrical configurations of this turbine unit were compared in an optimization process. It was illustrated that the distribution of mass flow through the different nozzle channels can be effectively controlled by varying the scroll cross-sectional area around the circumference. As for the vaned nozzle region, it was found that contouring the endwalls to generate a continuously-convergent passage results in an improvement of the vane-loading characteristics. Good agreement between the computed and measured static pressure along the scroll was obtained.

References

1 Tabakoff, W., Sheoran, Y., and Kroll, K,. "Flow Measurements in a Turbine Scroll," ASME *Journal of Fluids Engineering*, Vol. 102, No. 3, Sept. 1980, pp. 290–296.

2 Khalil, I. M., Tabakoff, W., and Hamed, A., "Losses in Radial Inflow Turbines," ASME *Journal of Fluids Engineering*, Vol. 98, Sept. 1976, pp. 364–373.

3 Kastner, L. J., and Bhinder, F. S., "A Method for Predicting the Performance of a Centripetal Gas Turbine Fitted with a Nozzleless Volute Casing," ASME Paper No. 75-GT-65.

4 Wallace, F. J., Cave, P. R., and Miles, J., "Performance of Inward Radial Flow Turbines Under Steady Flow Conditions with Special Reference to High Pressure Ratios and Partial Admission," *Proc. Instn. Mech. Engrs.*, Vol. 184, Part 1, No. 56, 1969–1970.

5 Futral, S. M., and Wasserbauer, C. A., "Off-Design Performance Prediction with Experimental Verification for a Radial Inflow Turbine," NASA TND 2621, 1965.

6 Lagneau, J. P., "Contribution to the Study of Advanced Small Radial Gas Turbines," VKI IN 38, Mar. 1970.

7 Sokhey, J., Tabakoff, W., and Hosny, W. M., "Flow Behaviour in Inlet Guide Vanes of Radial Turbines," NASA-CR-137632, Oct. 1975.

8 Katsanis, T., "Fortran Program for Calculating Transonic Velocities on a Blade-to-Blade Stream Surface of a Turbomachine," NASA TND-5427, Sept. 1969.

9 Hamed, A., Abdallah, S., and Tabakoff, W., "Flow Study in the Cross Sectional Plane of a Turbine Scroll," AIAA Paper No. 77-714 presented at the AIAA 10th Fluid and Plasma Dynamics Conference, Albuquerque, NM, June 27–29, 1977.

10 Hamed, A., Baskharone, E., and Tabakoff, W., "A Flow Study in Radial Inflow Turbine Scroll-Nozzle Assembly," ASME *Journal of Fluids Engineering*, Vol. 100, No. 1, Mar. 1978, pp. 31–36.

11 Baskharone, E., Hamed, A., and Tabakoff, W., "Flow in Nonrotating Passages of Radial Inflow Turbines," NASA-CR-159679, Sept. 1979.

12 Hamed, A., and Baskharone, E., "Analysis of the Three Dimensional Flow in a Turbine Scroll," ASME *Journal of Fluids Engineering*, Vol. 102, No. 3, Sept. 1980, pp. 297–301.

13 Dodge, P. R., "A Numerical Method for 2-D and 3-D Viscous Flows," *AIAA Journal*, Vol. 15, July 1977, pp. 961–965.

14 Baskharone, E., and Hamed, A., "A New Approach in Cascade Flow Analysis Using the Finite Element Method," *AIAA Journal*, Vol. 19, No. 1, Jan. 1981, pp. 65–71.

15 Zienkiewicz, O. C., *The Finite Element Method in Engineering Science*, McGraw-Hill, London, 1971.

16 Baskharone, E., "A New Approach in Turbomachinery Flow Analysis Using the Finite Element Method," Ph.D. thesis, University of Cincinnati, Ohio, Nov. 1979.

17 Hood, P., "Frontal Solution Program for Unsymmetric Matrices," *Int. J. Num. Meth. Engg.*, Vol. 10, No. 2, 1976, pp. 379–399.

Downloaded 01 Jun 2010 to 171.66.16.70. Redistribution subject to ASME license or copyright; see http://www.asme.org/terms/Terms_Use.cfm

W. Tabakoff
Professor.
Fellow ASME

B. V. R. Vittal
Graduate Research Assist.
Student Mem. ASME

B. Wood
Graduate Research Assist.
Student Mem. ASME

Department of Aerospace Engineering
and Applied Mechanics,
University of Cincinnati,
Cincinnati, Ohio 45221

Three-Dimensional Flow Measurements in a Turbine Scroll

A study was conducted to determine experimentally the flow behavior in combined scroll nozzle assembly of a radial inflow turbine. Hot film anemometry technique was used to measure the three-dimensional flow velocity in the scroll. The through-flow and secondary flow velocity components are measured at various points in three scroll sections.

Introduction

In recent years there has been considerable interest in the study of small radial gas turbines in order to improve their performance characteristics. Most of the research work has been concentrated on turbine rotors, since they were considered to have the most significant effect on turbine efficiency. Recently, research work has demonstrated a need for new design techniques in the turbine scroll and guide vanes.

At the present time the scroll designs are still based on one-dimensional flow calculations. Guide vane blades are merely designed to give the required flow turning angle. The inlet velocity distribution is assumed to be uniform from one guide vane inlet to another. Such an assumption is not realistic; a variation in the inlet velocity distribution exists and depends mainly on the scroll and the guide vane blade effects. Additionally, boundary layer buildup on scroll side walls has a blocking effect in the scroll passage. Consequently, each vane will have different inlet conditions, such as the inlet mass flow and the inlet flow incidence.

The secondary flow in the scroll results from the nonequilibrium between the pressure and the centrifugal forces on the scroll side walls. Nonuniformities in the flow properties at the scroll inlet also result in secondary flow. This effect is similar to the secondary flow in cascade passages and pipe bends. The secondary flow consists mainly of vortices, whose strength varies along the scroll, causing a circumferential variation in the flow parameters. This factor again leads to different inlet flow conditions in each guide vane channel.

Additional vortices are created in the scroll passage due to the flow discharge to the guide vanes. Such vortices are similar to the corner vortices, but are not stationary. They depend on the geometry of the scroll and nozzle entrance arrangements. Therefore, these distributions add to the three dimensional flow behavior affecting the guide vane inlet flow properties.

A new analysis which describes the flow behavior in combined scroll-nozzle assembly of radial inflow turbines is reported by Hamed, et al. [1]. This analysis provides a better understanding of the mutual interaction effects of the flow in scroll-nozzle assembly. In a different but parallel investigation, Hamed et al. [2] are presenting the solution for nonviscous rotational three-dimensional scroll flow which determines the velocity components in the scroll cross sectional planes. Very few experimental measurements of scroll flow can be found in the literature. Reference [3] reports a detailed experimental and analytical study of the losses in both the vaned and vaneless regions of a radial inflow turbine nozzle.

In order to study the complicated flow behavior in a scroll-nozzle assembly, an experimental program has been undertaken in the Department of Aerospace Engineering and Applied Mechanics at the University of Cincinnati. As a first step in this program, experimental measurements of the through-flow velocities in this scroll have been completed and reported in reference [4]. From these data, conclusions were drawn concerning the secondary flow behavior. This information was beneficial in the planning of the current procedures for the measurement of secondary flows in the scroll.

Research Scroll Facility

The test facility was designed to incorporate a complete radial inflow turbine scroll for testing using cold air. The most recent phase of experimental investigation was concerned with the measurement of the through-flow and secondary flow velocities at different scroll cross sections. It is hoped that with these data a better understanding of the scroll flow behavior will be obtained. The scroll used was a non-

Contributed by the Gas Turbine Division of THE AMERICAN SOCIETY OF MECHANICAL ENGINEERS and presented at the 28th International Gas Turbine Conference and Exhibit, Phoenix, Arizona, March 27-31, 1983. Manuscript received at ASME Headquarters December 27, 1983. Paper No. 83-GT-128.

Copyright © 1984 by ASME
Downloaded 01 Jun 2010 to 171.66.16.70. Redistribution subject to ASME license or copyright; see http://www.asme.org/terms/Terms_Use.cfm

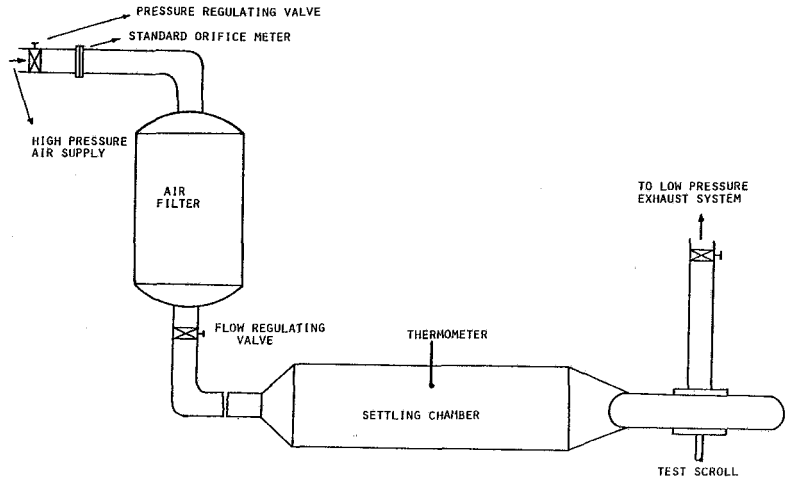


Fig. 1 Schematic diagram of the experimental setup

symmetric circular type with stator nozzle annulus consisting of 13 untwisted vanes. The turbine rotor was modified in such a way that the blades were removed and only the rotor hub was used in its place.

The scroll was originally part of a six kilowatt single shaft Brayton cycle space power system using a 0.1262 m (4.97 in.) radial inflow turbine. The design and fabrication details of the system are given in reference [5]. The cold performance evaluation of the radial inflow turbine is given in reference [6].

Figure 1 shows the schematic diagram of the experimental setup. High pressure air was supplied from four large storage tanks, the air passed through a remotely controlled pressure regulating valve, standard orifice meter, filter, and a flow regulating valve before entering the settling chamber. The temperature of the air was measured in the settling chamber. The filter was used to trap dust particles up to a nominal diameter of about three microns. This prolonged the operating life of the hot film sensor.

The air supply was regulated by the flow regulating valve to give an air mass flow of 0.453 kg/s (1 lb/s). The air mass flow was measured by a standard orifice meter. The air from the settling chamber was fed to the scroll inlet through a convergent duct. The duct was circular in shape and blended smoothly into the inlet of the scroll.

Experimental Investigation. A schematic diagram of the scroll is shown in Fig. 2. In the flow analysis of such a scroll, it is more convenient to define two cylindrical coordinate systems. The machine coordinate system (R, ϕ, Z) is a fixed frame of reference with its Z-axis as the machine shaft axis of the impeller. For the machine axes, the $\phi = 0$ line is 90 deg from the scroll entrance face as shown in Fig. 3. This set condition will be used for the purpose of discussion of the results. For the convenience of handling the experimental data in a specific scroll cross-section, it is necessary to define a local axes system (r, θ, X) which is attached to the center of any particular scroll cross-section under investigation. In this system, the X-axis is zero in the plane of the cross-section and

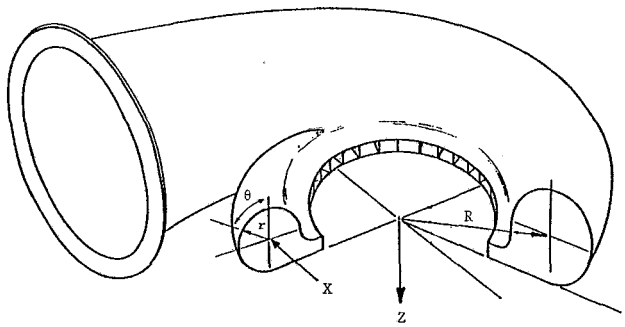


Fig. 2 Scroll schematic diagram

Nomenclature

d = diameter of the scroll cross section, m
m_c, m_b = angular increments to yaw angles, deg, (equations (A.9) and (A.10), Appendix)
$\dot{m}$ = mass flow rate, kg/s
Q = volume flow rate, m^3/s
r = radius of the scroll cross section, m
r_d = radial depth of the measuring point, cm
R = radius of curvature of the machine coordinate system, (Fig. 2)
$\bar{S}$ = the sensor axis (Fig. A.1)
$\mathbf{V}$ = flow velocity vector, m/s
V_h = horizontal component of the secondary flow velocity, m/s
V_s = secondary flow velocity, m/s
V_v = vertical component of secondary flow velocity, m/s
V_x = through-flow component of velocity, m/s
x = x-axis of probe coordinate system (Fig. A.1)
X = X-axis of scroll coordinate system (Fig. 2)
y = y-axis of probe coordinate system (Fig. A.1)
z = z-axis of probe coordinate system (Fig. A.1)
Z = Z-axis of scroll coordinate system (Fig. 2)
α = sensor yaw angle, deg (Fig. A.1)
ϵ = angle between the radius of curvature and the horizontal axis, deg (Fig. 5)
θ = angular position of the measuring parts, deg (Fig. 4)
θ_o = angle between sensors axis and x-axis, deg (Fig. A.1)
θ_p = probe pitch angle, deg (Fig. A.1)
θ_y = probe yaw angle, deg (Fig. A.1)
μ = dynamic viscosity, kg/m s
ρ = density, kg/m^3
ϕ = scroll angular coordinate, deg

Downloaded 01 Jun 2010 to 171.66.16.70. Redistribution subject to ASME license or copyright; see http://www.asme.org/terms/Terms_Use.cfm

is normal to this plane. Note that in the machine coordinate systems, the tangential direction at the center of any section coincides with the X-axis of the scroll cross-section (the so-called through-flow velocity direction).

Scroll Geometry. Since curvilinear flow channels with variable cross-sections offer no characteristic length, Reynolds number ($\mathbf{V}d/\nu$) alone based on the average velocity $\mathbf{V}$ of steady flow ceases to be a criterion of describing the flow, as it is used for straight pipe flow. However, a simple dimensional analysis carried out suggests that such flow can be geometrically and dynamically compared by defining two nondimensional numbers, namely ($\rho Q/\mu d$) and R/d where Q is the volume flow rate. In this work the scroll inlet mass flow Reynolds number was defined as

$$\frac{4}{\pi}\left(\frac{\dot{m}}{\mu d}\right)$$

and is equal to 2.607×10^5. Figure 3 shows three scroll section locations. The first cross-section is at $\phi = 0$ deg, the second at $\phi = 71$ deg, and the third at $\phi = 139$ deg.

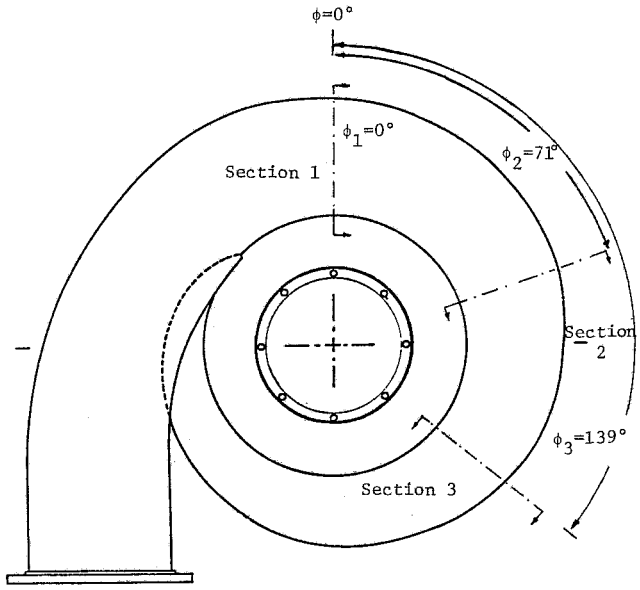


Fig. 3 Plan view of the scroll

Instrumentation. The air mass flow was measured using a standard orifice meter. The temperature of the air was measured in the settling chamber using a simple commercial dial type thermometer with a stem. No pressure measurements were made except at the orifice meter. The velocity measurements inside the scroll were made using the TSI model 1213-20 hot film slant sensor. The cylindrical sensor element is 0.0508 mm (0.002 in.) in diameter, 1.016 mm (0.040 in.) long, and is at a slant angle of 45 deg. It is coated with alumina and gold plated at the ends where it is fixed to the prongs. The prongs are 12.7 mm (0.5 in.) long.

Probe Mount and Flow Measurement. The positions of three scroll cross-sections where the measurements have been taken are shown in Fig. 3. At each section, specially designed probe ports were welded at discrete angular locations, which allowed the probes to survey the complete scroll cross-section. These ports were designed to mate properly with an automatic traversing mechanism. The probe was then mounted onto the electrically driven traversing mechanism. This permitted continuous movement of the probe into the cross-section along radial (r) lines in order to minimize experimentation time and human errors. The rate of transverse could also be varied. The depth position of the probe was read on a graduated scale mounted on the traversing mechanism.

Figure 4 gives the probe port locations for the three cross-sections. Figure 5 shows the relative positions of the three

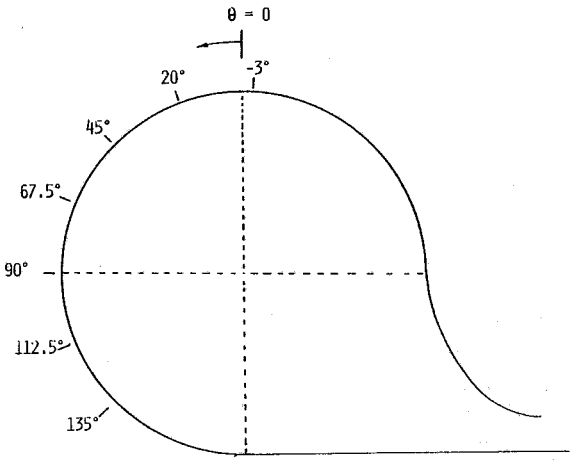
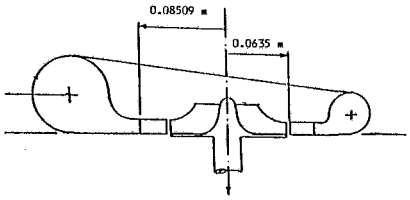


Fig. 4 Angular position of probe ports for the three cross-sections



SECTION	R	r	ϵ
1	0.1821 m	0.05156 m	16.46 deg.
2	0.1756 m	0.04445 m	14.66 deg.
3	0.1692 m	0.036576 m	12.49 deg.

EXIT NOZZLE HEIGHT = 0.011 m

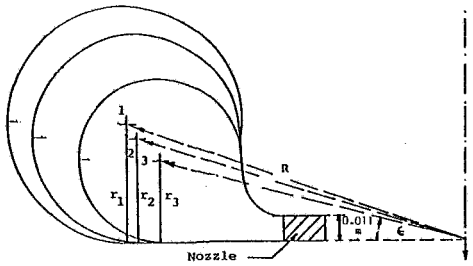


Fig. 5 Relative position of three sections with respect to the machine axis

Downloaded 01 Jun 2010 to 171.66.16.70. Redistribution subject to ASME license or copyright; see http://www.asme.org/terms/Terms_Use.cfm

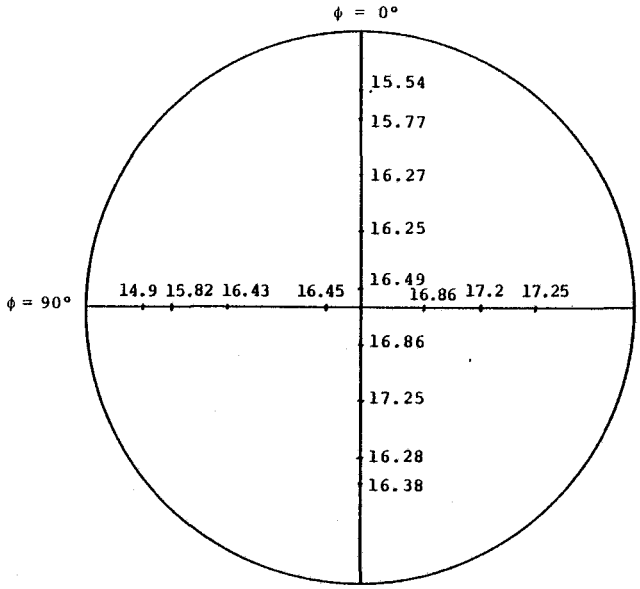


Fig. 6 The scroll inlet velocity distribution (m/s)

scroll sections with respect to the machine axis. The radius of curvature R from the center of the scroll section makes an angle ϵ to the scroll horizontal. A table attached to the figure shows the radii of curvature and the corresponding ϵ of the three sections.

Procedure. The high pressure air supply from air storage tanks was regulated to a pressure of 4.1368×10^5 N/m^2 gage (60 psig) at the orifice meter using a pressure regulating valve. The air supply was passed through an air filter to a settling chamber where the temperature was measured. The pressure drop across the orifice meter was varied with the flow regulating valve to give an actual air mass flow of 0.453 kg/s (1 lb/s). The air temperature did not vary appreciably from the nominal temperature of 21.11°C (70°F).

The flow velocity measurements inside the scroll were made using a hot film slant sensor. It was advantageous to use this sensor for three-dimensional flow measurements since it required only one channel of electronic circuitry, when compared to two or three for cross wire probes. This consequently minimized measurement errors. Also, the obstruction to the flow field was reduced. The operation, calibration, and the evaluation of velocities from the anemometer output signals are explained in the Appendix.

Results and Discussion

The scroll inlet velocity measurements were made at two port locations and the results are shown in Fig. 6. The total velocity vector at every point of measurement in the scroll cross-sections was resolved into three components. The through-flow component, V_x, and the two secondary flow components V_h and V_v. Figures 7(*a*), 7(*b*), and 7(*c*) show the measured through-flow velocities in each of the three sections. The contour lines of the through-flow velocity were obtained by normalizing the local measured velocities with respect to the scroll inlet average velocity of 16.36 m/s (53.7 ft/s). For all the measurements the mass flow rate was maintained at 0.453 kg/s (1 lb/s). The through-flow velocity contours are similar to the ones obtained using an x-probe given in reference [4]. The numerical values of the flow velocity components at various locations in the scroll are given in NASA Report CR-167920 [7].

Figure 8 shows the secondary flow velocity vectors at various points in scroll section 1. There are two secondary

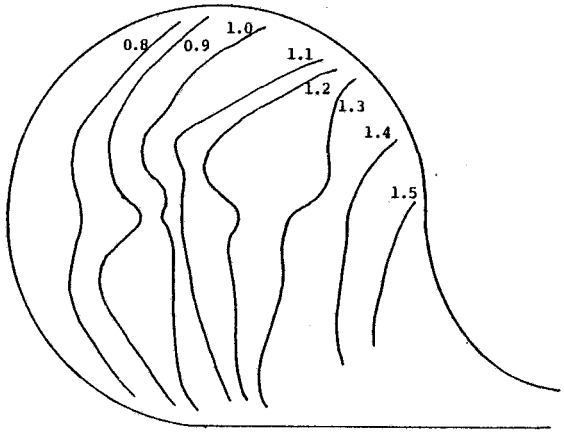


Fig. 7(*a*) Normalized through-flow velocity contours (Section 1)

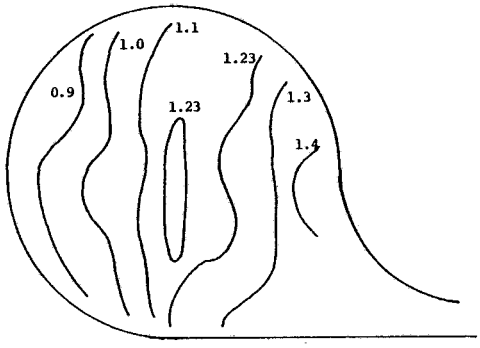


Fig. 7(*b*) Normalized through-flow velocity contours (Section 2)

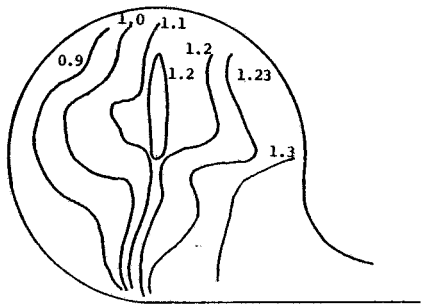


Fig. 7(*c*) Normalized through-flow velocity contours (Section 3)

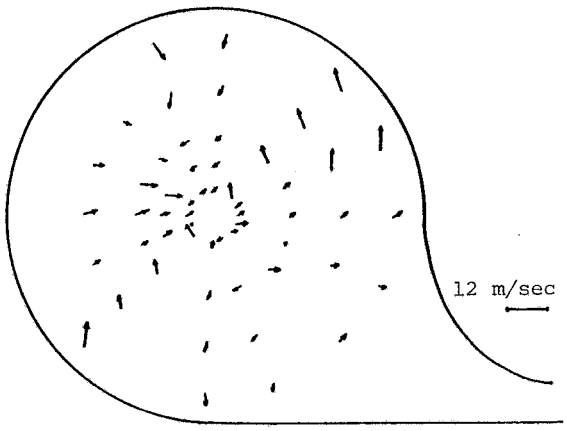


Fig. 8 Secondary flow velocity vectors (Section 1); (scale: 1 cm = 12 m/s)

Downloaded 01 Jun 2010 to 171.66.16.70. Redistribution subject to ASME license or copyright; see http://www.asme.org/terms/Terms_Use.cfm

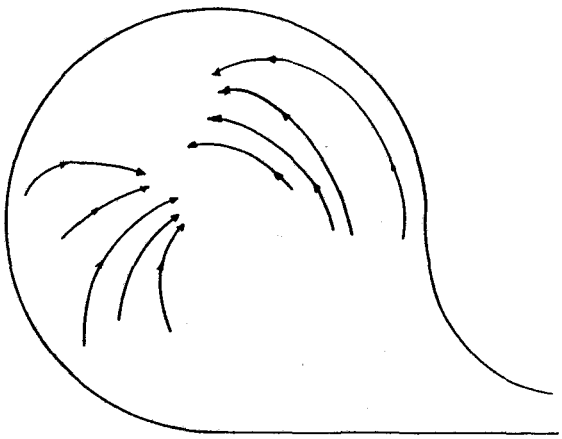


Fig. 9 Schematic diagram of recirculation zones (Section 1)

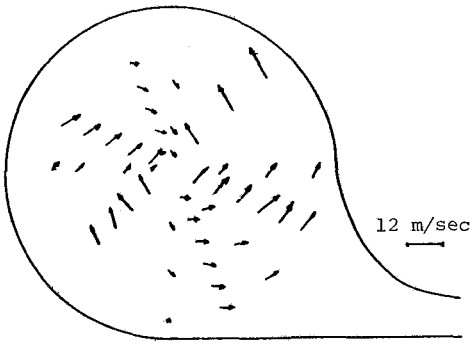


Fig. 10 Secondary flow velocity vectors (Section 2); (scale: 1 cm = 12 m/s)

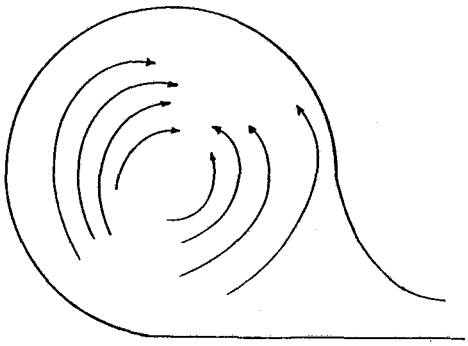


Fig. 11 Schematic diagram of recirculation zones (Section 2)

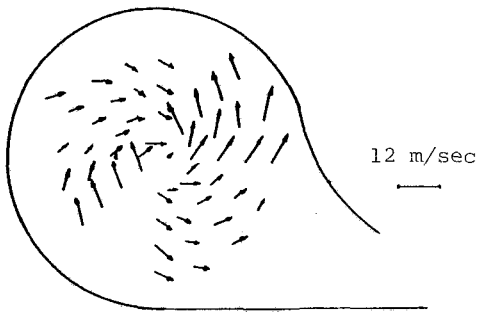


Fig. 12 Secondary flow velocity vectors (Section 3); (scale: 1 cm = 12 m/s)

flow currents observable in these data which are schematically shown in Fig. 9. The secondary flow pattern for scroll section 2 is shown in Fig. 10. Once again there are two secondary flow

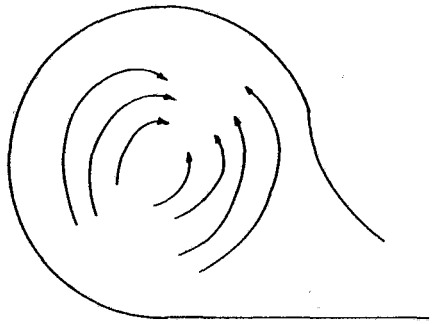


Fig. 13 Schematic diagram showing recirculation zones (Section 3)

loops as illustrated in Fig. 11. However, the flow parting position has rotated in the clockwise direction. The secondary flow pattern for scroll section 3 is shown in Figs. 12 and 13. Once again there are two recirculating zones and the flow parting position has rotated clockwise though not as much as that of the second section. The secondary flow currents observed during these tests are a result, in part, from a nonequilibrium between pressure and centrifugal forces. This imbalance, due to the nozzle discharge and the passage's curvature is directly related to the scroll geometry. For a better understanding of such phenomenon further testings are necessary for scroll having different design configurations. Presently we are measuring the secondary and through-flows in vaneless scrolls.

Acknowledgments

This research was sponsored by NASA Grant No. NAG3-26, Lewis Research Center.

The authors wish to express their appreciation for the useful discussions and suggestions provided by Mr. McLallin from NASA Lewis Research Center.

References

1 Hamed, A., Baskharone, E., and Tabakoff, W., "A Flow Study in Radial Inflow Turbine Scroll Nozzle Assembly," ASME *Journal of Fluids Engineering*, Vol. 100, Mar. 1978, pp. 31–36.

2 Hamed, A., Abdallah, S., and Tabakoff, W., "Flow Study in the Cross Sectional Planes of a Turbine Scroll," AIAA Paper No. 77-714, AIAA 10th Fluid and Plasma Dynamics Conference, Albuquerque, New Mexico, June 27–29, 1977.

3 Khalil, I., Tabakoff, W., and Hamed, A., "Losses in Radial Inflow Turbines," ASME *Journal of Fluids Engineering*, Vol. 98, Sept. 1976, pp. 364–373.

4 Tabakoff, W., Sheoran, Y., and Kroll, K., "Flow Measurements in a Turbine Scroll," ASME *Journal of Fluids Engineering*, Vol. 102, Sept. 1980, pp. 290–296.

5 Anon., "Design and Fabrication of the Brayton Cycle High Performance Turbine Research Package," Report APS-5281-R, AiResearch Mfg. Co. of Arizona, (NASA CR-72478), 1968.

6 Nusbaum, W. J., and Kofskey, M. G., "Cold Performance Evaluation of 4.97 Inch Radial Inflow Turbine Designed for Single Shaft Brayton Cycle Space Power System," NASA TND 5090, 1969.

7 Tabakoff, W., Vittal, B. V. R., and Wood, B., "Three-Dimensional Flow Measurements in a Turbine Scroll," Report NASA-CR 167920, July 1982.

8 Schmidt, D. P., and Okishi, T. H., "Multistage Axial-Flow Turbomachine Wake Production, Transport, and Interaction," Iowa State University No. ISU-ERI-AMES-77130, Nov. 1976.

9 Thermo Systems Inc., "Instruction Manual for Model 1125 Calibrator."

APPENDIX

Hot Film Velocity Measurement Technique

A schematic diagram of the probe along with coordinate axes used is shown in Fig. 14. The z-coordinate is along the axis of the probe and x-coordinate is located in such a way that the sensor lies in the x-z plane. The sensor axis $\bar{S}$ makes

Downloaded 01 Jun 2010 to 171.66.16.70. Redistribution subject to ASME license or copyright; see http://www.asme.org/terms/Terms_Use.cfm

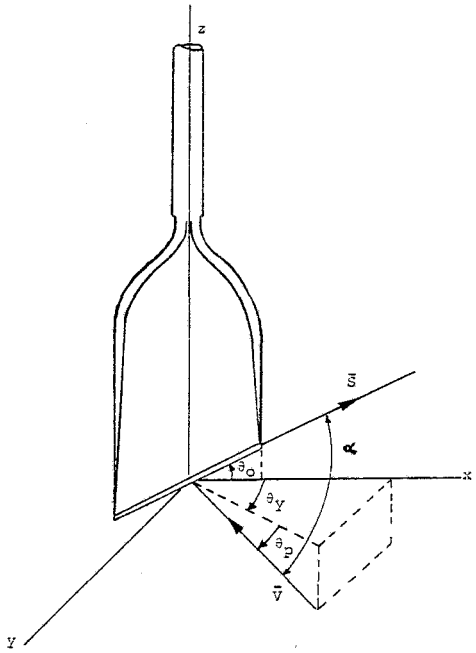


Fig. 14 Probe coordinate axes

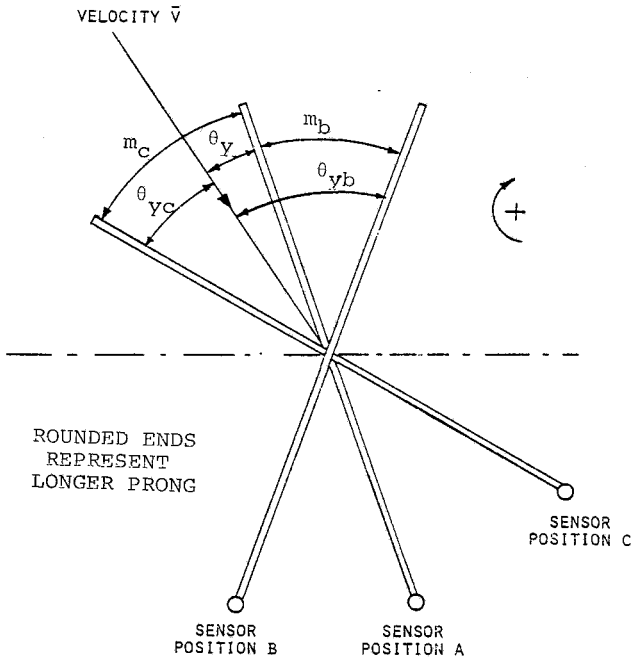


Fig. 15 Probe measurement positions and nomenclature, viewed from above along probe axis

an angle θ_o with the x-axis and α is the angle between the sensor axis and the flow velocity vector **V**. The direction of the velocity vector with respect to the probe is defined by θ_y, the probe yaw angle and θ_p, the probe pitch angle. A relationship among the various angles is given by the equation

$$\cos\alpha = \cos\theta_o \cos\theta_p \cos\theta_y + \sin\theta_o \sin\theta_p \qquad \text{(A1)}$$

A detailed description of the measurement procedure is given in reference [8].

Usually sensors are calibrated with flow normal to the sensor, i.e. sensor yaw angle $\alpha = 90$ deg. If a flow measurement is taken at a sensor angle other than 90 deg, in this case, the effective velocity V_e indicated by the sensor will

Table 1 Velocity = 76.19 m/s (250 ft/s)

θ_p Pitch angle deg	θ_y Yaw angle deg	Signal output volts	θ_p Pitch angle deg	θ_y Yaw angle deg	Signal output volts
−6	50	7.283	+3	50	7.216
	40	7.19		40	7.111
	30	7.121		30	6.87
	20	6.899		20	6.737
	10	6.813		10	6.606
	0	6.702		0	6.508
	−10	6.716		−10	6.529
	−20	6.875		−20	6.619
	−30	7.044		−30	6.737
	−40	7.136		−40	6.893
	−50	7.222		−50	7.113
−3	50	7.273	+6	50	7.191
	40	7.184		40	7.04
	30	7.073		30	6.817
	20	6.828		20	6.680
	10	6.743		10	6.535
	0	6.642		0	6.434
	−10	6.657		−10	6.467
	−20	6.757		−20	6.545
	−30	6.953		−30	6.686
	−40	7.093		−40	6.838
	−50	7.192		−50	7.063
0	50	7.247			
	40	7.145			
	30	6.96			
	20	6.782			
	10	6.675			
	0	6.579			
	−10	6.590			
	−20	6.687			
	−30	6.807			
	−40	7.002			
	−50	7.160			

be different from the actual flow velocity V. Schmidt and Okishi [8] used a second order empirical correlation to express the relationship between these two velocities as follows.

$$\frac{V_e}{V} = b_0 + b_1\alpha + b_2\theta_p + b_3 V + b_4\alpha^2 + b_5\theta_p^2 + b_6 V^2 + b_7\alpha\theta_p + b_8\alpha V + b_9\theta_p V \qquad \text{(A2)}$$

The coefficients b_0 through b_9 were determined using the calibration procedures given below.

Calibration Procedure. In order to obtain the coefficients for the foregoing equation, the probe was calibrated with the help of TSI Model 1125 calibrator [9] which uses a calibration nozzle. A probe fixture was developed to vary the yaw and pitch angles of the probe with respect to the flow from the nozzle. Initially, the probe was calibrated for flow normal to the sensor ($\alpha = 90$ deg) and the relationship between signal output and velocity was curve fitted using a polynomial curve fit. Using the probe fixture, the sensor was swept through various ranges of yaw and pitch angles. An example of a typical set of angular increments is shown in Table 1. The measurements shown in the table are only for one particular flow velocity. However, the calibration was carried out over the entire velocity vector envelope which was to be encountered in the experiment. The flow at the exit of the calibration nozzle was at about 21.11°C (70°F) and at atmospheric pressure. The air temperature in the scroll during measurements did not vary much from this temperature. Hence, no temperature correction was applied. However, since the air pressure was different, density corrections were applied to all the sensor output readings.

A computer program was developed to obtain the coefficients necessary for the equation (A2), from a least square curve fit of effective velocity calibration data obtained for different probe orientations and air speeds. Two sets of

Downloaded 01 Jun 2010 to 171.66.16.70. Redistribution subject to ASME license or copyright; see http://www.asme.org/terms/Terms_Use.cfm

coefficients were obtained. One for the velocity data at positive yaw angles and the other for the negative yaw angles.

The percentage error at each data point between the actual nozzle jet velocity and the velocity predicted by the polynomial relationship was calculated. Some of the errors were as low as 0.07 percent; however, the majority of them were around 0.4 percent, and none above 0.6 percent. The calibration did change even after 30-40 hr of actual running time. In order to inspect the accuracy of the V_e/V relationship (equation (2)), the percent error between the measured velocity and the predicted velocity ratio was calculated. The majority of errors was of the order of 1 percent.

Operation. The magnitude and direction of the velocity in the scroll at any one point was determined by taking the measurements at three probe angle orientations and reducing the data using equations (A1) and (A2). Referring to Fig. 15, if the three probe orientations are A, B, and C, the resulting six equations are:

For position A,

$$\frac{V_{e,a}}{V} = b_{0a} + b_{1a}\alpha_a + b_{2a}\theta_p + b_{3a}V + b_{4a}\alpha_a^2 + b_{5a}\theta_p^2 + b_{6a}V^2 + b_{7a}\alpha_a\theta_p + b_{8a}\alpha_a V + b_{9a}\theta_p V \quad \text{(A3)}$$

$$\cos\alpha_a = \cos\theta_o\cos\theta_p\cos\theta_y + \sin\theta_o\sin\theta_p \quad \text{(A4)}$$

For position B,

$$\frac{V_{e,b}}{V} = b_{0b} + b_{1b}\alpha_b + b_{2b}\theta_p + b_{3b}V + b_{4b}\alpha_b^2 + b_{5b}\theta_p^2 + b_{6b}V^2 + b_{7b}\alpha_b\theta_p + b_{8b}\alpha_b V + b_{9b}\theta_p V \quad \text{(A5)}$$

$$\cos\alpha_b = \cos\theta_o\cos\theta_p\cos\theta_{yb} + \sin\theta_o\sin\theta_p \quad \text{(A6)}$$

For position C,

$$\frac{V_{e,c}}{V} = b_{0c} + b_{1c}\alpha_c + b_{2c}\theta_p + b_{3c}V + b_{4c}\alpha_c^2 + b_{5c}\theta_p^2 + b_{6c}V^2 + b_{7c}\alpha_c\theta_p + b_{8c}\alpha_c V + b_{9c}\theta_p V \quad \text{(A7)}$$

$$\cos\alpha_c = \cos\theta_o\cos\theta_p\cos\theta_{yc} + \sin\theta_o\sin\theta_p \quad \text{(A8)}$$

Since the last two probe orientations are made by fixed angular increments with respect to the first,

$$\theta_{yb} = \theta_y + m_b \quad \text{(A9)}$$

$$\theta_{yc} = \theta_y - m_c \quad \text{(A10)}$$

The coefficients b_0 through b_9 in the equations (A3) to (A8) were known. The three effective velocities $V_{e,a}$, $V_{e,b}$, and $V_{e,c}$ being measured values, the foregoing six equations could be solved simultaneously for the six unknown variables α_a, α_b, α_c, θ_p, V, and θ_y. A computer code has been developed to solve the foregoing equations simultaneously using the Newton-Raphson numerical method. With V, θ_p, and θ_y determined, the velocity vector, **V** is completely specified with respect to the probe coordinate system. The velocity vector was then resolved into three components in the scroll coordinate system (horizontal velocity, through vector and vertical velocity).

The three probe measurement angles θ_y, θ_{yb}, and θ_{yc} were chosen that they lie in regions of high sensor sensitivity. To avoid probe prong interference, the shorter prong was always positioned into the flow upstream of the longer prong. First, the probe was rotated so as to face the flow direction, which is characteristically given by a minimum voltage output signal. The probe was then turned by 5 deg in the positive direction to get position A (Fig. 15) and the signal recorded. Position B was obtained by turning the probe by 30 deg in the positive direction and the reading taken. Finally the third reading was taken by rotating the probe in the negative direction by 30 deg from position A to obtain position C.

Downloaded 01 Jun 2010 to 171.66.16.70. Redistribution subject to ASME license or copyright; see http://www.asme.org/terms/Terms_Use.cfm

T. C. Prince
Engineer.

A. C. Bryans
Principal Engineer.

General Electric Company,
Aircraft Engine Business Group,
Lynn, Mass. 24048

Three-Dimensional Inviscid Computation of an Impeller Flow

The flow in a centrifugal impeller is analyzed by a quasi-three-dimensional streamline curvature method, by a three-dimensional Euler code, and by a three-dimensional finite element potential flow method. Comparison with Eckardt's published data for a backswept impeller shows that full three-dimensional methods better predict the loading at the hub and shroud.

Introduction

For three decades, the standard computational method for flow in a turbomachine has been based on the calculation of quasi-two-dimensional flows on intersecting surfaces. In many cases, a satisfactory quasi-three-dimensional solution for the flow throughout a blade row can be built up in this way. Most recent designs have depended on such a procedure, which is well accepted for axial flow machines.

Among the inherent limitations of the quasi-three-dimensional approximation is the need to neglect one of the three velocity components in each quasi-two-dimensional solution. In the most common quasi-three-dimensional procedure, the velocity vector of the flow is assumed to lie in a surface of revolution so that the quasi-three-dimensional solution is forced to have a greater degree of symmetry than the real flow. Some quasi-three-dimensional procedures relax this restriction, but not to the extent that they can model the important case of flow in a mixed flow rotor. In this case, where the main direction of flow lies between axial and radial, even an irrotational solution has significant velocity components which must depart from any surface which could be used in the quasi-two-dimensional model.

The use of a fully three-dimensional computational method eliminates the restriction just described and also removes the requirement to solve two coupled systems of equations. Two practical methods which have been described in the literature are the finite volume solution of the Euler equations [1] and the finite element solution of the potential flow equation [2]. The purpose of this paper is to examine the ability of these methods to predict an impeller flow for which published experimental data exist.

Experimental Data

The data published by Eckardt [3] were selected for their excellent quality and comprehensiveness. Since backswept blades are often employed with the intention of inhibiting separation and improving efficiency, Impeller "A" (Fig. 1) was selected. The computational methods of this investigation are intended for unseparated flows. Impeller "A" displays

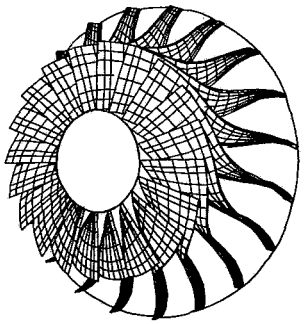


Fig. 1 Eckardt impeller "A"

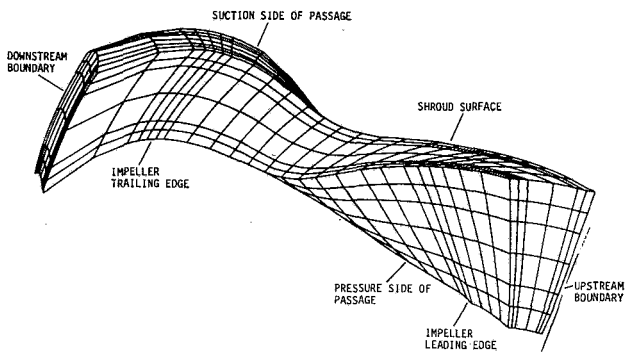


Fig. 2 Three-dimensional impeller analysis

significant internal separation, which may be typical of impellers designed in the past. Thus, it is a challenging computational problem, although it is more amenable than other impellers which appear in the literature.

The laser velocimeter data have been interpolated on the grid used by the computational codes to facilitate display and comparison with computational prediction. No attempt was made to smooth or extrapolate the data, so the plots made from the data appear somewhat rough. These plots still give a good picture of the flow.

The Euler Code

The Euler code is similar to that of Denton. The flow field is divided into 7000 control volumes, and an attempt is made

Contributed by the Gas Turbine Division of THE AMERICAN SOCIETY OF MECHANICAL ENGINEERS and presented at the 28th International Gas Turbine Conference and Exhibit, Phoenix, Arizona, March 27–31, 1983. Manuscript received at ASME Headquarters January 4, 1983. Paper No. 83-GT-210.

Copyright © 1984 by ASME
Downloaded 01 Jun 2010 to 171.66.16.70. Redistribution subject to ASME license or copyright; see http://www.asme.org/terms/Terms_Use.cfm

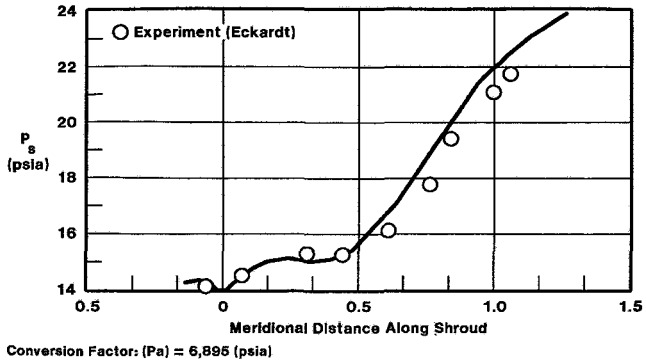


Fig. 3 Circumferential average pressure (potential code versus data)

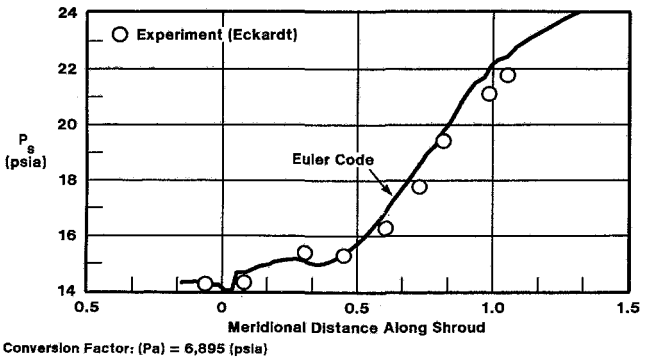


Fig. 4 Circumferential average pressure (Euler code)

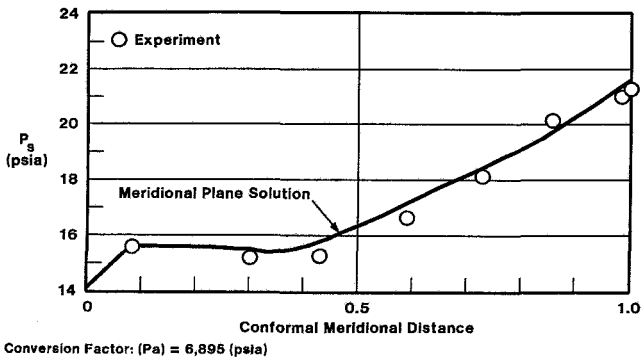


Fig. 5 Shroud pressure (meridional plane solution)

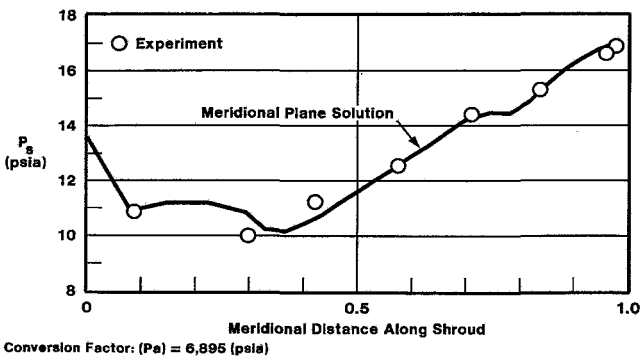


Fig. 6 Shroud pressure (maximum flow)

to satisfy the momentum, continuity, and energy equations in each such element by proceeding in a quasi-time-dependent manner. Inlet swirl is specified and exit static pressure is fixed. The requirement of continuity of flow quantities, including velocity around the trailing edge, determines the blade loading.

The grid (Fig. 2) is derived from the data used by a quasi-three-dimensional analysis system. The three-dimensional codes are not restricted to this type of grid, but this system is satisfactory for flows which are likely to be analyzed initially by quasi-two-dimensional methods.

In the test problem the Euler code does not run to an asymptotic "steady" solution, but must be stopped at the point where the solution appears most satisfactory. The numerical difficulties are associated with the extremely low velocities in the hub pressure side corner and the Courant-Friedrichs-Levy condition which limits the "time" step in accordance with the velocity.

This code requires over 3 hrs time on a VAX11-780 computer. A working set of at least 256 K bytes is required for efficient operation. While the resources required by this code are somewhat excessive for a computer of this class, the examination of results using interactive display is performed well by this type of computer.

Potential Flow Code

The three-dimensional potential flow code is based on the work of Laskaris. It employs the same data files as the Euler code, although it does not require as many degrees of freedom for satisfactory accuracy. Twenty-node brick and fifteen-node triangular prism elements are constructed with nodes coinciding with the grid intersections. All grid intersections (27 per brick) are employed in the numerical integration, but appropriate condensation leaves a maximum of 20 degrees of freedom per element in the mass flow influence matrix.

Specification of swirl and spanwise velocity on the grid inlet surface allow velocity potential to be fixed and these nodes to be condensed out of the flow matrix. The difference in potential between corresponding nodes in adjacent passages is fixed in the upstream and downstream regions, allowing further condensations. These boundary conditions fix the circulation on the blade. The resulting solution is examined later to determine whether the trailing edge loading is realistic. On the grid exit surface, a uniform mass flux is specified.

An initial solution is obtained by setting the density everywhere to the value corresponding to a local Mach number of 0.9 in the rotating reference frame, but setting the Mach number to zero in the influence coefficients. Thus the initial solution is quasi-incompressible. Two more outer Newton–Raphson iterations give the final compressible solution, provided that the Mach number is low enough to avoid choking.

The linearized equations using the mass flow influence matrix are solved by an approximate factorization conjugate gradients method. This approximate factorization is a Choleski factorization in which the matrix elements of the triangular factors are neglected if they are zero in the flow matrix. Thus the Choleski factor can be stored using the same sparse matrix pointer scheme as the flow matrix. Numerical tests have shown that the approximate factorization method requires twice as much computation per step as a simpler conjugate gradients method, but requires about a quarter of the number of steps.

This code requires a working set of 150 K bytes for efficient solution with about 700 degrees of freedom, and takes about 5 min on a VAX11-780 computer. When compared on the same grid with the Euler code, it requires about a third of the time, but produces a solution of much greater numerical accuracy, under the restriction to irrotational unchoked flows.

Eckardt Impeller Analysis

The optimum efficiency test case was analyzed at the given inlet conditions and rotational speed. Mass flow was increased slightly (2 percent in the finite element analysis) in order to match pressures in the inducer region. A further

Downloaded 01 Jun 2010 to 171.66.16.70. Redistribution subject to ASME license or copyright; see http://www.asme.org/terms/Terms_Use.cfm

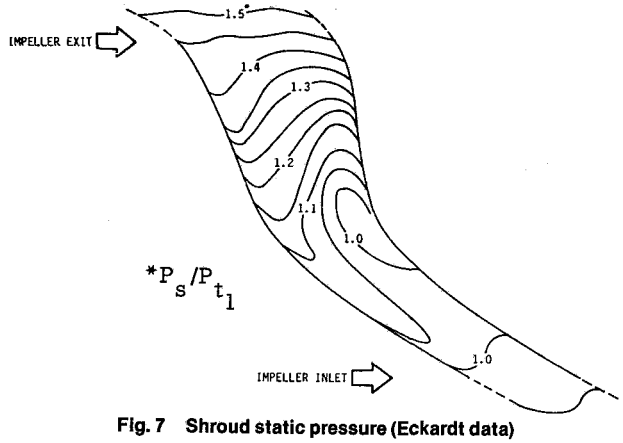


Fig. 7 Shroud static pressure (Eckardt data)

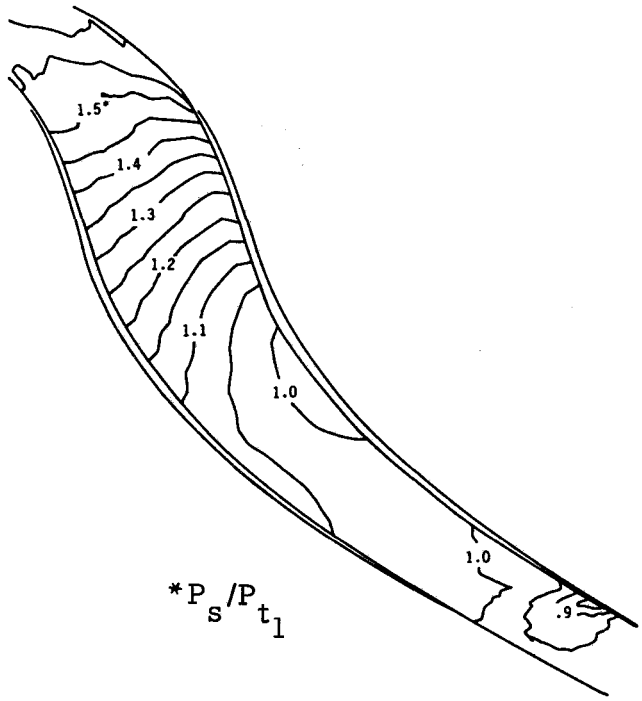


Fig. 8 Shroud pressure (three-dimensional Euler code)

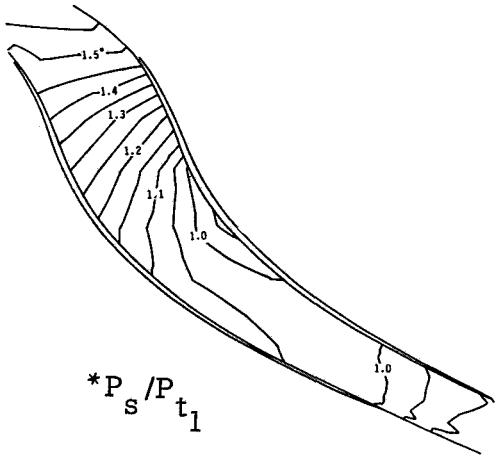


Fig. 9 Shroud pressure (finite element potential flow)

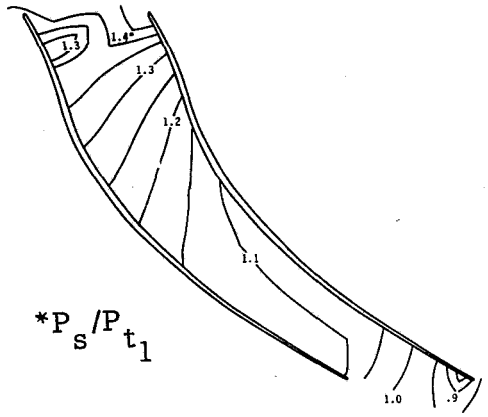


Fig. 10 Shroud pressure (quasi-three-dimensional analysis)

increase would be required to match pressure at the impeller exit. This increase in flow compensates for the lack of a model for boundary layer displacement thickness. Closer agreement could be obtained by the inclusion of polytropic efficiency in the calculation of gas properties. This could be justified only as a correlation of experimental data. Therefore, these calculations have assumed isentropic flow.

Figures 3 and 4 compare the circumferential average of the calculated pressure with the test data. The calculated pressure rise exceeds the test data since no provision is made for increasing boundary layer displacement in the region where the separated wake begins to develop. There is no significant difference between the finite element and the Euler code results.

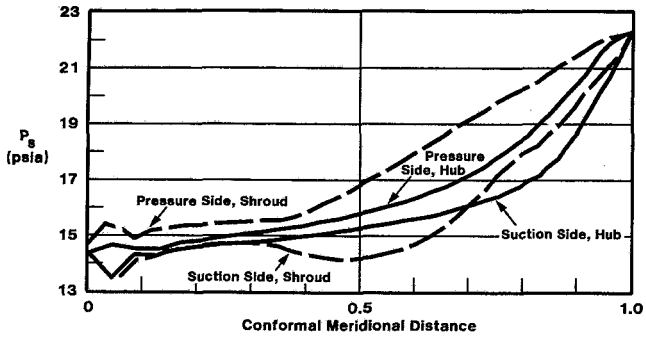
Figure 5 shows a similar comparison with the pressures computed in a meridional plane analysis. This analysis includes a loss correlation which permits a satisfactory comparison with experiment. Figure 6 shows the analysis of the maximum mass flow choked flow test case. The high losses experienced in this case require an adequate loss correlation to obtain reasonable agreement. This case was calculated also by the potential flow method; significantly higher pressure recovery is predicted in the absence of a boundary layer displacement model. These results show that a quasi-three-dimensional analysis with a good loss model is adequate to predict bulk properties such as these average shroud pressures. The full three-dimensional analysis has more value for examination of local detail of the flow.

Shroud Blade-to-Blade Pressure Distribution

Figure 7 represents Eckardt's plot of the blade-to-blade pressure measurements on the shroud. These contours appear to have been drawn with the intent of nearly matching pressure across the blade tip clearance, an effect which has not been modeled in the computation. Figure 8 shows that the Euler code predicts a similar pressure field with slightly more compression toward the exit. This difference is to be expected, as the wake, which is not reproduced in the computation, reduces the pressure recovery. Figure 9 shows a similar result from the finite element code, with slightly less pressure rise, and less numerical noise. The difference in pressure between the two analyses may be due to a small spurious entropy drop, which indicates inaccuracy in the Euler code solution of the energy equation. Figure 10 shows the equivalent quasi-three-dimensional solution. Although the quasi-three-dimensional solution has been matched to the circumferential average pressure by the use of a blockage factor which varies from inlet to exit, it does not predict the shape of these pressure contours and the blade to blade loading as well as the three-dimensional methods.

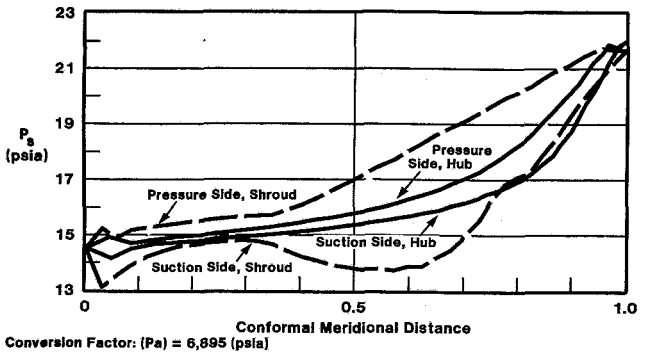
The plots of computational results from blade to blade use the transformed meridional coordinate associated with the conformal mapping from the blade-to-blade surface of revolution to a plane. This differs from the mapping used in Eckardt's pressure contour plot.

Downloaded 01 Jun 2010 to 171.66.16.70. Redistribution subject to ASME license or copyright; see http://www.asme.org/terms/Terms_Use.cfm



Conversion Factor: (Pa) = 6,895 (psia)

Fig. 11 Passage corner pressure (Euler code)



Conversion Factor: (Pa) = 6,895 (psia)

Fig. 12 Passage corner pressure (potential flow code)

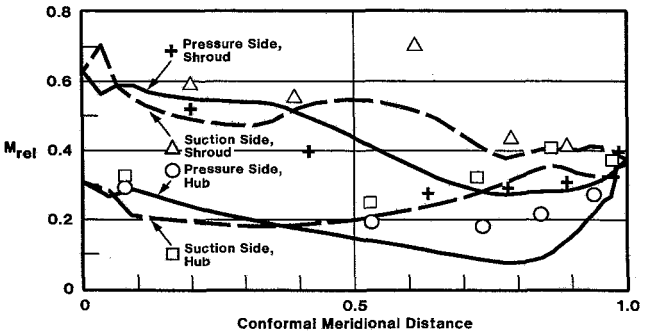


Fig. 13 Passage corner Mach number (Euler code)

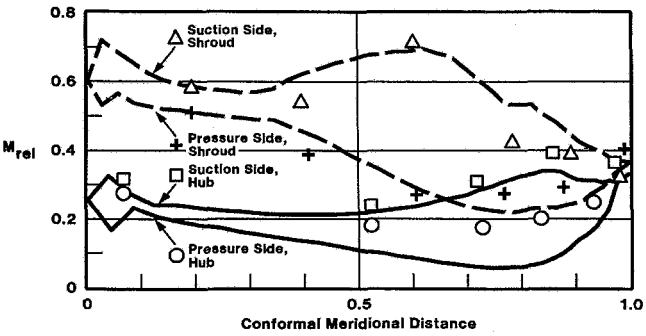


Fig. 14 Passage corner Mach number (potential flow code)

Analysis of Blade Loading at Hub and Tip

Figures 11 and 12 present the predictions of pressure in the four corners of the impeller passage. They agree well although the finite element code predicts somewhat more blade loading at the tip. Figures 13 and 14 show the equivalent predictions of relative Mach number. These show a weakness of the present Euler code; it is difficult to obtain accurate solutions for the velocity field. Inability to reach a converged solution

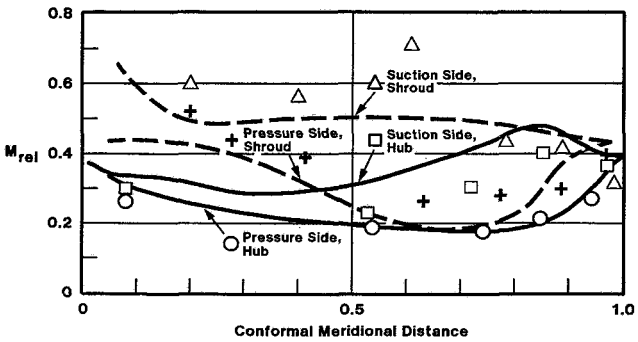


Fig. 15 Passage corner Mach number (quasi-three-dimensional analysis)

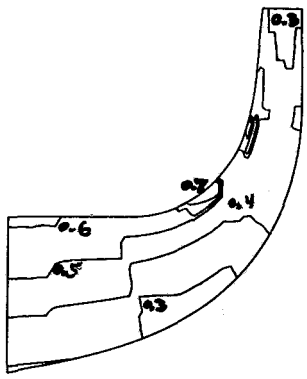


Fig. 16 Suction surface Mach number (velocimeter data)

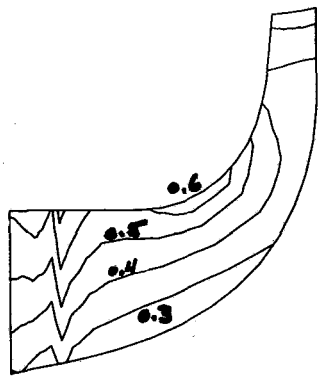


Fig. 17 Suction surface Mach number (potential flow)

has reduced the velocity gradients. While the effect has some qualitative relationship with the real flow, it is not a satisfactory solution, since the physics of the Euler equation formulation are the same as the potential flow and require consistency between velocity and pressure according to Bernoulli's equation (which is inherent in potential flow).

This problem might be solved more accurately if the energy equation were replaced by the isentropic relationships, but the energy equation incorporated in the Euler code is necessary for the solution of many transonic flows with shocks.

Figure 15 presents the relative Mach numbers in the corners obtained by quasi-three-dimensional analysis. This analysis does not predict as much diffusion in the suction side shroud corner and the pressure side hub corner as is shown by the three-dimensional analyses. It appears that the quasi-three-dimensional analysis misses the cumulative nonlinear addition of hub to shroud and pressure to suction side velocity gradients. To some extent, this is a result of an intentional modification of the stream tube thickness to match the blade-to-blade solution to the downstream conditions as given in the

Downloaded 01 Jun 2010 to 171.66.16.70. Redistribution subject to ASME license or copyright; see http://www.asme.org/terms/Terms_Use.cfm

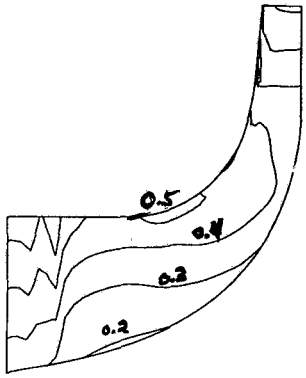


Fig. 18 Suction surface Mach number (Euler code)

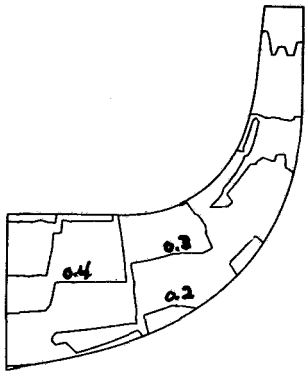


Fig. 19 Pressure surface Mach number (velocimeter data)

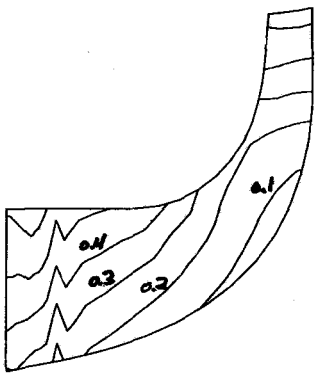


Fig. 20 Pressure surface Mach number (potential flow)

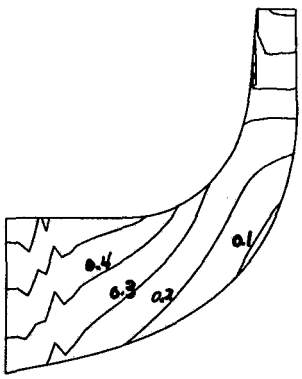


Fig. 21 Pressure surface Mach number (Euler code)

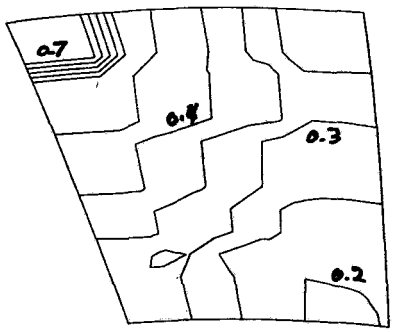


Fig. 22 Cross surface Mach number (velocimeter data)

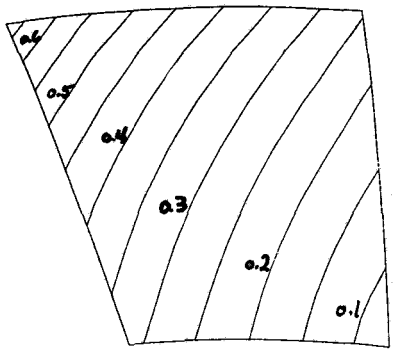


Fig. 23 Cross surface Mach number (potential flow)

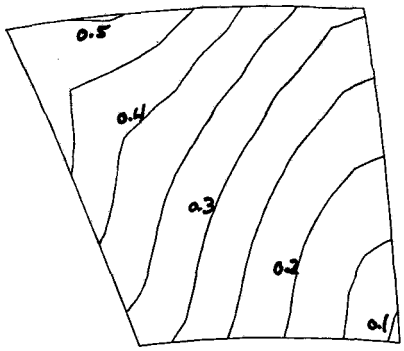


Fig. 24 Cross surface Mach number (Euler code)

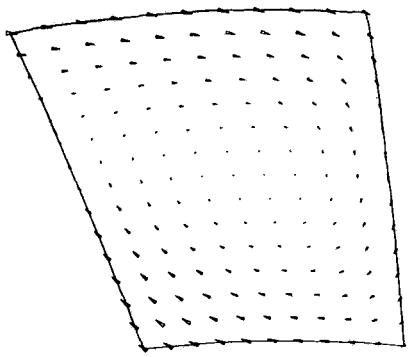


Fig. 25 Cross surface velocity vectors (potential flow)

test data. In this sense, the quasi-three-dimensional analysis was inconsistent with the three-dimensional analysis.

A rule of thumb in the design of impellers suggests that the blade loading coefficient

$$\left(\frac{P\,\text{pres} - P\,\text{suct side}}{2\,\text{dynamic head}}\right)$$

should not exceed 0.7; on this machine it reaches 0.8 at the tip, although it is very low in the inducer. Inviscid analysis predicts a loading of 1.2 at the hub. Velocimeter measurements indicate that the rule value of 0.7 was not

Downloaded 01 Jun 2010 to 171.66.16.70. Redistribution subject to ASME license or copyright; see http://www.asme.org/terms/Terms_Use.cfm

exceeded. A possible interpretation of this result is that such a design will generate a wake which grows until the loading is reduced to a value which can be sustained.

Comparison With Laser Velocimetry in Passage

Figures 16–18 present relative Mach number on the suction side of the passage (trailing face of the blade). Both the velocimeter data (Fig. 16) and the finite element analysis (Fig. 17) show a region where the Mach number exceeds 0.6 on the shroud in the elbow, where the quasi-three-dimensional analysis (Fig. 15) shows a peak Mach number of 0.5. The Euler analysis (Fig. 18) is generally in agreement with the finite element analysis. The velocimeter data show the beginning of the low velocity wake downstream of the peak Mach number. The wake moves away from the suction side as it moves downstream from its starting point. The Euler solution includes a smaller wakelike behavior, but, as previously mentioned, it is not a physically correct model of the real wake.

On the pressure side, the velocimeter data show Mach numbers less than 0.2 near the hub (Fig. 19). While this is higher than the predictions of finite element (Fig. 20) and Euler (Fig. 21) analysis, it is lower than the quasi-three-dimensional prediction. In general, the velocimeter data show slightly higher velocities than the three-dimensional analysis in the elbow region, presumably due to the lack of a boundary layer displacement growth in the analysis.

Figure 22 shows a cross section of velocimeter data at the surface of maximum hub to shroud velocity gradients. The finite element (Fig. 23) and Euler (Fig. 24) codes are in reasonable agreement, showing the extreme velocity gradient from pressure side hub to suction side shroud corner. The pressure gradients in this region may be expected to drive low energy fluid from the strongly diffusing hub pressure corner to the shroud suction corner, particularly since the inviscid flow also sweeps from the pressure side across the hub and up the suction side (Fig. 25). The hub to shroud pressure gradient is strong since the curvature effect of the hub and shroud is augmented by the lean of the blade.

Conclusions

Quasi-three-dimensional analyses currently in use provide an adequate model of the bulk properties of the flow. The combined local effects of blade lean and hub and shroud curvature are predicted more accurately by a full three-dimensional analysis. Still better results could be obtained if the boundary layer displacement effects could be modeled. Potential flow models are most satisfactory and economical when the generality of an Euler solution is not required. The existing Euler code is not as reliable as could be desired. Each of the fully three-dimensional methods provides useful information beyond that available in more approximate methods.

Acknowledgments

D. G. Holmes and T. E. Laskaris made available their three-dimensional finite element codes for incompressible radial and compressible axial turbomachinery. F. E. Hackert adapted their Euler and plotting codes to radial turbomachinery. D. Eckardt supplied the laser velocimetry data in tabular form.

References

1 Denton, J. D., and Singh, U. K., "Time Marching Methods for Turbomachinery Flow Calculation," VKI Lecture Series 7, 1979.

2 Laskaris, T. E., "Finite Element Analysis of Three-Dimensional Potential Flow in Turbomachines," *AIAA Journal*, Vol. 16, No. 7, July 1978, pp. 717–722.

3 Eckardt, D., "Flow Field Analysis of Radial and Backswept Centrifugal Compressor Impellers," *Performance Prediction of Centrifugal Pumps and Compressors*, edited by Gopalakrishnan, ASME New York, 1980, pp. 77–95.

Downloaded 01 Jun 2010 to 171.66.16.70. Redistribution subject to ASME license or copyright; see http://www.asme.org/terms/Terms_Use.cfm

Journal of Engineering for Gas Turbines and Power
Formerly Journal of Engineering for Power

Book Reviews

Aeroelasticity in Turbomachinery, Vol. 12, edited by P. Suter, published by the Federal Polytechnic Institute, Institute of Thermodynamics, Lausanne, Switzerland, 1981, 485 pages.

Aeroelasticity plays an increasingly important role in the design of turbomachinery, mainly because of a trend toward larger mass flows and higher peripheral speeds, leading to higher relative flow velocities, with a consequent increase in the flexibility and response of blading. This volume records the proceedings on this subject of the Second International Symposium, which was held in Switzerland in September 1980. A total of 31 papers, plus an interesting total evaluation of the symposium, comprise the volume.

Session 1 consists of papers on force and moment coefficients for high-deflection cascades, unsteady pressure distribution, and aerodynamic analysis of cascades in unsteady rotational flow. The session concludes with hydrodynamic interaction of cascades in incompressible flow.

Session 2 proceeds with cascade tests in wind tunnels. A number of the papers involve aeroelastic testing, damping of machinery blade variations, aerodynamic response of blade in pitching oscillation, with partial and full separation. The final paper in this session considers self-excited flow oscillation in low-pressure steam turbine cascades; this is a most interesting chapter on test methods and is well worth reading.

Session 3 treats theoretical methods, and among the subjects are stability and flutter analyses of turbine blades at low speeds and unsteady flow through a vibrating cascade. The last two papers consider stall flutter and quasi-stationary aerodynamic forces acting on a cascade of oscillating airfoils in subsonic flow. Although highly mathematical, this chapter should be read and not glanced over.

Session 4 focuses on vibration measurements. The reported papers deal with control of vibration in aeroelastic cascade experiments and method-of-force determination of the unsteady fluid dynamic forces from vibration response measurements. This problem is an extremely difficult one to resolve for turbomachinery blading, since the numerical problems associated with inverting the frequency response matrix lead to singularities.

Session 5 furnishes theoretical methods on unsteady flow in cascades. The topics considered are the effect of mean blade loading in supersonic cascade flutter, prediction of unstalled supersonic flutter in transonic fans, and stability analysis in coupled flexure-torsion vibrations. Although interesting, more work is required in this area.

Session 6 points to three additional efforts in unsteady supersonic flow in cascades. The reported papers concern periodic disturbances, effect of aspect ratio on unsteady aerodynamic forces induced by vibration, flutter in parallel shear flow, method of characteristic solution for finite oscillations due to supersonic effects, plus the nonstationary force ratios on blades of unsteady rotating rows in incompressible flow. This session continues the previous work on periodic disturbances acting on airfoils.

Session 7 treats experimental endeavors in turbomachinery. The topics discussed are measurement and prediction of aerodynamic damping of compressor blades, experimental and theoretical determination of the transfer function of a compressor, and practical experience with noncontact vibration systems. Although this session contains only four papers, each one reports on solid experimental information needed in bettering turbomachinery design.

The concluding chapter examines aerodynamically forced blade vibrations and related problems. The topics explored are inlet distortion and blade vibration in compressible flow, linear and nonlinear analysis of vortex whistle, and acoustic resonance of cascades and turbomachinery. This is a most interesting chapter, since acoustics can play havoc in design of turbomachinery. Acoustics are usually glossed over in aeroelastic considerations of turbomachinery design.

In summary, this book reveals the latest and best information on aeroelasticity, though much greater effort in both theoretical and experimental endeavors are required. For each of the various aspects of flutter, separate studies are required, and though much is known, we are still a long way from a comprehensive understanding of these phenomena. The reviewer recommends this volume to all engineers and scientists interested in the aeroelastic aspects of turbomachinery.

H. Saunders
General Electric Company
Schenectady, N.Y. 12345

Copyright © 1984 by ASME
Downloaded 01 Jun 2010 to 171.66.16.70. Redistribution subject to ASME license or copyright; see http://www.asme.org/terms/Terms_Use.cfm